Luminescent Nanoparticles for Drug Delivery and Detection

By

Sajni Haria

A thesis submitted to

The University of Birmingham

For the degree of

DOCTOR OF PHILOSOPHY



School of Chemistry

University of Birmingham

College of Engineering and Physical Sciences

March 2021

UNIVERSITY OF
BIRMINGHAM

University of Birmingham Research Archive

e-theses repository

This unpublished thesis/dissertation is copyright of the author and/or third parties. The intellectual property rights of the author or third parties in respect of this work are as defined by The Copyright Designs and Patents Act 1988 or as modified by any successor legislation.

Any use made of information contained in this thesis/dissertation must be in accordance with that legislation and must be properly acknowledged. Further distribution or reproduction in any format is prohibited without the permission of the copyright holder.

i. Abstract

This thesis shows the design of luminescent nanoparticles that can be used for theranostic applications in nanomedicine, focusing on drug delivery and detection. In this study, two nanoplatform designs are used.

Silica NPs are functionalised with luminescent Ln complexes, whilst simultaneously encapsulating an anticancer drug, in order to monitor drug release. This anticancer drug acts as a light harvesting unit for sensitised Ln luminescence, enabling drug sensing through 'on and off' Ln signals. We show the promising use of these NPs as diagnostic tools for drug sensing.

We also report the functionalisation of gold NPs with a dibenzoylmethane molecule attached via thiol bonds, with the ability to bind to Ln ions, and sensitise Ln luminescence.

i. Acknowledgements

First of all, I would like to express my sincere gratitude to my supervisor Professor Zoe Pikramenou for all of her support and guidance throughout my PhD which has been invaluable to me. Through working on a Masters project in her group, my research interests in nanomedicine were nurtured, so I would like to thank Zoe for giving me this opportunity to work in her group. Completing this PhD has represented a huge journey for me, giving me invaluable experiences and skills, and challenging me. I would also like to extend my sincere thanks to my second supervisor Dr Nik Hodges for his support and assistance, and all of the analytical and maintenance staff for all of their hard work.

I'm deeply grateful to all members, past and present, of the ZP and MJH groups including Menisha Manhota, Tasha Chauhan, Irene Theofilou, Andrew Carrod, Jamie Bradley, Zhilin Guo, Luke Watson, Sarah Akponasa, Patricia Girio, Elena del Giorgio, Asier Rodriguez Muguruza, and all master students, for their assistance at every stage of my research project. I also want to thank Garret from the Hodges group for his generous help in Biosciences! I want to specially thank my amazing friends Menisha, Tasha and Irene, who I am so lucky to have grown lifelong friendships with. And to Menisha, my silica buddy, I don't know what I would do without you! I would like to also thank some of my other friends in the department, Edd Wilkinson, Nick Cundy and Mat Wakeling, who have been there every step of the way since first year undergraduate! Thank you boys for giving me so much entertainment especially on games night (I will be beating you soon Edd and Mat…)! I can't forget my school friends, Maya Kotecha, Shanay West and Meera Shah, who have really reminded me the importance of friendship and been such a strong backbone in my life through this experience!

Finally, to my incredible family and Bhavik, whose belief in me has been my biggest motivation. I have not only written this PhD during Covid 19, but also under some challenging personal experiences, and so my gratitude for their unwavering support is unexplainable. Bhavik, thank you for being my shoulder to lean on during good and hard times, and for being so patient! Mum, dad, and Shiv, thank you for picking up my million phone calls a day during lockdown and seeing the end of the path for me, beyond the endless march!

iii. Contents

i. Abstract ..... *i*

i. Acknowledgements ..... *ii*

iii. Contents ..... *iii*

iv. Abbreviations ..... *vi*

List of Chemical Species Mentioned In General Literature vii

List of Compounds and Structures viii

1. General Introduction *1*

1.1. Drug Delivery Towards Cancer Therapy in Nanomedicine 1

1.2. Nanoparticles in Nanomedicine 5

1.3. Silica Nanoparticles 8

1.3.1. Mesoporous Silica Nanoparticles 8

1.3.2. Non-Porous Silica Nanoparticles 17

1.4. Gold Nanoparticles 19

1.4.1. Gold Nanoparticles in Nanomedicine 21

1.5. Lanthanide Luminescence and Historical Landmarks 22

1.5.1. The Use of Luminescence in Biological Systems 24

1.5.2. Lanthanides and their Coordination Chemistry 24

1.6. Thesis Aims and Objectives 48

1.7. Referenced Material 50

2. Luminescent Silica Nanoparticles for Drug Delivery and Detection *60*

2.1. Introduction 60

2.1.1. Camptothecin – An Anticancer Drug 60

2.1.2. Targeted Delivery of CPT Using Nanocarriers 63

2.1.3. CPT Delivery Using MSNs 66

2.1.4. MSNs Functionalised with Lanthanide Complexes as Imaging Labels 69

2.1.5. CPT Delivery Using Non-Porous Silica Nanoparticles 78

2.1.6. Non-Porous Silica Nanoparticles Funtionalised with Lanthanide Complexes as Luminescent Labels 81

2.2. Chapter Outline 84

2.3. Synthesis of Ligand, L 86

2.4. Synthesis and Characterisation of Porous Silica Nanoparticles 89

2.5. Functionalising MSNs with CPT and Ligand L 91

2.5.1. Drug Loaded Nanoparticles 91

2.5.2. Europium Coated MSNs using Ligand L 94

2.5.3. Sensitisation of Eu(III) by CPT 96

2.6. Synthesis and Characterisation of Non-Porous Silica Nanoparticles Doped with CPT 101

2.7. Lanthanide Coated SiO_2NPs 104

2.7.1. Luminescence Studies of Lanthanide Coated SiO_2NPs 107

2.8. Non-Porous Silica Nanoparticles Doped with CPT at Different Reaction Times 114

2.8.1. First method of synthesis of Non-Porous Silica Nanoparticles Doped with CPT 116

2.8.2. Emission Properties of CPT3⊂SiO_2NP_1 and the Respective Ln(III) Coated Nanoparticles 119

2.8.3. Second method of synthesis of Non-Porous Silica Nanoparticles Doped with CPT 124

2.8.4. Emission Properties of CPTn⊂SiO_2NP_2 and the Respective Ln(III) Coated Nanoparticles 128

2.9. Release of CPT from CPT⊂SiO_2NPs and Respective Lanthanide Coated Nanoparticles 134

2.9.1. Studying CPT Release from CPT0⊂SiO_2NP_1 135

2.9.2. Studying CPT Release from CPT0⊂Eu-L.SiO_2NP_1 in Water 141

2.10. Effect of CPT from CPT0⊂SiO_2NPs_1 and Respective Lanthanide Coated Nanoparticles on Lung Cancer Cells 145

2.10.1. Effect of CPT on Lung Cancer Cells after 24 hrs Incubation 147

2.10.2. Effect of CPT on Lung Cancer Cells after 72 hrs Incubation 148

2.10.3. Effect of Using a Physical Trigger on Toxicity of CPT to Lung Cancer Cells 154

2.11. Concluding Remarks 162

2.12. Referenced Material 164

3. Preparation of Gold Nanoparticles which Bind to Europium *..... 173*

3.1. Introduction 173

3.1.1. Lanthanide Coated Gold Nanoparticles 173

3.1.2. β-diketone Units as Sensitisers for Lanthanides 177

3.1.3. Coating Gold Nanoparticles with Ln(III) β-diketones and Potential Applications 189

3.2. Chapter Outline 192

3.3. Photophysical Properties of DBMSS and Binding to Europium 194

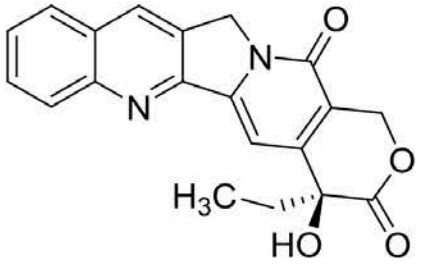
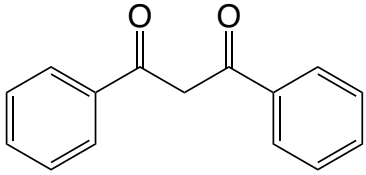
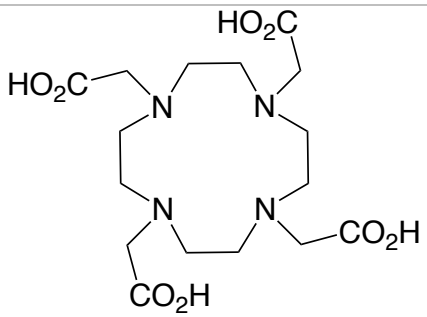
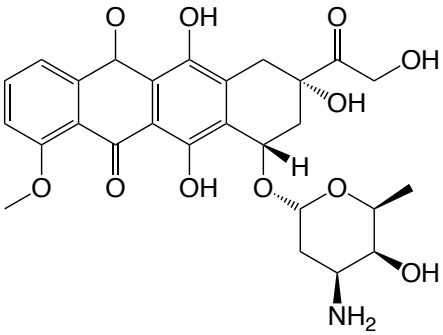
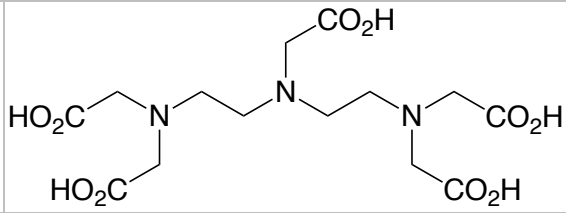
3.4. Luminescent Gold Nanoparticles with DBMSS and Europium 196

3.4.1. Preparation of Gold Nanoparticles 196
3.4.2. Photophysical Properties of Functionalised Gold Nanoparticles 200
3.4.3. Loading Europium onto Functionalised Gold Nanoparticles 202
3.4.4. Photophysical Properties of Europium Coated Gold Nanoparticles 206
3.4.5. Photophysical Properties of Purified Europium Coated Gold Nanoparticles 208
3.5. Concluding Remarks 216
3.6. Referenced Material 218
4. Conclusions and Further Work *222*
4.1. Thesis Conclusions 222
4.2. Future Work 223
5. Experimental *226*
5.1. General Experimental 226
5.2. Chapter 2 231
5.3. Chapter 3 244
5.4. Referenced Material 248
v. Appendix *249*
List of Appendicies 249

iv. Abbreviations

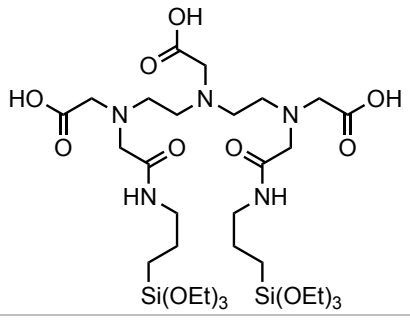
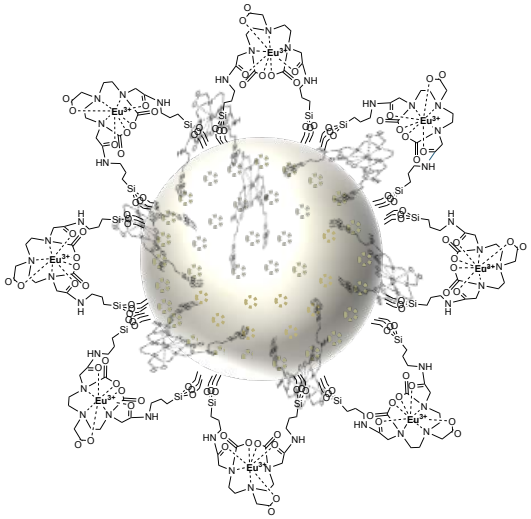
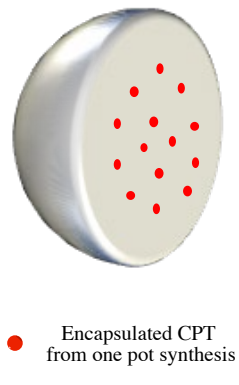
AuNP	Gold nanoparticle
CDT	Chemodynamic therapy
DNA	Deoxyribonucleic acid
DLS	Dynamic light scattering
EPR	Enhanced permeability and retention effect
FRET	Forster resonance energy transfer
HOMO	Highest occupied molecular orbital
Ln	Lanthanide
LUMO	Lowest unoccupied molecular orbital
MOF	Metal organic framework
MRI	Magnetic resonance imaging
MSN	Mesoporous silica nanoparticle
NIR	Near infrared light
NPs	Nanoparticles
PDI	Polydispersity index
PDT	Photodynamic therapy
PTT	Photothermal therapy
QD	Quantum dot
SAXRD	Small angle X-ray diffraction
SDDS	Smart drug delivery system
SEM	Scanning electron microscopy
SERS	Surface enhanced raman spectroscopy
SiO_2NP	Non-porous silica nanoparticles
SPECT	Single photon emission tomography
SPIONS	Supermagnetic iron oxide nanoparticles
SPR	Surface plasmon resonance
TEM	Transmission electron microscopy
UCNP	Upconverting nanoparticles
XRD	X-ray diffraction

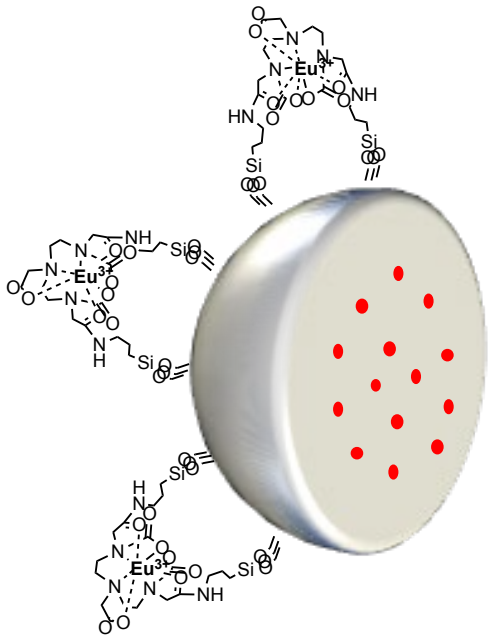
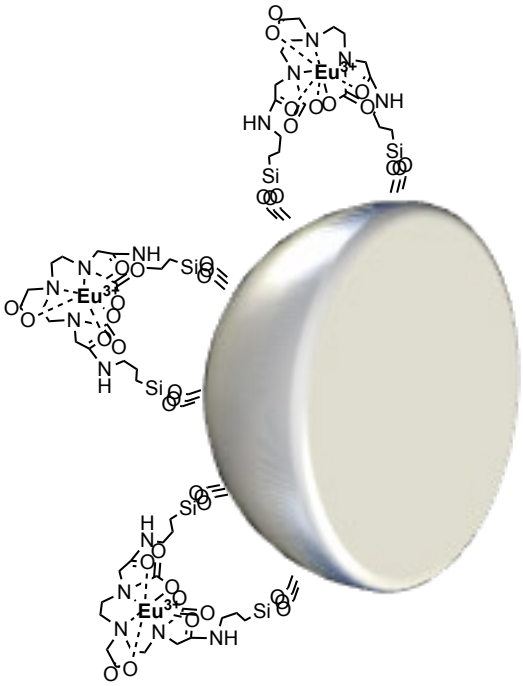
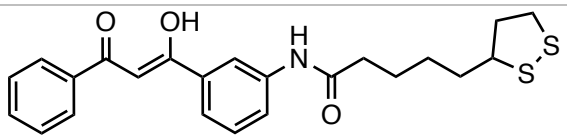
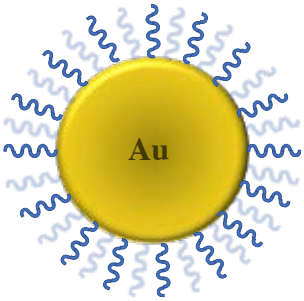
List of Chemical Species Mentioned In General Literature

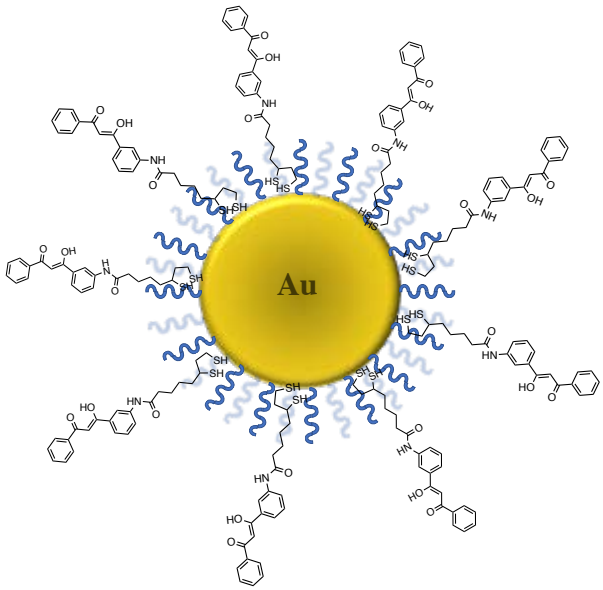
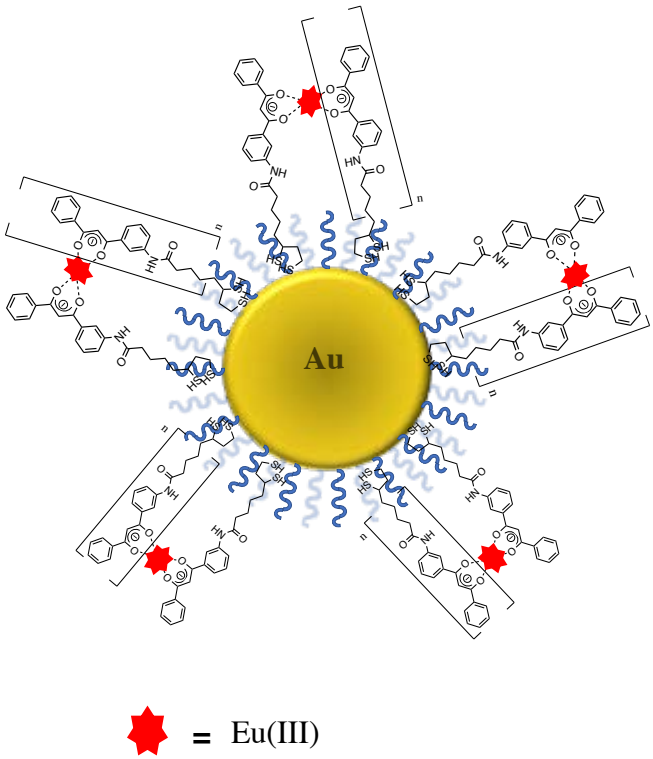
CPT	Camptothecin 
DBM	Dibenzoylmethane 
DOTA	
DOX	Doxorubicin 
DTPA	
FA	Folic acid
GA	Glycrrhetinic acid
GSH	Glutathione

HA	Hyaluronic acid
PEG	Polyethylene glycol
TEOS	Tetraethylorthosilicate
TOP	DNA topoisomerase enzyme

List of Compounds and Structures

L	
L.MSN	
CPT⊂SiO_2NP	

CPT⊂Ln-L.SiO_2NP	
Ln-L.SiO_2NP	
DBMSS	
AuNP. Z	

AuNP. Z + DBMSS	
AuNP. Z + DBMSS + Eu(III)	

1. General Introduction

1.1. Drug Delivery Towards Cancer Therapy in Nanomedicine

Cancer is defined as a group of diseases spreading through uncontrolled growth of abnormal cells, which can eventually result in death if untreated. It is well known that several lifestyle factors common in our generation such as smoking and alcohol consumption, aswell as an ageing population can increase risk[1, 2].

In 2018, cancer was the cause of 1 in every 6 deaths globally[3]. Fatalities caused by cancer are more than AIDS, tuberculosis and malaria combined, leading it to be the world's second largest death cause[3]. In USA alone, it is expected that nearly 1.9 million new cases of cancer will be diagnosed in 2021, with almost 608 570 fatalities approximated, roughly 1670 deaths a day[3]. These values don't account for the impact of COVID-19 on diagnosis of cancer. Worldwide, the diagnosis and treatment of cancer since 2020 was limited due to reduced access to hospitals and cancer centres during global lockdowns. The consequence of this global pandemic will have an unknown impact on future cancer statistics[4]. The International Agency for Research on Cancer suspects that by 2030, the amount of cases will rise to 21.7 million and, 13 million will be due to the growing and ageing population[2].

Nanomedicine offers a platform to apply nanoscale systems for the diagnosis and therapy of cancer, and has received significant attention. Additionally, advances in nanomedicine have seen a large contribution to the development of multifunctional nanosystems, enabling simultaneous targeting, delivery, tracking, and sensing of agents or analytes to specific sites. Specifically, in cancer therapies, such as the most common of which is chemotherapy, present many limitations. These include the non-selectivity of chemotherapeutic agents, leading to severe side effects and multidrug resistance. Moreover, poor water solubility of drugs means direct administration *in vivo* is challenging, and also leads to requirement of high dosages for effective treatments. This combined with the non-selectivity and high toxicity can affect drug resistance, *in vivo* degradation and fast excretion[5-7].

The emergence of nanoscale systems has had a major impact on the advances on drug delivery. This has led to targeted drug delivery, focusing on systems that have used nanocarriers. These include nanoparticles (NPs), liposomes, micellular systems and dendrimers[5-7]. Such nanoscale systems that have been categorised as 'smart drug delivery systems' (SDDS) consist of some key functionalities. For example, nanocarriers are able to transport and release drugs at a specific site in controlled manner. They have ability to enhance drug effect at tumour sites through targeting, usually achieved by functionalising nanosystems with ligands which recognise specific cancer cell receptors. Additionally, controlled drug release can be achieved by utilising triggers that can stimulate release. These often include using light to induce changes in the system triggering release, and others such as pH or redox potentials. Furthermore, optical labels are often used, or other diagnostic markers, allowing visualisation of the systems in the body (tracking the localisation of drugs, using probes to monitor release etc)[6-8].

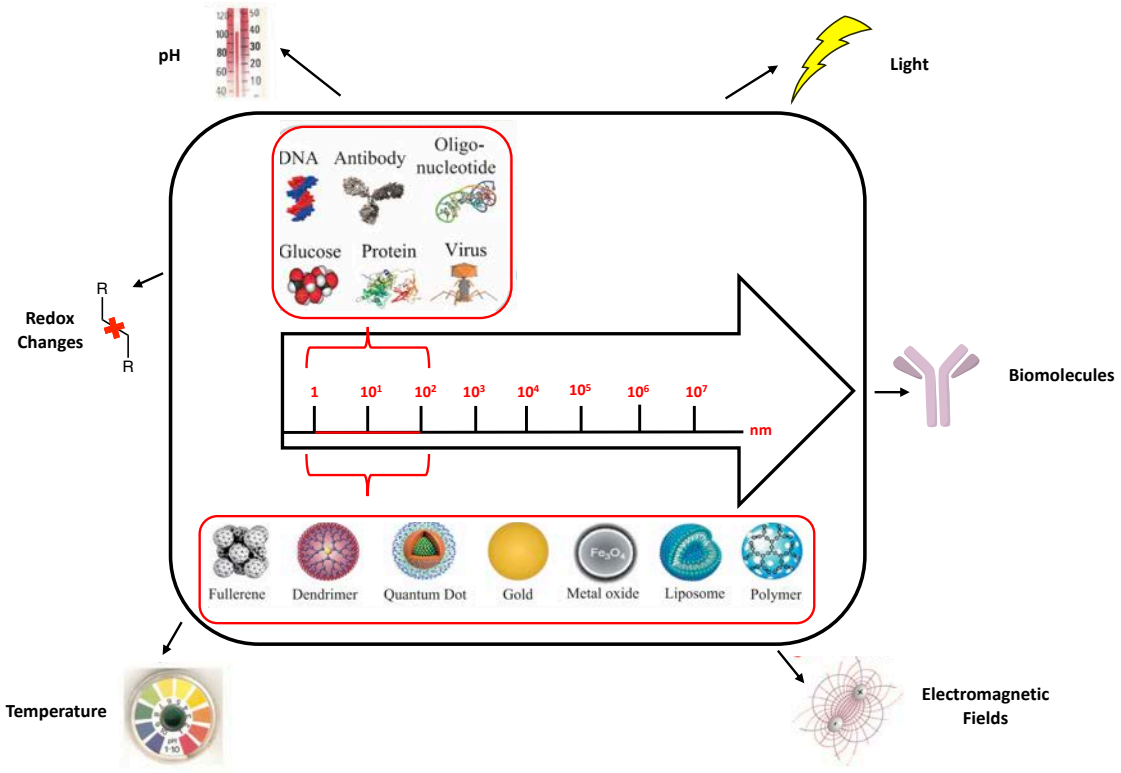


Figure 1.1

Schematic illustration of nanosystems used as nanocarriers for smart drug delivery systems, using stimuli responsive triggers to release drug. Image is redrawn from Kim *et. al.* and Lenggoro *et. al.*[6,9].

Table 1.1

Non ideal properties of drugs listed and how SDDS can improve their implications.

Non Ideal Properties of Drugs	**The Therapeutic Implications**	**Effect of Smart Drug Delivery Systems**
Poor water solubility	High hydrophobicity of most anticancer drugs cause poor water solubility issues	SDDS can provide hydrophobic pockets to carry hydrophobic anticancer drugs, with hydrophilic exteriors to enhance water solubility
Tissue damage from excretion	Unplanned leakage or excretion of drugs can lead to tissue damage	SDDS can offer controlled and regulated drug release aiding to reduce tissue damage from excretion
Rapid drug breakdown *in vivo*	This can lead to loss of activity of the drug	SDDS provides an environment for the drug to prevent premature release and degradation
Unfavourable pharmacokinetics	Clearance of drugs occur too rapidly from the body and often require high concentrations in doses	SDDS can help to reduce clearance and enable lower dosages
Poor biodistribution	Drugs affecting normal healthy cells as well as tumour cells can lead to severe side effects	SDDS help to reduce the volume of distribution with enhanced targeting of tumour sites and hence help to reduce side effects
Lack of selectivity for tumour cells	Consequential side effects can often limit amount of drug that can be administered. Low concentrations can result in minimal therapeutic effects	SDDS offers a platform to be able to load high concentrations of drugs in them and can be carried to the tumour site through the EPR effect. Functionalisation of SDDS can also aid in targeting specific sites.

Table 1 summarises the most common issues associated with free drug administration, and their implications which can be improved by SDDS[8]. The high hydrophobicity is a leading issue for most anticancer drugs, which in turn through poor water solubility, affects circulation of the drug around the body leading to other non-ideal properties as summarised. The enhanced permeability and retention (EPR) effect can improve these limitations using SDDS. The physiology of normal healthy tissue cells are highly different compared to tumour tissue cells, and can be exploited to deliver drugs to tumour sites. The vascular system of normal cells are uniformly structured and roughly 8 – 10 μm in diameter. Tumour blood vessels differ vastly, they are 20 – 100 μm in diameter, leaky, have abnormal capillaries and irregular flow. They have wide openings ranging from 200 nm – 1.2 μm, enabling small nanoscale materials to easily penetrate them leading to high accumulation of such nanosystems in tumour sites. Moreover, tumour cells cannot easily remove nanomaterials which also facilitate circulating nanomaterials to accumulate in tumours. This phenomenon is the EPR effect. Advances in nanomedicine have relied on the EPR effect to help enable accumulation of drugs at tumour sites in a targeted fashion[11, 15].

A review in 2018 summarised some of the examples on nanomedicines that were approved in the EU market. They ranged from nanoparticle formulations such as Abraxane (delivering paclitaxel) and Copaxone (Glatiramer acetate), to liposomes including examples like Caelyx (doxorubicin hydrochloride). Others included nanocomplexes, nanoemulsions, nanocrystals and polymer-protein conjugates[16].

1.2. Nanoparticles in Nanomedicine

Amongst all types of nanocarriers used in the designs of SDDS, NPs have been used extensively as the choice of nanocarriers, and continues to be a growing field in nanomedicine research. NPs have created a platform to enable major advances in diagnostics through imaging tools, and therapeutics with drug delivery[17]. After the pioneering work done by Brus and Ijima, who contributed to the development of research in nanoscience through developing nanoscience building blocks, NPs of all sizes and shapes have been created[17, 18].

NPs offer unique properties, some of which are shared by other nanocarriers such as dendrimers, but NPs can simultaneously encompass a wide range of properties. NPs create a platform that offers versatile possibilities for modifications and abilities to form multifunctional structures. Variations in surface modifications and ligands can create a host of applications in sensing, imaging, and targeted drug delivery. NPs can have enhanced stability due to large surface to volume ratios, vital for optimising drug loading[17]. The shape of NPs can also play a key part in their functions in nanomedicine. NPs of all sizes and shapes, such as nanorods, nanotubes, nanoplates, nanostars and so on have been created[17, 19-21]. As mentioned, NPs share the same advantages that SDDS provide. Increasing water solubility of drugs, protection of drug degradation and premature release, targeted delivery strategies, and decreasing toxicities of free drug[5].

A vital property that NPs offer are their optical properties, leading to NP imaging techniques widely used in diagnostics. The window for wavelengths of light that can be used to penetrate tissue is often an issue associated with organic dyes, due to narrow absorption profiles limiting excitation wavelengths. NPs present an opportunity to overcome the issues associated with this. Moreover, the use of light in NP systems offers a platform for applications in non-invasive therapy. NPs present a platform to use techniques such as luminescence, optical microscopy, surface enhanced Raman spectroscopy (SERS), and can be used in photodynamic therapy (PDT) and photothermal therapy (PTT)[17].

In drug delivery applications, NPs provide a strategy to perform targeted delivery of drugs to specific sites of interest and are achieved by two main methods. They are categorised as passive targeting and active targeting[5, 11].

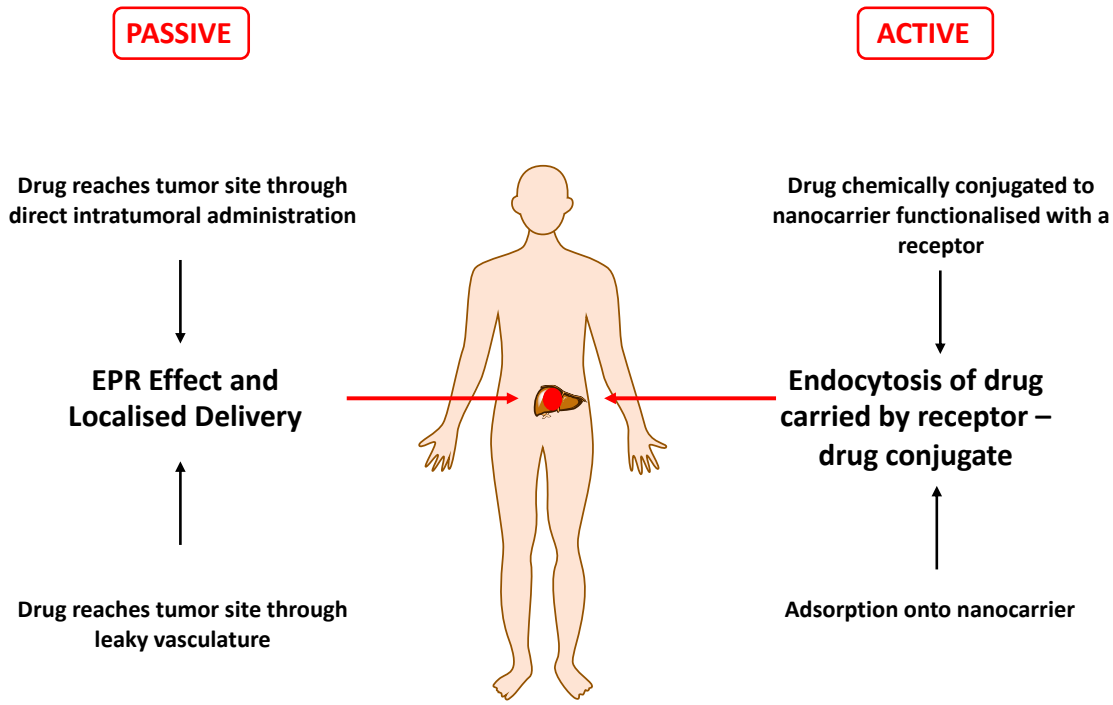


Figure 2.21

Schematic illustration of passive and active delivery strategies using NPs. Image is redrawn from Padhi *et. al.* and Parveen *et. al.*[5, 11].

The differences between normal and tumour tissues are exploited in passive targeting by relying on the EPR effect to deliver drugs to the tumour site. By relying on the EPR effect, high drug concentrations are required in order to avoid rapid clearance, and enhance accumulation at the tumour site. There have been many systems that incorporate anticancer drugs such as camptothecin (CPT), that have been investigated for release and tumour targeting[22-25].

Active targeting requires conjugation of receptors or targeting ligands to the nanocarrier that can promote specific site targeting, taking the drug and delivering it locally. Choice of ligands should have high affinity for cell receptors, and ones that are overexpressed at tumour sites. With targeting ligands, accumulation of drug at tumour site is carried by the active targeting, and uptake in drug molecules by tumour cells can occur through endocytosis [37, 26-28].

A diverse range of applications in therapeutics have emerged using NPs which include cancer therapy, antimicrobial activity, vaccines, gene delivery and targeted drug delivery (particularly to overcome side effects associated with chemotherapy)[5, 29-31]. Similarly, NPs offer a platform to be able to combine instrumentation to create diagnostic tools. Gold NPs (AuNPs) have been used widely as diagnostic labels for detection of diseases, with the ability to detect low concentrations of analytes[5, 32, 33]. NPs can also be modified with luminescent labels, for imaging techniques towards diagnosing diseases, and offer many advantages over organic dyes as labels. These include resistance to photobleaching, and ability to extend excitation windows using ligand functionalisation[5, 34-36].

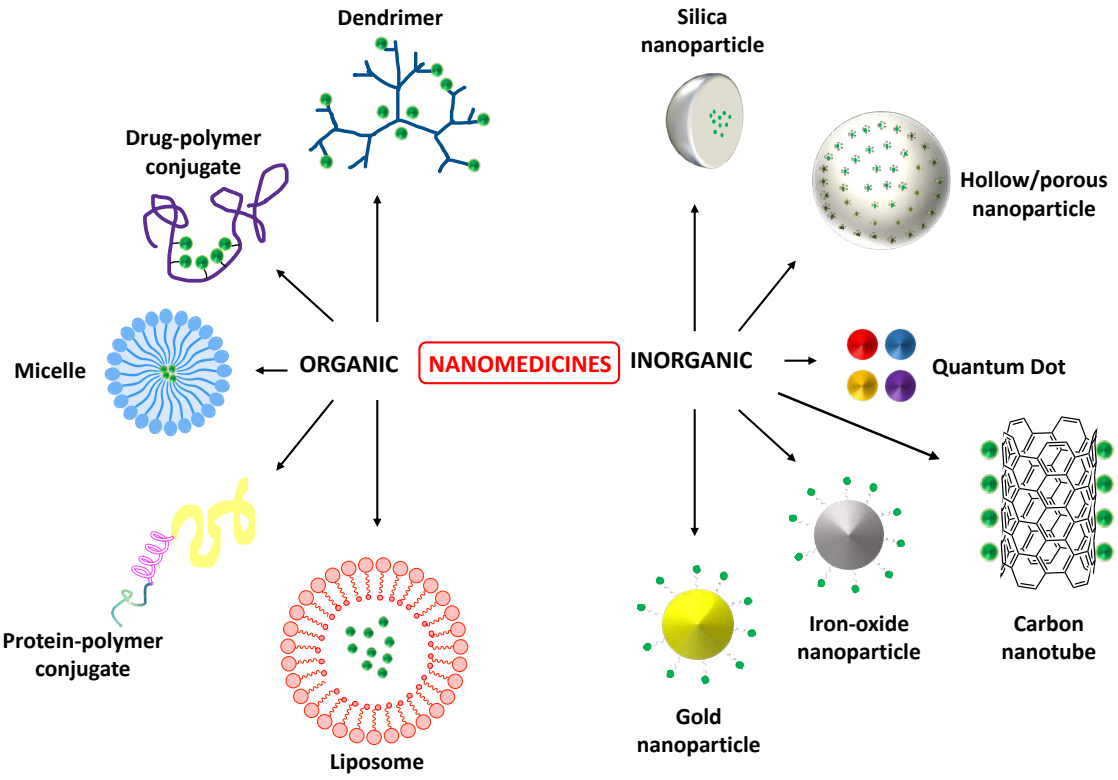


Figure 1.22

Schematic illustration of examples of nanomedicines used for therapeutics and diagnostics. Image redrawn from Cheng *et. al.*[15].

1.3. Silica Nanoparticles

A sub-category of inorganic NPs used in nanomedicine with growing attention, are silica NPs. They can be divided into two main classes of amorphous silica structures, mesoporous silica NPs (MSNs), and non-porous silica NPs (SiO_2NP).

1.3.1. Mesoporous Silica Nanoparticles

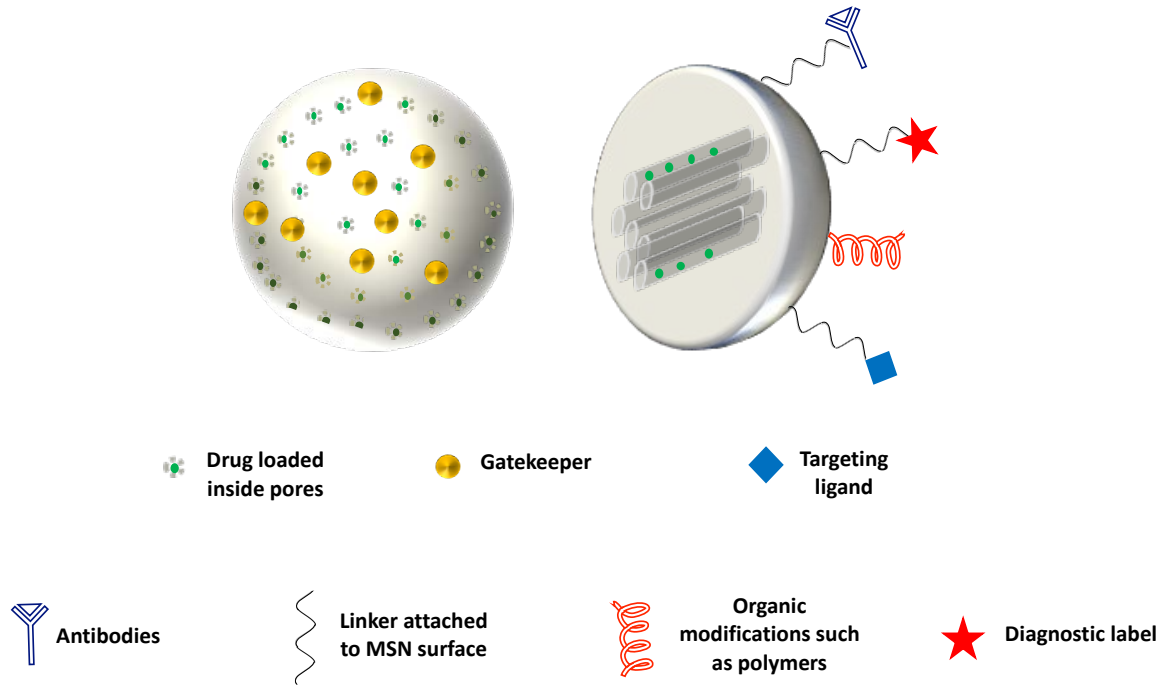


Figure 1.3.11

Schematic illustration of multifunctional MSNs as a platform for therapeutic applications in drug delivery, and as diagnostic tools. Image is redrawn from Bein *et. al.* and Lin *et. al.*[38, 39].

MSNs are porous silica NPs and have been extensively researched in nanomedicine as host matrices for drug molecules in specific areas such as drug delivery and targeting[42-51] and diagnostics[38, 40, 41]. Their attractive structural features that make them good hosts include their high surface area and pore volume enabling good opportunity for high drug loading capacities. The porous structures have tuneable pore sizes in addition to an ordered porous network, allowing channels inside the NPs to be used as a reservoir. MSNs are well known to have good biocompatibility and colloidal stability, making them good nanocarriers for organic

molecules. Furthermore, their surfaces can be easily functionalised through alkosilane chemistry, presenting a platform to create multifunctional MSNs to perform drug delivery with enhanced therapeutic efficiency with combination of diagnostic tools by using markers[5, 40, 38, 43, 52-57].

The synthesis of MSNs entails a two step sol-gel process that follows hydrolysis of Si-O bonds using a silica precursor, and condensation of the silica structure. For porous structures, surfactant templates are used to create an ordered network, and can be removed by calcination or extraction[73]. In the synthesis of MCM-41 MSNs, the surfactant templates form micelles with cationic head groups attracting negatively charged silicates from the silica precursor, producing layers to allow hydrolysis and condensation into an ordered meso-structure[52, 55]. It is argued that MSNs are formed either through monomer addition (particle growth occurs via addition of hydrolysed monomers after nucleation) or controlled aggregation (large NPs are formed through continuation of nucleation leading to primary NP aggregates).

For delivery to cells, nanoparticle internalisation occurs mostly through endocytosis, but the process is dependent on several factors. These factors range from size, shape, mesostructure and surface functionalisation and their properties[52]. MSNs that possess a range of shapes, sizes and porosity can have different effects on cellular uptake. After direct administration *in vivo*, multifunctional MSNs with loaded drug can be delivered specifically to desired tumour sites through the EPR effect. Importantly, after entering the bloodstream, due to defensive immune responses in the body, large NPs over approximately 100 – 120 nm can be cleared. Thus, it is essential that the physiochemical features of the NPs are taken into account for efficient biodistribution[38, 52].

MCM-41 MSNs

There are various types of MSNs that have been synthesised and developed. The first family of ordered MSNs was reported in 1992 by Mobil Corporation Scientists (MCM) classed as the M41s family[58, 59], including the most common used MSNs such as MCM-41 (2D hexagonal structure of pores) and SBA-15 (3D cubic structure of pores)[38, 42, 57]. M. Vallet-Regi *et. al.* reported for the first time in 2001, using MCM-41 MSNs as a reservoir for ibuprofen, and the

delivery of the drug. Passive drug delivery was performed, relying on diffusion of the drug out the pores[59]. Despite the attractive features of MSNs as nanocarriers, they are limited due to large NP sizes, and therefore there has been several efforts made to obtain smaller NPs[39]. Although MCM-41 materials obtain attractive and beneficial features, the fundamental issue with MCM-41 materials is their micrometre size making it challenging for the delivery to cells[12]. Varache *et. al.* reported the synthesis of MCM-41 MSNs in 2015, with optimised conditions yielding NPs with sizes between 60 – 150 nm, suitable for delivery applications. Base catalysed sol-gel synthesis was carried out, using NaOH. Through varying the NaOH concentration, they showed tunable pore structures could be achieved[60].

Characterisation of MSNs

Typical characterisation of MSNs involve size characterisation which can be carried out with microscopy techniques such as transmission electron microscopy (TEM) and scanning electron microscopy (SEM), in addition to dynamic light scattering (DLS). X-ray diffraction is also used often, to characterise the porosity of MSNs[54, 55, 61-63]. Varache *et*. al. demonstrated changes in MSN sizes through these characterisation techniques, in addition to N_2 sorption isotherms[60].

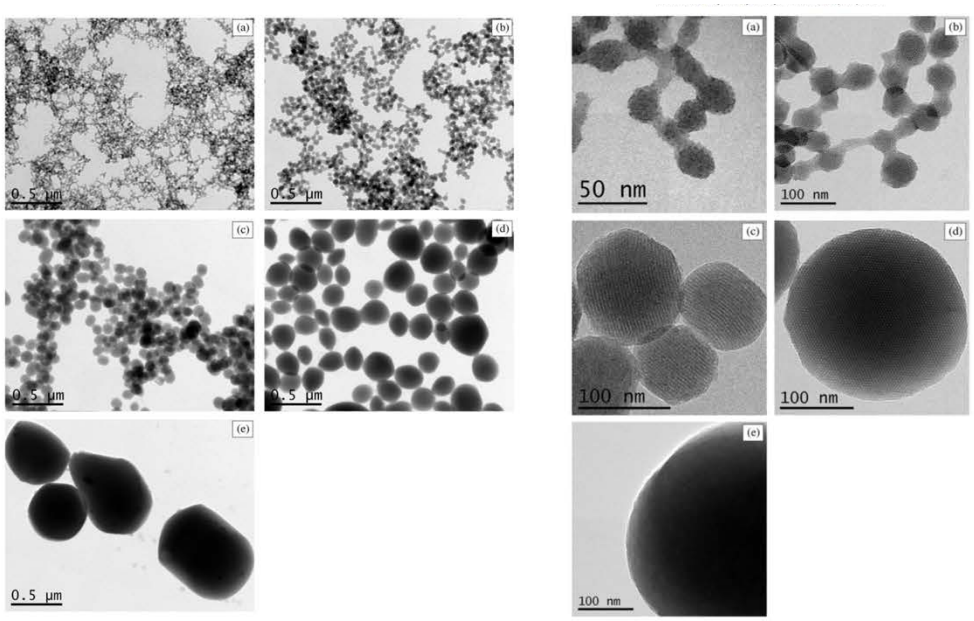


Figure 1.3.12

TEM and HRTEM images of MSNs prepared with different concentrations of NaOH taken from M. Vareche *et. al.* [60] : a) 5 mM b) 10 mM c) 15 mM d) 20 mM e) 25 mM.

TEM images showed the increase in MSN sizes as NaOH concentration was increased, and high resolution TEM (HRTEM) was used to demonstrate the porosity seen by the honeycomb like structure. Using DLS, they were able to determine the occurrence of aggregation at low concentrations, affecting light scattering. However, at high concentrations diameter to $Z_{average}$ ratios increased due to asymmetrical particles. XRD illustrated the formation of ordered MCM-41 MSNs at concentrations of NaOH between 12.5 mM and 22.5 mM, with defined peaks indexed at (100), (110), (200), and (210), indicative of a hexagonal mesoporous structure. Loss of porous structures were also characterised using XRD, shown at high concentrations with only one peak observed[60].

Therapeutic Drug Delivery using MSNs

Gatekeeping

The combination of MSNs and multifunctionality prospects has merged together applications in therapeutic and diagnostic use, in addition to stimuli responsive delivery of cargo. Often, premature release of drug molecules adsorbed inside the MSN structure can occur, which has led to stimuli responsive gatekeeping on MSNs to control drug release when a trigger is applied[6, 53].

pH responsive drug delivery systems are perhaps most commonly favoured due to the exploitation of pH differences between tumour tissue (acidic pH) and extracellular environments. Several strategies can be employed to design pH responsive systems, one including the hydrolysis of bonds, inducing detachment of gatekeeping ligands on the surface of MSNs, opening pores and enabling delivery[53].

Recently, Pan *et. al.* designed MSNs loaded with doxorubicin (DOX), an anticancer drug commonly delivered using MSNs, and gated with DOX and an aminopropyl based ligand. Their results showed negligible DOX release at neutral pH, but release was increased to 86 % in acidic environments. They ascribed this release due to hydrolysis of imine bonds in the acidic environment, leading to detachment of ligand and release of DOX. Additionally, anti-tumour efficacy of NPs were studied and showed accumulation in tumours occurring through the EPR

effect. Moreover, free DOX delivery obtained less tumour size inhibition compared to MSNs with DOX, showing the targeted properties of the system[53, 64].

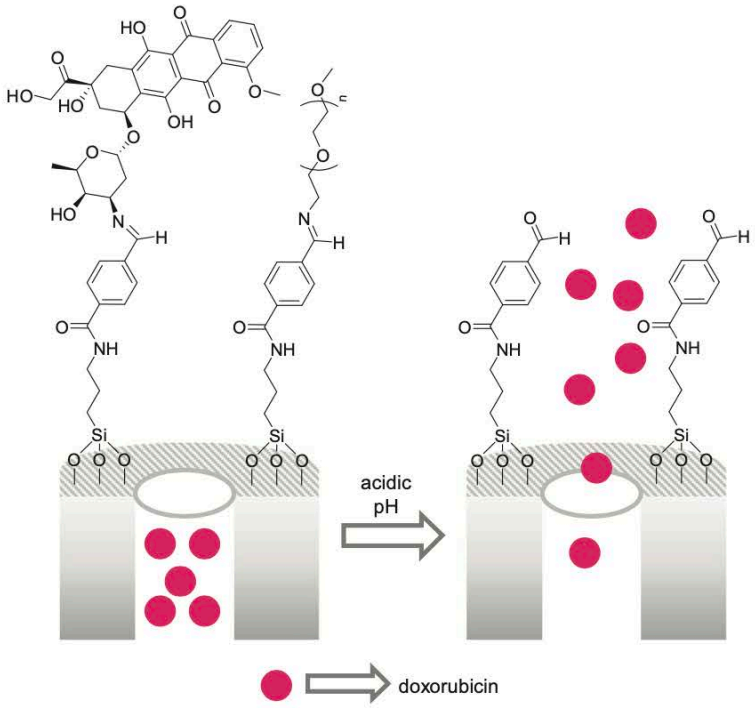


Figure 1.3.13

Schematic illustration of MSNs loaded with DOX, capped with DOX and an amino-based ligand responsive to hydrolysis in acidic environments, leading to DOX release. Image taken from Sancenon *et. al*[53].

Hydrolysis of bonds has been a clear strategy for pH triggered drug release[47-49, 53, 64-66] , in addition to electrostatic interactions such as protonation[67-69], and pH triggered degradation of gatekeepers[70-71].

Another important trigger often used are redox responsive systems due to the importance of oxidation and reduction reactions occurring in biological systems. Different concentrations of reducing agents in intracellular environments can be used to trigger drug release from redox responsive capped MSNs. Furthermore, redox activity is known to be elevated in tumour tissue due to higher concentrations of reducing agents like glutathione (GSH)[72-75]. Usually, this can occur through cleavage of disulphide bonds, exploiting the over expression of GSH at tumour sites, and also cleavage of bonds through presence of reactive oxygen species (ROS)[73, 77].

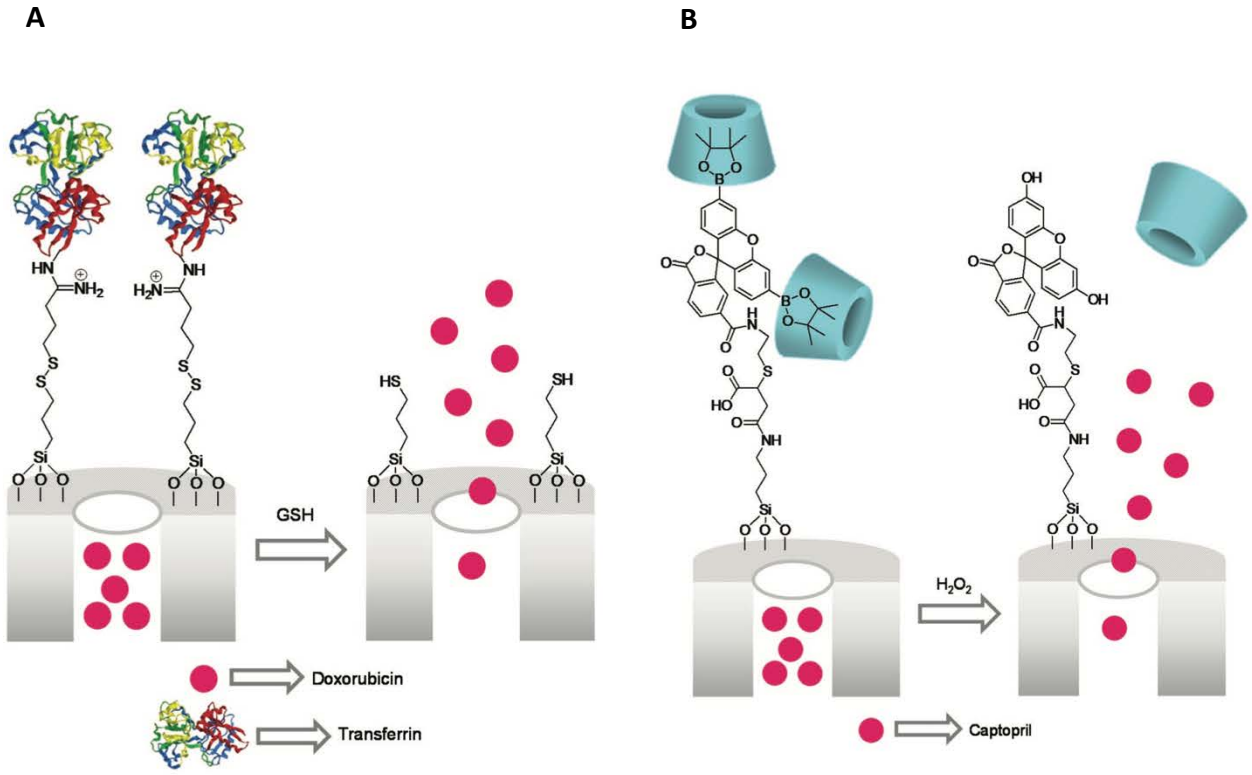


Figure 1.3.14

Schematic illustration of drug release through redox responsive systems using MSNs. A: MSNs loaded with DOX and capped with ligands that are sensitive to disulphide cleavage in the presence of GSH[72]. B: MSNs loaded with captopril and capped with a α–cyclodextrin containing a H_2O_2 sensitive probe in presence of ROS[76]. Cleavage links in both examples lead to drug delivery. Image taken from Sancenon *et. al*[53].

Light responsive drug delivery systems have generated much attraction due to the non-invasive capabilities of application of light to stimulate drug release. A major limitation of this attractive strategy however, is the ability to penetrate deep tissue and thus extending the excitation window beyond the UV range is required. Near infrared light (NIR) has provided a solution to this, and many examples of MSNs using light have included gold structures[50, 78], up-converting NPs (UCNPs)[79] and photosensitisers[80] to do this.

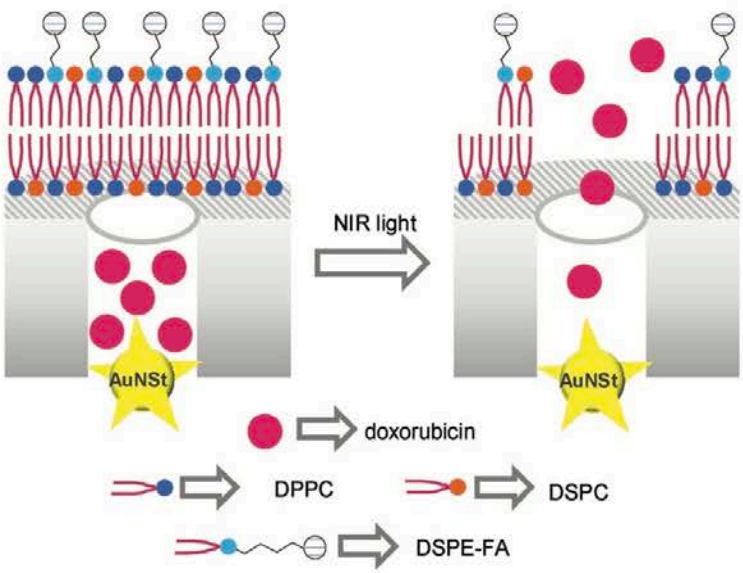


Figure 1.3.15

Schematic illustration of using light as a trigger to release DOX from folic acid (FA) functionalised MSNs at 808 nm[41]. Image taken from Sancenon *et. al*[53].

Many other triggers have also been used for drug delivery systems, including temperature responses, in addition to enzyme response systems[53]. This has created a vast host of different gatekeepers that have been used to cap MSNs, ranging from trigger responsive ligands, to inorganic moieties such as NPs[17, 41, 84-85] and organic moieties including DNA[82].

MSNs in Diagnostics

In order to understand the biological activity and efficacy of MSN SDDS *in vitro* and *in vivo*, diagnostic tools are essential to investigate the response of tumour cells to drug delivery, from stimuli responsive triggers or apoptosis of cells, in addition to being able to track accumulation and image it[38]. A vast range of diverse SDDS with diagnostic capabilities have been developed in order to learn more about drug uptake, its accumulation and effect on cancer cells. Fluorescent labels have been an attractive approach in the development of diagnostic SDDS, through attachment to the hydrophilic surface. There have been several types of fluorescent labels used ranging from QD[56], to organic dyes[38] and different types of

core-shell nanocomposites[52]. The use of markers enable the possibilities of using imaging techniques such as optical microscopy, magnetic resonance imaging (MRI), ultrasonic imaging and other techniques taking advantage of hybrid silica NPs[17, 86].

For instance, the diffusion processes for cargo moving inside mesopore channels have been studied, confirming the requirement for surface modifications to control adsorption and desorption processes. Brauchle *et. al.* investigated this through using single dye molecules and the anticancer drug DOX to image and study these processes[87].

Moreover, monitoring drug release has become desirable since the development of stimuli responsive SDDS, typically using optical markers either modified on the surface of MSNs, or encapsulated in the pores[88].

Lee *et. al.* designed MSNs with molecular valves in order to perform controlled drug delivery, in addition to monitoring the release. Their SDDS involved a Forster resonance energy transfer (FRET) donor (coumarin labelled cysteine MSNs), a fluorescent FRET acceptor being a β-CD acting as a cap blocking the pores, disulphide linkers as the redox responsive triggers for drug release, and a FRET donor-acceptor in order to monitor release in real time. Due to close proximity of the FRET acceptor to the FRET donor, through a disulphide link, FRET was achieved. After removal of the β-CD through redox responses to GSH environments, triggering release, FRET was turned off. Using the changes in this FRET signal, they were able to achieve real time drug release monitoring[89].

Zhang *et. al.* designed a lanthanide (Ln) based system using NIR Nd to emit in the NIR range, enabling deeper tissue penetration. By monitoring Nd luminescent signals in the NIR range, they were able to detect drug release. Their findings concluded drug release amounts and showed prolonged accumulation[90].

Luminescence lifetime imaging is also an attractive diagnostic tool, due to its abilities to reflect local changes, distinguishing signals above the autoflourescent background from biological media, and does not rely on spectral shift. Manet *et. al.* designed MSNs with carbon dots inside the porous structure, and carboamino groups on the surface. Luminescence

lifetimes up to 9 ns were detected upon excitation, and was easily discriminated against biological background fluorescence. Through this imaging technique, they were able to successfully monitor drug release.

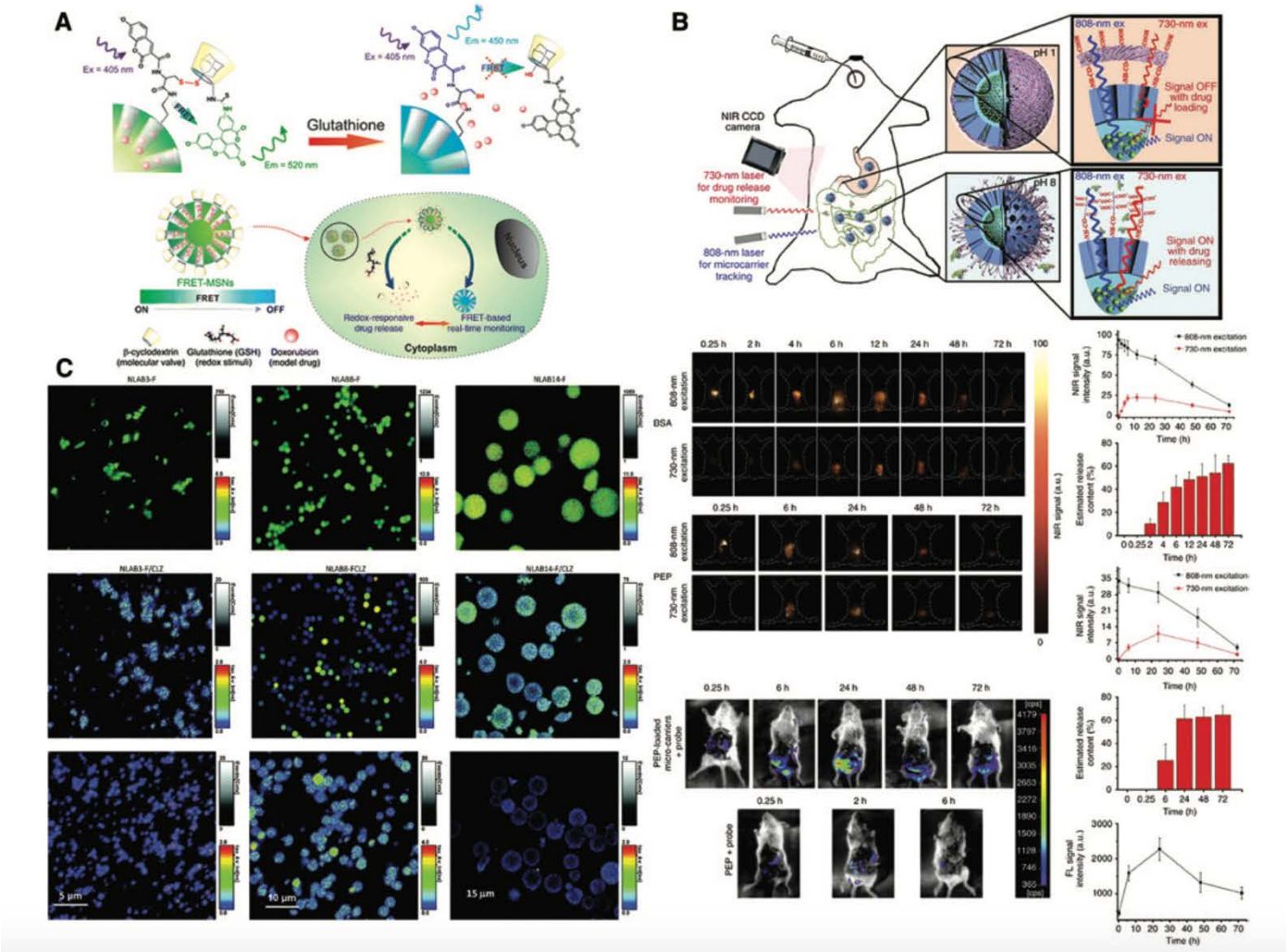


Figure 1.3.16

Examples of drug release monitored using fluorescent MSNs. A: Redox responsive FRET MSNs[89]. B: Using an InGaAs charge coupled device (CCD) camera to monitor drug release in the NIR range[90]. C: Monitoring drug release through luminescence lifetime imaging[91]. Image taken from Zhu *et. al.*[88].

1.3.2. Non-Porous Silica Nanoparticles

The second class of amorphous silica structures used for biomedical applications, are non-porous SiO_2NPs. SiO_2NPs can be used in SDDS as nanocarriers for drug molecules through encapsulation, or surface conjugation. SiO_2NPs offer the advantage of controlling different sizes and shapes, and can be used as a host for creating hybrid NPs (functionalisation with other NPs such as QDs, iron oxide NPs and gold NPs)[15, 93]. They have also shown better biosafety compared to MSNs[92].

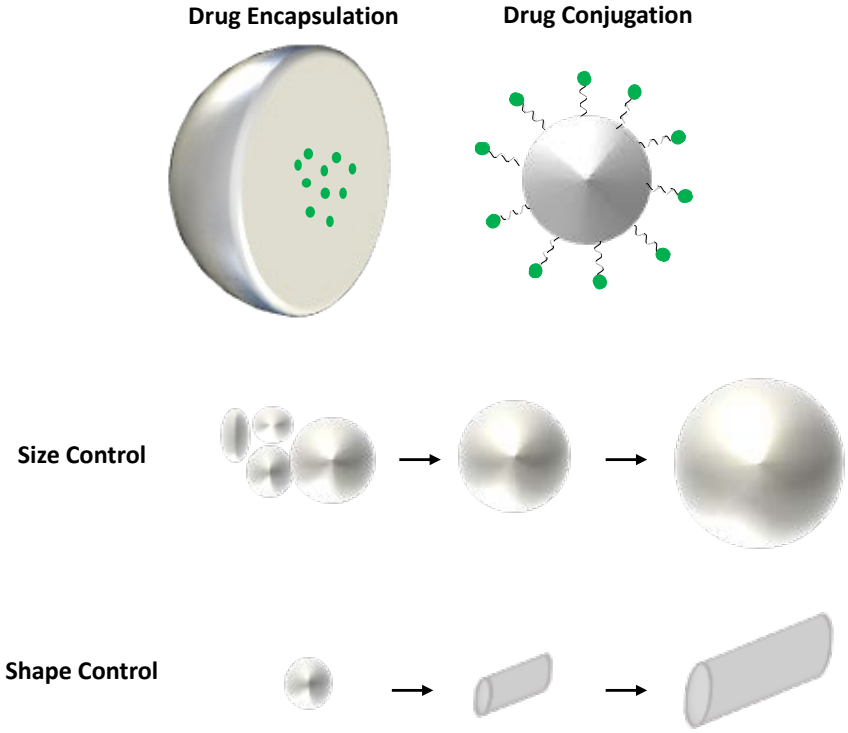


Figure 1.3.21

Schematic illustration of SiO_2NPs as nanocarriers, and their physiochemical properties which can be controlled. Image is redrawn from Cheng *et. al.*[15].

SiO_2NPs were first synthesised by Stober *et. al.* in 1968[94] using water, alcoholic solvent, ammonia and tetraalkoxysilane, to form monodisperse SiO_2NPs. Concentrations of components, different solvents and silica precursors have been investigated, and growth of silica has been determined. It is known that growth of SiO_2NPs occurs through condensation of hydrolysed monomers, followed by particle formation through siloxane aggregation. This

process is dependent on the ionic strength of solvents, and surface potentials of the silica particles. Consequentially, the concentrations of ammonia and water can affect the rate of hydrolysis and condensation, hence determining SiO_2NP sizes[15, 95]. Surface properties are not discussed here, as similar strategies of MSNs apply to SiO_2NPs.

Silica Nanoparticles in Drug Delivery

Similarly with other nanocarriers and MSNs, SiO_2NPs have been used as SDDS for a wide variety of materials ranging from drug molecules to biomolecules (proteins, peptides, DNA etc) for therapeutic applications in cancer. They have similar advantageous properties to MSNs as nanocarriers, such as controlled drug delivery, preventing premature release, protection of cargo from degradation, and prolonging blood circulation[15]. As seen on figure 1.3.21, there have been two strategies adopted to incorporate drugs into SiO_2NPs, which are encapsulation or conjugation. Encapsulation usually involves synthesis of SiO_2NPs with hollow centres for drug loading. This usually incorporates non covalent binding between drug molecules and the silica matrix, quite similar to adsorption in MSN pores[15, 96-99]. On the other hand, conjugation of drugs involves linking to the SiO_2NP surface through covalent bonds[15].

Other than spheres, several groups have studied SDDS using silica nanorattles, hollow silica-chitosan hybrid nanospheres, nanotubes and silica cross linked micelles[15, 100-104].

Silica Nanoparticles for Diagnostics

Similarly to MSNs, SiO_2NPs have been explored for carrying diagnostic probes, incorporating different markers for imaging techniques involving optical imaging and MRI. Dye doped SiO_2NPs have been used as an effective tool to merge nanotechnology and imaging to find synergic solutions and investigate SDDS. Particularly luminescence, where fundamental photochemistry deals with elementary processes such as light absorption and emission, to investigate complex functions. There has been extensive research in dye doped SiO_2NPs as luminescent probes for applications in nanomedicine ranging from sensing, to immunoassays, drug delivery and many more[98]. SiO_2NPs are photophysically inert, and so any functionalisation of diagnostic probes present efficient ability to produce imaging without silica interference. SiO_2NP designs can be tailored to amplify luminescence signals and

minimise quenching effects. Additionally, silica does not show toxicity and is a key advantage for use as a nanosystem in cancer diagnostics[98].

Silica NPs have been studied as tools for optical imaging, through the use of luminescent dyes, QDs and Ln complexes[15, 98, 106-109]. Furthermore, just as MSN structures, other imaging tools have also been extensively researched using SiO_2NPs as nanosystems in diagnostics, including common techniques such as MRI and PDT[15, 98, 110, 111].

1.4. Gold Nanoparticles

Gold NPs (AuNPs) have been widely employed in many applications within nanomedicine, such as delivery, sensing, and bioimaging, owing to several key advantages, including their unique optical properties.

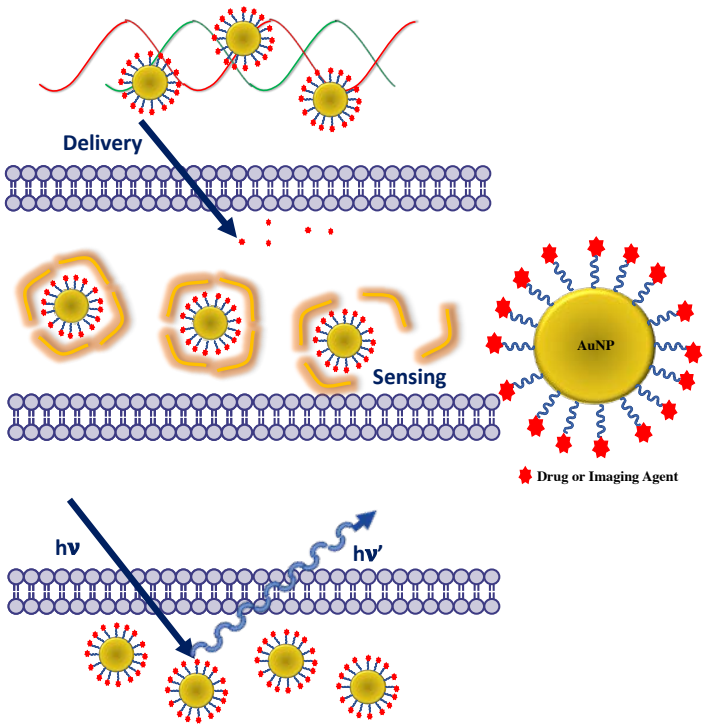


Figure 1.41

Schematic illustration of applications of gold NPs in nanomedicine. Image redrawn from Rotello *et. al.*[112].

Faraday first published work on AuNPs in 1857 reporting the red colour of the NPs attributed to the colloidal nature[112, 113]. The synthesis of AuNPs has been developed from a wide array of methods controlling factors such as size and shape[112, 114], mostly collated by Turkevich[115],

in the modern field of AuNP synthesis since the famous example from Faraday. The reduction of Au salt, usually from $HAuCl_4$, using trisodium citrate acts as a reducing agent and a stabilising agent. This process is important for surface functionalisation after the reduction of Au^{3+} to an inert Au^0, *via* subsequent replacement of citrate ions[114]. This was shown to be highly reproducible and yielded size distributions between diameters of 10 nm to 100 nm. Moreover, by controlling the Au : citrate ratio, it was found that the size of the colloidal NPs could be controlled[115].

AuNPs can be prepared with a range in diameters from 1 nm to 120 nm[114] giving rise to size and shape related optical properties, in addition to ranging colours as size increases[112]. The surface plasmon resonance (SPR) of AuNPs is a distinguishable characteristic unique for each size of nanoparticle. It is defined as ‘‘an electromagnetic frequency that induces a resonant coherent oscillation of the free electrons called the surface plasmon resonance, at the surface of a spherical nanoparticle if it is much smaller than the light wavelength’’[112]. The SPR enables us to spectroscopically observe the absorption band between 500 nm and 550 nm, arising from the oscillation of electrons. Factors such as size, shape, and surface functionalisation can influence this phenomenon, useful for monitoring the event of ligand attachment to the surface.

A large variety of molecules including surfactants, polymers, and dendrimers, can stabilise AuNPs *via* the use of thiolates exploiting the strong Au – S bond[112]. Replacement of citrate ions by thiolates is a facile method for surface functionalisation. The ease of this allows AuNPs to incorporate more than one type of imaging and targeting complexes and therefore can ideally be used as multimodal probes[92]. The multimodal functionality allows AuNPs to be detected by electron microscopy techniques and reflectance microscopy[115-117].

In addition, high concentrations of probes can be attached at a lower loading on the NPs due to their large surface to volume ratio. This also enables promotion of several binding site interactions facilitating the selective targeting of biological entities[118].

Functionalising Gold Nanoparticles

Approaches to coating gold NPs with metal complexes, and other inorganic entities, involve anchoring groups that can attach to the AuNP surface. There has been several different anchoring groups employed, but the most common of choice are soft thiols[115, 119-121]. The gold – sulphur bond is strong, and additionally groups with disulphides (two electron donating groups) provide stronger attachment, using groups such as lipoic acid derivatives and mercaptopyridines[122, 123]. The advantage of the strong Au-S bond enables favourable displacement of citrate ions, after AuNP synthesis forming stable NPs[115].

There have been many reports of different coatings on gold NPs, ranging from a wide array of entities. This has included *p* block material, such as fullerene clusters and silica coatings[119, 124-126] Organometallic complexes have been used as coatings too, due to excellent redox properties. Ferrocene complexes have been a common choice for this category, using thiols to attach to Au surfaces[127]. Transition metal complexes have also been used, especially for a strong interest in developing luminescent probes for biomedical applications. The Pikramenou group have reported many publications using transition metal complexes, such as iridium and ruthenium compounds with focuses on NPs localisation in cells and tracking [128-130].

However, to date, only a few examples of Ln coatings have been reported, compared to other entities[119, 120].

1.4.1. Gold Nanoparticles in Nanomedicine

AuNPs have been introduced into a wide range of biological applications in nanomedicine. Research has extensively demonstrated their advances in nanomedicine, from imaging, to sensing, host-guest interaction, electron microscopy and spectroscopy. AuNPs have been shown to possess size dependent optical properties, as mentioned due to the SPR effect. Additionally, the absorption and scattering of gold is often used beneficially for imaging techniques, due to their excellent contrast properties. They have been used for *in vivo* imaging, two photon luminescence, SERS, *in vivo* cancer therapy, and drug delivery, illustrating their broad theranostic applications[114-116, 128-130, 200, 201].

1.5. Lanthanide Luminescence and Historical Landmarks

The discovery of Ln elements has played a major role in developing luminescent materials. Ln luminescence has been used in many fields across technology, lighting and bioimaging, mainly driven by *f-f* transitions later explained[133]. A large portion of applications include lamps, bulbs, display phosphors, and lasers. The NdYAG laser is well known for its use in laser pointers, medicine, weapons and many more. Luminescent immunoassays and bioimaging are also well established fields of applications, not to mention their use also on security inks and counterfeit tags[133].

A review published by Bunzli in 2015 summarised eight historical Ln landmarks that have shaped the growing research in Ln luminescence and their applications[133].

In 1891, Carl Auer von Welsbach saw Cerium emission and the first industrial application of Lns was reported, the Auer light. He created the Auer light, an incandescent gas mantle that was formed by the addition of CeO_2 to ThO_2 which resulted in bright white emission upon heating[133].

Another significant discovery was made at the beginning of the 20th century, by George Urbain. His study of Eu(III) luminescence from dilutions in matrices, lead to the discovery of the orange – red emitting Y_2O_3:Eu phosphor. This bright phosphor had a quantum yield close to 1, and has been used in cathode ray tubes and fluorescent lamps since the 1960s[133-135].

In 1937, J. H. Van Vleck solved the puzzle of Ln optical spectra, decoding the nature of sharp transitions for most of the trivalent Ln(III) ions. He established the forbidden nature of these transitions, theorising the electric dipole nature were associated with the most intense transitions, and that they were caused by 'distortion of the electronic motion by crystalline fields'. Additionally, he also noted that vibronic lines in spectra were caused by interactions between electron motion and vibrations[133, 136].

In 1942, Weissman discovered what is now known today, as the antenna effect, a widely known method used to enhance Ln luminescence. He discovered that Ln luminescence can

be induced by excitation of organic ligands involved in Ln complexes. This finding proved to play a major part on the design of highly luminescent Ln complexes and materials[15, 133].

The Judd-Ofelt theory was developed by two authors, B.R Judd and G.S Ofelt, who independently published models for parameterisation of intensities of optical spectra. Although several assumptions are used to derive the parameters, the accuracy of the theory is remarkably successful[133, 137, 138].

Upconversion of Ln luminescence, developed initially for quantum counters, were found to be useful in many other applications such as lasers, security inks and markers. Recently, there have been many examples of upconverting NPs, used in biological applications such as drug release and bioimaging. This phenomenon was brought about by F. Auzel in 1966, who suggested that energy transfer between neighbouring Ln(III) ions can occur, and can be more efficient than ligand excitation. It is well known that Yb can be used as a sensitiser for upconverted Er(III) luminescence due to its large absorption at 980 nm, and hence Yb(III) doped materials have been developed[133, 139-143].

Ln luminescent immunoassays nowadays are an essential in medical research, and this unique idea originated from E. Soini and I. Hemmilä in the 1980s. This involved using conjugation of a Ln chelate to a specific antibody, and developed time resolved luminescent assays. Their proposal of these Ln based immunoassays cleverly exploited the unique properties of Lns[133, 143].

Lastly, the development of Er doped fibre amplifier, exploiting the rich electronic configuration of Er(III) enabled the design of multi level lasers[133, 144].

1.5.1. The Use of Luminescence in Biological Systems

The significance of non-invasive techniques for the diagnosis of diseases has become increasingly important. This has inspired the development of imaging techniques in cancer therapy, for diagnosis and examination of treatment efficiency[145]. Through this, luminescence imaging has emerged as a technique to meet the requirements of modern medicine. Light can carry energy that can interact with the biological surroundings, giving the opportunity to be able to penetrate tissue. There is a vast variety of optical probes that have been used as luminescent labels such as organic dyes, transition metal complexes and quantum dots[146].

Organic dyes have been extensively researched and are known to be highly emissive, but are however prone to photobleaching, and have short luminescent lifetimes. Transition metal complexes have also been used in biological imaging, advantageous of high excitation wavelengths beyond the UV region, but therefore have narrow Stokes shift limiting the luminescence detection. QDs are also highly emissive, with sharp emission bands and improved photostability than that of organic dyes, however their limitations include concerns over toxicity[146, 147].

Ln ions (Ln(III)) have emerged increasingly as attractive options as luminescent probes owing to their remarkable properties that prove to be advantageous over other optical probes. The unique chemistry of the *f* block is the core to their key properties that play a major role in Ln luminescence, attractive for not only bioimaging, but many other technological applications.

1.5.2. Lanthanides and their Coordination Chemistry

Their unique optical properties are explored here briefly to help us understand their chemistry and how they are used in their applications.

Electronic Configuration and Bonding

Lns are often found in rocks and minerals in the earth's crust, isolated as oxides and fluorides due to the instability of Lns in elemental form[148]. The high redox stability of Ln(III) mean they are usually found in their +3 oxidation state, as their 4*f* electrons are easily lost due to

shielding effects[148]. Therefore, the electronic configuration of the trivalent ions Ln(III),can be denoted as [Xe]$4f^n$ (n = 0-14).

Table 1.5.21

Electron configuration and ionic radii of Ln(III)[149].

Element	**Ln(III) Electronic Configuration**	**Ln(III) ionic radii/ Å**
^{57}La	[Xe]	1.250
^{58}Ce	[Xe]$4f^1$	1.220
^{59}Pr	[Xe]$4f^2$	1.200
^{60}Nd	[Xe]$4f^3$	1.175
^{61}Pm	[Xe]$4f^4$	------
^{62}Sm	[Xe]$4f^5$	1.140
^{63}Eu	[Xe]$4f^6$	1.120
^{64}Gd	[Xe]$4f^7$	1.105
^{65}Tb	[Xe]$4f^8$	1.090
^{66}Dy	[Xe]$4f^9$	1.075
^{67}Ho	[Xe]$4f^{10}$	1.055
^{68}Er	[Xe]$4f^{11}$	1.040
^{69}Tm	[Xe]$4f^{12}$	1.025
^{70}Yb	[Xe]$4f^{13}$	1.010
^{71}Lu	[Xe]$4f^{14}$	0.995

Across the Ln series, there is a general decreasing trend in ionic radii. Ln contraction causes this reduction in radius with increase in atomic number, arising from poor ability of *f* electrons to shield other valence electrons from the nucleus. The radial distribution function of Ln(III) ions (figure 1.5.21[150]) shows that 6*s* electrons penetrate the nucleus the deepest, with the 4*f* electrons lying closest to the nucleus. Due to shielding effects of the orbitals; 6*s* > 5*d* > 4*f*, the 4*f* electrons are easily lost. Although the 4*f*, 5*d*, and 6*s* orbitals are similar in energy, there is no orbital overlap with ligands due to the proximity of the 4*f* orbital to the nucleus, and hence the bonding interaction between Ln(III) and ligands is ionic[150].

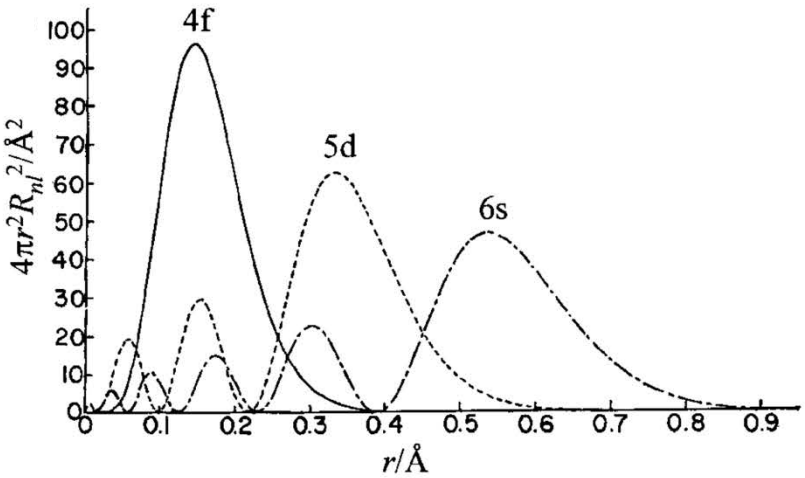


Figure 1.5.21

Radial distribution of the orbitals plotted as the probability of finding an electron at distance r from the nucleus of Ce[150].

Ln(III) ions are hard Lewis acids, and therefore prefer hard donor ligands containing O^-, F^-, and N^- electron pairs[155]. With mainly metal to ligand electrostatic interactions, hard donor ligands and non-directional bonding, Ln(III) ions prefer high coordination numbers usually between 6 to 12[155]. Steric hindrance can determine the structure where bulky ligands, such as bidentate ligands, can bind to the ion *via* the chelate effect being the driving force. The stability of complexes can increase by using structural preorganisation as a driving force[151]. This can be done by using macrocyclic caging ligands that can wrap around the Ln(III) ion, such as crown ethers[155], caging ligands such as DOTA, and linear ligands such as DTPA[152]. DTPA and DOTA ligands are widely known to be used as MRI contrast agents such as Gadopentetate Magnevist and Gadoterate Dotarem, as chelators for Gd(III) due to their cage like structures around the metal ion[152].

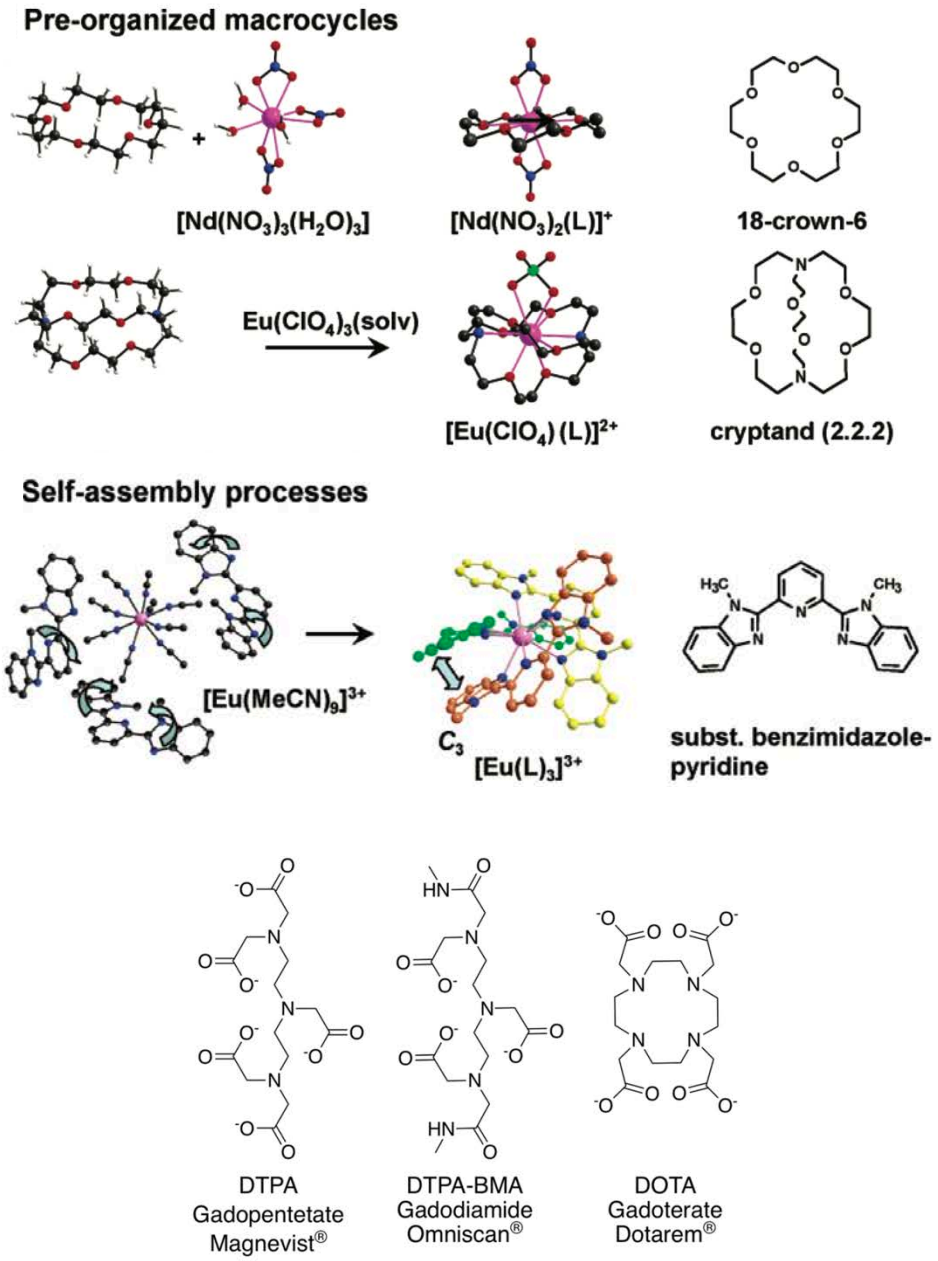


Figure 1.5.22

Schemes of structures demonstrating the chelate effect and structural preorganisation using macrocycles (top)[155], linear, and caging ligands (bottom)[152].

Optical Properties

The small radial extension of the 4*f* orbitals compared to the filled *s* and *d* shells, the shielding effect, is the very reason that leads to these unique optical properties of Ln(III) ions. The lack of interaction between 4*f* orbitals and ligand environment caused by the shielding from the coordination environment, leads to low Ln(III) absorption coefficients $\varepsilon = 1 - 10$ mol^{-1} dm^3 cm^{-1} [153, 155, 163]. Consequentially, *f*→*f* transition energies change little between compounds, giving rise to characteristic colours of Ln(III) ions[145].

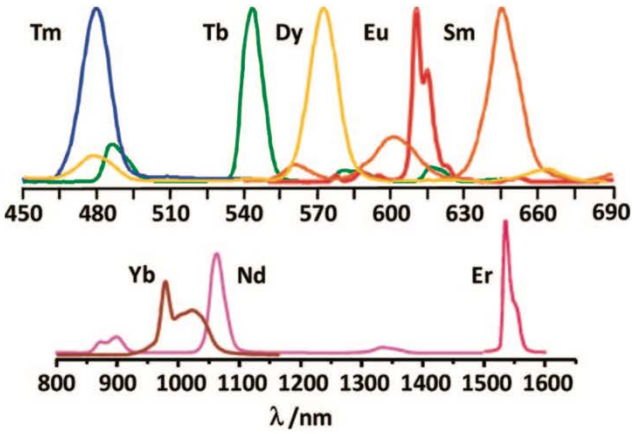


Figure 1.5.23

Luminescence spectra of Ln(III) β-diketones demonstrating characteristic Ln(III) colours. Image taken from Bunzli[145].

Secondly, the sharp bands in absorption and emission spectra arise from well defined *f*→*f* transition energies. Albeit the observation of these sharp bands in absorption and emission spectra, these transitions are forbidden by the Laporte selection rule, defined as $\Delta L = \pm 1$ only. The Laporte selection rule states that an electric dipole transition cannot occur in levels with the same centre of symmetry and hence *f-f* transitions are forbidden. However, these Laporte forbidden transitions become partially allowed due to vibronic coupling, influenced by the symmetry around the metal ion. As the metal – ligand bond vibrates, electron distribution changes around the bond and thus lowering the symmetry leading to vibronic coupling. Some of these induced electric dipole transitions are known to be very sensitive to changes in the Ln(III) coordination sphere, which are called hypersensitive transitions[145, 150, 162].

The electronic levels can be characterised by three quantum numbers, S, L and J (equation 1.5.21). As a result of the Ln high atomic numbers, and shielding effects, inter electron repulsion is caused as a consequence. This leads to splitting of the electronic levels[147, 162]. The spectroscopic energy levels can be described with a term symbol using Hund's rules based on spin orbit coupling and the heavy metal effect[145].

Equation 1.5.21

Form of Hund's rule to calculate term symbols.

$$^{2S+1}L_J$$

$$S = spin, L = orbital\ angular\ momentum, J = spin\ orbit\ coupling$$

Hund's rules includes three main requirements in order to determine the ground state of Ln(III) ions. The first rule requires that the spin multiplicity should be highest possible. The second rule states that if there are more than one terms with the same spin multiplicity, the term with the highest L (orbital angular momentum) is the ground state. Lastly, for electron shells more than half filled, the lowest J value is the ground state. However, for electron shells less than half filled, the highest J value is the ground state. These rules can therefore explain, for example, why the ground state of Eu(III) is $^7F_0$.The detected luminescence of Ln(III) ions usually arise from the lowest excited state to the ground state of each Ln, but there are examples that have detected luminescence from higher excited states[156, 157].

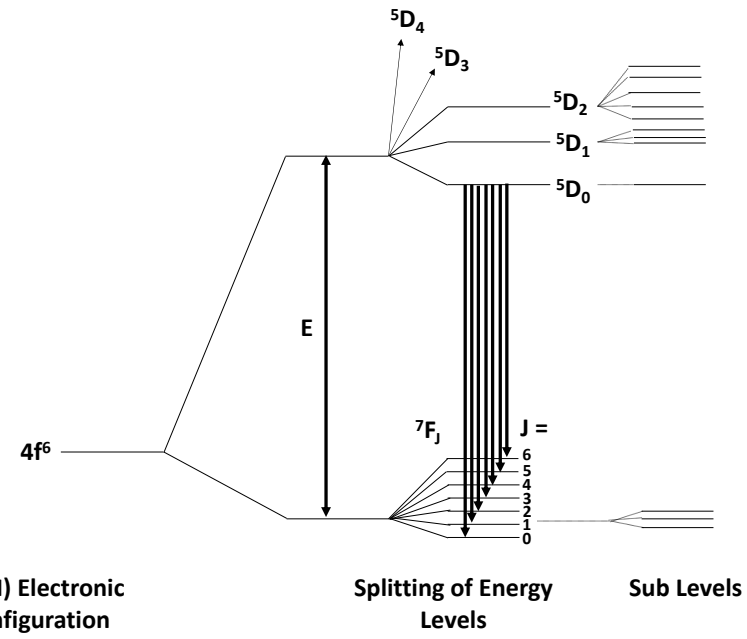


Figure 1.5.23

Luminescence spectra of Ln(III) β-diketones demonstrating characteristic Ln(III) colours. Image taken from Bunzli[145].

A review published by Binnemans in 2015, summarised well the interpretation of Eu(III) spectra. Figure 1.5.24 illustrates the splitting of energy levels, with the example of Eu(III), arising from three effects. The inter electron repulsion between the 4*f* electrons gives rise to the term symbols. Spin orbit coupling leads to splitting of these energy levels, caused by the interaction of the spin magnetic moment of the electron, and the magnetic field of the electron around the nucleus. Further splitting of these energy levels into sublevels can be caused by weak crystal field effect, where 4*f* electrons interact with the ligand field electrons[156, 162].

Sensitisation of Ln(III) Luminescence Using the Antenna Effect

The observation of weak *f*→*f* transitions in absorption and emission spectra can be achieved by direct excitation of the Ln(III) ion. For some metal ions, such as Eu(III) this can be efficient enough to detect emission, with the limitation of weak absorption. For Eu(III), the transition at 394 nm arising from $^5L_6 \leftarrow {}^7F_0$ is often used for direct excitation, but has a low molar absorption coefficient ε[156]. To overcome the challenges associated with weak absorption, and thus, weaker emission intensity, the antenna effect is used. The so called antenna effect, is

used to enhance Ln(III) luminescence with the use of sensitising units that include organic chromophores. Organic chromophores tend to have high ε, especially ligands designed with π-conjugation, as they are able to absorb light efficiently. Their strong ability to absorb light, enables energy transfer from the excited chromophore to the Ln(III) ions, resulting in enhanced luminescence intensity[145, 147, 164, 148-151, 155, 156]. This was discovered first in 1942 by Weissman, who observed intense Eu(III) luminescence from Eu(III) complexes that included dibenzoylmethane, salicylaldehyde and benzoylacetone chromophores[158].

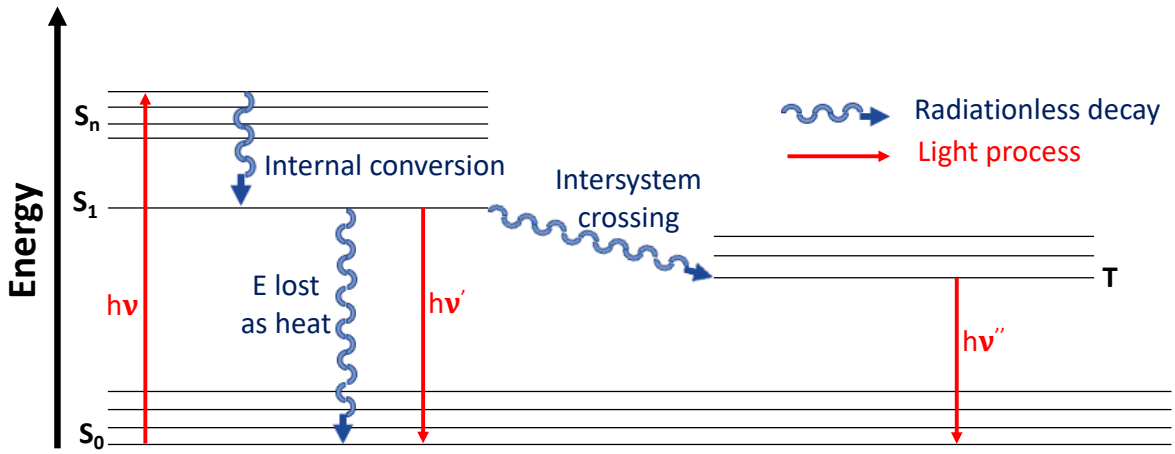


Figure 1.5.25

A Jablonski diagram illustrating the processes of excited states, by radiationless decay and radiative decay. S_0 ground state of sensitiser; S_1 first excited state of sensitiser; S_n excited states of sensitiser; T first excited triplet state of Ln(III)[145, 154].

The Jablonski diagram demonstrates the process of energy transfer from organic chromophores to Ln(III) in the antenna effect. Absorption of a photon from the sensitiser ground state to the ground excited state occurs, after which intersystem crossing can transfer energy to the ground excited state of Ln(III). There are two processes in which luminescence can be divided into, phosphorescence and fluorescence. Phosphorescence is slow and spin forbidden, where radiative decay occurs from the ground triplet excited state of Ln(III). Fluorescence, radiative decay from a spin allowed transition to the ground state, is however described as fast. This sensitisation process enables the population of the Ln(III) excited state usually in the UV range, giving rise to Ln(III) emission in the visible or NIR range. The difference

in the excitation and emission wavelength, the Stokes shift, is typically large for Ln complexes unlike organic complexes, resulting in improved detection[145, 147, 154, 162].

The excited state can be characterised by the lifetime τ, and quantum yield ϕ[162, 163].

Equation 1.5.22

Definition of luminescence lifetime τ.

$$\tau = \frac{1}{k_r + k_{nr} + k_p}$$

$$k_r = rate\ of\ radiative\ decay, k_{nr} = rate\ of\ non-radiative\ decay,$$
$$k_p = rate\ of\ photochemical\ decay\ from\ any\ further$$
$$photochemical\ reactions\ from\ excited\ states$$

Equation 1.5.23

Definition of luminescence quantum yield ϕ.

$$\phi = \frac{photons\ emitted}{photons\ absorbed}$$

Detection of energy transfer can be monitored by changes in these parameters. The luminescence intensities of ligand and Ln(III) can be monitored, in addition to the luminescence lifetimes.

Energy Transfer Mechanisms

There are two main mechanisms of energy transfer involved for the sensitisation process from a chromophore to a Ln(III) ion. The Dexter mechanism, also known as exchange mechanism requires good orbital overlap between ligand and metal as it involves a double electron transfer. It is usually short range, less than 10 Å and a non-radiative process, sometimes associated with quenching, and the reaction rate constant exponentially decays as distance increases[163].

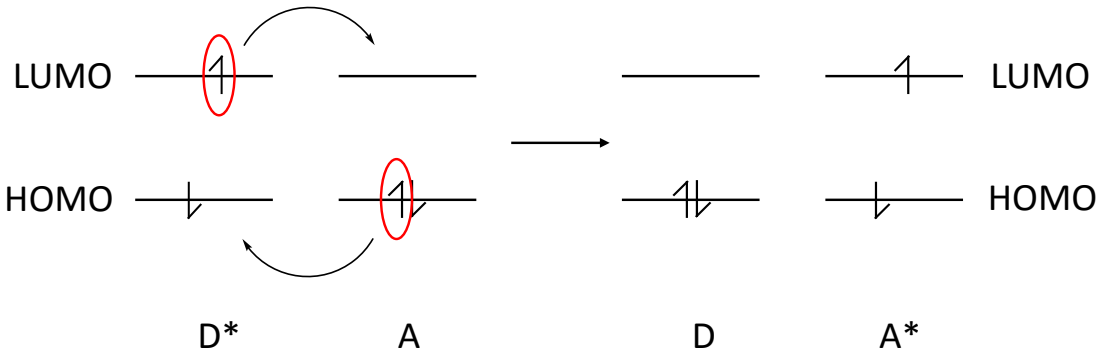


Figure 1.5.26

Schematic illustration drawn demonstrating the electron transfer process in the Dexter mechanism; D = donor and A = acceptor.

The second energy transfer mechanism is known as the Förster mechanism, or dipole-dipole mechanism. Here, the dipole moment of the excited donor state couples with the dipole moment of the Ln(III), the acceptor. This mechanism is specific for given ligand-metal complexes and usually lies at long distances, typically between 5 Å and 20 Å[163].

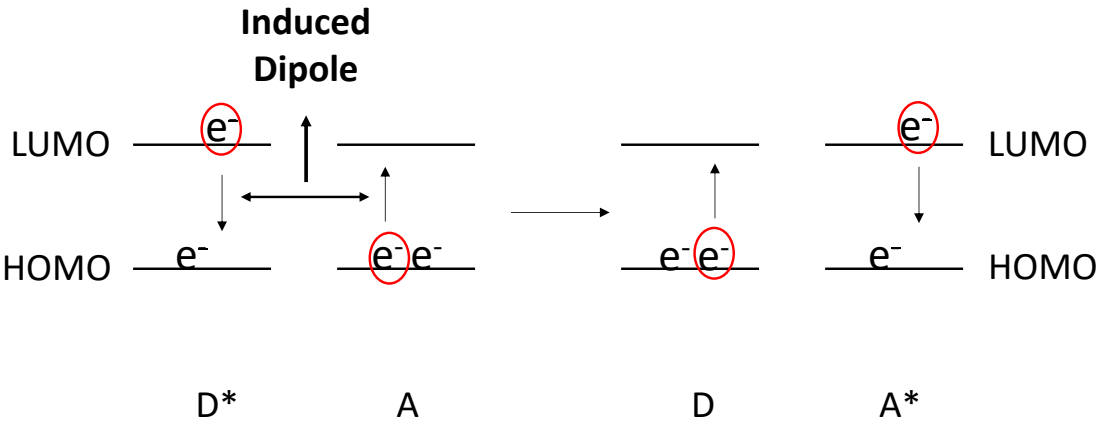


Figure 1.5.27

Schematic illustration drawn demonstrating the induced dipole coupling between the donor and acceptor in the Förster mechanism.

Ligand Design for Ln(III) Ions

In order to achieve optimal sensitised Ln(III) luminescence, the design and choice of the ligand is crucial. An ideal ligand aims to have good coordination ability to the metal ions, a high ε in order to absorb light strongly, and an appropriate energy gap between the excited state of the chromophore and the excited state of Ln(III)[150, 151, 159, 160].

Introducing an organic chromophore with high ε and ligand centred absorption in the UV range enables a large Stokes shift. This leads to reduction in background scattering, especially from biofluorescence in biological environments, and thus allows easy spectral discrimination. The introduction of a light harvesting chromophore, also overcomes the challenge of photobleaching associated with organic dyes. Energy transfer from organic chromophores to Ln(III) ions is usually fast, therefore reducing photobleaching[160].

The energy gap between the sensitiser and Ln(III) is important for efficient energy transfer, and so ligand design can be developed to fine tune the energy levels of the sensitiser. The closer the energy gap, the more efficient the energy transfer. Nevertheless, if the gap is too close, back energy transfer can occur from the excited Ln(III) to the sensitiser, decreasing Ln(III) luminescence, lifetime and quantum yield[160]. On the other hand, if the energy gap is too large, the Ln(III) excited state cannot be populated. Therefore, other processes such as radiative decay from the sensitiser can occur, as well as any energy lost as heat[154]. The energy gap is therefore usually required to be between 2500 cm^{-1} and 3500 cm^{-1} higher than the Ln(III) excited state[154].

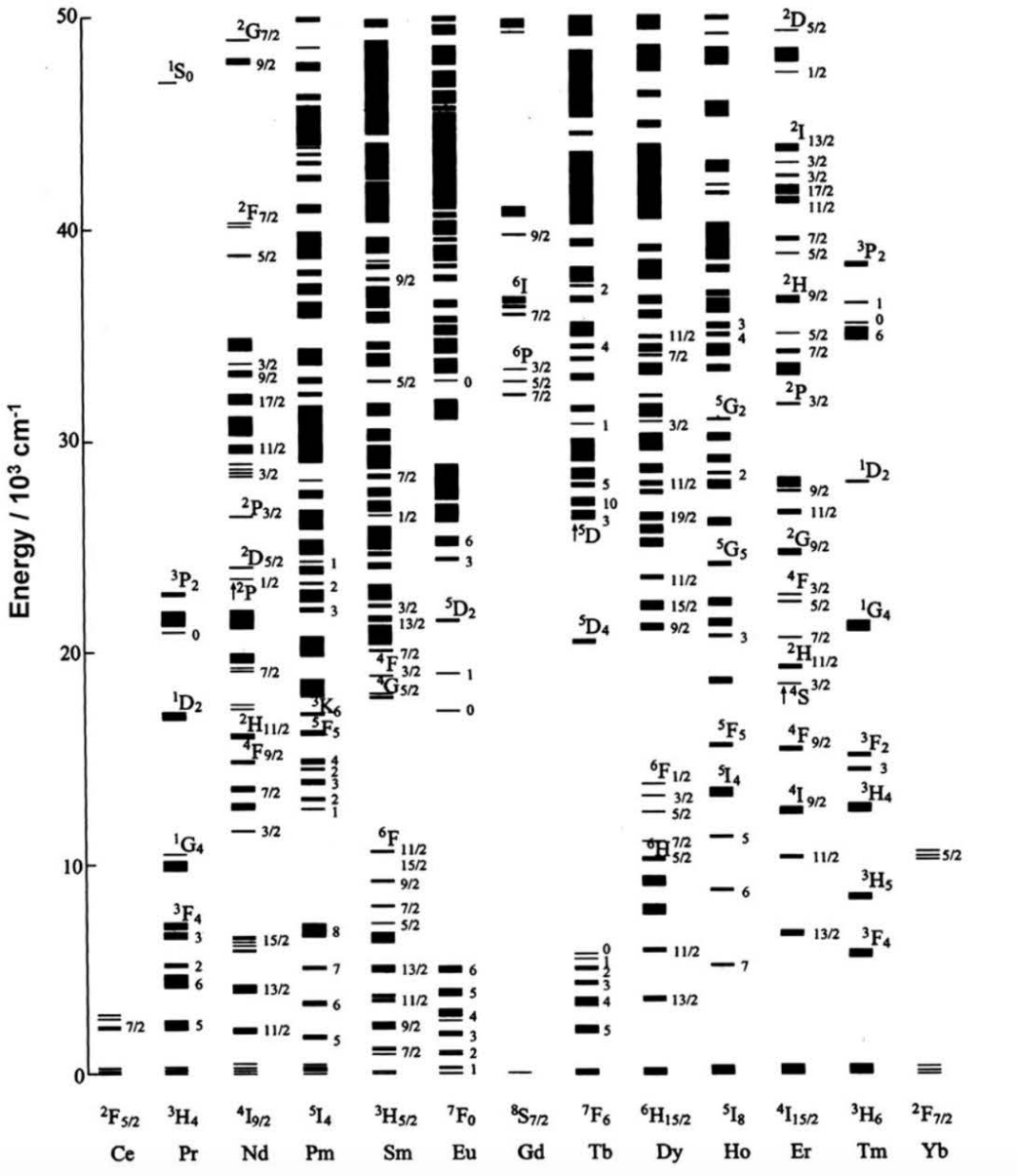


Figure 1.5.28

Energy level diagram for Ln(III) ions (doped as LaF_3)[154].

The coordination of Ln(III) ions to the ligands can be increased with the introduction of hard donor ligands containing O^-, F^-, and N^- electron pairs[155] in order to form thermodynamically stable Ln(III) complexes[147].

Lastly, the ligand design should shield the Ln(III) ions well from coordination to solvent molecules in order to inhibit radiation less decay affecting the luminescence.

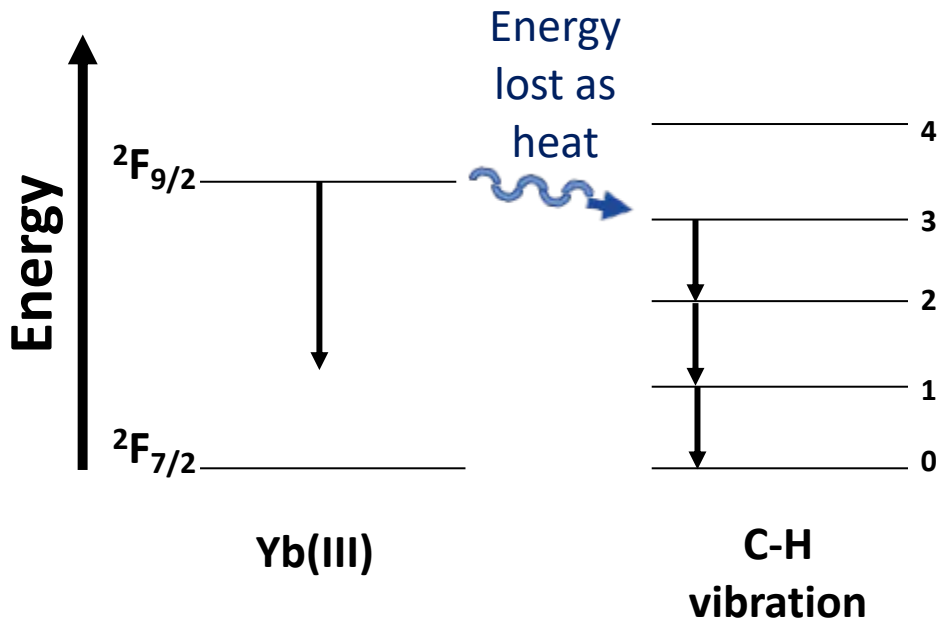


Figure 1.5.29

Quenching of $^2F_{9/2}$ energy level of Yb(III) by C-H oscillator shown the vibrational energy levels of CH. Image redrawn from Ning *et. al.*[160].

Non-radiative deactivation can occur from back energy transfer, thermal deactivation (both previously mentioned), but also through quenching. Vibrational coupling between Ln(III) ions and high energy vibrations from solvent interactions can significantly quench Ln(III) luminescence. The quenching of Ln(III) luminescence is demonstrated in figure 1.5.29, showing energy lost as heat from coupling to C-H vibrations. O-H vibrations also tend to quench Ln(III) luminescence, and so exclusion of coordination to water in solvents can be achieved by increasing coordination number. Replacement of these high energy vibrations can also reduce quenching, by introduction of deuteration such as C-D, O-D and fluorination C-F[147, 148, 160]. As previously mentioned, bulky cage like ligands such as DTPA and crown ethers are ideal candidates for overcoming coordination to solvent molecules[152, 155].

Near Infrared Emitting Ln(III)

NIR emitting Ln(III) ions have received great interest due to some key features of their optical properties. Their ability to emit in the NIR range means deeper penetration depth into biological tissue and thus increasing signal to noise ratio. Consequentially, imaging resolution is increased due to less background interference. This has enabled the use of non-invasive imaging techniques which are ideal for diagnostics and detection of cancer. They also undoubtedly have long lifetimes and much larger Stokes shift than visibly emitting Ln(III) ions[160].

The challenges associated however with NIR Ln(III) in biological imaging arise from low instrumental sensitivity in the emitting range. Secondly, to be able to overcome quenching from vibrational coupling to solvent molecules is more sensitive with NIR emitting Ln(III) ions[147, 160].

Overcoming these challenges links back to developing good ligand design for NIR Ln(III), with importance of exclusion to high energy vibrations using Ln cages, increasing lifetimes and also stability.

Obvious strategies have involved replacement of C-H vibrations with C-D resulting in increased emission due to deuteration. Hasegawa *et. al.* in 1996 observed the effect of deuteration on their Nd complex, resulting in enhanced emission. Gillin's group later quantified luminescence quenching from $Er(hfa)_3(H_2O)_2$ and the deuterated and hydrogenated $Cs[Er(hfa)_4]$. The important conclusion to be drawn from their work highlighted that the closest C-H oscillators were the largest contributors to Er(III) quenching, and also that neighbouring C-H oscillators have to be replaced[162, 165,-167].

Halogenation can also be used as an alternative, in cases where full deuteration is difficult. Fluorination is often commonly seen in addition to chlorination[162].

Coordination Structures for Highly Luminescent Lanthanide Complexes

In order to design ligand structures with the aim of forming highly luminescent complexes, there are many requirements that must be met, depending on the Ln and its application. The coordination sphere of Ln(III) ions can be tailored to find an antenna most suitable, whilst simultaneously avoiding coupling to high energy oscillations.

For efficient energy transfer between antennae and Ln(III) ions, positioning of excited states need to be considered. Tailoring ligands for this has been carried out by several research groups[168-174].

In addition to electronic considerations, the application of the Ln system is significant in the design of antennae. Antenna required for specific applications such as telecommunications, light emitting diodes and solar energy for example, need thermal stability. In display and optoelctronics, process polymers are often used. This is a common theme across lighting and display where polymer light emitting diodes are of interest. Resistance to photobleaching is important, as well as polymer architectures with interest in flexible displays[169, 174-180].

However, luminescent Ln complexes required as bioprobes used in bioimaging or immunoassays, need to be kinetically inert and thermodynamically stable[133]. Water solubility and saturated coordination spheres are important. For sensing applications, desirable ligands enable binding to analytes or Ln(III) ions, or even changes in redox potentials[48].

Gd contrast agents in MRI imaging has brought about an extensive amount of research in developing Gd complexes, which must compel some key requirements for this technique. Complexes must have high thermodynamic stability, as well be kinetically inert. High coordination numbers are important with a site left free for interaction with water molecules (crucial for MRI contrast enhancement). There have been two types of ligands that have been used for this, which are based on either twelve membered tetraazamacrocylic cyclen derivatives (cyclen = 1, 4, 7, 10-tetraazacyclododecane), and diethylenetriamine derivatives. These ligands can form good cage structures around the Ln(III) ion, driven by the chelate effect[181].

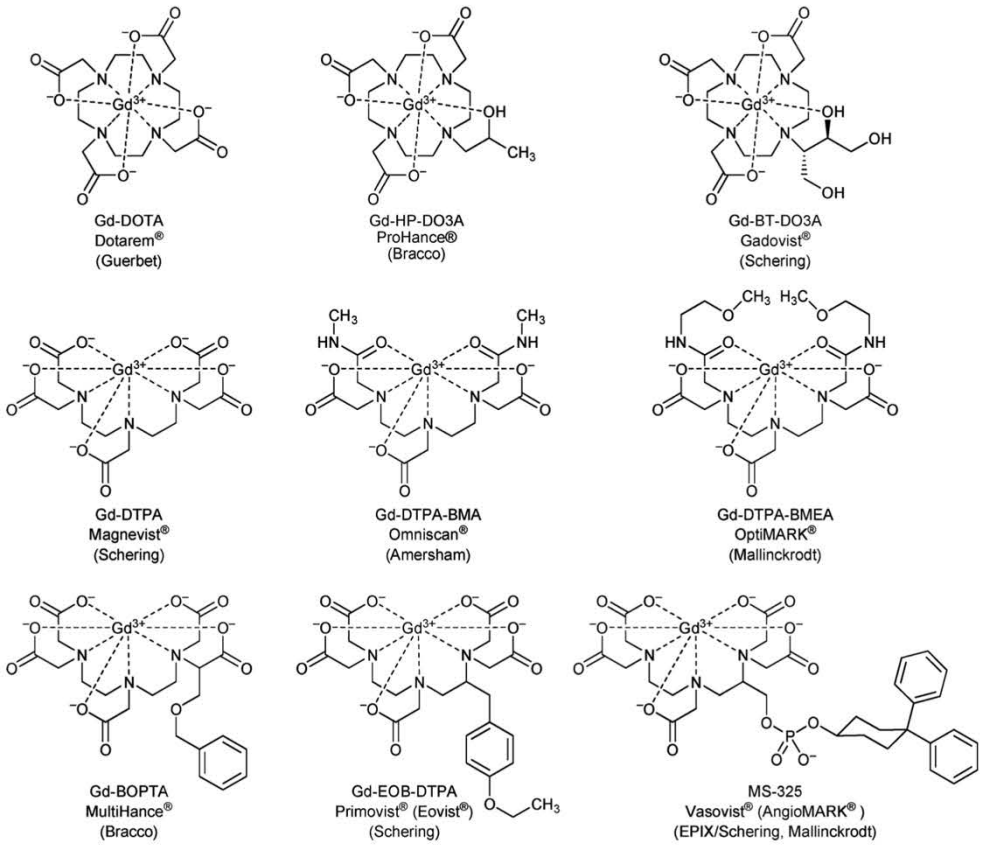


Figure 1.5.210

A scheme of contrast agents used clinically, demonstrating the cage like ligands used[181].

There has also been a huge effort made to develop modifications based on polydentate ligands like DOTA, and diethylenetriamines such as DTPA with different functionalities. Without conjugated R group functionalities, these molecules serve as good ligands regarding exclusion to water and other quenching moieties, in addition to high coordination environment. However, they don't necessarily present as an antenna without a light harvesting unit, and so these complexes have to either be excited directly at the Ln(III) ion or require to be conjugated to some other sensitising unit.

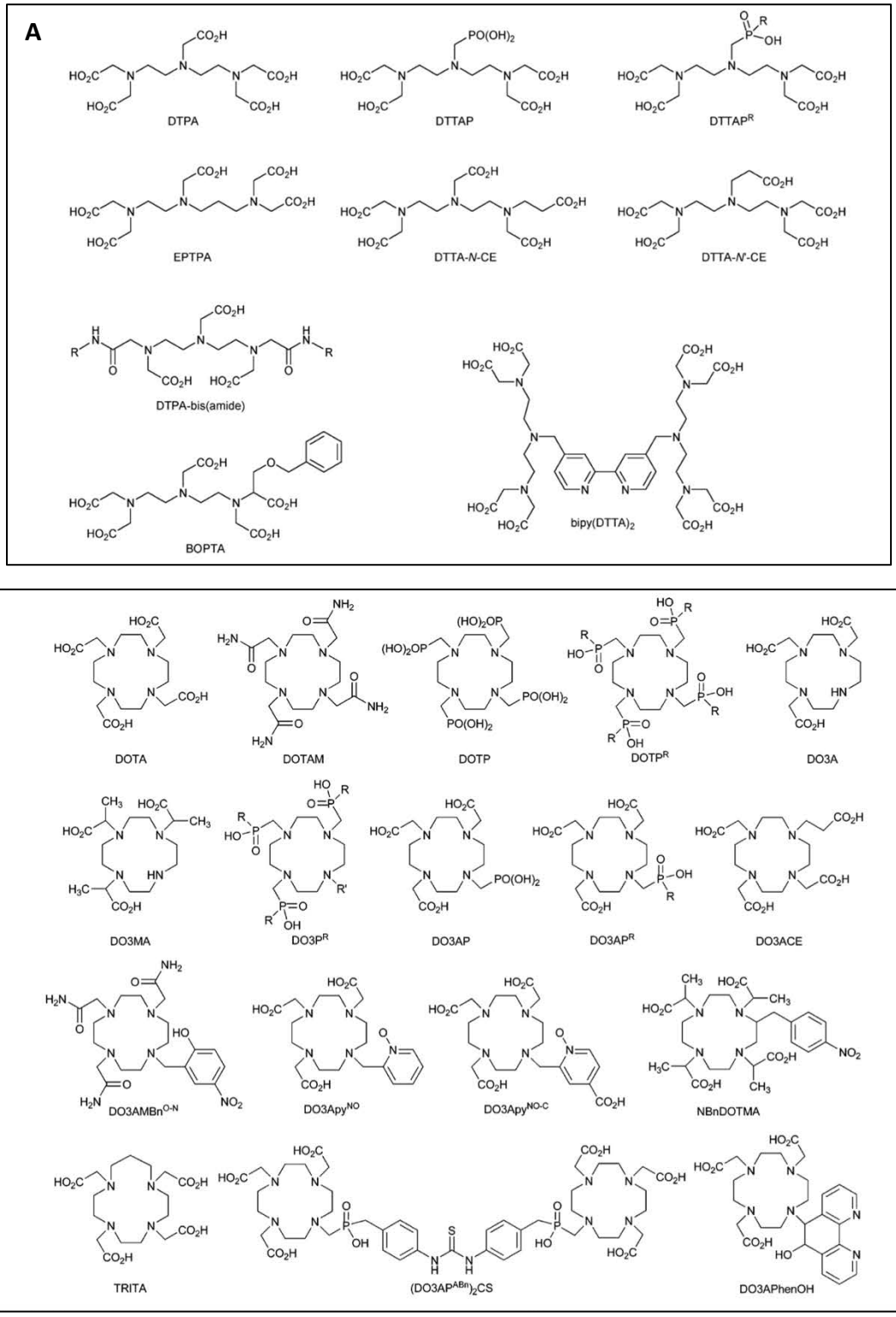


Figure 1.5.211

A scheme demonstrating different types of structural motifs used to design contrast agents. A: DTPA type ligand designs. B: DOTA type ligands[181].

Other than caging structures, there is a large library of other antenna, with light harvesting units, that have been designed and developed over the years in order to produce highly luminescent complexes. These come in all forms spanning from solids, solutions to hybrid materials and surfaces.

A vast majority of these complexes for visible emitting Ln luminescence, include Eu(III) due to specific optical properties[133]. For Eu(III), the large energy gap between the ground excited state $^5D_0$, and the ground emissive state $^7F_6$, is sufficient enough to minimise deactivation through vibrational coupling to high energy oscillations. Moreover, the lifetime from the ground excited state $^5D_0$ is up to milliseconds, enabling time gated detection. Eu(III) emission can also be very monochromatic, depending on its coordination environment. For instance, it's well known that Eu(III) complexes formed with β-diketones present spectra that are dominated by the $^5D_0 \rightarrow {}^7F_2$. Colour of Eu(III) complexes can also be tuneable, tailoring designs that favour $^5D_0 \rightarrow {}^7F_1$ transitions, a magnetic dipole transition, over other electric dipole transitions, shifting colours from red to orange. Ligand field has little effect on the $^5D_0$ with no splitting of levels, leading to facile discrimination of ^7J_F transitions[282].

β-diketones are well known as sensitisers for highly luminescent complexes, but there are many other ligand designs that have also been used[133].

Bunzli and co workers designed tridendate benzimidazole-subsitituted pyridine-2-carboxylates using 9 coordinate neutral homoleptic anhydrous Ln complexes. They achieved very efficient sensitisation with quantum yields as high as 71 % in solid state, and 52 % in solution (CH_2Cl_2)[133, 182].

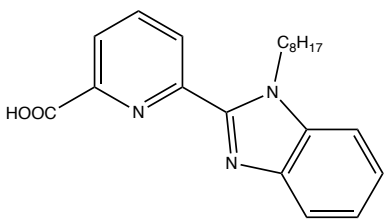


Figure 1.5.212

Structure of benzimidazole-substituted pyridine-2-carboxlate.

π-conjugation is a common theme in ligand designs, with hard donor electron donors such as O and N. Simple ligands such as 2,2'-bipyrimidine (bpm) are used often and have been reported to sensitise Eu(III) and Tb(III) luminescence with quantum yields of 70 % and 80 % respectively $[(Ln(NO_3)_3(bpm)_2]$[180].

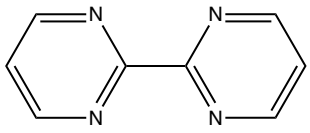


Figure 1.5.212

Structure of bpm.

Carboxylates are often used in ligand designs, offering electron donors using negatively charged O. Structures like DTPA and DOTA (figure 1.5.211) use these binding sites for caging in Ln(III) ions. High quantum yields, as high as 95 %, have been reported using polyaminocarboxylates[133].

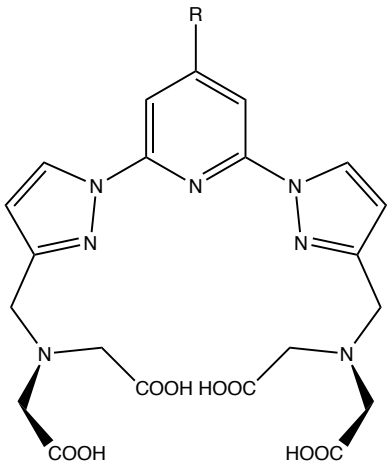


Figure 1.5.214

Structure of polyaminocarbozylate fitted with 4-carbomoyl-substituted pyridine[133].

The carboxylate in figure 1.5.214 was complexed to Tb(III) and achieved 95 % quantum yield. The π-conjugation provides a good light harvesting centre, with good ability to sensitise, whilst the hard N donor atoms provide strong binding. This combined with the carboxylates

provides a highly coordinated environment with caging around the Ln(III) ions, showing potential for high stability.

Macrocyclic derivatives have commonly been used as ligands due to their high coordination environments, minimising coordination to quenching molecules. Maury *et. al.* synthesised a series of Eu(III) and Tb(III) complexes based on triazacyclononane tris-pyridine carboxylates and methyl phosphinates[183].

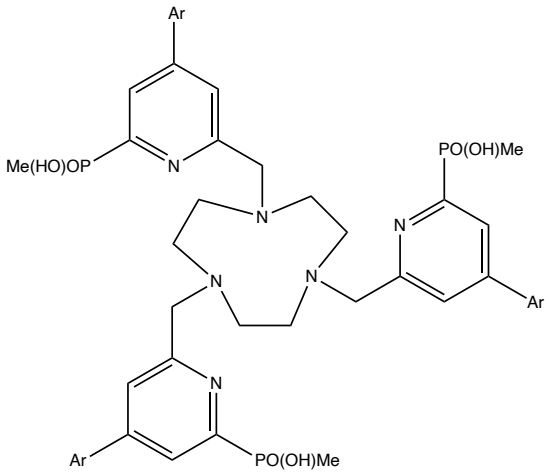


Figure 1.5.215

Structure of the functionalised phosphinate macrocyclic ligand used by Maury *et. al.*[183].

They reported 55 % quantum yield of Eu(ligand) and observed efficient energy transfer for their Eu(III) complexes. The advantage of using polydentate ligands can show additional sensing properties, by displacement of coordinated water molecules[183].

Other visible emitting Lns such as Sm(III) and Dy(III) are less luminescent due to their blue-shifted emission, compared to Eu(III), towards yellow colours[133].

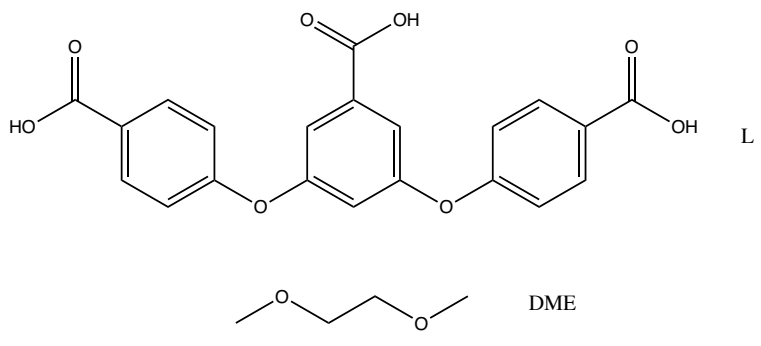


Figure 1.5.216

Structure of ligand L, and DME.

Metal organic frameworks (MOFs) have been used increasingly with Lns to produce a diversity of different topologies and architectures, combining the applications of MOFs (ion exchange, drug delivery, storage) and Ln advantages. MOFs offer several attractions for binding to Ln(III). They can accommodate high and flexible coordination environments. They also offer hard donor atoms like O and N containing ligands, and carboxylates. Liu *et. al.* formed novel dimeric Sm polymers, forming $[Sm_2(L)(DME)_2]_\infty$ reaching quantum yield of 17 % in solid state[184].

Petoud's group has dived into Ln research, designing metallocrowns to coordinate to Ln(III) ions. These designs are 'metal rich macrocycles' that form [Metal-N-O] repeated units. The oxygens are directed towards the inner of the macrocyclic rings, driven by preorganisation for encapsulating Ln(III) ions. With substituted functionalities, metallocrowns offer not only coordination to hard donor O atoms, but also through carboxylic acids which provide additional stability. To build multimetallic complexes, metallocrowns offer an attractive route often used by Petoud's group[171, 185].

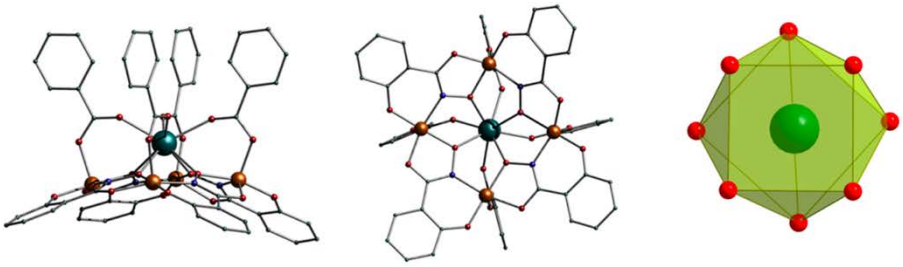


Figure 1.5.218

Molecular structure of metallocrown synthesised by Petoud *et. al.* coordinated to Dy(III)[185].

In 2016, Petoud *et. al.* synthesised a family of Ga(III)/Ln(III) metallocrown complexes. They detected luminescence from these complexes by excitation of the chromophoric ligands, generating spectra in the NIR range (Sm, Dy, Ho, Er, Yb) and the visible range (Sm, Eu, Tb, Dy, Tm). They reported high quantum yields showing good energy transfer capabilities, but uniquely reported the highest NIR quantum yield of 5.8 % reported for Yb(III) complex at the time[185].

Other ligands used include helicates[170, 186], cryptates[187-190], polyaminocarboxylates (and phosphinates)[191-195], and many other macrocyclic derivatives[196, 197].

NIR Ln complexes usually have much lower quantum yields, due to their higher affinity for vibrational coupling to quenching molecules. However deuteration, as discussed previously, can have a major effect in ligand designs[133]. Wong *et. al.* synthesised water soluble porphyrin based Yb(III) complexes and reported yields as high as 6 % for deuterated complexes, compared to 2 % (non-deuterated)[198].

Triple stranded trinuclear helicates have been used by Piguet, Petoud and corworkers[199], using transition metals as light harvesting units to transfer energy to Nd(III) in $[CrNdCr(ligand)_3]^{9+}$.

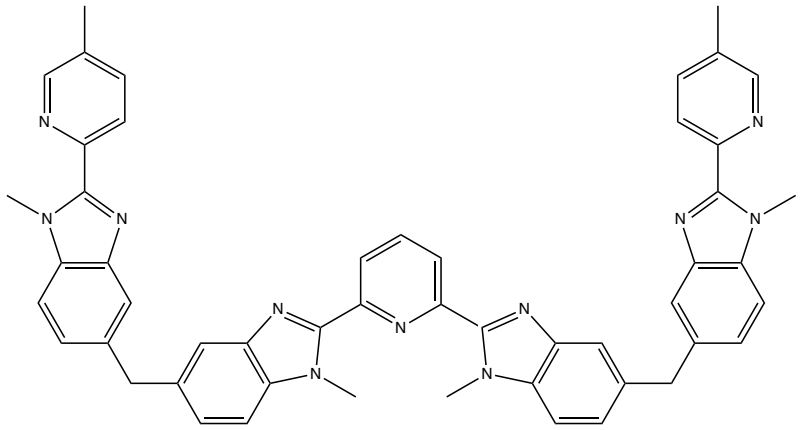


Figure 1.5.219

Trinuclear strand used by Piguet et. al.[199].

Advantages of Lanthanides as Luminescent Probes

Ln chemistry brings out some key characteristics that differentiate them as luminescent probes compared to others, such as organic dyes.

Their sharp narrow absorption and emission bands provide ‘‘elemental’’ characteristic emission, arising from shielding effects[160]. The lack of participation in covalent bonding, and hence any changes in the ligand environment has no effect on rearrangement of electrons, causing these fixed and sharp bands. This allows Ln emission to be easily distinguished, a great advantage for detection[160].

The visible, and even better, NIR emitting Ln(III) have large Stokes shifts caused by ligand excitation usually in the UV range, and Ln centred emission. A large Stokes shift, which is not common in organic dyes, is advantageous because it enables facile discrimination of emission spectra. It also reduces background scattering, beneficial for detection in biological environments where autofluorescence from biological serum occurs in the UV range[160].

Moreover, lanthanides are resistant to photobleaching, due to fast energy transfer, and therefore an additional reason as ideal probes over organic dyes[147, 160].

Their long lived lifetimes are a key attraction for application in biological imaging, arising from the slow relaxation of electrons from the excited Ln(III) caused by the forbidden Laporte transitions. This can lead to time gated measurements, and aids in reduction of background scattering as well as increased signal to noise ratios. It is important to note that for applications such as biological imaging, probes need to have water solubility, thermodynamic stability, long lifetimes and brightness, and the ability to excite over 405 nm. These requirements can be achieved by the correct ligand design[147, 160]. Notably, the use of NIR Lns are advantageous here due to their deep penetration into tissue previously discussed, which is attractive for non-invasive techniques.

Systems with multimodal functionality are also attractive for biological applications, and Lns provide simultaneous detection and sensing. By tailoring ligand design, different chemical species can be sensed by Ln(III) complexes based on the changes in energy transfer between the ligand and Ln(III).

1.6. Thesis Aims and Objectives

The aim of this thesis is to develop novel nanoscale platforms for theranostic applications in nanomedicine, focusing on drug delivery and detection, using luminescent Ln complexes as luminescent labels.

Silica NPs are used as one design to encapsulate a hydrophobic anticancer drug, which simultaneously acts as a Ln sensitiser enabling Ln luminescence signal detection. This design demonstrates the detection of drug release through an 'on and off' switch system monitored through changes in Ln luminescence signal (figure 1.61). The use of luminescent Ln complexes over typical organic probes is advantageous due to some key features. Their sharp emission spectra provide easy detection, in addition to large Stokes shifts enabling easy spectral discrimination. Long lived Ln lifetimes are also beneficial important for applications in biological imaging. Furthermore, use of NIR Lns provide deeper penetration into tissue as previously discussed, which is attractive for non-invasive techniques.

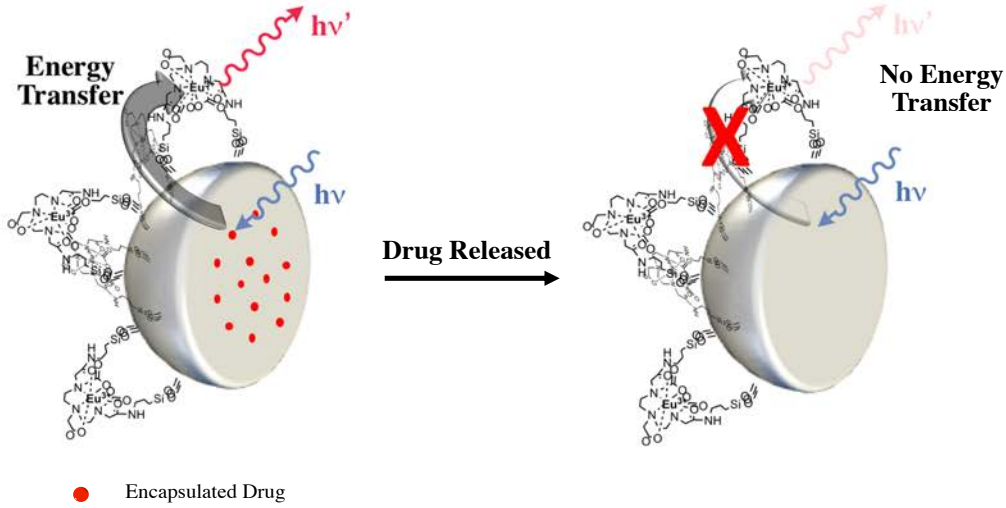


Figure 1.61

Schematic illustration of silica nanoparticle design carrying an anticancer drug inside, and functionalised with a luminescent Ln complex. The drug is able to sensitise Ln luminescence, turning signal 'on'. As drug is released from the nanoparticle design, Ln luminescence cannot be sensitised anymore, turning signal 'off'.

Gold NPs are used as a second design to create a nanoplatform for sensing Ln binding, and sensitising luminescence. They provide a platform in which multimodal systems can be developed, but also allowing high loading of luminescent Ln complexes at low concentrations, enhancing detection and sensitivity. β-diketone complexes have been used extensively as Ln chelators for applications in developing luminescent Ln immunoassays. Due to their key features, Lns are an attractive route to sensing and detecting analytes in immunoassays.

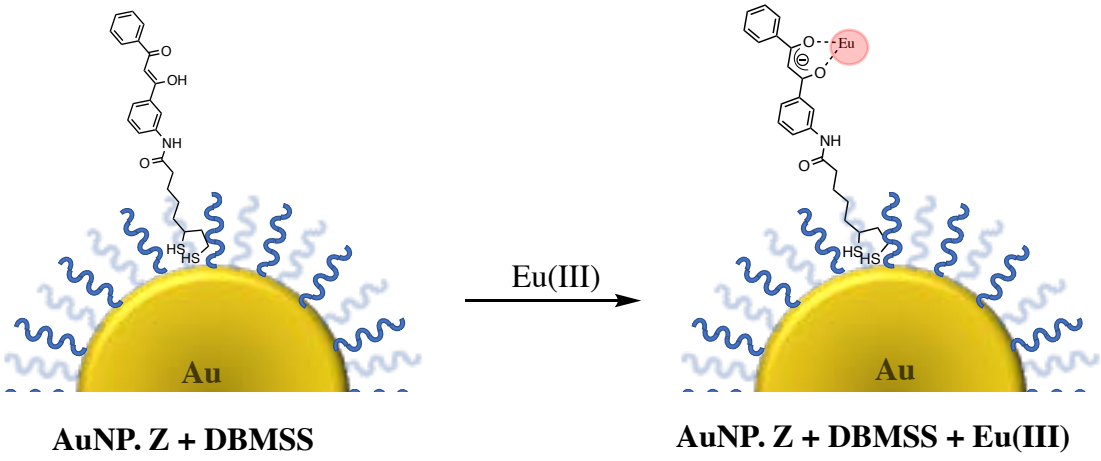


Figure 1.62

Schematic illustration of development of gold NPs functionalised with surface active DBM molecule, able to bind Eu(III) ions and sensitise luminescence.

1.7. Referenced Material

1. A. Jemal, F. Bray, M. M. Center, J. Ferlay, E. Ward and D. Forman, *CA. Cancer. J. Clin.,* 2011, **61**, 69-90
2. Global Cancer Facts and Figures Fourth Edition., *ACS*, 2015, 1
3. R. Siegel, K. Miller, H. Fuchs and A. Jemal, *Ca. Cancer. J. Clin.,* 2021, **7**1, 7–33
4. R. Siegel, K. Miller, H. Fuchs and A. Jemal, *Ca. Cancer. J. Clin.,* 2017, **71**, 7-33
5. S. Parveen, R. Misra and S. Sahoo, *Nanomedicine: NBM.,* 2012, **8**, 147-166
6. S. Baek, R. Singh, D. Khanal, K. Patel, E. Lee, K. Leong, W. Chrzanowski and H. Kim., *Nanoscale.,* 2015, **7**, 14191-14216
7. S. Mura, J. Nicolas and P. Couvreur, *Nat. Mater.,* 2013, **12**, 991-1003
8. T. Allen and P. Cullis, *Science*., 2004, **303**, 1818-1822
9. S. Saallah and I. Lenggoro, *Kona. Powder. Part. J.,* 2018, **35**, 89-111
10. H. Ulukan and P. Swaan, *Drugs.,* 2002, **62**, 2039-2057 ref 7
11. A. Behera and S. Padhi, *Environ. Chem. Lett.,* 2020, **18**, 1557-1567
12. Y. Wen, Y. Wang, X. Liu, W. Zhang, X. Xiong, Z. Han and X. Liang, *Cancer. Biol. Med.,* 2017, **14**, 363-370
13. Y. Pommier, *Nat. Rev. Cancer.,* 2006, **6**, 789-802
14. L. Fonseca, M. Sousa, D. Maia, L. Luna and O. Alves, *Nanoscale Adv.,* 2020, **2**, 1290-1300
15. L. Tang and J. Cheng, *Nano Today.,* 2013, **8**, 290-312
16. S. Soares, J. Sousa, A. Pais and C. Vitorino, *Front. Chem.,* 2018, **6**, 360
17. T. Doane and C. Burda, *Chem. Soc. Rev.,* 2012, **41**, 2885-2911
18. A. Alivastos, *ACS Nano.,* 2008, **2**, 1514-1516
19. C. Murphy, A. Gole, S. Hunyadi, J. Stone, P. Sisco, A. Alkilanu, B. Kinard and P. Hankins, *Chem. Commun.,* 2008, 544-557
20. S. Chen and D. Caroll, *Nano Lett.,* 2002, **2**, 1003-1007
21. P. Kumar, I. Pastoriza-Santos, B. IGonzalezez, F. Abajo and L. Liz-Marzan, *Nanotechnology.,* 2008, **19**, 015606
22. D. Jang, C. Moon and E. Oh, *Biomed Pharmacother.,* 2016, **80**, 162-172
23. K. Householder, D. DiPerna, E. Chung, G. Wohlleb, H. Dhruv, M. Berens and R. Sirianni, *Int. J. Pharm.,* 2015, **479**, 374-380
24. Y. Cirpanli, E. Allard, C. Passirani, E. Bilensoy, L. Lemaire, S. Calis and J. Benoit, *Int. J. Pharm.,* 2011, **403**, 201-206

25. D. Tang, F. Song, C. Chen, X, Wang and Y. Wang, *Nanotechonology.,* 2013, **24**, 145101
26. C. Zi, L. Yang, F. Xu, F. Dong, R. Ma, Y. Li, J. Zhou, Z. Ding, Z. Jiang and J. Hu, *Bioorg. Med. Chem. Lett.,* 2019, **29**, 243-237
27. J. Shi, P. Wu, Z. Jiang and X. Wei, *Eur. J. Med. Chem.,* 2014, **71**, 219-228
28. V. Yellepeddi, K. Vangara and S. Palakurthi, *J. Nanopart. Reticuloendothel. Syst.,* **15**, 1897
29. F. Cheng, C. Su, P. Wu and C. Yeh, *Chem. Commun.,* 2010, **46**, 3167-3169
30. H. Han, L. Mangala, J. Lee, M. Shahzah, H. Kim, D. Shen, E. Nam, E. Mora, R. Stone, C. Lee, J. Roh, A. Nick, G. Lopez-Berestein and A. Sood, *Clin. Cancer. Res.,* 2010, **16**, 3910-3922
31. K. Koziara, P. Lockman, D. Allen and R. Mumper, *J. Control. Release.,* 2004, **99**, 259-260
32. F. Corsi, C. De Palma, M. Colombo, R. Allevi, M. Nebuloni, S. Ronchi, G. Rizzi, A. Tosoni, E. Trabucchi, E. Clementi and D. Prosperi, *Small.,* 2009, **5**, 2555-2564
33. A. Escosura-Muniz, C. Sanchez-Espinel, B. Diaz-Freitas, A. Gonzalez-Fernandez, M. Maltez-da Costa and A. Merkoci, *Anal. Chem.,* 2009, **81**, 10268-10274
34. D. Brambilla, J. Nicolas, B. Le Droumaguet, K. Andrieux, V. Marsaud, P. Couraud and P. Couvreur, *Chem. Commun.,* 2010, **46**, 2602-2604
35. D. Kim, Y. Jeong and S. Jon, *ACS Nano.,* 2010, **4**, 3689-3696
36. F. Tang, F. He, H. Cheng and L. Li, *Langmuir.,* 2010, **26**, 11774-11778
37. Z. Zhou, Y. Piao, L. Hao, G. Wang, Z. Zhou and Y. Shen, *Nanoscale,* 2019, **11**, 15907-15916
38. C. Argyo, V. Weiss, C. Brauchle and T. Bein, *Chem. Mater*., 2014, **26**, 435−451
39. J. Vivero-Escoto, I. Slowing, B. Trewy and V. Lin, *Small.,* 2010, **6**, 1952-1967
40. M. Liong, J. Lu, M. Kovochich, T. Xia, S. Ruehm, A. Nel, F. Tamanoi and J. Zink, *ACS Nano.,* 2008, **2**, 889-896
41. J. Lee, N. Lee, T. Kim, J, Kim and T. Hyeon, *Acc. Chem. Res.,* 2011, **44**, 893-902
42. S. Natarajan and S. Selvaraj, *RSC Adv.,* 2014, **4**, 14328-14334
43. B. Murugan, L. Narashimhan Ramana, S. Gandhi, S. Sethuraman and U. M. Krishnan, *J. Mater. Chem. B*., 2013, **1**, 3494–3505
44. Z. Li, J. Barnes, A. Bosoy, J. Stoddart and J. Zink, *Chem. Soc. Rev.,* 2012, **41**, 2590
45. P. Yang, S. Gai and J. Lin, J. *Chem. Soc. Rev.,* 2012, **41**, 3679-3698

46. W. Cheng, C. Liang, X. Wang, H. Tsai, G. Liu, Y. Peng, J. Nie, L. Huang, L. Mei and X. Zeng, *Nanoscale,* 2017, **9**, 17063-17073
47. X. Xu, C. Wu, A. Bai, X. Liu, H. Lv, Y. Liu, *J. Nanomater.,* 2017, **2017**, 2069685-2069698
48. D. Yang, N. Wang, H. Ji, S. Sun, J. Dong, Y. Zhong, C. Qian and H. Xu, *RSC Adv.,* 2018, **8**, 38987-38994
49. L. Li, W. Sun, L. Li, Y. Liu, L. Wu, F. Wang, Z. Zhou, Z. Zhang and Y. Huang, *Nanoscale,* 2017, **9**, 314-325
50. J. An, X. Yang, K. Cheng, X. Song, L. Zhang, C. Li, X. Zhang, Y. Xuan, Y. Song, B. Fang, X. Hou, Y. Zhao and B. Liu, *ACS Appl. Mater. Interfaces***.,** 2017**, *9***, 41748-41759
51. L. Hou, Y. Zheng, Y. Wang, Y. Hu, J. Shi, Q. Liu, H. Zhang and Z. Zhang, *ACS Appl. Mater. Interfaces.,* 2018, **10**, 21927-21938
52. Z. Tao, *RSC Adv.,* 2014, **4**, 18961-18980
53. A. Garcia-Fernandez, E. Aznar, R. Martinez-Manez and F. Sancenon, *Small.,* 2020, **16**, 1902242-1902304
54. J. Lu, M. Liong, J. Zink and F. Tamanoi, *Small*., 2007, **3**, 1341-1346
55. R. Narayan, U. Nayak, A. Raichur and S. Garg, *Pharmaceutics.,* 2018, **10**, 118-167
56. Y. Wang, Q. Zhao, N. Han, L. Bai, J. Li, J. Liu, E. Che L. Hu, Q. Zhang, T. Jiang and S. Wang, *Nanomedicine: NBM.,* 2015, **11**, 313-327
57. M. Vallet-Regi, F. Balas and D. Arcos, *Angew. Chem. Int. Ed.,* 2007, **46**, 7548-7558
58. C. Kresge, M. Leonowicz, W. Roth, J. Vartuli and J. Beck, *Nature.,* 1992, **359**, 710-712
59. M. Vallet-Regi, A. Ramila, R. P. del Real and J. Perez-Pariente, *Chem. Mater.,* 2001, **13**, 308-311
60. M. Varache, I. Bezverkhyy, L. Saviot, F. Bouyer, F. Baras and F. Bouyer, *J. Non-Cryst. Solids.,* 2015, **408**, 87-97
61. J. Cheng, Q. Ding, J. Wang, L. Deng, L. Yang, L. Tao, H. Lei and S. Lu, *Nanoscale.,* 2016, **8**, 2011-2021
62. S. Wu, Q. Deng, X. Huang and X. Du, *ACS Appl. Mater. Interfaces.,* 2014, **6**, 15217-15223
63. M. Martinez-Carmona, D. Lozano, M. Colilla and M. Vallet-Regi, *RSC Adv.,* 2016, **6**, 50923-50932
64. X. Zeng, G. Liu, W. Tao, Y. Ma, X. Zhang, F. He, J. Pan, L. Mei and G. Pan, *Adv. Funct. Mater.,* 2017, **27,** 1605985
65. J. Liu, X. Guo, Z. Luo, J. Zhang, M. Li and K. Cai, *Nanoscale*., 2018, **10**, 13737

66. S. Yang, D. Chen, N. Li, Q. Xu, H. Li, F. Gu, J. Xie and J. Lu, *Small*., 2016, **12**, 360
67. M. Babaei, K. Abnous, S. M. Taghdisi, S. A. Farzad, M. T. Peivandi, M. Ramezani and M. Alibolandi, *Nanomedicine.,* 2017, **12**, 1261
68. B. Gupta, H. Ruttala, B. Poudel, S. Pathak, S. Regmi, M. Gautam, K. Poudel, M. Sung, W. Ou, S. Jin, J. Jeong, S. Ku, H. Choi, C. Yong and J. Kim, *ACS Appl. Mater. Interfaces.,* 2018, **10,** 24392
69. P. Yin, T. Pongkulapa, H. Cho, J. Han, N. Pasquale, H. Rabie, J. Kim, J. Choi and K. Lee, *ACS Appl. Mater. Interfaces.,* 2018, **10**, 26954
70. J. Wang, D. Xu, T. Deng, Y. Li, L. Xue, T. Yan, D. Huang, D. Deng, *ACS Appl. Nano Mater.,* 2018, **1**, 1976
71. H. Xue, Z. Yu, Y. Liu, W. Yuan, T. Yang, J. You, X. He, R. Lee, L. Li and C. Xu, *Int. J. Nanomed.,* 2017, **12,** 5271
72. Y. Tian, R. Guo, Y. Jiao, Y. Sun, S. Shen, Y. Wang, D. Lu, X. Jiang and W. Yang, *Nanoscale Horiz.,* 2016, **1,** 480
73. H. Liu, X. Luan, H. Feng, X. Dong, S. Yang, Z. Chen, Q. Cai, Q. Lu, Y. Zhang, P. Sun, M. Zhao, H. Chen, J. Lovell and C. Fang, *Adv. Funct. Mater.,* 2018, **28**, 1801118
74. X. Chen, D. Li, A. Lin, J. Xu, L. Wu, H. Gu, Z. Huang, J. Liu, Y. Zhang and X. Yin, *Int. J. Nanomed.,* 2018, **13**, 3661
75. S. Zhao, M. Xu, C. Cao, Q. Yu, Y. Zhou and J. Liu, *J. Mater. Chem. B.*, 2017, **5**, 6908
76. S. Y. Tan, C. Teh, C. Y. Ang, M. Li, P. Li, V. Korzh ans Y. Zhao, *Nanoscale* 2017, **9**, 2253
77. D. Shao, M. Li, Z. Wang, X. Zheng, Y. Lao, Z. Chang, F. Zhang, M. Lu, J. Yue, H. Hu, H. Yang, L. Chen, W. Dong and K. Leong, *Adv. Mater.,* 2018, **30**, 1801198
78. J. Xu, X. Wang, Z. Teng, G. Lu, N. He and Z. Wang, *ACS Appl. Mater. Interfaces.,* 2018, **10**, 24440
79. Y. Zhang, K. Ren, X. Zhang, Z. Chao, Y. Yang, D. Ye, Z. Dai, Y. Liu and H. Ju, *Biomaterials.,* 2018, **163**, 55
80. M. Xuan, J. Shao, J. Zhao, Q. Li, L. Dai and J. Li, *Angew. Chem. Int. Ed.,* 2018, **57**, 6049
81. C. Lai, B. Trewyn, D. Jeftinija, K. Jeftinija, S. Xu, S. Jeftinija and V. Lin, *J. Am. Chem. Soc.,* 2003, **125**, 4451–4459
82. Z. Zhang, D. Balogh, F. Wang, S. Sung, R. Nechushtai and I. Willner, *ACS Nano*., 2013, **7**, 8455–8468

83. F. Muhammad, W. Qi, A. Wang, J. Gu, J. Du and G. Zhu, *J. Mater. Chem. B.,* 2015, **3**, 1597-1604
84. H. Y. Lu, Y. J. Chang, N. C. Fan, L. S. Wang, N. C. Lai, C. M. Yang, L. C. Wu and J. A. Ho, *Biomaterials.,* 2015, **42**, 30-41
85. A. Renner, S. Ilyas, H. Shlosser, A. Szymura, S. Roitsch, K. Wennhold and S. Mathur, *Langmuir.,* 2020, **36**, 14819-14828
86. Y. Chen, H. Chen and J. Shi, *Adv. Mater*., 2013, **25**, 3144
87. B. Ruuhle, M. Davies, T. Lebold, C. Braüchle and T. Bein, *ACS Nano.,* 2012, **6**, 1948
88. F. Zheng, W. Xiong, S. Sun, P. Zhang and J. Zhu, *Nanophotonics.,* 2019, **8**, 391-413
89. J. Lai, B. Shah, E. Garfunkel and K. Lee, *ACS Nano.,* 2013, **7**, 2741–2750
90. R. Wang, L. Zhou, W. Wang, X. Li and F. Zhang, *Nat. Commun.,* 2017, **8**, 14702
91. S. Valetti, J. Wankar, M. Ericson, A. Feiler and I. Manet, *J. Mater. Chem. B.,* 2017, **5**, 3201–32011
92. Z. Xu , S. Liu, Y. Kang and M. Wang, *Nanoscale.,* 2015, **7**, 5859-5868
93. Y. Piao, A. Burns, J. Kim, U. Wiesner and T. Hyeon, *Adv. Funct. Mater*., 2008, **18**, 3745-3758
94. W. Stober, A. Fink and E. Bohn, *J. Colloid. Interface. Sci*., 1968, **26**, 62-69
95. A. Blaaderen, J. Geest and A. Vrij, *J. Colloid. Interface. Sci*., 1992, **154**, 481-501
96. D. Lewis, V. Dore, N. Rogers, T. Mole, G. Nash, P. Angeli and Z. Pikramenou, *Langmuir.,* 2013, **29**, 14701-14708
97. D. Zhang, Z. Wu, J. Xu, J. Liang, J. Li and W. Yang, *Langmuir.,* 2010, **26**, 6657-6662
98. M. Montalti, L. Prodi, E. Rampazzo and N. Zaccheroni, *Chem. Soc. Rev.,* 2014, **43**, 4243-4268
99. L. Rossi, L. Shi, F. Quina and Z. Rosenzweig, *Langmuir.,* 2005, **21**, 4277-4280
100. L. Li, Y. Guan, H. Liu, N. Hao, T. Liu, X. Meng, C. Fu, Y. Li, Q. Qu, Y. Zhang, S. Ji, L. Chen, D. Chen and F.Tang, *ACS Nano.,* 2011, **5**,7462—7470
101. H. Liu, D. Chen, L. Li, T. Liu, L. Tan, X. Wu and F. Tang, *Angew. Chem. Int. Ed*., 2011, **50,** 891—895
102. E. Yan, Y. Fu, X. Wang, Y. Ding, H. Qian, C. Wang, Y. Hu, X. Jiang, *J. Mater. Chem*., 2011, **21,** 3147—3155
103. K. Hu, K. Hsu and C. Yeh, *Biomaterials*., 2010, **31**, 6843—6848

104. F. Chi, Y. Guo, J. Liu, Y. Liu and Q. Huo, *J. Phys. Chem. C.,* 2010, **114**, 2519—2523
105. L. Accomasso, E. Rocchietti, S. Raimondo, F. Catalano, G. Alberto, A. Giannitti, V. Minieri, V. Turinetto, L. Orlando, S. Saviozzi, G. Caputo, S. Geuna, G. Martra and C. Giachino, *Small.,* 2012, **8**, 3192—3200
106. P. Sharma, N. Bengtsson, G. Walter, H. Sohn, G. Zhou, N. Iwakuma, H. Zeng, S. Grobmyer, E. Scott and B. Moudgil, *Small*., 2012, **8**, 2856—2868
107. K. Hayashi, M. Nakamura and K. Ishimura, *Chem. Commun*., 2012, **48**, 3830—3832
108. M. Helle, E. Rampazzo, M. Monchanin, F. Marchal, F. Guillemin, S. Bonacchi, F. Salis, L. Prodi and L. Bezdetnaya, *ACS Nano*., 2013, **7**, 8645–8657
109. E. Rampazzo, F. Boschi, S. Bonacchi, R. Juris, M. Montalti, N. Zaccheroni, L. Prodi, L. Calderan, B. Rossi, S. Becchi and A. Sbarbati, *Nanoscale*., 2012, **4**, 824–830
110. A. Bumb, C. Regino, M. Perkins, M. Bernardo, M. Ogawa, L. Fugger, P. Choyke, P. Dobson and M. Brechbiel, *Nanotechnology*., 2010, **21**, 175704
111. J. Kim, Y. Kim, J. Kim, K. Kang, E. Tae, H. Youn, D. Kim, S. Kim, J. Kwon, M. Cho, Y. Lee, J. Jeong, J. Chung and D. Lee, *Nanomedicine*., 2012, **7**, 219–229
112. Y. Yeh, B. Creran and V. Rotello, *Nanoscale.,* 2012, **4**, 1871-1880
113. M. Faraday, *Philos. Trans. R. Soc. London*., 1857, **147**, 145–181
114. E. Boisselier and D. Astruc, *Chem. Soc. Rev.,* 2009, **38**, 1759 – 1882
115. D. Lewis and Z. Pikramenou, *Coord. Chem. Rev.,* 2014, **273-274**, 213-225
116. A. Davies, D. Lewis, S. Watson, S. Thomas and Z. Pikramenou, *PNAS.,* 2012, **109**, 1862-1867
117. N. Rogers, S. Claire, R. Harris, S. Farabi, G. Zikeli, I. Styles, N. Hodges and Z. Pikramenou, *Chem Comm.,* 2014, **50**, 617-619
118. S. Comby, E. Surender, O. Kotova, L. Truman, J. Molloy, and T. Gunnlaugsson, *Inorg. Chem.,* 2014, **53**, 1867-1879
119. F. Dumur, E. Dumas and C. Mayer, *Nanomaterials.,* 2020, **10**, 548
120. A. Jungemann, N. Feliu, I. Bakaimi, M. Hamaly, A. Alkilany, I. Chakraborty, A. Masood, M. Casula, A. Kostopoulou, E. Oh, K. Susumu, M. Stewart, I. Medintz, E. Stratakis, W. Parak and A. Kanaras, *Chem. Rev.,* 2019, **119**, 4819–4880
121. P. Selvakannan, S. Mandal, R. Pasricha, S. Adyanthaya, M. Sastry, *Chem. Commun.,* 2002, **13**, 1334–1335
122. H. Yao, O. Momozawa, T. Hamatani and K. Kimura, *Chem. Mater., 2001*, **13**, 4692–4697

123. H. Zhang, S. Evans, J. Henderson, R. Miles and T. Shen, *J. Phys. Chem. B.,* 2003, **107**, 6087–6095
124. M. Dzwonek, D. Załubiniak, P. Piatek, G. Cichowicz, S. Meczynska-Wielgosz, S. Stepkowski, M. Kruszewski, A. Wieckowska and R. Bilewicz, *RSC Adv.,* 2018, **8**, 14947–14957
125. H. Fujihara and H. Nakai, *Langmuir.,* 2001, **17,** 6393–6395
126. C. Hanske, M. Sanz-Ortiz and L. Liz-Marzán, *Adv. Mater.,* 2018, **30**, 1707003
127. R. Stiles, R. Balasubramanian, S. Feldberg and R. Murray, *J. Am. Chem. Soc.,* 2008, **130**, 1856–1865
128. N. Rogers, H. Jeffery, S. Claire, D. Lewis, G. Zikeli, N. Hodges, S. Egginton, G. Nash and Z. Pikramenou, *Nanomedicine.,* 2017, **12**, 2725-2740
129. S. King, S. Claire, R. Tiexeira, A. Dosumu, A. Carrod, H. Dehgani, M. Hannon, A. Ward, R. Bricknell, S. Botchway, N. Hodges and Z. Pikramenou, *J. Am. Chem. Soc.,* 2018, **140,** 10242-10249
130. A. Dosumu, S. Claire, L. Watson, P. Girio, S. Osborne, Z. Pikramenou and N. Hodges, *J. Am. Chem. Soc. Au.,* 2021, **1**, 174-186
131. S. Sung, H. Holmes, L. Wainwright, A. Toscani, G. Stasiuk, A. White, J. Bell, J. Wilton-Ely, *Inorg. Chem.,* 2014, **53**, 1989–2005
132. D. Lewis, T. May, J. MacPherson and Z. Pikramenou, *Chem. Commun.,* 2006, 1433-1435
133. J. Bunzli, *Coord. Chem. Rev.,* 2015, **293-294**, 19-47
134. J. Bunzli and S. Eliseeva, *Chem. Sci.,* 2013, **4**, 1939–1949
135. S. Shionoya and W. Yen, Phosphor Handbook, CRC Press Inc., Boca Raton, FL, 1999
136. J. Van Vleck*, J. Phys. Chem*., 1937, **41**, 67–80
137. B. Judd, *Phys. Rev.,* 1962, **127**, 750
138. G. Ofelt, *J. Chem. Phys.,* 1962, **37**, 511–520
139. F. Auzel, *C.R. Acad. Sci. Paris Ser. B.,* 1966, **262**, 1016
140. F. Auzel, *Chem. Rev.*, 2004, **104**, 139–173
141. Q. Liu, W. Feng and F. Li, *Coord. Chem. Rev*., 2014, **273**, 100-110
142. B. Liu, C. Li, D. Yang, Z. Hou, P. Ma, Z. Cheng, H. Lian, S. Huang and J. Lin, *Eur. J. Inorg. Chem.*, 2014, **2014**, 1906–1913
143. E. Soini and H. Kojola*, Clin. Chem.*, 1983, **29**, 65–68
144. R. Mears, L. Reekie, S. Poole and D. Payne, *Electron. Lett*., 1986, **22,** 159–160

145. J. Bunzli, *Chem. Rev.,* 2010, **110**, 2729-2755
146. J. Bunzli, *J. Lumin.,* 2016, **170**, 866-878
147. J. Monteiro, *Molecules.,* 2020, **25**, 2089-2123
148. R. Teo, J. Termini and H. Gray, *J. Med. Chem.,* 2016, **59**, 6012-602419
149. P. D'Angelo, A. Zitolo, V. Migliorati, G. Chillemi, M. Duvail, P. Vitorge, S. Abadie and R. Spezia, *Inorg. Chem.,* 2011, **50**, 4752-4759
150. S. Eliseeva and J. Bunzli, *Chem. Soc. Rev.,* 2010, **39**, 189-227
151. J. Bunzli and C. Piguet, *Chem. Rev.,* 2002, **102**, 1897-1928
152. J. Rees, G. Deblonde, D. An, C. Ansoborlo, S. Gauny, R. Abergel, *Sci. Rep.,* 2018, **8**, 4419-4428
153. D. Lewis and Z. Pikramenou, *Coord. Chem. Rev.,* 2014, **273-274**, 213-225
154. J. Bunzli, *Eur. J. Inorg. Chem.,* 2017, 5058-5063
155. J. Bunzli, *Acc. Chem. Res.,* 2006, **39**, 53-61
156. K. Binnemans, *Coord. Chem. Rev.,* 2015, **295**, 1-45
157. J. Moore, R. Lord, G. Cisneros and M. Allen, *J. Am. Chem. Soc.,* 2012, **134**, 17372-17375
158. S. Weissman, *J. Chem. Phys.,* 1942, **10**, 214-217
159. D. Manna and T. Ghanty, *Phys. Chem. Chem. Phys.,* 2012, **14**, 11060-11069
160. Y. Ning and M Zhang, *Coord. Chem. Rev.,* 2019, **399**, 1-19
161. J. Bunzli and S. Eliseeva, *Ln Luminescence.,* 2010, **7**, 1-45
162. J. Bunzli, *Coord. Chem. Rev.,* 2015, **293-294**, 19-47
163. J. Bunzli and C. Piguet, *Chem. Soc. Rev.,* 2005, **34**, 1048-1077
164. M. Rajendran, E. Yapici and L. Miller, *Inorg. Chem.,* 2014, **53**, 1839-1853
165. Y. Hasegawa, Y. Kimura, K. Murakoshi, Y. Wada, J. Kim, N. Nakashima, T. Yamanaka and S. Yanagida, *J. Phys. Chem.,*1996, **100**, 10201–10205
166. Y. Hasegawa, Y. Wada and S. Yanagida*, J. Photochem. Photobiol. C: Photochem. Rev.,* 2004, **5,** 183–202
167. L. Winkless, R. Tan, Y. Zheng, M. Motevalli, P. Wyatt and W. Gillin, *Appl. Phys. Lett.,* 2006, **89,** 111115
168. A. Bettencourt-Dias and J. Rossini, *Inorg. Chem.,* 2016, **55**, 9954-9963
169. J. Andres and K. Borbas, *Inorg. Chem*., 2015, **54**, 8174−8176
170. M. Berwick, D. Lewis, A. Jones, R. Parslow, T. Dafforn, H. Cooper, J. Wilkie, Z. Pikramenou, M. Britton and A. Peacock, *J. Am. Chem. Soc.,* 2014, **136**, 1166−1169

171. E. Trivedi, S. Eliseeva, J. Jankolovits, M. Olmstead, S. Petoud and V. Pecoraro, *J. Am. Chem. Soc*., 2014, **136**, 1526−1534
172. J. Routledge, M. Jones, S. Faulkner and M. Tropiano, *Inorg. Chem*., 2015, **54**, 3337−3345
173. A. Bettencourt-Dias, *Dalton Trans.,* 2007, 2229−2241
174. H. Xu, Q. Sun, Z. An, Y. Wei and X. Liu, *Coord. Chem. Rev*., 2015, **293−294**, 228−249
175. Y. Hasegawa and T. Nakanishi., *RSC Adv*., 2015, **5**, 338−353
176. H. Meng, *Polym. Electron*., 2013, 37−63
177. L.Ying, C. Ho, H. Wu, Y. Cao and W. Wong, *Adv. Mater*., 2014, **26**, 2459−2473
178. X. Wang, H. Chang, J. Xie, B. Zhao, B. Liu, S. Xu, W. Pei, N. Ren, L. Huang and W. Huang, *Coord. Chem. Rev*., 2014, **273–274**, 201−212
179. J. Lehr, P. D. Beer, S. Faulkner and J. Davis, *Chem. Commun*., 2014, **50**, 5678−5687
180. G. Zucchi, O. Maury, P. Thuery, F. Gumy, J. Bünzli, M. Ephritikhine, *Chem. Eur. J*., 2009, **15,** 9686–9696
181. P. Hermann, J, Kotek, V. Kubicek and I. Lukes, *Dalton Trans.,* 2008, 3027-3047
182. N. Shavaleev, S. Eliseeva, R. Scopelliti and J. Bünzli, *Chem. Eur. J.,* 2009, **15**, 10790-10802
183. M. Soulie, F. Latzko, E. Bourrier, V. Placide, S. Butler, R. Pal, J. Walton, P. Baldeck, B. Le Guennic, C. Andraud, J. Swier, L. Lamarque, D. Parker and O. Maury, *Chem. Eur. J*., 2014, **20**, 8636–8646
184. X. Wei, L. Yang, S. Liao, M. Zhang, J. Tian, P. Du, W. Gu and X. Liu, *Dalton Trans*., 2014, **43**, 5793–5800
185. C. Chow, S. Eliseeva, E. Trivedi, T. Nguyen, J. Kampf, S. Petoud and V. Pecoraro, *J. Am. Che. Soc.,* 2016, **138**, 5100-5109
186. E. Deiters, B. Song, A. Chauvin, C. Vandevyver, F. Gumy and J. Bünzli, *Chem. Eur. J.,* 2009, **15**, 885–900
187. S. Eliseeva, G. Aubeck, F. Mourik, A. Cannizzo, B. Song, E. Deiters, A. Chauvin, M. Chergui and J. Bunzli, J*. Phys. Chem. B.,* 2010, **114,** 2932
188. B. Alpha, J. Lehn and G. Mathis, *Angew. Chem*., 1987, **99**, 259-266
189. S. Petoud, S. Cohen, J. Bunzli, and K. Raymond, J*. Am. Chem. Soc*., 2003, **125**, 13324
190. A. Bour-Dolle, M. Allali, J. Mulatier, B Le Guennic, J. Zwier, P. Baldeck, J. Bunzli, C. Andraud, L. Lamarque and O. Maury, *Inorg. Chem*., 2011, **50**, 4987
191. V. Mukkala, C. Sund, M. Kwiatkowski, P. Pasanen, M. Hogberg, J. Kankare and H. Takalo, *Helv. Chim. Acta.,* 1992, **75**, 1621-1623

192. G. Piszczek, B. Maliwal, I. Gryczynski, J. Dattelbaum and J. Lakowicz, J. *Fluoresc*., 2001, **11**, 101–107
193. P. Kadjane, M. Starck, F. Camerel, D. Hill, N. Hildebrandt, R. Ziessel and L. J. Charbonniere, *Inorg. Chem*., 2009, **48**, 4601
194. N. Katia, A. Lecointre, M. Regueiro-Figueroa, C. Platas-Iglesias and L. Charbonniere, *Inorg. Chem*., 2011, **50**, 1689
195. M. Starck, P. Kadjane, E. Bois, B. Darbouret, A. Incamps, R. Ziessel and L. Charbonniere, *Chem. Eur. J.*, 2011, **17**, 9164 – 9179
196. M. Li and P. Selvin, *J. Am. Chem. Soc*., 1995, **117**, 8132
197. Y. Bretonniere, M. Cann, D. Parker and R. Slater, *Org. Biomol. Chem*., 2004, **2**, 1624 – 1632
198. T. Zhang, X. Zhu, C. Cheng, W. Kwok, H. Tam, J. Hao, D. Kwong, W. Wong and K. Wong, *J. Am. Chem. Soc*., 2011, **133**, 20120–20122
199. L. Aboshyan-Sorgho, H. Nozary, A. Aebischer, J. Bunzli, P. Morgantini, K. Kittilsved, A. Hauser, S. Eliseeva, S. Petoud and C. Piguet, *J. Am. Chem. Soc*., 2012, **134,** 12675–12684
200. H. Huang, S. Barua, G. Sharma, S. Dey and K. Rege, *J. Control. Release.,* 2011, **155**, 344-357
201. P. Chen, S. Mwakari and A. Oyelere, *Nanotechnol. Sci. Appl.,* 2008, **2**, 45-65

2. Luminescent Silica Nanoparticles for Drug Delivery and Detection

2.1. Introduction

2.1.1. Camptothecin – An Anticancer Drug

CPT is a naturally occurring, highly hydrophobic alkaloid acting as an anticancer drug. Its anticancer properties and potency, came about after its discovery and isolation from a Chinese tree, *Camptotheca acuminata* Decne, in the 1966. The discovery of CPT, in search for steroids, occurred during screening of a large amount of plants, where each of the samples were tested for antibacterial, antitumour and antiviral activity[1-3].

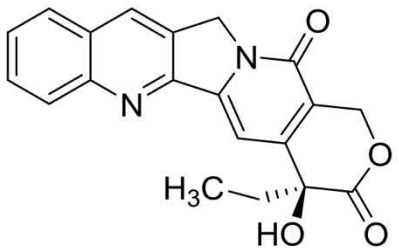


Figure 2.1.11
Structure of CPT.

CPT's Target and How It Can Cause Apoptosis

CPT, and its derivatives, are unique for various reasons, but the first and most important being that it only has one known target. Nuclear DNA topoisomerase 1 (TOP 1) is an enzyme that cleaves one strand of DNA and is the only known target for CPT. TOP 1 enzymes are needed in order to relax supercoiled DNA and is essential for DNA replication and transcription. TOP 1 enzymes form a cleavage complex which occurs during a cleavage reaction in the process of relaxing supercoiled DNA. During this reaction TOP 1 enzymes are vulnerable to inhibitors such as CPT. Inhibitors can cause collisions between DNA replication forks and cleavage

complexes, leading to formation of long lived TOP 1 – DNA complexes that can be trapped by CPT. These collisions can leads to breaking of the DNA strand, arresting DNA fork replications, and breaking down the TOP 1 – DNA bond, leading to apoptosis[2, 4].

Moreover, the cytotoxic activity of CPT can also be completely inactivated in presence of basic conditions[2]. CPT molecules can penetrate cells easily and are able to target the TOP 1 enzyme within minutes after exposure[4]. In addition, CPT was selected as an anticancer drug based on its selectivity, as opposed to its potency. CPT molecules have low affinities for TOP 1 enzymes and usually are high drug concentrations are required for trapping the enzyme, but it selectively only targets the TOP 1 enzyme[2].

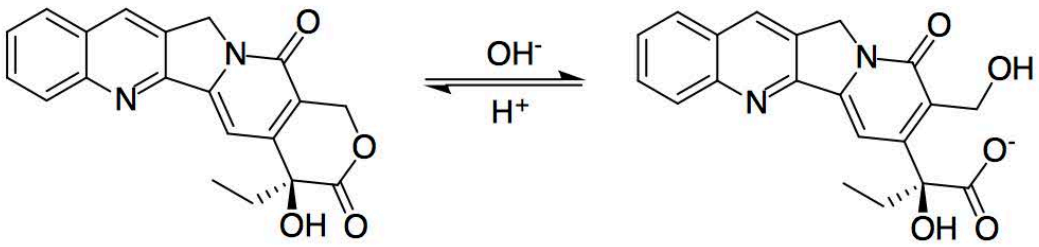


Figure 2.1.12

Reaction scheme of the reversible hydrolysis of the lactone form to the open ringed carboxylate taken from Pommier[5].

Despite the unique features that make CPT and its derivatives an attractive anticancer drug, it has some limitations. In order for DNA damage TOP 1 cleavage complexes need to live long enough for this, but is limited by the fast diffusion of CPT from TOP 1 cleavage complexes. Therefore, in order to remain as cleavage complexes for long enough, CPT doses must be given for a prolonged period of time. Another limitation involves side effects produced by CPT, and limits dosages that can be given safely to patients. Thirdly, as mentioned, the active lactone can readily convert into the inactive carboxylate, and is actually known to bind strongly to serum albumin[4].

CPT Derivatives

Despite encouraging toxicity results from early clinical trials, severe side effects such as myelosuppression, diarrhoea and hemorrhagic cystitis were observed. In addition, before the 1970s, sufficient information on CPT's mechanism of action was not known. Poor water solubility issues of the hydrophobic drug were also said to be a possible cause for the observed toxicity in trials. Water soluble salts of CPT were developed enabling direct administration, but however showed losses in antitumour activity due to the chemical modifications[1, 8].

To date, there are two CPT derivatives used clinically, topotecan hydrochloride (Hycamtin) and irinotecan hydrochloride (Camptostar). They are FDA approved, the former by GlaxoSmithKline, and latter by Pfizer. They are both water soluble CPT derivatives and can be infused intravenously. Hycamtin is used for treatment against metastatic ovarian cancer, and Camptostar for metastatic colorectal cancer[2-4, 9]. Onivyde, a nanosystem developed to deliver irinotecan using liposomes was FDA approved in 2015 for the treatment of pancreatic cancer, and has been tested for other malignancies[3, 10]. There have been major advances in the field of nanomedicine for developing SDDS revolutionising diagnostics and therapeutics in cancer treatments by delivering drugs controllably, in stable systems, in addition to multimodal functionalities. This has been seen across the field with other drugs, such as paclitaxel. Abraxane is a formulation of paclitaxel loaded albumin NPs, FDA approved, for treating metastatic breast cancer[2].

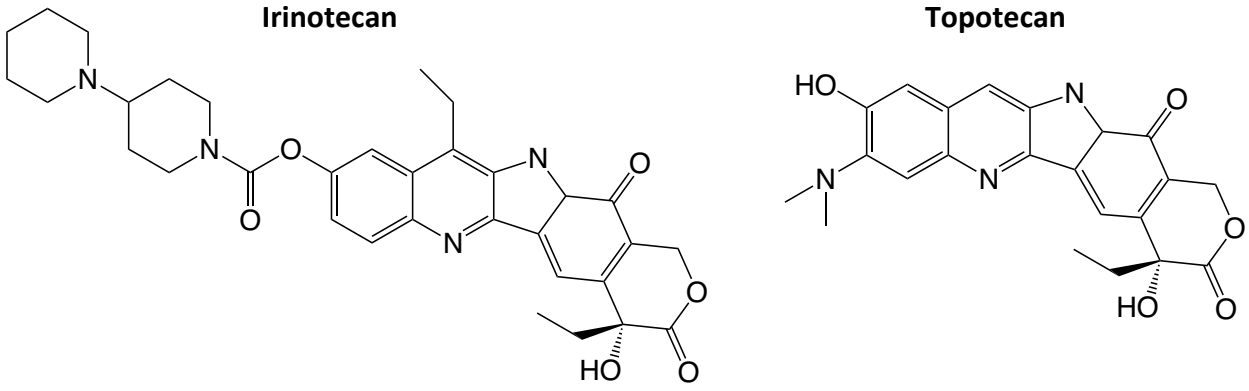


Figure 2.1.13

Structures of CPT derivatives irinotecan and topotecan.

All limitations associated with CPT (free drug biodegradability, deficient biodistribution and unfavourable pharmacokinetics) can be overcome by nanomedicine[6]. Nanomedicine offers a platform where water solubility issues and biocompatibility can be improved, as well as prolonging the time periods for anticancer drugs in the body, and hence improving accumulation of drugs at tumour sites[3].

2.1.2. Targeted Delivery of CPT Using Nanocarriers

Similarly, nanocarrier systems for delivery of CPT have been explored extensively which have included three main categories: carrier aided delivery systems, prodrug coupled delivery of CPT, and carrier free nanodrug delivery systems[3].

Carrier Aided Drug Delivery Systems

Usually, loss of drug activity arises from fast metabolism of the drugs in the body and effectivity is reduced. Carried aided drug delivery systems can enhance the therapeutic effect of the drug through intravenous administration and hence accumulation in the body can be improved. Several nanocarriers with different sizes and structures have been developed, including liposomes, NPs (polymeric, inorganic, metal NPs, iron oxide NPs and carbon nanotubes)[3, 11]. Surface modification of these nanocarriers has also been shown to enhance biodistribution of the carriers.

Table 2.1.21

Summary of some carrier aided drug delivery systems for CPT derivatives that have been trialled[3].

Product Name	Nanocarrier System	Drug	Treatment
IHL-205 (Yakult Honsha)[12]	Liposome	Irinotecan	Solid tumours
INX-0076 (Brakiva, Tekmira)[13]	Liposome	Topotecan	Solid tumours
CRLX-101 (Cerulean Pharma)[14]	Cyclodextrin nanoparticle	Camptothecin	Solid tumours, renal cell
Lipotecan (TLC388) (Taiwan Liposome)[15]	Polymeric micelle	TLC388 – CPT derivative	Carcinoma, rectal cancer, non-small cell lung cancer, liver cancer, renal cancer
NK-012 (Nippon Kayaku)[16]	PEG polymeric micelle	SN-38 – active metabolite of irinotecan	Solid tumours, small cell lung cancer, breast cancer

Polymer functionalised nanocarriers for delivering CPT based on natural polymers and synthetic polymers have been used[17, 18]. Lipid based nanocarriers utilising liposomes have also been extensively used[3, 10, 12, 13]. Their unique structure enables loading of drugs into hydrophobic pockets with hydrophilic environments. Moreover, inorganic NPs have widely been used as they provide diagnostic tools with abilities to facilitate techniques such as imaging, and simultaneous delivery[19-23].

Prodrug Coupled Drug Delivery Systems

Prodrugs are modified versions of drugs compounds that can be converted into their active forms after exposure to specific environments or triggers[2, 3]. Nanodrugs can be formed through $\pi-\pi$ conjugation of hydrophobic drugs via hydrogen bonding, and there have been

studies using CPT to create nanofibers through this interaction[2, 24]. Some of other examples of prodrug coupled delivery of CPT and its derivatives have been summarised in table 2.1.22.

Table 2.1.22

Summary of some prodrug coupled drug delivery systems for CPT derivatives that have been trialled[3].

Product Name	Nanocarrier System	Drug	Treatment
CT-2106 (CTI Biopharma)[25]	Nanoparticle and polyglutamic acid drug conjugate	Camptothecin	Colon cancer, ovarian cancer
MAG_CPT (Pfizer)[26]	Nanoparticle and (2-hydroxypropyl)methacrylamide drug conjugate	Camptothecin	Solid tumours
NKTR-102 (Nektra)[27]	Nanoparticle and PEG drug conjugate	Irinotecan	Breast cancer, ovarian cancer, colorectal cancer

Carrier Free Drug Delivery Systems

Despite the advantages nanocarriers bring for targeted drug delivery, they can be limited due to safety issues, as well as to the zero therapeutic activity of the actual carriers themselves. It has been reported that some systems can cause high toxicity and inflammation in the kidneys, which has led to developing other strategies without the use of carriers[3, 28, 29]. Nanodrugs with ability to form via self-assembly of drug molecules has been a key strategy for this[30, 31].

2.1.3. CPT Delivery Using MSNs

The incorporation of CPT into MSN designs has been studied by several groups previously, investigating many factors such CPT cytotoxicity from the SDDS systems, cellular uptake and any enhancement through application of targeting ligands, studying controlled release stimulated by triggers, and monitoring drug release.

Tamanoi *et. al.* have studied the incorporation of CPT in MSN structures extensively. They have achieved drug delivery to a range of human cancer cell lines showing the promising uses of MSNs as nanocarriers[32, 46-48]. Their study was a significant report of demonstrating antitumour drug delivery using MSNs, in addition to showing significant tumour suppression in mice treated with CPT loaded MSNs. They later investigated targeting effects using CPT loaded MSNs functionalised with FA[46]. Through surface modification with FA they observed enhanced potency suppressing tumours.

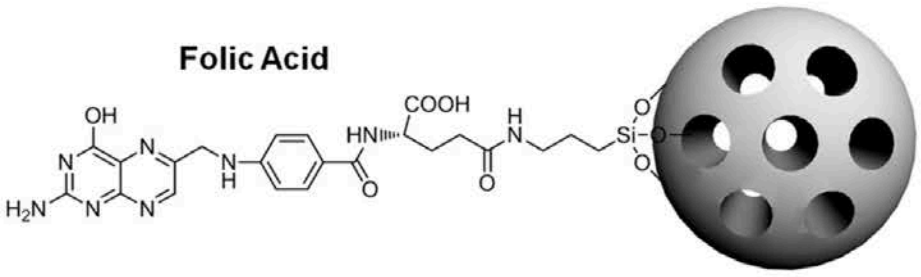


Figure 2.1.31

Illustration of FA modified MSNs by Tamanoi *et. al.,* image is taken from Tamanoi *et. al*[46].

Modification of MSN surfaces with targeting ligands such as FA has become a widely used strategy particularly for improving cellular uptake, and thus increased CPT effect[46, 48, 49]. MSN models modified with hyaluronic acid (HA) have also been studied with CPT encapsulation inside the pores. HA selectively targets cancer cells which overexpress the CD44 protein, and thus, HA modified MSNs can lead to fast uptake through receptor mediated endocytosis[46, 50].

Great attention has focused on CPT delivery through overexpression of biomolecules in cancer cells, leading to dissociation of linkages and hence CPT release. Disulphide-based SDDS have particularly grown much attraction, owing to intracellular GSH triggered release. Some examples have demonstrated designs of MSNs with CPT covalently linked, compared to adsorption of free drug molecules in the pores for controlled release[51, 52].

Botella *et. al.* designed SDDS using MSNs in order to investigate when, where, and how CPT was released into cells. Synthesised derivatives of CPT were linked through a disulphide bond to rhodamine loaded MSNs. When in presence of intracellular GSH, drug release was triggered through cleavage of the disulphide link, and showed NP stability when in absence of GSH[52]. Miao *et. al.* reported the SDDS utilising MSNs and manganese oxide coated superparamagnetic iron oxide NPs (SPIONs) as caps on MSN pores regulating CPT release. Simultaneously, they also achieved to create a diagnostic effect arising from the SPIONs, achieving MRI imaging for diagnosis and tracking therapeutic effects[53].

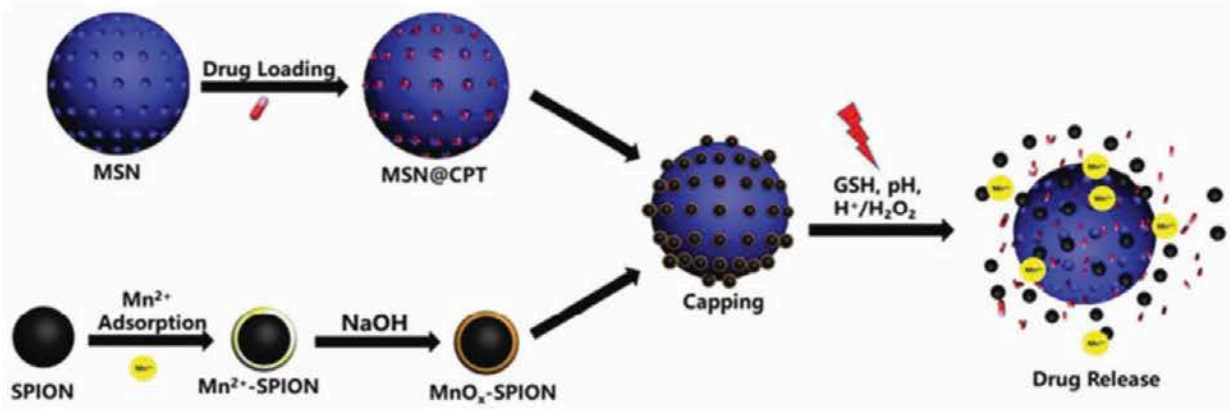


Figure 2.1.32

Schematic illustration of SDDS formed using MSNs and SPIONs with CPT encapsulation in pores, in order to perform controlled drug release when in presence of GSH. Image is taken from Gao *et. al.*[51].

MSN systems carrying CPT have also been studied for synergistic effects through combination chemotherapy. This principle involves the co-delivery of multiple anticancer drugs, with independent mechanisms of action, in order to achieve enhanced therapeutic effect. SDDS aimed for release of combined anticancer drugs involving CPT has commonly been studied with DOX. The therapeutic combination of CPT and DOX has grown much interest as they are

both TOP inhibitors (TOP1 and TOP2 respectively), therefore leading to enhanced chemotherapy[54-59].

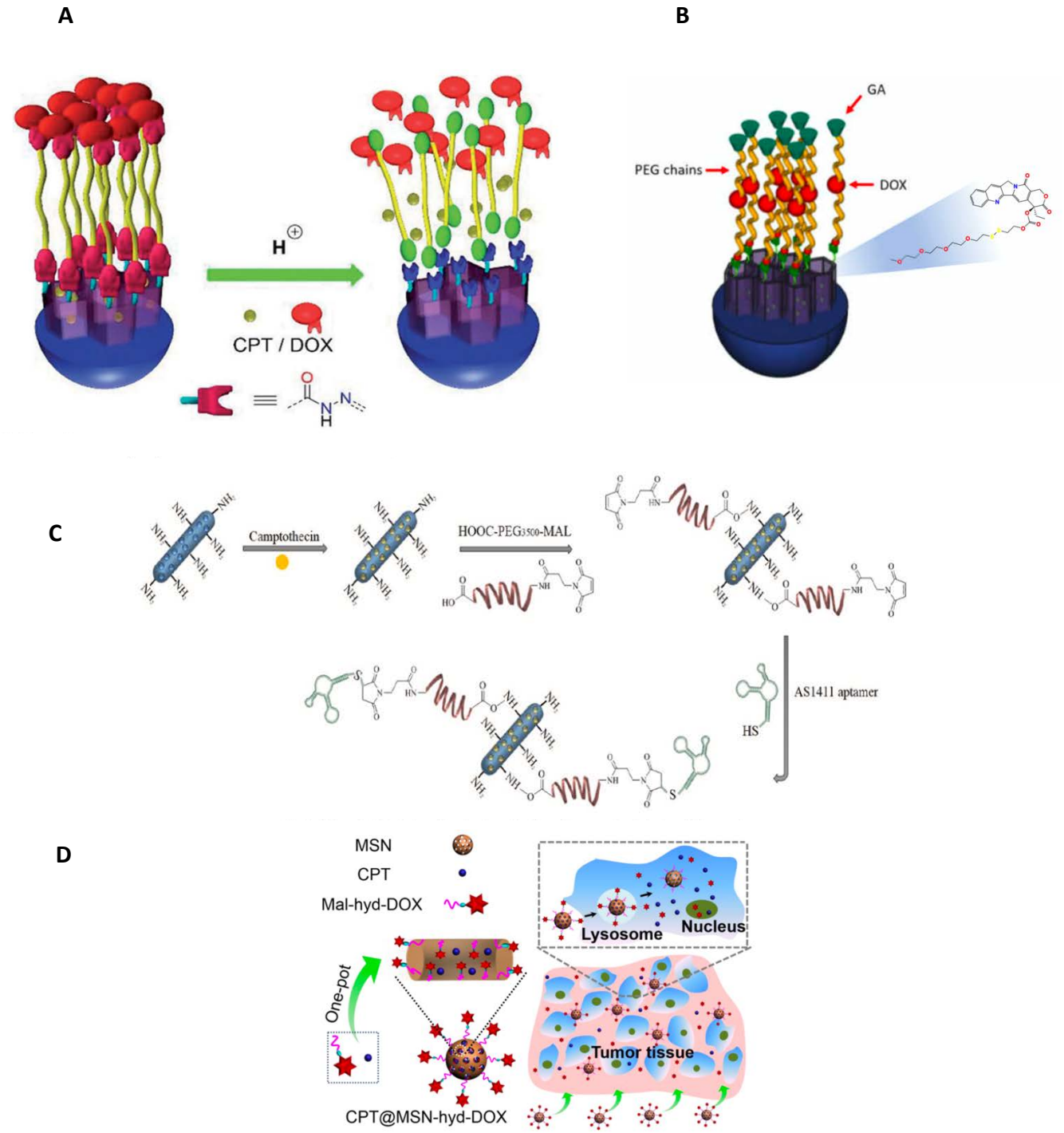


Figure 2.1.33

Examples of SDDS utilising MSNs for codelivery of CPT and DOX. A: Schematic illustration of pH responsive MSNs with CPT loaded in pores, and DOX attached to the MSN surface acting as a cap sensitive to acidic environments triggering release[54]. B: Schematic illustration of MSNs modified with glycrrhetinic acid (GA), PEG and DOX, with CPT loaded pores. At acidic pH, PEG chains are cleaved, triggering DOX and CPT release[55]. C: Schematic illustration of rod shaped MSNs loaded with CPT and surviving shRNA expressing plasmid (iSur DNA), and surface tagged with As1411 DNA aptamers[56]. D: Schematic illustration of CPT loaded MSNs modified with DOX, and release stimulated by pH response[57].

These examples commonly have shown triggered drug release through pH sensitive environments[54, 55, 57]. Interestingly, Alibolandi *et. al.* created SDDS with rod shaped MSNs for the codelivery of CPT and iSur (figure 2.1.33, C). CPT was loaded into PEGylated rod shaped MSNs with iSur, and the surface was tagged with a DNA aptamer for enhanced cellular uptake. Their choice of NP shape aimed to enhance uptake and drug loading due to high aspect ratios of rod shaped NPs. The larger surface area allows more interaction with cells hence enabling enhanced cellular uptake, in addition to the surface tagged with DNA aptamers. They observed a significant tumour growth suppression with their system in tumour bearing mice and improved survival rate[57].

It is clear that MSNs have been extensively used as nanocarriers for CPT, improving free CPT limitations arising from solubility issues and hydrophobicity[32, 36, 46-61, 62, 63, 65].

2.1.4. MSNs Functionalised with Lanthanide Complexes as Imaging Labels

The use of luminescent labels, as mentioned previously, has presented the opportunity for SDDS to perform diagnostic techniques to assess tumour sizes and locations, but also assessments of therapeutic effects from drug delivery treatments. A diverse range of luminescent labels have been used commonly from organic dyes to transition metal complexes. The emergence of Ln ions as luminescent labels for SDDS have brought about many advantages over other labels. Their advantages as luminescent labels in biological systems, and their unique *f* block chemistry giving rise to these properties are explained in section 1.5.2.

The ease of surface modification of silica NPs has allowed SDDS platforms to grow multifunctional NP systems, from application of therapeutic effects from drug delivery to enhanced efficacy from targeting ligands, and the ability to investigate properties of these systems through diagnostic markers. The development of multifunctional SDDS has attractive properties but remains a challenge in incorporating several diagnostic markers such as magnetic imaging and optical imaging labels. Previous efforts have involved organic dyes bringing luminescent properties to MSN systems, and iron oxide NPs bringing magnetic properties. Limitations however of these strategies include poor photostability of dyes, and

thus optimal release efficacy. Hwang *et. al.* reported the synthesis of Ln doped MSN frameworks, by encapsulating Eu/Gd oxide NPs in MSN porous structure. They were used as anticancer drug delivery chemotherapeutic agents by loading DOX in the structures, luminescent markers, MRI contrast agents, and NIR irradiation for single oxygen sensitisers for PDT therapy (and simultaneous DOX release)[66].

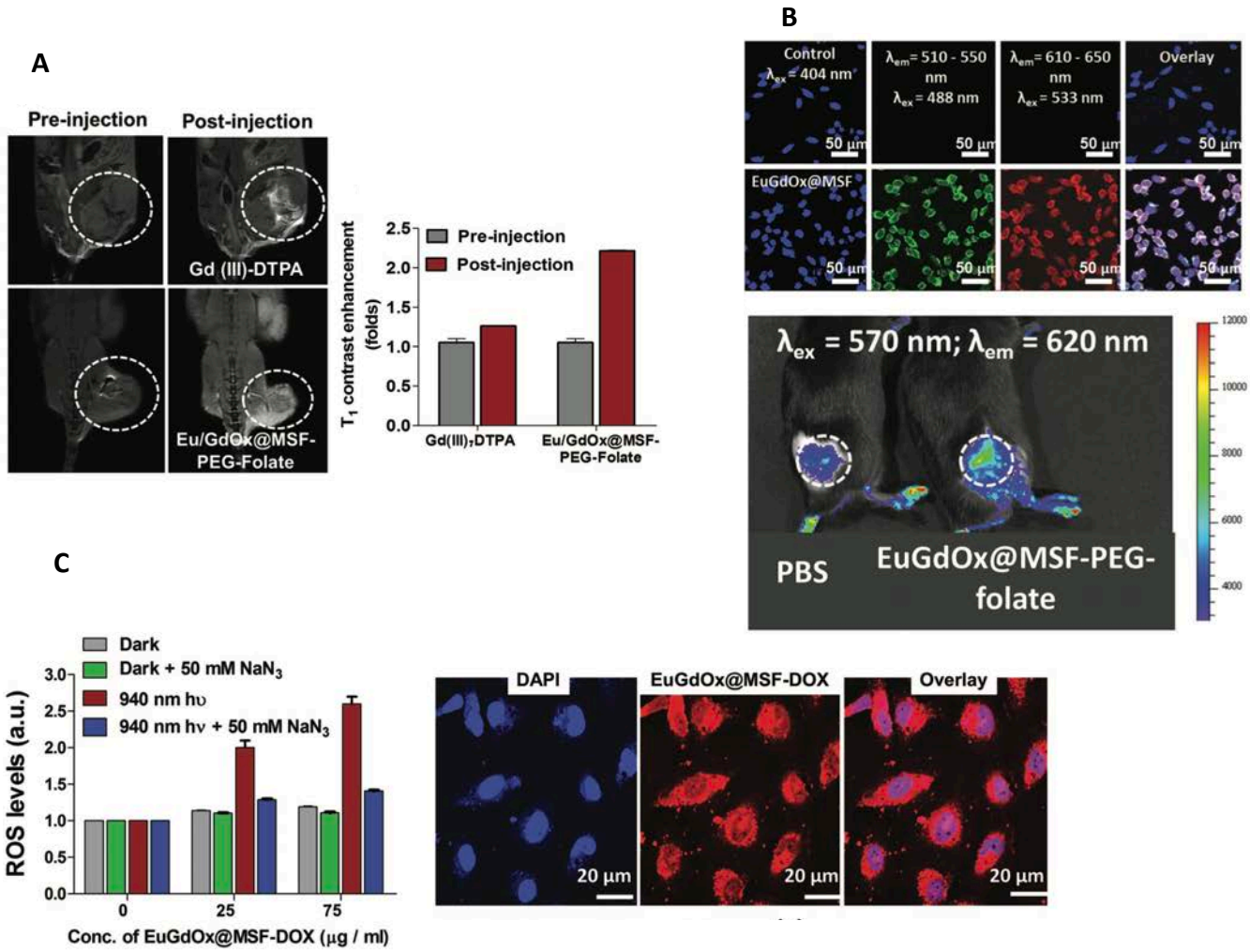


Figure 2.1.41

Multifunctional properties of the Ln doped MSN framework synthesised by Hwang *et. al.* A left: *In vivo* T_1 weighted MRI images of tumour bearing mice injected with commercial Gd-DTPA compared to the SDDS synthesised. A right: The T_1 contrast agents enhancement comparison. B top: Confocal fluorescence microscopy imaging of the Ln doped MSN framework in HeLa cells at 488 nm and 533 nm. B bottom: *In vivo* fluorescence imaging of PBS and the Ln doped MSN framework injected in tumour bearing mice, 1 h after injection. C: ROS levels of the NPs at different concentrations, incubated in HeLa cells for 4 h. Images taken from Hwang *et. al.*[66].

They were able to demonstrate the magnetic properties of the Ln doped MSN framework using *in vivo* T_1-weighted MRI images of melanoma tumour bearing mice. Luminescence properties of the NPs were also demonstrated using Ln luminescence spectroscopy, confocal fluorescence imaging and *in vivo* fluorescence imaging of the tumour bearing mice. Moreover, they performed *in vitro* combined chemo-photodynamic therapy of the drug loaded MSNs in HeLa cells[66].

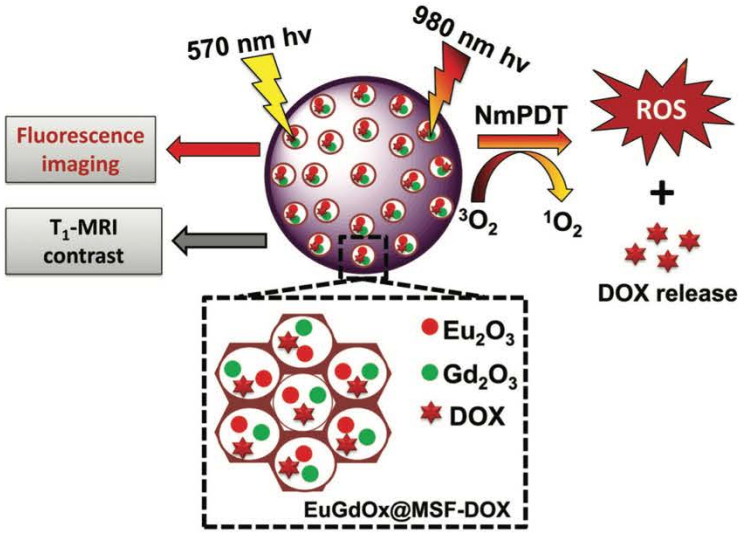


Figure 2.1.42

Schematic illustration of the multifunctional SDDS developed by Hwang *et. al.* Image taken from Hwang *et. al.*[66]. The schematic represents the ability to visualise visible fluorescence emission by λ_{exc} = 570 nm and λ_{em} = 620 nm from intratumoral injection of EuGdOx@MSF-DOX, and formation of $^1O_2$ by NIR λ_{exc} = 980 nm leading to ROS and release of DOX without addition of photosensitisers.

Lin *et. al.* also reported the synthesis of a multifunctional SDDS using MSNs to perform CPT delivery. Dual mode imaging was used arising from incorporation of Eu(III), a luminescent Ln, and Gd(III), a Ln with magnetic properties. Furthermore, they incorporated stimuli triggered drug release through modification of the surface with HA, in addition to gatekeeping for controlled release[67].

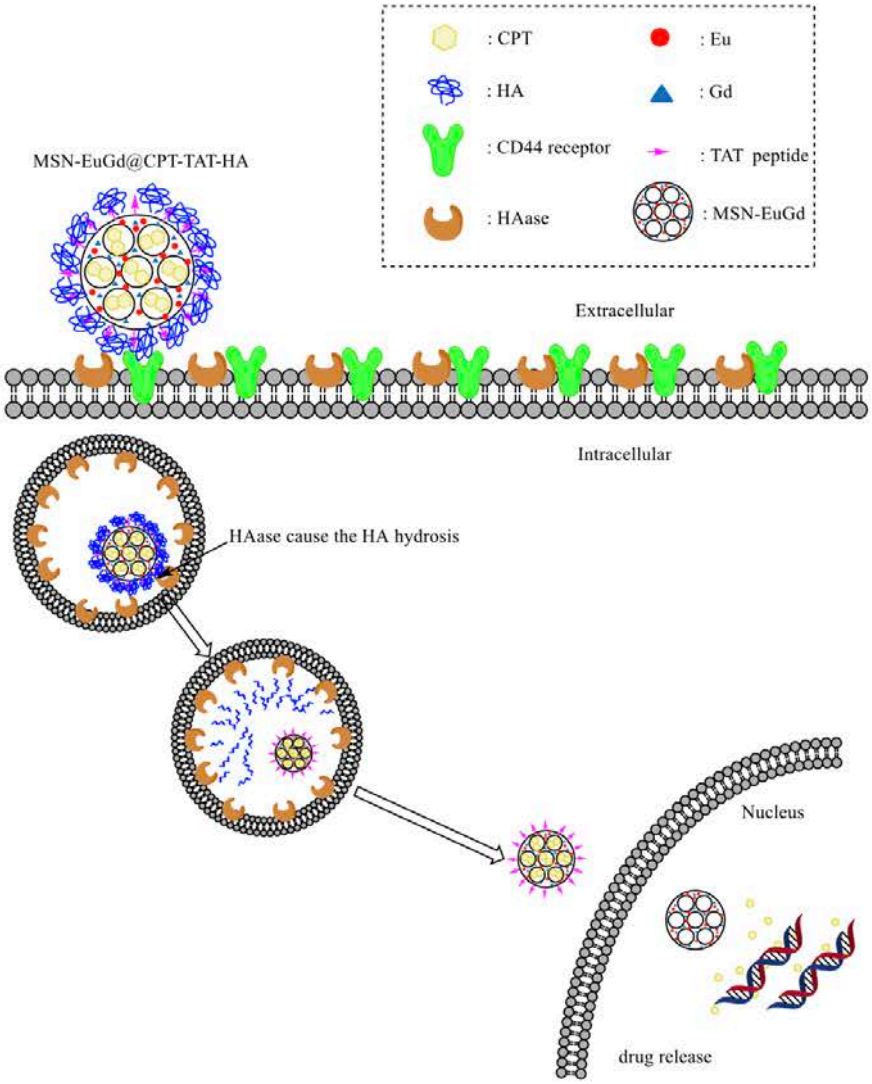


Figure 2.1.43

Schematic illustration of SDDS using MSNs loaded with CPT, Eu(III) and Gd(III), and surface modified with HA and a nuclear penetrating peptide (TAT peptide). Image is taken from Lin *et. al.*[67].

HA was chosen for this system due to its selectivity for CD44 receptors which are overexpressed in cancer cells, hence aiding drug delivery through endocytosis from selective HA-CD44 binding. In addition, a TAT peptide was used as a nuclear target which also aided targeted delivery of CPT to the nucleus in cancer cells for release. The release was triggered by changes in pH (from physiological conditions to acidic environments in tumour cells), breaking down HA on the surface and leading to CPT release. Simultaneously, HA also acted

as a gatekeeper due to its polymeric properties, enabling controlled release and prevention of premature release. The dual imaging properties of the SDDS demonstrated biodistribution of CPT from drug release, and showed the attachment of the NPs to cell membranes owing to targeting HA and TAT molecules[67].

A similar system has previously been reported by Lin *et. al.* which also utilised Ln doped MSNs (EuGd-MSNs) for CPT delivery. In this case, the MSNs were modified with FA, and CPT through disulphide linkage[68].

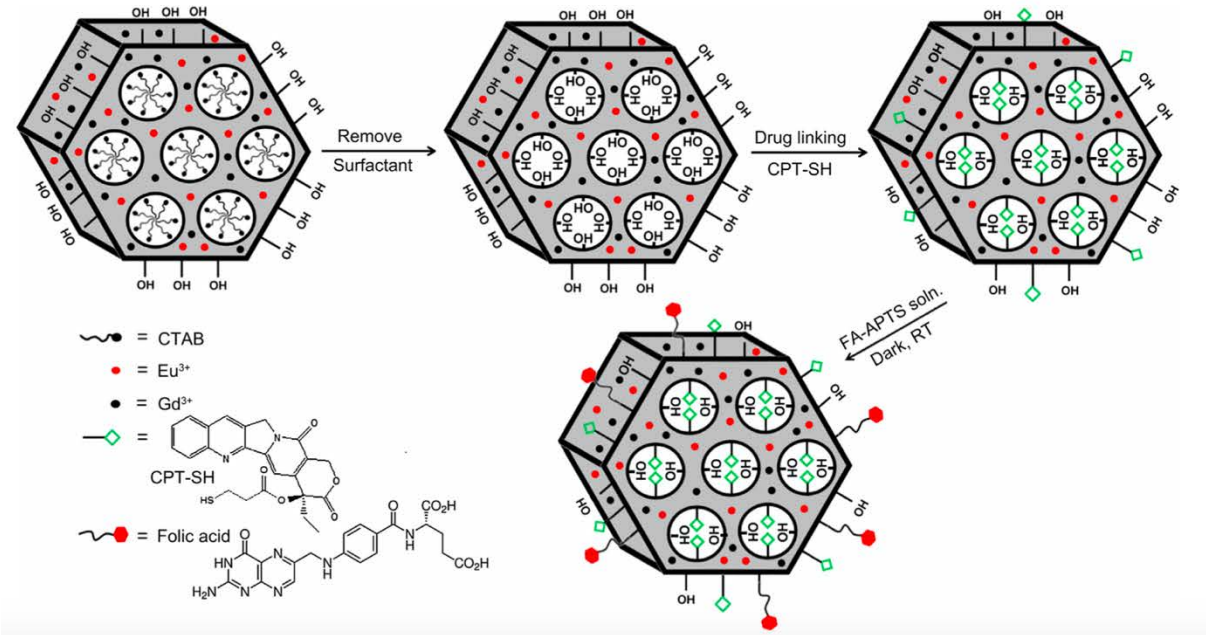


Figure 2.1.44

Schematic illustration of EuGd-CPT and FA- modified MSNs. Image taken from Lin *et. al.*[68].

It is evident that Ln doped MSNs have attracted much attention due to the luminescent properties enabling tracking of NP accumulation. Here, Eu(III) was chosen due to its long luminescent lifetimes, and Gd(III) for its recognition as T_1 contrast agent for MRI. Disulphide linkage of CPT to the MSN surface was the chosen strategy here, in attempt to overcome the low solubility of free CPT. Through reduction cleavage of the link, Lin *et. al.* developed a system to deliver unmodified CPT molecules in a controlled manner, triggered by intracellular

reducing enzymes (GSH). Surface modification also involved FA attachment as a targeting ligand due to its selectivity for folate receptors which are overexpressed in cancer cells[68].

Other than luminescent labels, Ln functionalised MSN systems have also incorporated other *f* block metals capable of MRI imaging (as seen)[66-68, 81], and radiotherapy[69]. Mathis *et. al.* developed a novel nanosystem incorporating Eu(III) complexes into amino functionalised MSNs, in addition to radioactive $^{177}LuCl_3$[69].

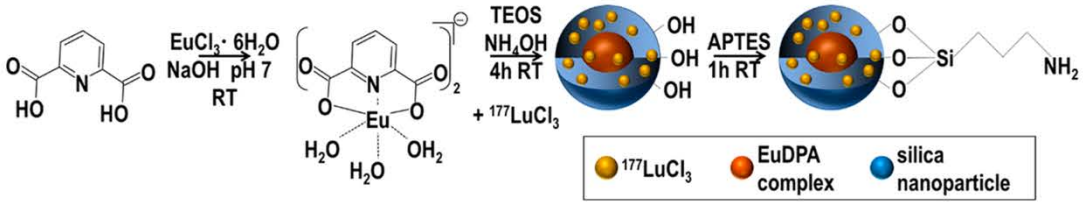


Figure 2.1.45

Schematic illustration of Lu-Eu/MSN-NH_2 hybrid NP system. Image taken from Mathis *et. al.*[69].

By incorporation of a tracer amount of ^{177}Lu into Eu(III) sites, radioactivity was switched on leading to dual mode imaging and tumour radiotherapy. Imaging techniques (single photon emission tomography (SPECT) and computed tomography (CT) imaging) were used to investigate biodistribution of the NPs for studying uptake in mice *in vivo*. They used an HT-29 tumour xenograft mouse model to evaluate antitumour efficacy of the radioactive labelled MSNs, to demonstrate the potential therapeutic applications of the functionalised MSNs[69].

There has been a lot of interest in developing Ln doped upconversion NPs (UCNPs), explored for applications in cancer theranostics due to some key factors. Some research in this field has seen the combination of UCNPs and silica NPs to created multifunctional NPs for imaging and drug delivery[68]. Common luminescent probes used such as organic dyes, QDs and metal complexes tend to require UV excitation sources which limit their applications in theranostics. UV excitation leads to low tissue penetration depth, low signal to noise ratios arising from background autofluorescence, long term irradiation causing DNA damage, and possible safety concerns of metal toxicities. A strategy to overcome these issues is using NIR light excitation,

enabling deeper tissue penetration, and thus reducing background autofluorescence and minimising photodamage to biological tissue[70-72]. UCNPs are able to convert low energy emission to high energy emission and is a process where two or more photons are combined to create a high energy photon, essentially an anti-Stokes shift. They usually have high excitation wavelengths, 980 nm or 808 nm in the NIR range, good for deep tissue penetration. Background autofluorescence is completely eliminated as NIR excitation is used. Furthermore, multimodality can be introduced by using UCNPS by doping different Ln ions. Lastly, resistance to photobleaching allows *in vitro* and *in vivo* theranostic monitoring[70, 73-76].

Coating the surface shell of UCNPs gives a hydrophilic platform for improving solubility, but also for modifications to the surface. Mesoporous silica shells and hollow mesoporous silica shells have been used as coatings on UCNPs, to develop theranostic SDDS. The porous structures, as described earlier, provide large surface area and an ability to carry drugs, as well as easy surface functionalisation[3, 118]. Hollow mesoporous silica shells (yolk-shell structures) have also attracted much interest due to the hollow structure, large pore volumes, and high surface to volume ratios[70, 78].

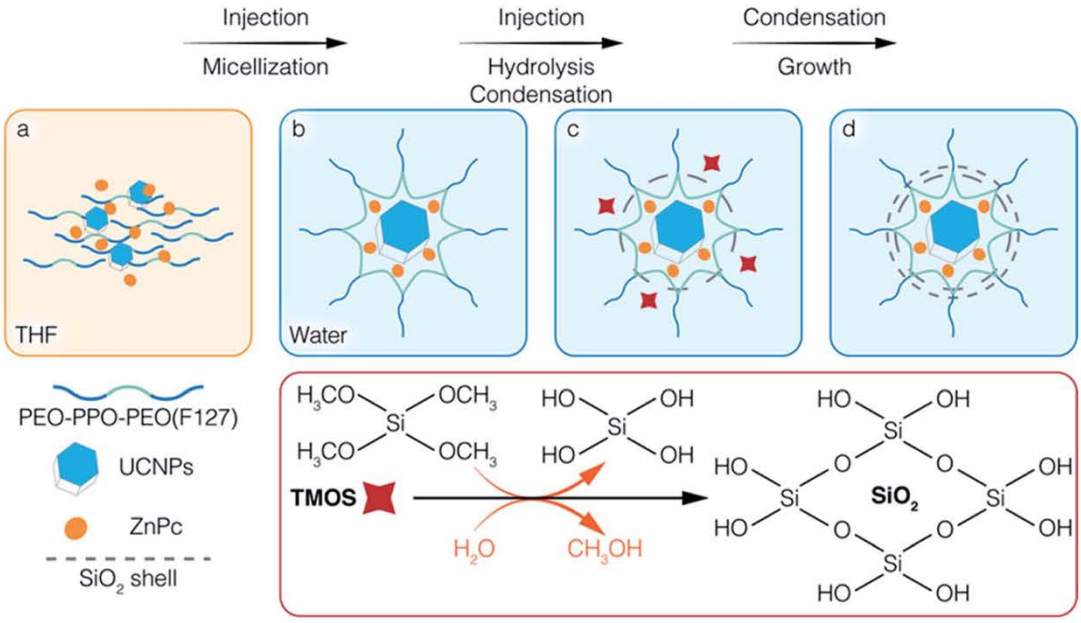


Figure 2.1.46

Schematic illustration of formation of silica coated UCNPs carrying drugs (ZnPc). Image is taken from Vetrone *et. al.*[79]. An amphiphilic triblock copolymer (ethylene oxide)$_{106}$(propylene oxide)$_{70}$(ethyelene oxide)$_{106}$ (PEO-PPO-PEO) forms micelles in water confining the hydrolysis and condensation of silica precursor TMOS leading to a silica shell cross linked micelle. Polymeric micelle and silica nanocapsules are formed with UCNPs and ZnPC which acts as a drug (photosensitiser).

Vetrone and co workers reported a one pot synthesis of Er(III) and Yb(III) doped UCNPs, and a photosensitiser zinc phthalocyanine (ZnPc) in silica shells. Their theranostic NPs demonstrated good colloidal stability and showed PDT effect against chemo resistant breast cancer cells (BT474 cells), in addition to negative contrast enhancement for MRI (T_2 weighted)[79].

Another example of a multimodal theranostic platform created for synergistic therapy, combining chemodynamic (CDT) and photodynamic (PDT) therapy, was reported by Yang *et. al.*[80]. Their design involved a porous silica shell coating UCNPs for upconversion luminescence (UCL), CT, and MRI (trimodal imaging) for synergistic CDT, PDT and gas therapy. Copper peroxide nanodots and PEG were loaded into the pores. These nanodots were decomposed in the acidic environment, after endocytosis into cancer cells, in turn causing the release of Cu ions and H_2O_2 formation subsequently leading to CDT achievement. PDT efficacy was enhanced through hypoxia relief and depletion of GSH, in addition to DNA damage through the release of ROS levels. Furthermore, the trimodality of the SDDS arising from the Ln ions enabled monitoring the treatment in real time[80].

Similarly to UCNPs, other NIR Ln examples have been studied on MSNs[84, 85], as well as other Ln functionalised MSNs[84-86].The combination of CPT and Lns has been reported with utilising MSNs as a nanocarrier[68, 69]. Wang and co-workers reported the synthesis of silica coated UCNPs, with GSH cleavable disulphide bonds attached to link CPT to the silica shell. Low intensity NIR light was used to trigger PDT avoiding photodamage to healthy cells, and also enabling enhanced synergistic effects through GSH triggered release of CPT[73].

Camptothecin and Lanthanides

GSH responsive theranostics utilising UCNPs has many examples combining Lns and CPT. As previously discussed, disulphide cleavage by interaction with GSH has been employed often to release CPT from drug delivery systems[70, 90, 91].

Other examples reported of combining CPT and Lns in nanosystems to produce applications in theranostics has also been observed[90, 91]. Wong *et. al* devised a Ln nanoplatform for CPT delivery, incorporating dual imaging capabilities[90].

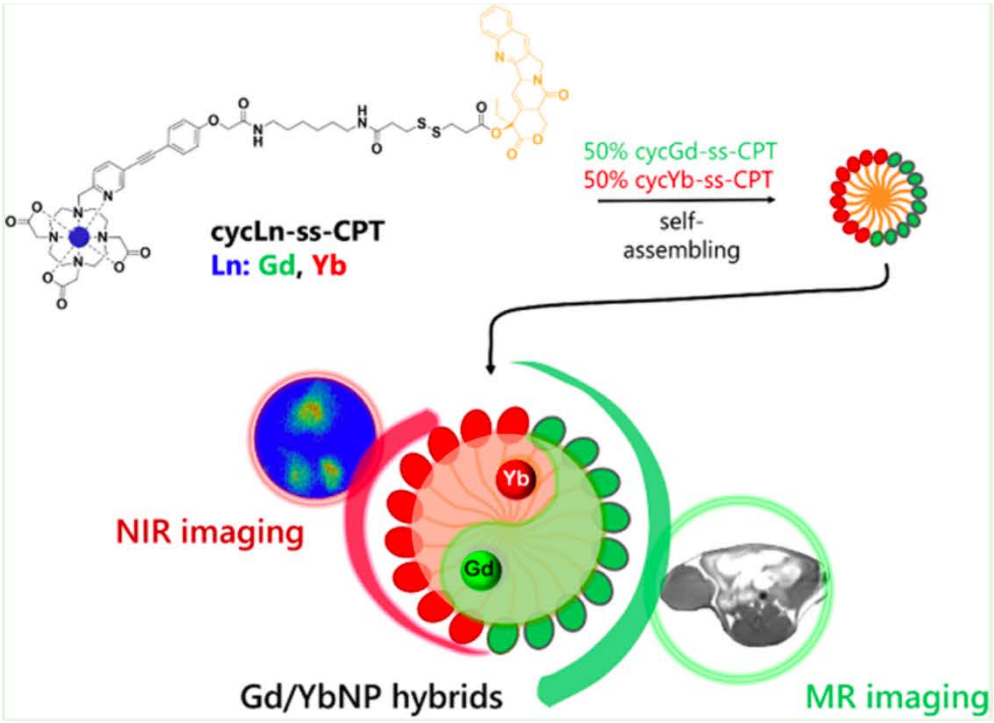


Figure 2.1.47

Schematic illustration of Ln self-assembled nanocomposites using a Ln – cyclen complex, with attachment to CPT through disulphide linkage responsive to GSH rich environments. Dual imaging capabilities were developed through incorporation of magnetic Gd(III) for MRI imaging, and NIR luminescent Yb(III) for NIR imaging. Image taken from Wong *et. al.*[90].

CPT was incorporated as a prodrug to overcome well known limitations of CPT such as poor solubility and inactive carboxylate conversion in physiological conditions. Cyclen derived macrocycles were used as choice of coordinating ligands for Gd(III) and Yb(III) due to high stability as chelators. CPT molecules were conjugated to Ln-cyclen complexes through disulphide linkage, and CPT encapsulation was formed through self-assembly of the micellular NPs. In presence of tumour cells rich in GSH concentrations, CPT release was triggered. Real time MRI and NIR imaging was used to monitor the CPT release. Increase in Yb(III)

luminescence was observed after GSH activation, confirming CPT drug release which was monitored through NIR imaging. In addition, T_1 contrast enhanced performance was achieved in solution and *in vivo*, showing the potential applications as a theranostic platform.

2.1.5. CPT Delivery Using Non-Porous Silica Nanoparticles

Great interest has focused on drug delivery using SiO_2NPs, after the approval of ultrasmall SiO_2NPs by the US FDA for clinical trials in 2011 for cancer imaging[58, 94]. SiO_2NPs have been employed as drug carriers for not only CPT, but other anticancer drugs such as DOX.

Wang and co-workers reported the development of two SiO_2NP prodrug systems for synergistic drug release through stimuli response triggers[58]. It is known that the combination of CPT and DOX is favourable for cancer therapy due to their TOP enzyme targets[54-59]. GSH and acidic pH were chosen as stimuli triggers for drug release, commonly seen for other MSN systems as mentioned previously. Tumour environments feature low pH values due to high CO_2 levels and high metabolic rates, and GSH rich regions are also found in tumour cells. Wang *et. al.* exploited these common features of tumour environments to release CPT and DOX. CPT and DOX were covalently encapsulated in the SiO_2NPs, via the Stober method[93] through co-condensation with the silica precursor. CPT molecules were encapsulated through a cleavable GSH responsive disulphide bond conjugated to silane groups. However, DOX beared a hydrazone pH responsive bond. This strategy was chosen in order to minimise undesired premature drug release upon response to GSH and acidic environments. Their prodrug NP system aimed to achieve improved features over MSNs such as easier synthesis, higher circulation in the blood and better biocompatibility[58].

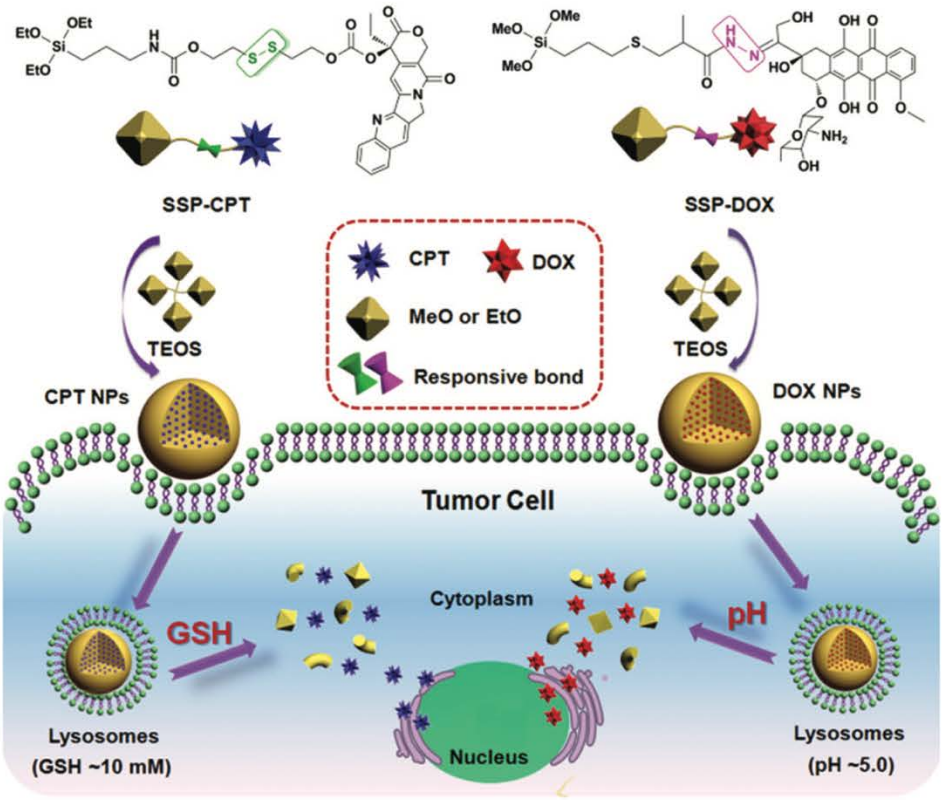


Figure 2.1.51

Schematic illustration of modified prodrugs CPT and DOX for encapsulation in SiO_2NPs via the Stober method. NPs were taken up into tumour cells via endocytosis, followed by GSH and pH triggered drug release of CPT/DOX from the prodrugs, to free drug release. Image is taken from Wang *et. al.*[58].

UV-Vis spectroscopy and luminescence was used to show the presence of both drugs in the silica matrix. Similar techniques such as TEM and DLS was used here to characterise NP sizes and morphology yielding sizes between 50 – 200 nm. *In vitro* drug release studies demonstrated effective proliferation inhibition of HeLa cells, and furthermore, the synergistic effect was studied against free drug studies showing improved efficacy.

In contrast, Corma and co-workers designed surfaced modified SiO_2NPs for CPT delivery with covalent conjugation, rather than encapsulation[95]. Despite the development of water soluble CPT derivatives, irinotecan and topotecan, these analogues show less activity than CPT.

Corma *et. al.* aimed to incorporate CPT, and improve limitations associated with the inactive carboxylate ring, through substitution on the OH group of the drug molecule. They summarised previous research that focused on attachment of CPT through substitution at the OH, but it was clear that efficient solubility was a problem. Herein, they reported a SiO_2NP drug delivery platform for CPT through linkage at the OH position. Solubility enhancement was aimed through surface functionalisation with trihydroxysilylpropyl carboxylate groups (THSC), ionised at physiological pH and hence improving colloidal stability through electrostatic repulsion[95].

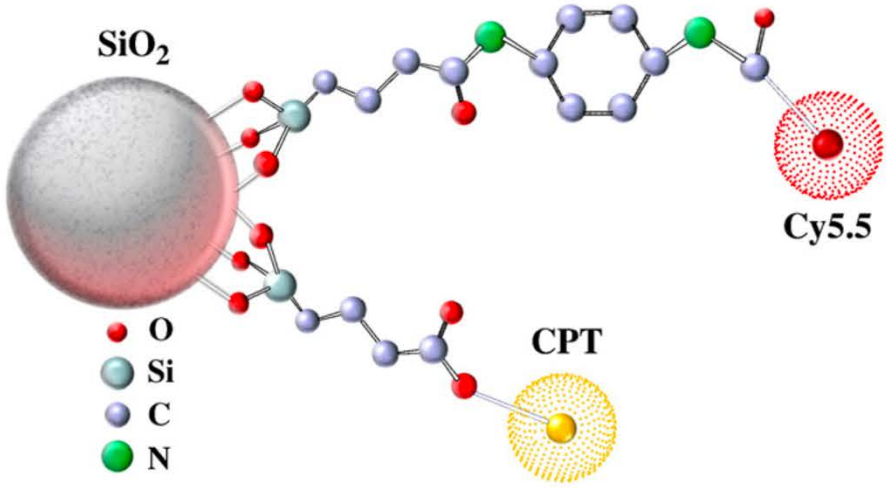


Figure 2.1.52

Schematic illustration of CPT conjugated SiO_2NPs, functionalised with THSC groups and labelled with Cy5.5, a luminescent label enabling *in vivo* luminescence imaging. Image taken from Corma *et. al* [95].

In vitro studies were investigated to show cell internalisation, through endocytosis, and also cytotoxicity against HeLa (cervix cancer cell line) and HT-29 Fluc (colorectal cancer cell line). Biodistribution *in vivo* was studied in mice using *in vivo* and *ex vivo* luminescence imaging, and lastly therapeutic efficacy assays were studied to show tumour suppressing growth after treatment.

2.1.6. Non-Porous Silica Nanoparticles Funtionalised with Lanthanide Complexes as Luminescent Labels

Hybrid organic-inorganic Ln based nanosystems have attracted great interest, not only in nanomedicine, but also in optics and photonics[97]. Combination of Lns on silica nanosystems has also been extensively researched, just as seen in MSN systems, due to multimodal imaging potentials and synergistic diagnostic efficacy[98].

UCNPs, as mentioned earlier, have emerged as a unique class of luminescent probes, exhibiting advantageous properties in diagnostics, from converting NIR light into visible and UV, to penetrating tissue deep in bioimaging applications. Limitations of UCNPs have shown that fine control of particle size and distribution of Ln doping can be challenging. Lin *et. al.* constructed silica coated UCNPs ($Gd_2(WO_4)_3$:Yb(III)/Ho(III)) by one pot co-precipitation creating NPs with uniform distribution and exhibiting enhanced yellow luminescence[98]. An amphiphilic polymer, polyethylenimine (PEI), was functionalised on the surface to improve hydrophilicity. Temperature sensing of the NPs were achieved by using the fluorescence intensity ratio (FIR) method, and were found to exhibit sensing properties through thermally coupling of $^5F_{5(1)}$/ $^5F_{5(2)}$ levels of Ho(III). The T_1 weighted MRI properties of Gd(III) also enabled enhanced effect *in vitro* and *in vivo*. Furthermore, a cisplatin and platinum drug *cis, cis, trans*-diamminedichlorodisuccinato-platinum(*iv*) (*c,c,t*-$Pt(NH)_3Cl_2(OOCCH_2CH_2COOH)_2$) (DSP) was conjugated to the $Gd_2(WO_4)_3$:Yb(III)/Ho(III)@SiO_2NP, and were found to achieve stronger inhibition than cisplatin and plain $Gd_2(WO_4)_3$:Yb(III)/Ho(III))@SiO_2NP on CT26 cancer cells. The NIR and MRI containing Ln SiO_2NPs were shown to be a promising tool in cancer theranostics, showing enhanced therapeutic effects compared to cisplatin and DSP, and bimodal imaging[98].

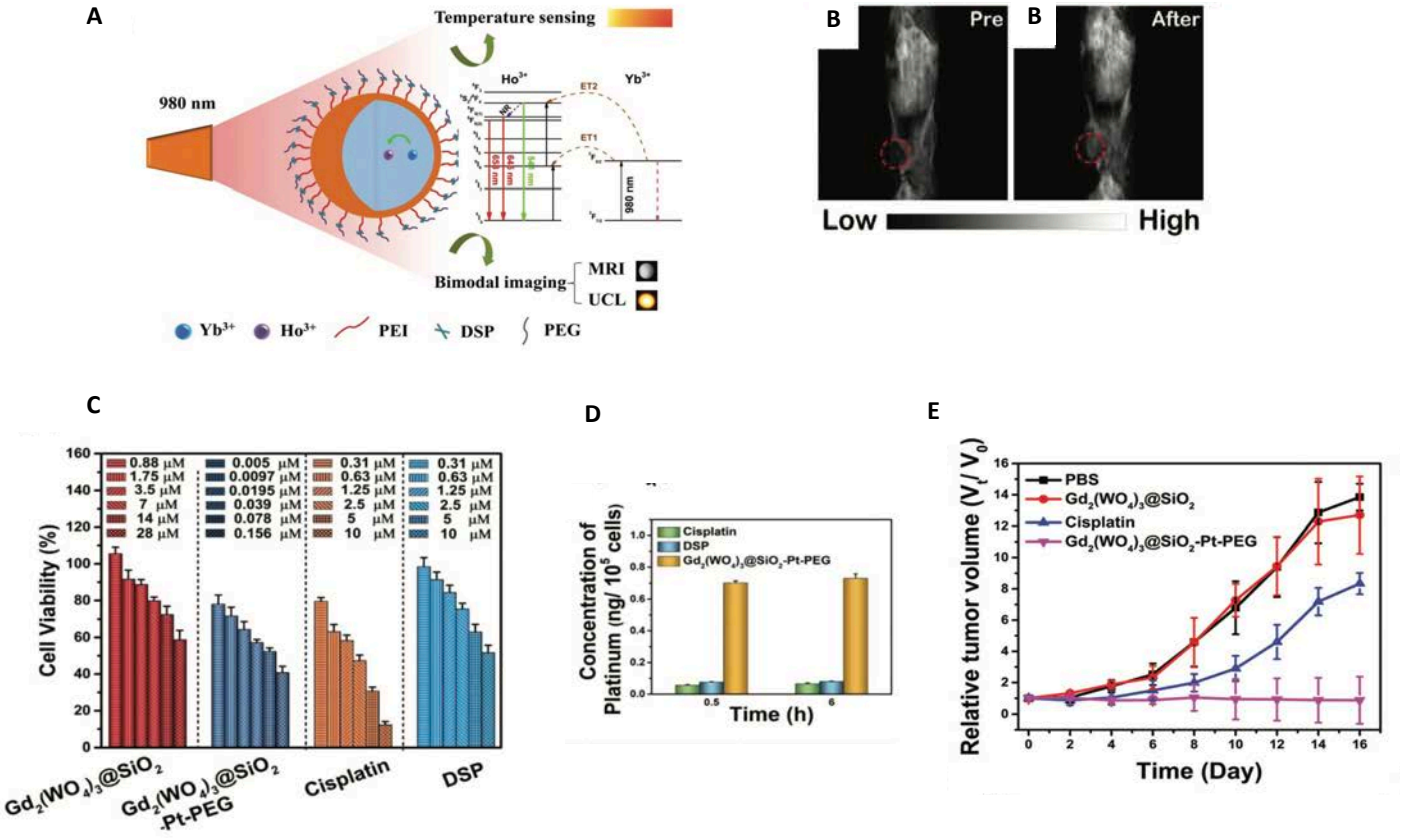


Figure 2.1.61

Diagnostic techniques used by Lin and co-workers. A: schematic illustration of temperature sensing, and bimodal imaging (upconversion luminescence (UCL) and MRI). B left: T_1 weighted MRI pre injection. B right: T_1 weighted MRI after injection. C: Cell viability assay after incubation of 48 h with $Gd_2(WO_4)_3$@SiO_2NP, $Gd_2(WO_4)_3$@SiO_2NP-Pt-PEG, cisplatin, and DSP. D: Measuring the amount of endocytosis caused by the different drugs at different times. E: Changes in mice tumour sizes dependent on the different treatments given. Images are taken from Lin *et. al.* [98].

Dual visible-NIR luminescent SiO_2NPs were developed for applications in cellular imaging by Mustafina *et. al.*[99]. Due to the unique Ln photophysical properties, Ln based luminescence was chosen as the route to developing diagnostic SiO_2NPs with ability to provide better imaging quality from enhanced signal to noise ratio, than organic lumophores. Dual luminescence abilities with an NIR probe was important due to improved tissue penetration upon excitation. Additionally, by using combination of Lns, luminescent wavelengths are tuneable, and also enabled metal to metal energy transfer. Mustafina and co- workers presented the complexation of *p*=sulfonatothiacalix[4]arene (TCAS) Tb(III) and Yb(III)presented the complexation of *p*=sulfonatothiacalix[4]arene (TCAS) Tb(III) and Yb(III)

complexes, doped into the silica matrix, utilising ligand to metal, and metal to metal energy transfer for enhanced visible and NIR luminescence[99, 100].

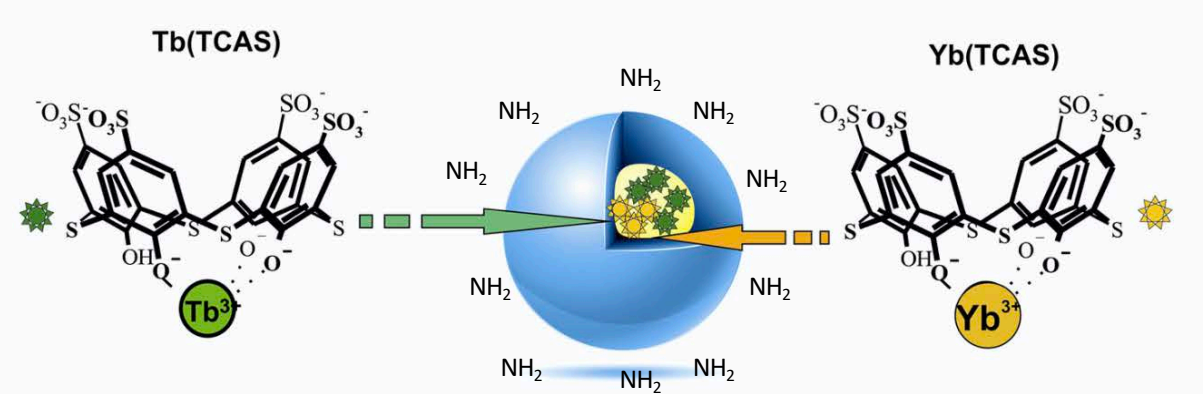


Figure 2.1.62

Schematic illustration summarising the process of encapsulation of Tb(III) and Yb(III) TCAS complexes in SiO_2NPs, functionalised with amino groups. Image is modified from Mustafina *et. al.*[98].

Other than ligand to metal energy transfer, the close proximity of the Ln complexes to each other in the silica matrix enabled metal to metal energy transfer (Tb → Yb), and enhanced NIR Yb(III) luminescence was observed with ratios at 2 : 1 (Tb : Yb). NPs with 2 : 1 ratio of the Lns exhibited enhanced toxicity to lung cancer cells (A549) compared to control NPs, demonstrated by cytotoxicity assay. Luminescent confocal microscopy was also used tracking green luminescence for studying cellular uptake by human embryo cells (W1-38) after 24 h incubation. The green luminescent NPs were located in the cytoplasm of cells, and the confocal images confirmed cell internalisation under Tb centred luminescence. The NIR centred luminescence from Yb(III) was not explored, but presented an opportunity for scope in this field to monitor cell internalisation with deep penetration depths[98].

As seen, common Lns chosen as luminescent markers have seen many studies in the uses of Eu(III), Tb(III) and Yb(III) (NIR), creating highly luminescent complexes for applications in cancer diagnostics.

2.2. Chapter Outline

This chapter is concerned with the preparation of novel silica NPs encapsulating an anticancer drug, **CPT**, for drug delivery applications. The NPs are also coated with luminescent Ln complexes, based on a DTPA framework ligand, as a diagnostic tool through detection of Ln luminescence. **CPT** has a high absorption coefficient, and absorbs light efficiently, enabling energy transfer to Ln ions resulting in sensitised luminescence.

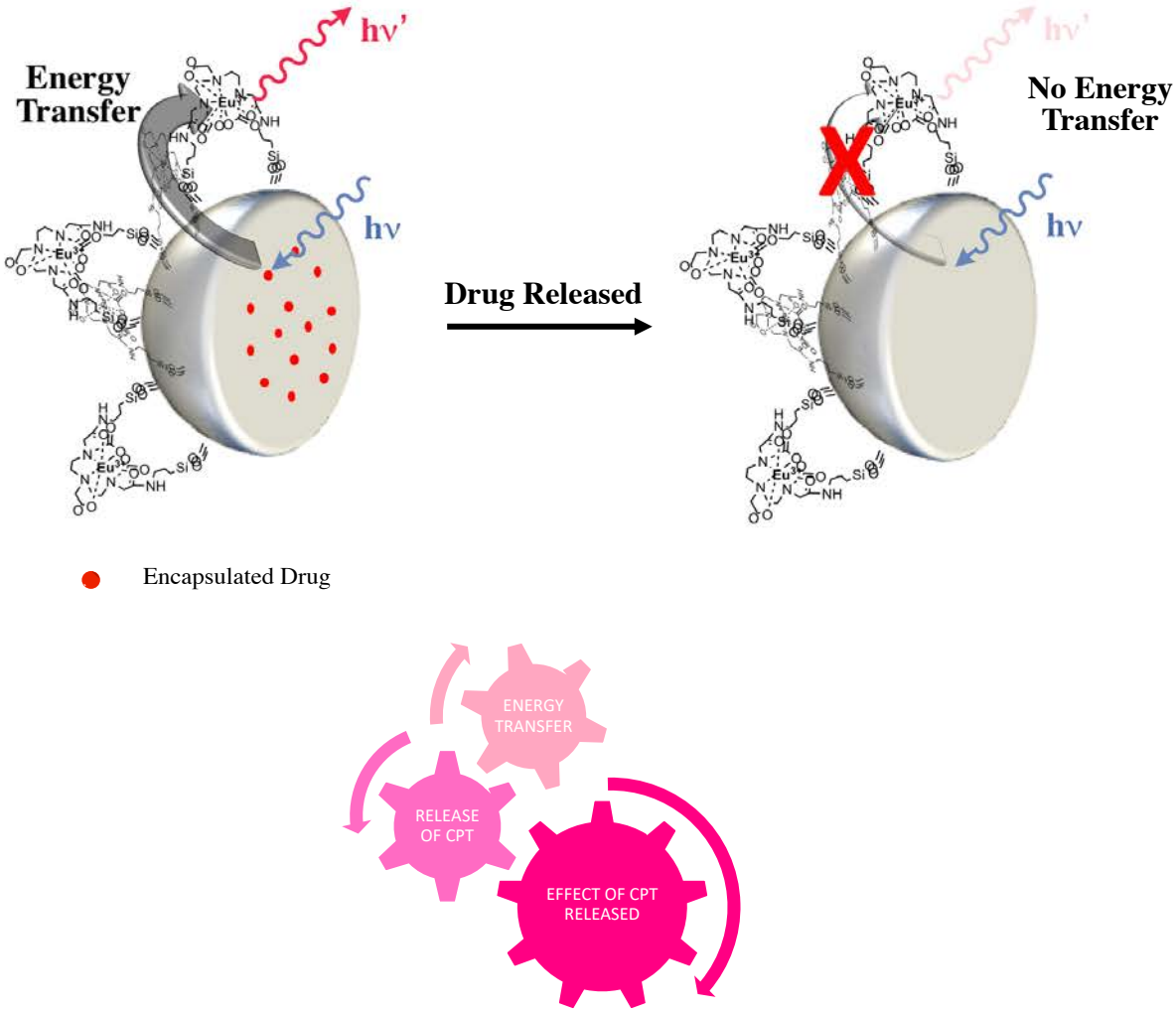


Figure 2.21

Schematic illustration of silica nanoparticle design carrying **CPT**, and functionalised with a luminescent DTPA-Ln complex. An 'on and off' switch system of Ln luminescence signal is created through the detection of drug release. The project aims include: achieving sensitised energy transfer from **CPT** to Ln(III) complex in the nanoparticle design, monitoring **CPT** release from the NPs, and investigating the effect of released **CPT** on A549 lung cancer cells.

Herein, the synthesis and characterisation of ligand **L**, and silica NPs are reported. The photophysical properties of complexation to Eu(III) ions, and sensitisation of Eu(III) luminescence from **CPT** in solution are investigated as proof of concept. The luminescence properties of the nanoparticle designs developed are investigated, using Eu(III) and NIR Lns Nd(III) and Yb(III). The functionalised NPs are then used to show **CPT** release, monitored using UV-Vis absorbance, in order to calculate % release, and indications of which **CPT** form is being released. Once the release was studied, the effect of **CPT** was studied using cytotoxic assays on lung cancer A549 cells, to examine the toxicity of the released drug.

2.3. Synthesis of Ligand, L

The ligand **L** was chosen as the Ln chelator, with silane legs for attachment to silica NPs. **L** is a derivative of diethylenetriaminepentaacetic acid (DTPA) and provides a caged structure around Ln(III) ions, and is known to have a high binding constant[113-116].

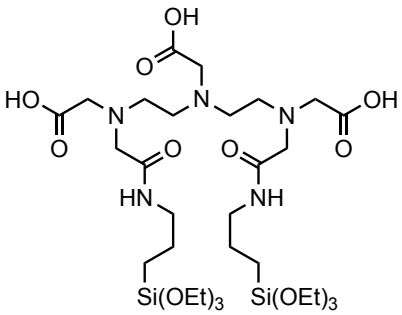


Figure 2.31

Structure of **L**

The synthesis of **L** was achieved from a one step reaction, with starting material DTPA bis anhydride[102].

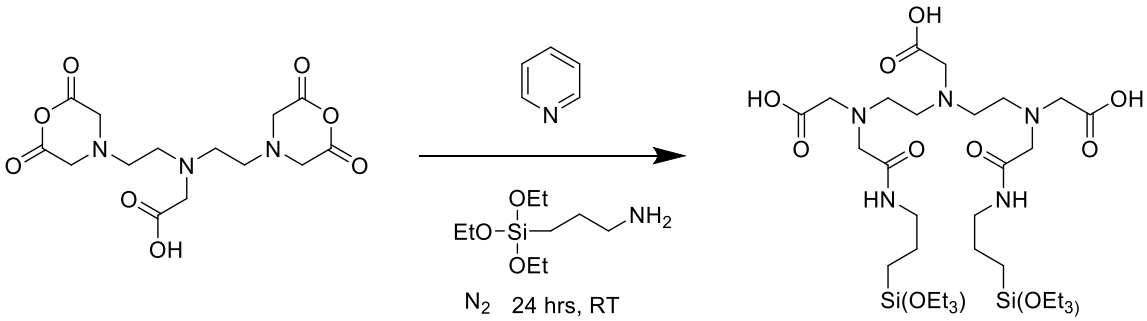


Figure 2.32

Reaction scheme of **L.**

DTPA bis anhydride was dissolved and stirred in anhydrous pyridine prior to addition of 3-aminopropyl triethoxysilane (APTES) (giving the silica legs). This reaction was carried out in anhydrous conditions overnight before collection of the product **L**[102]. Copious amounts of hexane was used to precipitate **L** in addition to stirring in an ice bath. A lot of time was required for this step as well as keeping solutions overnight in the fridge to help precipitate **L**. The ligand was then isolated via filtration and checked by ^{1}H NMR and ^{13}C NMR and mass spectrometry (see appendix figure 1) .

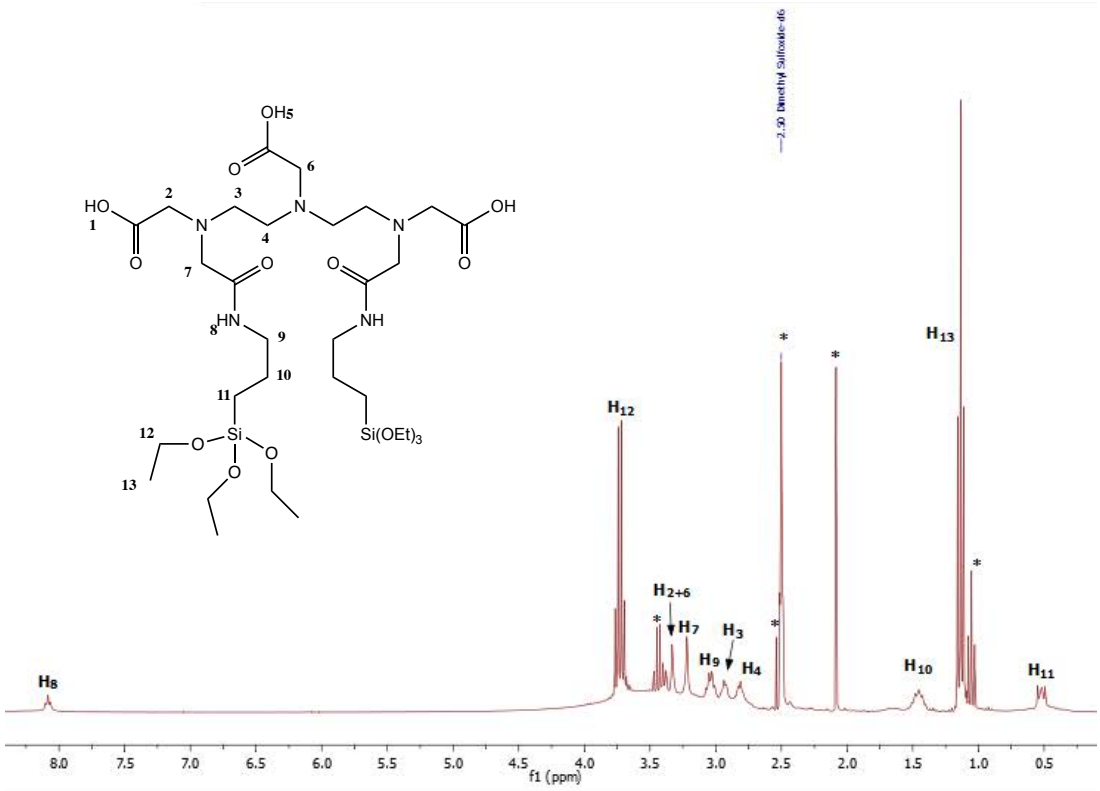


Figure 2.33

The 300 MHz ^{1}H NMR spectrum of **L** recorded in d*6*-DMSO. The solvent peak at 2.54 ppm is formed by DMSO C*H*$_3$. The solvent peak at 2.08 ppm arises from acetone traces, and the peak at 1.05 ppm arises from ethanol traces.

11 of the 13 proton environments were detected (O*H* protons excluded). The amide bond formation arising from the signal in the aromatic region at 8.08 ppm of H_8, N*H*CO, represented as a triplet, is indicative of successful synthesis of **L**. Triplets are detected in the aliphatic region at δ_H 2.94 ppm and 2.81 ppm corresponding to H_3 and H_4 respectively. The proton shifts for H_2 and H_6 superimpose into a singlet at 3.33 ppm integrating for 6H, arising from the

change in symmetry from DTPA bis anhydride to **L**, and the new positioning of H_2 next to a carboxylic acid instead of an anhydride. H_{2+6} and H_7 are also shifted from their δ_H DTPA bis anhydride, due to a greater electron withdrawing effect from the new amide bond, also indicative of successful formation. Additionally, the silane legs H_{12} and H_{13} are detected as a quartet at 3.73 ppm (6H), and a triplet at 1.14 ppm (9H) respectively.

The ^{13}C NMR spectrum of **L** was also recorded in d*6*-DMSO (see appendix figure 2) and revealed 10 of 11 carbon environments, perhaps due to superimposed peaks in the range 170 – 180 ppm arising from *C* = O environments (only two were detected instead of 3). Only one environment has a negative signal corresponding to the *C*H_3 group on the end of the silane legs. The combination of mass spectrometry, ^1H NMR and ^{13}C NMR confirm the successful synthesis of ligand **L**.

2.4. Synthesis and Characterisation of Porous Silica Nanoparticles

Mesoporous silica NPs (**MSNs**) were synthesised following a modified Stober synthesis, forming ordered MCM-41 type **MSNs**[103-105]. The synthesis of **MSNs** are briefly discussed in section 1.3.1.

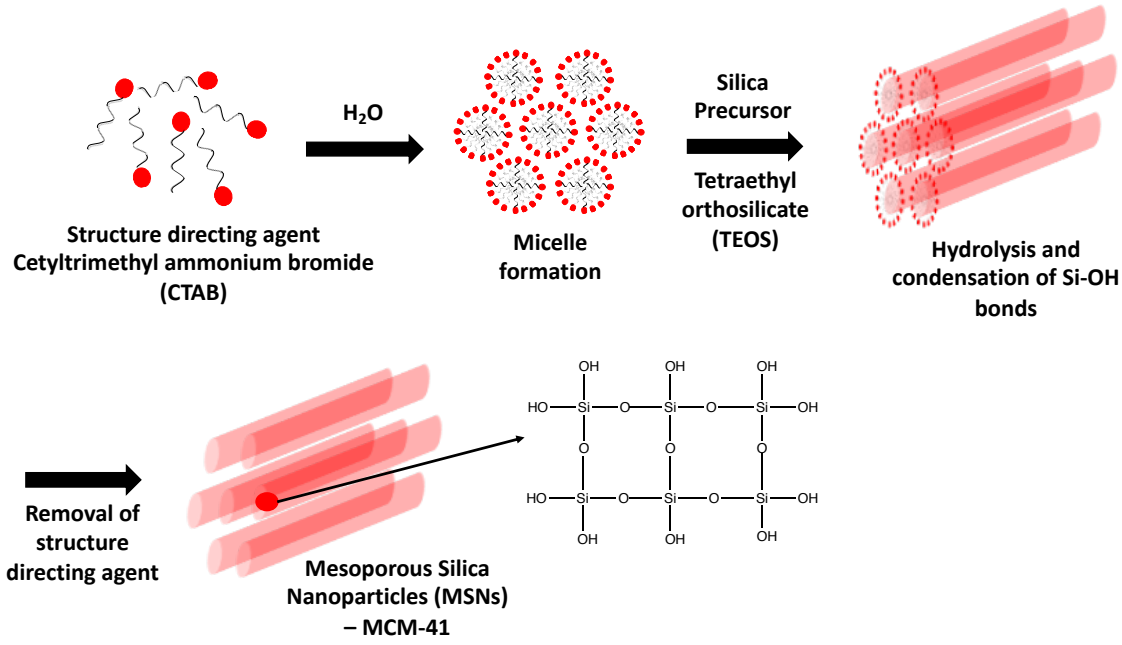


Figure 2.41

Schematic illustration of the formation of MCM-41 **MSNs** using a base catalysed Stober method. Image redrawn from Mehmood *et. al.*[106].

A silica precursor, tetraethyl orthosilicate (TEOS) was used to form the silica network around the CTAB micelles directing the structure of MCM-41 **MSNs**, *via* hydrolysation and condensation around the micelles in basic conditions. The base controls the rate of condensation, and hence the nucleation and growth of the NPs. After CTAB removal, *via* either acid extraction or calcination, spherical **MSNs** are formed with a Si-OH network arranged in an hexagonal array, characteristic of MCM-41 NPs[103].

The enhanced permeation and retention (EPR) effect is dependent on nanoparticle charge and size. To deliver **MSNs** loaded with drug, it is important to synthesis nanoparticle sizes

with diameters < 200 nm to avoid clearance from the bloodstream and hence unnecessary accumulation in non-specific organs. Varache *et*. *al*. previously reported the effect of NaOH concentration on nanoparticle sizes, controlling the rate of condensation[105]. Based on this, we modified the Stober method by controlling the NaOH concentration, using 12.5 mM NaOH to yield sizes between 100 nm – 200 nm retaining a narrow size distribution. Furthermore, we also observed a size dependence of the NPs on the speed of TEOS addition during the synthesis. Over 10 minutes, the speed of TEOS was increased, and a decrease in nanoparticle size was observed.

Table 2.41

DLS sizes of NPs dependent on speed of TEOS additions over 10 minutes.

Sample	**TEOS/ μL (over 10 mins)**	**Size d/ nm Number Distribution**	**PDI**
1	250 (x5)	140 ± 40	0.09
2	625 (x2)	120 ± 40	0.11
3	1250 (x1)	95 ± 30	0.14

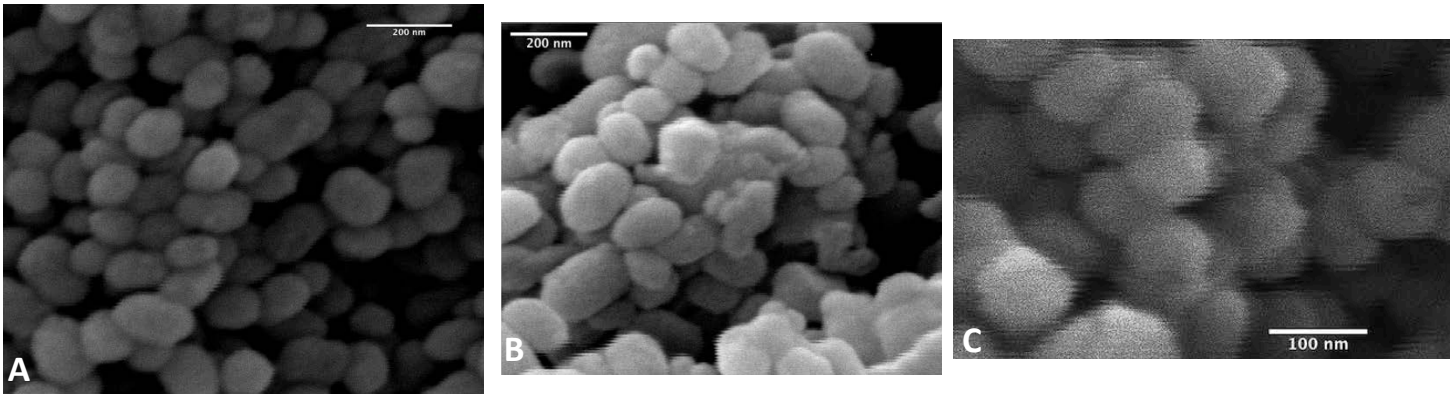


Figure 2.43

SEM images of corresponding samples to Table 2.41. A: Sample 1, average diameter size 130 nm. B: Sample 2, average diameter size 120 nm, C: Sample 3, average diameter size 100 nm. SEM diameters averaged from 10 NPs (5 for C).

MSNs were characterised by Dynamic Light Scattering (DLS) and Scanning Electron Microscopy (SEM). The hydrodynamic diameter of **MSNs** (table 2.41) suggests sizes decreasing from 140 nm to 95 nm as the speed of TEOS addition was increased over 10 minutes, all with good Polydispersity Index (PDI). The PDI here gives us an indication of a narrow size distribution with monodisperse NPs in solution, with a value < 0.2. The SEM images (figure 2.42) of the corresponding samples demonstrate the characteristic spherical morphology of **MSNs**, but more importantly confirm the nanoparticle sizes and the decreasing size trend[105].

2.5. Functionalising MSNs with CPT and Ligand L

2.5.1. Drug Loaded Nanoparticles

Traditionally, reports of drug delivery using **MSNs** load cargo after synthesis of the NPs[107-110]. This is usually carried out by typically stirring a mixture of the drug and NPs, and purified *via* centrifugation to collect the drug loaded NPs. Synthesised **MSNs** were loaded with anticancer drug **CPT** and their characterisation were carried out using DLS, SEM, Small Angle X-ray diffraction (SAXD), and solid state UV-Vis absorption spectroscopy.

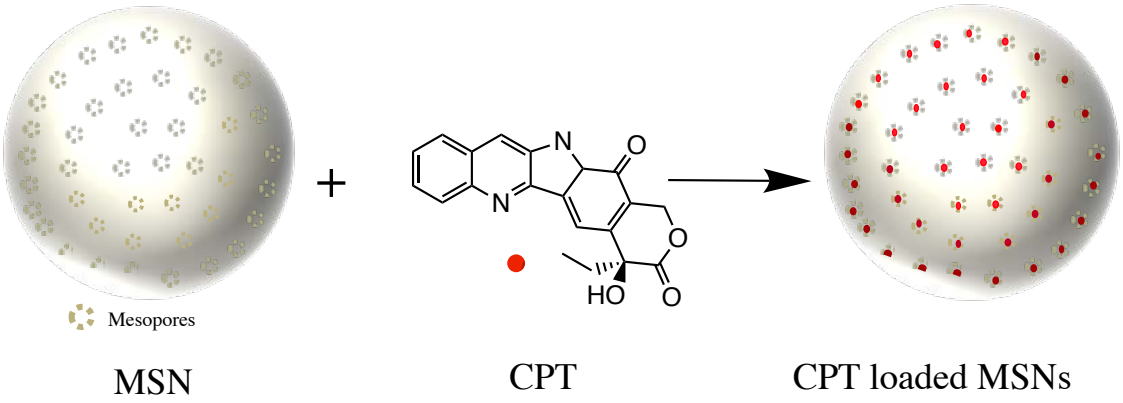


Figure 2.5.11

Schematic illustration of synthesis route to collection of **CPT** loaded **MSNs**.

Table 2.5.11

DLS sizes of **MSNs** and drug loaded **MSNs**.

Sample	Size d/ nm Intensity Distribution	PDI
MSNs	156 ± 29	0.148
CPT loaded **MSNs**	116 ± 17	0.518

Table 2.5.12

Zeta potentials of **MSNs** and drug loaded **MSNs**.

Sample	Zeta Potential ζ/ mV
MSNs	-34 ± 6
CPT loaded **MSNs**	9 ± 7

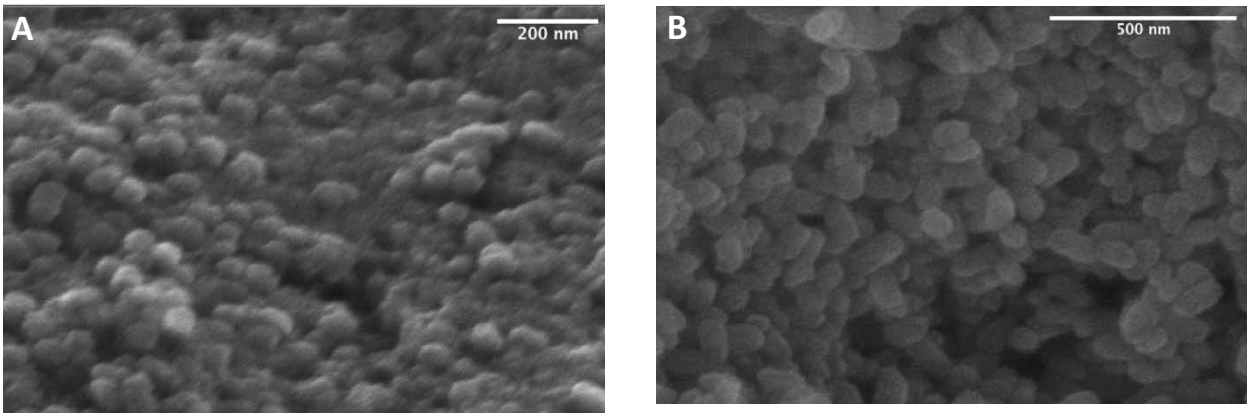


Figure 2.5.12

A: SEM image of **MSNs**, average diameter 60 nm. B: SEM image of **CPT** loaded **MSNs**, average diameter 72 nm. SEM diameters averaged from 10 NPs.

DLS analysis provides the hydrodynamic diameter of the NPs in solution, hence the larger values (table 2.5.11) compared to actual size obtained by SEM (figure 2.5.12). The PDI of the MSNs show a good narrow size distribution, whose value increases after loading with **CPT**, due to the incorporation of the drug in the pores and adsorbed on the surface. The morphology and size is observed to be stable after SEM imaging of the **CPT** loaded **MSNs**. The zeta potentials of the respective NPs were measured, which is an indication of surface charge. There was a large difference observed of 43 mV after drug loading, taking the zeta potential to a positive value of 9 mV. This drastic change suggests clearly the adsorption of **CPT** on the negative SiO_2 surface of the **MSNs**, hence the change to a positive value, as expected.

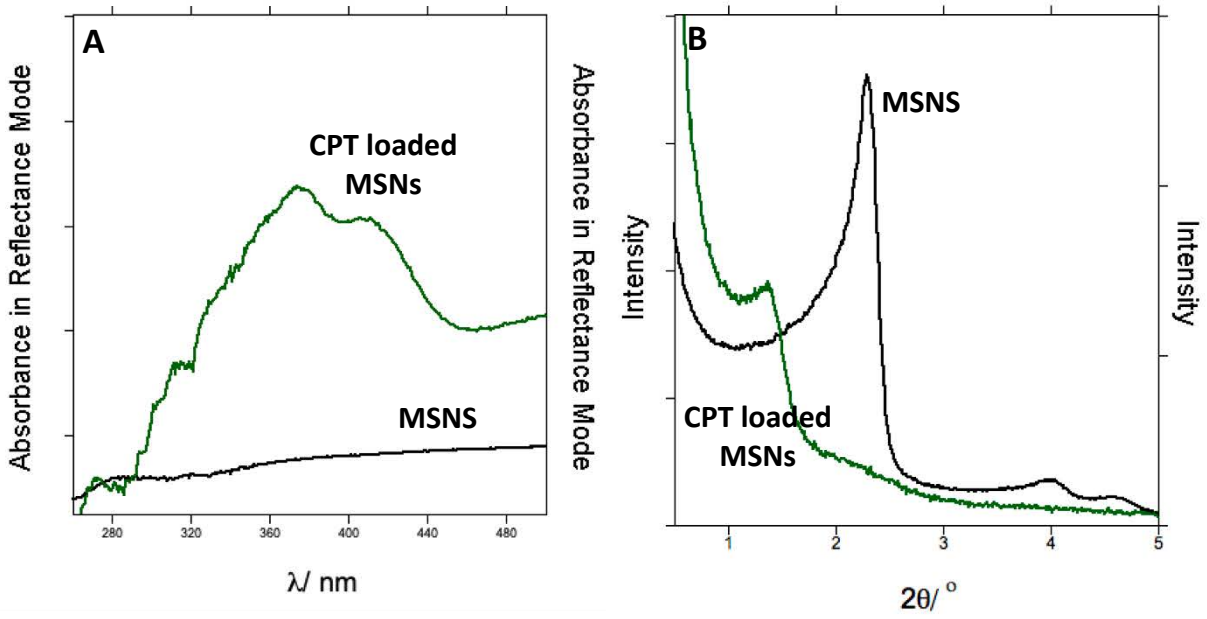


Figure 2.5.13

A: Solid state UV-Vis absorption of **MSNs** (black) and **CPT** loaded **MSNs** (green). B: SAXD patterns of **MSNs** (black) and **CPT** loaded **MSNs** (green).

The structural properties of the NPs were investigated by SAXD, to confirm the arranged order of the silica network in MCM-41 type **MSNs**[105]. Figure 2.5.13 B represents the SAXD patterns of **MSNs**, and **CPT** loaded **MSNs**. The diffraction pattern of the **MSNs** was observed to exhibit one intense peak at a 2θ value of 2.3 °, followed by two shoulders. This is a very characteristic

pattern of MCM-41 NPs, with the peaks indexing for (100), (110) and (200) as expected, confirming the disordered structure and 2D hexagonal array of mesopores. After loading with **CPT**, we observed a decrease in intensity and a shift in 2θ value, suggesting a change in pore diameter. This can be assumed to be attributed to the relationship between 2θ and diameter, arising from Bragg's law[105], and therefore a change in porosity post CPT incorporation.

Solid state UV-Vis absorption was used to investigate the presence of the drug in the NPs after loading. The plain **MSNs** control shows no absorbance as expected, compared to the **CPT** loaded **MSNs** with a λ_{max} of 370 nm, in agreement with solution UV-Vis absorption of **CPT**, confirming the presence of the drug within the NPs (see appendix, figure 8).

2.5.2. Europium Coated MSNs using Ligand L

MSNs were stirred with **L** and purified *via* centrifugation to collect **L.MSN**. Eu(III) was titrated in to the nanoparticle solution to form **Eu- L.MSN**, monitored by luminescence.

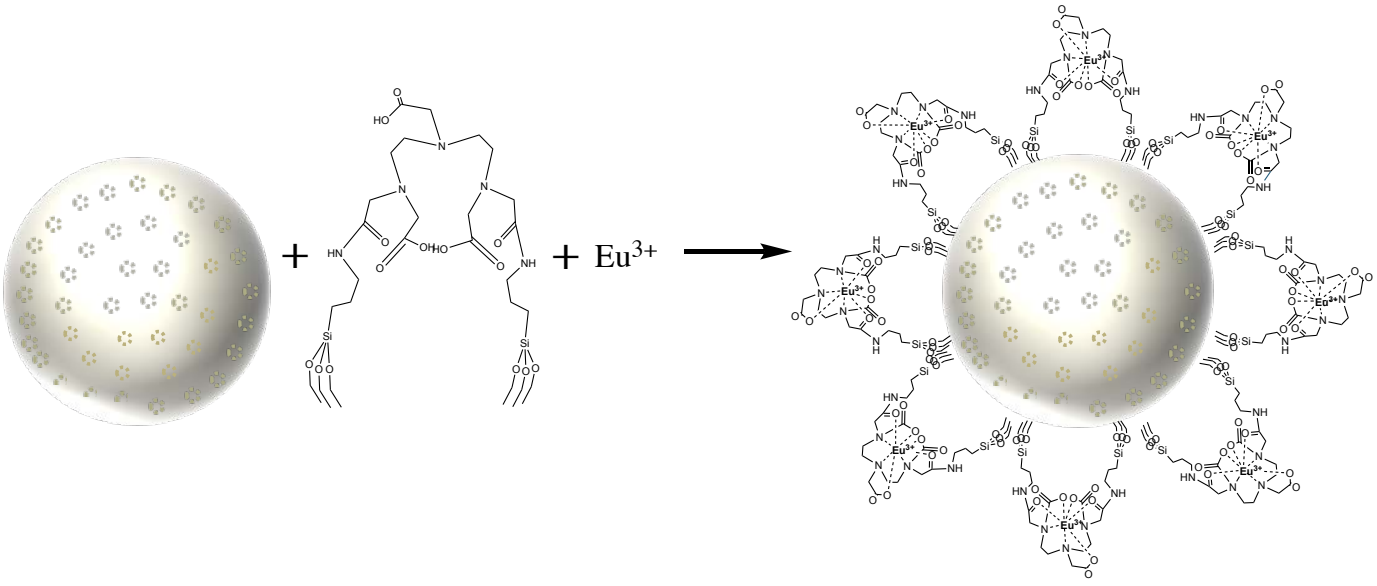


Figure 2.5.21

Schematic illustration of design route to **L.MSN** complexed to Eu(III).

The luminescence study of **L.MSN** complexed to Eu(III) was performed to investigate if the binding event could be observed by monitoring the Eu(III) emission.

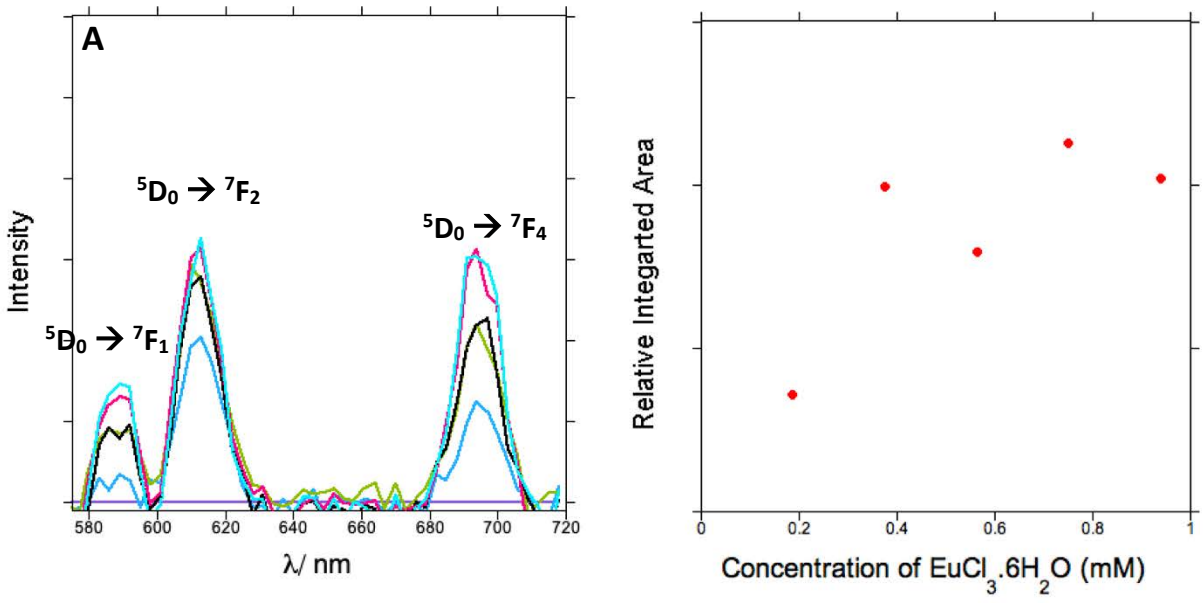


Figure 2.5.22

A: Emission spectrum of the binding between Eu(III) and **L.MSN**, λ_{exc} = 394 nm. Eu(III) (18 mM) was titrated into a solution of **L.MSN** (0.7 mg mL^{-1}) to a final concentration of Eu(III) of 0.94 mM. B: A plot of relative integrated area between λ = 601 nm – 628 nm against Eu(III) concentration. Emission spectra corrected for PMT and instrument response.

As Eu(III) was titrated into a solution of the ligand and **MSNs**, the Eu(III) emission was monitored as the metal ion was excited directly at λ_{exc} = 394 nm. An increase in emission intensity was observed and detected at three characteristic transitions of $^5D_0 \rightarrow {}^7F_{1,2,4}$. The hypertensive transition at 615 nm ($^5D_0 \rightarrow {}^7F_2$) shows high intensity, and is comparable with the electric dipole transition $^5D_0 \rightarrow {}^7F_4$ at and 690 nm. The increase in intensities of these transitions indicate the successful binding between the metal ion and **L.MSN**. This observation can be attributed to the exclusion of water molecules surrounding the metal ion, as the ligand binds to Eu(III), in addition to hypersensitive transitions of Eu(III)[111, 112].

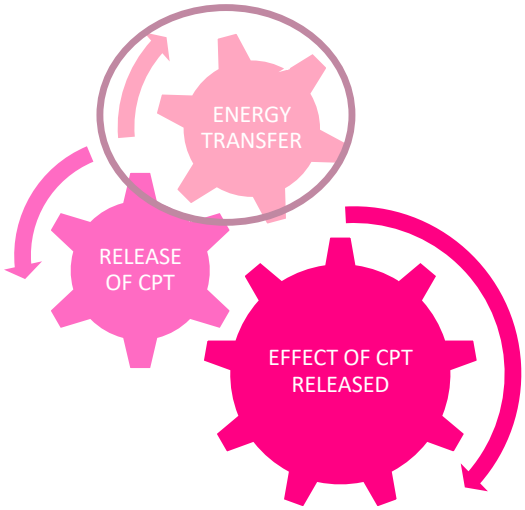
The change in intensity of the transitions observed in the emission spectra also indicate successful binding between Eu(III) and **L**, credited to hypersensitive transitions. Hypersensitive transitions of Lns are induced by the decrease in symmetry around the metal ion as the coordination sphere is filled. Due to shielding effects, it's known that the Ln 4*f*

orbitals do not interact well with *d* orbitals of ligands, and therefore any ligand field stabilisations effects are considered to be negligible. The interaction between the Ln 4*f* and ligand *d* orbitals can become more prominent due to hypersensitive *f-f* transitions. When coordinated to water molecules Eu(III) is in a highly symmetrical environment, where only magnetic dipole transitions are allowed ($\Delta L = 0$, $\Delta J = 0, 1$). After coordination to a ligand the symmetry is lowered, giving rise to changes in intensities as electric dipole transitions become allowed (ΔL and $\Delta J = 0, 2, 4, 6$)[111, 112, 119-121].

DTPA ligand frameworks are known to have high stability constants, usually $K = 10^{15}$, important for the stability of the Ln complexes[113-116]. The polydentate ligand **L** can have a coordination number of 9 using hard oxygen and nitrogen donors, as the ligand saturates the ion's coordination sphere, the exclusion of water minimises quenching from high energy *OH* vibrations[114, 117, 118]. The saturation around the metal ion, with a high coordination number, was the main attraction behind the ligand design, with the silane legs enabling attachment to silica NPs *via* the Si – O bond.

2.5.3. Sensitisation of Eu(III) by CPT

The first major step to the project was to determine the energy transfer process that could occur using the anticancer drug **CPT**, to sensitise Ln(III) luminescence.



CPT is a highly conjugated molecule with a high absorption coefficient, ε_{350} (MeOH) = 20000 mol^{-1} dm^3 cm^{-1} (see appendix figure 10) in agreement with literature values[122, 123, 125]. With

the role as a drug for targeted tumour sites, the high conjugation and ε enables **CPT** to simultaneously act as a sensitiser for Ln(III) ions.

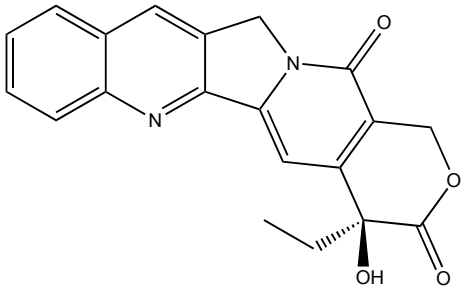


Figure 2.5.31

Structure of **CPT**.

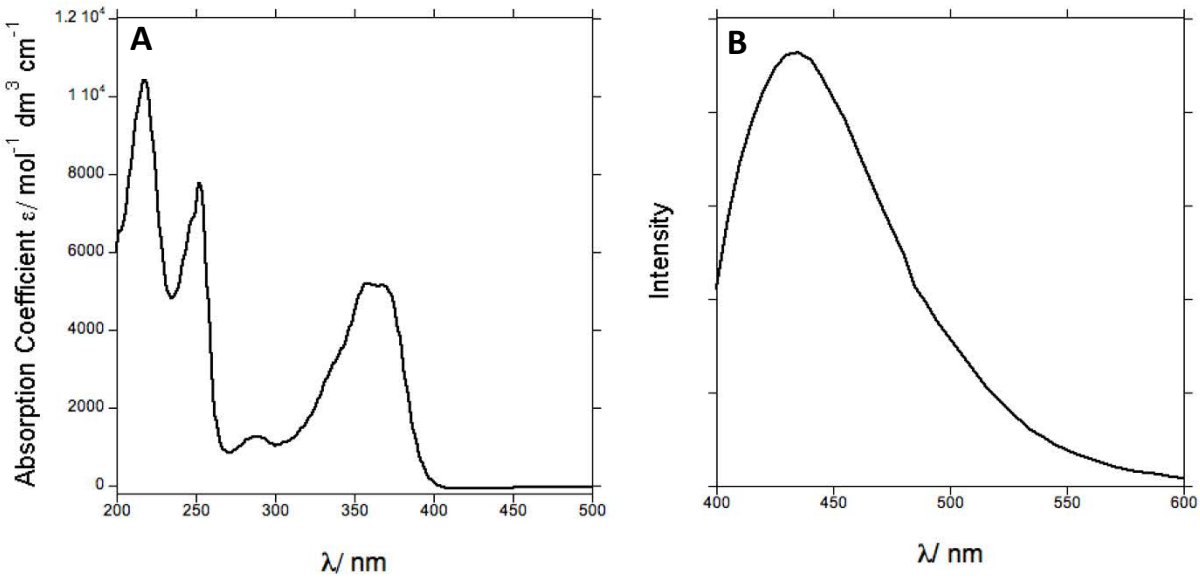


Figure 2.5.32

A: UV-Vis spectrum of **CPT** (30 μM, MeOH). B: Emission spectrum of **CPT** (30 μM, MeOH), λ_{exc} = 350 nm. Emission spectra corrected for PMT and instrument response.

CPT exhibits absorbance with an intense shoulder at λ_{max} = 360 nm attributed to $\pi \rightarrow \pi^*$ transition, and two other bands at λ_{max} = 250 nm, and 220 nm[106, 124, 125] . The emission of **CPT** in MeOH can be monitored at λ_{max} = 430 nm with an excitation wavelength of 350 nm, giving

a Stokes shift of 80 nm. With a high absorption coefficient, and emission between 400 nm – 500 nm, we can exploit **CPT** as a sensitiser for Ln ions.

To study the sensitisation, the emission of Eu(III) was monitored in a solution of the metal ion and **CPT**, in the presence of base.

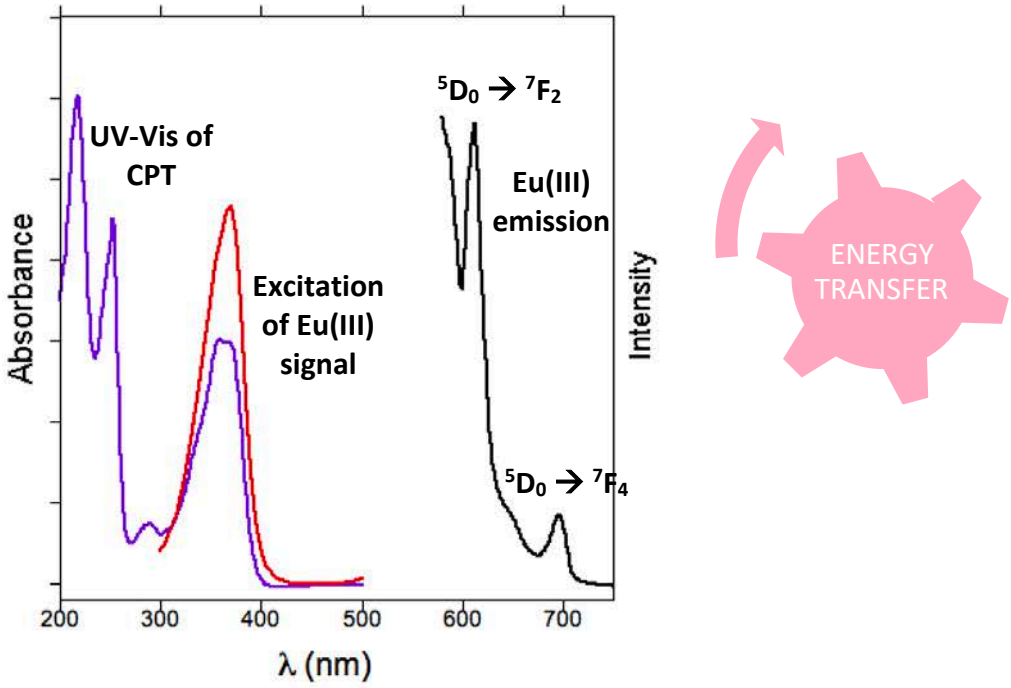


Figure 2.5.33

Photophysical characterisation of Eu(III) emission sensitised by **CPT** in solution. **CPT** absorbance (30 μM, MeOH) (purple), Eu(III) excitation at λ_{em} = 615 nm (red), Eu(III) emission (0.03 mM) from sensitisation of **CPT** (30 μM, MeOH), λ_{exc} = 350 nm. Emission spectra corrected for PMT and instrument response. Excitation spectra corrected for lamp response.

In a solution of **CPT** in the presence of base, Eu(III) emission was detected by characteristic sharp lines at λ_{em} = 615 nm ($^5D_0 \rightarrow {}^7F_2$) and 695 nm ($^5D_0 \rightarrow {}^7F_4$), with the $^5D_0 \rightarrow {}^7F_2$ transition being most intense. The absence of other Eu(III) transitions suggests the low symmetrical environment around the metal ion when coordinated to **CPT**[111]. The detected signal

suggested energy transfer from **CPT** due to the excitation wavelength of 350 nm used to obtain the Eu(III) emission. To confirm this, the excitation spectrum at λ_{em} = 615 nm of the $^5D_0 \rightarrow {}^7F_2$ transition was investigated. The spectrum (figure 2.5.33, red) shows good overlap with the **CPT** solution UV-Vis absorbance spectrum (figure 2.5.33, purple) indicating that at the excitation wavelength of 350 nm, the population of the Eu(III) excited state giving rise to emission is most intense at this wavelength. To further prove this observation, the energy transfer between **CPT** and Eu(III) was monitored spectroscopically.

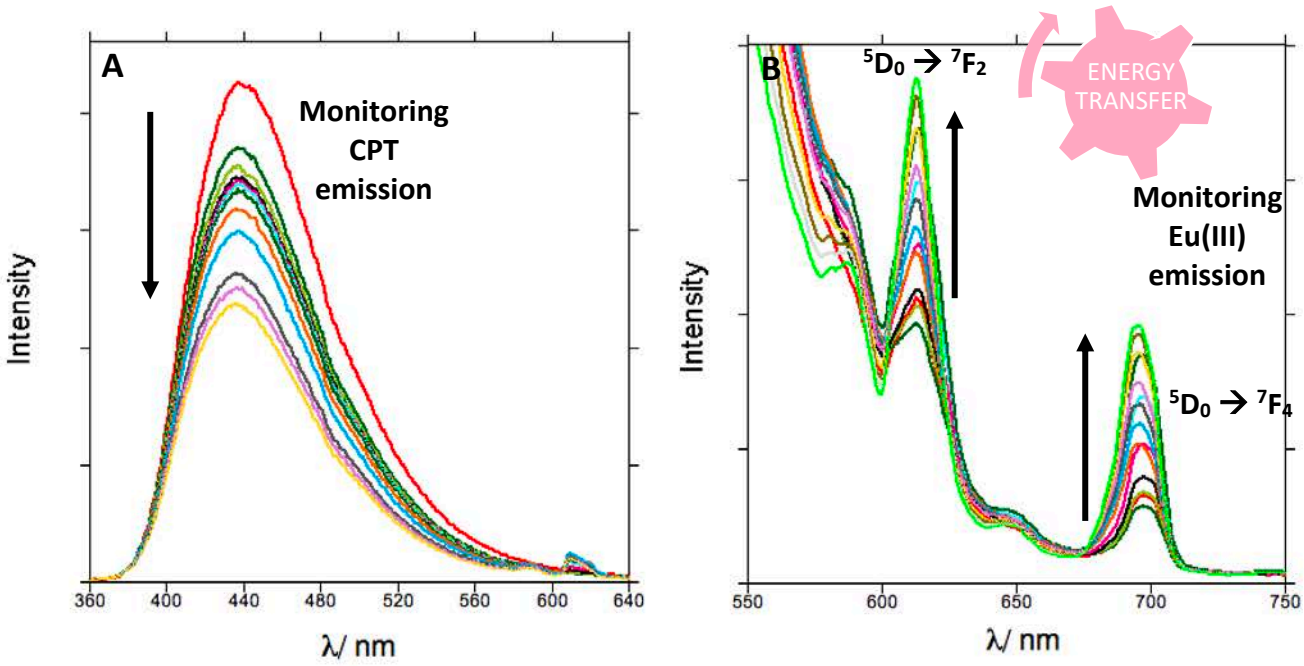


Figure 2.5.34

Emission spectra of Eu(III) (5 mM) titrated into **CPT** (0.05 mM, MeOH) to a final concentration of Eu(III) 1.7 mM, and **CPT** 0.03 mM, λ_{exc} = 350 nm. A: monitoring **CPT** emission. B: monitoring Eu(III) emission. Emission spectra corrected for PMT and instrument response.

As the metal ion was titrated into a solution of the drug, a decrease in **CPT** emission was observed at λ_{em} = 430 nm, and simultaneously an increase in Eu(III) emission was monitored. Moreover, the comparable intensity ratio between the $^5D_0 \rightarrow {}^7F_2$ and $^5D_0 \rightarrow {}^7F_4$ transitions indicate the sensitivity to environmental changes as Eu(III) is titrated into a solution of **CPT**[111].

This luminescence study was important to show the energy transfer occurring between the drug and the metal ion, detected by the changes in emission signal as the process occurred.

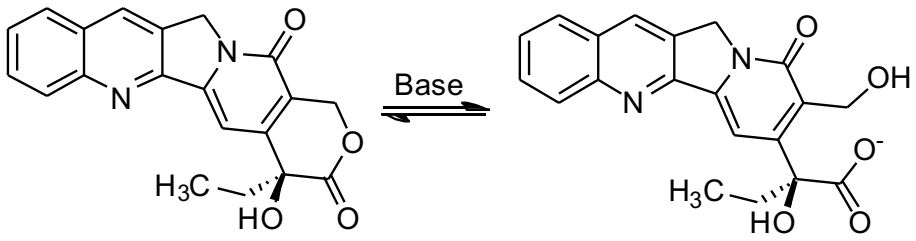


Figure 2.5.35

Ring opening of **CPT** in the presence of base, forming the carboxylate and providing a binding site for coordination to Eu(III).

The Eu(III) emission signal detected was confirmed to be as a result of sensitisation from **CPT**, in the presence of base. Under basic conditions, **CPT** can undergo ring opening forming the carboxylate, whose properties are inactive as an anticancer drug[122, 126-129]. It is well known that the drug exists in its natural form as a lactone, and many studies have reported to show the inactivity of the carboxylate form. In this case in presence of base, we have created a binding site for the metal ion enabling the sensitisation process in solution, as a proof of study. However, this is not ideal for the diagnostic applications of the NP design created. In order to have good potential as a nanocarrier, simultaneously monitoring drug release *via* Ln luminescence, it is imperative that we are able to sensitise Ln emission using the closed ring **CPT** in NPs.

Furthermore, it is essential to note that the sensitisation process from the drug to the Eu(III) centre in solution, in absence of base, was not successful. With no binding site on the sensitising unit, Eu(III) emission signal cannot be detected, and thus signified the requirement for a nanocarrier to hold the active drug in close proximity to enable energy transfer.

2.6. Synthesis and Characterisation of Non-Porous Silica Nanoparticles Doped with CPT

Non-porous silica NPs were synthesised in order to create a one pot synthesis, essentially creating NPs with the drug templated in the structure, and thus providing a potential solution to keep **CPT** in its active form and simultaneously act as a sensitising unit.

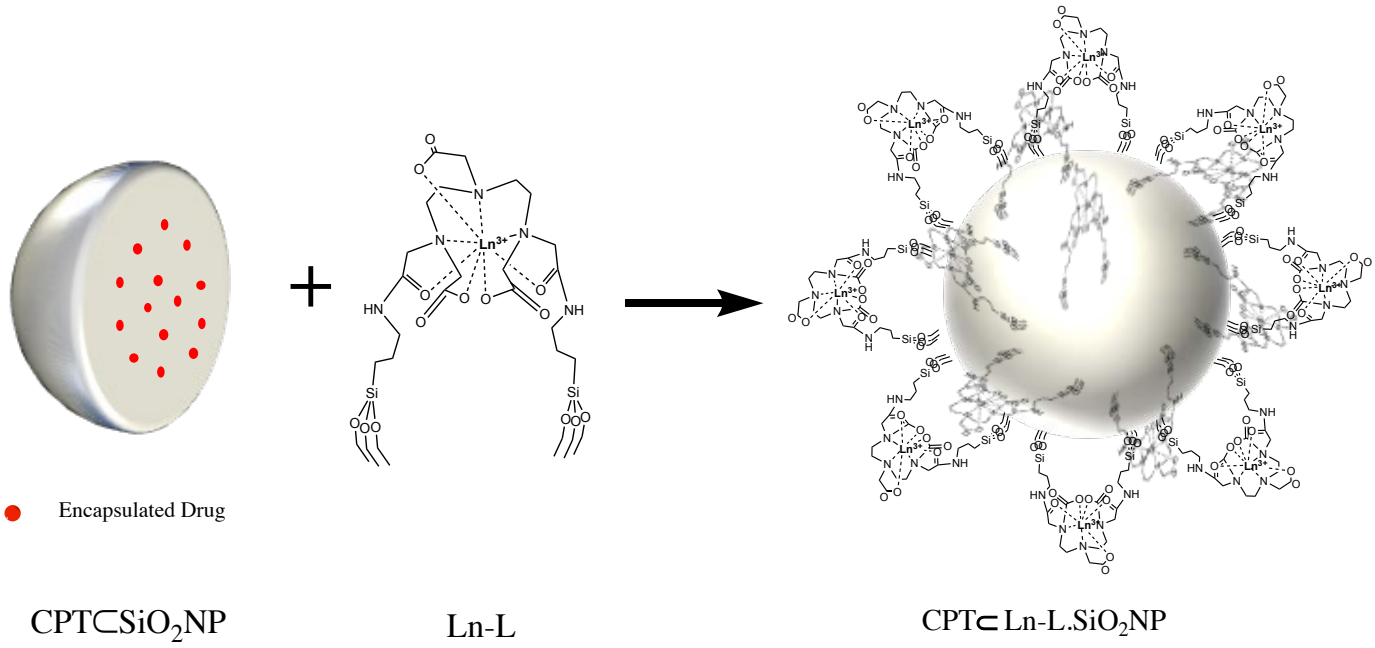


Figure 2.61

Schematic illustration of synthesis route to **CPT⊂Ln-L.SiO_2NP**.

Non-porous silica NPs (**SiO_2NP**) doped with **CPT** were synthesised based on the Stober method, using TEOS as the silica precursor, and ammonia as the base catalyst[130-132]. This method has been used previously for preparing dye doped silica NPs by Pikramenou *et. al.* by generally adding the dye at the beginning of the reaction[132]. The hydrolysis of TEOS and condensation into oligomers, followed by aggregation and growth of the primary particles to secondary particles occurs[132, 137]. The addition of the drug at the beginning of the reaction enables interaction with the primary particles, giving opportunity to inclusion within the aggregation and growth of the particles. This synthesis was used to create encapsulated **CPT** in silica NPs, forming **CPT⊂SiO_2NP**. The NPs were characterised by DLS, SEM, and solid state UV-Vis absorption.

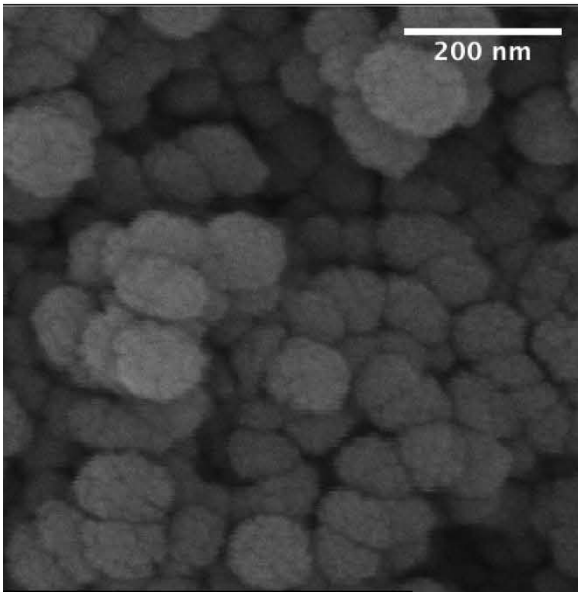


Figure 2.62

SEM image of **CPT⊂SiO$_2$NP**, average diameter 95 nm. SEM diameter averaged from 10 NPs.

Table 2.61

Hydrodynamic diameter of NPs by DLS.

Sample	Size d/ nm Intensity Distribution	PDI
CPT⊂SiO$_2$NP	83 ± 26	0.095

Table 2.62

Zeta potentials of NPs by DLS.

Sample	Zeta Potential ζ/ mV
SiO$_2$NP	-50 ± 9
CPT⊂SiO$_2$NP	-51 ± 14

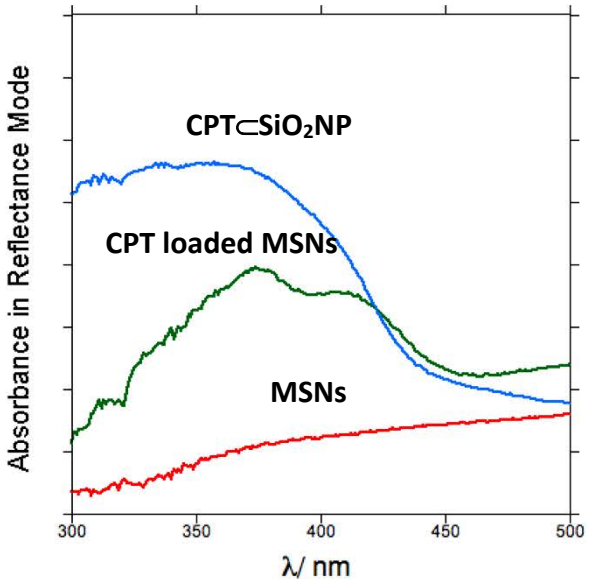


Figure 2.63

Solid state UV-Vis absorption of **CPT** functionalised NPs; **CPT⊂SiO₂NP** (blue), **CPT** loaded **MSNs** (green), **SiO₂NP** (red).

The hydrodynamic diameter of **CPT⊂SiO₂NP** by DLS is 70 nm with a good PDI, showing a good narrow distribution of sizes in the nanoparticle solution (table 2.61). This observation was confirmed by SEM showing the NPs to be on average 95 nm in diameter, with good spherical shape and no aggregation (figure 2.62). The zeta potential was also measured against control **SiO₂NP** with no drug, to investigate whether the drug was included in the NPs mostly, rather than adsorbed on the nanoparticle surface (table 2.62). The very negative zeta potential of -51 mV suggests that **CPT** has been successfully encapsulated inside the NPs, dominating over any drug molecules that may be adsorbed on the surface. The large difference between the zeta potentials of **CPT⊂SiO₂NP** and **CPT** loaded **MSNs** (table 2.5.12) suggests that this is the case. Any adsorbed **CPT** molecules on the surface would significantly change the potential to a more positive value (table 2.5.12). Solid state UV-Vis absorbance was used to detect the presence of **CPT** in the NPs (figure 2.63), confirming the success of the encapsulation. The presence of the absorption between λ_{max} = 350 nm and 400 nm can be attributed to **CPT**, with good overlap of **CPT** loaded **MSNs**, confirming the observation.

2.7. Lanthanide Coated SiO_2NPs

The synthesis to forming **CPT⊂Ln-L.SiO_2NP** (figure 2.61) (Ln(III) = Eu, Yb, Nd), was carried out, and purified *via* centrifugation before collecting the NPs. Their sizes were characterised by DLS and SEM, and additionally their surface charge by measuring the zeta potential.

Table 2.71

Hydrodynamic diameter of NPs by DLS.

Sample	Size d/ nm Intensity Distribution	PDI
CPT⊂SiO_2NP	83 ± 26	0.095
CPT⊂Eu-L.SiO_2NP	80 ± 42	0.272
CPT⊂Nd-L.SiO_2NP	84 ± 39	0.243
CPT⊂Yb-L.SiO_2NP	94 ± 63	0.298

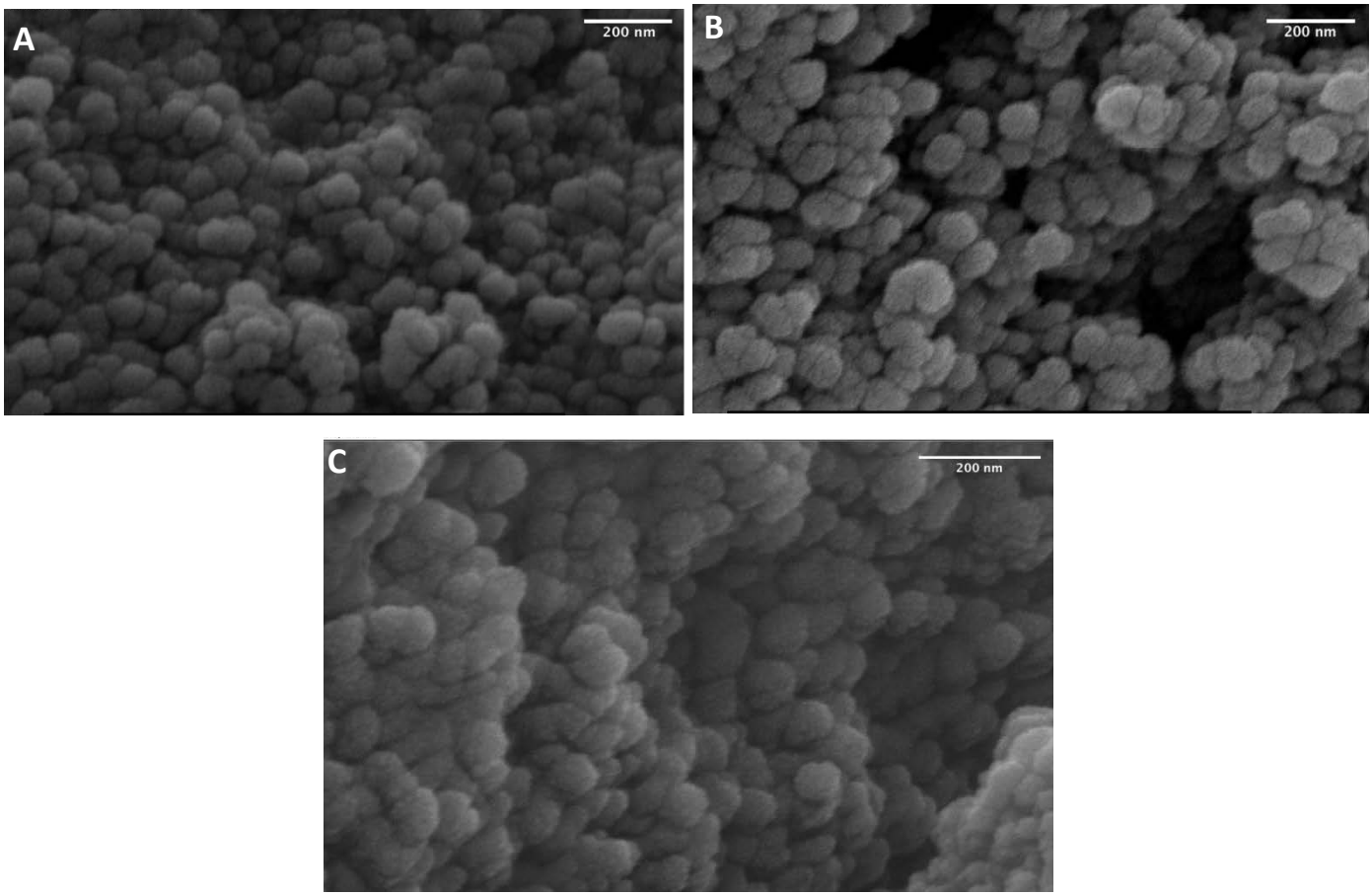


Figure 2.71

SEM images of **CPT⊂Ln-L.SiO_2NP**. A: Ln(III) = Eu, average diameter 79 nm. B: Ln(III) = Nd, average diameter 89 nm. C: Ln(III) = Yb, average diameter 75 nm. SEM diameters averaged from 10 NPs.

Table 2.72

Zeta potentials of the NPs measured by DLS.

Sample	Zeta Potential ζ/ mV
CPT⊂SiO_2NP	-51 ± 14
CPT⊂Eu-L.SiO_2NP	-24 ± 10
CPT⊂Nd-L.SiO_2NP	-18 ± 12
CPT⊂Yb-L.SiO_2NP	-24 ± 5

The hydrodynamic diameters of the Ln coated **SiO_2NP**s were measured using DLS (table 2.71). Upon coating of the **CPT⊂SiO_2NP** with the Ln complexes, no significant change was observed in the size distribution due to the small size of **L** compared to the NPs. They were measured with PDI values between 0.2 – 0.3, as expected after coating of the NPs. The sizes and morphology were confirmed by SEM imaging (figure 2.71). The zeta potentials of the corresponding NPs were also measured to obtain their surface charge, indication of a change to the surface after coating. An increase in zeta potential of 27 mV (**CPT⊂Eu-L.SiO_2NP** and **CPT⊂Yb-L.SiO_2NP**) and 33 mV (**CPT⊂Nd- L.SiO_2NP**) was observed after coating **CPT⊂SiO_2NP**. This was a good indication of successful coating onto the **CPT⊂SiO_2NP**s, observed by the large positive change in zeta potential.

2.7.1. Luminescence Studies of Lanthanide Coated SiO_2NPs

We have previously proved the successful energy transfer between **CPT** and Eu(III), in the presence of base in solution. The use of **SiO_2NPs** to firstly carry the drug to its target site acting as a nanocarrier, and secondly to hold **CPT** in its active form (figure 2.5.35) in close proximity to the metal ion to allow sufficient energy transfer[113], was implemented. If this is achievable, Ln(III) luminescence signal from sensitisation of **CPT** can be used to determine whether the drug has been released, or not. The synthesis to forming **CPT⊂Ln-L.SiO_2NP** (figure 2.61) (Ln(III) = Eu, Yb, Nd), was carried out, and purified *via* centrifugation before collecting the NPs.

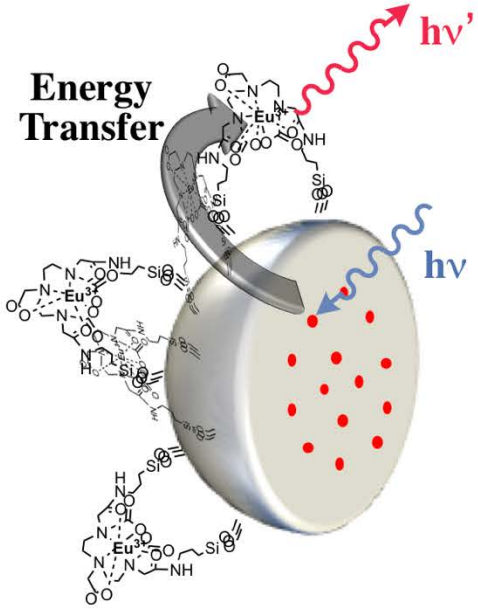


Figure 2.7.11

Schematic illustration of the energy transfer from **CPT** to **Ln-L** in the Ln coated **SiO_2NP** system, $h\nu < h\nu'$.

The Ln(III) luminescence signal was monitored from **CPT⊂Ln-L.SiO_2NP** NPs using λ_{exc} = 350 nm.

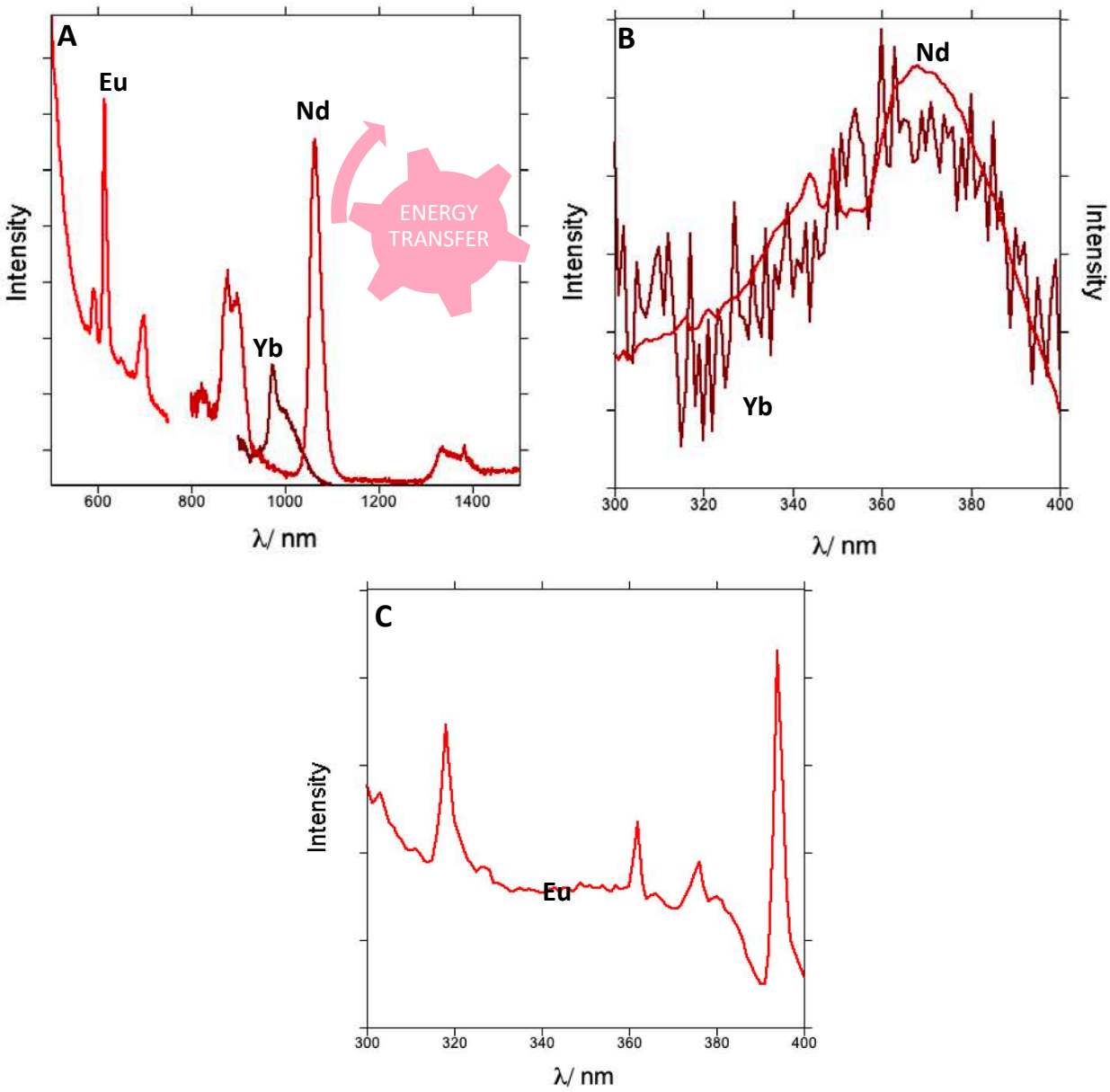


Figure 2.7.12

A: Solid state emission spectra of **CPT⊂Ln-L.SiO$_2$NP**, monitoring Ln emission, Ln(III) = Eu (red), Yb (brown), Nd (maroon), λ_{exc} = 350 nm. B: Excitation spectra of **CPT⊂Ln-L.SiO$_2$NP**, monitoring Ln excitation, Ln(III) = Yb (brown) and Nd (maroon) at their respective emission bands; λ_{em} = 975 nm (Yb) and 1060 nm (Nd). C: Excitation spectra of **CPT⊂Eu-L.SiO$_2$NP** monitoring Eu excitation at λ_{em} = 615 nm. Emission spectra corrected for PMT and instrument response. Excitation spectra corrected for lamp response.

The solid state emission signal was detected for each Ln(III) NP system by sensitisation of **CPT** at λ_{exc} = 350 nm. The characteristic emission signal was collected for the Eu(III) NPs, observed by three sharp peaks at λ_{em} = 590 nm, 615 nm and 695 nm ($^5D_0 \rightarrow {}^7F_{1,2,4}$ respectively), with the hypersensitive $^5D_0 \rightarrow {}^7F_2$ transition at λ_{em} = 615 nm being most intense. The high intensity of this transition indicates low symmetry around the Eu(III) ion and in addition, the transitions are not observed to be split (Stark levels), also indicating only one equivalent site for each Eu(III) ion[111, 135]. The difference in intensities of each transition reflects the hypersensitivity effect, previously discussed in section 2.5.2, suggesting the Ln complex has retained its stability post addition to **CPT⊂SiO$_2$NP**[112]. The intensity can be seen to tail down before we are able to detect Eu(III) signal, which can be attributed to the strong **CPT** emission tailing down. Due to the high ε and therefore, strong emission signal of **CPT**, a difference of 185 nm between λ_{max} = 615 nm (EuIII) and 430 nm (**CPT**), is only just sufficient enough in this case to detect the visible emitting Ln(III). With proof of concept of the drug's ability to sensitise Eu(III) (section 2.5.3), and the latter Eu(III) solid state emission signal from **CPT⊂Eu-L.SiO$_2$NP** (figure 2.7.12, A) using λ_{exc} = 350 nm, was strong evidence of successful energy transfer in the nanoparticle system designed. This was an imperative result that showed great potential for the 'on-off' switch system, but more significantly to use near infra-red (NIR) Ln. NIR emitting Lns are an attractive choice due to their ability to penetrate tissue deeper, and the reduced interference from background luminescence of biomolecules. Additionally, with a large difference in λ_{max} between **CPT** emission and NIR Ln(III) emission, the NIR Ln(III) signal can be optimised[118, 136].

The characteristic emission signal for Nd(III) from **CPT⊂Nd-L.SiO$_2$NP** was collected at λ_{em} = 890 nm ($^4F_{3/2} \rightarrow {}^4I_{9/2}$), 1060 nm ($^4F_{3/2} \rightarrow {}^4I_{11/2}$) and 1335 nm ($^4F_{3/2} \rightarrow {}^4I_{13/2}$), with the $^4F_{3/2} \rightarrow {}^4I_{11/2}$ transition being most intense. Yb(III) emission signal, albeit weaker, was also detected from **CPT⊂Yb-L.SiO$_2$NP** at λ_{em} = 975 nm ($^2F_{5/2} \rightarrow {}^2F_{7/2}$)[118]. An excitation wavelength of λ_{exc} = 350 nm was also used here (in addition to **CPT⊂Eu-L.SiO$_2$NP**) to monitor the respective emission signal from each Ln(III), providing strong evidence for good energy transfer from **CPT** to Ln(III) within the designed system. To further confirm this, the excitation spectra of **CPT⊂Ln-L.SiO$_2$NP** (Ln(III) = Yb and Nd) were recorded at their respective most intense transitions: λ_{em} = 975 nm (Yb) and λ_{em} = 1060 nm (Nd). Good overlap between the spectra

was observed between 300 nm to 400 nm, in agreement with **CPT** UV-Vis absorbance (see appendix figure 19), confirming the observed Ln(III) emission was a result of energy transfer from **CPT**. Furthermore, the excitation spectra allows us to identify that the respective transitions $^2F_{5/2} \rightarrow {}^2F_{7/2}$ (Yb) and $^4F_{3/2} \rightarrow {}^4I_{11/2}$ (Nd) are most intensely populated when λ_{exc} = 375 nm. The excitation spectra of **CPT⊂Eu-L.SiO$_2$NP** at λ_{em} = 615 nm was also recorded but unlike figure 2.7.12 B, showed inefficient energy transfer perhaps arising from the smaller Stokes shift between **CPT** absorbance and Eu(III) emission at 620 nm.

The **CPT** emission and excitation was also monitored from the **CPT⊂Ln-L.SiO$_2$NP** (Ln(III) = Eu, Yb, Nd) NPs.

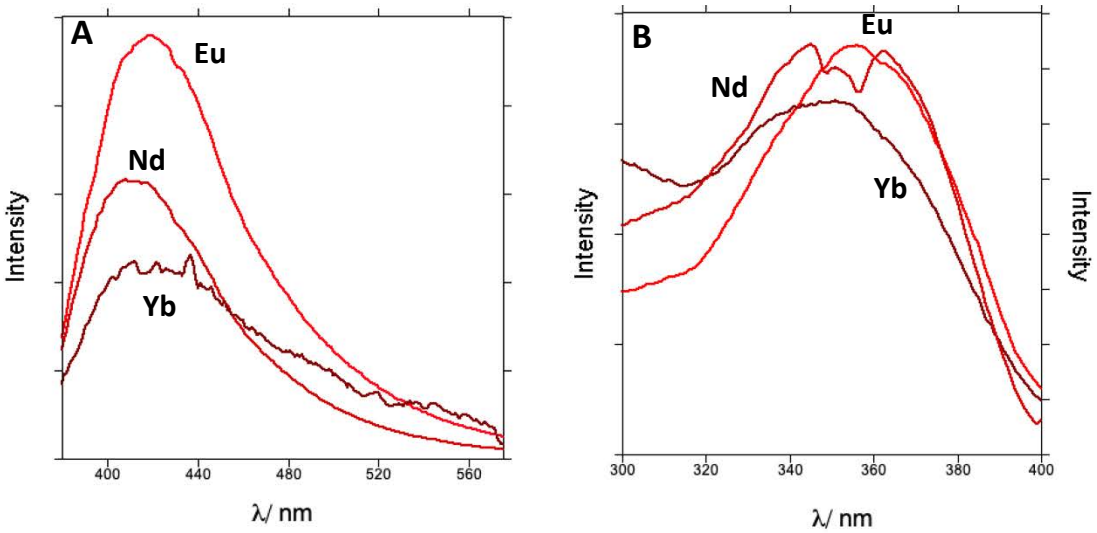


Figure 2.7.13

A: Solid state emission spectra of **CPT⊂Ln-L.SiO$_2$NP**, monitoring **CPT** emission, Ln(III) = Eu (red), Yb (brown), Nd (maroon), λ_{exc} = 350 nm. B: Excitation spectra of **CPT⊂Ln-L.SiO$_2$NP**, monitoring **CPT** excitation, Ln(III) = Eu (red), Yb (brown), Nd (maroon), at their respective emission bands; λ_{em} = 420 nm. Emission spectra corrected for PMT and instrument response. Excitation spectra corrected for lamp response.

Strong **CPT** emission was recorded for each nanoparticle system using the same excitation wavelength, λ_{exc} = 350 nm. Good overlap was observed between each NP system; λ_{em} = 420 nm (Ln(III) = Eu and Yb), and λ_{em} = 410 nm (Ln(III) = Nd), which was also reflected in their

respective excitation spectra, in good agreement with **CPT** UV-Vis absorbance (see appendix figure 19).

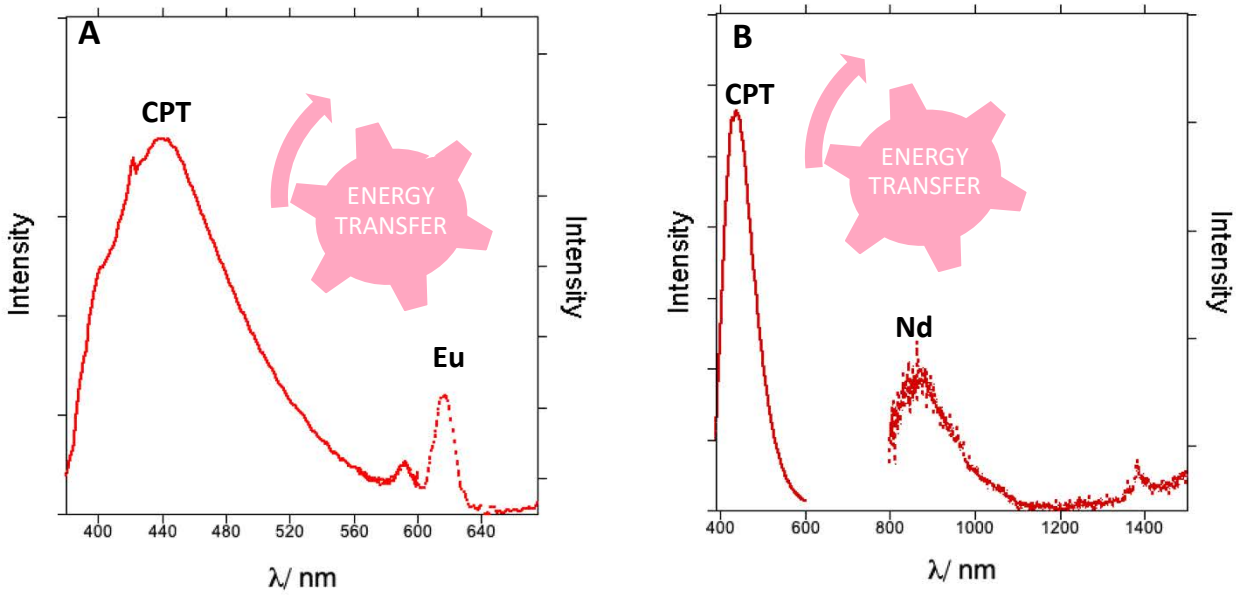


Figure 2.7.14

A: Solution emission spectra of **CPT⊂Eu-L.SiO$_2$NP** in water (1 mg mL^{-1}, H_2O), monitoring **CPT** emission (red, solid), and Eu(III) emission (red, dotted), λ_{exc} = 350 nm. B: Solution emission spectra of **CPT⊂Nd-L.SiO$_2$NP** in D_2O (1 mg mL^{-1}, D_2O), monitoring **CPT** emission (maroon, solid), and Nd(III) emission (maroon, dotted), λ_{exc} = 350 nm. Emission spectra corrected for PMT and instrument response.

The emission signal in solution was also detected for the Eu(III) and Nd(III) NP system by sensitisation of **CPT** at λ_{exc} = 350 nm (figure 2.7.14 A and B respectively). The characteristic emission signal was collected for the Eu(III) NPs observed by two sharp peaks at λ_{em} = 590 nm and 615 nm ($^5D_0 \rightarrow {}^7F_{1,2}$ respectively). The high intensity of the hypersensitive transition, also observed in solid state, correlates with the low symmetry around the Eu(III) ion[111]. Monitoring the Nd(III) emission signal proved difficult despite using D_2O and inert conditions, however the signal at λ_{em} = 890 nm ($^4F_{3/2} \rightarrow {}^4I_{9/2}$), and 1335 nm ($^4F_{3/2} \rightarrow {}^4I_{13/2}$) was observed, unusually without the detection of the $^4F_{3/2} \rightarrow {}^4I_{11/2}$ transition at λ_{em} = 1060 nm. This could be a consequential effect of quenching mechanisms, especially sensitive for NIR Lns[118]. Monitoring

Yb(III) emission signal from **CPT⊂Yb-L.SiO$_2$NP** in solution was not successful due to the inert conditions required for detection of the NIR signal in solution[118]. The solution emission observed however, for both **CPT⊂Eu-L.SiO$_2$NP** and **CPT⊂Nd-L.SiO$_2$NP** was an important result, in addition to the solid state emission and corresponding excitation spectra (figure 2.7.12), as this was proof of the nanoparticle design holding **CPT** at a sufficient distance from **Ln-L** to sensitise Ln(III) emission (figure 2.7.11).

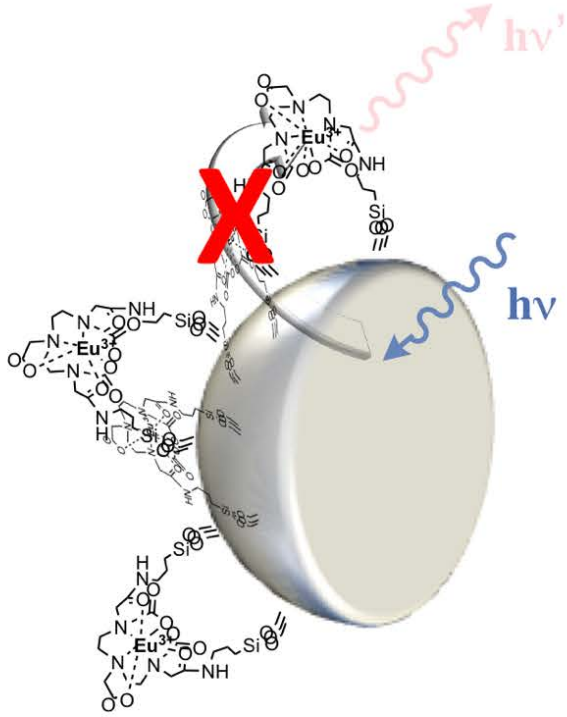


Figure 2.7.15

Schematic illustration of control **Ln-L.SiO$_2$NP** NPs (Ln(III) = Eu, Yb, Nd) in absence of **CPT**.

Control experiments of the respective nanoparticle systems without **CPT** (figure 2.7.15), were also recorded to aid the evidence of **CPT** sensitisation in order to observe Ln(III) emission.

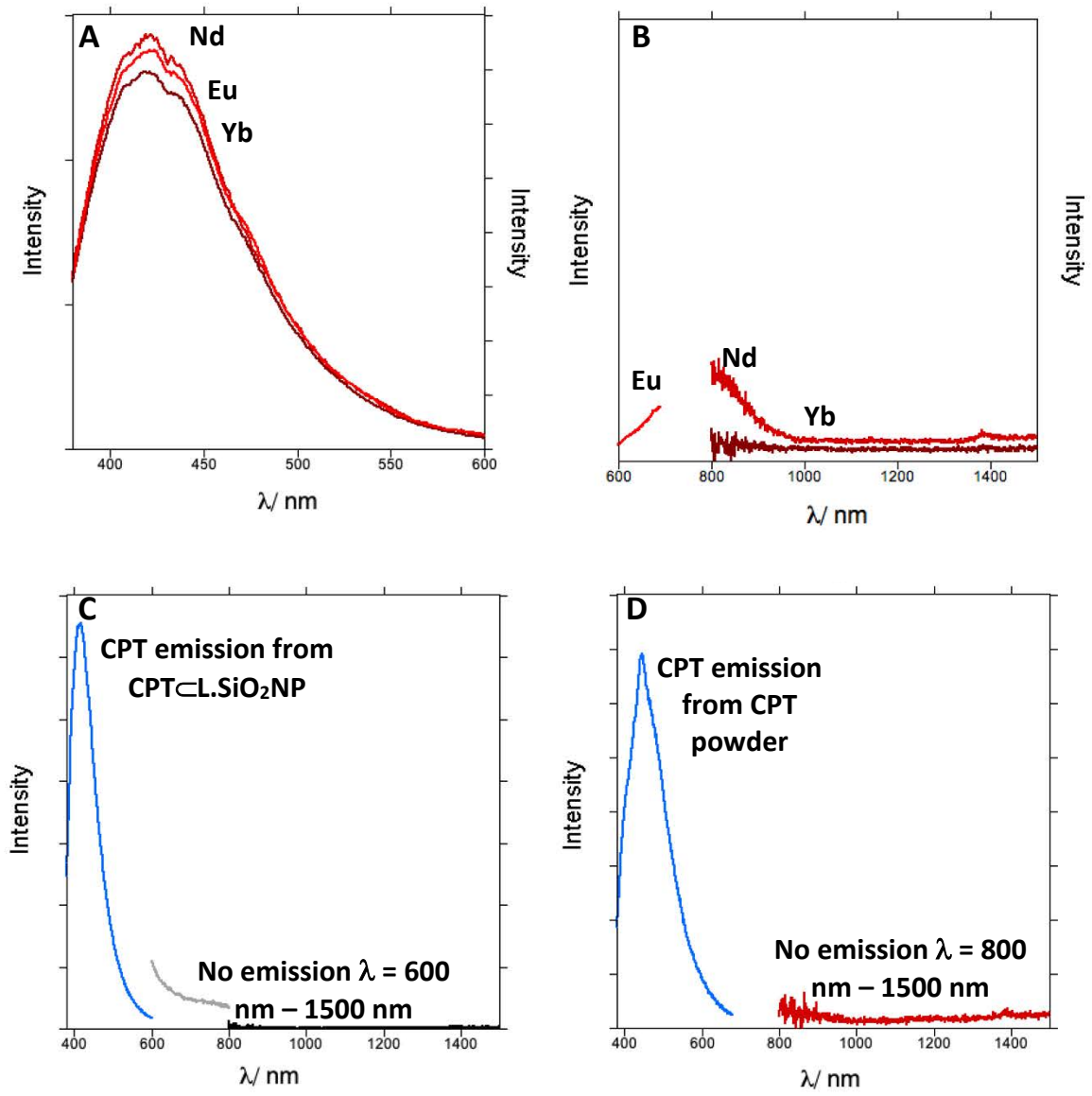


Figure 2.7.16

Solid state emission spectra of control experiments **Ln-L.SiO$_2$NP** (Ln(III) = Eu, Yb, Nd), λ_{exc} = 350 nm. A: Emission spectra of **Ln-L.SiO$_2$NP** in the visible range, Ln(III) = Eu (red), Yb (brown), Nd (maroon). B: Emission spectra of **Ln-L.SiO$_2$NP** in the visible – NIR range, Ln(III) = Eu (red), Yb (brown), Nd (maroon). C: Emission spectra of **CPT⊂L.SiO$_2$NP**; **CPT** emission (blue), emission in the Ln(III) visible (grey) and NIR (black) range. D: Emission spectra of **Nd-L.SiO$_2$NP** mixed with **CPT** powder, **CPT** emission (blue), emission in the Ln(III) NIR range (maroon). Emission spectra corrected for PMT and instrument response.

Control experiments were conducted from **Ln-L.SiO$_2$NP** (in absence of **CPT**), **CPT⊂L.SiO$_2$NP** (in absence of Ln(III)), and **Nd-L.SiO$_2$NP** mixed with **CPT** powder. Emission was monitored in in the **CPT** and Ln(III) emission ranges to confirm the necessity of **CPT**'s presence within the designed system to observe sufficient energy transfer.

Firstly, the emission of **Ln-L.SiO$_2$NP** in absence of **CPT**, was monitored in the visible and NIR range using λ_{exc} = 350 nm (figure 2.7.16, A and B). Scattering of **SiO$_2$NPs** was observed in the same range as **CPT** emission, and this was confirmed by monitoring changes in λ_{em} as λ_{exc} was changed every 5 nm (see appendix figure 23). Zero **CPT** emission was observed between λ_{max} = 400 nm – 600 nm as expected. These control experiments also show zero emission signal in the Ln(III) visible and NIR range (figure 2.7.16, B), in addition to zero **CPT** emission in absence of the drug (figure 2.7.16, A). This confirmed the necessity of the drug's presence within the designed system, in order to observe the Laporte forbidden Ln(III) emission enhanced *via* sensitisation. Secondly, the emission of control **CPT⊂L.SiO$_2$NP** NPs were also monitored (figure 2.7.16, C), in absence of metal ions to show no interference from **CPT** emission beyond λ_{max} = 600 nm. Lastly, figure 2.7.16 D shows the emission of **Nd-L.SiO$_2$NP** mixed with **CPT** powder. **CPT** emission was observed as expected at λ_{max} = 440 nm, but no Nd(III) emission signal was detected in the NIR range. This control experiment showed the necessity of **CPT**'s presence to be within the nanoparticle system designed and encapsulated in the **SiO$_2$NP** to be within proximity to the metal ions, in order to observe Ln(III) emission due to efficient energy transfer.

Combining the conclusions gathered from the control experiments (figure 2.7.16), in addition to the observed solid state emission of **CPT⊂Ln-L.SiO$_2$NP** (Ln(III) = Eu, Nd and Yb) and the respective excitation spectra (figure 2.7.12), and more importantly the solution emission spectra of **CPT⊂Ln-L.SiO$_2$NP** (Ln(III) = Eu and Nd) (figure 2.7.14), shows strong evidence confirming the energy transfer process successfully occurring in these nanoparticle systems, without the presence of base.

2.8. Non-Porous Silica Nanoparticles Doped with CPT at Different Reaction Times

Ln(III) emission was successfully detected from **CPT⊂Ln-L.SiO$_2$NP**, from **CPT** sensitisation, synthesised by adding the drug in the beginning of the **SiO$_2$NP** reaction as discussed in section 2.6. The synthesis was based on the Stober method, following Lewis *et. al.*, who covalently incorporated Iridium complexes throughout a silica core in 2013[132]. The Pikramenou group previously also prepared dye doped silica NPs with the complex $[Ru(phen)_3]^{2+}$ [137].

Interestingly, this dye doped method was reported to show emission dependent properties on the time of the addition of the dye by Yang *et. al.*[133].

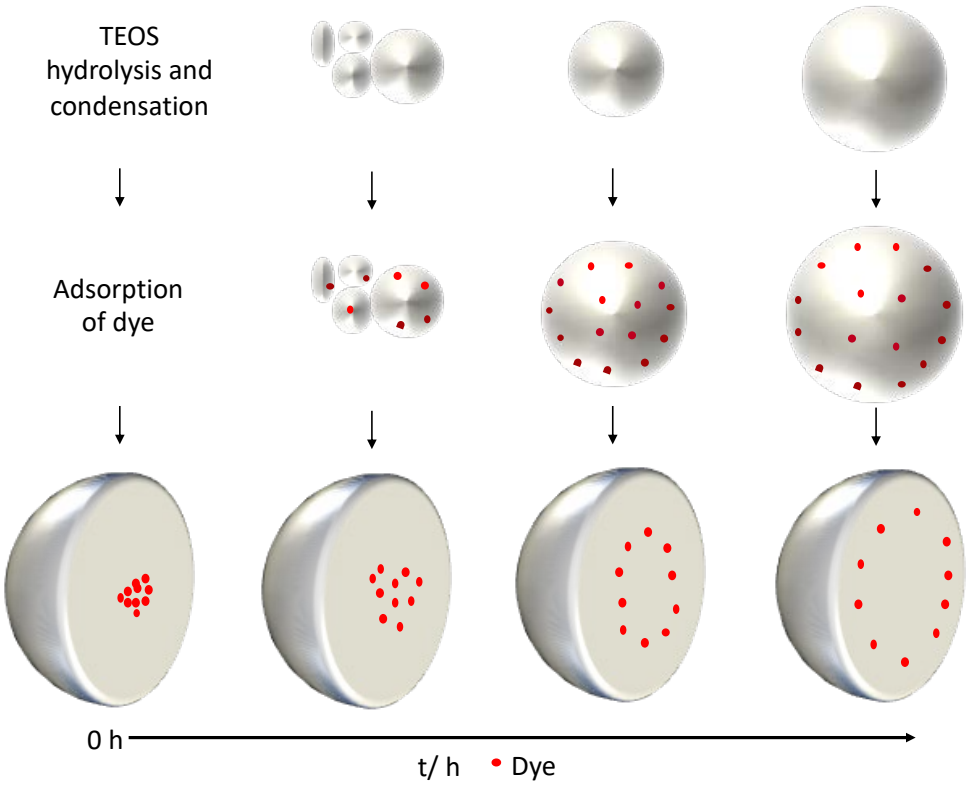


Figure 2.81

Schematic illustration of silica species at different times along the Stober process corresponding to the different times of addition of dye. Image is redrawn from Yang *et. al.*[133].

They found the emission properties of the dye doped NPs were dependent on the time of dye addition. Based on the experimental results found, they proposed the growth of the dye doped NPs, redrawn in figure 2.81. Introducing their dye at the beginning of the reaction enabled rapid TEOS hydrolysis and condensation, in the presence of ammonia, and therefore created a greater opportunity for dye molecules to come into contact with each other by interacting with the hydrolysing TEOS. Introducing the dye further into the reaction after the primary particles have been consumed and the growth of secondary particles becomes prominent, favoured adsorption of the dye onto the surface. The silica monomers can then deposit on the adsorbed dye, however if the dye is introduced much further into the reaction time the dye cannot be protected by a silica protection later[133].

Using this proposed mechanism as a guide, different **CPT⊂SiO₂NP** NPs were synthesised with the drug added at 3 h, with the same solvent concentrations used as per section 1.6. This was proposed to investigate whether the emission properties of **CPT⊂Ln-L.SiO₂NP** could be enhanced. Based on the hypothetical growth of dye doped silica NPs (figure 2.81), if **CPT** is added further into the reaction; 3 h, where the drug molecules are spaced out closer to the surface, in increasing proximity to **Ln-L**, the efficiency of the energy transfer process could be enhanced.

2.8.1. First method of synthesis of Non-Porous Silica Nanoparticles Doped with CPT

CPT⊂SiO₂NP NPs were synthesised as per section 2.6, with the dye added at 3 h, forming **CPT3⊂SiO₂NP_1**. The NPs synthesised in section 2.6 (dye added at 0 h) were renamed **CPT0⊂SiO₂NP_1** (and respectively **CPT0⊂Ln-L.SiO₂NP_1)**, and their properties were compared to **CPT3⊂SiO₂NP_1**.

The synthesis to form **CPT⊂Ln-L.SiO₂NP** (figure 2.61) (Ln(III) = Eu, Yb, Nd), was carried out (as per section 2.7), and purified *via* centrifugation before collecting the NPs. Their sizes were characterised by DLS and SEM, and additionally their surface charge by measuring the zeta potential.

Table 2.8.11

Hydrodynamic diameter of NPs by DLS.

Sample	Size d/ nm Intensity Distribution	PDI
CPT3⊂SiO₂NP_1	129 ± 49	0.129
CPT3⊂Eu-L.SiO₂NP_1	88 ± 55	0.230
CPT3⊂Nd-L.SiO₂NP_1	88 ± 21	0.372
CPT3⊂Yb-L.SiO₂NP_1	69 ± 29	0.207

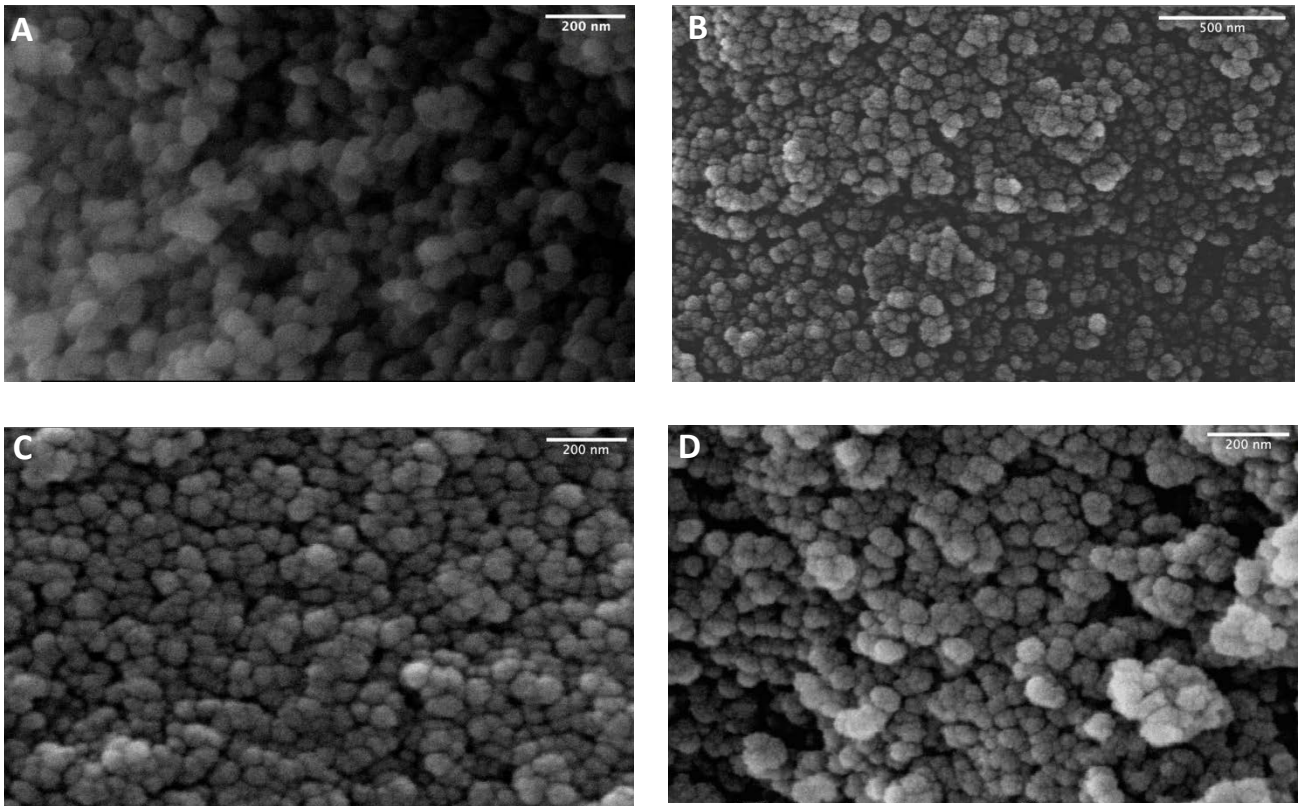


Figure 2.8.11

SEM images of **CPT3⊂Ln-L.SiO$_2$NP_1**. A: **CPT3⊂SiO$_2$NP_1**, average diameter 70 nm. B: Ln(III) = Eu, average diameter 52 nm. C: Ln(III) = Nd, average diameter 55 nm. D: Ln(III) = Yb, average diameter 54 nm. SEM diameters averaged from 10 NPs.

Table 2.8.12

Zeta potentials of the NPs measured by DLS.

Sample	Zeta Potential ζ/ mV
CPT3⊂SiO$_2$NP_1	-42 ± 8
CPT3⊂Eu-L.SiO$_2$NP_1	-28 ± 11
CPT3⊂Nd-L.SiO$_2$NP_1	-25 ± 6
CPT3⊂Yb-L.SiO$_2$NP_1	-21 ± 5

The hydrodynamic diameters of **CPT1⊂SiO$_2$NP_3** and the respective Ln coated **SiO$_2$NP**s were measured using DLS (table 2.8.11). Upon coating of the **CPT⊂SiO$_2$NP** with the Ln complexes, no significant change was observed in the size distribution due to the small size of **L** compared to the NPs. They were measured with PDI values between 0.2 – 0.3, as expected after coating of the NPs. The sizes and morphology were confirmed by SEM imaging (figure 2.8.11). The zeta potentials of the corresponding NPs were measured obtaining their surface charge, an indication of a change to the surface after coating. A small increase in zeta potential of 9 mV from **CPT0⊂SiO$_2$NP_1** to **CPT3⊂SiO$_2$NP_1** was observed, suggesting some **CPT** interaction with the surface. This could be explained by the location of the encapsulated **CPT** in **CPT3⊂SiO$_2$NP_1** (figure 2.81) closer to the surface (favouring adsorption closer to surface as **CPT** was added later in the synthesis), but is also within error. However, the substantial negativity of the zeta potential still suggests sufficient encapsulation of **CPT** by comparison to **CPT** loaded **MSNs** (9 mV), a significant difference from **CPT3⊂SiO$_2$NP_1**. A further larger increase in zeta potential was observed after coating with the Ln(III) complexes; 14 mV (**CPT3⊂Eu-L.SiO$_2$NP_1**), 17 mV (**CPT3⊂Nd-L.SiO$_2$NP_1**) and 21 mV (**CPT3⊂Yb-L.SiO$_2$NP_1**). The positive change in zeta potential showed the successful coating onto the **CPT⊂SiO$_2$NP**s.

2.8.2. Emission Properties of CPT3⊂SiO_2NP_1 and the Respective Ln(III) Coated Nanoparticles

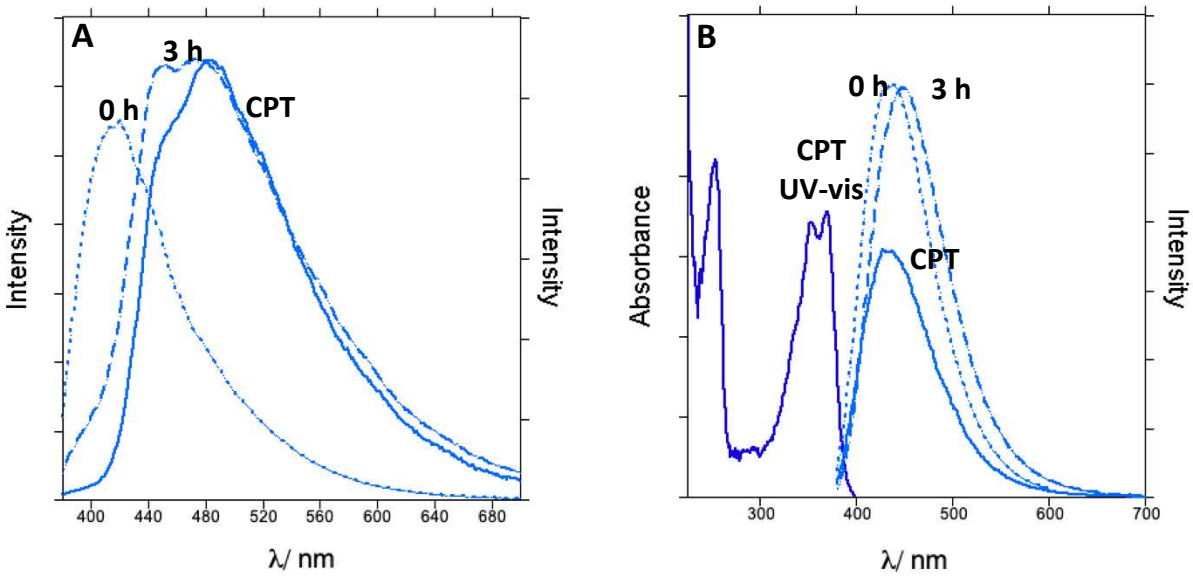


Figure 2.8.21

Emission spectra of **CPT** and **CPTn⊂SiO_2NP_1** NPs, n = 0 h, 3 h, at λ_{exc} = 360 nm. A: Solid state emission spectra of **CPT0⊂SiO_2NP_1** (blue, dotted), **CPT3⊂SiO_2NP_1** (blue, dashed) and **CPT** powder (blue, solid). B: Solution emission spectra of **CPT0⊂SiO_2NP_1**(blue, dotted) (1 mg mL^{-1}, H_2O), **CPT0⊂SiO_2NP_1** (blue, dashed) (1 mg mL^{-1}, H_2O) and **CPT** (blue, solid) (0.025 mM, H_2O), compared to solution **CPT** absorbance (dark blue) (0.025 mM, H_2O). Emission spectra corrected for PMT and instrument response.

The solid state emission spectra of the NPs were compared (figure 2.8.21, A) using λ_{exc} = 360 nm. The emission of **CPT0⊂SiO_2NP_1** lies at λ_{em} = 415 nm, a hypsochromic shift from the emission of **CPT3⊂SiO_2NP_1** at λ_{em} = 465 nm, and the emission of **CPT** powder lies at λ_{em} = 480 nm. This observation is also mirrored in the solution emission spectra of the NPs. The emission of **CPT0⊂SiO_2NP_1** lies at λ_{em} = 435 nm, again a hypsochromic shift from the emission of **CPT3⊂SiO_2NP_1** at λ_{em} = 450 nm. The blue shift in emission observed from adding the dye before 3 h (at the beginning: 0 h) was also observed by Yang *et. al.*[133]. The slight blue shifted change in **CPT** emission, in comparison to **CPT** encapsulated in **SiO_2NP**s has previously been reported too, by Wang *et. al.*[133]. Wang and co-workers, similarly designed a nanocarrier using **SiO_2NP**s to co-deliver **CPT** and **DOX**, using GSH and pH responsive triggers. Both of the emission spectra for the prodrug NPs showed similar emission to the drug molecules alone, but similarly observed a blue shift in **CPT** emission[138].

It is known for **CPT** to be able to form dimers, and form stacking interactions when packed together[108, 124, 139-141]. D. Dvoranova *et. al.* in 2013 optimised the structures of CPT and its π-dimer using UV-Vis spectroscopy and DFT calculations[124]. It was found their study implied that the existence of two strong shoulders in the UV-Vis spectra of CPT (figure 2.8.21, B) at 350 nm, but more to the blue-shifted shoulder to be explained by π-π interactions holding the CPT molecules in a heat to tail orientation. Self-aggregation also prevents hydrolysis of CPT, preserving the drug in its active form. pH can also influence the chemical equilibrium of CPT between the lactone and carboxylate (figure 2.5.35), in turn influencing the interactions between CPT molecules in the NPs. Fonseca *et. al.* in 2020 proposed the association of CPT molecules with each other on the surface of graphene oxide (GO) and GO decorated with MSNs (GO-MSNs) through hydrogen bonding and π-π stacking interactions[108].

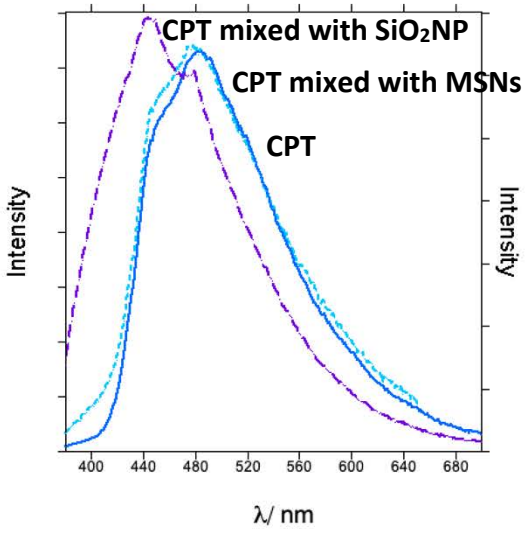


Figure 2.8.22

Solid state emission spectra of **CPT** (blue) compared to **CPT** mixed with **MSNs** (turquoise, dotted) and **CPT** mixed with **SiO_2NP** (purple, dashed) at λ_{exc} = 360 nm. Emission spectra corrected for PMT and instrument response.

The structure of **CPT** emission band shows a shoulder at 450 nm, which is also mirrored in the control experiments of **CPT** mixed with **MSNs** and **SiO_2NP** (shoulder at 450 nm and 480 nm respectively). These suggest signs of possible vibronic coupling, indicating some interaction between **CPT** molecules when packed as a solid.

In light of this information, the blue shift in the emission of **CPT0⊂SiO$_2$NP_1** compared to **CPT3⊂SiO$_2$NP_1** could be explained by the packing of **CPT** molecules close together, rather than spread out when the drug is added later in the reaction (figure 2.81). The proposed mechanism by Wang *et. al.* shows the dye to pack closely together when added at 0 h[138]. The emission properties of **CPTn⊂SiO$_2$NP_1** follow a similar trend to the dye doped NPs suggesting a similar mechanism for **CPTn⊂SiO$_2$NP_1**.

CPT3⊂Ln-L.SiO$_2$NP_1 NPs were prepared similarly to **CPT0⊂Ln-L.SiO$_2$NP_1** and their emission was monitored.

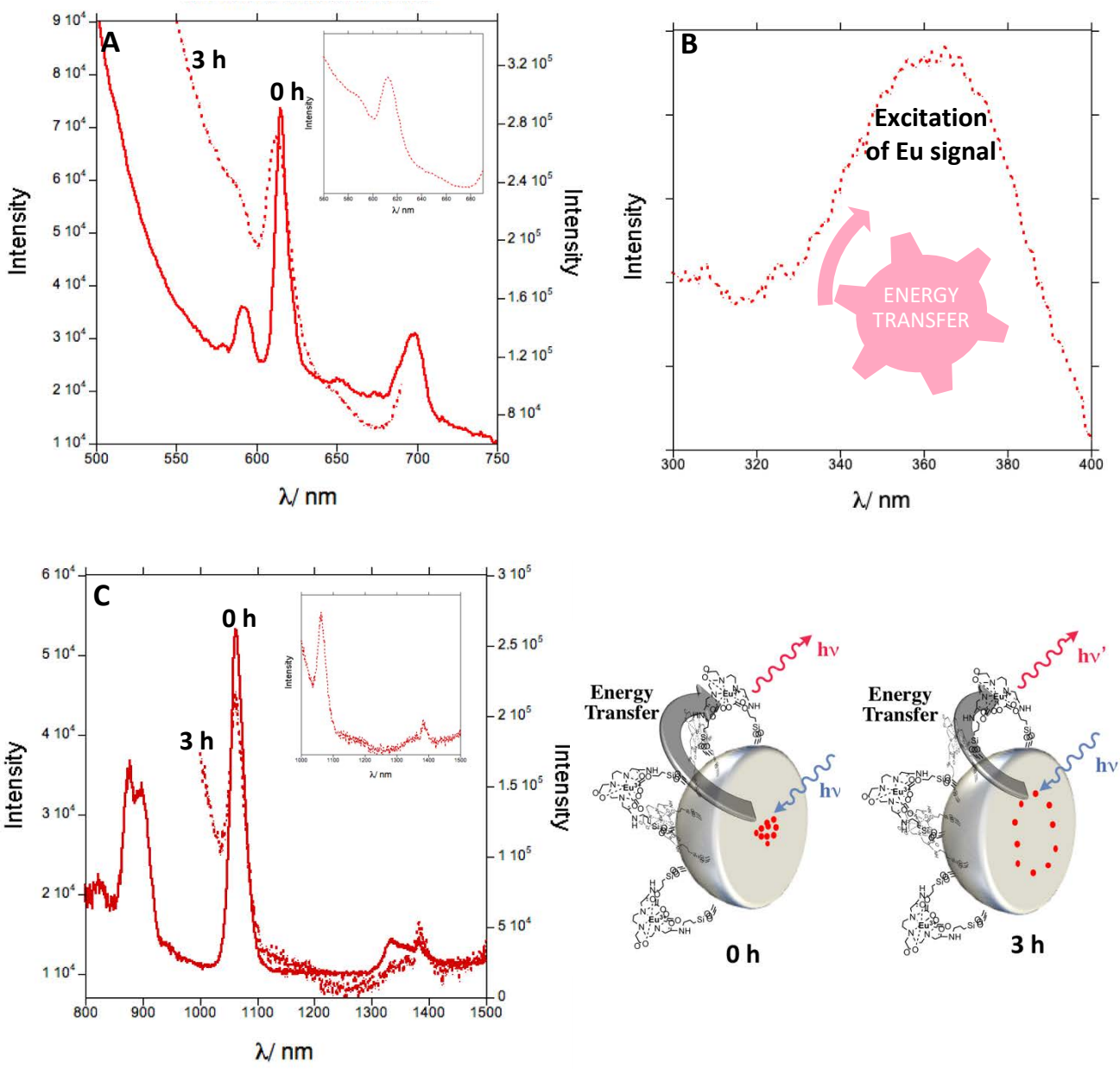


Figure 2.8.23

Solid state emission spectra of **CPTn⊂Ln-L.SiO$_2$NP_1,** n = 0 h, 3 h, monitoring Ln emission, Ln(III) = Eu (red), and Nd (maroon), λ_{exc} = 350 nm, and corresponding excitation spectra. A: Solid state emission spectra of **CPT3⊂Eu-L.SiO$_2$NP_1** (red, dotted) compared to **CPT0⊂Eu-L.SiO$_2$NP_1** (red, solid). B: Excitation spectrum of **CPT3⊂Eu-L.SiO$_2$NP_1** at λ_{em} = 615 nm. C: Solid state emission spectra of **CPT3⊂Nd-L.SiO$_2$NP_1** (maroon, dotted) compared to **CPT0⊂Nd-L.SiO$_2$NP_1** (maroon, solid). Emission spectra corrected for PMT and instrument response. Excitation spectra corrected for lamp response.

The Ln(III) emission signal was monitored of **CPT3⊂Ln-L.SiO$_2$NP_1** using λ_{exc} = 350 nm. The detection of Ln(III) signal was only successful for **CPT3⊂Eu-L.SiO$_2$NP_1** (figure 2.83, A) and **CPT3⊂Nd-L.SiO$_2$NP_1** (figure 2.8.23, C).

The solid state emission signal was detected for the Eu(III) NPs, observed by one sharp peak at λ_{em} = 615 nm, the hypersensitive transition ($^5D_0 \rightarrow {}^7F_2$). The intensity of the other transitions, as observed for **CPT0⊂Eu-L.SiO$_2$NP_1** were not detected, suggesting the likely reason being less efficient energy transfer, in contrast to changes in the Eu(III) coordination sphere (presence of transitions can depend on the coordination sphere)[111]. The emission signal of **CPT3⊂Eu-L.SiO$_2$NP_1** (figure 2.8.23, A, dotted line) was compared to **CPT0⊂Eu-L.SiO$_2$NP_1** (figure 2.8.23, A, solid line) and elucidated the weaker signal of Eu(III) emission from the **CPT3⊂Eu-L.SiO$_2$NP_1** NP. The excitation scan was also recorded for these NPs (figure 2.8.23, B), confirming the energy transfer process occurring from **CPT** to Eu(III), in agreement with **CPT** UV-Vis absorbance.

The solid state emission signal was also detected for the Nd(III) NPs at λ_{em} = 1060 nm (($^4F_{3/2} \rightarrow {}^4I_{11/2}$) and 1335 nm ($^4F_{3/2} \rightarrow {}^4I_{13/2}$), with the $^4F_{3/2} \rightarrow {}^4I_{11/2}$ transition being most intense, as expected. The Nd(III) signal in this case was also weaker than **CPT0⊂Nd-L.SiO$_2$NP_1** (figure 2.8.23, C), outlined by the lower intensity and detection of only two transitions, missing $^4F_{3/2} \rightarrow {}^4I_{9/2}$.

The solid state emission signal for **CPT** was also monitored (figure 2.8.24).

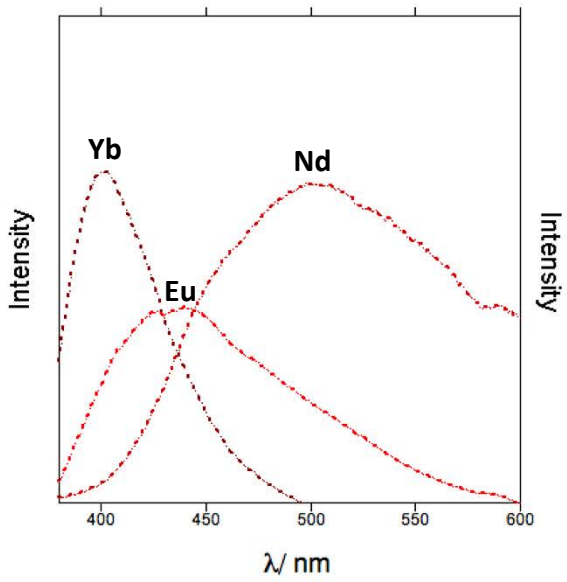


Figure 2.8.24

Solid state emission spectra of **CPT3⊂Ln-L.SiO$_2$NP_1,** monitoring **CPT** emission, Ln(III) = Eu (red), Nd (maroon) and Yb (brown), λ_{exc} = 350 nm. Emission spectra corrected for PMT and instrument response.

Despite the hypothetical mechanism of silica growth with **CPT** (figure 2.81) mentioned previously, potentially enhancing the emission signal with the drug molecules lying closer to the surface, this was not the observed result. The emission signal was only detected for Eu(III) and Nd(III) NPs with 3 h doping, and their signal was much weaker than **CPT0⊂Eu-L.SiO$_2$NP_1**.

2.8.3. Second method of synthesis of Non-Porous Silica Nanoparticles Doped with CPT

CPT⊂SiO$_2$NP NPs were synthesised with concentrations following Pikramenou *et. al.* with the dye added at 3 h and 0 h, investigating the emission properties again searching for potential enhanced luminescence[35]. The concentration of TEOS in this synthesis is higher and concentration of base (NH_4OH) lower compared to method 1, and is known that changes in base concentration affects NP size due to rates of condensation changing[105]. These NPs were named **CPTn⊂SiO$_2$NP_2**, n = 3 h and 0 h, (and respectively **CPTn⊂Ln-L.SiO$_2$NP_2**).

The synthesis to forming **CPTn⊂Ln-L.SiO$_2$NP_2** (see schematic illustration in figure 2.61) (Ln(III) = Eu, Yb, Nd), was carried out (as per section 2.7), and purified *via* centrifugation before collecting the NPs. Their sizes were characterised by DLS and SEM, and additionally their surface charge by measuring the zeta potential.

Table 2.8.31

Hydrodynamic diameter of NPs by DLS.

Sample	Size d/ nm Intensity Distribution	PDI
CPT0⊂SiO_2NP_2	255 ± 52	0.013
CPT0⊂Eu-L.SiO_2NP_2	116 ± 44	0.348
CPT0⊂Nd-L.SiO_2NP_2	111 ± 48	0.289
CPT0⊂Yb-L.SiO_2NP_2	108 ± 49	0.309
CPT3⊂SiO_2NP_2	240 ± 48	0.002
CPT3⊂Eu-L.SiO_2NP_2	150 ± 32	0.05
CPT3⊂Nd-L.SiO_2NP_2	181 ± 55	0.276
CPT3⊂Yb-L.SiO_2NP_2	107 ± 57	0.344

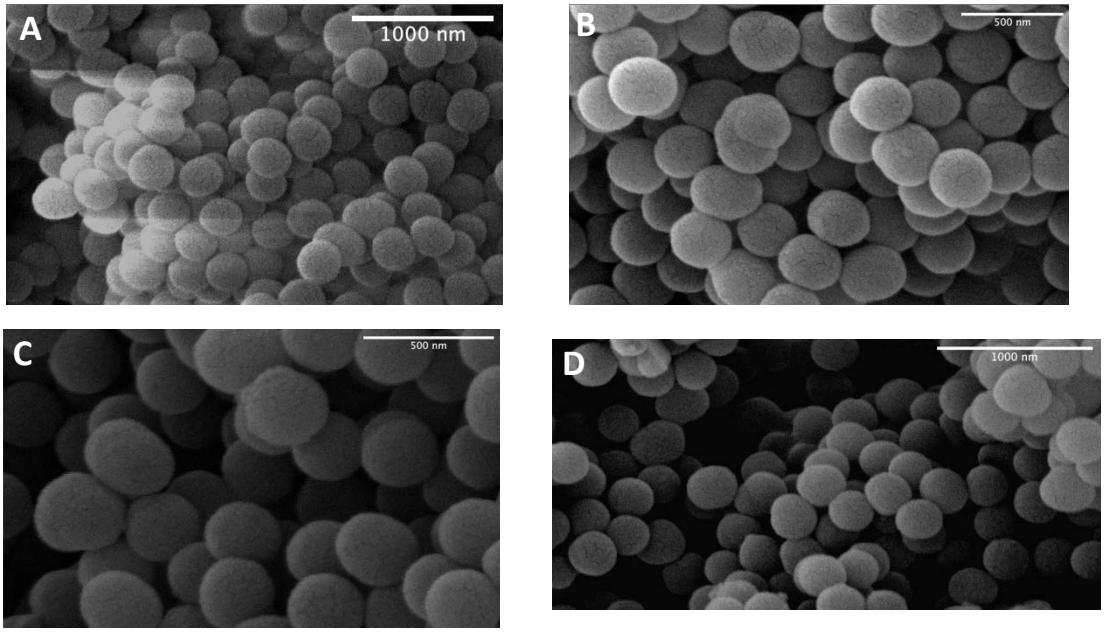


Figure 2.8.31

SEM images of **CPT0⊂Ln-L.SiO_2NP_2**. A: **CPT0⊂SiO_2NP_2** average diameter 272 nm. B: Ln(III) = Eu, average diameter 266 nm. C: Ln(III) = Nd, average diameter 265 nm. D: Ln(III) = Yb, average diameter 283 nm. SEM diameters averaged with 10 NPs (5 for C).

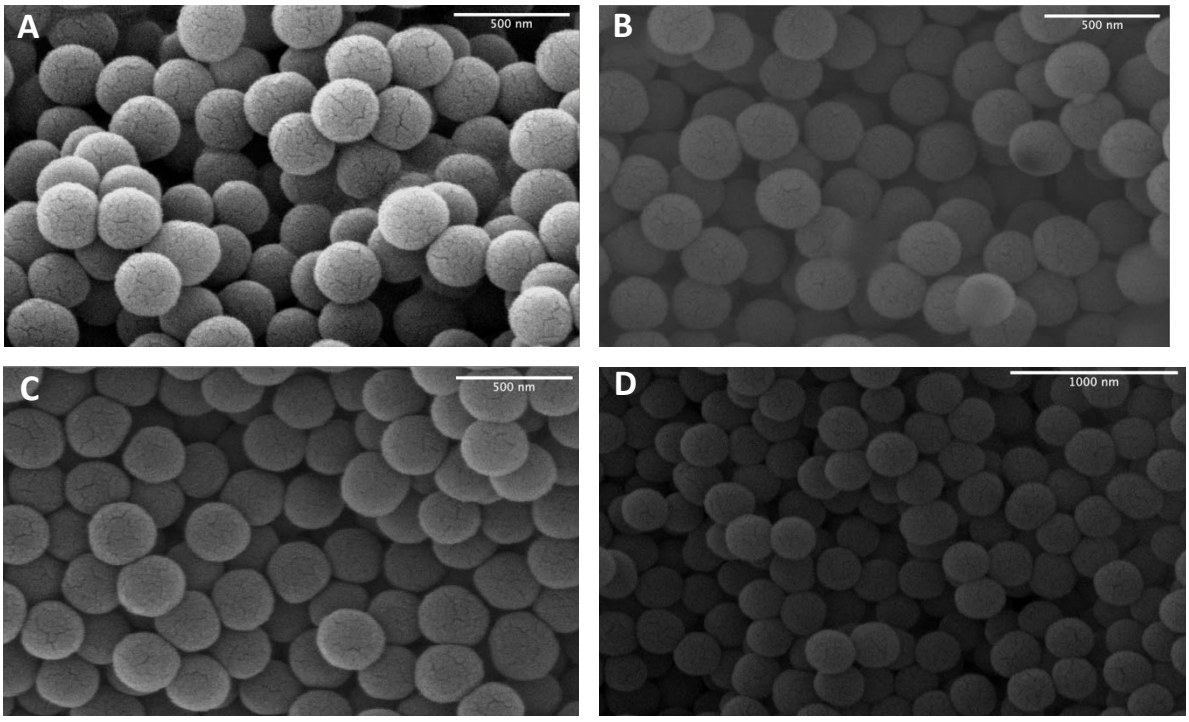


Figure 2.8.32

SEM images of **CPT3⊂Ln-L.SiO$_2$NP_3**. A: **CPT3⊂SiO$_2$NP_3** average diameter 267 nm. B: Ln(III) = Eu, average diameter 241 nm. C: Ln(III) = Nd, average diameter 242 nm. D: Ln(III) = Yb, average diameter 257 nm. SEM diameters averaged with 10 NPs.

Table 2.8.32

Zeta potentials of the NPs measured by DLS.

Sample	Zeta Potential ζ/ mV
CPT0⊂SiO$_2$NP_2	-21 ± 7
CPT0⊂Eu-L.SiO$_2$NP_2	-17 ± 5
CPT0⊂Nd-L.SiO$_2$NP_2	-23 ± 20
CPT0⊂Yb-L.SiO$_2$NP_2	-17 ± 10
CPT3⊂SiO$_2$NP_2	-17 ± 6
CPT3⊂Eu-L.SiO$_2$NP_2	-17 ± 9
CPT3⊂Nd-L.SiO$_2$NP_2	-13 ± 5
CPT3⊂Yb-L.SiO$_2$NP_2	-21 ± 5

The hydrodynamic diameters of **CPTn⊂SiO$_2$NP_2** and the respective Ln coated **SiO$_2$NP**s were measured using DLS (table 2.8.31). Both **CPT0⊂SiO$_2$NP_2** and **CPT3⊂SiO$_2$NP_2** were measured to be 255 nm and 240 nm respectively by DLS, with good PDI values showing a good narrow size distribution. In both cases, upon coating of the **CPT⊂SiO$_2$NP** with the Ln complexes, a decrease in size, although arguably could be within error due to the small size of **L** compared to the NPs. They were measured with PDI values between 0.2 – 0.3, as expected after coating of the NPs. The sizes and morphology were confirmed by SEM imaging (figure 2.8.31 and 2.8.32). The zeta potentials of the corresponding NPs were measured obtaining their surface charge. An increase in zeta potential of 30 mV from **CPT0⊂SiO$_2$NP_1** to **CPT0⊂SiO$_2$NP_2** was observed, suggesting that the encapsulation of **CPT** interaction in **CPT0⊂SiO$_2$NP_2** could be further spread out than **CPT0⊂SiO$_2$NP_1** possibly due to the larger size of the **CPT0⊂SiO$_2$NP_2** NPs. A similar trend was observed with **CPT3⊂SiO$_2$NP_n** (n = method 1 or method 2), where an increase of 25 mV was observed which could be explained by the location of the encapsulated **CPT** in **CPT3⊂SiO$_2$NP_1** (figure 2.81) closer to the surface. Again, the comparison made to **CPT** loaded **MSNs** suggests that, despite the change in zeta potential, there is still sufficient encapsulation of **CPT** in the NPs. A further larger increase in zeta potential was observed after coating with the Ln(III) complexes. The positive change in zeta potential showed the successful coating onto the **CPT⊂SiO$_2$NP**s.

2.8.4. Emission Properties of CPTn⊂SiO_2NP_2 and the Respective Ln(III) Coated Nanoparticles

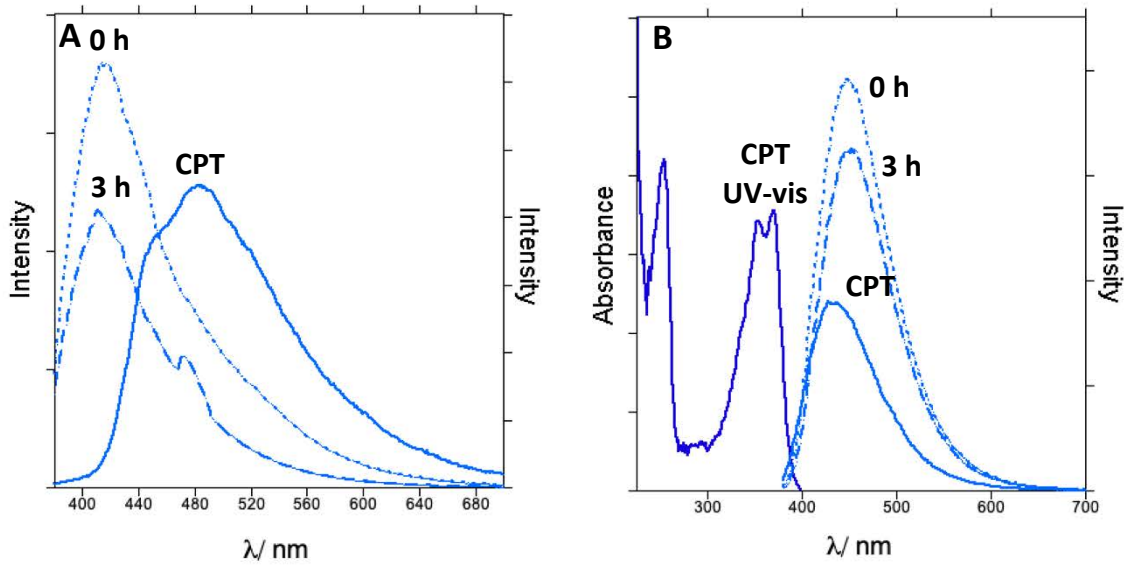


Figure 2.8.41

Emission spectra of **CPT** and **CPTn⊂SiO_2NP_2** NPs, n = 0 h, 3 h, at λ_{exc} = 360 nm. A: Solid state emission spectra of **CPT0⊂SiO_2NP_2** (blue, dotted), **CPT3⊂SiO_2NP_2** (blue, dashed) and **CPT** powder (blue, solid). B: Solution emission spectra of **CPT0⊂SiO_2NP_2** (blue, dotted) (1 mg mL^{-1}, H_2O), **CPT3⊂SiO_2NP_2** (blue, dashed) (1 mg mL^{-1}, H_2O) and **CPT** (blue, solid) (0.025 mM, H_2O), compared to solution **CPT** (dark blue) (0.025 mM, H_2O). Emission spectra corrected for PMT and instrument response.

The solid state emission spectra of the NPs were compared (figure 2.8.41, A) using λ_{exc} = 360 nm. The emission of **CPT0⊂SiO_2NP_2** lies at λ_{em} = 415 nm, slightly redshifted from the emission of **CPT3⊂SiO_2NP_2** at λ_{em} = 410 nm, and the emission of **CPT** powder lies at λ_{em} = 480 nm. Similar trend in blue shifted emission from **CPT** to the encapsulated NPs was also observed in this case[133], with possible vibronic coupling suggested from the irregularity of the spectra (figure 2.8.41, A) correlating with **CPT** interactions in close proximity[108, 124]. The solution emission of **CPT0⊂SiO_2NP_2** lies at λ_{em} = 450 nm, and the emission of **CPT3⊂SiO_2NP_2** at λ_{em} = 450 nm.

CPTn⊂Ln-L.SiO_2NP_2 (n = 0 h and 3 h) NPs were prepared similarly to **CPTn⊂Ln-L.SiO_2NP_1** and their emission was monitored.

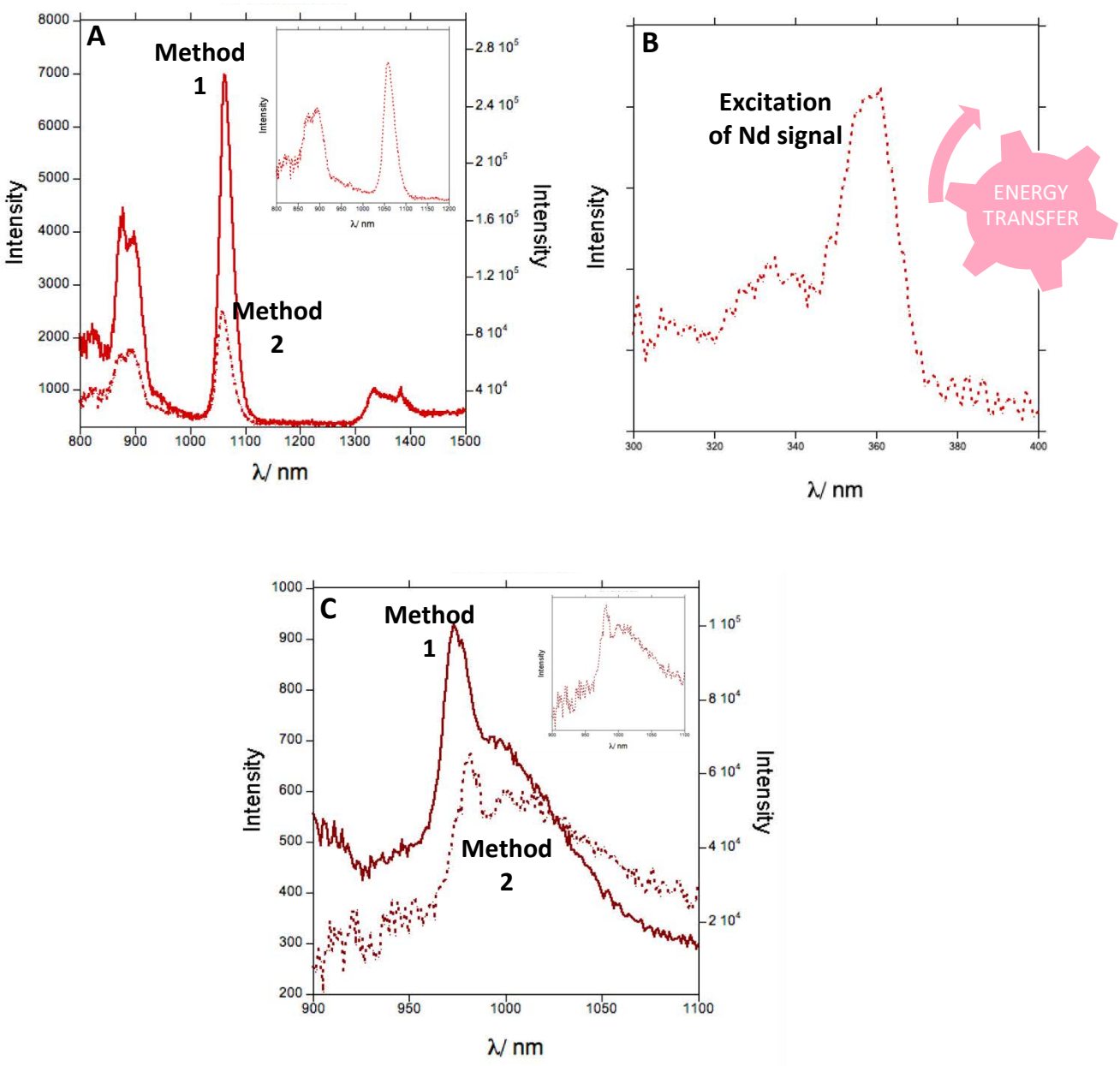


Figure 2.8.42

Solid state emission spectra of **CPT0⊂Ln-L.SiO$_2$NP_n,** n = method 1, method 2, monitoring Ln emission, Ln(III) = Nd (maroon) and Yb (brown), λ_{exc} = 350 nm, and corresponding excitation spectra. A: Solid state emission spectra of **CPT0⊂Nd-L.SiO$_2$NP_2** (maroon, dotted) compared to **CPT0⊂Nd-L.SiO$_2$NP_1** (maroon, solid). B: Excitation spectrum of **CPT0⊂Nd-L.SiO$_2$NP_2** at λ_{em} = 1060 nm. C: Solid state emission spectra of **CPT0⊂Yb-L.SiO$_2$NP_2** (brown, dotted) compared to **CPT0⊂Yb-L.SiO$_2$NP_1** (brown, solid). Emission spectra corrected for PMT and instrument response. Excitation spectra corrected for lamp response.

The Ln(III) emission signal was monitored of **CPT0⊂Ln-L.SiO$_2$NP_2** using λ_{exc} = 350 nm. The detection of Ln(III) signal was only successful for **CPT0⊂Nd-L.SiO$_2$NP_2** (figure 2.8.42, A) and ~~of~~ **CPT0⊂Yb-L.SiO$_2$NP_2** (figure 2.8.42, C).

The solid state emission signal was detected for the Nd(III) NPs at λ_{em} = 880 nm ($^4F_{3/2} \rightarrow {}^4I_{9/2}$), and λ_{em} = 1060 nm ($^4F_{3/2} \rightarrow {}^4I_{11/2}$), with the $^4F_{3/2} \rightarrow {}^4I_{11/2}$ transition being most intense, as expected. The Nd(III) signal was compared to of **CPT0⊂Nd-L.SiO$_2$NP_1** (figure 2.8.42, A), and was much weaker observed by the low intensity, and detection of only two transitions, missing $^4F_{3/2} \rightarrow {}^4I_{9/2}$. The excitation of the Nd(III) signal at the most intense transition $^4F_{3/2} \rightarrow {}^4I_{11/2}$, λ_{em} = 1060 nm was recorded confirming the energy transfer process from the drug.

The solid state emission signal was also detected for the Yb(III) NPs, observed by one sharp peak at λ_{em} = 980 nm ($^2F_{5/2} \rightarrow {}^2F_{7/2}$). The emission signal here was also noticeably weaker in comparison to of **CPT0⊂Yb-L.SiO$_2$NP_1**.

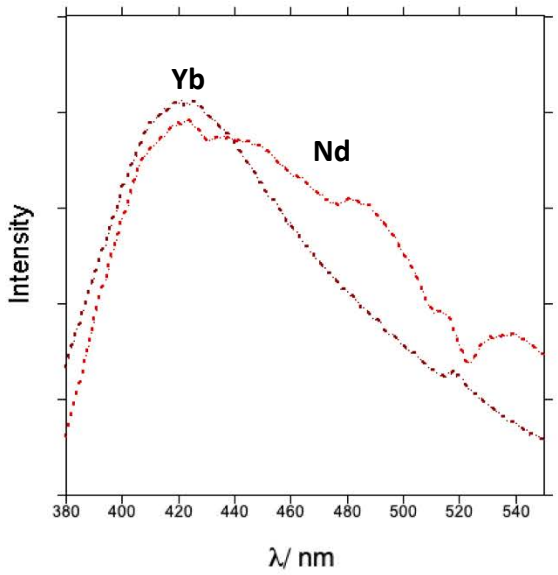


Figure 2.8.43

Solid state emission spectra of **CPT0⊂Ln-L.SiO$_2$NP_2,** monitoring CPT emission, Ln(III) = Nd (maroon) and Yb (brown), λ_{exc} = 350 nm. Emission spectra corrected for PMT and instrument response.

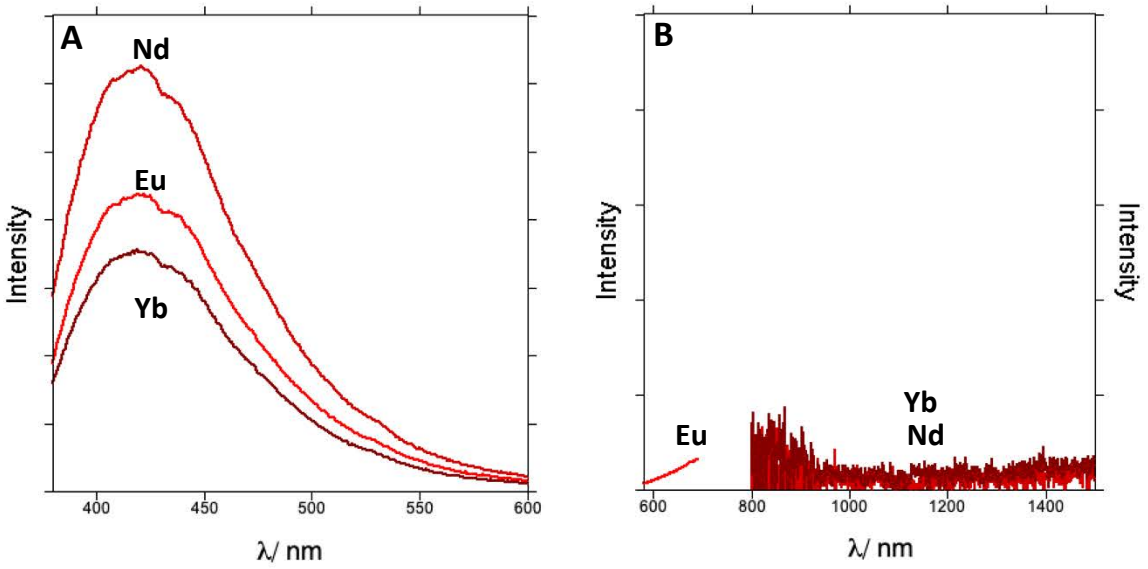


Figure 2.8.44

Solid state emission spectra of control experiments of **Ln-L.SiO$_2$NP_2** (Ln(III) = Eu, Yb, Nd), λ_{exc} = 350 nm. A: Emission spectra of **Ln-L.SiO$_2$NP_2** in the visible range, Ln(III) = Eu (red), Yb (brown), Nd (maroon). B: Emission spectra of **Ln-L.SiO$_2$NP_2** in the visible – NIR range, Ln(III) = Eu (red), Yb (brown), Nd (maroon). Emission spectra corrected for PMT and instrument response.

The emission of **Ln-L.SiO$_2$NP_2**, in absence of **CPT**, was monitored in the visible and NIR range using λ_{exc} = 350 nm (figure 2.8.44, A and B). Only scattering attributed to the **SiO$_2$NP**s was observed in the visible range between λ_{max} = 400 nm – 600 nm as expected (see appendix figure 23). More importantly, the control experiments also show zero emission signal in the Ln(III) visible and NIR range (figure 2.8.44, B), which is the same result as previously observed (section 2.7). This experiment was an additional control to illustrate the necessity of the drug's presence within the designed system, in order to observe the emission attributed from the sensitisation of **CPT**.

Table 2.8.41

Summary of emission properties from **CPTn⊂Ln-L.SiO$_2$NP_1,** n = 0 h, 3 h.

Sample	0 h	3 h
CPTn⊂Eu-L.SiO$_2$NP	✓	✓
CPTn⊂Nd-L.SiO$_2$NP	✓	✓
CPTn⊂Yb-L.SiO$_2$NP	✓	×

Table 2.8.42

Summary of emission properties from **CPTn⊂Ln-L.SiO$_2$NP_2**, n = 0 h, 3 h.

Sample	0 h	3 h
CPTn⊂Eu-L.SiO$_2$NP	×	✓
CPTn⊂Nd-L.SiO$_2$NP	✓	×
CPTn⊂Yb-L.SiO$_2$NP	✓	×

With proof of concept, we showed the ability of **CPT** to sensitise Ln(III) luminescence in solution, in presence of base (section 2.5.3, figure 2.5.33). The collected characteristic Eu(III) emission signal suggested energy transfer from the drug, which was proved by the excitation spectrum, in addition to monitoring the decrease in **CPT** emission and simultaneously the increase in Eu(III) emission.

After synthesis of **CPTn⊂SiO$_2$NP_x** (x = method 1, method 2) (n = 0 h, 3 h) and the respective Ln coated NPs, we were able to successfully detect Ln(III) luminescence using λ_{exc} = 350 nm from **CPT0⊂Ln-L.SiO$_2$NP_1** (Ln(III) = Eu, Nd and Yb), **CPT3⊂Ln-L.SiO$_2$NP_1** (Ln(III) = Eu and Nd) (section 2.7.1 and section 2.8.2 respectively), **CPT0⊂Ln-L.SiO$_2$NP_2** (Ln(III) = Nd and Yb) and **CPT3⊂Ln-L.SiO$_2$NP_2** (Ln(III) = Eu) (section 2.8.3) summarised in tables 2.8.41 and 2.8.42. This could be attributed to the smaller sizes of NPs from method 1 (0 h and 3 h) compared to the larger sizes obtained from method 2 (0 h and 3 h), and therefore having better sensitisation as the distance between **CPT** and Ln(III) is closer in the smaller NPs. Furthermore, the

comparison of luminescence studies from 0 h and 3 h (for both methods) shows more successful spectra from 0 h studies. This could be attributed to the fact that when forming **CPTn⊂Ln-L.SiO$_2$NP_x** from **CPTn⊂SiO$_2$NP_x**, some **CPT** is release in solution as the Ln-**L** coated NPs are made. As this occurs **CPT** spreads out towards the surface (figure 2.8.45) and therefore **CPT** could be packed closer to the surface in **CPT0⊂Ln-L.SiO$_2$NP_x**, compared to having less **CPT** close to the surface in **CPT3⊂Ln-L.SiO$_2$NP_x** as sufficient amount of **CPT** has released to result in less efficient energy transfer from 3 h NPs.

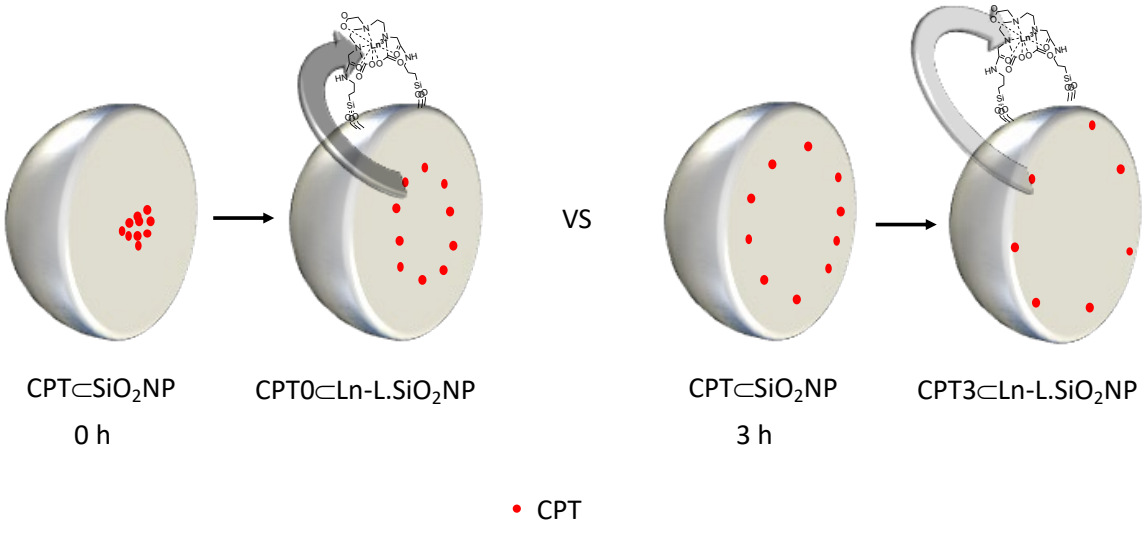
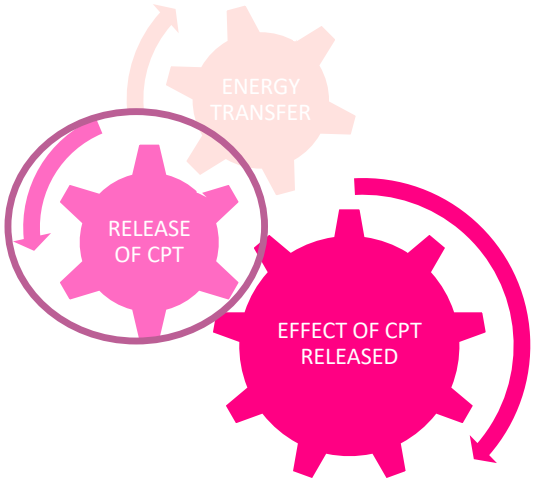


Figure 2.8.45

Schematic illustration of positioning of **CPT** in **CPTn⊂Ln-L.SiO$_2$NP** demonstrating better sensitisation from 0 h NPs compared to 3 h NPs.

The energy transfer was shown by the detection of characteristic sharp emission lines in the spectra, corresponding excitation spectra, and control experiments of **Ln-L.SiO$_2$NP** in absence of **CPT**. Furthermore, the detection of Ln luminescence from **CPT0⊂Ln-L.SiO$_2$NP_1** (Ln(III) = Eu and Nd) in solution was important, showing the success of our design (encapsulating and holding **CPT** in the NPs, with the ability to sensitise luminescence). This experiment confirms the energy transfer process occurring from **CPT** adsorbed within the NPs and not from free **CPT** in solution.

2.9. Release of CPT from CPT⊂SiO_2NPs and Respective Lanthanide Coated Nanoparticles



After successfully showing the energy transfer process is occurring to obtain sensitised Ln luminescence, we moved on to monitoring drug release, and hence leading to the investigation of drug release efficacy. Monitoring drug release from SDDS has been employed as an attractive strategy for diagnostic purposes, using functionalised multimodal systems carrying the ability to perform theranostic applications[142]. There have been several methods used to monitor drug release from **SiO_2NPs,** ranging from high performance liquid chromatography (HPLC)[143] to UV-Vis absorbance and luminescence spectroscopy[108, 144-146]. The unique photophysical properties of **CPT** , with high ε and luminescence in the UV range consequentially led to the use of UV-Vis absorbance to detect **CPT** release[108]. Furthermore, the UV-Vis absorbance and luminescence of **CPT** studies have shown differences in band shapes, dependent on pH values of the drug. This was an additional reason to use UV-Vis absorbance for detecting **CPT** release, and investigating the form of the drug upon release. It is known that **CPT** can easily hydrolyse from the active lactone form to the inactive carboxylate form. These structures have been studied by UV-Vis, and have shown differences in band shapes[108, 126, 160].

2.9.1. Studying CPT Release from CPT0⊂SiO_2NP_1

Preliminary release studies from other NPs were studied (see appendix figure 39, 40, 42), however we chose to investigate just with **CPT0⊂SiO_2NP_1** due to the successful luminescence studies acquired by the Ln coated NPs.

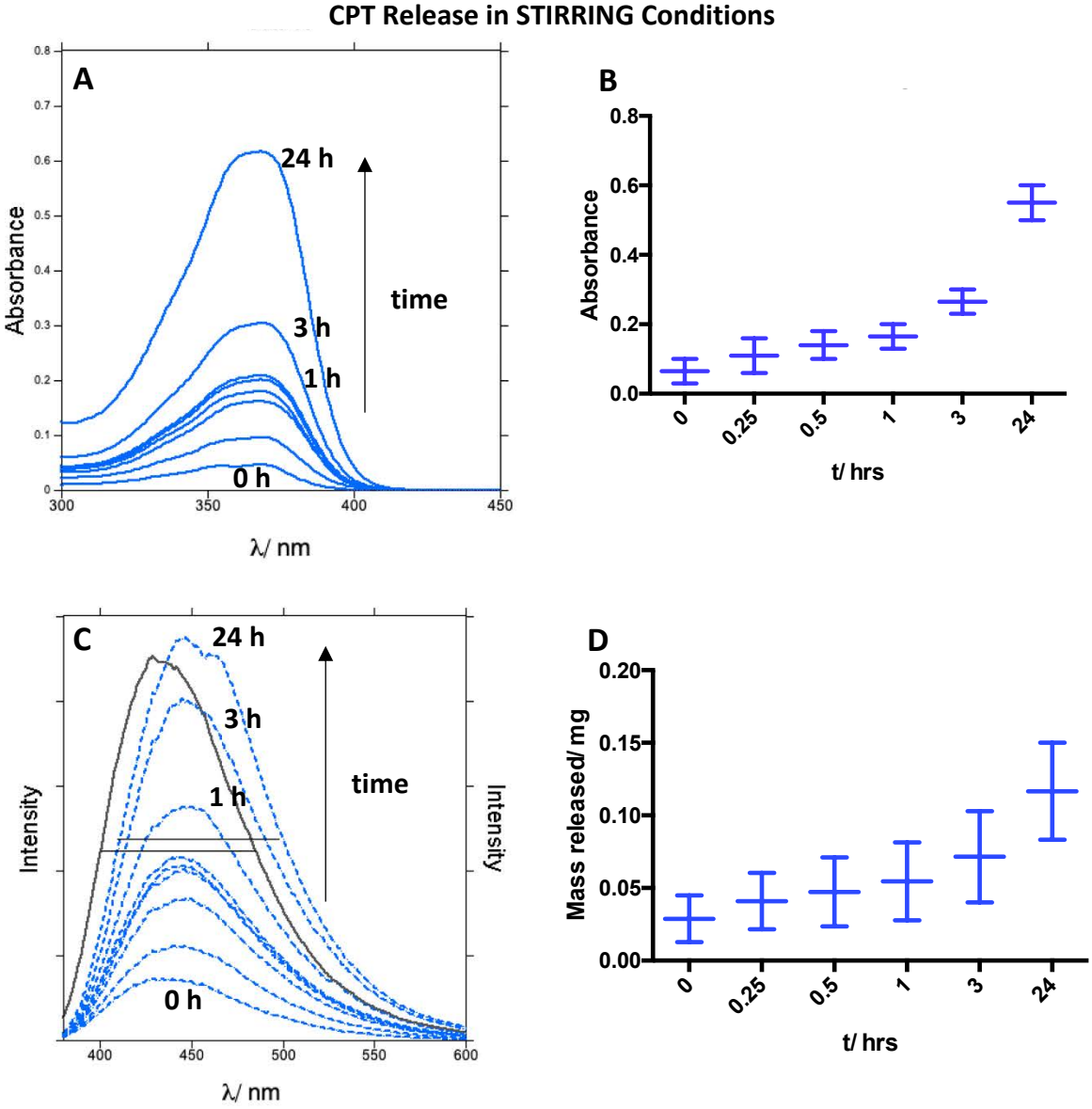


Figure 2.9.11

Release of **CPT** from **CPT0⊂SiO_2NP_1** (1 mg mL^{-1}, H_2O, stirring at 37 °C) up to 24 hrs studied by UV-Vis absorbance. A: UV-Vis absorbance of **CPT** released from **CPT0⊂SiO_2NP_1**. B: A scatter graph showing the absorbance of **CPT** released against time. C: Emission of **CPT** released from **CPT0⊂SiO_2NP_1** (blue dotted) compared to **CPT** emission (0.1 mM, H_2O), λ_{exc} = 350 nm. Emission spectra corrected for PMT and instrument response. D: The mass of **CPT** released from **CPT0⊂SiO_2NP_1** calculated from UV-Vis absorbance.

In order to conduct the experiment 37 ^{o}C, a dispersion of **CPT0⊂SiO$_2$NP_1** was stirred to keep T constant. Aliquots of 1 mL from the solution were taken and centrifuged in order to remove any excess NPs, leaving behind just any drug that was released into solution. The UV-Vis absorbance of the aliquot was measured at time intervals up to 24 hrs, and returned back to the solution after measurement.

An increase in UV-Vis absorbance was observed, as expected, as more **CPT** was released into the solution from **CPT0⊂SiO$_2$NP_1**. From the UV-Vis absorbance study, the **CPT** absorbance was used to calculate the mass of **CPT** released (from the Beer-Lambert law). To calculate % release of **CPT**, the drug loading of **CPT0⊂SiO$_2$NP_1** was also required. This was calculated from the **CPT** absorbances of supernatants measured after synthesis of **CPT0⊂SiO$_2$NP_1** to account for any excess **CPT** in solution after synthesis and hence give an estimated mass of **CPT** loaded[144-146]. The table below summarises the methodology leading up to the calculation of the drug loading (see table 5.11 in chapter 5 for calculations of mass of **CPT** from the supernatant absorbance).

Equation 2.9.11

$$c\ of\ \boldsymbol{CPT} = \frac{superntant\ absorbance\ taken\ from\ graph}{\varepsilon_{CPT\ in\ solvent} L}$$

Equation 2.9.12

$$moles\ of\ \boldsymbol{CPT} = conc \times vol \quad mass\ of\ \boldsymbol{CPT} = moles \times RMM_{CPT}$$

Table 2.9.11

Table of values calculated from UV-Vis absorbance of **CPT0⊂SiO$_2$NP_1** in order to determine drug loading.

Sample	**Supernatant Absorbance**	**Concentration of CPT/ mM**	**Moles**	**Mass/ mg**	**Mass of CPT added to synthesis CPT0⊂SiO$_2$NP_1/ mg**	**Drug Loading/ %**
CPT0⊂SiO$_2$NP_1	0.8	0.05	1.4 x 10^6	0.48	17	97

Using the Beer-Lambert Law (A = εcL), the concentration and thus mass of **CPT** released in the supernatant was obtained[108, 144-147]. Using the knowledge of how much drug was added to the synthesis of **CPT0⊂SiO₂NP_1,** and excess **CPT** after synthesis of **CPT0⊂SiO₂NP_1**, the drug loading was calculated.

Equation 2.9.13

$$\boldsymbol{Estimated\ mass\ of\ CPT\ loaded} = mass\ of\ CPT\ added\ to\ synthesis - mass\ of\ CPT\ release$$

Equation 2.9.14

$$\boldsymbol{Efficieny\ of\ Drug\ Loading} = \frac{estimated\ mass\ of\ CPT\ loaded}{mass\ of\ CPT\ added\ to\ synthesis} \times 100$$

0.09 mg was calculated to be the estimated mass of CPT loaded.

Equation 2.9.15

$$\boldsymbol{Mass\ of\ CPT\ loaded\ per\ mass\ of\ SiO2NP} = \frac{mass\ of\ CPT\ added\ to\ synthesis - mass\ of\ CPT\ released}{total\ mass\ of\ \mathrm{CPT1{\subset}SiO2NP0\ synthesis}}$$

Using this, and the mass of **CPT** loaded per mass of SiO_2NP, the % of **CPT** released was calculated.

Equation 2.9.14

$$\boldsymbol{CPT\ released\ at\ 24\ h} = \frac{mass\ of\ CPT\ released\ at\ 24\ h}{estimated\ mass\ of\ CPT\ loaded} \times 100$$

Table 2.9.12

Table of values showing % release of CPT from **CPT0⊂SiO₂NP_1.**

Sample	**Mass of CPT loaded per mass of SiO_2NP/ mg**	**Mass of CPT released/ mg**	**% Release**
CPT0⊂SiO₂NP_1	0.09	0.08	89

89 % of **CPT** was released from **CPT0⊂SiO₂NP_1** over 24 h, whilst stirring at 37 °C. The emission of the released **CPT** was also measured. The full width at half maximum of the emission spectra were compared to **CPT** in H_2O, and no broadening was observed. Interestingly, a red shift in maxima was observed over time, from λ_{max} 435 nm to 450 nm. Looking back at section 2.8, Wang *et*. *al*. observed emission dependent properties on their silica NPs doped with a Ruthenium complex at different time points[133]. The proposed synthesis of the non-porous **CPT⊂SiO₂NP** was discussed (figure 2.81), and we observed a similar trend in emission properties (figure 2.8.21). The emission of **CPT3⊂SiO₂NP_1** was red shifted from **CPT0⊂SiO₂NP_1**, where the drug particles would have been more spread out rather than packed in the centre. The red shift observed in the emission of the drug release potentially suggests the pattern observed by Wang *et. al.* may also apply to **CPT⊂SiO₂NP.** As the **CPT** is released from **CPT0⊂SiO₂NP_1**, particles that may be packed in the centre slowly move towards the edge of the silica network and into solution.

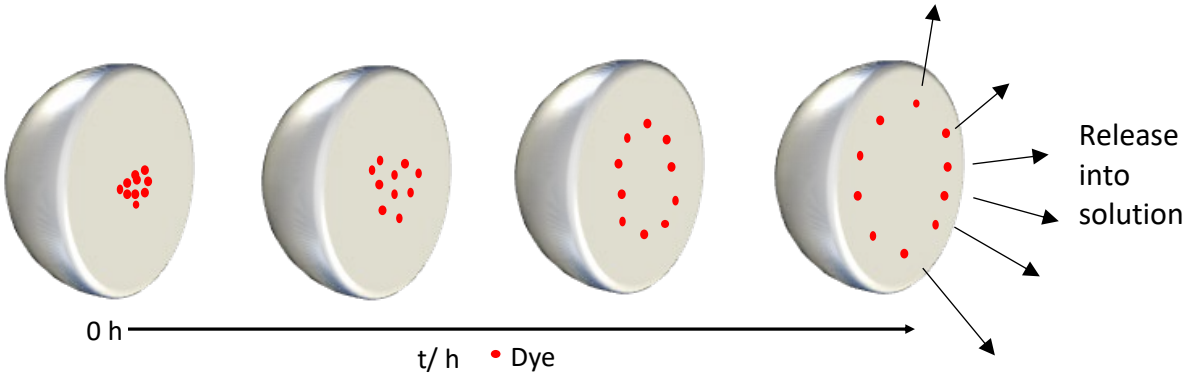


Figure 2.9.12

Schematic illustration of release of CPT from **CPT0⊂SiO₂NP_1** showing the movement of drug particles travelling towards edge of silica network and into solution.

As drug particles move away from the centre of the nanoparticle, this resembles a similar position to the drug particles when **CPT** is doped at 3 h (**CPT3⊂SiO₂NP_1**). The red shift in emission from release of the drug could be following the trend explained here.

To compare, the release of the drug was studied in static conditions in order to show the effect of physical force applied when stirring.

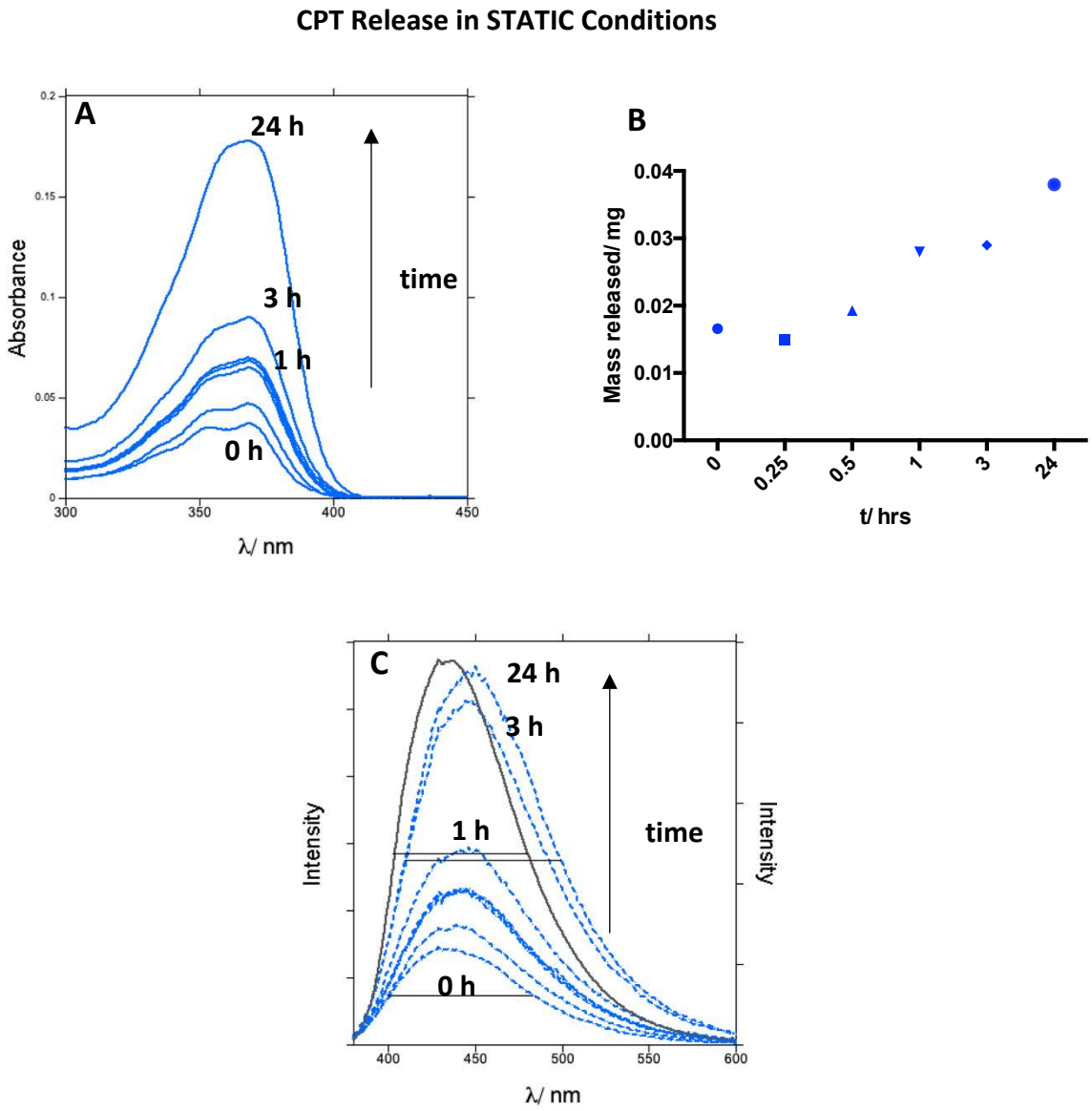


Figure 2.9.13

Release of **CPT** from **CPT0⊂SiO$_2$NP_1** (1 mg mL^{-1}, H_2O, RT) up to 24 hrs studied by UV-Vis absorbance. A: UV-Vis absorbance of **CPT** released from **CPT0⊂SiO$_2$NP_1.** B: The mass of **CPT** released from **CPT0⊂SiO$_2$NP_1** calculated from UV-Vis absorbance. C: Emission of **CPT** released from **CPT0⊂SiO$_2$NP_1** (blue dotted) compared to **CPT** emission (0.1 mM, H_2O), λ_{exc} = 350 nm. Emission spectra corrected for PMT and instrument response.

CPT0⊂SiO$_2$NP_1 NPs were kept in a falcon tube in H_2O stationary on a lab bench. Aliquots of 1 mL from the solution were taken and centrifuged in order to remove any excess NPs, leaving

behind just any drug that was released into solution. The UV-Vis absorbance of the aliquot was measured at time intervals up to 24 hrs, and returned back to the solution after measurement.

An increase in UV-Vis absorbance was observed, as more **CPT** was released into the solution from **CPT0⊂SiO$_2$NP_1**, however the absorbance values observed were much lower as expected. In static conditions, with no physical trigger to the NPs, the release of the drug was much slower. The absorbance was used to calculate the mass of **CPT** released. Using the previous calculations, the % of **CPT** released was calculated.

Table 2.9.12

Table of values showing % release of CPT from **CPT0⊂SiO$_2$NP_1 .**

Sample	**Mass of CPT loaded per mass of SiO$_2$NP/ mg**	**Mass of CPT released/ mg**	**% Release**
CPT0⊂SiO$_2$NP_1	0.09	0.04	44

With static conditions at RT, only 44 % of drug particles were released from **CPT0⊂SiO$_2$NP_1** demonstrating the slower release with the change of conditions. The slower release from static conditions also strongly supports the successful encapsulation of **CPT** in the NPs previously observed from luminescence studies.

Emission spectra (figure 2.9.13 C) show a red shift in λ_{max} from 0 h to 24 h. This follows the trend that was observed by the release of **CPT0⊂SiO$_2$NP_1** at 37 ^{o}C, stirring, supporting that the suggested mechanism is correct.

Drug release studies from the experiments showed the change in UV-Vis band from the start, observed by two shoulders at the λ_{max} maxima, growing into a broad band. The broad band corresponds to $\pi-\pi^*$ transitions in the carboxylate form, also reported by Alves *et. al.*[108]. These observations suggest a mixture of active and inactive forms of **CPT**, perhaps dominated by the lactone after long experiment times under reversible hydrolysis conditions[108].

2.9.2. Studying CPT Release from CPT0⊂Eu-L.SiO_2NP_1 in Water

After observing the ability to release the drug from the unfunctionalised **CPT0⊂SiO_2NP_1**, with a physical trigger (stirring) at 37 °C, but also in static conditions, we studied the release of the drug from **CPT0⊂Eu-L.SiO_2NP_1**. If the release of the drug could be detected from the Ln coated NPs, the amount of release occurring outside of a cellular environment can give us an insight into the amounts of drug that could be released in cells, and their effect. To mimic conditions in cells, release was performed at 37 °C in H_2O, stirring to keep temperature constant.

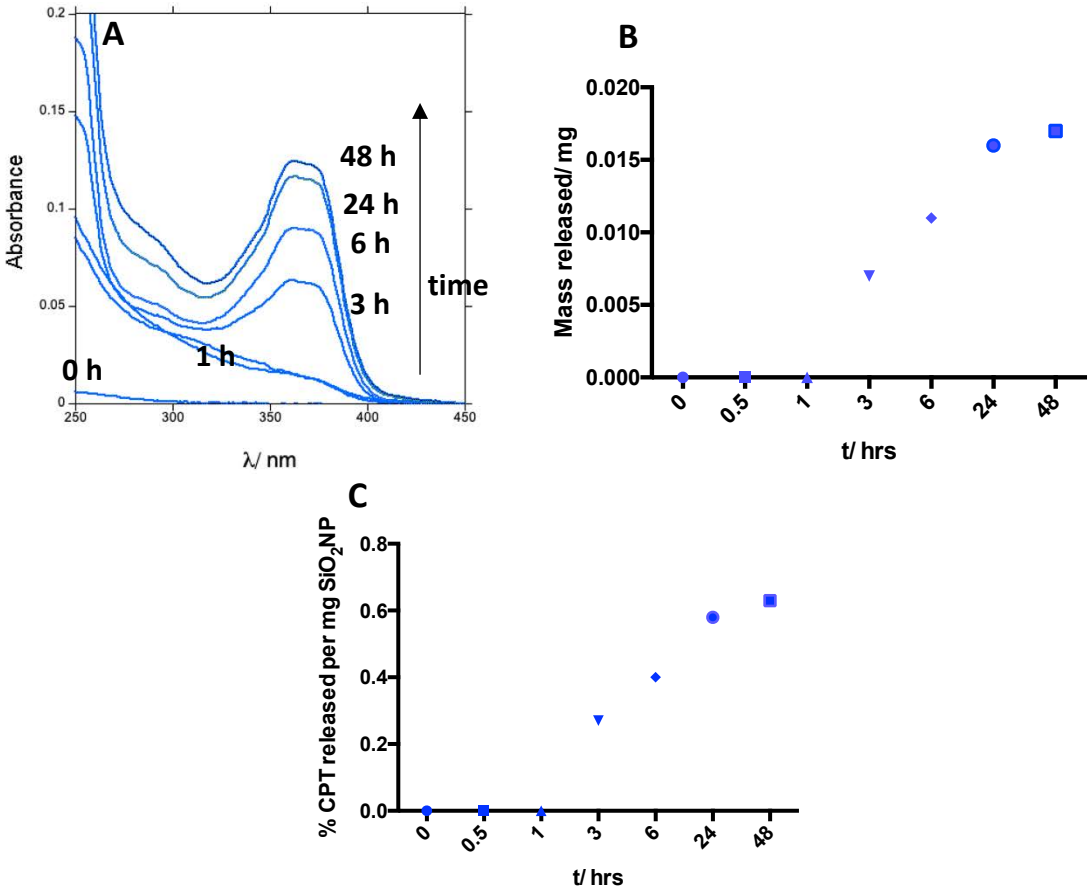


Figure 2.9.21

Release of **CPT** from **CPT0⊂Eu-L.SiO_2NP_1** (1 mg mL^{-1}, H_2O, 37 °C) stirring up to 48 hrs, studied by UV-Vis absorbance. A: UV-Vis absorbance of **CPT** released from **CPT0⊂Eu-L.SiO_2NP_1**. B: The mass of **CPT** released from **CPT0⊂Eu-L.SiO_2NP_1**calculated from UV-Vis absorbance. C: The % of **CPT** released per every mg of **SiO_2NP**.

A dispersion of **CPT0⊂Eu-L.SiO$_2$NP_1** was stirred at 37 ^{o}C in water. Aliquots of 1 mL from the solution were taken and centrifuged in order to remove any excess NPs, leaving behind just any drug that was released into solution. The UV-Vis absorbance of the aliquot was measured at time intervals up to 48 hrs, and returned back to the solution after measurement.

An increase in UV-Vis absorbance was observed, as expected, albeit with values much lower than the unfunctionalised **CPT0⊂SiO$_2$NP_1**, corresponding with the low values of mass released (figure 2.9.21 B). The lower and slower release of the drug from the Ln coated NPs can be attributed to the surface of the silica network being capped by the Eu(III) complex, slowing down the release of **CPT** into solution. Functionalisation of silica NPs (porous and non-porous) has remained an attractive method to perform controlled drug release, in addition to preventing premature release through gatekeeping[148-155] as well as passive drug release *via* diffusion through the silica network[156-159]. The UV-Vis absorbance results show that with the surface being functionalised, we can slow down the release enabling a controlled method of release for experiments in cells.

Similarly, the absorbance was used to calculate the mass of **CPT** released. Drug loading of **CPT0⊂Eu-L.SiO$_2$NP_1** was measured using UV-Vis absorbance of the supernatant of **CPT0⊂Eu-L.SiO$_2$NP_1** after synthesis. This was used to calculate the % release of **CPT**.

Table 2.9.21

Table of values showing % release of CPT from **CPT0⊂Eu-L.SiO$_2$NP_1** after 48 hrs.

Sample	**Mass of CPT loaded per mass of SiO$_2$NP/ mg**	**Mass of CPT released/ mg**	**% Release**
CPT0⊂Eu-L.SiO$_2$NP_1	2.75	0.2	0.7

Drug release studies mirrored the same observations, resulting in the observation of broad **CPT** band, indicating difficult investigation of distinguishable **CPT** forms.

To demonstrate the use of the NPs as a diagnostic application, the emission of the NPs were monitored after release to show the promising use of our design. This strongly illustrates our aim to detect drug release through monitoring changes in Ln(III) luminescence (see figure 2.21 in chapter outline).

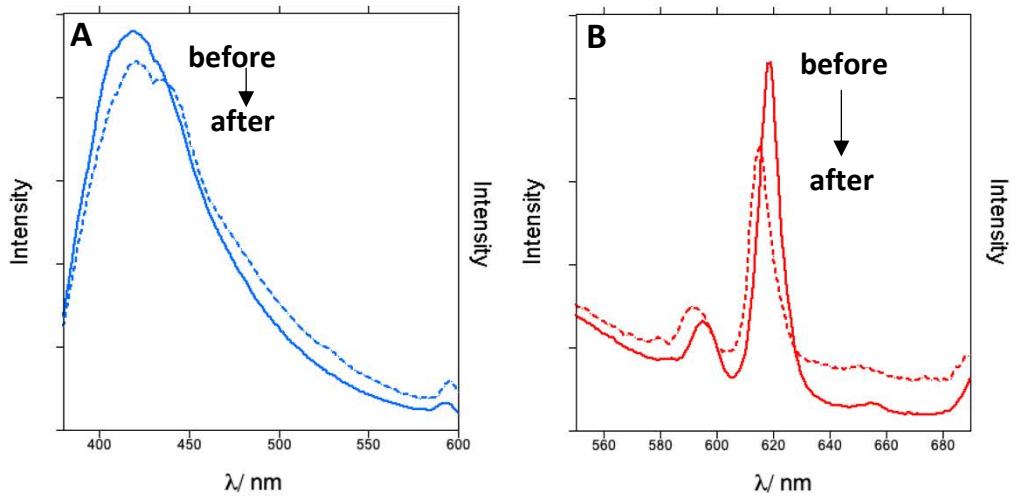


Figure 2.9.22

Changes in emission compared before and after release of **CPT** from **CPT0⊂Eu-L.SiO$_2$NP_1** at 24 h, solid state, λ_{exc} = 350 nm. A: Monitoring **CPT** emission from **CPT0⊂Eu-L.SiO$_2$NP_1** before release (blue solid line) compared to emission of **CPT0⊂Eu-L.SiO$_2$NP_1** after release (blue dotted line). B: Monitoring Eu(III) emission from **CPT0⊂Eu-L.SiO$_2$NP_1** before release (red solid line) compared to emission of **CPT0⊂Eu-L.SiO$_2$NP_1** after release (red dotted line). Emission spectra corrected for PMT and instrument response.

Table 2.9.22

Summary of the integrated area under the peak for each spectra.

Emission signal	Area under peak before release	Area under peak after release	% Decrease After Release
CPT	3.8 x 10^7	3.7 x 10^7	3
CPT0⊂Eu-L.SiO$_2$NP_1 $^5D_0 \rightarrow {}^7F_1$	2.9 x 10^7	9.5 x 10^5	97
CPT0⊂Eu-L.SiO$_2$NP_1 $^5D_0 \rightarrow {}^7F_2$	4.5 x 10^6	2.6 x 10^6	42

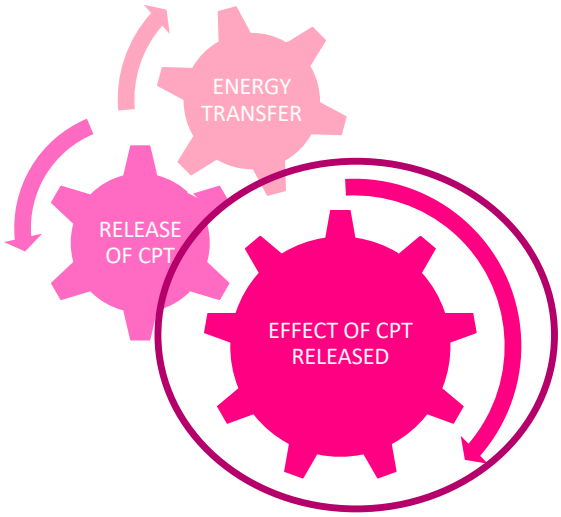
The emission properties of **CPT0⊂Eu-L.SiO$_2$NP_1** were characterised before and after 24 h release of the drug, monitoring both **CPT** and Eu(III) signal (figure 2.9.22). The area under the peak for each spectra was integrated using Kaleidagraph (table 2.9.22).

A decrease in **CPT** emission was observed from **CPT0⊂Eu-L.SiO$_2$NP_1** after release (figure 2.9.22, A), as expected. This result was confirmed by the integrated area under the peak when monitoring **CPT** emission signal from λ_{max} = 380 nm to 500 nm (table 2.9.22). A red shift in **CPT** emission signal was also detected after release, which is an additional result supporting the observations of redshift in emission from **CPT0⊂SiO$_2$NP_1**.

Eu(III) emission signal was detected after release of the drug from **CPT0⊂Eu-L.SiO$_2$NP_1**. In both cases, before and after release, transitions of Eu(III) emission were detected: $^5D_0 \rightarrow {}^7F_{1,2}$. Eu(III) emission signal before release was detected at λ_{max} = 595 nm ($^5D_0 \rightarrow {}^7F_1$) and the most intense transition at λ_{max} = 620 nm ($^5D_0 \rightarrow {}^7F_2$). Emission signal after release was detected at λ_{max} = 590 nm ($^5D_0 \rightarrow {}^7F_1$) and also the most intense transition at λ_{max} = 615 nm ($^5D_0 \rightarrow {}^7F_2$). In both transitions, a decrease in integrated area under the peak was observed from λ_{max} = 583 nm to 604 nm ($^5D_0 \rightarrow {}^7F_1$), and λ_{max} = 604 nm to 629 nm ($^5D_0 \rightarrow {}^7F_2$).

The decrease in emission signal for both **CPT** and Eu(III) emission signal was an imperative result obtained during the project and strongly showed the design's concept to be used as a diagnostic tool. Through monitoring changes in Eu(III) emission signal, **CPT** release can be detected due to less efficient energy transfer, enabling the use of light to monitor drug release from this system.

2.10. Effect of CPT from CPT0⊂SiO_2NPs_1 and Respective Lanthanide Coated Nanoparticles on Lung Cancer Cells



After successfully showing the energy transfer process is occurring to obtain sensitised Ln luminescence, we moved on to the next major step in our project. It was observed that through UV-Vis studies, the determination of **CPT** forms between carboxylate and lactone forms were difficult, and indicated possible mixtures. Through investigation of the cytotoxic effect of **CPT** released from the functionalised NPs, the effect of the released drug could be studied in view of our application for our design.

To study the cytotoxic effect of **CPT** we used the *in vitro* MTT (3-(4, 5-dimethylthiazolyl-2)-2, 5-diphenyltetrazolium bromide) assay. MTT assays are a metabolic viability based assay that use salts such as MTT to screen the anti-proliferative properties of compounds being tested giving indications on cell viability and cytotoxicity. It is a colorimetric assay in which yellow coloured MTT is reduced to purple formazan crystals in the metabolically active cells. These cells contain NAD(P)H dependent oxidoreductase enzymes which reduce MTT to formazan. A solubilisation solution (DMSO) is used to dissolved the formazan crystals and the resulting purple colour absorbance is measured in a spectrometer between 500 – 600 nm. The colour of the solution correlates to the number of viable cells (the darker the colour, the more viable number of cells)[161].

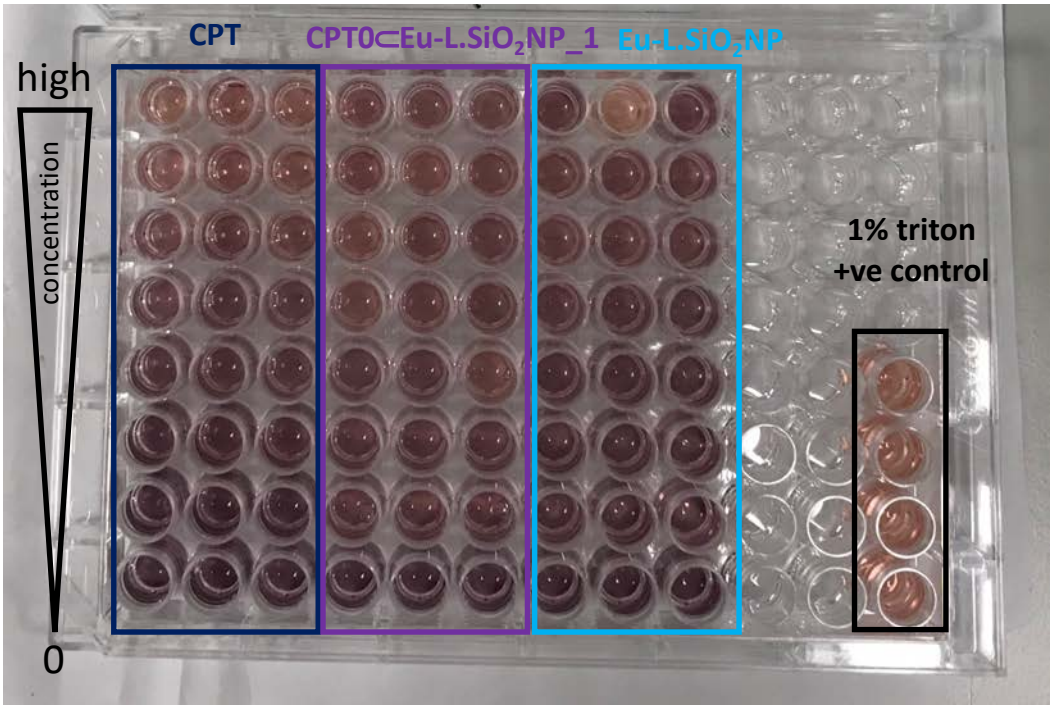


Figure 2.101

Image of 96-well plate of A549 lung cancer cells incubated at 72 hr with **CPT** (7 concentrations from dilution of 500 nM, DMSO), **CPT0⊂Eu-L.SiO$_2$NP** (7 concentrations from dilution of 2 mg mL^{-1}), **Eu-L.SiO$_2$NP ((**7 concentrations from dilution of 2 mg mL^{-1}) and positive control of 1 % triton. This image represents the change in intensity of purple colour of the controls after formation of formazan crystals using DMSO.

Figure 2.101 illustrates the correlation between the colour of the purple solution and the number of viable cells. As the concentration of both **CPT** and **CPT0⊂Eu-L.SiO$_2$NP** drops, the purple colour is darker indicating there are a higher number of viable cells with low concentrations of these controls. The change is much smaller in control **Eu-L.SiO$_2$NP** in absence of **CPT**.

2.10.1. Effect of CPT on Lung Cancer Cells after 24 hrs Incubation

A cell viability assay was performed on A549 cancer cells with **CPT0⊂Eu-L.SiO$_2$NP_1** at 24 hrs incubation to initially test the effect of the drug.

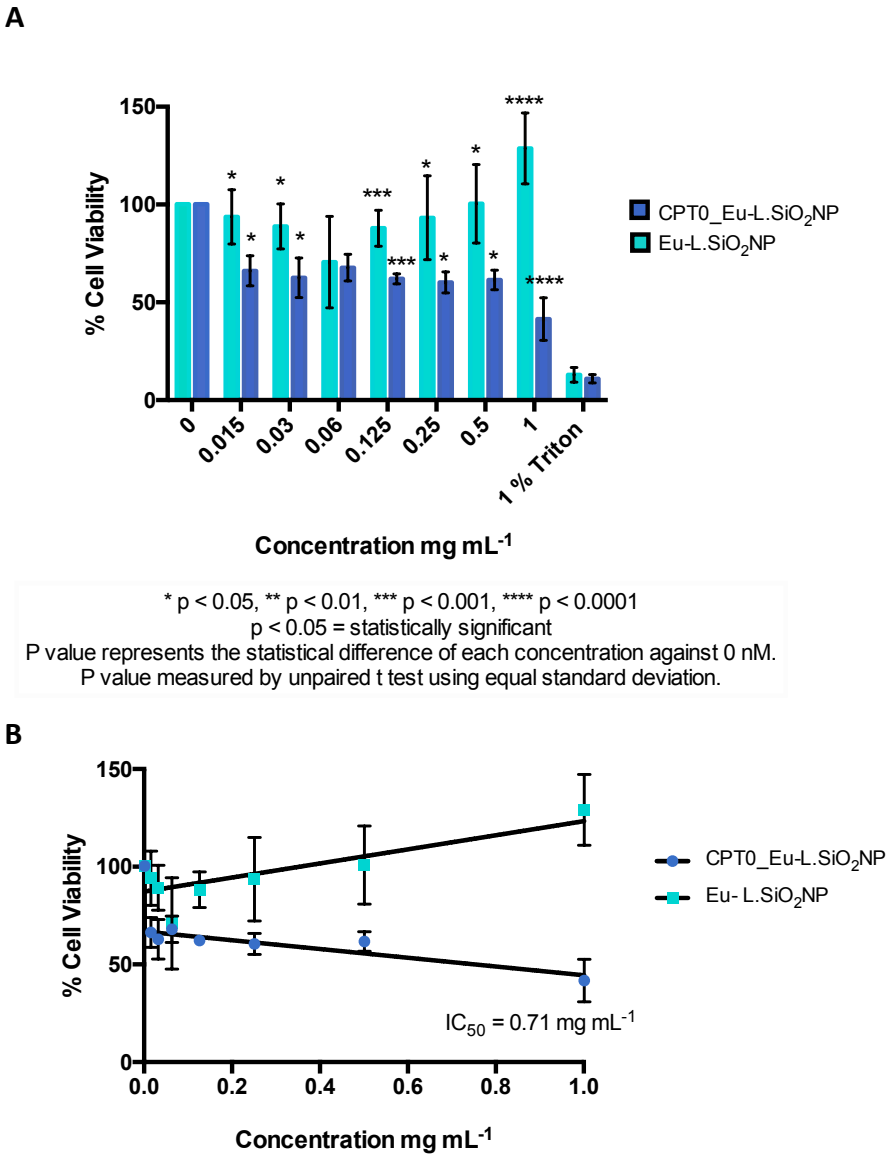


Figure 2.10.11

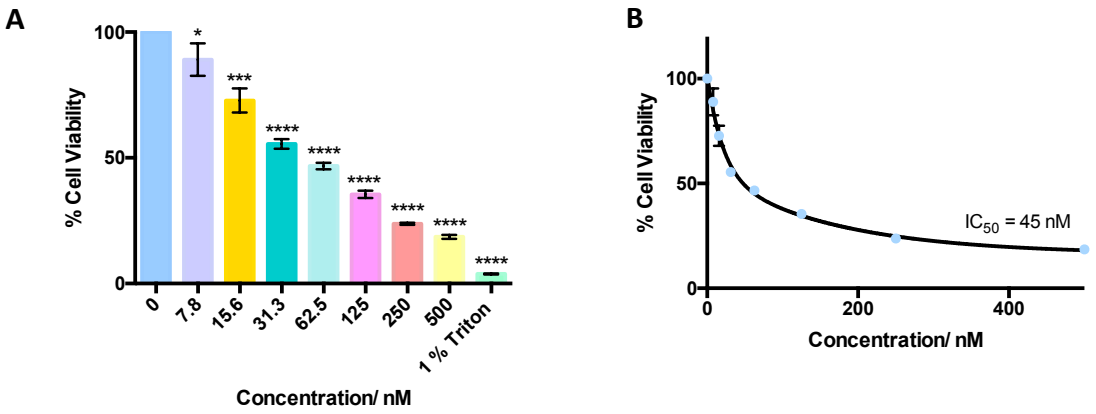
A: In vitro cytotoxicity MTT assay showing percentage cell viability of A549 cells after 24h incubation with **CPT0⊂Eu-L.SiO$_2$NP_1** (blue) (7 concentrations from dilution of 1 mg mL^{-1}, cultured cell media) and **Eu-L.SiO$_2$NP_1** (green) ((7 concentrations from dilution of 1 mg mL^{-1}, cultured cell media), with a positive control of 1% triton. P value represents the statistical significant difference of each concentration against 0 nM, $p < 0.05$ is significantly different. The P value was measured by an unpaired t test with equal SD B: IC$_{50}$ curve of **CPT0⊂Eu-L.SiO$_2$NP_1** (blue circle) in cell media, incubation time of 24h in A549 cells; 0.71 mg mL^{-1}, and **Eu-L.SiO$_2$NP_1** (green square) in cell media, incubation time of 24h in A549 cells.

Cell viability was measured in one experiment, where each concentration consisted of triplicate wells. The error bars for each data point represent the mean with standard deviation (SD) of these measurements. The IC_{50} value of CPT (in DMSO) in A549 cells at 24 h incubation was not found with the concentrations used, but the IC_{50} of **CPT0⊂Eu-L.SiO$_2$NP_1** was found to be 0.71 mg mL^{-1} at these conditions.

Interestingly, no decreasing dependence on increasing concentration of **Eu-L.SiO$_2$NP_1** was observed, but in fact some increase in % cell viability at 24h incubation, which has been observed before for **SiO$_2$NPs**[162]**.** More significantly, a decrease in cell viability with increasing concentrations of **CPT0⊂Eu-L.SiO$_2$NP_1** suggested toxicity arising from **CPT** within these NPs. To obtain the IC_{50} of **CPT**, but also further investigate the toxicity of the NPs, the experiment was repeated at a longer incubation time of 72h to paint the full picture.

2.10.2. Effect of CPT on Lung Cancer Cells after 72 hrs Incubation

After observing some toxicity to A549 cancer cells from **CPT0⊂Eu-L.SiO$_2$NP_1**, a cell viability assay was performed 72 hrs incubation to support the observation of **CPT** toxicity.



* p < 0.05, ** p < 0.01, *** p < 0.001, **** p < 0.0001
p < 0.05 = statistically significant
P value represents the statistical difference of each concentration against 0 nM.
P value measured by unpaired t test using equal standard deviation.

Figure 2.10.21

A: *In vitro* cytotoxicity MTT assay showing percentage cell viability of A549 cells after 72h incubation with **CPT** (7 concentrations from dilution of 500 nM, DMSO) with a positive control of 1% triton. The P value was measured by an unpaired t test with equal SD. B: IC_{50} curve of **CPT** in DMSO, incubation time of 72h in A549 cells, 45 nM.

Cell viability was measured in four independent experiments, where each experiment consisted of at least triplicate wells at each concentration. The error bars for each data point represent the mean with standard deviation (SD) of these measurements. The IC_{50} value of CPT (in DMSO) in A549 cells was found to be 45 nM, at 72 h incubation period. All experiments resulted in a concentration dependent decrease in the cell viability, as expected.

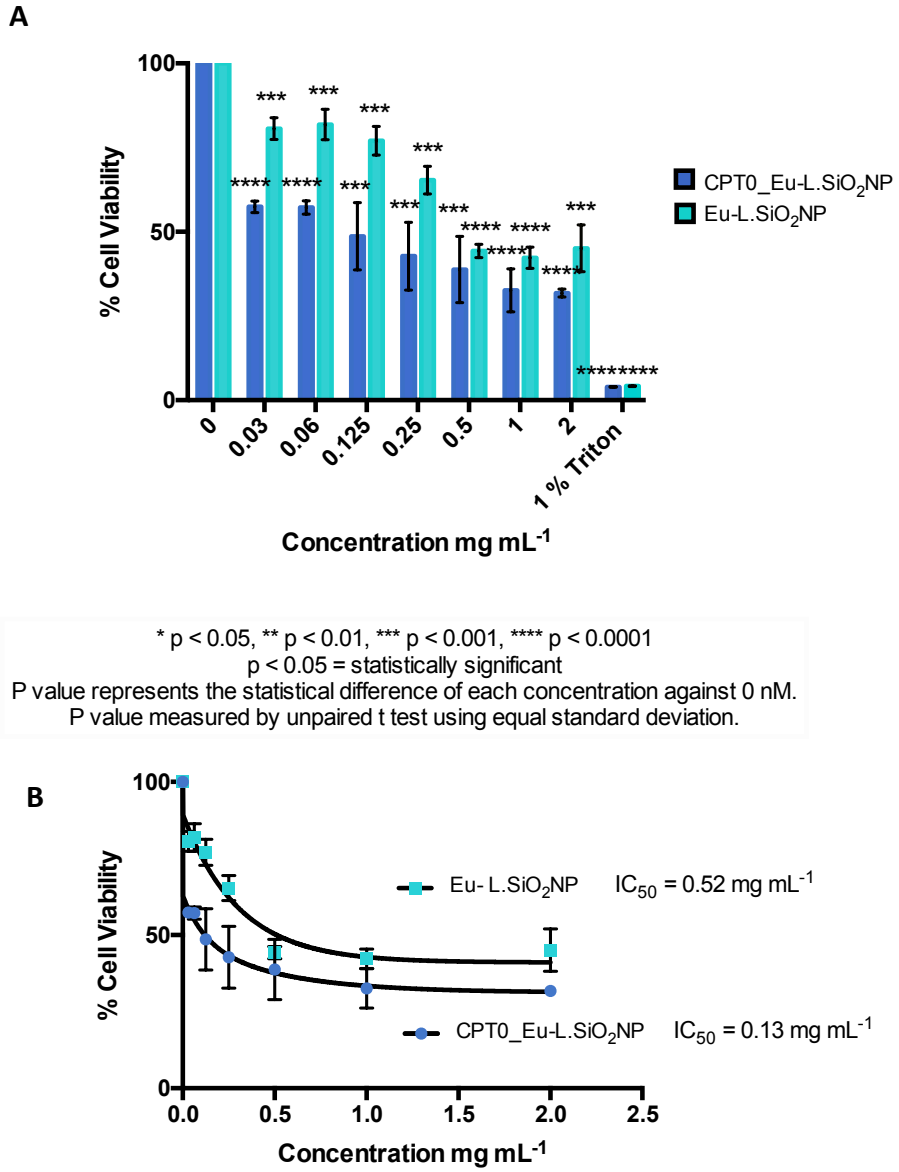


Figure 2.10.22

A: *In vitro* cytotoxicity MTT assay showing percentage cell viability of A549 cells after 72h incubation with **CPT0⊂Eu-L.SiO$_2$NP_1** (blue) (7 concentrations from dilution of 2 mg mL^{-1}, cultured cell media) and **Eu-L.SiO$_2$NP_1** (green) ((7 concentrations from dilution of 2 mg mL^{-1}, cultured cell media), with a positive control of 1% triton. B: IC_{50} curve of **CPT0⊂Eu-L.SiO$_2$NP_1** (blue circle) in cell media, incubation time of 72h in A549 cells; 0.13 mg mL^{-1}, and **Eu-L.SiO$_2$NP_1** (green square) in cell media, incubation time of 72h in A549 cells; 0.52 mg mL^{-1}.

Cell viability of the functionalised NPs were measured in one experiment, with triplicate wells at each concentration. The error bars for each data point represent the mean with standard deviation (SD) of these measurements. A general trend of decreasing cell viability on increasing concentration dependence was observed for all sets of NPs, as expected similarly to figure 2.10.11. More importantly, a significant difference between the **CPT** containing NPs and **SiO_2NP** was obtained, suggesting the increase in cell death was arising from **CPT** toxicity to the cells (as seen previously with a 24 h incubation period).

It is imperative to look at the difference between **CPT0⊂Eu-L.SiO_2NP_1** and **Eu-L.SiO_2NP_1**. At concentrations up to 0.125 mg mL^{-1} of NPs there is between 80-100 % cell viability of **Eu-L.SiO_2NP_1** which is not significant enough to be attributed as toxic. However there is a significant drop in cell viability at these concentrations of **CPT0⊂Eu-L.SiO_2NP_1** strongly suggesting toxicity to cells from **CPT** within these NPs. This result is mirrored in the IC_{50} values of the NPs: **CPT0⊂Eu-L.SiO_2NP_1** (0.13 mg mL^{-1}) is much lower than **Eu-L.SiO_2NP_1** (0.52 mg mL^{-1}), giving a window of suggested concentrations of NPs for dosage.

Table 2.10.21

Summary of **CPT** concentration released from **CPT0⊂Eu-L.SiO_2NP_1** at 1 mg mL^{-1} and 0.125 mg mL^{-1}.

	1 mg mL^{-1}	**0.125 mg mL^{-1}**
Mass of **CPT** released/ mg	0.017	0.002
Estimated theoretical concentration of **CPT** released/ nM	4.8×10^4	6×10^3

The estimated theoretical concentration of **CPT** released from **CPT0⊂Eu-L.SiO_2NP_1** at 0.125 mg mL^{-1} at 72 hrs was calculated based on results obtained from UV-Vis absorbance of release studies of **CPT0⊂Eu-L.SiO_2NP_1** in water (figure 2.9.21). If the same % of **CPT** was released from **CPT0⊂Eu-L.SiO_2NP_1** at 0.125 mg mL^{-1}, 6×10^3 nM of **CPT** would be released into A549 cells. This concentration is 130 times larger in magnitude to the IC_{50} value of **CPT** in A549 cells (45 nM).

To compare the concentration of **CPT** released against the IC_{50} value of **CPT** (45 nM) in a negative scenario, similar calculations were made in the hypothetical situation of only 1% **CPT** release occurring using values from figure 2.9.21.

Table 2.10.22

Summary of **CPT** concentration released from **CPT0⊂Eu-L.SiO$_2$NP_1** at 1 mg mL^{-1} and 0.125 mg mL^{-1} if only 1 % of drug molecules were released.

	1 mg mL^{-1}	**0.125 mg mL^{-1}**
Mass of **CPT** released/ mg	1.7×10^{-4}	2×10^{5}
Estimated theoretical concentration of **CPT** released/ nM	480	60

If only 1 % of **CPT** was released at 72 hrs, compared to the results obtained from UV-Vis absorbance (figure 2.9.31), 60 nM of **CPT** would be released at 0.125 mg mL^{-1} of **CPT0⊂Eu-L.SiO$_2$NP_1**. This is only just larger in magnitude than the IC_{50} value of **CPT** in A549 cells at 72 hrs incubation. If such an extreme negative result was observed, more than 50 % cell viability would be observed, supporting the evident toxicity arising from **CPT**.

The cell viability of unfunctionalised **CPT0⊂SiO$_2$NP_1** was also measured at 72 hrs incubation.

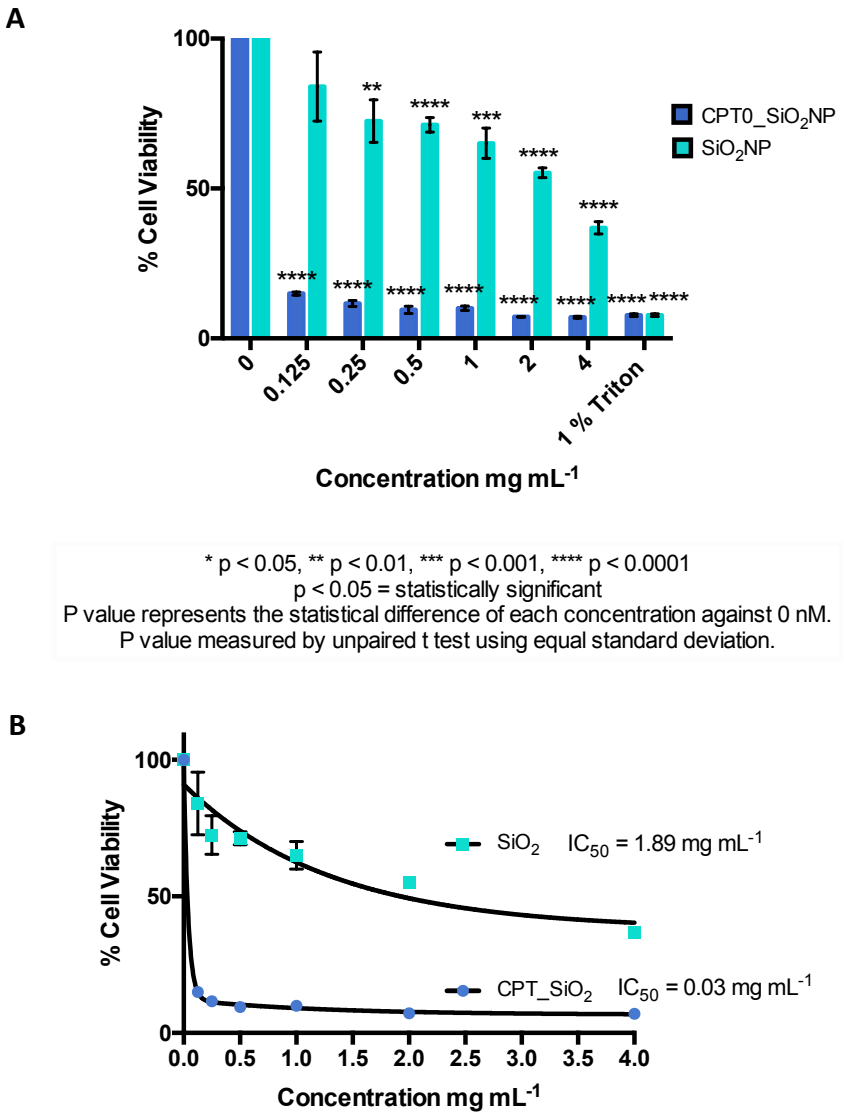


Figure 2.10.23

A: In vitro cytotoxicity MTT assay showing percentage cell viability of A549 cells after 72h incubation with **CPT0⊂SiO$_2$NP_1** (blue) (6 concentrations from dilution of 4 mg mL^{-1}, cultured cell media) and **SiO$_2$NP** (green) ((6 concentrations from dilution of 4 mg mL^{-1}, cultured cell media), with a positive control of 1% triton. B: IC$_{50}$ curve of **CPT0⊂SiO$_2$NP_1** (blue circle) in cell media, incubation time of 72h in A549 cells; 0.03 mg mL^{-1}, and **SiO$_2$NP** (green square) in cell media, incubation time of 72h in A549 cells; 1.89 mg mL^{-1}.

In vitro cytotoxicity was conducted in one experiment consisting of triplicate concentrations. The error bars for each data point represent the mean with standard deviation (SD) of these measurements.

As seen previously with the functionalised **CPT0⊂Eu-L.SiO_2NP_1**, the same trend was mirrored here in decreasing cell viability with increasing nanoparticle concentration. The difference in toxicity between **CPT0⊂SiO_2NP_1** and **SiO_2NP** is much more magnified in this experiment, confirming the toxicity to cells can be attributed to **CPT**. The toxicity arising from **CPT** is also concentration dependent as explained earlier. In this case, we are to look at concentrations up to also 0.125 mg mL^{-1} where **SiO_2NP** shows between 80 – 100 % cell viability, but there is a significant drop down to 14 % cell viability at 0.125 mg mL^{-1} **CPT0⊂SiO_2NP_1**.

Table 2.10.23

Summary of **CPT** concentration released from **CPT0⊂SiO_2NP_1** at 1 mg mL^{-1} and 0.125 mg mL^{-1} at 24 hrs.

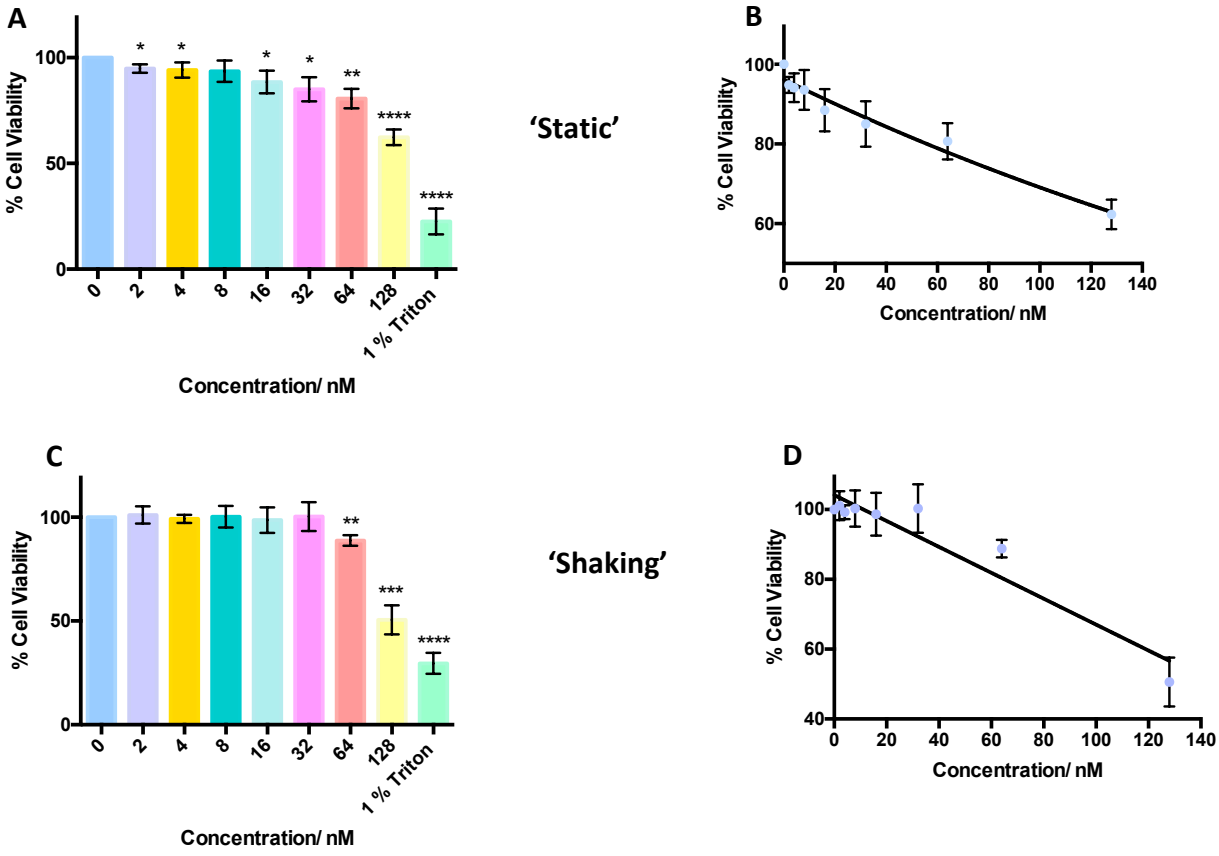
	1 mg mL^{-1}	**0.125 mg mL^{-1}**
Mass of **CPT** released/ mg	0.04	4×10^3
Estimated theoretical concentration of **CPT** released/ nM	11×10^3	1.4×10^3

Values were taken from release study of **CPT⊂SiO_2NP** in water, in static conditions (figure 2.9.13). The theoretical concentration of **CPT** released from **CPT⊂SiO_2NP** at 0.125 mg mL^{-1} at 24 hrs was calculated. Just after 24 hrs, 1.4×10^3 nM of **CPT** would be released, 300 times larger in magnitude than the IC_{50} value of **CPT**. As the release study of **CPT⊂SiO_2NP** was only studied up to 24 hrs, we can only predict that this number would be much larger at 72 hrs due to the expected increased **CPT** release.

To consider a negative scenario where only 1 % **CPT** release occurred, 14 nM of **CPT** would be released. This is lower than the IC_{50} value of **CPT** (45 nM). In order to have an effect resulting in more than 50 % cell viability, only 3.5 % of **CPT** would have to be released giving an estimated amount of 50 nM release (5 nM more than the IC_{50} value of **CPT**). This negative result enables us to predict that more than enough **CPT** would have an effect on cancer cells at 0.125 mg mL^{-1} of NPs.

2.10.3. Effect of Using a Physical Trigger on Toxicity of CPT to Lung Cancer Cells

To further investigate the toxicity, shaking conditions were used to mimic the release studies of the NPs kept stirring at 37 °C. In order to use these conditions a shaking incubator was used to mimic the physical movement. 96-well plates were used and incubation time period was shortened to 6 hrs due to feasibility of retaining cell growth outside a CO_2 chamber. The 96 well-plates were kept shaking in an incubator at 37 °C outside a CO_2 chamber. For the corresponding static experiment, a 96 well plate was kept inside the CO_2 chamber at 37 °C.



* p < 0.05, ** p < 0.01, *** p < 0.001, **** p < 0.0001
p < 0.05 = statistically significant
P value represents the statistical difference of each concentration against 0 nM.
P value measured by unpaired t test using equal standard deviation.

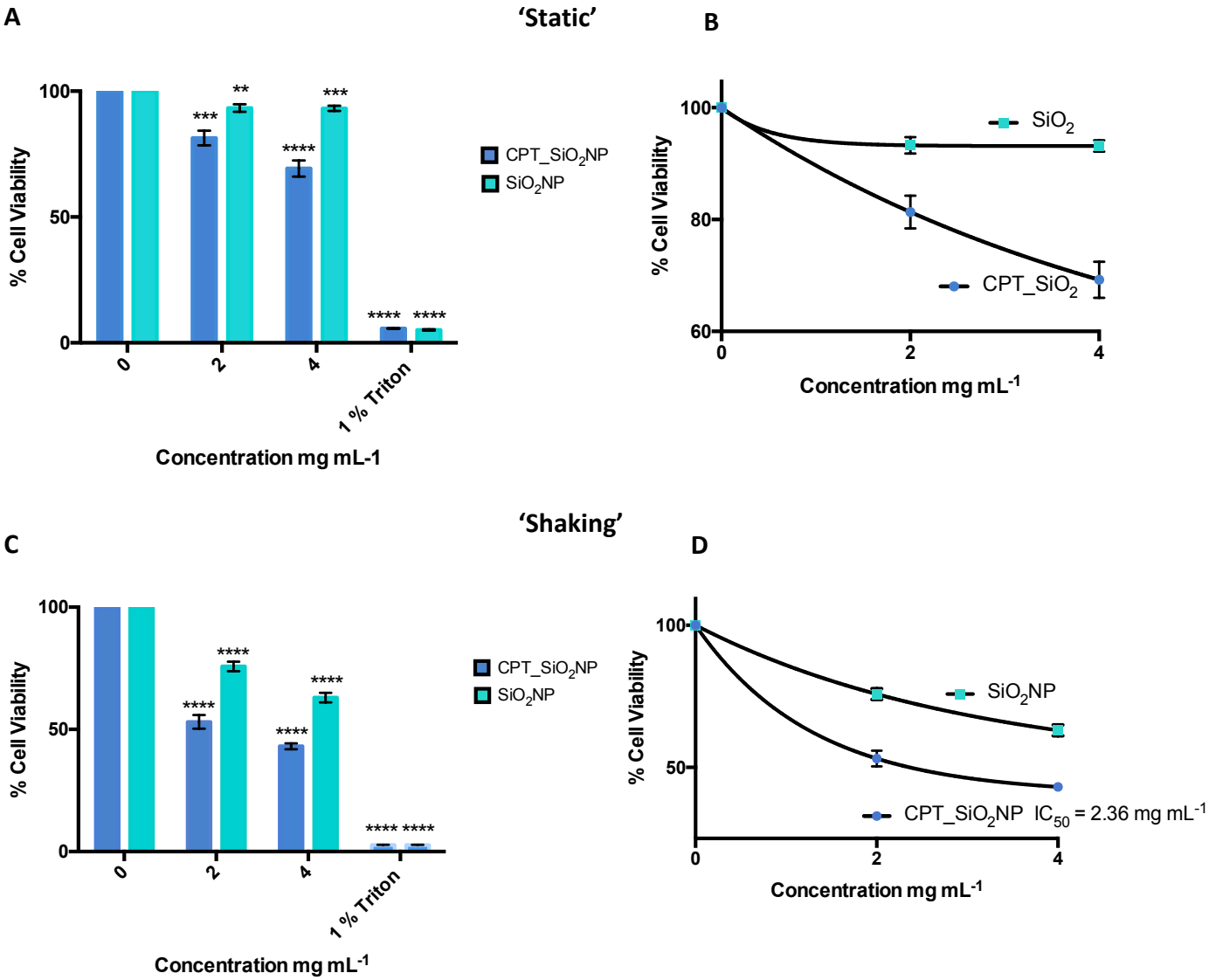
Figure 2.10.31

A: : *In vitro* cytotoxicity MTT assay showing percentage cell viability of A549 cells after 6h incubation with **CPT** (7 concentrations from dilution of 128 nM, DMSO) with a positive control of 1% triton. B: IC_{50} curve of **CP**T in DMSO, incubation time of 6h in A549 cells. C: *In vitro* cytotoxicity MTT assay showing percentage cell viability of A549 cells after 6h incubation, with 96-well plate shaking at 37 °C, with **CPT** (7 concentrations from dilution of 128 nM, DMSO) with a positive control of 1% triton. D: IC_{50} curve of **CPT** in DMSO, incubation time of 6h shaking in A549 cells.

The cell viability of **CPT** at 6h incubation was measured, conducted in two experiments (one static kept in the CO_2 chamber at 37 ^oC, one shaking at 37 ^oC in an incubator) consisting of triplicate concentrations. The error bars for each data point represent the mean with standard deviation (SD) of these measurements. P value represents the statistical significant difference of each concentration against 0 nM, $p < 0.05$ is significantly different. The P value was measured by an unpaired t test with equal SD.

A faster drop in cell viability was observed in the shaking experiment, as expected, due to the forced physical force applied. Although the IC_{50} values for **CPT** at 6h incubation with A549 cells were not quite reached, this experiment showed us the difference in toxicity to the cells after applying a physical trigger such as shaking.

As we previously saw, the difference in toxicity between unfunctionalised **CPT0⊂SiO$_2$NP_1** and **SiO$_2$NP** was much more magnified. Therefore, we first studied the toxicity of the unfunctionalised NPs comparing toxicities between conditions (static and stirring) at 6 h incubation. This approach was chosen in the hope that we would observe a clear difference at such a short incubation time period, which may be harder to detect with **CPT0⊂Eu-L.SiO$_2$NP_1**.



* p < 0.05, ** p < 0.01, *** p < 0.001, **** p < 0.0001
p < 0.05 = statistically significant
P value represents the statistical difference of each concentration against 0 nM.
P value measured by unpaired t test using equal standard deviation.

Figure 2.10.32

A: *In vitro* cytotoxicity MTT assay showing percentage cell viability of A549 cells after 6h incubation, 'static' with **CPT0⊂SiO₂NP_1** (blue) (3 concentrations from dilution of 4 mg mL^{-1}, cultured cell media) and **SiO₂NP** (green) (3 concentrations from dilution of 4 mg mL^{-1}, cultured cell media), with a positive control of 1% triton. B: IC_{50} curve of **CPT0⊂SiO₂NP_1** (blue circle) in cell media, and **SiO₂NP** (green square) in cell media, incubation time of 6h in A549 cells. C: *In vitro* cytotoxicity MTT assay showing percentage cell viability of A549 cells after 6h incubation, 'shaking' with **CPT0⊂SiO₂NP_1** (blue) (3 concentrations from dilution of 4 mg mL^{-1}, cultured cell media) and **SiO₂NP** (green) (3 concentrations from dilution of 4 mg mL^{-1}, cultured cell media), with a positive control of 1% triton. D: IC_{50} curve of **CPT0⊂SiO₂NP_1** (blue circle) in cell media, and **SiO₂NP** (green square) in cell media, incubation time of 6h, 'shaking' in A549 cells.

The cell viability of **CPT0⊂SiO$_2$NP_1** and **SiO$_2$NP** at 6 h incubation was measured, conducted in two experiments (one static kept in the CO_2 chamber at 37 ^oC and one shaking at 37^oC in an incubator) consisting of triplicate concentrations. The error bars for each data point represent the mean with standard deviation (SD) of these measurements. P value represents the statistical significant difference of each concentration against 0 nM, $p < 0.05$ is significantly different. The P value was measured by an unpaired t test with equal SD.

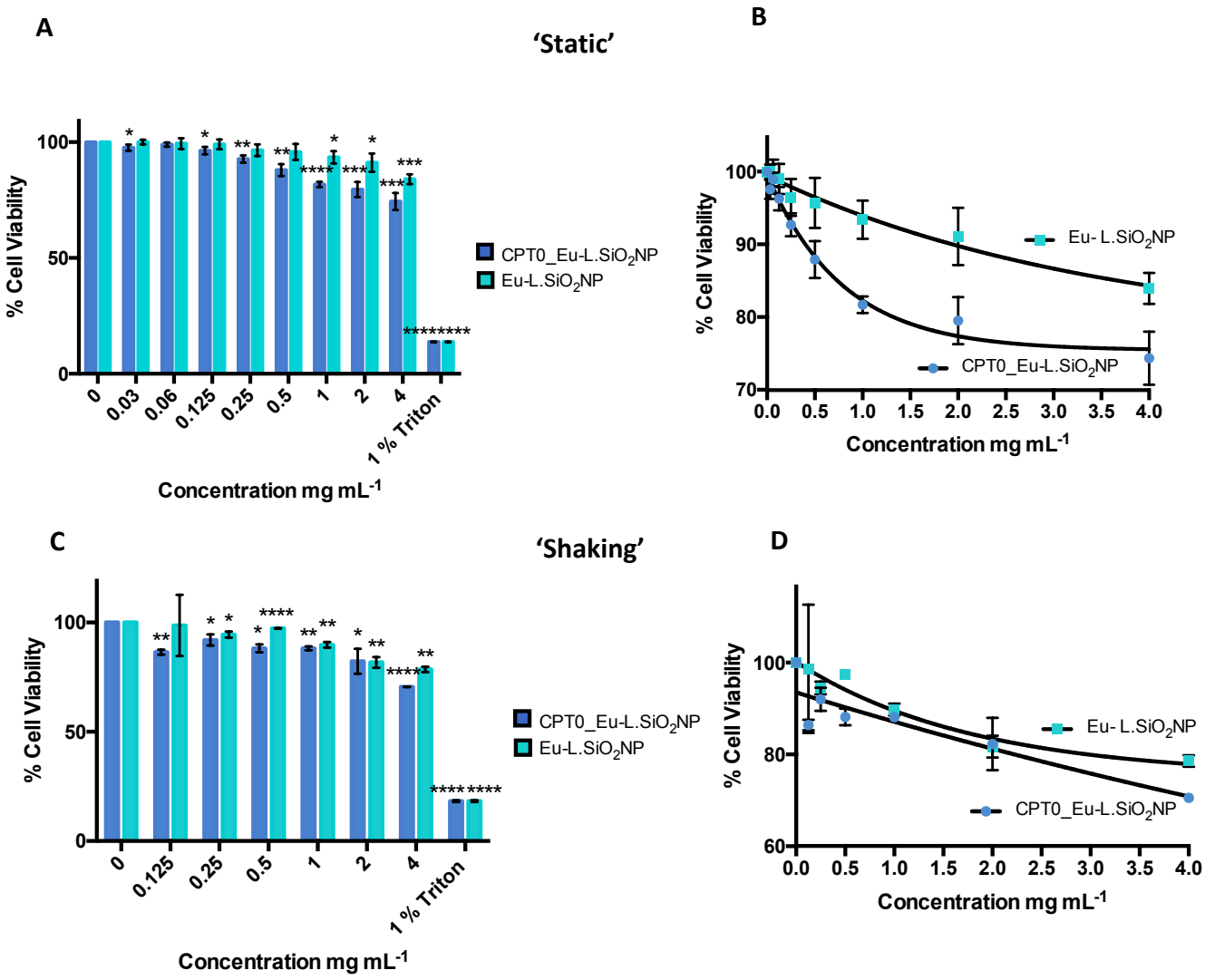
A clear difference can be seen between the static and shaking experiments; a faster decrease in % cell viability was observed with the shaking experiment in 6h compared to static. Additionally, we can also see the difference in toxicity between **CPT0⊂SiO$_2$NP_1** and **SiO$_2$NP**, adding to the evident results from the 72h incubation of the NPs previously, although it is concentration dependent.

Firstly, looking at the static experiment (figure 2.10.32, A and B), there was no significant drop in % cell viability of **SiO$_2$NP** up to 4 mg in 6 h (> 90 %), and hence any toxicity to the cells (< 80 %) can be attributed to the drug. At 6 h incubation, the lowest % cell viability that was reached was 69 %, although not as large, still a significant drop to strongly suggest the toxicity to the cells can safely be assumed to be arising from **CPT**.

In the shaking experiment (figure 2.10.32, C and D), increased toxicity to the cells was observed with both **CPT0⊂SiO$_2$NP_1** and **SiO$_2$NP**, assumed due to the physical trigger applied as expected. The concentration range in which we can expect 80 – 100 % cell viability with **SiO$_2$NP** is up to 1.48 mg mL^{-1}, at which **CPT0⊂SiO$_2$NP_1** shows 60 % cell viability. We can assume when up to this concentration (1.48 mg mL^{-1}), the toxicity seen can be attributed solely to **CPT** within the NPs.

Now, comparing the two experiments, we should look at the cell viability at 1.48 mg mL^{-1}. **CPT0⊂SiO$_2$NP_1** shows 85 % cell viability in the static experiment, much less than when shaking at 60 %. This is also mirrored in the **SiO$_2$NP**s (93 % in the static experiment compared to 80 % in the shaking experiment). A larger decrease was observed in % cell viability due to the physical trigger applied, as previously seen in release studies of static experiments

compared to stirring the NPs. This is important to note as we have attempted to show the results of the larger effect observed, given this should occur in the bloodstream once the NPs have been administered.



* p < 0.05, ** p < 0.01, *** p < 0.001, **** p < 0.0001
p < 0.05 = statistically significant
P value represents the statistical difference of each concentration against 0 nM.
P value measured by unpaired t test using equal standard deviation.

Figure 2.10.33

A: *In vitro* cytotoxicity MTT assay showing percentage cell viability of A549 cells after 6h incubation, 'static' with **CPT0⊂Eu-L.SiO$_2$NP_1** (blue) (8 concentrations from dilution of 4 mg mL^{-1}, cultured cell media) and **Eu-L.SiO$_2$NP_1** (green) (8 concentrations from dilution of 4 mg mL^{-1}, cultured cell media), with a positive control of 1% triton. B: IC_{50} curve of **CPT0⊂Eu-L.SiO$_2$NP_1** (blue circle) in cell media, and **Eu-L.SiO$_2$NP_1** (green square) in cell media, incubation time of 6h in A549 cells. C: *In vitro* cytotoxicity MTT assay showing percentage cell viability of A549 cells after 6h incubation, 'shaking' with **CPT0⊂Eu-L.SiO$_2$NP_1** (blue) (6 concentrations from dilution of 4 mg mL^{-1}, cultured cell media) and **Eu-L.SiO$_2$NP_1** (green) (6 concentrations from dilution of 4 mg mL^{-1}, cultured cell media), with a positive control of 1% triton. D: IC_{50} curve of **CPT0⊂Eu-L.SiO$_2$NP_1** (blue circle) in cell media, and **⊂Eu-L.SiO$_2$NP_1** (green square) in cell media, incubation time of 6h, 'shaking' in A549 cells.

The cell viability of **CPT0⊂Eu-L.SiO$_2$NP_1** and **Eu-L.SiO$_2$NP_1** at 6 h incubation was measured, conducted in two experiments (one static kept in the CO_2 chamber at 37 ^oC, one shaking at 37 ^oC in an incubator) consisting of at least duplicate concentrations. The error bars for each data point represent the mean with standard deviation (SD) of these measurements. P value represents the statistical significant difference of each concentration against 0 nM, $p < 0.05$ is significantly different. The P value was measured by an unpaired t test with equal SD.

The difference between the static experiment and shaking is not as evident in this case with the functionalised NPs. There definitely is a higher decrease in % cell viability of **CPT0⊂Eu-L.SiO$_2$NP_1** with the physical trigger applied in the shaking experiment, with 70 % cell viability compared to 74 % when static. Albeit a much smaller difference, the decrease in viability looks much steeper in the shaking experiment. There is also a notable difference between the **Eu-L.SiO$_2$NP_1** NPs. The cell viability of **Eu-L.SiO$_2$NP_1** drops down to 78 % at 4 mg mL^{-1} when shaking, however the cell viability only drops to 84 % when static. A similar trend in a steeper decrease with increasing concentration of **Eu-L.SiO$_2$NP_1** is also observed between the two experiments.

Specifically looking at the static experiment firstly (figure 2.10.33, A and B), we can see that after 1.29 mg mL^{-1}, the cell viability of **CPT0⊂Eu-L.SiO$_2$NP_1** drops just below 80 % whilst maintaining an insignificant decrease in cell viability with **Eu-L.SiO$_2$NP_1** (93 % at 1.29 mg mL^{-1}). This decreases slightly to 84 % at 4 mg mL^{-1} (still higher than the % cell viability of **CPT0⊂Eu-L.SiO$_2$NP_1** at 1.29 mg mL^{-1}), as **CPT0⊂Eu-L.SiO$_2$NP_1** drops to 74 % at the highest concentration of 4 mg mL^{-1}. From this experiment, we would have to look administering in the ranges between 1.29 mg mL^{-1} and 4 mg mL^{-1} based on these results.

Now, looking at the shaking experiment (figure 2.10.33, C and D), there is a much smaller difference between **CPT0⊂Eu-L.SiO$_2$NP_1** and **Eu-L.SiO$_2$NP_1** up to approximately 2.5 mg mL^{-1}. The difference in % cell viability after this concentration seems to spread apart as we would expect from the drug containing NPs **CPT0⊂Eu-L.SiO$_2$NP_1** compared to the **Eu-L.SiO$_2$NP_1**, and reaches a lower percentage cell viability of 78 % (**CPT0⊂Eu-L.SiO$_2$NP_1**) at 4 mg mL^{-1}.

Table 2.10.31

Summary of estimated **CPT** concentration released from **CPT0⊂Eu-L.SiO$_2$NP_1** at 4 mg mL^{-1} at 6 hrs.

	1 mg mL^{-1}	**4 mg mL^{-1}**
Mass of **CPT** released/ mg	0.011	0.044
Estimated theoretical concentration of **CPT** released/ nM	3.2 x 10^4	1.3 x 10^5

Values were taken from release study of **CPT0⊂Eu-L.SiO$_2$NP_1** in water (figure 2.9.11). The theoretical concentration of **CPT** released from **CPT0⊂SiO$_2$NP_1** at 4 mg mL^{-1} at 6 hrs was calculated. Although this is estimated on release studies in water, it is likely the concentration released from **CPT0⊂Eu-DTPA.SiO$_2$NP_1** will be higher than the IC_{50} of **CPT** at 6 hrs (129 nM). This would ensure a significant decrease in cell viability would occur with a 4 mg mL^{-1} dosage.

The effect of using a physical trigger has become more apparent. We observed from release studies that the effect of the physical motion (figure 2.9.11 and 2.9.13) results in higher release (up to 24 hrs by UV-Vis absorbance). This was reflected in the MTT assays of **CPT0⊂Eu-L.SiO$_2$NP_1** and **CPT0⊂SiO$_2$NP_1**. Table 2.10.32 summarises all the important conclusions gathered from the MTT assays of all controls.

Table 2.10.32

Summary of important conclusions gathered from observed MTT assays.

Incubation Time	**CPT0⊂Eu-L.SiO_2NP_1** vs **Eu-L.SiO_2NP_1**	**CPT0⊂SiO_2NP_1** vs ⊂**SiO_2NP**
72 hrs	• Clear difference up to 0.125 mg mL^{-1} showing toxicity arising only from **CPT** in this concentration range • 48 % cell viability with **CPT0⊂Eu-L.SiO_2NP_1** at 0.125 mg mL^{-1}	• Difference in cell viability is much more prominent between drug containing NPs and silica NPs • 14 % cell viability with **CPT0⊂SiO_2NP_1** at 0.125 mg mL^{-1} • Shows faster apoptosis with unfunctionalised **CPT0⊂SiO_2NP_1** as release is not controlled
6 hrs	• Difference between controls in shaking experiment are not as obvious as in the static experiment • However a higher drop in cell viability is achieved in shaking experiment • Concentration dependent	• Difference between controls in shaking experiment are clearer as in the static experiment • Higher drop in cell viability is achieved in shaking experiment • Concentration dependent

The cell viability assays also confirm that the toxicity to A549 cells can be attributed solely to **CPT** from the NPs at concentrations that show no significant cell death from the control NPs compared to drug included NPs. The effect of **CPT** on A549 cells was important to study, to show successful toxicity and the release of **CPT** into the cells is in its active form. This was not deduced from release studies using UV-Vis absorbance and emission due to the similarity of **CPT** absorbance bands at pH < 5[108, 160]. However, the key information taken from the cytotoxic assays demonstrates the effect of pH environments enabling reversible reactions from basic carboxylate **CPT** molecules to active lactones.

2.11. Concluding Remarks

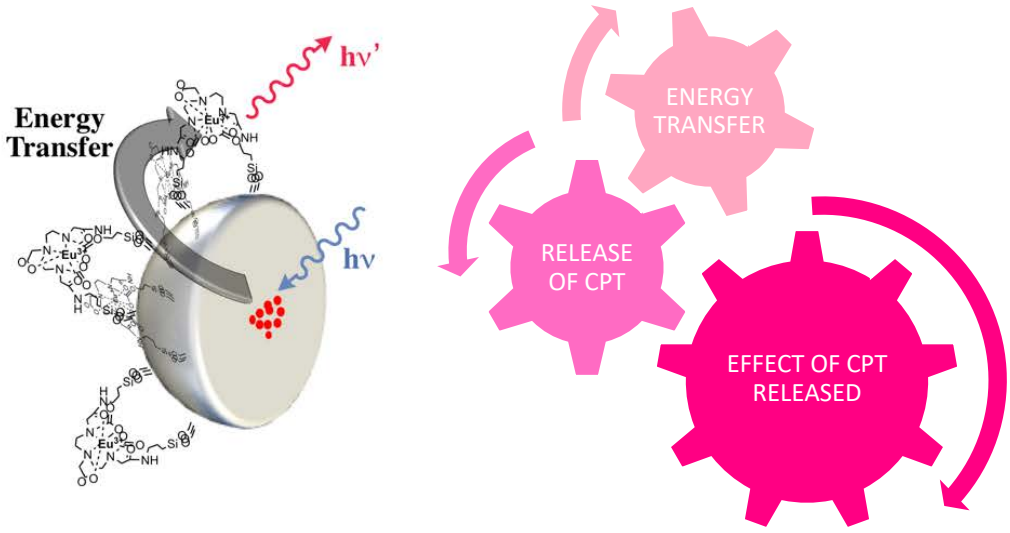


Figure 2.111

Schematic illustration of our novel design of **CPT⊂Ln-L.SiO$_2$NP** as a theranostic tool for drug delivery and drug release detection, demonstrating successful sensitised energy transfer for Ln luminescence detection, monitoring **CPT** release, and investigating the toxicity of **CPT** on A549 lung cancer cells.

After synthesis and characterisation of ligand **L** and **SiO$_2$NPs**, in addition to luminescence studies of ligand complexation, the sensitisation of Ln(III) luminescence by **CPT** absorption was studied. The sensitisation of Eu(III) luminescence from **CPT** in solution was successfully studied as proof of concept, demonstrating the drug's ability to act as a simultaneous light harvesting unit, in addition to therapeutic applications (section 2.5.3.).

After successful sensitisation observed, the design of the silica system was developed and studied by luminescence spectroscopy. Non-porous **SiO$_2$NPs** were used as the nanocarrier, despite the advantages of MSNs, due to the ability to encapsulate **CPT** without chemical modification, in hope to perform drug release in the active lactone form. Eu(III), Nd(III) and Yb(III) luminescence was detected from **CPT0⊂Ln-L.SiO$_2$NP_1** (section 2.7.1.) from successful

energy transfer from **CPT** within the NP design. This was confirmed by excitation spectra, solution emission spectra of **CPT0⊂Ln-L.SiO$_2$NP_1** (Ln(III) = Eu and Nd), and control experiments. Despite weaker energy transfer, observed by the presence of strong **CPT** emission (figure 2.7.14), successful sensitisation to Ln(III) occurred, demonstrating the success of the NP design.

The release of **CPT** from **CPT0⊂SiO$_2$NP_1** and **CPT0⊂Eu-L.SiO$_2$NP_1** were studied in water. The capping of the NPs by the Eu(III) ligand demonstrated a clear reduction in **CPT** release. Although % release statistics were arguably low, it was later observed by MTT assay studies, that the release was sufficient enough to observe toxicity to A549 cells by **CPT** solely. The release studies also showed a decrease in Eu(III) luminescence signal after release, measured by the integrated area under the peak, demonstrating promising potential as a diagnostic tool for drug release detection.

The effect of **CPT** released was studied using MTT assay on A549 lung cancer cells, to determine the effect of the NP system, in addition to acquiring more information on what form of the drug is released. UV-Vis release studies indicated a mixture of lactone and carboxylate forms of **CPT** were released over time. MTT assays demonstrated efficient **CPT** toxicity to A549 cells, dependent on concentration, which was attributed to **CPT** solely. The effect of a physical trigger was applied, mimicking release study experiments, and demonstrated an increase in cytotoxicity when applied.

The preparation of novel luminescent Ln coated **SiO$_2$NPs** demonstrated the ability to perform theranostic applications in nanomedicine. This design offers a promising platform for therapeutic drug delivery, in addition to detection of drug release through monitoring Ln luminescence changes.

2.12. Referenced Material

1. H. Ulukan and P. Swaan, *Drugs.,* 2002, **62**, 2039-2057
2. A. Behera and S. Padhi, *Environ. Chem. Lett.,* 2020, **18**, 1557-1567
3. Y. Wen, Y. Wang, X. Liu, W. Zhang, X. Xiong, Z. Han and X. Liang, *Cancer. Biol. Med.,* 2017, **14**, 363-370
4. Y. Pommier, *Nat. Rev. Cancer.,* 2006, **6**, 789-802
5. S. Saallah and I. Lenggoro, *Kona. Powder. Part. J.,* 2018, **35**, 89-111
6. L. Fonseca, M. Sousa, D. Maia, L. Luna and O. Alves, *Nanoscale Adv.,* 2020, **2**, 1290-1300
7. L. Tang and J. Cheng, *Nano Today.,* 2013, **8**, 290-312
8. A. Guiotto, M. Canevari, P. Orsolini, O. Lavanchy, C. Deuschel, N. Kaneda, A. Kurita, T. Matsuzaki, T. Yaegashi, S. Sawada and F. Veronese, *J. Med. Chem.,* 2004, **47**, 1280-1289
9. F. Li, T. Jiang, Q. Li and X. Ling, *Am. J. Cancer. Res.,* 2017, **7**, 2350-2394
10. Y. Lamb and L. Scott, *Drugs.,* 2017, **77**, 785-792
11. S. Mura, J. Nicolas and P. Couvreur, *Nat. Mater.,* 2013, **12**, 991-1003
12. J. Infante, V. Keedy, S. Jones, W. Zamboni, E. Chan, J. Bendell, W. Lee, H. Wu, S. Ikeda, H. Kodaira, M. Rothenburg and H. Burris, *Cancer. Chemother. Pharmacol.,* 2012, **70**, 699-705
13. P. Tardi, E. Choice, D. Masin, T. Redelmeier, M. Bally and T. Madden., *Cancer. Res.,* 2000, **60**, 3389-3393
14. S. Gaur, Y. Wang, L. Kretzner, L. Chen, T. Yen, X. Wu,Y. Yuan, M. Davis and Y. Yen, *Nanomedicine.,* 2014, **10**, 1477-1486
15. S. Ghamande, C. Lin, D. Cho, G. Shapiro, E. Kwak and M. Silverman, Y. Tseng, M. Kuo, W. Mach, S. Hsu, T. Coleman, J. Yang, A. Cheng, M. Ghalib, I. Chaudhary and S. Goel, *Invest. New. Drugs,* 2014, **32**, 445-451
16. T. Hamaguchi, T. Doi, T. Eguchi-Nakajima, K. Kato, Y. Yamada, Y. Shimada, N. Fuse, A. Ohtsu, S. Matsumoto, M. Takanashi and Y. Matsumura, *Clin. Cancer. Res.,* 2010, **16**, 5058-5066
17. J. Chen, Y. Tsai, M. Tsai, S. Lee, M. Wei, S. Kuo and M. Shieh, *Part. Part. Syst. Charact.,* 2017, **34**, 1600424

18. K. Min, K. Park, Y. Kim, S. bae, S. Lee, H. Jo, R. Park, I. Kim, S. Jeong K. Kim and I. Kwon, *J. Control. Release.,* 2008, **127**, 208-218
19. H. Huang, S. Barua, G. Sharma, S. Dey and K. Rege, *J. Control. Release.,* 2011, **155**, 344-357
20. H. Na, I. Song and T. Hyeon, *Adv. Mater.,* 2009, **21**, 2133-2148
21. M. Liong, J. Lu, M. Kovochich, T. Xia, S. Ruehm, A. Nel, F. Tamanoi and J. Zink, *ACS Nano.,* 2008, **2**, 889-896
22. P. Lee, Y. Chiou, J. Wong, C. Peng and M. Shieh, *Biomaterials.,* 2013, **34**, 8756-8765
23. X. Liu, A. Situ, Y. Kang, K. Villabroza, Y. Liao, C. Chang, T. Donahue, A. Nel and H. Meng, *ACS Nano.,* 2016, **10**, 2702-2715
24. Z. Zhou, Y. Piao, L. Hao, G. Wang, Z. Zhou and Y. Shen, *Nanoscale,* 2019, **11**, 15907-15916
25. J. Homsi, G. Simon, C. Garrett, G. Springett, R. De Conti, A. Chiappori, P. Munster, M. Burton, S. Stromatt, C. Allievi, P. Angiuli, A. Eisenfeld, D. Sullican and A. Daud, *Clin. Cancer. Res.,* 2007, **13**, 5855-5861
26. D. Bissett, J. Cassidy, J. Bono, F. Muirhead, M. Main, L. Robson, D. Fraier, M. Magne, C. Pellizzoni, M Porro, R. Spinelli, W. Speed and C. Twelves, *Br. J. Cancer,* 2004, **91**, 50-55
27. A. Awada, A. Garcia, S. Chan, G. Jerusalem, R. Coleman, M. Huizing, A. Mehdi, S. O'Reilly, J. Hamm, P. Barrett-Lee, V. Cocquyt, K. Sideras, D. Young, C. Zhao, Y. Chia. U. Hoch. A. Hannh and E. Perez, *Lancet. Oncol.,* 2013, **14**, 1216-1225
28. P. Huang, D. Wang, Y. Su, W. Huang, Y. Zhou, D. Cui, Z. Zhu and D. Yan, *J. Am. Chem. Soc.,* 2014, **136**, 11748-11756
29. Y. Li, Y. Yang, F. An, Z. Liu, X. Zhang and X. Zhang, *Nanotechonology.,* 2013, **24**, 015103
30. D. He, W. Zhang, H. Deng, S. Huo, Y. Wang, N. Gong, L. Deng, Z. Liang and A. Dong, *Chem. Commun.,* 2016, **52**, 14145-14148
31. Y. Zhao, F. Chen, Y. Pan, Z. Li, X. Xue, C. Okeke, Y. Wang, C. Li, L. Peng, P. Wang, X. Ma and X. Liang, *ACS. Appl. Mater. Int.* 2015, **7**, 19295-19305
32. R. Narayan, U. Nayak, A. Raichur and S. Garg, *Pharmaceutics.,* 2018, **10**, 118-167
33. Y. Zhang, K. Ren, X. Zhang, Z. Chao, Y. Yang, D. Ye, Z. Dai, Y. Liu and H. Ju, *Biomaterials.,* 2018, **163**, 55
34. M. Xuan, J. Shao, J. Zhao, Q. Li, L. Dai and J. Li, *Angew. Chem. Int. Ed.,* 2018, **57**, 6049

35. C. Lai, B. Trewyn, D. Jeftinija, K. Jeftinija, S. Xu, S. Jeftinija and V. Lin, *J. Am. Chem. Soc.,* 2003, **125**, 4451–4459
36. Z. Zhang, D. Balogh, F. Wang, S. Sung, R. Nechushtai and I. Willner, *ACS Nano*., 2013, **7**, 8455–8468
37. F. Muhammad, W. Qi, A. Wang, J. Gu, J. Du and G. Zhu, *J. Mater. Chem. B.,* 2015, **3**, 1597-1604
38. H. Y. Lu, Y. J. Chang, N. C. Fan, L. S. Wang, N. C. Lai, C. M. Yang, L. C. Wu and J. A. Ho, *Biomaterials.,* 2015, **42**, 30-41
39. A. Renner, S. Ilyas, H. Shlosser, A. Szymura, S. Roitsch, K. Wennhold and S. Mathur, *Langmuir.,* 2020, **36**, 14819-14828
40. Y. Chen, H. Chen and J. Shi, *Adv. Mater*., 2013, **25**, 3144
41. B. Ruuhle, M. Davies, T. Lebold, C. Braüchle and T. Bein, *ACS Nano.,* 2012, **6**, 1948
42. F. Zheng, W. Xiong, S. Sun, P. Zhang and J. Zhu, *Nanophotonics.,* 2019, **8**, 391-413
43. J. Lai, B. Shah, E. Garfunkel and K. Lee, *ACS Nano.,* 2013, **7**, 2741–2750
44. R. Wang, L. Zhou, W. Wang, X. Li and F. Zhang, *Nat. Commun.,* 2017, **8**, 14702
45. S. Valetti, J. Wankar, M. Ericson, A. Feiler and I. Manet, *J. Mater. Chem. B.,* 2017, **5**, 3201–11
46. J. Lu, Z. Li, J. Zink and F. Tamanoi, *Nanomedicine: NBM.,* 2012, **8**, 212-220
47. J. Lu, M. Lion, S. Sherman, T. Xia, M. Kovochich, A. Nel, J. Zink and F. Tamanoi, *Nanobiotechonology.,* 2007, **3**, 89-95
48. J. Lu, M. Lion, Z. Li, J. Zink and F. Tamanoi, *Small*., 2010, **6**, 1794-1805
49. P. Botella and E. Rivero-Buceta, *J. Control. Release.,* 2017, **247**, 28-54
50. M. Ma, H. Chen, Y. Chen, K. Zhang, X. Wang, X. Cui and J. Shi, *J. Mater. Chem.,* 2012, **22**, 5615-5621
51. D. Zhang, L. Li, X. ji and Y. Gao, *New. J. Chem.,* 2019, **43**, 18673-18684
52. C. Muniesa, V. Vicente, M. Quesada, S. Saez-Atienzar, J. Blesa, I. Abasolo, Y. Fernandez and P. Botella, *RSC Adv*., 2013, **3**, 15121–15131
53. S. Ren, J. Yang, L. Ma, X. Li, W. Wu, C. Liu, J.He and L. Miao, *ACS Appl. Mater. Interfaces*., 2018, **10**, 31947–31958
54. M. Llinas, G. Matrinez-Edo, A. Cascante, I. Porcar, S. Borros and D. Sanchez-Garcia, *Drug Delivery.,* 2018, **25**, 1137-1146

55. G. Matrinez-Edo, C. Fornaguera, S. Borros and D. Sanchez-Garcia, *Pharmaceutics.,* 2020, **12**, 1048

56. M. Babei, K. Abnous, S. Taghdisi, S. Taghavi, A. Saljooghi, M. Ramezani and M. Alibolandi, *Eur. J. Pharm. Biopharm.,* 2020, **156**, 84-96

57. Z. Li, Y. Liu, X. Wang, L. Liu, J. Hu, G. Luo, W. Chen, L. Rong and X. Zhang, *ACS Appl. Mater. Interfaces.,* 2013*,* **5**, 7995-8001

58. Z. Xu , S. Liu, Y. Kang and M. Wang, *Nanoscale.,* 2015, **7**, 5859-5868

59. Z. Li, H. Li, L. Liu, Z. You, C. Zhang and Y. Wang, *RSC Adv.,* 2015, **5**, 77097-77105

60. T. Xia, M. Kovochich, M. Liong, H. Meng, S. Kabehie, S. George, J. Zink and A. Nel, *ACS Nano*., 2009, **3**, 3273–3286

61. D. Ferris, J. Lu, C. Gothard, R. Yanes, C. Thomas, J. Olsen, J. Stoddart, F. Tamanoi and J. Zink, *Small*., 2011, **7**, 1816–1826

62. S. Parveen, R. Misra and S. Sahoo, *Nanomedicine: NBM.,* 2012, **8**, 147-166

63. Z. Tao, *RSC Adv.,* 2014, **4**, 18961-18980

64. A. Garcia-Fernandez, E. Aznar, R. Martinez-Manez and F. Sancenon, *Small.,* 2020, **16**, 1902242-1902304

65. Y. Wang, Q. Zhao, N. Han, L. Bai, J. Li, J. Liu, E. Che L. Hu, Q. Zhang, T. Jiang and S. Wang, *Nanomedicine: NBM.,* 2015, **11**, 313-327

66. P. Kalluru, R. Vankayala, C. Chiang and K. Hwang, *Adv. Funct. Mater.,* 2016, **26**, 7908-7920

67. Z. Wu, C. Lee and H. Lin, *Cancers.,* 2019, **11**, 697

68. M. Chan and H. Lin, *Biomaterials.,* 2015, **46**, 149-158

69. R. Viana, L. Costa, A. Hannon, M. Filho, E. Falcao, M. Vicente, S. Junior and J. Mathis, *ACS Appl. Nano. Mater.,* 2020, **3**, 8691-8701

70. Y. Wang, S. Song, S. Zhang and H. Zhang, *Nano Today.,* 2019, **25**, 38-67

71. Y. Du, B. Xu, T. Fu, M. Cai, F. Li and Y. Zhang, *Chemical Society.,* 2010, **132**, 1470-1471

72. J. Zhou, M. Yu, Y. Sun, X. Zhang, X. Zhu, Z. Wu, D. Wu and F. Li, *Biomaterials.*, 2011, **32**, 1148-1156

73. F. Wang and X. Liu, *Chem. Soc. Rev.,* 2009, **38**, 976-989

74. M. Haase, H. Scafer, *Angew. Chem. Int. Ed.,* 2011, **50**, 5808-5829

75. F. Auzel, *Chem Rev.,* 2004, **104**, 139-173

76. Y. Sun, X. Zhu, J. Peng and F. Li, *ACS Nano.,* 2013, **7**, 11290-11300

77. J. Liu, W. Bu, S. Zhang, F. Chen, H. Xing, L. Pan, L. Zhou, W. Peng and J. Shi, *Chemistry.,* 2012, **18**, 2335-2341

78. F. Tang, L. Li and D. Chen, *Adv. Mater.,* 2012, **18**, 12512-12521

79. M. Wang, Y. Zhang, M. Ng, A. Skripka, T. Cheng, X Li, K. Bhakoo, A. Chang, F. Rosei, and F. Vetrone, *Chem. Sci.,* 2020, **11**, 6653-6661

80. S. Liu, W. Li, S. Dong, F. Zhang, Y. Dong, B. Tian, F. He, S. Gai and P. Yang, *Nanoscale.,* 2020, **12**, 24146-24161

81. L. Zhao, X. Ge, G. Yan, X. Wang, P. Hu, L. Shi, O. Wolfbeis, H. Zhang and L. Sun, *Nanoscale.,* 2017, **9**, 16012-16023

82. R. Sabio, S. Santagneli, M. Gressier, J. Caiut, W. Pazin, I. Leite, N. Inada, R. da Silva, S. Riberiro and M. Menu, *Nanotechnology.,* 2020, **31**, 085709

83. A. Kaczmarek, D. Esquivel, J, Ouwehand, P. Voort, F. Romero-Salguero and R. Deun, *Dalton Trans.,* 2017, **46**, 7878-7887

84. E. DeOliveira, C. Neri, O. Serra and A. Prado, *Chem. Mater.,* 2007, **19**, 5437-5442

85. R. Pallares, P. Agbo, X. Liu, D. An, S. Gauny, S. Zeltmann, A. Minor and J. Abergel, *ACS Appl. Mater. Interfaces.,* 2020, **12**, 40078-40084

86. Y. Liu, L. Sun, J. Liu, X. Peng, X. Ge, L. Shi and W. Huang, *Dalton Trans.,* 2015, **44**, 237-246

87. J. Shi, T. Wang, Y. You, M. Akhtar, Z. Liu, F. Han, Y Li and Y. Wang, *Nanoscale.,* 2019, **11**, 13078-13088

88. K. Zhu, G. Liu, J. Hu and S. Liu, *Biomacromolecules.,* 2017, **18**, 2571-2582

89. C. Yue, C. Zhang, G. Alfranca, Y. Yang, X. Jiang, Y. Yang, F. Pan, J. de la Fuente and D. Cui, *Theranostics*., 2016, **6**, 456–469

90. Y. Zhang, X. Ma, H. Chau, W. Thor, L. Jiang, S. Zha, W. Fok, H. Mak, J. Zhang, J. Cai, C. Ng, H. Li, D. Parker,L. Li, G. Law and K. Wong, *ACS Appl. Nano. Mater.,* 2021, **4**, 271-278

91. L. Yao, Y. Hu, Z. Liu, X. Ding, J. Tian and J. Xiao, *Mol. Pharmaceutics.,* 2019, **16**, 846-855

92. Y. Piao, A. Burns, J. Kim, U. Wiesner and T. Hyeon, *Adv. Funct. Mater*., 2008, **18**, 3745—3758

93. W. Stober, A. Fink and E. Bohn, *J. Colloid. Interface. Sci*., 1968, **26**, 62-69

94. R. Friedman, J. *Natl. Cancer Inst*., 2011, **103,** 1428–1429

95. P. Botella, I. Abasolo, Y. Fernandez, C. Muniesa, S. Miranda, M. Quesada, J. Ruiz, S. Junior and A. Corma, *J. Control. Release.,* 2011, **156**, 246-257
96. B. Riva, M. Bellini, E. Corvi, P. Verderio, E. Rozek, B. Colzani, S. Avvakumova, A. Ragherieri, M. Rizzuto, C. Morasso, M. Colombo and D. Prosperi, *J. Control. Release.,* 2018, **519**, 18-26
97. F. Artizzu, D. Loche, D. Mara, L. Malfatti, A. Serpe, R. Deun and M. Casula, *J. Mater. Chem. C.,* 2018, **6**, 7479-7486
98. G. Liu, Y. Chen, M. Jia, Z. Sun, B. Ding, S. Shao, F. Jiang, Z. Fu, P. Ma and J. Lin, *Dalton Trans.,* 2019, **48**, 10537-10546
99. S. Fedorenko, D. Gilmanova, A. Mukhametshina, I. Nizameev, K. Kholin, B. Akhmadeev, A. Voloshina, A. Sapunova, S. Kuznetsova, A. Daminova, S. Katsyuba, R. Zairov and A. Mustafina, *J. Mater. Sci.,* 2019, **54**, 9140-9154
100. A. Mustafina, S. Fedorenko, O. Konovalova, A. Menshikova, N. Shevchenko, S. Soloveva, A. Konovalov and I. Antipin, *Langmuir.,* 2009, **25**, 3146-3151
101. J. van Hest, G. Blab, H. Gerritsen, C. Donega and A. Meijerink, *Nanoscale Res. Lett.,* 2016, **11**, 261
102. K. Taylor-Pashow, J. D. Rocca and W. Lin, *Nanomaterials.,* 2012, **2**, 1-14
103. Z. Tao, *RSC Adv.,* 2014, **4**, 18961-18980
104. R. Narayan, U. Nayak, A. Raichur and S. Garg, *Pharmaceutics.,* 2018, **10**, 118-167
105. M. Varache, I. Bezverkhyy, L. Saviot, F. Bouyer, F. Baras and F. Bouyer, *J. Non-Cryst. Solids.,* 2015, **408**, 87-97
106. A. Mehmood, H. Ghafar, S. Yaqoob, U. Gohar and B. Ahmad, *J. Develop. Drugs.,* 2017, **6**, 1000174
107. M. Martinez-Carmona, D. Lozano, M. Colilla and M. Vallet-Regi, *RSC Adv.,* 2016, **6**, 50923-50932
108. L. Fonseca, M. Sousa, D. Maia, L. Luna and O. Alves, *Nanoscale Adv.,* 2020, **2**, 1290-1300
109. S. Ren, J. Yang, L. Ma, X. Li, W. Wu, C. Liu, J.He and L. Miao, *ACS Appl. Mater. Interfaces*., 2018, **10**, 31947–31958
110. M. Llinas, G. Matrinez-Edo, A. Cascante, I. Porcar, S. Borros and D. Sanchez-Garcia, *Drug Delivery.,* 2018, **25**, 1137-1146
111. K. Binnemans, *Coord. Chem. Rev.,* 2015, **295**, 1-45

112. M. Hatanaka and S. Yabushita, *Theor Chem Acc.,* 2014, **133**

113. J. Bunzli and C. Piguet, *Chem. Soc. Rev*., 2005, **34**, 1048-1077

114. J. Bunzli, *Acc. Chem. Res*., 2006, **39**, 53-61

115. A. K. Hagan and T. Zuchner, *Anal. Bioanal. Chem*., 2011, **400**, 2847-2864

116. D. J. Lewis, F. Moretta, A. T. Holloway and Z. Pikramenou, *Dalton Trans.,* 2012, 41, 13138-13146

117. J. Rees, G. Deblonde, D. An, C. Ansoborlo, S. Gauny, R. Abergel, *Sci. Rep.,* 2018, **8**, 4419-4428

118. Y. Ning and M Zhang, *Coord. Chem. Rev.,* 2019, **399**, 1-19

119. S. Eliseeva and J. Bunzli, *Chem. Soc. Rev.,* 2010, **39**, 189-227

120. D. Lewis and Z. Pikramenou, *Coord. Chem. Rev.,* 2014, **273-274**, 213-225

121. J. Bunzli, *Coord. Chem. Rev.,* 2015, **293-294**, 19-47

122. K. Steenkeste, E. Guiot, F. Tfibel, P. Pernot, F. Merola, P. Georges and M. Fontaine-Aupart, *Chemical Physics.,* 2002, **275**, 93-108

123. Y. Zhang, Y. Cao, Y. Yang, J. Chen and Y. Liu, *Chem. Commun.,* 2014, **50**, 13066-13069

124. D. Dvoranova, M. Bobenicova, S. Soralova and M. Breza, *Chem. Phys. Lett.,* 2013, **580**, 141-144

125. N. Sanna, G. Chillemi, L. Gontrani, A. Grandi, G. Mancini, S. Castelli, G. Zagotto, C. Zazza, V. Barone, and A. Desideri. *J. Phys. Chem. B,.* 2009, **113**, 5369-5375

126. I. Chourpa, J. Millot, G. Sockalingum, J. Riou and M. Manfait, *BBA.,* 1998, **1379**, 353-366

127. J. Lu, Z. Li, J. Zink and F. Tamanoi, *Nanomedicine: NBM.,* 2012, **8**, 212-220

128. D. Zhang, L. Li, X. ji and Y. Gao, *New. J. Chem.,* 2019, **43**, 18673-18684

129. C. Muniesa, V. Vicente, M. Quesada, S. Saez-Atienzar, J. Blesa, I. Abasolo, Y. Fernandez and P. Botella, *RSC Adv*., 2013, **3**, 15121–15131

130. L. Tang and J. Cheng, *Nano Today.,* 2013, **8**, 290-312

131. W. Stober, A. Fink and E. Bohn, *J. Colloid. Interface. Sci*., 1968, **26**, 62-69

132. D. Lewis, V. Dore, N. Rogers, T. Mole, G. Nash, P. Angeli and Z. Pikramenou, *Langmuir.,* 2013, **29**, 14701-14708

133. D. Zhang, Z. Wu, J. Xu, J. Liang, J. Li and W. Yang, *Langmuir.,* 2010, **26**, 6657-6662

134. L. Rossi, L. Shi, F. Quina and Z. Rosenzweig, *Langmuir.,* 2005, **21**, 4277-4280

135. M. Pietraszkiewicz, O. Pietraszkiewicz, J. Karpiuk, A. Majka, G. Dutkiewicz, T. Borowiak, A. Kaczmarek and R. Deun, *J. Lumin*., 2016, **170**, 411–419
136. J. Monteiro, *Molecules.,* 2020, 25, 2089-2123
137. D. Lewis, V. Dore, M. Goodwin, A. Savage, G. Nash, P. Angeli and Z. Pikramenou, *Meas. Sci. Technol.,* 2012, **23**, 084004
138. Z. Xu , S. Liu, Y. Kang and M. Wang, *Nanoscale.,* 2015, **7**, 5859-5868
139. A. Behera and S. Padhi, *Environ. Chem. Lett.,* 2020, **18**, 1557-1567
140. Y. Wen, Y. Wang, X. Liu, W. Zhang, X. Xiong, Z. Han and X. Liang, *Cancer. Biol. Med.,* 2017, **14**, 363-370
141. Z. Zhou, Y. Piao, L. Hao, G. Wang, Z. Zhou and Y. Shen, *Nanoscale,* 2019, **11**, 15907-15916
142. F. Zheng, W. Xiong, S. Sun, P. Zhang and J. Zhu, *Nanophotonics.,* 2019, **8**, 391-413
143. Y. Yan, J. Fu, T. Wang and X. Lu, *Acta Biomaterialia.,* 2017, **51**, 471-478
144. P. Zhang, T. Wu and J. Kong, *ACS Appl. Mater. Int.,* 2014, **6**, 17446-17453
145. M. Martinez-Carmona, D. Lozano, M. Colilla and M. Vallet-Regi, *RSC Adv.,* 2016, **6**, 50923-50932
146. L. Chen, B, Chen, X. Liu, Y. Xu, L. Zhang, Z. Cheng and X. Zhu, *J. Mater. Chem. B.,* 2016, **4**, 3377-3386
147. D. Swinehart, *J. Chem. Educ.,* 1962, **39**, 333-335
148. S. Baek, R. Singh, D. Khanal, K. Patel, E. Lee, K. Leong, W. Chrzanowski and H. Kim., *Nanoscale.,* 2015, **7**, 14191-14216
149. A. Garcia-Fernandez, E. Aznar, R. Martinez-Manez and F. Sancenon, *Small.,* 2020, **16**, 1902242-1902304
150. C. Muniesa, V. Vicente, M. Quesada, S. Saez-Atienzar, J. Blesa, I. Abasolo, Y. Fernandez and P. Botella, *RSC Adv*., 2013, **3**, 15121–15131
151. S. Ren, J. Yang, L. Ma, X. Li, W. Wu, C. Liu, J.He and L. Miao, *ACS Appl. Mater. Interfaces*., 2018, **10**, 31947–31958
152. M. Llinas, G. Matrinez-Edo, A. Cascante, I. Porcar, S. Borros and D. Sanchez-Garcia, *Drug Delivery.,* 2018, **25**, 1137-1146
153. G. Matrinez-Edo, C. Fornaguera, S. Borros and D. Sanchez-Garcia, *Pharmaceutics.,* 2020, **12**, 1048

154. M. Babei, K. Abnous, S. Taghdisi, S. Taghavi, A. Saljooghi, M. Ramezani and M. Alibolandi, *Eur. J. Pharm. Biopharm.,* 2020, **156**, 84-96

155. Z. Li, Y. Liu, X. Wang, L. Liu, J. Hu, G. Luo, W. Chen, L. Rong and X. Zhang, *ACS Appl. Mater. Interfaces.,* 2013*,* **5**, 7995-8001

156. S. Parveen, R. Misra and S. Sahoo, *Nanomedicine: NBM.,* 2012, **8**, 147-166

157. A. Behera and S. Padhi, *Environ. Chem. Lett.,* 2020, **18**, 1557-1567

158. K. Householder, D. DiPerna, E. Chung, G. Wohlleb, H. Dhruv, M. Berens and R. Sirianni, *Int. J. Pharm.,* 2015, **479**, 374-380

159. D. Tang, F. Song, C. Chen, X, Wang and Y. Wang, *Nanotechonology.,* 2013, **24**, 145101

160. M. di Nunzio, B. Cohen and A. Douhal, *J. Phys. Chem. A.,* 2011, **115**, 5094-5104

161. Y. Rai, R. Pathak, N. Kumari, D. Sah, S. Pandey, N. Kalra, R. Soni, B. Dwarakanath and A. Bhatt, *Sci. Rep.,* 2018, **8**, 1531

162. J. Chang, K. Chang, D. Hwang and Z. Kong, *Environ. Sci. Technol.,* 2007, **41**, 2064-2068

3. Preparation of Gold Nanoparticles which Bind to Europium

3.1. Introduction

3.1.1. Lanthanide Coated Gold Nanoparticles

The advantage of using Ln(III) lumophores as bioprobes for applications in modern medicine has been discussed. These, coupled with the advantages of using AuNPs as carriers for these probes, offer a platform for creating a diverse range of multimodal NPs that are also able to serve several purposes such as sensing, diagnosing, and therapy.

There has generally been two approaches to incorporating Ln complexes on AuNPs. The complexes can be assembled prior to NPs synthesis and can then be attached to AuNPs. This can occur through reduction of the gold salt (i.e. *in situ*), or bound post synthesis of AuNPs by ligand exchange. The second approach involves assembling the Ln complexes on the AuNP surface by attaching monolayers of ligands and the titration of Ln(III) ions to form the complexed coatings[1].

The first report of Ln coated gold NPs was not until 2006, by the Pikramenou group. Eu(III) complexes were assembled on AuNPs displaying characteristic red luminescence[2]. The ligand design involved a DTPA core, with hard donor atoms such as N and O, providing good and stable coordination to Eu(III), in addition to two aromatic thiols providing sensitisation, and an anchor to the AuNP surface.

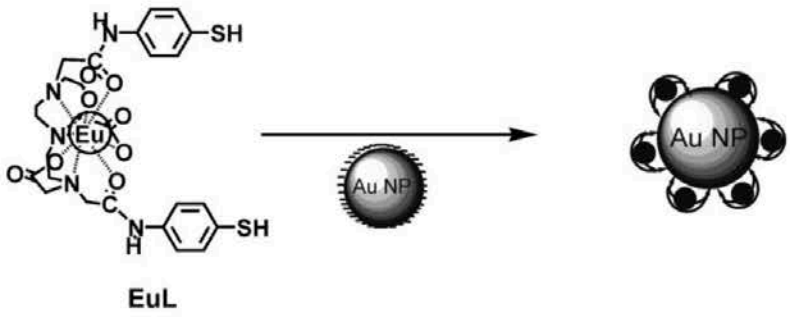


Figure 3.1.11

Schematic illustration of the AuNP scaffold designed by Pikramenou *et. al.,* using the displacement of citrate ions to form the Ln coated AuNPs. Image taken from Pikramenou *et. al*[2].

Using the advantage of AuNP SPR effects, they were able to characterise the coating of the NPs using UV-Vis absorption by observing the modifications to the gold surface. Techniques such as transmission electron microscopy (TEM) were employed, in order to examine nanoparticle sizes and morphology. Interestingly, they observed luminescence quenching of the Eu(III) coated NPs, which has been reported by deactivation through excited states of the AuNP surface. This can depend on the distance between the chromophore and the AuNP surface[2, 3].

This two-step approach to synthesise water soluble, luminescent AuNPs has become a design backbone for applications in nanomedicine field. In 2012, Pikramenou *et. al.* synthesised luminescent AuNPs and the pHLIP peptide with the aim of targeting the cytoplasm of cells with a pH controlled delivery. The design of the Eu(III) complex is similar to the previous example, a binding site for Eu(III) desiring the requirement for a high coordination number and saturation, and a sensitising unit using quinoline rings with an aliphatic spacer attached to Au surface using thiolates[4].

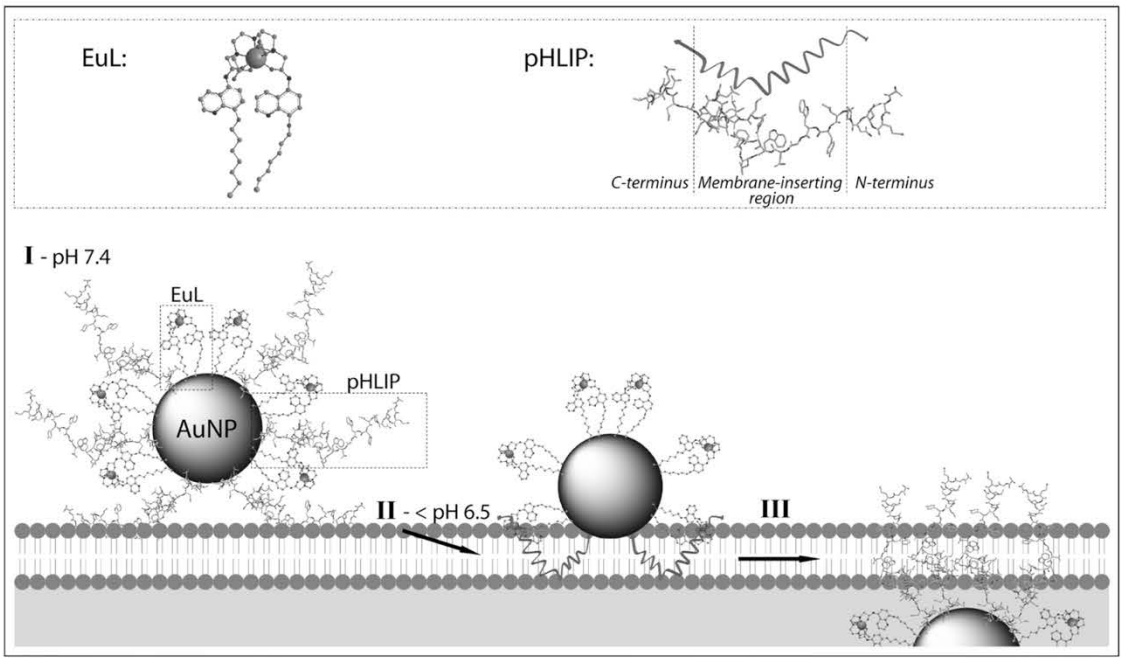


Figure 3.1.12

Schematic illustration of luminescent AuNPs coated with a Eu(III) complex and pHLIP, and the hypothesised translocation into cells controlled by pH. Image taken from Pikramenou *et. al.*[4].

In acidic environment, pH < 6.5, the pHLIP peptide inserts across the C-terminus membrane and internalises into human platelets rapidly. The peptide is able to form a transmembrane helix upon change of pH and therefore can insert across the cell membrane. With the advantage of multimodality from AuNPs, TEM and reflectance-mode confocal microscopy was used to locate the AuNP cores in the platelets and in addition, using luminescence microscopy to image Eu(III) emission from the metal centres. To confirm the presence of Eu(III) in the platelets, time resolved luminescence measurements and luminescence spectra from microscopy images showed characteristic sharp lines and long lifetimes. The Pikramenou group have shown the exciting potential of AuNP scaffolds in biological applications, by coating with more than one type of agent, creating a design approach for targeting a vast host of biological tissue. The scaffold also allows multimodal imaging as used here[4].

With the best of knowledge, the first report of near-infrared (NIR) emitting Lns combined with AuNPs was published by Truman *et. al.* in 2012[5, 6]. NIR emitting Lns are extremely attractive for bio-imaging applications due to deeper tissue penetration and reduced interference from background biofluorescence, and light scattering[5].

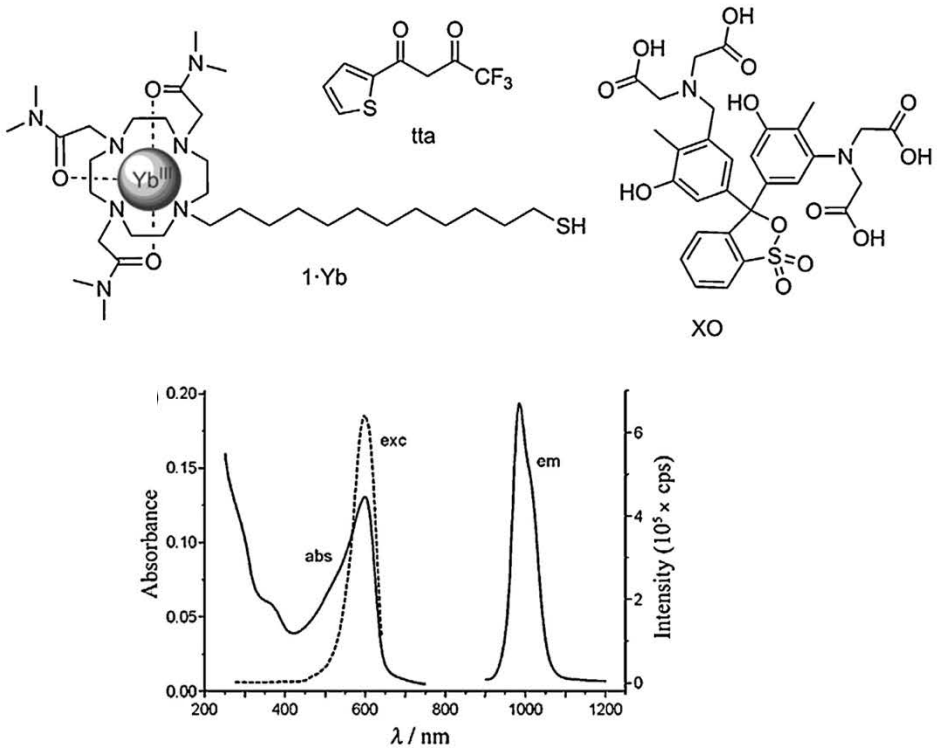


Figure 3.1.13

A schematic illustration of NIR emitting pH responsive NPs (top). Photophysical characterisation of the Yb(III) complex resulting in Yb(III) emission from sensitised energy transfer of the XO ligand. Image taken from Pikramenou *et. al.*[5].

Albeit a different route to attachment to AuNPs *via* a modified two phase Brust method[5], Yb(III) complexed to a thiolated cyclen was used to coat the NPs. Uniquely, there are three sensitising units that could be used to switch on Yb(III) emission: tta ligand (4,4,4-trifluoro-1-(thiophen-2-yl)butane-1,3-dione), nta ligand (4,4,4-trifluoro-1-(naphthalen-2-yl)butane-1,3-dione) or XO (xylenol orange) (figure 3.1.13). They found the emission of Yb(III) to be highly pH dependent, pH > 4 switched on emission to a maximum of pH 4.6, then decreasing to a

constant intensity at pH 5.6-8.0. By cycling through the pH ranges, they were able to show the switchable 'on-off' system of Yb(III) emission.

The potential of Ln bioprobes used for biomedical applications has been shown to be enhanced by conjugation to AuNPs. Such high concentrations, at which the Ln complex can be toxic, can be loaded onto AuNPs allowing to create effective nano-scaffolds with low concentrations. By introducing the presence of multimodal functionalities, different analytes can be detected in one assay, targeting of specific sites can occur, as well as simultaneous tracking of NPs[8]. To date, AuNPs are still largely studied due to their photophysical properties (SPR effect) and facile synthesis. A wide range of Ln complexes have been used to coat gold NPs for these reasons[3, 4, 7-14].

3.1.2. β-diketone Units as Sensitisers for Lanthanides

Organic complexes using transition metals are often used in bio-imaging applications. Complexes such as $[Ru(bpy)_3]^{2+}$ derivatives have higher excitation wavelengths, closer to the visible region of the electromagnetic spectrum, and are favoured for imaging type applications[4, 5, 15]. A major hindrance of sensitised Ln luminescence is the higher energy required for excitation, with wavelengths in the UV region of the electromagnetic spectrum[16]. These wavelengths cannot penetrate deep into tissue, but can also be damaging to tissue. Despite this, and the fact that organic probes can obtain high quantum yields, their broad emission signal can interfere with background emission from bio-luminescence[16].

β-diketonate ligands and derivatives are widely used to form highly emissive Ln complexes. With appropriate functionalities in addition to π-conjugation running through the molecule, flexibility is enabled in the excitation window where longer wavelengths can be used. β-diketonates provide a negatively charged binding site naturally forming neutral complexes with Ln(III) ions with a 3 : 1 ratio of β-diketonate : Ln(III). The π-conjugation running through the molecule enables strong absorption features over a range of wavelengths for the $\pi-\pi^*$ transition. This makes β -diketonate ligands good light harvesting units, and strong sensitisers for Ln(III) luminescence. Their sensitisation for strong Eu(III) luminescence is well known, owing to appropriate energy transfer arising from the energy gap between the excited triplet level of the ligand, and excited Eu(III) ion. However, with electron donation from six O atoms

(from three β-diketonates), Ln(III)- β-diketonate complexes are often coordinated to at least one water molecule, and thus isolated as hydrates. Consequently, this can lead to quenching of emission via coordination to high energy O-H oscillations. A common method to overcome this challenge, which has been increasingly adopted, is to add ancillary ligands in order to replace water molecules. These ancillary ligands can often bear additional chromophoric properties, enabling additional sensitisation, and tailoring of excitation wavelengths[16-18, 38].

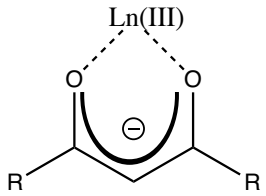


Figure 3.1.21

Base structure of β-diketonates binding to Ln(III) ion.

The Marques group synthesised Ln compounds for potential applications as anticancer agents, synthesised a series of Ln complexes using three β-diketonates and a phenanthroline derivative (Ln = Sm, Eu, Tb)[17].

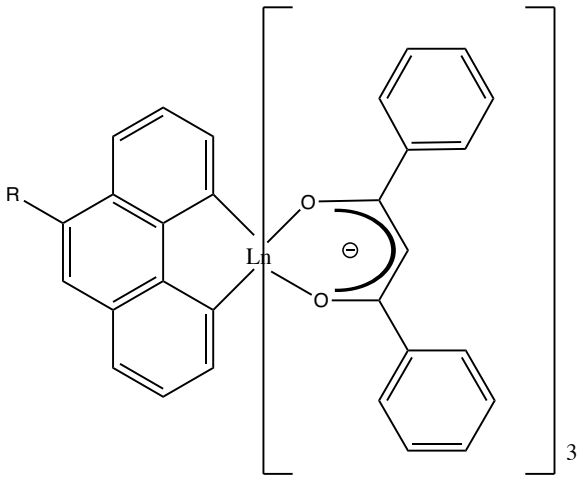


Figure 3.1.22

Structure of the complexes synthesised by Marques *et. al*, $Ln(DBM)_3(phen)$[17].

Many N-heterocyclic chromophoric ligands such as phenanthroline, pyridine and bipyridine are usually seen complexed to Ln(III) ions alongside β-diketonates. The π-conjugation provides an additional chromophore centre, but have also been used as DNA intercalators due to planarity, as well as sensitisers in PDT. Through ligand excitation (DBM), they detected Sm(III) and Eu(III) emission, in addition to ligand emission. Interestingly, in PBS, no ligand centred emission was detected, and only sharp Ln(III) peaks corresponding to Sm(III) and Eu(III) transitions. This suggested either quenching of ligand in PBS, or complete efficient energy transfer[17].

An additional method to overcome quenching pathways which reduce Ln(III) complex luminescence, particularly involved for NIR Ln(III) ions, is fluorination. Fluorination of β-diketonates is common, reducing the number of C-H oscillations and replaced with C-F. Fluorination brings about a challenge in that with electron attractive nature of flouritinated bonds, coordination to negatively charged Ln(III) ions is harder. Bunzli *et. al.* combined four benzoyltrifluoroacetone (BFTA) moieties to design a fluorinated β-diketonate podand, connected by methoxy groups to enable sufficient flexibility for coordination to Ln(III). With this large chelate effect, and octa-coordinated, they expected high binding constants[19].

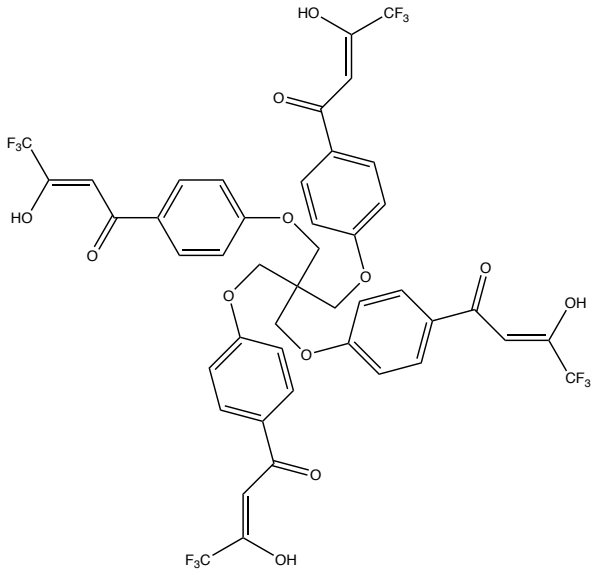


Figure 3.1.23

Structure of the fluorinated β-diketonate podand designed by Bunzli *et. al.*[19].

Due to heavy fluorination, the Ln(III) complexes (Ln = Sm, Gd, Yb and Er) were only soluble in DMF and DMSO which are highly polar solvents. Their luminescence studies showed efficient energy transfer for sensitisation of Sm(III), Yb(III) and Er(III) emission. They also used energy transfer from Yb(III) → Er(III) to further enhance Er(III) emission .

Patra *et. al.* synthesised four ternary Ln(III) complexes (Ln = Eu and Tb), all involving 1,1,1-trifluoro-3-(2-theonyl)acetone (TTA), and studied for interactions with DNA, and DNA photocleavage. Their design involved three β-diketonates (negatively charged), and one bidentate ligand (chalcone) conjugated with fluorine. The design aimed to have a saturated coordination environment, in order to minimised non-radiative transitions (quenching). With the high vibrational energy of C-F oscillations, higher than that of C-H, CF_3 groups can enhance luminescence by decreasing the non-radiative decay processes[20-22].

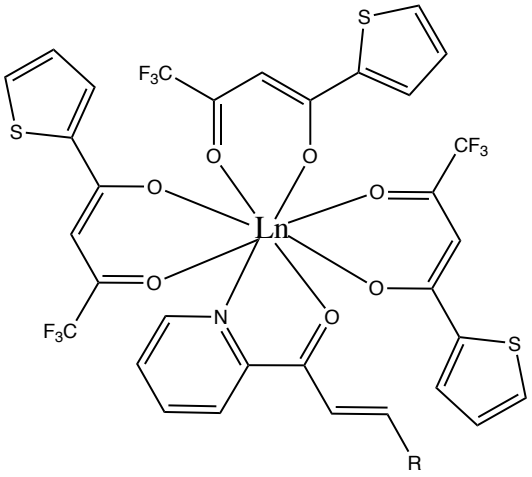


Figure 3.1.24

Structure of Ln complexes designed by Patra *et. al*., R = anthracene or pyrene[20].

Their chalcone containing and TTA complexes showed strong luminescence from all complexes (Eu and Tb), showing good energy transfer from the TTA ancillary sensitising unit. The ligands containing pyrene or anthracene acted as good photosensitisers for DNA photocleavage by generation of ROS species.

β-diketones and Eu(III) Luminescence

Luminescent Eu(III) materials are highly attractive arising from their well suited nature as visible red emitters in optoelectronics, and as luminescent labels in bioprobes. As a ligand for Ln(III) complexes, it has already been established its effectiveness in sensitisation and ability to form highly luminescent complexes, often seen with ancillary ligands to aid minimisation of quenching processes. This is especially prominent for Eu(III) ions due to the appropriate positioning of the electronic levels of $^5D_0$ state and the triplet states of β-diketonates. *Via* internal conversion, transitions from higher excited Eu(III) states can occur (such as $^5D_1$). The matching of energy levels is a key feature in the luminescence properties of Eu(III) β-diketonate complexes[16].

It seems advances in the design of highly luminescent Eu(III) β-diketonate complexes has focused largely on extending the excitation window from UV to visible range in order for use in biological applications. Additionally, as mentioned, designs have involved expanding Eu(III) coordination sphere through adducts and ancillary ligands[16, 38].

Iftikhar and Hasan recently published luminescence studies of novel ternarny $Eu(DBM)_3(impy)$ (DBM = anionic 1,3-dibenzoylmethane) (impy = 2-(1H-imidazol-2-yl)pyridine) forming a coordination sphere of eight donor atoms.

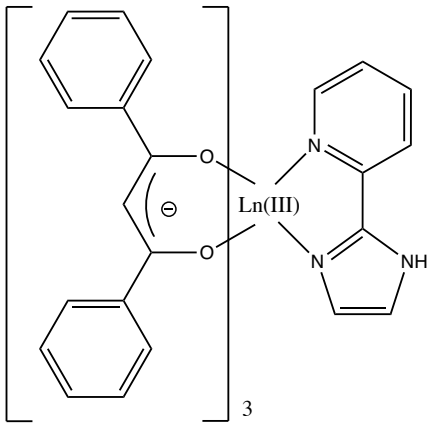


Figure 3.1.25

Structure of $Ln(DBM)_3(impy)$, Ln = Eu and Gd[38].

The impy ligand coordinates to Eu(III) via the imidazolyl and pyridyl N atoms, in addition to the six O atoms donated by the tris-β-diketonates, forming a coordination number of eight. However, the impy ligand brings about an asymmetric environment and can create distortion of the Eu(III) complex, which can result in enhanced luminescence. They found a distorted square antiprismatic geometry with the Eu(III) complex, encapsulating the Eu(III) ion inside with the high coordination sphere, and thus compelled with structural needs for efficient sensitisation[38].

Excitation spectra were recorded by monitoring the emission at $^5D_0 \rightarrow {}^7F_2$, and demonstrated efficient ligand to metal transfer indicated by the absence of *f→f* transitions in the excitation spectra (sometimes seen with Eu(III)). This confirmed efficient sensitisation from the DBM ligand. With determination of the triplet states of DBM and impy, they found that the energy gap between $E_{triplet}$ of DBM and $^5D_0$ was sufficient enough for efficient energy transfer. However, they could not rule out any losses in luminescence due to energy transfer from DBM to impy, or the higher excited level $^5D_1$ of Eu(III)[38].

One of the important features of Eu(III) luminescence spectra are the high amount of information obtained from the transitions observed, which are indications of geometries around Eu(III), which was used in this case[38].

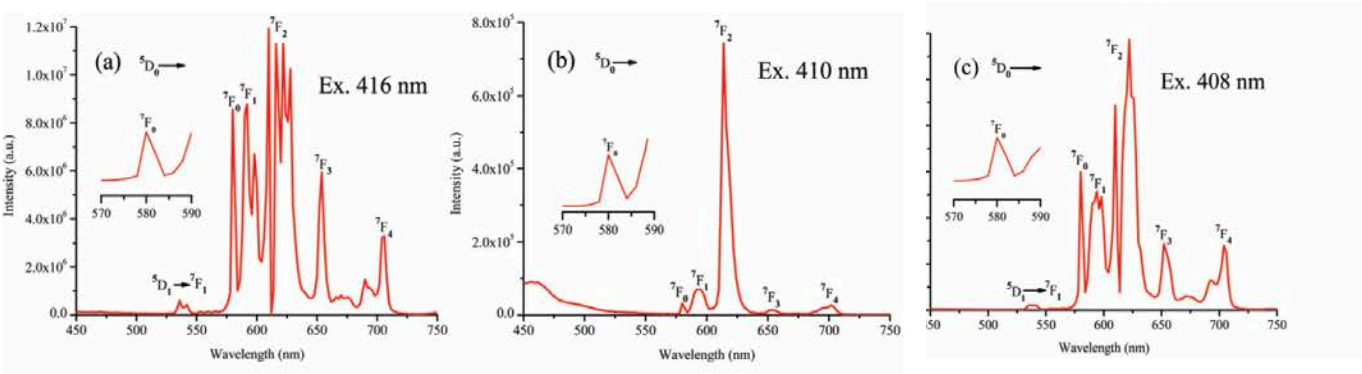


Figure 3.1.26

Emission spectra of $Eu(DBM)_3(impy)$ in solid state (a), chloroform (b) and as a hybrid film (c). Image taken from Iftikhar *et. al.*[38].

In solution, it is clear the luminescence was dominated by the hypersensitive $^5D_0 \rightarrow {}^7F_2$ transition, and hence the red colour of $Eu(DBM)_3$(impy). Luminescence from the higher excited state $^5D_1 \rightarrow {}^7F_1$ was also observed in the hybrid film. However, the significance of the information gained from Eu(III) spectra can be explained by the splitting of the $^5D_0 \rightarrow {}^7F_2$ transition observed in solid state and the hybrid film, telling us a lot about the symmetry around Eu(III). Further splitting of these transitions arises from the Stark effect, and is influenced by ligand field effects[23]. Splitting of the magnetic dipole transition $^5D_0 \rightarrow {}^7F_1$ (independent of ligand environment) clarifies the unsymmetrical environment and agrees with the distorted square antiprismatic geometry[71]. No splitting of the $^5D_0 \rightarrow {}^7F_0$ indicates only one site for Eu(III) in every phase, in agreement also with their crystal structure results[38].

Furthermore, the ratio of luminescence intensities of the transitions (mainly the electric dipole transitions, $^5D_0 \rightarrow {}^7F_{0,2,4}$) depend heavily on the environment around Eu(III). Increases in intensity of these transitions are usually observed in complexes with low symmetry, when compared to $^5D_0 \rightarrow {}^7F_{1,3}$ (magnetic dipole transitions which are independent of the environment)[39].

In addition, the detection of the strong $^5D_0 \rightarrow {}^7F_2$ transition, which was not expected due to its forbidden nature in distorted square antiprismatic geometries, indicated J mixing. Similarly is the case with the magnetic dipole transitions $^5D_0 \rightarrow {}^7F_{1,3}$ (solid and hybrid film) arising from J mixing[38, 39].

The interpretation of Eu(III) spectra can be very informative, as demonstrated by Iftikhar *et. al*., and is an important factor in why Eu(III) ions are a common choice for designing luminescent Ln(III) complexes.

More recently, Tadokoro *et. al*. synthesised Ln(III) β-diketonate complexes (Ln = Eu and Tb) for incorporation into Nafion film used for energy saving materials. They were able to achieve reversible emission between red emitting Eu(III) and green emitting Tb(III) via pH adjustment. The ligand of choice used here was N-(2-pyridinyl)benzoylacetamide (HPBA), a β-diketone containing an amide and a pyridine ring[24].

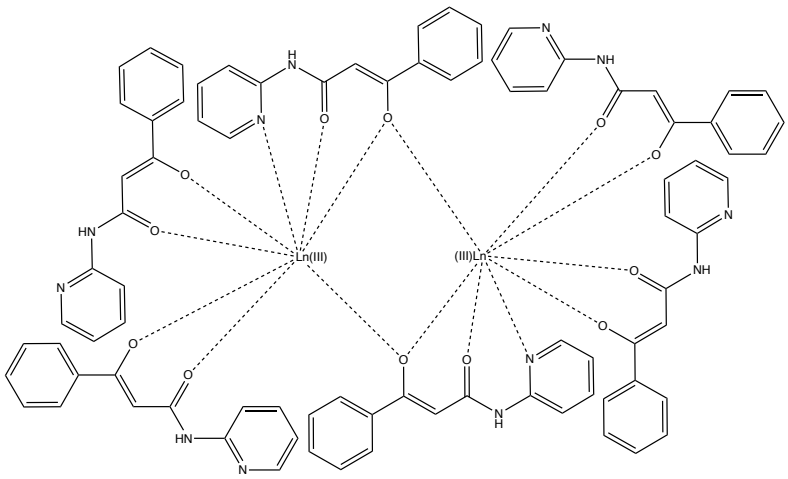


Figure 3.1.27

Structure of $Ln_2(PBA)_6$ by Tadokoro *et. al.*[24].

HPBA has been used before, due to the unique ability of the ligand to increase its triplet excitation energy. The amide and pyridine containing β-diketone is able to do this due to the presence of an amide group, facilitating energy transfer from ligand to metal. The pyridine ring also has importance, in that pH can be adjusted, enabling tuneable emission wavelengths. This arises from protonation and deprotonation of the β-diketone, causing changes in the S_1 and T_1 levels[24-26].

They were able to switch between red and green emission (Eu(III) and Tb(III) respectively) by controlling pH. Under basic conditions they detected Eu(III) emission, and under acidic conditions they detected Tb(III) emission.

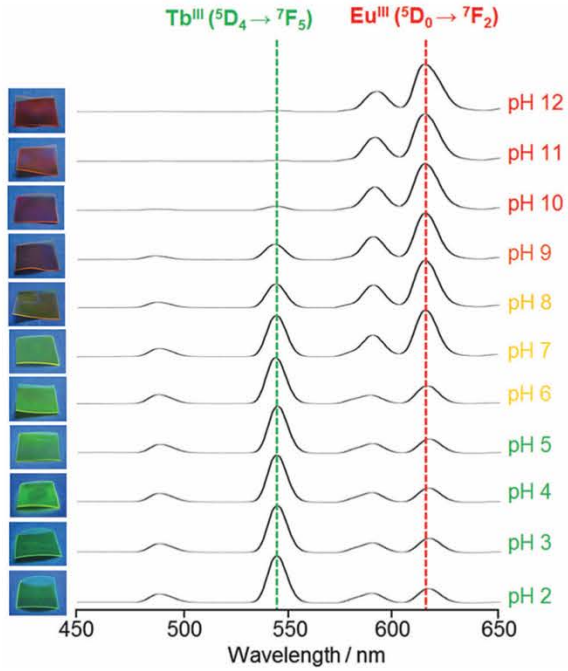


Figure 3.1.28

Emission spectra demonstrating dependence on pH conditions. Image taken from Tadokoro *et. al*.[26].

Similarly, they were able to extract geometrical information from the Eu(III) spectrum by comparing the intensities of $^5D_0 \rightarrow {}^7F_2$ and $^5D_0 \rightarrow {}^7F_1$ transition. The large ratio of $^5D_0 \rightarrow {}^7F_2$: $^5D_0 \rightarrow {}^7F_1$ indicated low symmetry around the Eu(III) ion.

Reddy *et. al*. reported the synthesis of a novel luminescent bioprobe for use in live cell imaging, with a high quantum yield of 25 % and a long luminescent lifetime of 398 ms. Their main goal in the design of the complex was to extend the excitation window, that is usually limited to the UV range, and selective localisation in regions of interest in the cell[27].

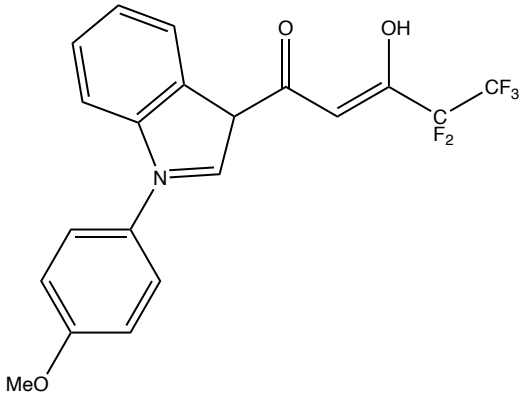


Figure 3.1.29

Structure of the β-diketone complex synthesised by Reddy *et. al*., HpfphOCH$_3$IN[27].

The Eu(III) complex consisted of three HpfphOCH$_3$IN ligands, accompanied by one ancillary ligand (a phosphine oxide ligand). Low temperature phosphorescence studies giving triplet state energy levels of the ligand showed appropriate energy transfer from ligand to Eu(III) $^5D_0$ state. This was reflected in the absence of Eu(III) absorption bands, and the absence of ligand emission from the complex, indicating efficient sensitisation. The luminescence spectrum was dominated by the $^5D_0 \rightarrow {}^7F_2$ transition, suggesting low site symmetry. Additionally, the presence of only one peak detected for $^5D_0 \rightarrow {}^7F_0$ transition, indicated only one environment around the Eu(III) ion existed. The high quantum yield and long luminescence lifetimes were achieved by excitation at 405 nm, showing it's promising use for cell imaging applications[27].

Another field of research that has relied on Ln probes is the detection of Cu^{2+} ions and sulphide ions. High levels of copper has been associated with liver damage, increased blood pressure and other neurodegenerative diseases. Hence, research has followed monitoring and sensing Cu^{2+} and sulphide ions[32, 33]. Using Lns, due to their unique properties such as long lived luminescence (and time gated measurements), has become more attractive. However, before the work published by Wu *et. al.,* most complexes obtained low luminescence quantum yields. Wu *et. al*. reported the synthesis of a new Eu(III) β–diketone complex with a high quantum yield and long luminescent lifetime[28].

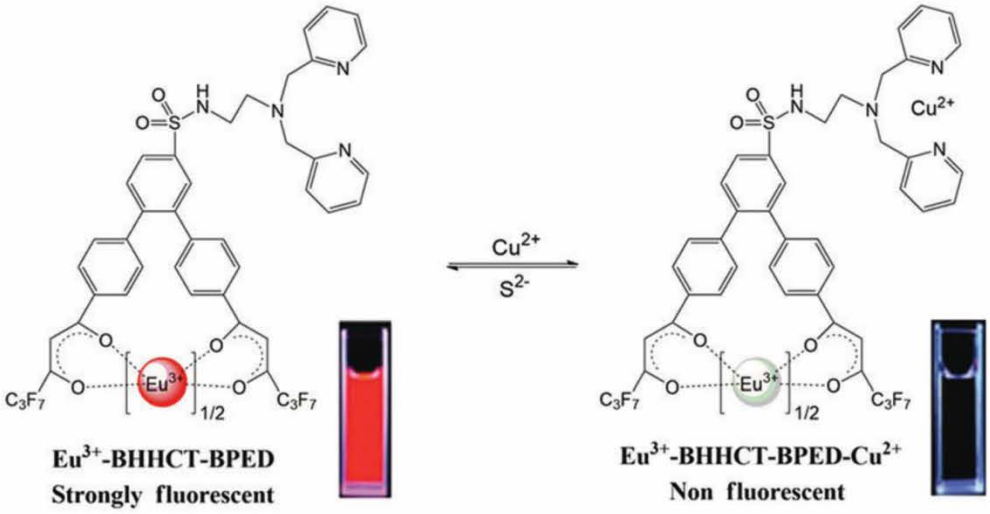


Figure 3.1.210

Mechanism of sensing Cu^{2+} and sulphide ions using the Eu(III) β-diketone complex. Image taken from Wu *et. al*[28].

When coordinated to Cu^{2+} ions, emission of Eu(III) at the hypersensitive $^5D_0 \rightarrow {}^7F_2$ transition was quenched. This was reversed by the addition of sulphide ions, removing Cu^{2+} ions as CuS, recovering the Eu(III) emission. This reversible effect enabled on – off sensing of the two species. The Eu(III) complex also showed a high luminescence quantum yield of 57 %, and a long lifetime of 810 ms[28].

In the Pikramenou group, research into derivatives of $Eu(DBM)_3$ has included syntheses of bis(β-diketone) ligands in aid to improve emission qualities of the simple $Eu(DBM)_3$ complex[34, 40].

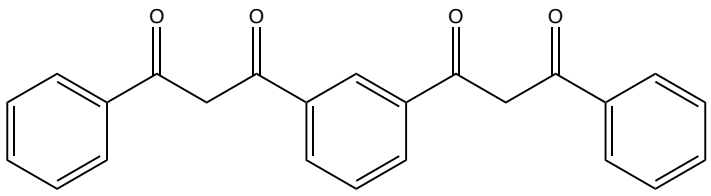


Figure 3.1.211

Structure of bis-DBM with the ability to bind to two metal ion centres in its anionic structure.

Pikramenou *et. al.* developed complexes using β-diketone ligands joined by 1,3-phenylene spacer to bind to Ln ions and observe sensitised emission. The aim to increase Ln(III) emission compared to the original $Ln(DBM)_3$ was carried out through the design of having two binding sites for metal ions.

Their measured luminescence quantum yield of the dinuclear Eu(III) bis(β-diketone) complex in DMF was 5 %, higher than that of the mononuclear Eu(III) complex $Eu(DBM)_3$, attributed to the additional lumophore. Their luminescence properties showed appropriate positioning of the triplet ligand state, in order to efficiently sensitise Eu(III), Sm(III) and Nd(III) emission. Moreover, high energy O-H oscillations were excluded from the quadruple stranded complexes and displayed stronger luminescent properties[40].

Pikramenou *et. al*. have also used bis(β-diketones) to form luminescent racks of dinuclear Eu(III) complexes, desired for systems with high light output[31].

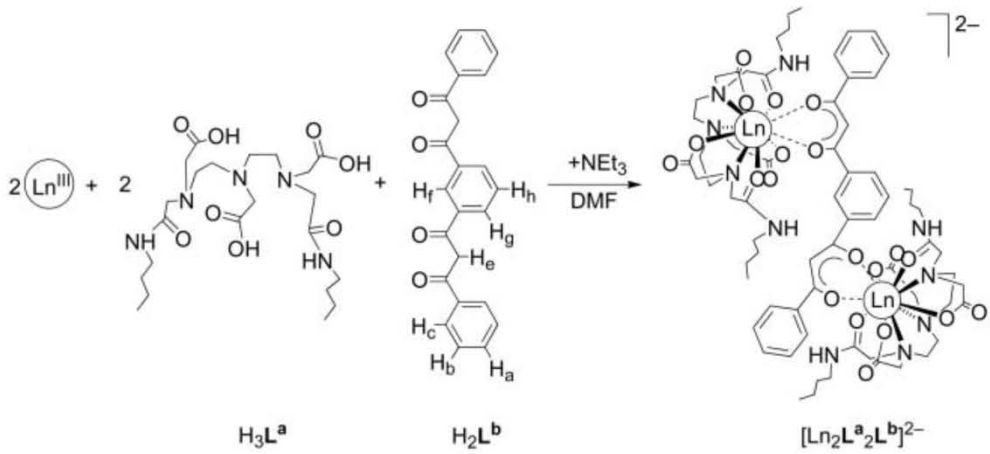


Figure 3.1.212

Scheme of heteroligand assembly, used by controlling Ln coordination with a multidentate ligand and a bis(β-diketone). Image taken from Pikramenou *et. al*.[31].

The spacer in the bis(β-diketone) involves a rigid phenylene, in order to act as a rack for enabling attachment of two Eu(III) ions, but also provides chromophoric properties[31].

The wide variety of Eu(III) β-diketone complexes that have been developed to form highly luminescent complexes for various applications is tremendous. Significantly, for use in bioimaging, it is evident that research has focused on extending the excitation window from UV to visible, and also designing ligands with appropriate energy transfer abilities. The π-conjugation of these complexes, modifications of the β-diketone through fluorination, and addition of ancillary ligands with hard donor atoms such as N, has helped facilitate this[16-31, 38, 40].

3.1.3. Coating Gold Nanoparticles with Ln(III) β-diketones and Potential Applications

There have been few reports of Ln complexes with β-diketones used to coat gold NPs[41, 42]. Both examples in this case, have been designed for potential applications in sensing and displacement assays.

Ln complexes are especially useful for sensing and detection of analytes in immunoassays, a field very much developed using Lns due to their advantages. Luminescent Ln bioprobes began to become popular from the mid 1970s using β-diketonates and polyaminocarboxylates as chelates for Ln complexes (Eu, Sm, Tb and Dy) in time resolved luminescent assays[34, 35].

In an immunoassay, concentration dependent signal of an analyte is created by using labelled antibodies (with lumophores, radioisotopes, enzymes). The challenge presented by immunoassays include high background signal from analytes thus reducing sensitivity and ranges of detection. The advantage of using Ln complexes is their long lived luminescence lifetimes, enabling time gated measurements in order to reduce background interference, and hence increasing sensitivity and detection. It's important that the assays are able to detect low concentrations of analytes, even when in the presence of other biological molecules such as proteins. It can be imagined that in a mixture of proteins, detection of a specific protein can be challenging, especially when samples can be highly complex[33].

These assays can be generally divided into two categories, heterogenous and homogenous immunoassays. Heterogenous assays are associated with binding to analytes through molecules immobilised on a solid substrate, and have been commercialised under dissociation enhanced Ln fluorometric immunoassay (DELFIA)[34, 36, 37].

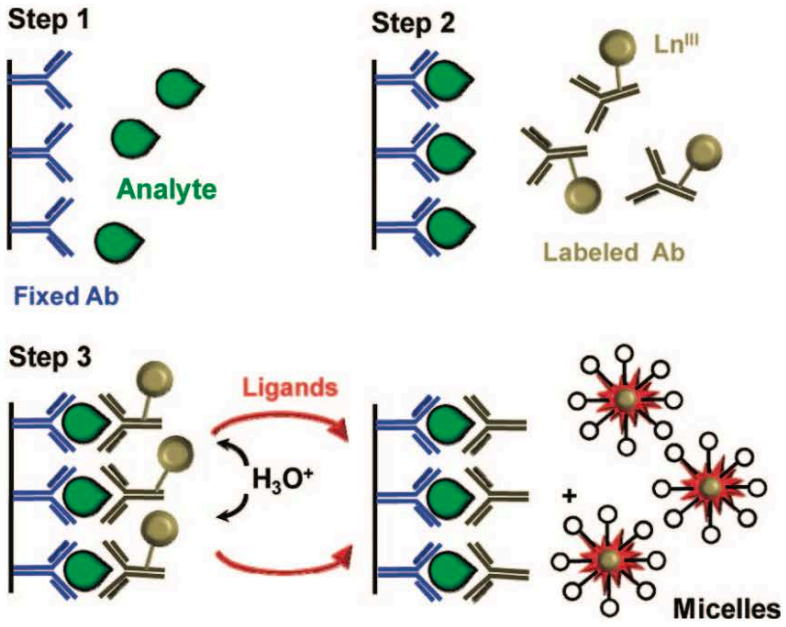


Figure 3.1.31

A schematic diagram demonstrating the principles of a heterogeneous immunoassay from Bunzli[34].

Homogenous assays rely on the principles of Forster resonance energy transfer (FRET) to detect analytes in solution. The analyte of interest is coupled to two antibodies, one with a Ln and one with an organic acceptor. Dipole-dipole interactions at long range enable energy transfer from the Ln to the acceptor[34, 36].

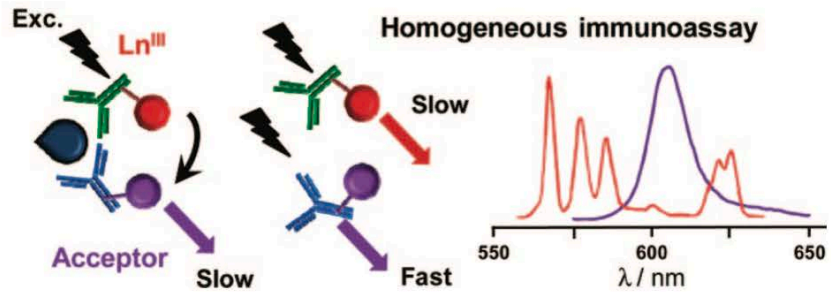


Figure 3.1.32.

Schematic diagram representing homogeneous immunoassays from Bunzli[34].

With large Stokes shift of Ln complexes, excitation windows can be tailored to move away from acceptor absorption, hence making Ln systems suitable as FRET donors in immunoassays.

β-diketone complexes have often been employed as Ln chelators for applications in luminescent immunoassays. With the advantage of stable and neutral tris-β-diketone complexes, a high coordination environment is provided, and appropriate sensitisation. There have also been examples of two β-diketones held by spacers, forming tetradentate ligands[33].

However, the advantages of this can be magnified by using functionalised gold NPs. With high loading of luminescent Ln probes at low concentrations and multimodal functionality, it provides a platform for enhancing detection and sensitivity in Ln immunoassays.

3.2. Chapter Outline

This chapter is concerned with the design of luminescent **AuNPs** coated with a surface active DBM molecule attached *via* thiol groups, developing a platform for sensing Eu(III) ions and sensitising Ln luminescence.

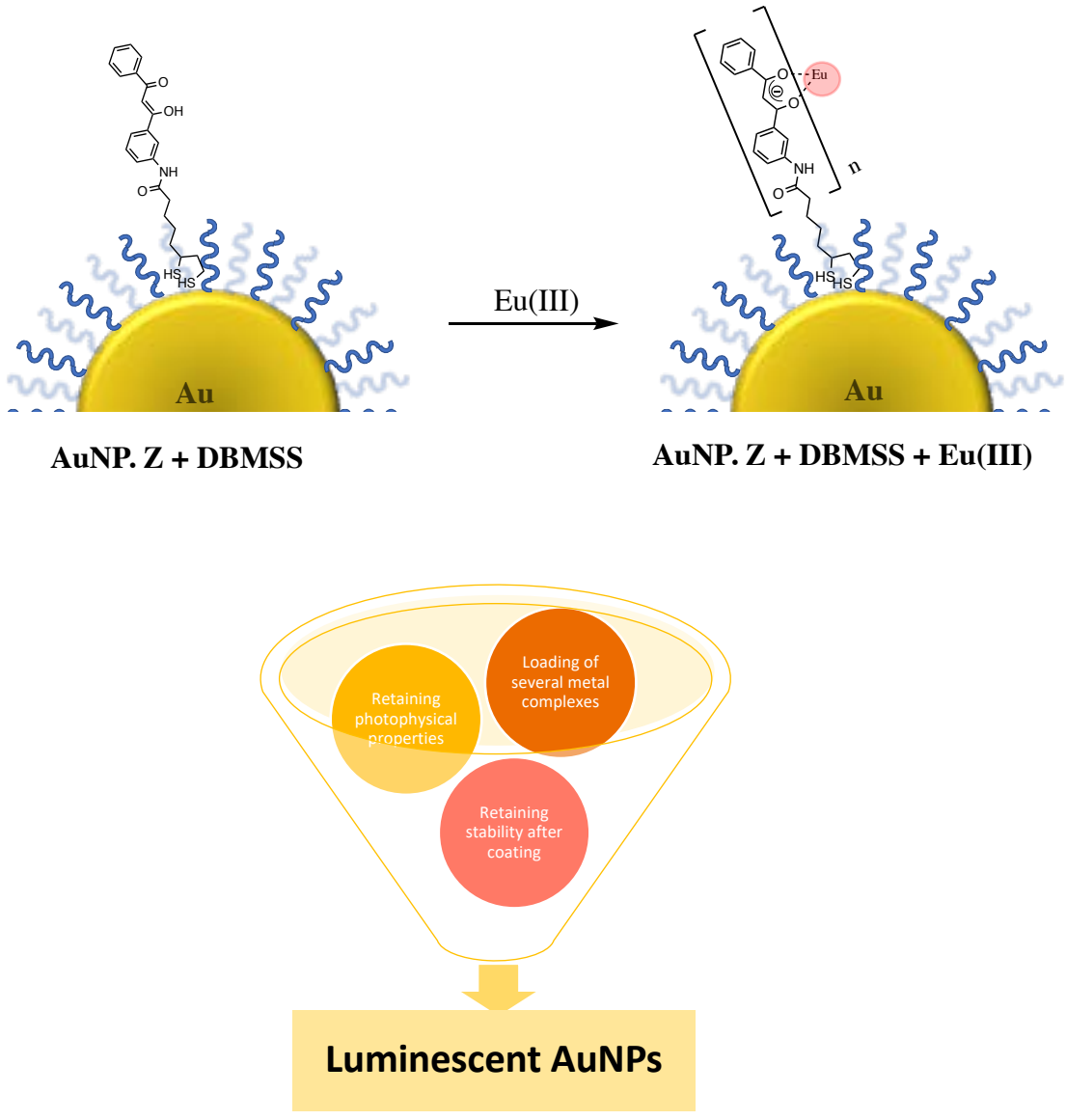


Figure 3.21

Schematic illustration of development of gold NPs functionalised with surface active DBM molecule, **DBMSS**, able to bind Eu(III) ions and sensitise luminescence. This design aims to design luminescent NPs whilst retaining good stability and photophysical properties upon coating with **DBMSS** and Eu(III).

Herein, the surface functionalisation of gold NPs with **DBMSS**, and their photophysical properties are reported. The coated NPs show binding to Eu(III) ions, monitored by luminescence and UV-Vis absorbance, successfully sensitising Eu(III) emission with long lived lifetimes.

3.3. Photophysical Properties of DBMSS and Binding to Europium

The **DBMSS** ligand synthesis was performed by J. Lilley according to reaction schemes described in his thesis[43]. The photophysical characterisation of **DBMSS**, and its binding to Eu(III) was investigated before preparation of functionalised NPs. The UV-Vis absorption of **DBMSS** and **Eu(DBMSS)$_3$** (figure 3.41) is shown here.

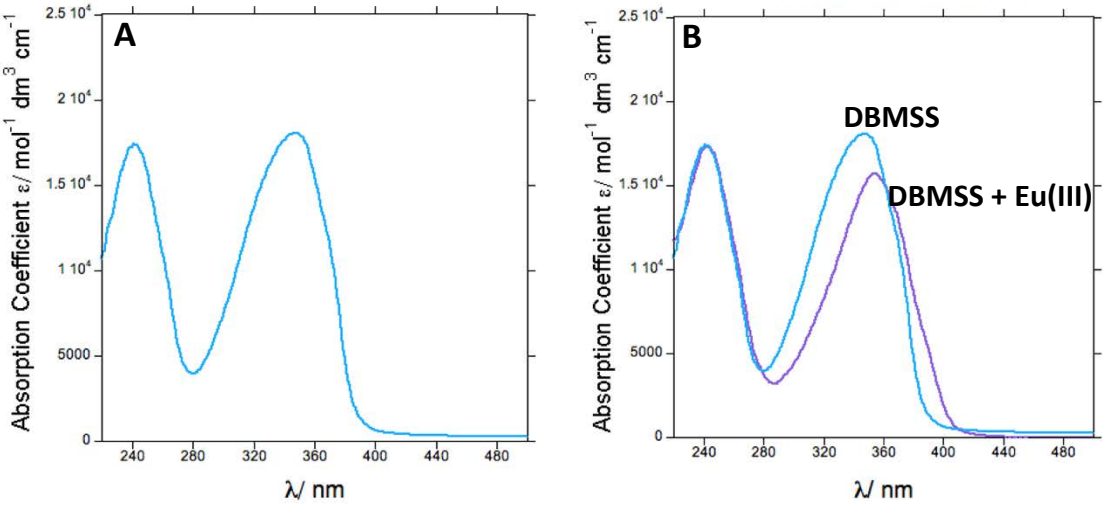


Figure 3.31

A: UV-Vis spectrum of **DBMSS** (0.016 mM, MeOH). B: Change in **DBMSS** absorption (blue) (0.05 mM, 10 % MeOH) upon addition of Eu(III) (0.017 mM, 10 % MeOH) (purple) in H_2O. Data is in good agreement with J. Lilley[43].

The UV-Vis absorption spectrum of **DBMSS** in MeOH shows two intense bands at λ_{max} = 350 nm and 240 nm (ε = 13000 mol^{-1} dm^3 cm^{-1} and ε = 12000 mol^{-1} dm^3 cm^{-1} respectively, see appendix figure 43). The two bands can be attributed to $\pi^* \rightarrow \pi$ transitions from the aryl groups. These values are in agreement with other DBM functionalised molecules previously reported in literature[38, 44-46, 47].

The UV-Vis absorption spectrum (figure 3.31, B) shows a bathochromic shift in λ_{max} from 350 nm to 355 nm after coordination to the ion, suggesting successful binding to the **DBMSS** ligand[47].

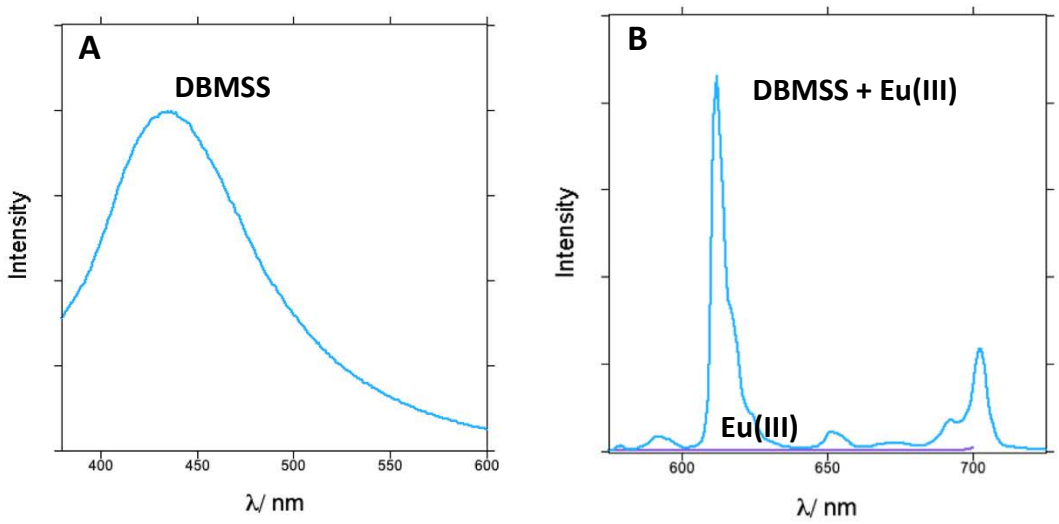


Figure 3.32

A: Emission spectrum of **DBMSS** (0.016 mM, MeOH), λ_{exc} = 350 nm. B: Emission spectrum of **DBMSS** (0.05 mM, 10 % MeOH) upon addition of $EuCl_3.6H_2O$ (0.017 mM, 10 % MeOH) (blue) in H_2O. Emission of $EuCl_3.6H_2O$ (purple) (0.017 mM, MeOH), λ_{exc} = 350 nm. Emission spectra corrected for PMT and instrument response. Data is in good agreement with J. Lilley[43].

The emission of **DBMSS** in MeOH shows one intense peak at λ_{max} = 435 nm when excited at λ_{exc} = 350 nm[48]. The Eu(III) *f-f* emission signal was monitored by using λ_{exc} = 350 nm (figure 3.32, B). The characteristic Eu(III) emission was in the visible region with detection of five transitions. The very weak, and strictly forbidden $^5D_0 \rightarrow {}^7F_0$ transition at λ_{max} = 580nm was observed. The detection can inform us about the geometry around Eu(III), indicating the metal ion occupies a site with C_{nv}, C_n or C_s symmetry. The $^5D_0 \rightarrow {}^7F_1$ transition at λ_{max} = 590 nm was observed, but the most intense transition detected was at λ_{max} = 612 nm attributed to the hypersensitive transition $^5D_0 \rightarrow {}^7F_2$, which is characteristically strong in β-diketones[39]. The high intensity, compared to $^5D_0 \rightarrow {}^7F_1$, is often associated with low symmetry of the metal ion. The $^5D_0 \rightarrow {}^7F_3$ (λ_{max} = 650 nm) and $^5D_0 \rightarrow {}^7F_4$ (λ_{max} = 702 nm) were both detected, with the latter being more intense. As more **DBMSS** can bind to the ion, the symmetry around Eu(III) changes, giving rise to change in intensities for transitions compared to $EuCl_3.6H_2O$[49]. Due to known weak absorption of *f* elements and their weak emissive nature arising from Laporte forbidden transitions, the excitation of **DBMSS + Eu(III)** at 350 nm strongly suggests the Eu(III) emission signal can be attributed to sensitisation from **DBMSS**[50]. This is further demonstrated by the zero Eu(III) emission signal of $EuCl_3.6H_2O$ when using λ_{exc} = 350 nm. The absence of the **DBMSS** ligand disables sensitisation and hence no emission signal.

3.4. Luminescent Gold Nanoparticles with DBMSS and Europium

3.4.1. Preparation of Gold Nanoparticles

To design luminescent NPs, following synthesis yielding gold NPs with diameter 13 nm (**AuNP**), a fluorinated surfactant Zonyl FSA was used to coat the surface prior to functionalisation (**AuNP. Z**). **AuNP. Z** was purified via centrifugation and then coated with **DBMSS. DBMSS** was treated with hydrazine for reduction of thiol bonds to attach to **AuNP** surface, followed by coordination to Eu(III).

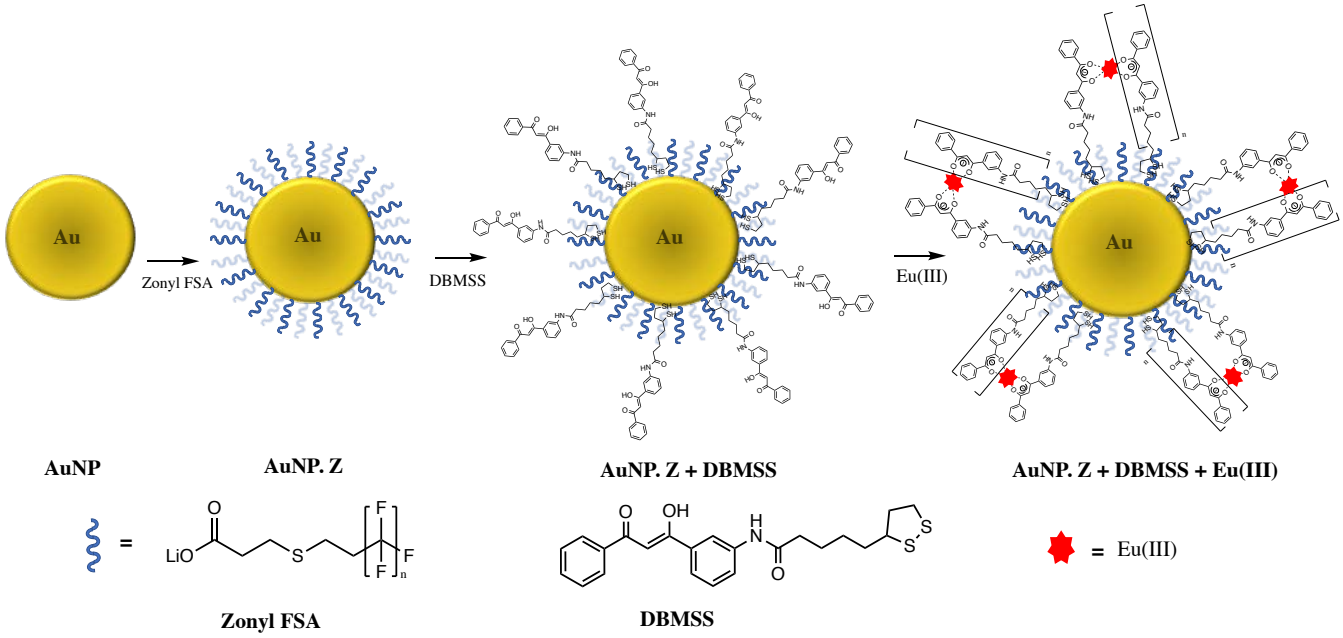


Figure 3.4.11

Schematic design of preparation of luminescent **AuNP** via functionalisation with **DBMSS** followed by Eu(III) addition.

Monodisperse and water soluble **AuNP** were synthesised using the improved Turkevich method, with some modifications[4, 51, 52] involving optimisation of reagent concentrations to achieve narrow size distributions of 13 nm **AuNP**s. Sizes of NPs were characterised by DLS (table 3.4.11) and TEM (figure 3.4.12), and surface charge measured by zeta potentials (table 3.4.12).

Table 3.4.11

DLS characterisation for functionalised NPs.

Sample	Intensity Distribution/ nm	Number Distribution/ nm	PDI
AuNP	21 ± 7	13 ± 3	0.154
AuNP. Z	31 ± 11	18 ± 4	0.218
AuNP. Z + DBMSS	138 ± 52	78 ± 28	0.171
AuNP. Z + DBMSS + Eu(III)	161 ± 66	88 ± 34	0.184

DLS sizing analysis suggests the **AuNP** are *ca.* diameter of 13 nm by number distribution as expected, with a PDI value of 0.154 demonstrating good monodispersity in the nanoparticle solution. After coating with fluorinated surfactant Zonyl FSA (figure 3.4.11), an increase in size is observed due to the addition of the polymer onto the surface stabilising the NPs. A much larger increase in diameter is observed after functionalisation with the **DBMSS** ligand, from 21 nm to 131 nm by intensity, and a further, albeit smaller increase, 27 nm after incorporation of Eu(III). The PDI values of each step are all within acceptable range, confirming a good narrow size distribution and no signs of aggregation, which was also confirmed by UV-Vis absorbance as seen. The small increase in diameter observed after incorporation of Eu(III) into **DBMSS** moieties on the **AuNP** surface is within the error of **AuNP. Z + DBMSS**.

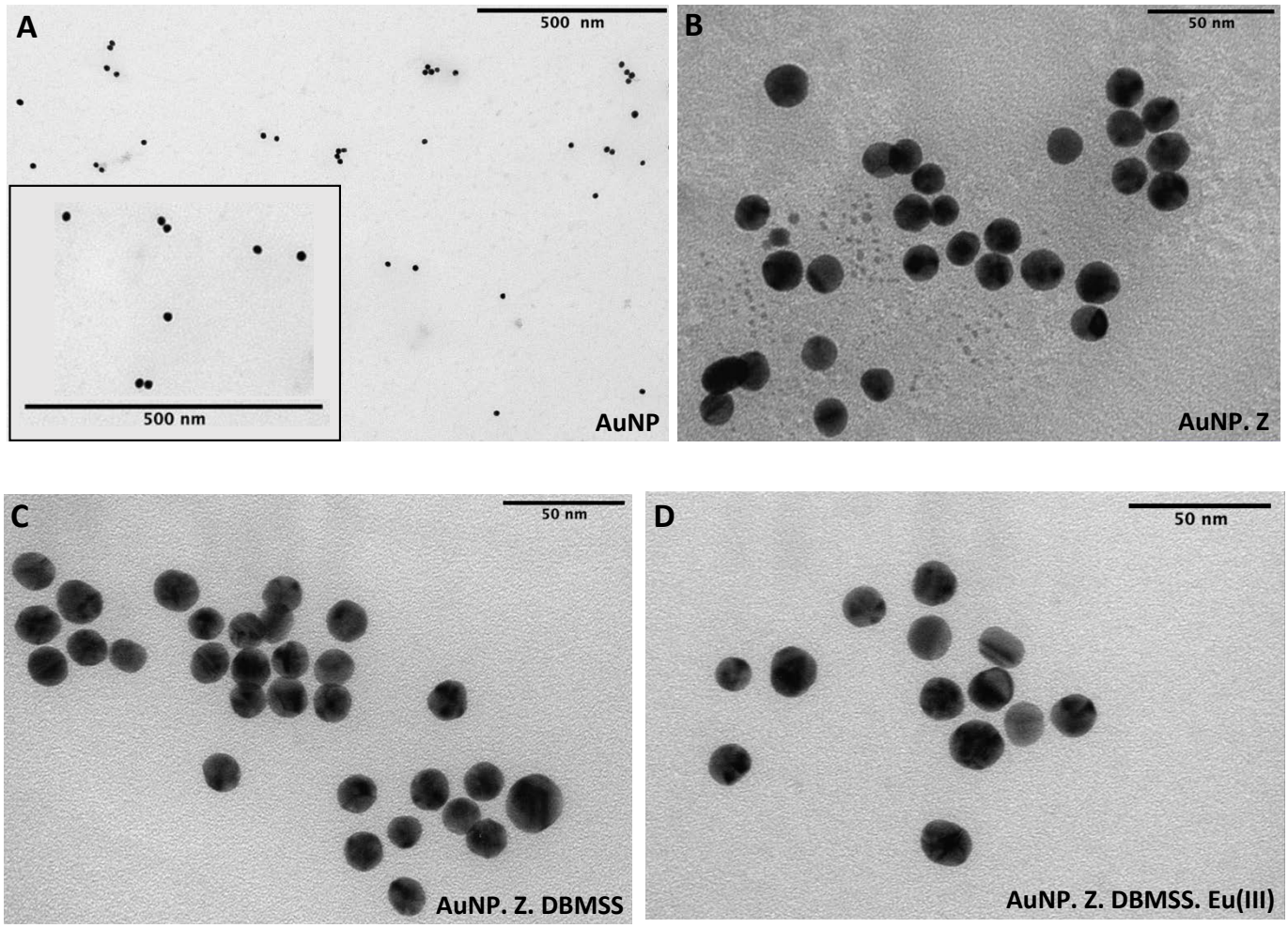


Figure 3.4.12

TEM images of **AuNP** samples. A: **AuNP** (1.15 nM, H_2O) average diameter 13 nm. B: **AuNP. Z** (0.7 nM, H_2O) average diameter 16 nm. C: **AuNP. Z + DBMSS** (0.85 nM, H_2O) average diameter 18 nm. D: **AuNP. Z + DBMSS + Eu(III)** (0.8 nM, H_2O) average diameter 17 nm. Diameter averages were calculated using 10 NPs per image.

TEM was used in order to investigate the actual size of **AuNP** from stock solution, in order to calculate **AuNP** concentrations. Moreover, this technique also enables us to further assess the monodispersity of the NPs, in addition to the shape and size. DLS analysis (table 3.4.12) gave us good indication of monodisperse NPs, obtained by the PDI values, but also the general increasing trend in size upon coating of the NPs. The **AuNP** diameter size was measured to be 13 nm by TEM with good monodispersity and a narrow size distribution observed (figure 3.4.12, A). Upon stabilisation with Zonyl FSA, an increase in size was observed, with an

average diameter of 16 nm, in good agreement with DLS analysis, and showed good monodispersity with these NPs (figure 3.4.12, B). A further increase in diameter size was observed after coating with **DBMSS** again showing good monodispersity in the nanoparticle solution (figure 3.4.12, C). No further change in size was observed by TEM upon coordination to Eu(III), although detected by DLS, with good monodispersity (figure 3.4.12, D). Although the increasing trend in size is observed by TEM, the increments are much smaller than DLS analysis. However, this can be expected by DLS as the hydrodynamic diameter in solution is measured explaining the large dramatic increases observed. TEM has shown good spherical shape of **AuNP**, which has been retained upon coating, with good monodispersity.

Table 3.4.12

Zeta potentials of **AuNP** samples.

Sample	Zeta Potential ζ/ mV
AuNP	-40 ± 5
AuNP. Z	-35 ± 8
AuNP. Z + DBMSS	-67 ± 9
AuNP. Z + DBMSS + Eu(III)	-52 ± 10

The zeta potentials of the **AuNP** samples were measured obtaining their surface charge, where changes in values upon functionalisation can indicate the success of surface modification dependent on the charge of the molecules. The zeta potential of uncoated **AuNP** was -40 mV, as expected due to the negatively charged citrate ions stabilising the gold surface after synthesis. Small change (within error) is observed after stabilisation with Zonyl FSA obtaining a zeta potential of -35 mV. A large negative increase of 32 mV was observed after coating with the **DBMSS** ligand, which was expected due to the presence of hydrazine in order to reduce the thiols for attachment to gold. After incorporation of Eu(III) onto **AuNP. Z + DBMSS**, a zeta potential of -52 mV was measured. A positive increase of 15 mV was observed due to the presence of the positively charged trivalent ion. This was not as a

dramatic change as expected, possibly attributed to the fact that not all **DBMSS** sites may be occupied after incorporation of the metal ion.

3.4.2. Photophysical Properties of Functionalised Gold Nanoparticles

The photophysical properties of **AuNP** and corresponding functionalised NPs were characterised by surface plasmon resonance (SPR) (figure 3.4.21) using UV-Vis absorbance.

Prior to coating the surface of **AuNP** with **DBMSS**, the NPs were stabilised using fluorinated polymer Zonyl FSA. The use of surfactants and polymers can be beneficial for functionalised AuNP designs as they can prevent aggregation induced by positively charged complexes interacting with negatively charged citrate ions[74]. The necessity of their use on AuNPs has been previously reported in our group. The preparation of charged complexes $Ru(bpy)^{2+}$, $Ir(ppy)_2(bpy)^{2+}$, and DTPA derivative ligands coated on AuNPs have benefited from the use of Zonyl and pHLIP stabilising the NPs[4, 50, 53-55].

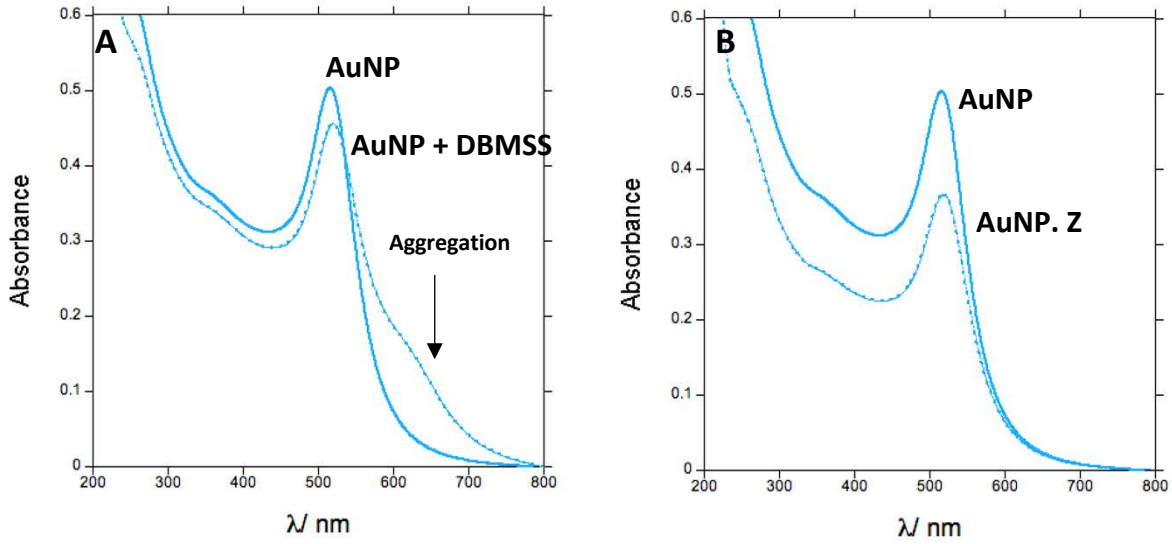


Figure 3.4.21

A: Change in SPR of **AuNP** (solid line) (1.2 nM in H_2O)as μL additions of 1 mM **DBMSS** in MeOH is titrated in to a final concentration of 1 μM to prepare **AuNP + DBMSS** (dotted line) (0.85 nM in H_2O). B: Change in SPR of **AuNP** (solid line) (1.2 nM in H_2O) after stabilisation with Zonyl to prepare **AuNP. Z** (dotted line) (0.88 nM in H_2O).

Direct loading of **DBMSS** onto **AuNP** to prepare **AuNP + DBMSS**, resulted in aggregation of the NPs (figure 3.4.21, A). Perturbation is observed in the UV-Vis spectrum of demonstrated from the growth in the **AuNP** SPR band between 600 nm – 700 nm, characteristic of aggregated and destabilised AuNPs[56, 57]. Upon addition of Zonyl FSA, a bathochromic shift in **AuNP** SPR was observed from λ_{max} = 515 nm to 518 nm, indicative of an interaction between the surfactant and the **AuNP** surface (figure 3.5.21, B).

The surfactant modified NPs, **AuNP. Z**, were isolated and purified *via* centrifugation, followed by titrating the **DBMSS** ligand onto the surface of **AuNP. Z** monitored by UV-Vis absorption (figure 3.4.22).

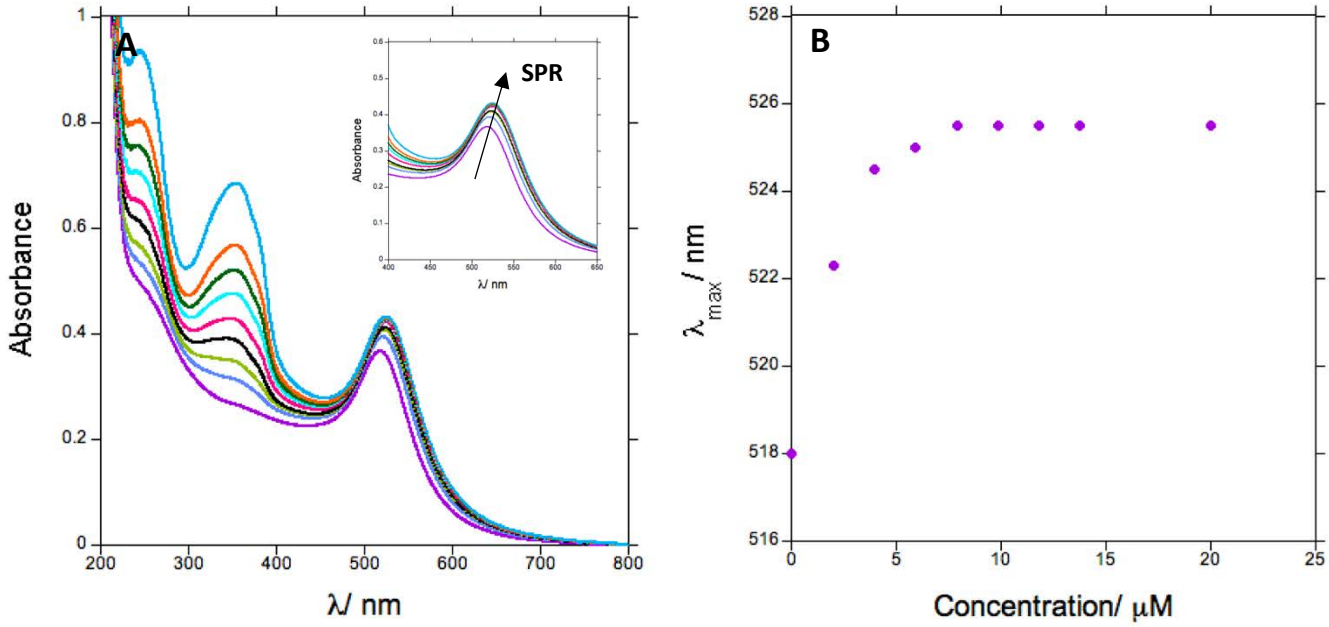


Figure 3.4.22

A: Change in SPR of **AuNP. Z + DBMSS** (0.88 nM **AuNP. Z** + 19.5 μM **DBMSS**) as μL additions of 1 mM **DBMSS** in MeOH is titrated in to a final concentration of 19.5 μM **DBMSS**. Figure 3.4.22, A insert shows the SPR shift from $\boldsymbol{\lambda}_{max}$ from 518 nm to 525.5 nm. B: A plot of $\boldsymbol{\lambda}_{max}$ against **DBMSS** concentration to show the binding on **AuNP**.

As the surface is functionalised with **DBMSS**, a bathochromic shift in the **AuNP** SPR is observed from λ_{max} = 518 nm to a saturation point of λ_{max} = 525.5 nm, an overall shift of 7.5 nm. This optimised data showed further shift in SPR λ_{max} in contrast to J. Lilley, who observed a plateau at λ_{max} = 524 nm (**AuNP. Z** (3.2 nM in H_2O), **DBMSS** (11.32 mM, MeOH)). It should be noted that there is no perturbation observed here as seen in figure 3.4.21, due to the presence of Zonyl FSA, stabilising the NPs preloading with **DBMSS**. The increase in intensity of the band at λ_{max} = 350 nm is attributed to the absorption of the aryl rings of the **DBMSS** ligand.

3.4.3. Loading Europium onto Functionalised Gold Nanoparticles

After successful coating of the **AuNPs** with the **DBMSS** ligand, taken to saturation, the next step in our design to create luminescent AuNPs was to load Eu(III) onto **AuNP. Z + DBMSS**. Eu(III) was titrated in to prepare **AuNP. Z + DBMSS + Eu(III)**, and hence Eu(III) emission signal was monitored from sensitisation of the **DBMSS** ligand.

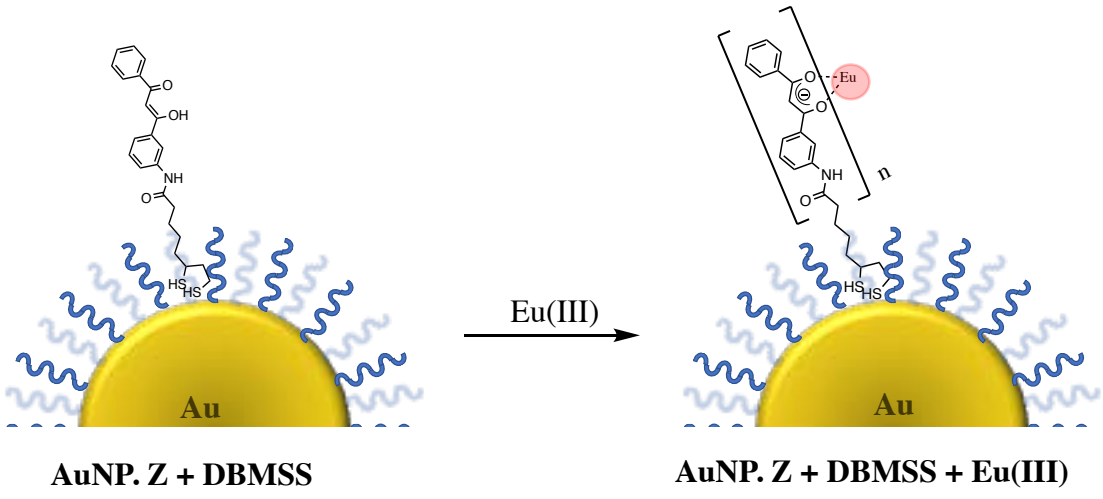


Figure 3.4.31

Schematic design of preparing **AuNP. Z + DBMSS + Eu(III)** (0.7 nM **AuNP. Z** + 19.5 μM **DBMSS** + 3.3 μM **Eu(III)**) showing more than one **DBMSS** moieties binding to Eu(III).

The loading of Eu(III) onto **AuNP. Z + DBMSS** was monitored by UV-Vis (figure 3.4.32).

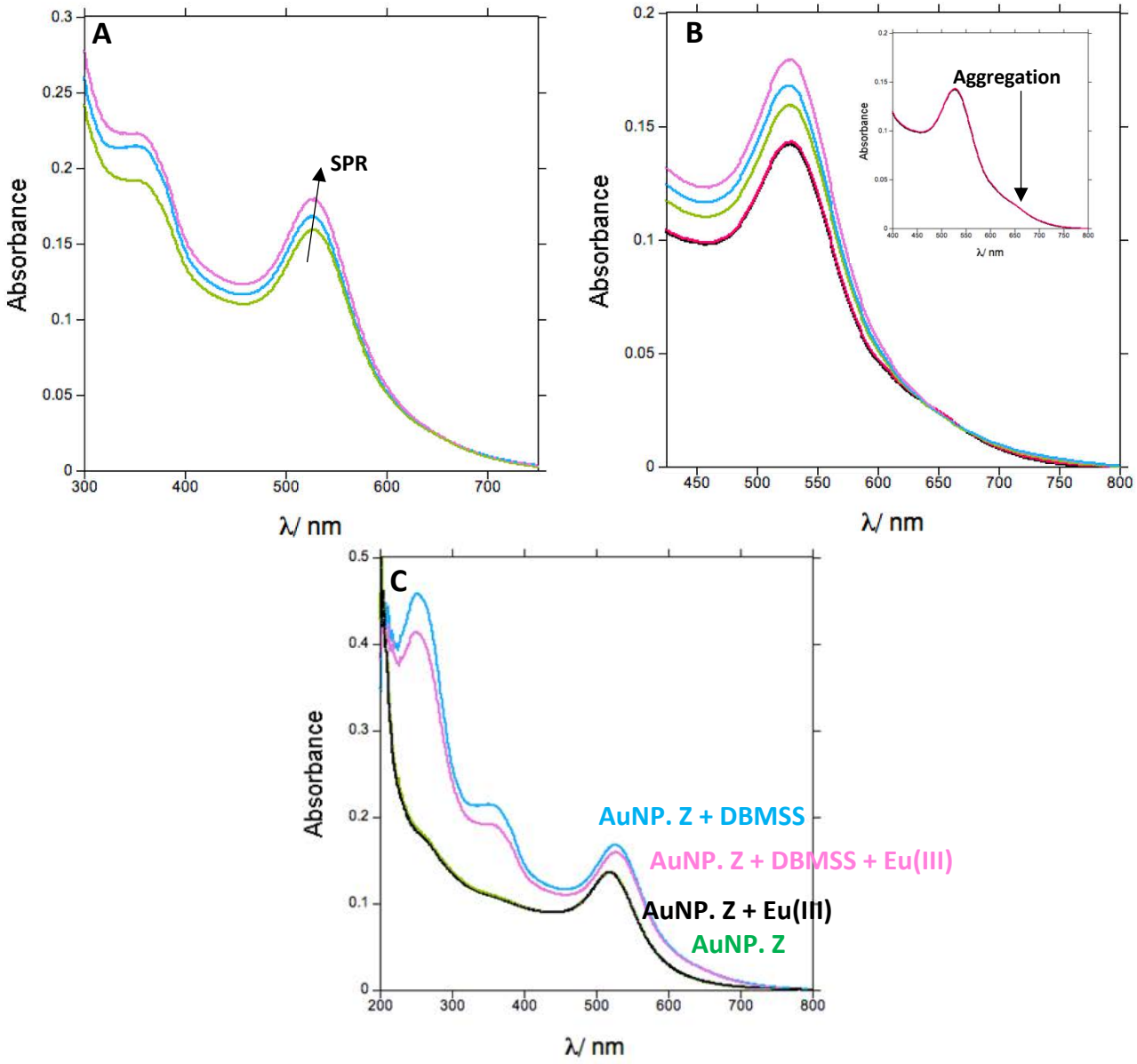


Figure 3.4.32

A: Change in SPR of **AuNP. Z + DBMSS** (0.7 nM **AuNP. Z** + 19.5 μM **DBMSS**) as μL additions of 0.2 mM Eu(III) in MeOH is titrated in to a final concentration of 3.3 μM.
B: Aggregation of **AuNP. Z + DBMSS + Eu(III)** (0.7 nM **AuNP. Z** + 19.5 μM **DBMSS** + 4.8 **Eu(III)**) as total concentration of 4.8 μM Eu(III) in MeOH is titrated. Figure 3.4.32, B insert shows the perturbation in the SPR band illustrating aggregation by UV Vis between λ = 600– 700 nm.
C: Control experiment comparing SPR shifts between **AuNP. Z + DBMSS** (blue) (0.7 nM **AuNP. Z** + 19.5 μM **DBMSS**), **AuNP. Z + DBMSS + Eu(III)** (pink (0.7 nM **AuNP. Z** + 19.5 μM **DBMSS + 3.3 Eu(III)**), **AuNP. Z** (green) (0.7 nM in H_2O), and **AuNP. Z + Eu(III)** (black) (0.7 nM **AuNP. Z** + 3.3 μM **Eu(III)**).

As Eu(III) is titrated in, a bathochromic shift in the **AuNP** SPR of 1 nm is observed from λ_{max} = 526 nm to 527 nm. Albeit the binding occurring between the ion and the aryl rings of **DBMSS** is away from the **AuNP** surface, the observed shift confirms the modification of the **AuNP** surface due to the interaction between the incubated Eu(III) and the **AuNP** surface. The experiment also allows us to identify the saturation point, whereby a maximum concentration of 3.3 μM Eu(III) can be added before aggregation (figure 3.4.32, B). Furthermore, there is in fact also a redshift in **DBMSS** absorption of λ_{max} = 358 nm to 361 nm after coordination to Eu(III). The observed redshift was mirrored in the λ_{max} shift observed in **DBMSS + Eu(III)** (figure 3.31, B).

In addition to the titration of Eu(III) loaded onto **AuNP. Z + DBMSS**, control **AuNP** SPR shifts were compared to investigate if the incorporation of Eu(III) onto the functionalised NPs, confirmed successful binding to the **DBMSS** moieties. The UV-Vis of **AuNP. Z + Eu(III)** was monitored, in absence of **DBMSS**, showing no shift in **AuNP** SPR. This observation matches the **AuNP. Z** SPR at λ_{max} = 518 nm, demonstrating the necessity of **DBMSS** on **AuNP** for Eu(III) to be complexed, and hence this interaction detected by UV-Vis. The control experiment (figure 3.4.32, C), along with the small shift in **AuNP** SPR (figure 3.4.32, A), and **DBMSS** (figure 3.41, B), confirms our result of Eu(III) successfully binding to **DBMSS** moieties on **AuNP. Z. + DBMSS**.

Table 3.4.31

Summary of **AuNP** SPR, and **DBMSS** UV-Vis absorbance shifts.

Sample	AuNP SPR λ_{max}	DBMSS λ_{max}
AuNP	515	-----
AuNP. Z	518	-----
AuNP. Z + DBMSS	526	358
AuNP. Z + DBMSS + Eu(III)	527	361

Inductively coupled plasma mass spectrometry (ICP-MS) was conducted on **AuNP. Z + DBMSS + Eu(III)**. This technique can be used to detect the amount of metals in samples at low levels detection (parts per billion) and therefore can be used to quantify number of complexes per **AuNP**. The ratios between Eu atoms and Au atoms, and the calculated number of Au atoms per NP can reveal the number of Eu complexes per NP (see appendix table 47)[58-60]. ICP-MS revealed an average of 3200 ± 300 Eu(III) complexes per NP.

At a total of 3.3 μM of Eu(III) titrated onto **AuNP. Z + DBMSS** resulted in approximately 3200 metal complexes per NP. For an approximation of **DBMSS** moieties, with the assumption of 3 : 1 binding, we can approximate that (at least) 9600 **DBMSS** moieties were occupying the **AuNP** surface, at a final concentration of 19.5 μM **DBMSS**. This however is a rough estimate, and it is unclear how many **DBMSS** moieties are bound per Eu(III) ion at this stage.

3.4.4. Photophysical Properties of Europium Coated Gold Nanoparticles

Following preparation of **AuNP. Z + DBMSS + Eu(III)**, the luminescence properties of the functionalised NPs were investigated. Eu(III) emission signal was monitored *via* sensitisation of the **DBMSS** ligand at λ_{exc} = 350 nm (figure 3.4.41).

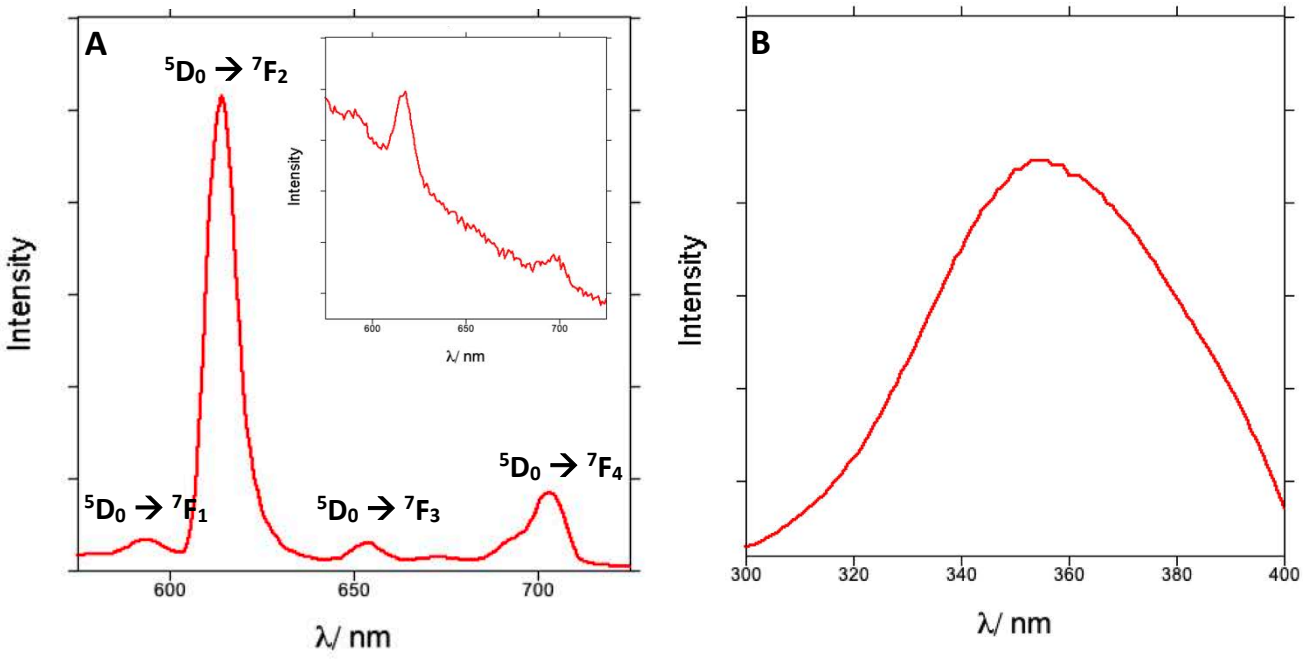


Figure 3.4.41

A: Monitoring Eu(III) emission of **AuNP. Z + DBMSS + Eu(III)** (0.7 nM **AuNP. Z** + 19.5 μM **DBMSS** + 3.3 μM **Eu(III)**, pH 9), λ_{exc} = 350 nm. Figure A insert shows emission of **AuNP. Z + DBMSS + Eu(III)** before pH adjustment (0.7 nM **AuNP. Z** + 19.5 μM **DBMSS** + 3.3 μM **Eu(III)**, pH 7), λ_{exc} = 350 nm. B: Excitation of **AuNP. Z + DBMSS + Eu(III)** (0.7 nM **AuNP. Z** + 19.5 μM **DBMSS** + 3.3 μM **Eu(III)**, pH 9) at λ_{em} = 616 nm. Emission spectra corrected for PMT and instrument response. Excitation spectra corrected for lamp response. Data is in good agreement with J. Lilley[43].

After complexation of Eu(III) into **AuNP. Z + DBMSS** at a final concentration 3.3 μM Eu(III), the characteristic Eu(III) emission signal was detected at between 575 nm and 725 nm from **DBMSS** sensitisation, and four characteristic transitions were observed. Noticeably, the detection of the $^5D_0 \rightarrow {}^7F_0$ transition was absent, but it is often very weak. A similar trend in transition intensities to **DBMSS + Eu(III)** (figure 3.32) was observed. Detection of $^5D_0 \rightarrow {}^7F_1$ transition was at λ_{max} = 594 nm, but the most intense was the hypersensitive transition $^5D_0 \rightarrow {}^7F_2$ at λ_{max} = 614 nm. The $^5D_0 \rightarrow {}^7F_3$ and $^5D_0 \rightarrow {}^7F_4$ transitions at λ_{max} = 653 nm and λ_{max} = 702

nm were also detected[39, 61, 62]. The effect of pH was shown by the change in intensities and detection of other hypersensitive transitions (3.4.41 figure A insert) after increasing pH to 9, reflecting a change in the coordination sphere of Eu(III), by interaction with the solvent, resulting in enhanced emission intensity and detection of hypersensitive transitions[39, 63].

The excitation of **AuNP. Z + DBMSS + Eu(III)** at λ_{em} = 614 nm was monitored in order to demonstrate the sensitisation giving rise to Eu(III) emission from **DBMSS**. The excitation spectrum allows us to identify that emitting level, J = 2, at λ_{em} = 614 nm can be populated most intensely when λ_{exc} = 350 nm, in agreement with **DBMSS** UV-Vis absorption (see appendix figure 48), confirming energy transfer from **DBMSS** to Eu(III).

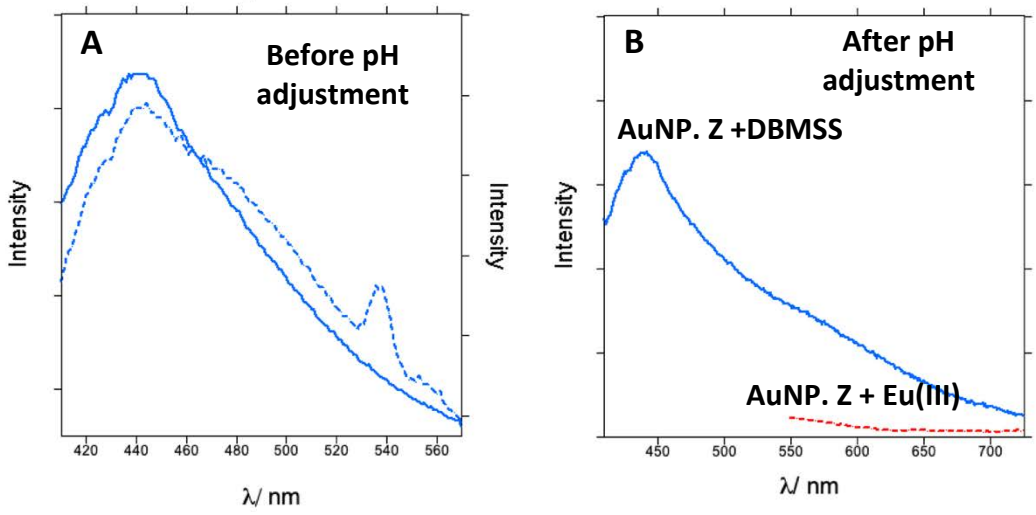


Figure 3.4.42

A: Monitoring **DBMSS** emission of **AuNP. Z + DBMSS + Eu(III)** (blue, dotted) (0.7 nM **AuNP. Z** + 19.5 μM **DBMSS** + 3.3 μM **Eu(III)**, pH 9) compared to **AuNP. Z + DBMSS + Eu(III)** before pH adjustment (blue) (0.7 nM **AuNP. Z** + 19.5 μM **DBMSS** + 3.3 μM **Eu(III)**, pH 7), $\boldsymbol{\lambda}_{exc}$ = 350 nm. B: Monitoring emission of control experiments **AuNP. Z + DBMSS** (blue) (0.7 nM **AuNP. Z** + 19.5 μM **DBMSS**) and **AuNP. Z + Eu(III)** (red, dotted) (0.7 nM **AuNP. Z** + 3.3 μM **Eu(III)**), $\boldsymbol{\lambda}_{exc}$ = 350 nm. Emission spectra corrected for PMT and instrument response.

The decrease in **DBMSS** emission (figure 3.4.42, A) shows energy transfer has increased from the sensitiser to Eu(III) resulting in improved Eu(III) detection. The change in **DBMSS** emission after pH adjustment of **AuNP. Z + DBMSS + Eu(III)** (figure 3.4.42, B) also interestingly shows the detection from the higher excited state, $^5D_1 \rightarrow {}^7F_1$ at λ_{max} = 537 nm, absent in **AuNP. Z + DBMSS + Eu(III)** before pH adjustment[64]. This result also strongly supports the evidence of

the effect of pH due to optimisation of the coordination sphere around Eu(III), and the energy transfer from **DBMSS** to Eu(III).

Control experiment of **AuNP. Z + Eu(III)** (figure 3.4.42, B) was measured in order to show the necessity of **DBMSS** presence on the NPs in order to detect Eu(III) emission, using the antenna effect. Without a sensitiser, Ln(III) emission is weak due to forbidden Laporte transitions. No emission was detected where Eu(III) emits, strongly supporting the addition of **DBMSS** was required for Ln(III) detection. **AuNP. Z + DBMSS** shows emission at λ_{max} = 440 nm, attributed to **DBMSS**.

Eu(III) emission was successfully detected by adjusting pH, and sensitisation from **DBMSS** was confirmed through excitation spectra and control experiments. However, **AuNP. Z + DBMSS** was not purified before complexation to Eu(III) and therefore there is possibility that some **DBMSS** moieties may be unbound. Hence, due to possible complexation of Eu(III) to unbound **DBMSS**, the emission detected in figure 3.3.41 cannot solely be attributed to bound **DBMSS** moieties on the **AuNP** surface. Consequentially, the approximated value of Eu(III) complexes per NP may in truth be somewhat lower after purification.

3.4.5. Photophysical Properties of Purified Europium Coated Gold Nanoparticles

Incorporation of Eu(III) into purified **AuNP. Z. DBMSS** (0.7 nM **AuNP. Z** + 19.5 μM **DBMSS** purified) was investigated, in order to determine the photophysical properties with only bound **DBMSS**. Purification of **AuNP. Z + DBMSS** was performed using a Sephadex G10 column to remove unbound **DBMSS**, collecting **AuNP. Z. DBMSS**.

The addition of less **DBMSS** was also investigated. In section 3.4.2, it was shown by a titration of **DBMSS** onto **AuNP. Z** that after 10 μM of **DBMSS** added to **AuNP. Z** (figure 3.4.22) a plateau was reached. This suggested full coating of the **AuNP** surface had been reached beyond this point, and any **DBMSS** molecules added up to 10 μM should be bound to the Au surface. Therefore, in addition to purified **AuNP. Z. DBMSS**, **AuNP. Z + DBMSS** (0.7 nM **AuNP. Z** + 10 μM **DBMSS**) was also investigated.

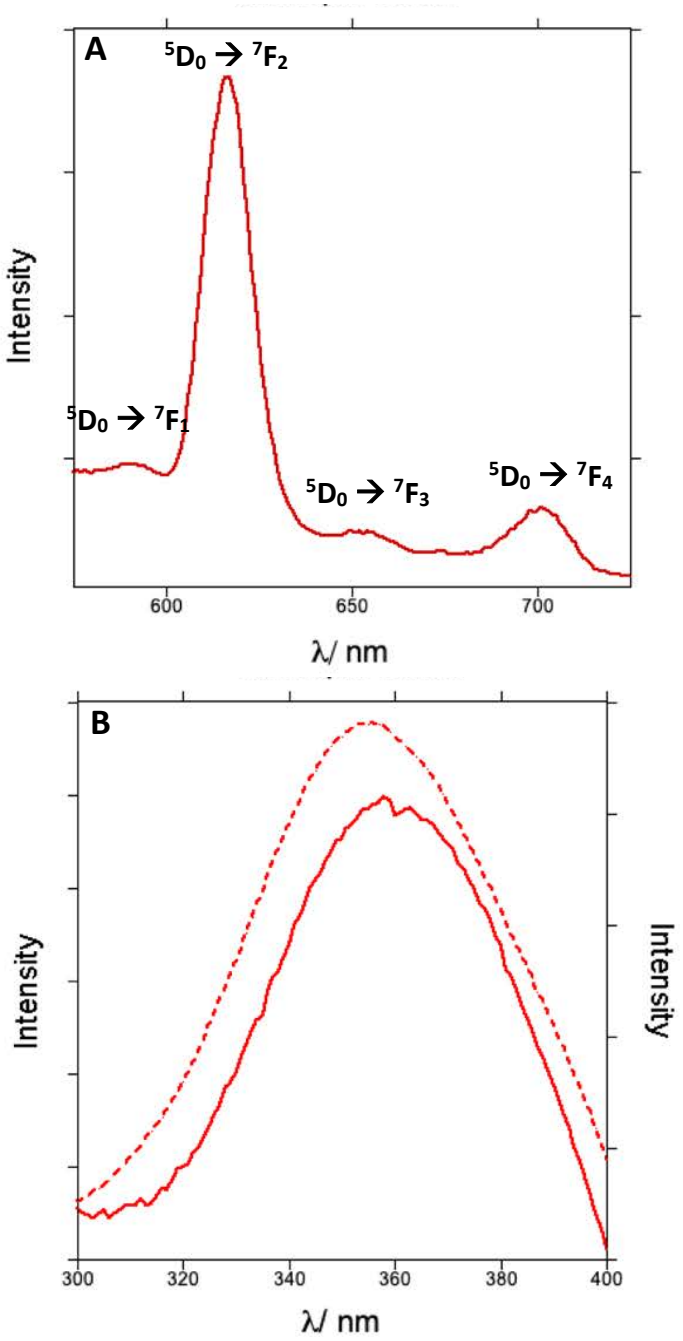


Figure 3.4.43

A: Monitoring Eu(III) emission of **AuNP. Z. DBMSS + Eu(III)** (purified **AuNP. Z + DBMSS** (0.7 nM **AuNP. Z** + 19.5 μM **DBMSS** +3.3 μM **Eu(III)**, pH 9) , λ_{exc} = 350 nm. B: Excitation of **AuNP. Z. DBMSS + Eu(III)** (red) (purified **AuNP. Z + DBMSS** (0.7 nM **AuNP. Z** + 19.5 μM **DBMSS**) +3.3 μM **Eu(III)**, pH 9) and **AuNP. Z + DBMSS + Eu(III)** (red, dotted) (0.7 nM **AuNP. Z** + 10 μM **DBMSS** + 3.3 μM **Eu(III)**)at λ_{em} = 616 nm. Emission spectra corrected for PMT and instrument response. Excitation spectra corrected for lamp response.

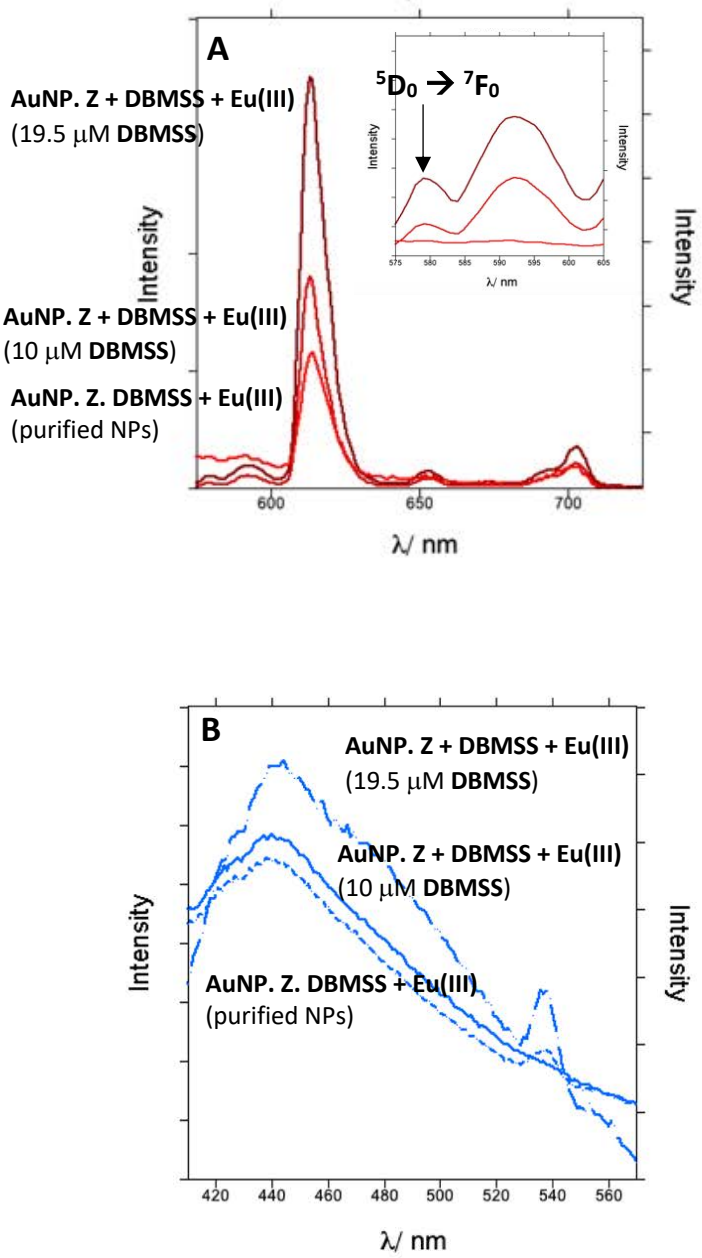


Figure 3.4.44

A: Monitoring Eu(III) emission of **AuNP. Z + DBMSS + Eu(III)** (brown) (0.7 nM **AuNP. Z** + 19.5 μM **DBMSS** +3.3 μM **Eu(III)**, pH 9), **AuNP. Z + DBMSS + Eu(III)** (maroon) (0.7 nM **AuNP. Z** + 10 μM **DBMSS** +3.3 μM **Eu(III)**, pH 9) and **AuNP. Z. DBMSS + Eu(III)** (red) (purified **AuNP. Z + DBMSS** (0.7 nM **AuNP. Z** + 19.5 μM **DBMSS** +3.3 μM **Eu(III)**, pH 9) $\boldsymbol{\lambda}_{exc}$ = 350 nm. Figure A insert shows the $^5D_0 \rightarrow {}^7F_0$ transition magnified between $\boldsymbol{\lambda}_{max}$ = 575 nm – 605 nm.

B: Monitoring **DBMSS** emission of **AuNP. Z + DBMSS + Eu(III)** (blue, dashed) (0.7 nM **AuNP. Z** + 19.5 μM **DBMSS** +3.3 μM **Eu(III)**, pH 9), **AuNP. Z + DBMSS + Eu(III)** (blue, dotted)) (0.7 nM **AuNP. Z** + 10 μM **DBMSS** +3.3 μM **Eu(III)**, pH 9) and **AuNP. Z. DBMSS + Eu(III)** (blue) (purified **AuNP. Z + DBMSS** (0.7 nM **AuNP. Z** + 19.5 μM **DBMSS** +3.3 μM **Eu(III)**, pH 9), $\boldsymbol{\lambda}_{exc}$ = 350 nm. Emission spectra corrected for PMT and instrument response.

Albeit weaker, Eu(III) emission was detected from **AuNP. Z. DBMSS + Eu(III)** (purified NPs), observed at four transitions. Emission was detected at λ_{max} = 590 nm ($^5D_0 \rightarrow {}^7F_1$), the hypersensitive transition at λ_{max} = 614 nm ($^5D_0 \rightarrow {}^7F_2$), λ_{max} = 652 nm ($^5D_0 \rightarrow {}^7F_3$) and λ_{max} = 701 nm ($^5D_0 \rightarrow {}^7F_4$)[39]. **AuNP. Z. DBMSS + Eu(III)** (purified NPs) presented more background scattering after purification, attributed to organic emission from **DBMSS**.

The emission of Eu(III) from **AuNP. Z + DBMSS + Eu(III)** (final concentration 10 μM **DBMSS**) was much more intense, but reduced compared to **AuNP. Z + DBMSS + Eu(III)** (final concentration 19.5 μM **DBMSS**) (figure 3.4.44). Interestingly, the weak $^5D_0 \rightarrow {}^7F_0$ transition was only detected for **AuNP. Z + DBMSS + Eu(III)** (final concentration 19.5 μM **DBMSS**) and **AuNP. Z + DBMSS + Eu(III)** (final concentration 10 μM **DBMSS**) shown in figure 3.4.44 A insert. The absence of this transition in **AuNP. Z. DBMSS + Eu(III)** (purified NPs) could suggest either a change in symmetry around the Eu(III) ion[39], or the weak transition is not detectable due to the more prominent background scattering from **DBMSS**. Additionally, the $^5D_0 \rightarrow {}^7F_0$ can be used to determine how many Eu(III) sites occur from splitting of the peaks but usually requires high sensitivity in the instrument[39]. However, what this does tell us, is that all emission detected from **AuNP. Z. DBMSS + Eu(III)** (purified NPs) can be attributed solely to energy transfer from only bound **DBMSS** on the **AuNP** surface, due to the purification process. Excitation spectra of the new **AuNPs**, **AuNP. Z. DBMSS + Eu(III)** (purified NPs) and **AuNP. Z + DBMSS + Eu(III)** (final concentration 10 μM **DBMSS**) also confirm sensitisation from **DBMSS**.

Monitoring **DBMSS** emission from the NPs (figure 3.5.44, B) also supports the effect of pH by the observation of the transition at λ_{max} = 537 nm attributed to $^5D_1 \rightarrow {}^7F_1$.

The lifetime **DBMSS + Eu(III)** (1 : 1, 2 : 1, 3 : 1) (see section 3.1.2 for discussion on β-diketones forming 3 : 1 complexes with Ln(III)) was measured and compared to the lifetime of the NPs in order to determine the coordination of Eu(III) to **DBMSS** on the **AuNP** surface.

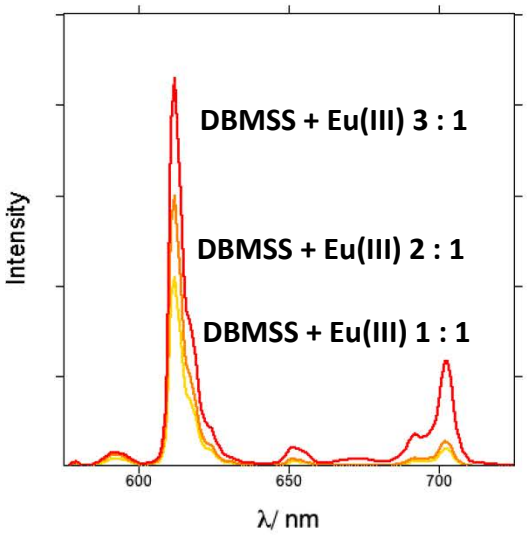


Figure 3.4.45

Emission of **DBMSS + Eu(III)** (1 : 1, 2 : 1, 3 : 1), λ_{exc} = 350 nm . A solution of **DBMSS** (0.05 mM, 10 % MeOH) titrated with $EuCl_3.6H_2O$ (0.016 mM, 0.025 mM, 0.05 mM, 10 % MeOH) in H_2O. Emission spectra corrected for PMT and instrument response.

Table 3.4.41

Lifetime global analysis of **DBMSS + Eu(III)** (1 : 1, 2 : 1, 3 : 1), fitted with a χ^2 between 1 and 1.1, measuring τ at λ_{em} = 615 nm. A solution of **DBMSS** (0.05 mM, 10 % MeOH) titrated with $EuCl_3.6H_2O$ (0.016 mM, 0.025 mM, 0.05 mM, 10 % MeOH) in H_2O.

	1 : 1		**2 : 1**		**3 : 1**	
	f_i/ %	τ_1/ μs	f_i/ %	τ_1/ μs	f_i/ %	τ_1/ μs
Component 1	32	160	19	150	32	170
Component 2	68	330	81	360	68	370

The lifetime of **DBMSS + Eu(III)** was recorded in water, and fitted using global analysis with a χ^2 between 1 and 1.1. The long component lifetime observed for 1 : 1 was 330 μs, which increased to 370 μs as the ratio of **DBMSS** : **Eu(III)** increased to 3 : 1. The lifetime of $Eu(DBM)_3$ in MeOH has previously been reported as 390 μs[65]. There are also reports of other DBM and Eu(III) complexes, often seen with another ancillary ligand such as $Eu(DBM)_3(phen)$ which has

been previously reported at 493 μs, and $Eu(DBM)_3.2H_2O$/PMMA complex bound to PMMA resin at 672 μs[66, 67]. The shorter lifetime measured of **DBMSS** : **Eu(III)** 3 : 1 in H_2O seems reasonable here. The longer lifetime of $Eu(DBM)_3$(phen) can be attributed to the additional ligand phenanthroline, excluding more water molecules and simultaneously increasing the efficiency of sensitisation. The longer lifetime of $Eu(DBM)_3.2H_2O$/PMMA arises from the presence of ligands in PMMA.

Table 3.4.42

Lifetime global analysis of **AuNP** samples with **DBMSS** and **Eu(III)** fitted with a χ^2 between 0.9 and 1.2.

	AuNP. Z + DBMSS + Eu(III) in *excess* of **DBMSS** (19.5 μM)		**AuNP. Z + DBMSS + Eu(III)** at **DBMSS** *saturation* point (10 μM)		**AuNP. Z. DBMSS + Eu(III)** *purified* NPs	
	f_i/ %	τ_1/ μs	f_i/ %	τ_1/ μs	f_i/ %	τ_1/ μs
Component 1	12	97	43	120	31	88
Component 2	88	240	57	280	69	280

The lifetime of the **AuNP** samples were recorded in water, and fitted with IRF, using global analysis with a χ^2 between 0.9 and 1.2. The lifetime of **AuNP. Z + DBMSS + Eu(III)** (final concentration 10 μM **DBMSS**) showed biexponential behavior with a long lifetime of 280 μs. The lifetime of purified **AuNP. Z. DBMSS + Eu(III)** also showed biexponential behavior with a long lifetime of 280 μs.Considering the ratio of **DBMSS** to **Eu(III)** on **AuNP. Z + DBMSS + Eu(III)** (final concentration 10 μM **DBMSS**) is 3 : 1, as a final concentration of 3.3 μM was titrated onto **AuNP. Z + DBMSS** (final concentration of 10 μM **DBMSS**), the lifetime is lower than that of **DBMSS + Eu(III)** (all ratios, table 3.4.1). This suggests partial occupation of binding sites on the **AuNP** surface. Decrease in lifetimes can also arise from deactivation pathways. it's well known that the deactivation of the Eu(III) excited state (and other Ln(III)) is sensitive to non-radiative processes. This includes back energy transfer and thermal deactivation, but more relevant, deactivation via vibrational coupling between coordinated solvent molecules and Eu(III)[68, 69]. Although the lower lifetimes suggesting only partial binding to **DBMSS**, the lifetimes are long lived and very characteristic of Ln(III) ions.

The quantum yields of the purified NPs were measured and compared to **DBMSS + Eu(III) (3 : 1).** This was achieved using an integrated sphere attachment in the Edinburgh instrument (see experimental section 5.1). Spectral scans were ran in the excitation scatter region (of **DBMSS**) of the reference solvent (water) and of the sample (**DBMSS + Eu(III)** and purified NPs). Emission scans were also ran of these samples (reference solvent and samples) in the emission range (of Eu(III)). Using F980 software, the data was processed (see section 5.1 and equation 5.17) determining the quantum yields of each sample.

Table 3.4.43

Quantum yield compared between **DBMSS + Eu(III) (3 : 1)** and **AuNP. Z. DBMSS + Eu(III)** (purified NPs).

Sample	Quantum Yield Φ/ %
DBMSS + Eu(III) (3 : 1)	1.92
AuNP. Z. DBM + Eu(III) (purified NPs)	0.32

The luminescence quantum yields of the Eu(III) samples were measured at room temperature in water. The quantum yield of **DBMSS + Eu(III) (3 : 1)** was measured as 1.92 %. The quantum yield of hydrated $Eu(DBM)_3(H_2O)$ has been previously reported as 1 %, in good agreement with the experimental result of 1.92 %[70]. This can also be compared to the quantum yield of $Eu(DBMSS)_3(phen)$ measured at 4.9 %, higher than that **DBMSS + Eu(III) (3 : 1)** due to the extra sensitising group phenanthroline[71].

The luminescence quantum yield of **AuNP. Z. DBM + Eu(III)** (purified NPs) dropped to 0.32 % as expected. This is in good agreement with reported values in literature. Rai *et. al.* reported their complex $Eu(DBM)_2.2H_2O$/PMMA as 0.42 %[73]. The decrease in quantum yields and lifetimes from solution **DBMSS + Eu(III)** to **AuNP. Z. DBM + Eu(III)** as discussed can be attributed to partial binding of **DBMSS** sites, or quenching from **AuNP**. It has been reported previously in the Pikramenou group the deactivation of lifetimes of metal complexes on Au surfaces due to energy or electron transfer from these complexes to the Au surfaces[4]. This

could be determined by preforming $Eu(DBMSS)_3$ and then coating **AuNP. Z** and comparing lifetimes.

This can further be supported through additional analysis of binding estimation. The concentration of **DBMSS** can be compared to the concentration of **AuNP** for purified **AuNP. Z. DBMSS + Eu(III)** and **AuNP. Z + DBMSS + Eu(III)** (10 mM final concentration **DBMSS**). The concentration of **DBMSS** can be calculated through Beer Lambert law ($A = \varepsilon cL$).

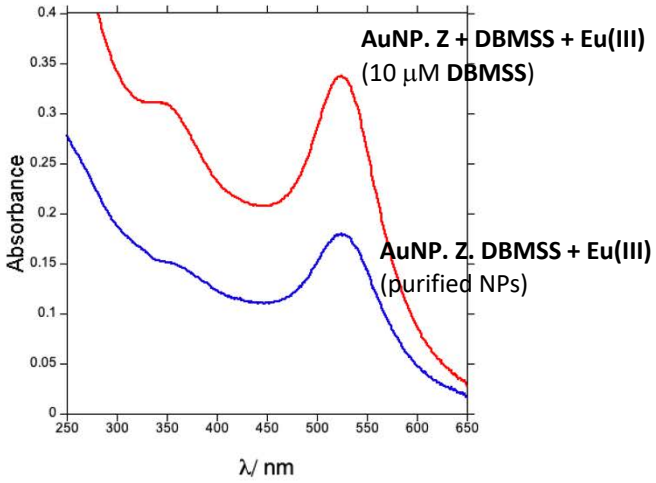


Figure 3.4.46

UV-Vis absorbance **AuNP. Z. DBMSS + Eu(III)** (0.9 nM, blue) and **AuNP. Z + DBMSS + Eu(III)** (10 mM final concentration DBMSS) (1.7 nM, red)

The concentration of **DBMSS** in **AuNP. Z. DBMSS + Eu(III)** (purified NPs) calculated from $A = \varepsilon cL$ (ε = 13000 mol^{-1} dm^3 L^{-1}, see appendix figure 43) is 15500 nM. Comparing this to the concentration of **AuNP** already calculated to be 1.5 nM, this gives a ratio of 7700 : 1 **DBMSS : AuNP**. If 3 : 1 binding was true, this would mean there were 2600 Eu(III) complexes on the Au surface, and if partial binding was occurring then less than 2600 Eu(III) complexes were bound to the Au surface. These numbers are an approximation of course as the absorbance of **DBMSS** is hard to distinguish on the absorbance graph. ICP-MS revealed that 3200 Eu(III) complexes were present in **AuNP. Z +DBMSS + Eu(III)** (at saturation point 19.5 μM **DBMSS)** prior to purification. Thus, the estimation of 2600 complexes or less in purified **AuNP. Z. DBMSS + Eu(III)** makes logical sense perhaps due to partial binding, or quenching from **AuN**

3.5. Concluding Remarks

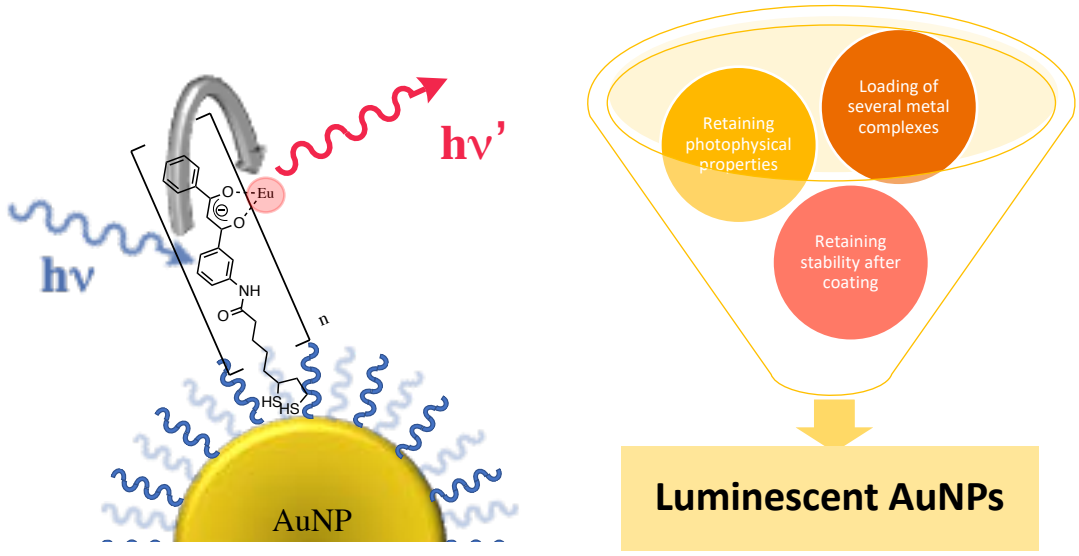


Figure 3.51

Schematic illustration of the design creating luminescent AuNPs functionalised with **DBMSS** and Eu(III) with the aim to retain good stability and photophysical properties upon coating.

Preliminary studies of photophysical properties of **DBMSS** and **DBMSS + Eu(III)** were studied to obtain $\varepsilon_{\mathbf{DBMSS}}$. Their luminescence properties revealed useful information of the Eu(III) coordination environment.

Functionalised **AuNPs** were characterised by DLS, zeta potential, TEM and UV-Vis absorbance. These confirmed successful surface modifications. The changes in size by DLS analysis (table 3.4.12), with shape and monodispersity are in good agreement with TEM (figure 3.4.12), and surface charge by zeta potentials (table 3.4.13), and strongly suggest successful surface modification whilst retaining good shape and a narrow size distribution.

Luminescence, and UV-Vis absorbance studies revealed **DBMSS** retained photophysical properties upon coating. Initial photophysical characterisation after Eu(III) incubation, studied both by SPR changes (figures 3.4.22 and 3.4.32) and luminescence properties of **AuNP. Z + DBMSS + Eu(III)** (figure 3.4.41) (excess of **DBMSS** (19.5 μM)), confirm the successful

modifications with strong evidence from control experiments. The luminescence properties were concluded after further investigation with **AuNP. Z. DBM + Eu(III)** (purified NPs), resulting in long lifetimes suggesting partial occupation of binding sites and a luminescence quantum yield of 0.32 %.

These studies demonstrate the successful design of luminescent **AuNPs,** retaining good stability and photophysical properties upon coating with **DBMSS** and **Eu(III).** The design showed the ability to coordinate many metal complexes (3200 Eu(III) complexes onto **AuNP. Z + DBMSS + Eu(III)** (final concentration of 19.5 μM **DBMSS**)), resulting in intense luminescent properties. After purification of NPs, the design demonstrated good ability in retaining these properties, resulting in long luminescent lifetime and quantum yield. Our approach to designing luminescent Eu(III) coated **AuNPs,** stabilised with a fluorinated surfactant, show promising potential as a scaffold for future designs incorporating other Ln(III) ions, with the ability to still enable binding to **DBMSS** and **Ln(III)**.

3.6. Referenced Material

1. F. Dumur, E. Dumas and C. Mayer, *Nanomaterials.,* 2020, **10**, 548
2. D. Lewis, T. May, J. MacPherson and Z. Pikramenou, *Chem. Commun.,* 2006, 1433-1435
3. S. Osborne and Z. Pikramenou, *Faraday Discuss.,* 2015, **185**, 219-231
4. A. Davies, D. Lewis, S. Watson, S. Thomas and Z. Pikramenou, *PNAS.,* 2012, **109**, 1862-1867
5. D. Lewis and Z. Pikramenou, *Coord. Chem. Rev.,* 2014, **273-274**, 213-225
6. L. Truman, S. Comby and T. Gunnlaugsson, *Angew. Chem, Int. Ed.,* 2012, **51**, 9624-9627
7. S. Comby, E. Surender, O. Kotova, L. Truman, J. Molloy, and T. Gunnlaugsson, *Inorg. Chem.,* 2014, **53**, 1867-1879
8. M. Brust, M. Walker, D. Bethell, D. Schifrin and R. Whyman, *J. Chem. Soc. Chem. Commun.,* 1994, 801
9. S. Comby and T. Gunnlaugsson, *ACS Nano.,* 2011, **5**, 7184-7197
10. M. Yon, C. Pibourret, J. Marty and D. Ciuculescu-Pradines, *Nanoscale Adv.,* 2020, **2**, 4671
11. L. Moriggi, C. Cannizzo, E. Dumas, C. Mayer, A. Ulianov and L. Helm, *J. Am. Chem. Soc.,* 2009, **131**, 10828-10829
12. M. Ferriera, J. Goncalves, B. Mousavi, M. Prata, S. Rodrigues, D. Calle, P. Lopez-Larrubia, S. Cerdan, T. Rodrigues, P. Ferreira, L. Helm, J, Martins and C. Geraldes, *Dalton Trans*., 2015, **44**, 4016
13. J. Massue, S. Quinn and T. Gunnlaugsson, *J. Am. Chem. Soc*, 2008, **130**, 6900–6901
14. J. Liu, Z. Xiong, J. Zhang, C. Peng, B. Klajnert-Maculewicz, M. Shen and X. Shi, *ACS Appl. Mater. Interfaces*., 2019, **11**, 15212−15221
15. N. Rogers, H. Jeffery, S. Claire, D. Lewis, G. Zikeli, N. Hodges, S. Egginton, G. Nash and Z. Pikramenou, *Nanomedicine.,* 2017, **22**, 2725-2740
16. M. Reddy, V. Divya and R. Pavithran, *Dalton Trans.,* 2013, **42**, 15249-15262
17. M. Campello, E. Palma, I. Correia, P. Paulo, A. Matos, J. Rino, J. Coimbra, J. Pessoa, D. Gambino, A. Paulo and F. Marques, *Dalton Trans.,* 2019, **48**, 4611-4624
18. K. Binnemans, P. Lanaerts, K. Driesen and C. Gorller-Walrand, *J. Mater. Chem.,* 2004, **14,** 191-195
19. S. Biju, Y. Eom, J. Bunzli and H. Kim, *J. Mater. Chem. C.,* 2013, **1**, 6935-6944
20. S. Dasari and A. Patra, *RSC Adv.,* 2017, **7**, 44272-44281

21. D. Raj, S. Biju and M. Reddy, *Inorg. Chem.,* 2008, **47**, 8091–8100
22. P. Martin-Ramos, C. Coya, A. Alvarez, M. Silva, C. Zaldo, J. Paixao, P. Chamorro-Posada and J. Martın- Gil, *J. Phys. Chem. C*, 2013, **117**, 10020–10030
23. M. Pietraszkiewicz, O. Pietraszkiewicz, J. Karpiuk, A. Majka, G. Dutkiewicz, T. Borowiak, A. Kaczmarek and R. Deun, *J. Lumin*., 2016, **170**, 411–419
24. H. Kamebuchi, T. Yoshioka and M. Tadokoro, *Mater. Adv.,* 2020, **1**, 569-573
25. J. Xu, L. Jia, N. Jin, Y. Ma, X. Liu, W. Wu, W. Liu, Y. Tang and F. Zhou, *Chem. Eur. J.,* 2013, **19**, 4556
26. X. Li, H. Chen, A. Kirillov, Y. Xie, C. Shan, B. Wang, C. Shi and Y. Tang, I*norg. Chem. Front.*, 2016, **3**, 1014
27. T. George, M. Krishna and M. Reddy, *Dalton Trans.,* 2016, **45,** 18719-18729
28. Y. Wang, H. Wang, X. Zhao, Y. Jin, H. Xiong, J. Yuan and J. Wu, *New. J. Chem.,* 2017, **41**, 5981-5987
29. Z. Dai, L. Tian, B. Song, Z. Ye, X. Liu and J. Yuan, *Anal. Chem*., 2014, **86**, 11883–11889
30. Y. Yip, G. Law and W. Wong, *Dalton Trans*., 2016, **45**, 928–935
31. M. Catsano-Briones, A. Bassett, L. Meason, P. Ashton and Z. Pikramenou, *Chem. Commun.,* 2004*,* 2832-2833
32. J. Massue, S. Quinn and T. Gunnlaugsson, *J. Am. Chem. Soc*, 2008, **130**, 6900–6901
33. E. Soini and I. Hemmila, *Clin. Chem.,* 1979, **25**, 353
34. J. Bunzli, *Chem. Rev.,* 2010, **110**, 2729-2755
35. C. Bonnet, J. Massue, S. Quinn and T. Gunnlaugsson, *Org. Biomol. Chem.*, 2009, **7**, 3074–3078
36. R. Teo, J. Termini and H. Gray, *J. Med. Chem.,* 2016, **59**, 6012-602419
37. A. Hagan and T. Zuchner, *Anal. Bioanal. Chem.,* 2011, **400**, 2847–2864
38. N. Hasan and K. Iftikhar, *New. J. Chem.,* 2019, **43**, 2479-2489
39. K. Binnemans, *Coord. Chem. Rev.,* 2015, **295**, 1-45
40. A. Bassett, S. Magennis, P. Glover, D. Lewis, N. Spencer, S. Parsons, R. Williams, L. De Cola and Z. Pikramenou, *J. Am. Chem. Soc.,* 2004, **126**, 9413-9424
41. J. Massue, S. Quinn and T. Gunnlaugsson, *J. Am. Chem. Soc*, 2008, **130**, 6900–6901
42. E. Soini and I. Hemmila, *Clin. Chem.,* 1979, **25**, 353
43. J. Lilley Thesis, University of Birmingham, 2013

44. J. Hubaud, I. Bombarda, L. Decome, J. Wallet and E. M. Gaydou, *J. Photochem. and Photobiol. B: Biol.*, 2008, **92**, 103 – 109
45. I. Malina, N. Juhnevics and V. Kampers, *P EST ACA SCI.,* 2016, **66**, 493-500
46. M. Mryczek, J. Zawadiak and T. Piotrowski, *Eur. J. Chem.,* 2011, **3**, 289-294
47. S. Biju, Y. Eom, J. Bunzli and H. Kim, *J. Mater. Chem. C.,* 2013, **1**, 6935-6944
48. I. Malina, K. Traskovskis, N. Lesina and A. Vembris, *Dyes Pigm.,* 2019, **163**, 257-266
49. M. Hatanaka and S. Yabushita, *Theor Chem Acc.,* 2014, **133**
50. D. Nie, Z. Chen, Z. Bian, J. Zhou, Z. Liu, F. Chen, Y. Zhao and C. Huang, *New. J. Chem.,* 2007, **31**, 1639-1646
51. M. Wuithschick, A. Birnbaum, S. Witte, M. Sztucki, U. Wainio, N. Pinna, L. Rademann, F. Emmerling, R. Kraehnert and J. Polte, *ACS Nano.,* 2015, **9**, 7052-7071
52. N. Rogers, H. Jeffery, S. Claire, D. Lewis, G. Zikeli, N. Hodges, S. Egginton, G. Nash and Z. Pikramenou, *Nanomedicine.,* 2017, **22**, 2725-2740
53. S. Osborne and Z. Pikramenou, *Faraday Discuss.,* 2015, **185**, 219-231
54. S. King, S. Claire, R. Tiexeira, A. Dosumu, A. Carrod, H. Dehgani, M. Hannon, A. Ward, R. Bricknell, S. Botchway, N. Hodges and Z. Pikramenou, *J. Am. Chem. Soc.,* 2018, **140,** 10242-10249
55. N. Rogers, S. Claire, R. Harris, S. Farabi, G. Zikeli, I. Styles, N. Hodges and Z. Pikramenou, *Chem Comm.,* 2014, **50**, 617-619
56. F. Schulz, T. Vossmeyer, N. Bastus and H. Weller, *Langmuir.,* 2013, **29**, 9897-9908
57. Y. Yeh, B. Creran and V. Rotello, *Nanoscale.,* 2012, **4**, 1871-1880
58. J. Shang and Z Gao, *Chem. Soc. Rev.,* 2014, **43**, 7267-7278
59. W. Haiss, N. Thanh, J. Aveyard and D. Fernig, *Anal. Chem.,* 2007, **79**, 4215-4221
60. R. Carney, J. Kim, H. Qian, R. Jin, H. Mehenni, F. Stellacci and O. Bakr, *Nat. Commun.,* 2011, **7**, 335
61. N. Hasan and K. Iftikhar, *New. J. Chem.,* 2019, **43**, 2479-2489
62. M. Hatanaka and S. Yabushita, *Theor. Chem. Acc.,* 2014, **133**, 1517-1532
63. J. Moore, R. Lord, G. Cisneros and M. Allen, *J. Am. Chem. Soc.,* 2012, **134**, 17372-17375
64. D. Wei, Z. Fan, Y. Huang and H. Seo, *J. Mater. Chem. C.,* 2020, **8**, 15717-15727
65. W. Dawson, J. Kropp and M. Windsor, *J. Chem. Phys.,* 1966, **45**, 2410-2418
66. H. Liu, Y. Lee, S. Park, K. Jang and S. Kim, *J. Lumin*, 2004, **110**, 11-16
67. R. Weissleder and V. Ntziachristos, *Nat. Med.,* 2003, **9**, 123-128

68. J. Monteiro, *Molecules.,* 2020, 25, 2089-2123

69. R. Teo, J. Termini and H. Gray, *J. Med. Chem.,* 2016, **59**, 6012-6024

70. E. Niyama, H. Brito, M. Cremona, E. Teotonio, R. Reyes, G. Brito and M. Felinto, *Spectrochimica Acta Part A.,* 2005, **61**, 2643-2649

71. P. Nockemann, E. Beurer, K. Driesen, R. Deun, K. Hecke, L. Meervelt and K. Binnemans, *Chem. Commun.,* 2005, 4354-4356

72. H. Liu, Y. Lee, S. Park, K. Jang and S. Kim, *J. Lumin.*, 2004, **110**, 11-16

4. Conclusions and Further Work

4.1. Thesis Conclusions

Our approach to developing luminescent NPs entailed the design of two nanosystems.

The preparation and design of novel **SiO_2NP**s coated with luminescent **Ln-L**, encapsulated with an anticancer drug **CPT**, demonstrated the promising potential as a platform for theranostic applications. The design showed successful therapeutic delivery of **CPT** to A549 lung cancer cells, causing apoptosis arising from **CPT**, in addition to monitoring drug release through detection of Ln(III) luminescence changes. This design shows promising potential contribution to the field of NPs in nanomedicine, offering a platform for facile development of luminescent **SiO_2NPs**. The conclusions demonstrate good proof of concept of encapsulation of a hydrophobic anticancer drug. Moreover, the $\pi-\pi$ conjugated structure of **CPT** enabled efficient light absorption, and hence good sensitisation, and this attribute can be applied to other hydrophobic drugs with high ε.

The design of luminescent **AuNPs** stabilised with a fluorinated surfactant, Zonyl FSA, demonstrated excellent photophysical properties upon coating with the β–diketone ligand, **DBMSS**, and Eu(III). The preparation of the NPs illustrated efficient retention of stability, even after coating with the two species, in addition to the ability to bind several metal complexes. This design demonstrates promising potential in building Ln coated **AuNPs** for potential applications in Ln luminescent immunoassays. The ability to perform high loading of luminescent Ln probes at low concentrations, in addition to potential future multimodal functionalities, offers a platform for enhancing Ln luminescence detection and sensitivity in immunoassays.

4.2. Future Work

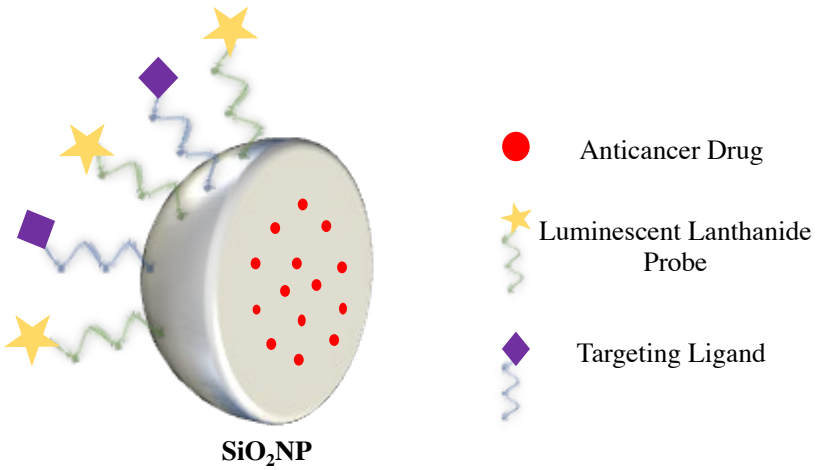


Figure 4.21

Schematic illustration of our novel **SiO_2NP** design encapsulating an anticancer drug, functionalised with luminescent Ln complexes and potential targeting species for future work.

Although successful Ln(III) luminescence *via* **CPT** sensitisation was observed in the **CPT0⊂Ln-L.SiO_2NP_1** system, the release and consequential effect of **CPT** was studied from **CPT0⊂Eu-L.SiO_2NP_1**. Future work should look to extend these studies **CPT⊂Ln-L.SiO_2NP** (Ln(III) = Nd and Yb). The importance of using NIR Lns is an advantageous tool for applications in bioimaging of these Ln systems, due to their deeper tissue penetration depth. This will enable higher sensitivity, higher signal to noise ratio and reduced background luminescence, which are advantageous for non-invasive techniques in bioimaging.

In addition, this project could look to encapsulating other hydrophobic anticancer drugs, creating a platform to develop several theranostic **SiO_2NPs** with different drugs and targets. It has been commonly seen (see section 2.1.3.) that co-delivery of **CPT** with other drugs (which target the same enzyme), such as DOX, can enhance synergistic effects of therapeutic drug delivery. Moreover, the already clinically used **CPT** derivatives, irinotecan and topotecan, can be encapsulated. With a **CPT** backbone in their structures, efficient sensitisation looks promising, and can therefore be used in the **SiO_2NPs** system, detecting their release through

changes in Ln luminescence. This work can extend to study the imaging in cells, in order to pick up Ln signals from the **CPT⊂Ln-L.SiO$_2$NP** NPs.

Irinotecan **Topotecan**

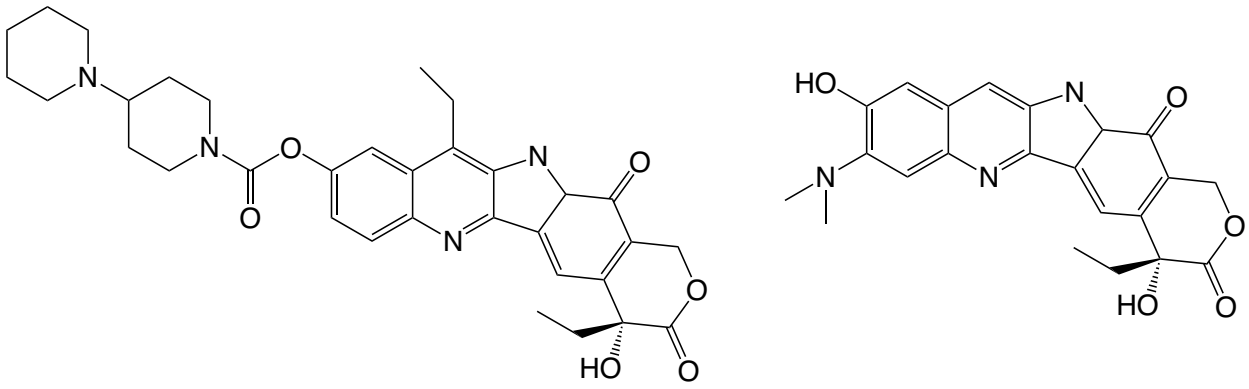


Figure 4.22

Structures of CPT derivatives irinotecan and topotecan.

Furthermore, as a design with the ability to develop multimodal functionality, this project can look into the attachment of specific targeting ligands. Research in theranostic silica NPs has seen the attachment of targeting moieties such as folic acid (see section 2.1.3.), in addition to possessing stimuli responsive behaviours, such as pH. These designs can lead to the development of **CPT⊂SiO$_2$NP** functionalised with **Ln-L** to detect drug release, and targeting ligands to allow controlled release acquired by stimuli responsive triggers.

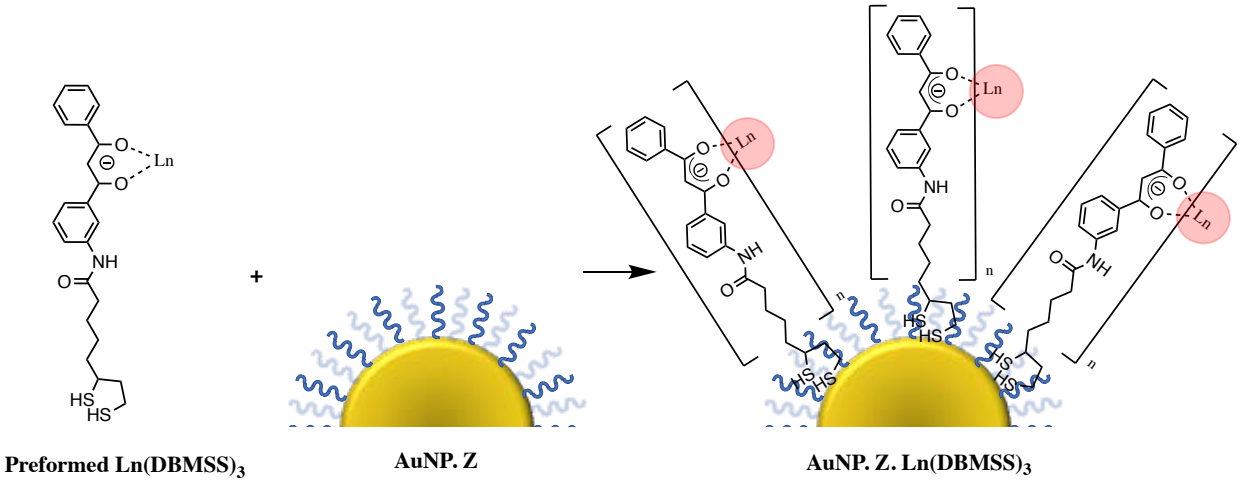


Figure 4.22

Schematic illustration of different route to creating luminescent **AuNPs** *via* the attachment of preformed Ln-β-diketones.

Studies of our luminescent **AuNPs** were performed through coordination to Eu(III) after coating the NPs with **DBMSS**. Future work can be extended to look into coating **AuNPs** with preformed **Eu(DBMSS)$_3$,** hence having potentially enhanced luminescence properties by increasing the partial binding seen in the studies (not all Eu(III) sites were occupied) to a 3 : 1 ratio.

Furthermore, as mentioned previously, the use of NIR Lns is beneficial for applications in luminescent Ln immunoassays. NIR Lns provide higher signal to noise ratios and reduced background scatter, therefore enhanced detection and sensitivity. The incorporation of NIR Lns, such as Nd(III) and Yb(III), will be a useful option as a design for luminescent **AuNPs**.

Preliminary studies have shown the stability of coated **AuNPs** were retained through the use of PEG, instead of Zonyl FSA. Future work can look into the full coating of **AuNPs** stabilised with PEG, for comparison of photophysical properties, in addition to the extent of loading of metal complexes.

5. Experimental

5.1. General Experimental

General Use of Reagents

All glassware was cleaned with deionised water and acetone, and dried overnight in a 180 ^{o}C oven prior to use. For NP synthesis, glassware was cleaned with aqua regia, and rinsed well with milli Q water, before drying in a 180 ^{o}C oven prior to use. All anhydrous solvents were dried over 3 Å molecular sieves under $N_{2(g)}$ for 6 h. All chemical materials and solvents were purchased from Sigma Aldrich UK or Fischer.

NMR Spectroscopy

^{1}H NMR data was obtained on a Brüker AVIII300 NMR spectrometer at 300 MHz, as stated, and ^{13}C NMR data was obtained on a a Brüker AVIII400 NMR spectrometer at 101 MHz. Deuterated solvents were used, and data was processed on MestReNova, with each spectra referenced to the appropriate residual solvent peak.

MS data was obtained using micro mass liquid chromatography TOF using electrospray negative or positive, as stated.

UV-Vis Absorbance Spectroscopy

UV-Vis absorbance data was obtained on a Varian Cary 5000 spectrometer, with baseline correction for each experiment according to appropriate solvent used. 1 cm path length quartz cuvettes were used. Solid state UV-Vis spectra were acquired using the solid state attachment and zero baseline correction was used. UV-Vis spectra were plotted using Kaleidagraph software.

Absorption coefficients ε were calculated using Beer Lamberts law.

Equation 5.11

$$A = \varepsilon c L$$

$$where\ A = absorbance, c = concentration, L = path\ length$$

Drug Release Calculations from UV-Vis Absorbance Spectroscopy

Drug release was calculated through UV-Vis absorbance data, to obtain mass of **CPT** released from absorbance values of supernatant spectra. Drug release studies were plotted using Kaleidagraph and GraphPad Prism software.

Equation 5.12

$$\boldsymbol{Estimated\ mass\ of\ CPT\ loaded} = mass\ of\ CPT\ added\ to\ synthesis - excess\ CPT$$

Equation 5.13

$$\boldsymbol{Efficieny\ of\ Drug\ Loading} = \frac{Estimated\ mass\ of\ CPT\ loaded}{mass\ of\ CPT\ added\ to\ synthesis} \times 100$$

Equation 5.14

$$\boldsymbol{Mass\ of\ CPT\ loaded\ per\ mass\ of\ SiO2NP} = \frac{Estimated\ mass\ of\ CPT\ loaded}{total\ mass\ of\ \mathrm{CPT}\subset\mathrm{SiO2NP\ synthesis}}$$

Table 5.11

Calculation of mass released at 24 h (or any time point) through absorbance of supernatant taken from the release experiment.

Sample	**Supernatant Absorbance**	**Concentration of CPT/ mM**	**Moles**	**Mass**
CPT⊂SiO₂NP	Taken from graph	$c = \frac{A}{\varepsilon_{CPT\ in\ solvent} L}$	$moles = conc \times vol$	$mass = moles \times RMM_{CPT}$

Equation 5.15

$$\%\ \boldsymbol{CPT\ released\ at\ 24\ h} = \frac{mass\ of\ CPT\ released\ at\ 24\ h}{estimated\ mass\ of\ CPT\ loaded} \times 100$$

AuNP Concentration Calculations from UV-Vis Absorbance Spectroscopy

The λ SPR of **AuNP**s were used to calculate the concentrations of functionalised **AuNP**s[1]. For example:

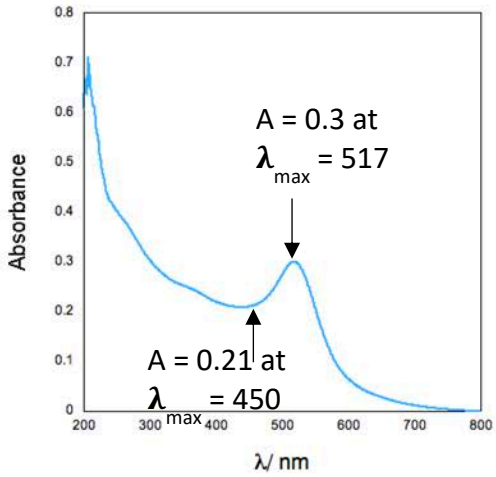


Figure 5.11

UV-Vis absorbance of stock **AuNP** after synthesis.

Equation 5.15

$$c = \frac{A_{450}}{\varepsilon_{450}}$$

$$where\ c = concentration\ of\ \boldsymbol{AuNP}\ stock\ and$$

$$\varepsilon_{450}\ has\ values\ for\ each\ AuNP\ size\ determined\ by\ TEM[1]$$

$$\varepsilon_{450} = 1.39 \times 10^{8} (d = 13\ nm), c = 1.51\ nM\ (AuNP\ stock)$$

Equation 5.16

$$c = \frac{A_{coated\ \boldsymbol{AuNP}\ at\ \lambda_{max}\ SPR}}{A_{\boldsymbol{AuNP}\ stock\ at\ \lambda_{max}\ SPR}}$$

$$where\ c = concentration\ of\ coated\ \boldsymbol{AuNP}$$

Luminescence Spectroscopy

Luminescence and excitation spectra were obtained on an Edinburgh Instruments FLSP920, Edinburgh Instruments or Photon Technology International (PTI) QM-1 luminescence spectrometer. The Edinburgh Instruments FLSP920 was fitted with a 450 W Xenon arc lamp. The detection source was an R928 visible, or NIR as stated, Hamamatsu photomultiplier tube.

Luminescence spectra were recorded using either F900 software or F980 software, and 1 cm path length quartz cuvettes were used. The PTI spectrometer was fitted with a 75 W PowerArc Xe lamp, and a Hamamatsu R928 digital photomultiplier tube as the detector (PMT). Luminescence spectra were recorded using Felix 32 software, and 1 cm path length quartz cuvettes were used.

Luminescence Quantum Yield

Luminescence quantum yield data was obtained using an integrating sphere attachment, using F980 software to process the data. 1 cm path length matched Quartz cuvettes were used. Equation below represents how the quantum yield data is obtained where η represents the data collected as per equation 5.17 and processed by the software.

Equation 5.17

$$\eta = \frac{E_s - E_r}{S_r - S_s}$$

$$where\ E = \ spectral\ scans\ of\ the\ emission\ range\ recorded\ from\ 525 - 725\ nm,$$

$$S = \ spectral\ scans\ in\ the\ excitaion\ scatter\ region\ recorded\ from\ 330 - 370\ nm\ ,$$

$$r = reference\ solvent$$

Luminescence lifetimes were obtained with the same detection sources as mentioned, and were recorded using a microsecond flashlamp. Lifetime data was recorded by the F900 software, and analysed using Edinburgh Instruments FAST software.

Nanoparticle Characterisation

DLS and Zeta Potential

DLS and Zeta potential data were acquired using Malvern Zetasizer nano ZSP. Samples were recorded using disposable 1 cm cuvettes for DLS size analysis, and a folded capillary cell for zeta potential measurements. Standard operating procedures (SOP) were used to run samples.

SEM

SEM images were obtained using XL30 ESEM-FEG (Philips) under high vacuum at 20 kV electron beam and 20000 x magnification. Samples were placed as powders on a conductive plate and coated with gold.

TEM

TEM images were obtained using JOEL 1200 EX TEM microscope. Samples were prepared *via* drying onto a 200 mesh formvar-coated copper grid.

Small angle X-ray diffraction

Small angle X-ray diffraction (SA-XRD) was carried out using Panalytical Empyrean diffractometer (Malvern Instruments Ltd, UK). This used a Cu Kα and radiation (40 kV, 40 mA). The diffraction patterns were recorded over the range 0.5° – 6° (2θ) with a 0.01 ° step.

ICP-MS

ICP-MS measurements were acquired on a 7500cx ICPMS at the University of Warwick. This technique can quantify amounts of metal (ppb) in samples by comparing ratios between Ln atoms and Au atoms. The number of Au atoms per **AuNP** can be calculated[2] as per equation 5.18, in order to calculate number of Ln complexes per **AuNP** (equation 5.19) .

Equation 5.18[2]

$$N = \frac{\pi}{6}\frac{\rho D^3}{M} N_A, N = 30.89602\ D^3$$

$$where\ N = number\ of\ atoms\ per\ \boldsymbol{AuNP}, \rho = density\ of\ gold,$$

$$D = core\ diameter\ of\ \boldsymbol{AuNP}\ taken\ from\ TEM,$$

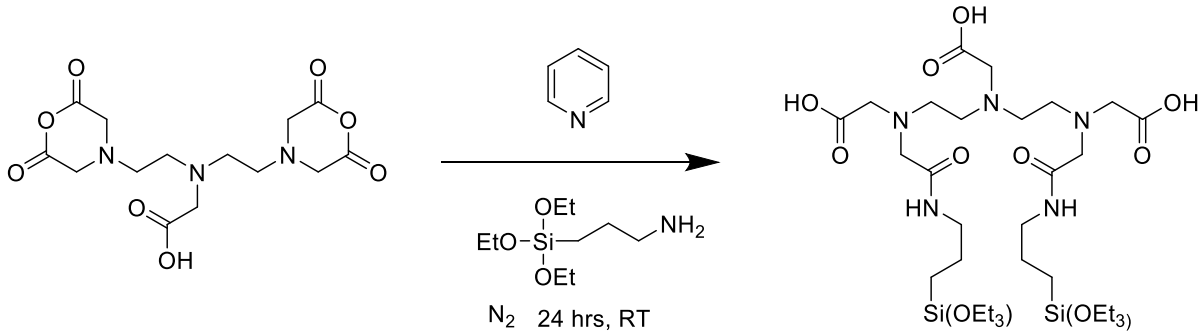
$$M = atomic\ weight\ of\ gold,\ _{N_A} = Avogadro\ constant$$

Equation 5.19

$$number\ of\ Ln\ complexes\ per\ \boldsymbol{AuNP} = \frac{N\ (N = number\ of\ atoms\ per\ \boldsymbol{AuNP})}{Au\ atoms : Eu\ atoms\ ratio}$$

5.2. Chapter 2

Ligand L – modified literature procedure from K. Taylor-Pashow *et. al.*[5]

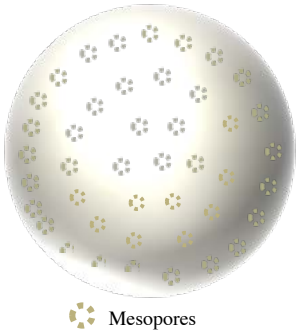


Diethylenetriaminepentaacetic acid dianhydride (2 g) was dissolved in anhydrous pyridine (44 mL) under $N_{2(g)}$. To the stirred solution, 3-aminopropyl triethoxysilane APTES (2.9 mL) was added. The solution was left to stir under $N_{2(g)}$ for 24h at room temperature. The resulting mixture was reduced down to 30 mL upon rotary evaporation. The product was precipitated using hexane (160 mL), stirred in an ice bath under $N_{2(g)}$. The product was left to precipitate further overnight in a fridge. The product was isolated via Buchner filtration and washed with hexane (5 x 40 mL) and left to air dry[5]; (4.15 g, 96%); ^{1}H NMR δ_H (300 MHz, d*6*-DMSO) 8.08 (2H, s, N*H*CO), 3.73 (12H, q, J = 6.96, OC*H*$_2$CH$_3$), 3.33 (6H, s, N*H*$_2$COOH), 3.22 (4H, s, N*H*$_2$CON), 3.04 (2H, m, J = 7.11, NC*H*$_2$Et), 2.94 (4H, t, J = 6.16, NC*H*$_2$CH$_2$N), 2.81 (4H, t, J = 6.16, NCH$_2$C*H*$_2$N), 1.45 (4H, m, J = 7.11, NCH$_2$C*H*$_2$CH$_2$), 1.14 (18H, t, J = 6.96, C*H*$_3$), 0.52 (4H, t, J = 7.5, NCH$_2$CH$_2$C*H*$_2$). ^{13}C{^{1}H} δ_C (100 MHz, d6-DMSO) 18.7, 19.0, 23.2, 41.6, 51.0, 51.4, 52.6, 55.8, 56.5, 58.2, 170.5, 173.1. MS (ES-TOF)$^-$ *m/z*: 798.4008 [M – H]$^-$.

Ln-L

Ligand **L** (0.18 mmol, 100 mg) was dissolved in tetrabutylammonium hydroxide (5 mL, 40% aqueous) and stirred for 30 min at room temperature. The Ln solution (3 equiv, 1 mL) in water was dropped into the solution and left to stir for a further 30 min at room temperature. The solution was kept in the freezer overnight to further aid precipitation and collected by suction filtration[12]. Owing to the paramagnetic nature of Ln (Ln(III) = Eu, Nd, Yb), individual assignments of proton environments for the given experimental conditions were not possible. The NMR spectra were recorded but due to the prescence of paramagnetic Ln the peaks were broad and could not be assigned. ^{1}H NMR δ_H (300 MHz, d*6*-DMSO) 3.38, 1.55, 1.31, 0.93 (**Eu-L**). 3.85, 1.54, 1.29, 0.91 (**Nd-L**). 3.15, 1.53, 1.3, 0.92 (**Yb-L**).

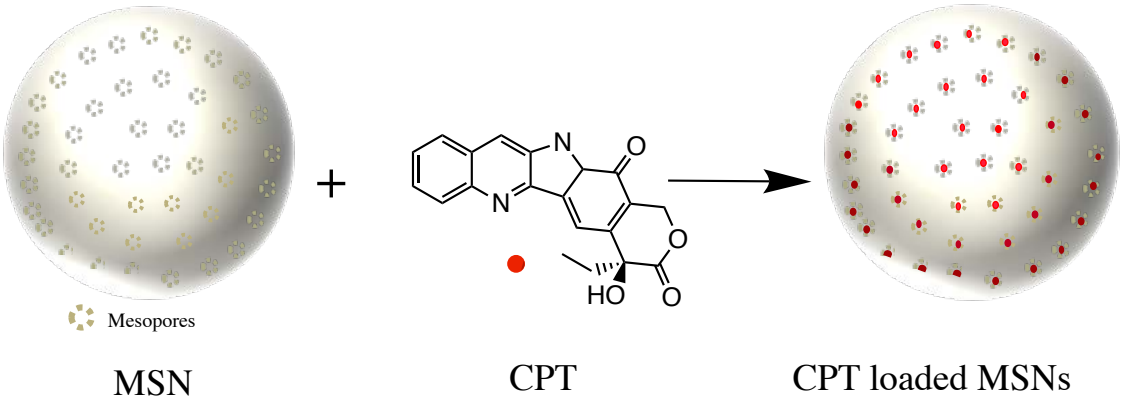
MCM-41 MSNs



MSN

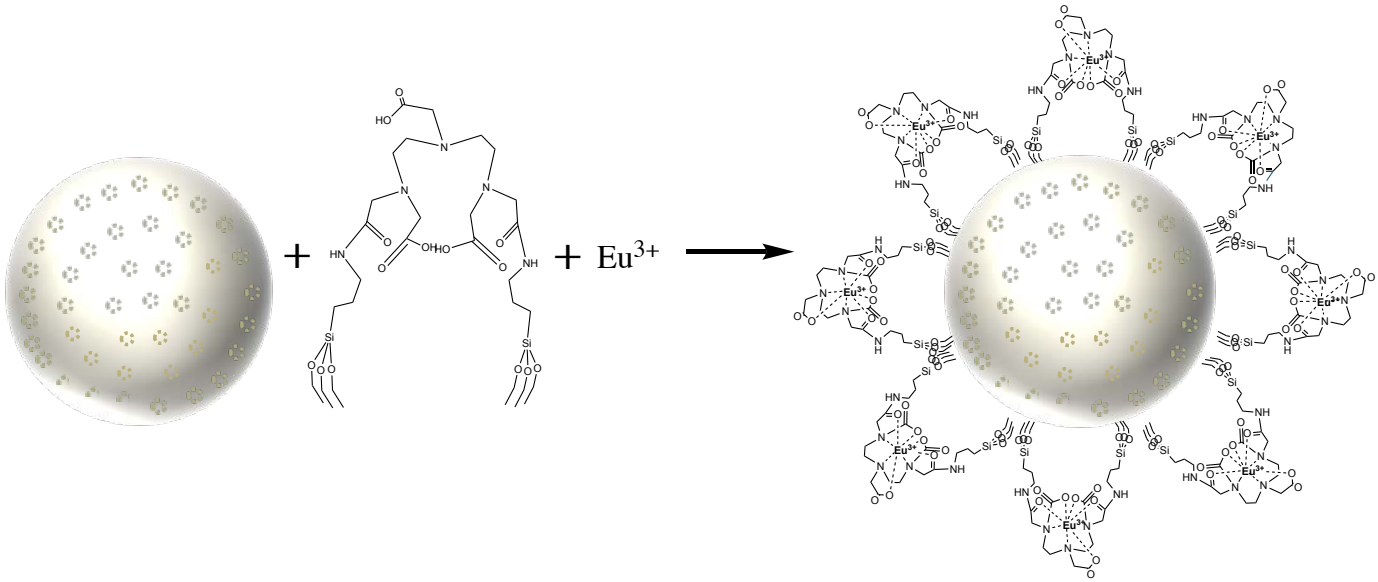
MSNs were synthesised according to the modified Stober method[6]. Aqueous NaOH solution (12.5 mM) was added to a premixed solution of ethyl trimethyl ammonium bromide (CTAB) (0.25 g) dissolved in water (120 mL), and heated to 80 ^{o}C. Tetraethoxyorthosilicate (TEOS) (1.25 mL) was dropped into the solution and the reaction was stirred for 2h. The product was centrifuged at 7830 rpm for 20 min, the supernatant was removed and the NPs were washed with water (x 3). To remove the CTAB surfactant, the collected NPs were redispersed in MeOH (50 mL) and concentrated HCl (6 mL), and left to stir at 70 ^{o}C for 24 h. The NPs were centrifuged at 7830 rpm for 20 min, washed with water (x 3), and dried under vacuum. Diameter 156 ± 29 nm (DLS intensity distribution), PDI = 0.148, ζ -34 ± 6 mV.

CPT Loaded MSNs



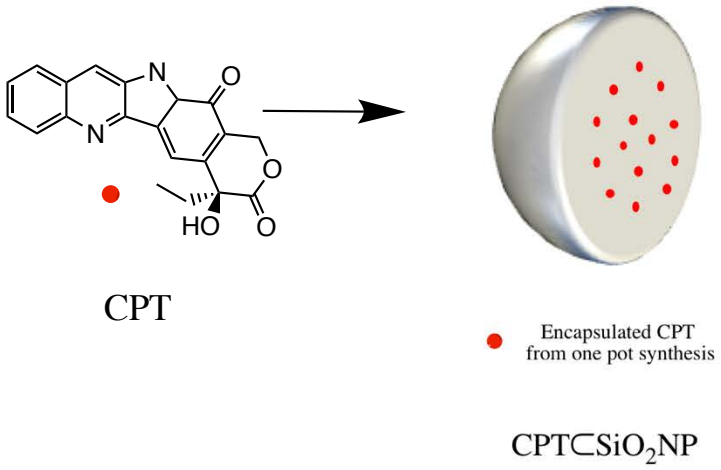
The **CPT** loading into **MSNs** was based on the ratio of TEOS : **CPT** (1 : 0.005) of **CPT0⊂SiO$_2$NP_1**. In this context, **CPT** (10 mg) and **MSNs** (220 mg) were stirred together in MeOH (10 mL) at room temperature for 24 h. The NPs were centrifuged at 7830 rpm for 20 min, washed with water (x 3), and dried under vacuum. Diameter 116 ± 17 nm (DLS intensity distribution), PDI = 0.148, ζ +9 ± 7 mV.

L.MSN



MCM-41 MSNs (0.1 g) were mixed with **L** (0.6 g, 0.8 mmol), and the mixture was refluxed in anhydrous toluene (10 mL) at 100 ^{o}C overnight. The solution was left to cool before nanoparticle collection via centrifugation. The NPs were centrifuged at 7830 rpm for 20 mins and washed with EtOH (x 3), and dried under vacuum[8]. Complexation was confirmed by luminescence spectroscopy.

CPT0⊂SiO$_2$NP_1



CPT encapsulated silica NPs were prepared according to the Stober method[9]. Ammonium hydroxide (1.5 mL, 40 mmol) was added to a premixed solution of **CPT** (16 mg mL^{-1}, 0.04 mmol, EtOH), EtOH (25 mL), and TEOS (2 mL in 5 mL EtOH, 9 mmol). The solution was stirred for 2 hrs at RT, then sonicated for 15 mins, and stirred for a further 1 h at RT. The NPs were collected by centrifugation at 7830 rpm for 20 mins and washed with water (x 3), and dried under vacuum. Diameter 83 ± 26 nm (DLS intensity distribution), PDI = 0.095, ζ -51 ± 14 mV.

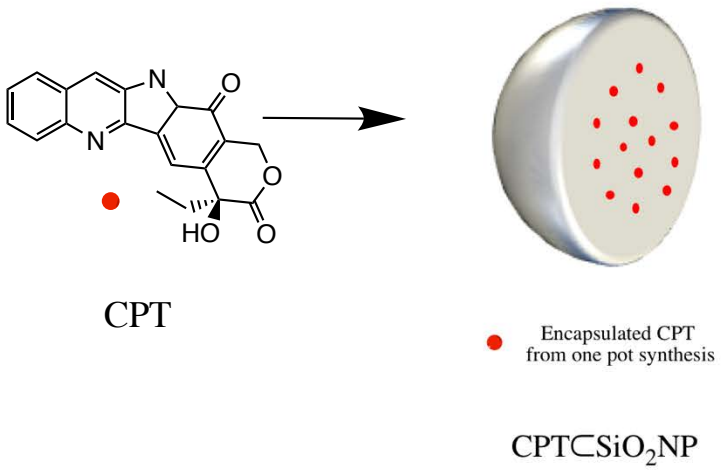
CPT3⊂SiO$_2$NP_1

CPT encapsulated silica NPs were prepared according to the Stober method[9]. Ammonium hydroxide (1.5 mL, 40 mmol) was added to EtOH (25 mL), and TEOS (2 mL in 5 mL EtOH, 9 mmol). The solution was stirred at RT, and a solution of **CPT** (16 mg mL^{-1}, 0.04 mmol, EtOH) was added after 3 hrs. The solution was left to stir overnight. The NPs were collected by centrifugation at 7830 rpm for 20 mins and washed with water (x 3), and dried under vacuum. Diameter 129 ± 49 nm (DLS intensity distribution), PDI = 0.129, ζ -42 ± 8 mV.

CPT5⊂SiO$_2$NP_1

CPT encapsulated silica NPs were prepared according to the Stober method[9]. Ammonium hydroxide (1.5 mL, 40 mmol) was added to EtOH (25 mL), and TEOS (2 mL in 5 mL EtOH, 9 mmol). The solution was stirred at RT, and a solution of **CPT** (16 mg mL^{-1}, 0.04 mmol, EtOH) was added after 5 hrs. The solution was left to stir overnight. The NPs were collected by centrifugation at 7830 rpm for 20 mins and washed with water (x 3), and dried under vacuum. Diameter 77 ± 18 nm (DLS intensity distribution), PDI = 0.028, ζ -21 ± 9 mV.

CPT0⊂SiO$_2$NP_2

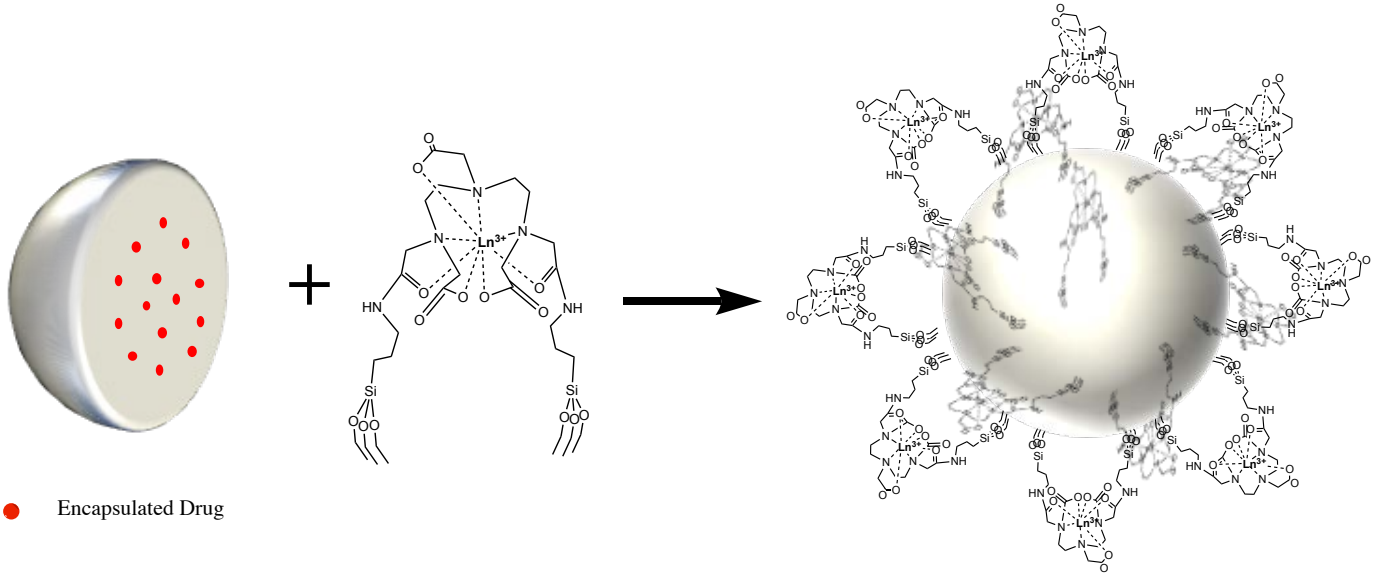


CPT encapsulated silica NPs were prepared according to the Stober method[10]. Tetraethoxyorthosilicate (TEOS) (2.4 mL, 17 mmol) was added to a premixed solution of EtOH (26.55 mL), ammonium hydroxide (1.88 mL, 48 mmol) and water (1.57 mL) stirring at 25 °C, 150 rpm. A solution of CPT (16 mg mL^{-1}, 0.04 mmol, EtOH) was added at 0 hrs and left to stir overnight at 25 °C. The NPs were centrifuged at 7830 rpm for 20 min, washed with water (x 3), and dried under vacuum). Diameter 255 ± 52 nm (DLS intensity distribution), PDI = 0.013, ζ -21 ± 7 mV.

CPT3⊂SiO$_2$NP_2

CPT encapsulated silica NPs were prepared according to the Stober method[9]. Ammonium hydroxide (1.5 mL, 40 mmol) was added to EtOH (25 mL), and TEOS (2 mL in 5 mL EtOH, 9 mmol). The solution was stirred at RT, and a solution of **CPT** (16 mg mL^{-1}, 0.04 mmol, EtOH) was added after 3 hrs. The solution was left to stir overnight. The NPs were collected by centrifugation at 7830 rpm for 20 min and washed with water (x 3), and dried under vacuum. Diameter 240 ± 48 nm (DLS intensity distribution), PDI = 0.002, ζ -17 ± 6 mV.

CPTn⊂Ln-L.SiO$_2$NP_x



Ln-L (Ln(III) = Eu, Nd and Yb) was added in excess to **CPTn⊂SiO$_2$NP_x** (n = 0 h, 3 h, x = method 1 or method 2) at a weight ratio 10 : 1, and stirred at room temperature overnight in MeOH. The NPs were collected by centrifugation at 7830 rpm for 20 min, washed with water (x 3), and dried under vacuum.

Sample	Size d/ nm Intensity Distribution	PDI	Zeta Potential ζ/ mV
CPT0⊂Eu-L.SiO$_2$NP_1	80 ± 42	0.272	-24 ± 10
CPT0⊂Nd-L.SiO$_2$NP_1	84 ± 39	0.243	-18 ± 12
CPT0⊂Yb-L.SiO$_2$NP_1	94 ± 63	0.298	-24 ± 5
CPT3⊂Eu-L.SiO$_2$NP_1	88 ± 55	0.230	-28 ± 11
CPT3⊂Nd-L.SiO$_2$NP_1	88 ± 21	0.372	-25 ± 6
CPT3⊂Yb-L.SiO$_2$NP_1	69 ± 29	0.207	-21 ± 5
CPT0⊂Eu-L.SiO$_2$NP_2	116 ± 44	0.348	-17 ± 5
CPT0⊂Nd-L.SiO$_2$NP_2	111 ± 48	0.289	-23 ± 20
CPT0⊂Yb-L.SiO$_2$NP_2	108 ± 49	0.309	-17 ± 10
CPT3⊂Eu-L.SiO$_2$NP_2	150 ± 32	0.05	-17 ± 9
CPT3⊂Nd-L.SiO$_2$NP_2	181 ± 55	0.276	-13 ± 5
CPT3⊂Yb-L.SiO$_2$NP_2	107 ± 57	0.344	-21 ± 5

Sample Preparation for SEM

SEM imaging was carried out on the following NPs. Samples were placed as powders on a carbon stub and coated with gold.

Sample	Size d/ nm
MSNs	60
CPT loaded MSNs	72
CPT0⊂SiO$_2$NP_2	95
CPT0⊂Eu-L.SiO$_2$NP_1	79
CPT0⊂Nd-L.SiO$_2$NP_1	89
CPT0⊂Yb-L.SiO$_2$NP_1	75

CPT3⊂SiO_2NP_1	79
CPT3⊂Eu-L.SiO_2NP_1	52
CPT3⊂Nd-L.SiO_2NP_1	55
CPT3⊂Yb-L.SiO_2NP_1	54
CPT5⊂SiO_2NP_1	90
CPT0⊂SiO_2NP_2	272
CPT0⊂Eu-L.SiO_2NP_2	266
CPT0⊂Nd-L.SiO_2NP_2	265
CPT0⊂Yb-L.SiO_2NP_2	283
CPT3⊂SiO_2NP_2	267
CPT3⊂Eu-L.SiO_2NP_2	241
CPT3⊂Nd-L.SiO_2NP_2	242
CPT3⊂Yb-L.SiO_2NP_2	257
Eu-L.SiO_2NP_1	78
Nd-L.SiO_2NP_1	80
Yb-L.SiO_2NP_1	72
Eu-L.SiO_2NP_2	442
Nd-L.SiO_2NP_2	355
Yb-L.SiO_2NP_2	430

Drug Loading Studies

UV-Vis absorbance of first supernatant from centrifuge wash after synthesis of **CPTn⊂SiO_2NP_x** and **CPTn⊂Ln-L.SiO_2N_x** were measured. Mass of **CPT** released was calculated using UV-Vis absorbance and **CPT** $\varepsilon_{solvent}$ (see equation 5.11 and 5.12).

Sample	CPT Released/ mg	CPT Added to Reaction/ mg	Drug Loading/ %
CPT0⊂SiO_2NP_1	4.8	16.8	71
CPT3⊂SiO_2NP_1	4.9	16.8	71
CPT0⊂SiO_2NP_2	15.3	16.7	8
CPT3⊂SiO_2NP_2	11.8	16.8	30
CPT0⊂Eu-L.SiO_2NP_1	0.2	12	98

CPT Release from CPT0⊂SiO_2NP_1 Monitored by UV-Vis Absorbance

A dispersed solution of **CPT0⊂SiO_2NP_1** (1 mg mL^{-1}, H_2O or cultured cell media as stated) was stirred at 37 °C. Aliquots of 1 mL were taken, and centrifuged at 7830 rpm for 2 mins. UV-Vis absorbance of supernatants were measured up to experiment time as stated, and returned back to the solution.

For static release, **CPT0⊂SiO_2NP_1** (1 mg mL^{-1}, H_2O or cultured cell media as stated) were kept in a stationary falcon tube at RT, or in a water bath at 37 °C as stated. Aliquots of 1 mL were taken, and centrifuged at 7830 rpm for 2 mins. UV-Vis absorbance of supernatants were measured up to experiment time as stated, and returned back to the solution.

MTT Assay – IC_{50} Determination of CPT on A549 Cells – Assisted with Dr Nik Hodges

To determine the cell viability, the MTT assay was used. Cells culture was previously carried out, maintained at 37 °C in a humidified chamber (5% CO_2, 95% air) in 75 cm^2 cell culture flasks containing of media (15 mL). Cells were seeded at 6500 cells per well in a 96-well plate in of growth medium (100 µL) (DMEM + PSG + 10% FBS), and left incubated overnight to allow attachment. The next day, media was removed and replaced with of fresh media (100 µL) containing the test compounds at different concentrations, and triplicates per sample taken into consideration. Test compounds were **CPT** dissolved in DMSO (0 – 500 nM) prepared from

1 mM stock solution and 0.1% v/v triton x-100 positive control. Cultures were incubated for 24 h and 72 h at 37 ^{o}C in a humidified chamber (5% CO_2, 95% air). Following incubation, media was removed and cells were washed with PBS (200 µL) before adding fresh media (200 µL) containing (4,5-Dimethyl-2-thiozolyl)-2,5-diphenyl-2H-tetrazolium bromide (MTT) (0.5 mg mL^{-1}), and incubated for a further 2.5 hrs at 37 ^{o}C. The media was removed carefully, and replaced with DMSO (100 µL) to dissolve the blue formazan product. The 96-well plate was rocked gently at room temperature in the dark to aid dissolution. Absorbance was measured at 570 nm using a Bio-Tek FL600 plate reader against a DMSO blank. Experiments were performed in triplicates and the relative cell viability was expressed a percentage relative to the untreated negative control cells. Data was plotted using GraphPad Prism software.

MTT Assay – Toxicity of CPT0⊂Eu-L.SiO$_2$NP_1 and CPT0⊂SiO$_2$NP_1 on A549 Cells – Assisted with Dr Nik Hodges

To determine the cell viability, the MTT assay was used. Cells culture was previously carried out, maintained at 37 ^{o}C in a humidified chamber (5% CO_2, 95% air) in 75 cm^2 cell culture flasks containing of media (15 mL). Cells were seeded at 6500 cells per well in a 96-well plate in of growth medium (100 µL) (DMEM + PSG + 10% FBS), and left incubated overnight to allow attachment. The next day, media was removed and replaced with of fresh media (100 µL) containing the test compounds at different concentrations, and triplicates per sample taken into consideration. Test compounds were **CPT0⊂Eu-L.SiO$_2$NP_1** and **Eu-L.SiO$_2$NP_1** (0 – 2 mg mL^{-1}) and **CPT1⊂SiO$_2$NP_0** and **SiO$_2$NP** (0 – 4 mg mL^{-1}), and 0.1% v/v triton x-100 positive control. Cultures were incubated for (24 h as stated) 72 h at 37 ^{o}C in a humidified chamber (5% CO_2, 95% air). Following incubation, media was removed and cells were washed with PBS (200 µL) before adding fresh media (200 µL) containing (4,5-Dimethyl-2-thiozolyl)-2,5-diphenyl-2H-tetrazolium bromide (MTT) (0.5 mg mL^{-1}), and incubated for a further 2.5 hrs at 37 ^{o}C. The media was removed carefully, and replaced with DMSO (100 µL) to dissolve the blue formazan product. The 96-well plate was rocked gently at room temperature in the dark to aid dissolution. Absorbance was measured at 570 nm using a Bio-Tek FL600 plate reader against a DMSO blank. Experiments were performed in triplicates and the relative cell viability was expressed a percentage relative to the untreated negative control cells. Data was plotted using GraphPad Prism software.

MTT Assay – IC_{50} Determination of CPT on A549 Cells at 6 hrs Incubation – Garret Rochford

To determine the cell viability, the MTT assay was used. Cells culture was previously carried out, maintained at 37 °C in a humidified chamber (5% CO_2, 95% air) in 75 cm^2 cell culture flasks containing of media (15 mL). Cells were seeded at 6500 cells per well in a 96-well plate in of growth medium (100 µL) (DMEM + PSG + 10% FBS), and left incubated overnight to allow attachment. The next day, media was removed and replaced with of fresh media (100 µL) containing the test compounds at different concentrations, and triplicates per sample taken into consideration. Test compounds were **CPT** dissolved in DMSO (0 – 128 nM) prepared from 1 mM stock solution and 0.1% v/v triton x-100 positive control. Cultures were incubated for 6 h at 37 °C in a humidified chamber (5% CO_2, 95% air) for static experiment, and 6 h rocking in an incubator outside of a humidified chamber, for shaking experiment. Following incubation, media was removed and cells were washed with PBS (200 µL) before adding fresh media (200 µL) containing (4,5-Dimethyl-2-thiozolyl)-2,5-diphenyl-2H-tetrazolium bromide (MTT) (0.5 mg mL^{-1}), and incubated for a further 2.5 hrs at 37 °C. The media was removed carefully, and replaced with DMSO (100 µL) to dissolve the blue formazan product. The 96-well plate was rocked gently at room temperature in the dark to aid dissolution. Absorbance was measured at 570 nm using a Bio-Tek FL600 plate reader against a DMSO blank. Experiments were performed in triplicates and the relative cell viability was expressed a percentage relative to the untreated negative control cells. Data was plotted using GraphPad Prism software.

MTT Assay – Toxicity of CPT0⊂Eu-L.SiO_2NP_1 and CPT0⊂SiO_2NP_1 on A549 Cells Mimicking Release Study Conditions – Garret Rochford

To determine the cell viability, the MTT assay was used. Cells culture was previously carried out, maintained at 37 °C in a humidified chamber (5% CO_2, 95% air) in 75 cm^2 cell culture flasks containing of media (15 mL). Cells were seeded at 6500 cells per well in a 96-well plate in of growth medium (100 µL) (DMEM + PSG + 10% FBS), and left incubated overnight to allow attachment. The next day, media was removed and replaced with of fresh media (100 µL) containing the test compounds at different concentrations, and triplicates (and duplicates as stated) per sample taken into consideration. Test compounds were **CPT0⊂Eu-L.SiO_2NP_1** and **Eu-L.SiO_2NP_1** (0 – 4 mg mL^{-1}) and **CPT0⊂SiO_2NP_1** and **SiO_2NP** (0 – 4 mg mL^{-1}), and 0.1% v/v triton x-100 positive control. Cultures were incubated for 6 h at 37 °C in a humidified chamber

(5% CO_2, 95% air) for static experiment, and 6 h rocking in an incubator outside of a humidified chamber, for shaking experiment. Following incubation, media was removed and cells were washed with PBS (200 µL) before adding fresh media (200 µL) containing (4,5-Dimethyl-2-thiozolyl)-2,5-diphenyl-2H-tetrazolium bromide (MTT) (0.5 mg mL^{-1}), and incubated for a further 2.5 hrs at 37 ^{o}C. The media was removed carefully, and replaced with DMSO (100 µL) to dissolve the blue formazan product. The 96-well plate was rocked gently at room temperature in the dark to aid dissolution. Absorbance was measured at 570 nm using a Bio-Tek FL600 plate reader against a DMSO blank. Experiments were performed in triplicates and the relative cell viability was expressed a percentage relative to the untreated negative control cells. Data was plotted using GraphPad Prism software.

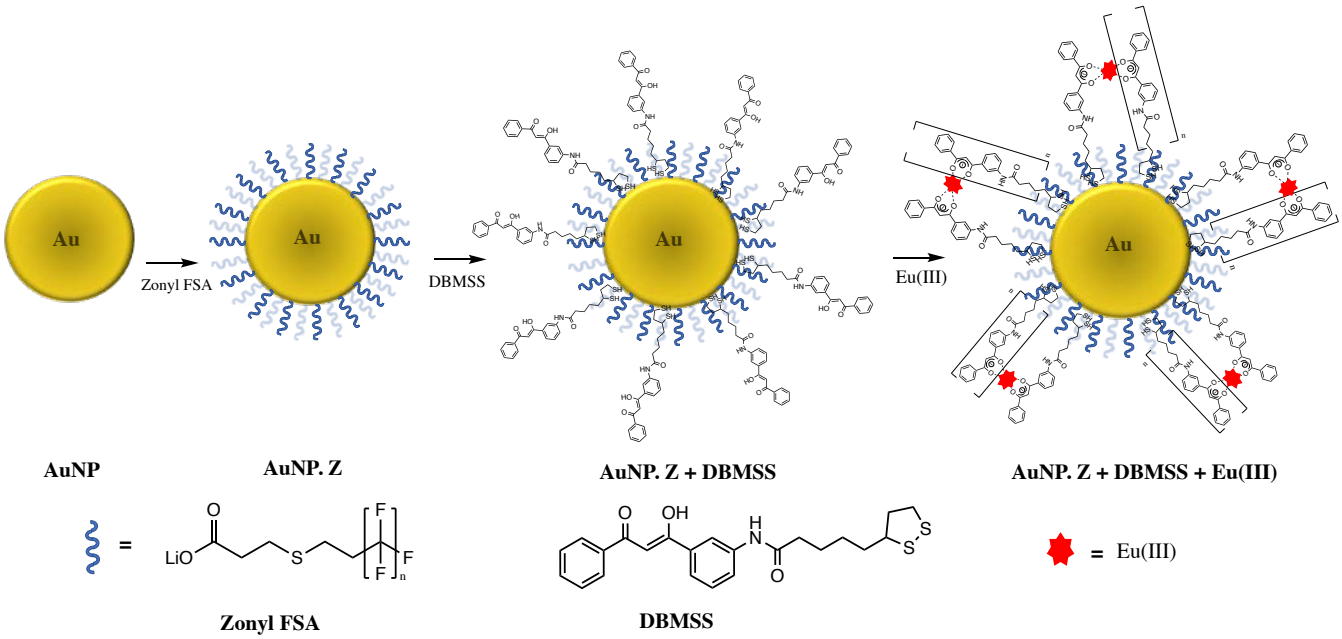
5.3. Chapter 3

DBMSS

DBMSS was synthesised by J. Lilley[12].

List of NMR data confirming synthesis of **DBMSS** performed by J Lilley, published in his thesis[12]:

i. ^{1}H NMR spectrum of **DBMSS** in d_6-DMSO
ii. ^{13}C NMR spectrum of **DBMSS** in d_6-DMSO
iii. MS $(ES\text{-}TOF)^{+}$ of DBMSS
iv. HSQC of aromatic region of **DBMSS** in d_6-DMSO
v. HSQC of aliphatic region of **DBMSS** in d_6-DMSO
vi. HMBC of DBMSS in d_6-DMSO
vii. HMBC of aromatic region of **DBMSS** in d_6-DMSO
viii. HMBC of aliphatic region of **DBMSS** in d_6-DMSO



AuNP

Preliminary experiments were carried out using **AuNP** synthesised by Irene Theofilou, used for demonstration of **AuNP** stability using Zonyl, and **DBMSS** titration onto **AuNP**. Experiments for further coating processes and photophysical characterisation were

synthesised. The protocol for synthesising 13nm AuNPs was based on a previously published method by Turkevich *et. al.*[3,4]. All the glassware was washed with aqua regia ($HCl:HNO_3$, 3:1) and dried in the oven. A solution of trisodium citrate dihydrate (60.5 mg, 0.21 mmol), citric acid (13.8 mg, 0.07 mmol) and ethylenediaminetetraacetic acid (EDTA) (1.1 mg, 0.004 mmol) in 100 mL ultrapure water was vigorously stirred and brought to reflux. After 15 minutes, a solution of preheated to 80 ^oC gold (III) chloride trihydrate ($HAuCl_4.3H_2O$) (7.9 mg, 0.02 mmol) in 25 mL ultrapure water was rapidly added. After a further 15 minutes of reflux, the heat was turned off and the solution was left to cool to room temperature forming 1.51 nM **AuNP.** λ_{max} (H_2O): 517 nm (SPR). Diameter 13 ± 3 nm (DLS number distribution), PDI = 0.154, ζ -40 ± 8 mV.

AuNP. Z

2.5 % Zonyl FSA solution in ultrapure water (10 μL) was added to 1.5 nM **AuNP** (1 mL) and stirred for 10 minutes at room temperature. This was centrifuged at 10, 000 g for 30 minutes, the supernatant was removed and the pellet was resuspended in ultrapure water (1 mL) to form **AuNP. Z,** λ_{max} (H_2O): 518 nm (SPR). Diameter 18 ± 4 nm (DLS number distribution), PDI = 0.218, ζ -35 ± 8 mV.

AuNP. Z + DBMSS (final concentration 19.5 μM DBMSS)

DBMSS treated with hydrazine (MeOH) (20 μL, 1 mM) was titrated into 0.7 nM (1 mL) solution of **AuNP. Z** and stirred for 10 minutes. λ_{max} (H_2O): 526 nm (SPR). Diameter 78 ± 28 nm (DLS number distribution), PDI = 0.171, ζ -67 ± 9 mV.

AuNP. Z + DBMSS (final concentration 10 μM DBMSS)

Deprotonated **DBMSS** (MeOH) (10 μL, 1 mM) was titrated into 0.7 nM (1 mL) solution of **AuNP. Z** and stirred for 10 minutes. λ_{max} (H_2O): 525 nm (SPR).

AuNP. Z + DBMSS + Eu(III) (final concentration 19.5 μM DBMSS + 3.3 μM Eu(III))

Eu(III) (MeOH) (20 mL, 0.2 mM) was titrated into 0.85 nM (1 mL) solution of **AuNP. Z + DBMSS**, pH adjusted to 9, and stirred for 10 minutes. λ_{max} (H_2O): 527 nm (SPR). Diameter 88 ± 34 nm (DLS number distribution), PDI = 0.184, ζ -52 ± 10 mV.

AuNP. Z + DBMSS + Eu(III) (final concentration 10 μM DBMSS + 3.3 μM Eu(III))

Eu(III) (MeOH) (20 mL, 0.2 mM) was titrated into 0.85 nM (1 mL) solution of **AuNP. Z + DBMSS,** pH adjusted to 9, and stirred for 10 minutes. λ_{max} (H_2O): 525 nm (SPR).

AuNP. Z. DBMSS

AuNP. Z + DBMSS (0.7 nM **AuNP. Z** + 19.5 μM **DBMSS** + 3.3 mM **Eu(III)** was purified using column chromatography with Sephadex G10. The collected NPs were named **AuNP. Z. DBMSS** (0.9 nM, 1 mL, H_2O).

AuNP. Z. DBMSS + Eu(III)

Eu(III) (MeOH) (20 mL, 0.2 mM) was titrated into 0.9 nM (1 mL) solution of **AuNP. Z. DBMSS,** pH adjusted to 9, and stirred for 10 minutes. λ_{max} (H_2O): 525 nm (SPR).

ICPMS of AuNP. Z + DBMSS + Eu(III) (final concentration 19.5 μM DBMSS + 3.3 μM Eu(III))

– Sample digestion carried out by J. Bradley

ICPMS data of ***AuNP. Z + DBMSS + Eu(III)*** was collected in triplicates to give an average number of Eu(III) complexes per NP. See equations 5.18 and 5.19 in section 5.1.

Table 5.31

Table summarising data collected from ICPMS of ***AuNP. Z + DBMSS + Eu(III) (final concentration 19.5 mM DBMSS + 3.3 mM Eu(III))***

Measurement Runs	**Au Atoms/ ppb**	**Eu Atoms/ ppb**	**Au : Eu Atoms** $= \frac{Au\ atoms}{Eu\ toms}$	**Au Atoms per NP** See equation 5.18	**Eu(III) Complexes per NP** $= \frac{Au\ atoms\ per\ NP}{Au{:}\,Eu\ ratio}$
1	505	26	20	N = 30.9 x d^3 (67880)	3445
2	605	26	24	67880	2865
3	511	24	21	67880	3170

Sample Preparation for TEM

TEM imaging was carried out on **AuNPs** and coated NPs with **DBMSS** and Eu(III). For all samples, 20 μL was added to a 200 mesh formvar coated copper grid, and left to dry overnight: **AuNP** (1.5 nM), **AuNP. Z** (0.7 nM), **AuNP. Z + DBMSS** (19.5 μM **DBMSS**) (0.85 nM), **AuNP. Z + DBMSS + Eu(III)** (19.5 μM **DBMSS**) (0.8 nM).

AuNP. PEG-SH – AuNP were provided by I. Theofilou

10 μL PEG-SH (1 mM) was added to **AuNP** (1.1 nM, 1 mL, H_2O) and stirred for 30 minutes at room temperature. This was centrifuged at 10, 000g for 30 minutes, the supernatant was removed and the pellet was resuspended in ultrapure water (1 mL) to form **AuNP. PEG-SH.** λ_{max} (H_2O): 518 nm (SPR). Diameter 16 ± 5 nm (DLS number distribution), PDI = 0.235.

AuNP. PEG-SH + DBMSS ((final concentration 24 μM DBMSS)

DBMSS treated with hydrazine (MeOH) (25 μL, 1 mM) was titrated into **AuNP. PEG-SH** (1.8 nM, 1 mL, H_2O) and stirred for 10 minutes. λ_{max} (H_2O): 524 nm (SPR). Diameter 107 ± 40 nm (DLS number distribution), PDI = 0.216.

5.4. Referenced Material

1. W. Haiss, N. Thanh, J. Aveyard and D. Fernig, *Anal. Chem.,* 2007, **79**, 4215-4221
2. J. Shang and Z Gao, *Chem. Soc. Rev.,* 2014, **43**, 7267-7278
3. N. Rogers, H. Jeffery, S. Claire, D. Lewis, G. Zikeli, N. Hodges, S. Egginton, G. Nash and Z. Pikramenou, *Nanomedicine.,* 2017, **22**, 2725-2740
4. F. Shculz, T. Homolka, N. Bastus, V. Puntes, H. Weller and T. Vossmeyer, *Langmuir.,* 2014, **35**, 10779-10784
5. K. Taylor-Pashow, J. D. Rocca and W. Lin, *Nanomaterials.,* 2012, **2**, 1-14
6. M. Varache, I. Bezverkhyy, L. Saviot, F. Bouyer, F. Baras and F. Bouyer, *J. Non-Cryst. Solids.,* 2015, **408**, 87-97
7. A. Paula, R. Junior, D. Martinez, E. Paredes-Gamero, H. Nader, N. Duran, G. Justo and O. Alves, *ACS Appl. Mater. Interfaces.,* 2013, **5**, 8387-8393
8. M. Laprise-Pelletier, M. Bouchoucha, J. Lagueux, P. Chevallier, R. Lecomte, Y. Gossuin, F. Kleitz and M. A. Fortin., J. Mater. Chem. B., 2015, **3**, 748-758
9. L. Rossi, L. Shi, F. Quina and Z. Rosenzweig, *Langmuir.,* 2005, **21**, 4277-4280
10. D. Zhang, Z. Wu, J. Xu, J. Liang, J. Li and W. Yang, *Langmuir.,* 2010, **26**, 6657-6662
11. J. Lilley Thesis, University of Birmingham, 2013
12. L. Rossi, L. Shi, N. Rosenzweig and Z. Rosenzweig, *Biosens. Bioelectron.,* 2006, **21**, 1900-1906

v. Appendix

List of Appendicies

1. MS(ES-TOF)$^-$ of **L.**
2. ^{1}H and ^{13}C NMR of **L.**
3. ^{1}H NMR of **Eu-L.**
4. ^{1}H NMR of **Nd-L**.
5. ^{1}H NMR of **Yb-L.**
6. DLS analsysis and zeta potential of **MSNs**.
7. DLS analsysis and zeta potential of **CPT loaded MSNs**.
8. UV-Vis absorbance comparsion of **CPT** and **CPT loaded MSNs**.
9. SAXRD of **L.MSN** and **CPT loaded MSNs**.
10. **CPT** ε_{MeOH}.
11. **CPT** ε_{H2O}
12. **CPT** ε_{EtOH}.
13. DLS analsysis and zeta potential of **CPT0⊂SiO$_2$NP_1.**
14. Zeta potential of **SiO$_2$NP.**
15. DLS analsysis and zeta potential of **CPT0⊂Eu-L.SiO$_2$NP_1.**
16. DLS analsysis and zeta potential of **CPT0⊂Nd-L.SiO$_2$NP_1.**
17. DLS analsysis and zeta potential of **CPT0⊂Yb-L.SiO$_2$NP_1.**
18. Comparison of **CPT0⊂Ln-L.SiO$_2$NP_1** excitation spectra to **CPT** UV-Vis absorbance.
19. DLS analsysis, zeta potential, and SEM of **Eu-L.SiO$_2$NP_1.**
20. DLS analsysis, zeta potential, and SEM of **Nd-L.SiO$_2$NP_1.**
21. DLS analsysis, zeta potential, and SEM of **Yb-L.SiO$_2$NP_1.**
22. Emission scatter of plain **SiO$_2$NP.**
23. DLS analsysis and zeta potential of **CPT3⊂SiO$_2$NP_3.**
24. DLS analsysis and zeta potential of **CPT3⊂Eu-L.SiO$_2$NP_1.**
25. DLS analsysis and zeta potential of **CPT3⊂Nd-L.SiO$_2$NP_1.**
26. DLS analsysis and zeta potential of **CPT3⊂Yb-L.SiO$_2$NP_1.**
27. DLS analsysis and zeta potential of **CPT0⊂SiO$_2$NP_2.**
28. DLS analsysis and zeta potential of **CPT0⊂Eu-L.SiO$_2$NP_2.**

29. DLS analsysis and zeta potential of **CPT0⊂Nd-L.SiO_2NP_2.**
30. DLS analsysis and zeta potential of **CPT0⊂Yb-L.SiO_2NP_2.**
31. DLS analsysis and zeta potential of **CPT3⊂SiO_2NP_2.**
32. DLS analsysis and zeta potential of **CPT3⊂Eu-L.SiO_2NP_2.**
33. DLS analsysis and zeta potential of **CPT3⊂Nd-L.SiO_2NP_2.**
34. DLS analsysis and zeta potential of **CPT3⊂Yb-L.SiO_2NP_2.**
35. DLS analsysis, zeta potential, and SEM of **Eu-L.SiO_2NP_2.**
36. DLS analsysis, zeta potential, and SEM of **Nd-L.SiO_2NP_2.**
37. DLS analsysis, zeta potential, and SEM of **Yb-L.SiO_2NP_2.**
38. Preliminary release studies from **CPT3⊂SiO_2NP_1.**
39. Preliminary release studies from **CPT5⊂SiO_2NP_1.**
40. DLS analsysis, zeta potential, and SEM of **CPT5⊂SiO_2NP_1.**
41. Preliminary release studies from **CPT loaded MSNs.**
42. **DBMSS** ε_{MeOH}.
43. DLS analysis and zeta potential of **AuNP.**
44. DLS analysis and zeta potential of **AuNP. Z**.
45. DLS analysis and zeta potential of **AuNP. Z + DBMSS** (final concentration of 19.5 μM **DBMSS**).
46. DLS analysis and zeta potential of **AuNP. Z + DBMSS + Eu(III)** (final concentration of 19.5 μM **DBMSS** + 3.3 μM Eu(III)).
47. Table summarising ICP-MS values.
48. UV-Vis absorbance and excitation overlap of **DBMSS + Eu(III)** and **AuNP. Z + DBMSS + Eu(III).**
49. Lifetimes of **DBMSS + Eu(III)** at different ratios.
50. Preliminary studies of changes in UV-Vis absorption upon addition of **DBMSS** to **AuNP. PEG-SH.**
51. DLS analysis and zeta potential of **AuNP** (provided by I. Theofilou).
52. DLS analysis and zeta potential of **AuNP. PEG-SH.**
53. DLS analysis and zeta potential of **AuNP. PEG-SH + DBMSS** (final concentration of 24 μM **DBMSS**)

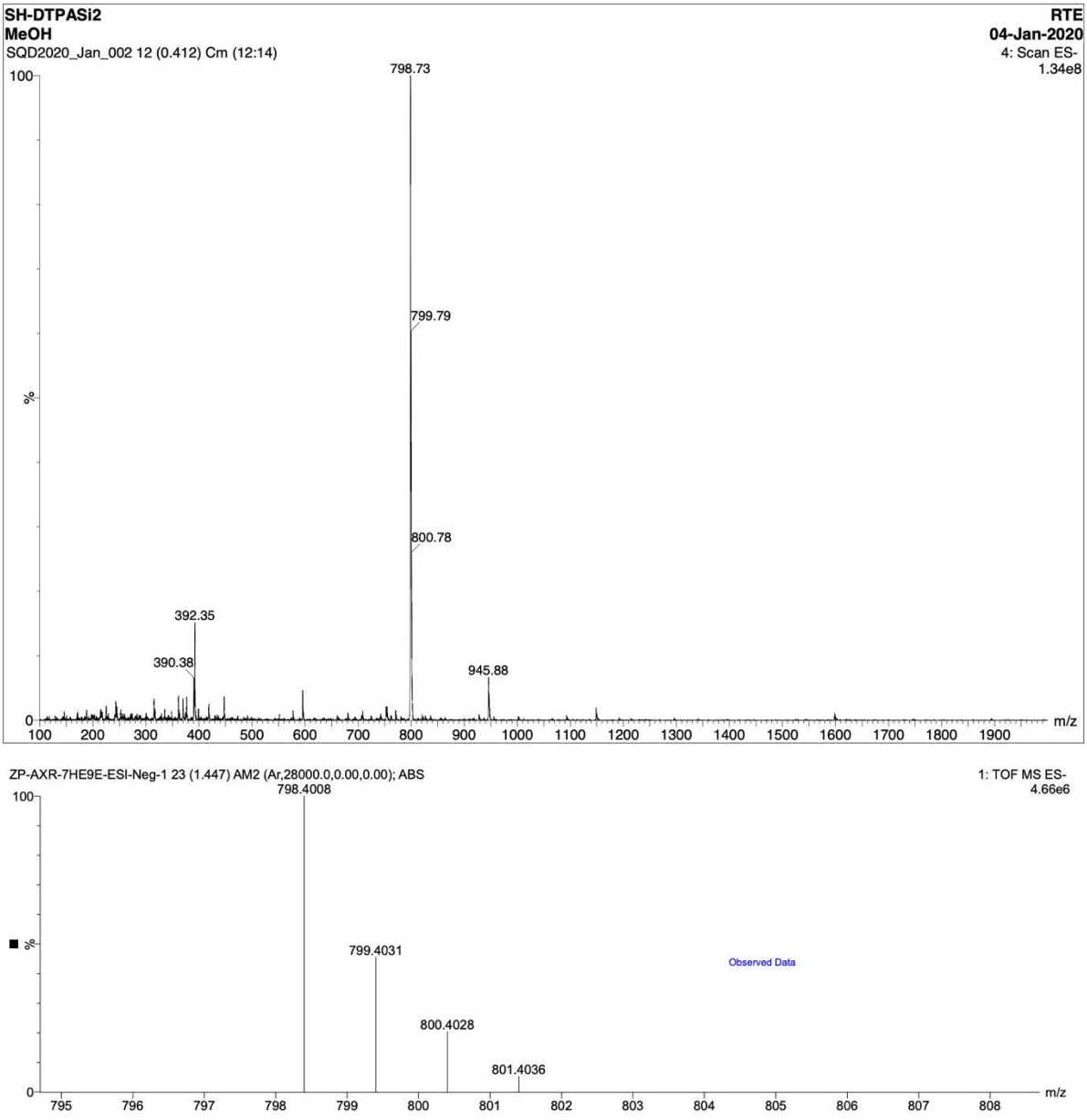


Figure 1

Mass spectrum of **L.** Accurate mass spectrum taken by Asier Rodriguez-Muguruza.

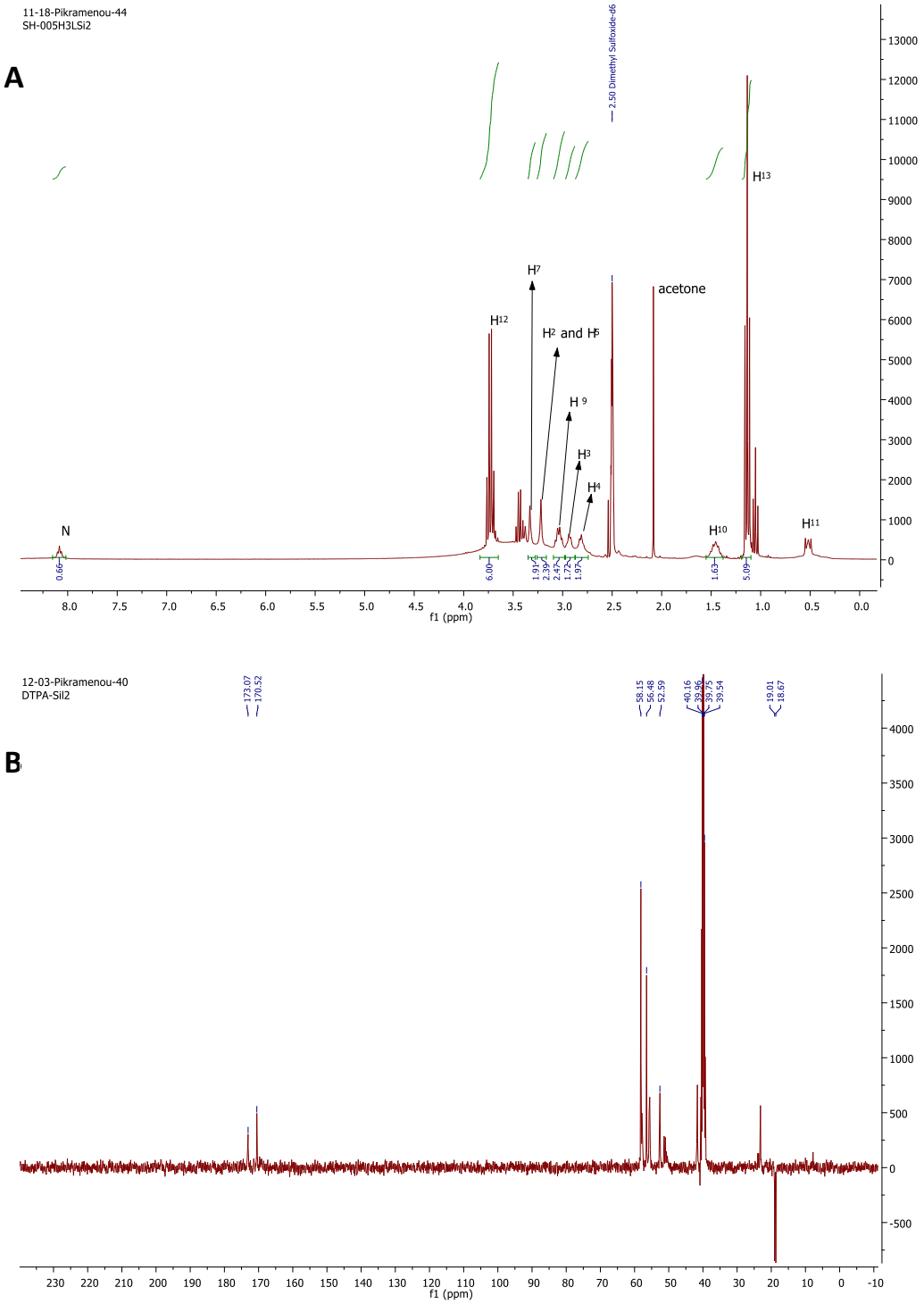


Figure 2

A: The 300 MHz ^{1}H NMR spectrum of **L** recorded in d*6*-DMSO. The solvent peak at 2.54 ppm is formed by DMSO C*H*$_3$. The solvent peak at 2.08 ppm arises from acetone traces, and the peak at 1.05 ppm arises from ethanol traces. B: The ^{13}C NMR spectrum of **L** recorded in d*6*-DMSO.

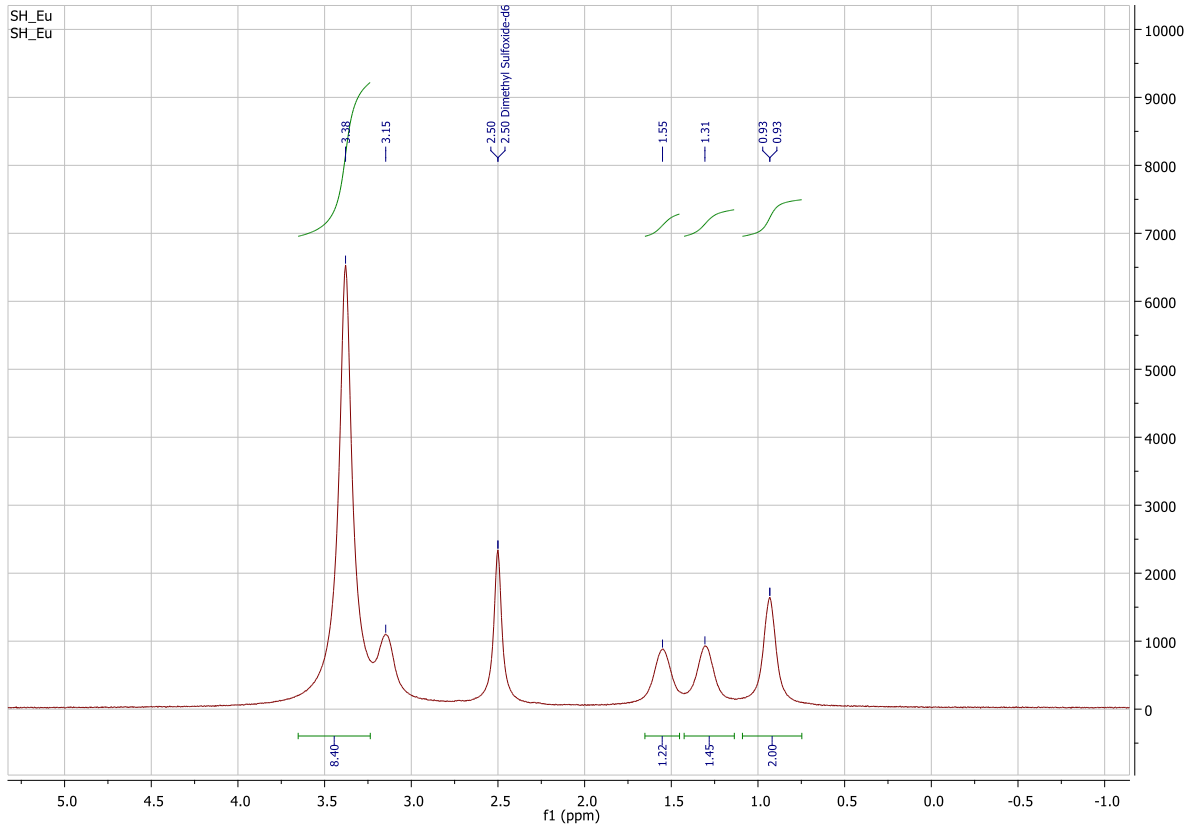


Figure 3

The 300 MHz ^{1}H NMR spectrum of **Eu-L** recorded in d*6*-DMSO. The solvent peak at 2.54 ppm is formed by DMSO C*H*$_3$. The solvent peak at 3.3 ppm arises from residual water.

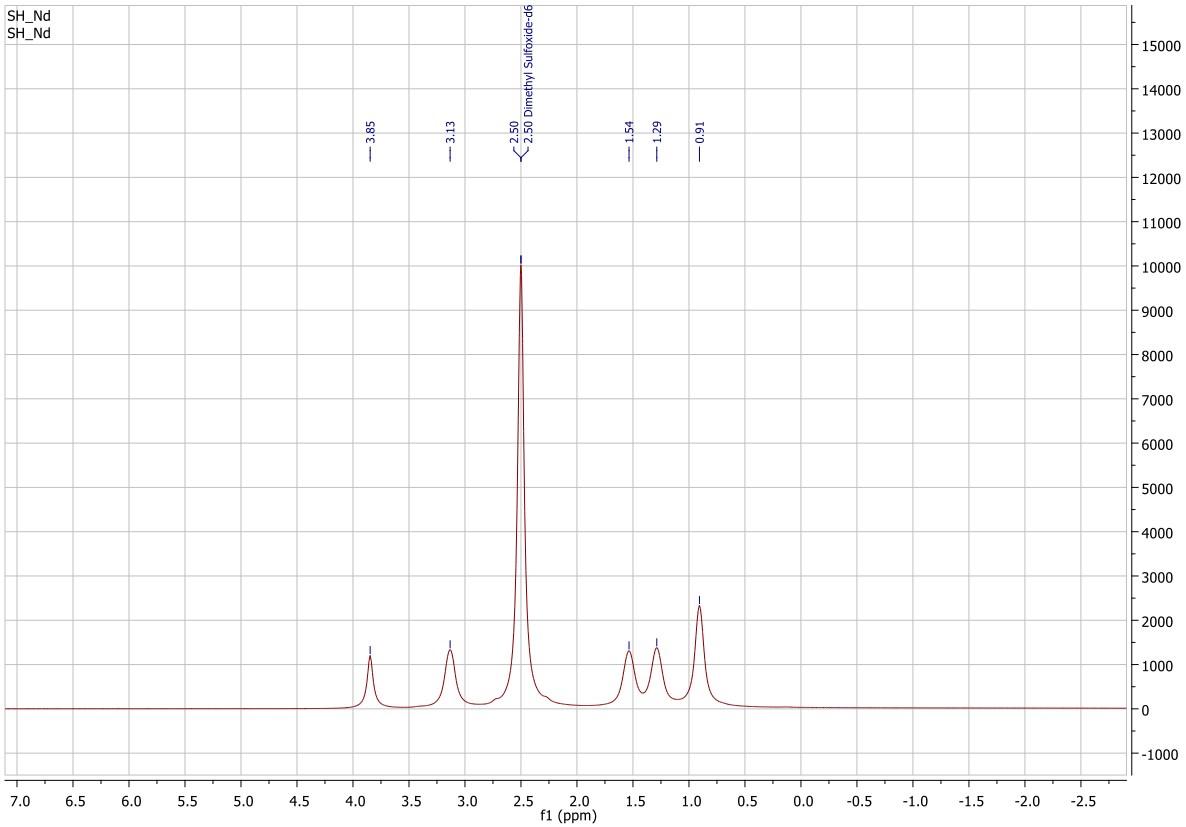


Figure 4

The 300 MHz ^{1}H NMR spectrum of **Nd-L** recorded in d*6*-DMSO. The solvent peak at 2.54 ppm is formed by DMSO CH_3. The solvent peak at 3.3 ppm arises from residual water.

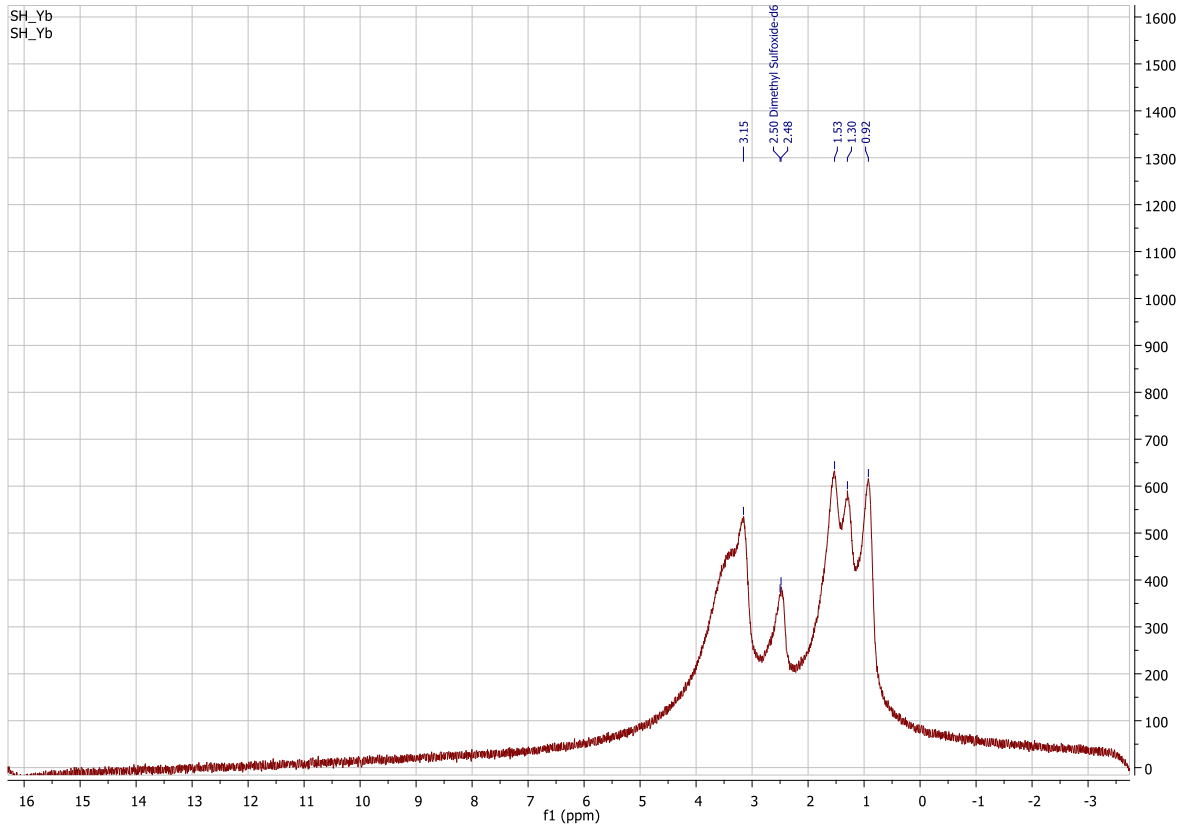


Figure 5

The 300 MHz ^{1}H NMR spectrum of **Eu-L** recorded in d*6*-DMSO. The solvent peak at 2.54 ppm is formed by DMSO C*H*$_3$. The solvent peak at 3.3 ppm arises from residual water.

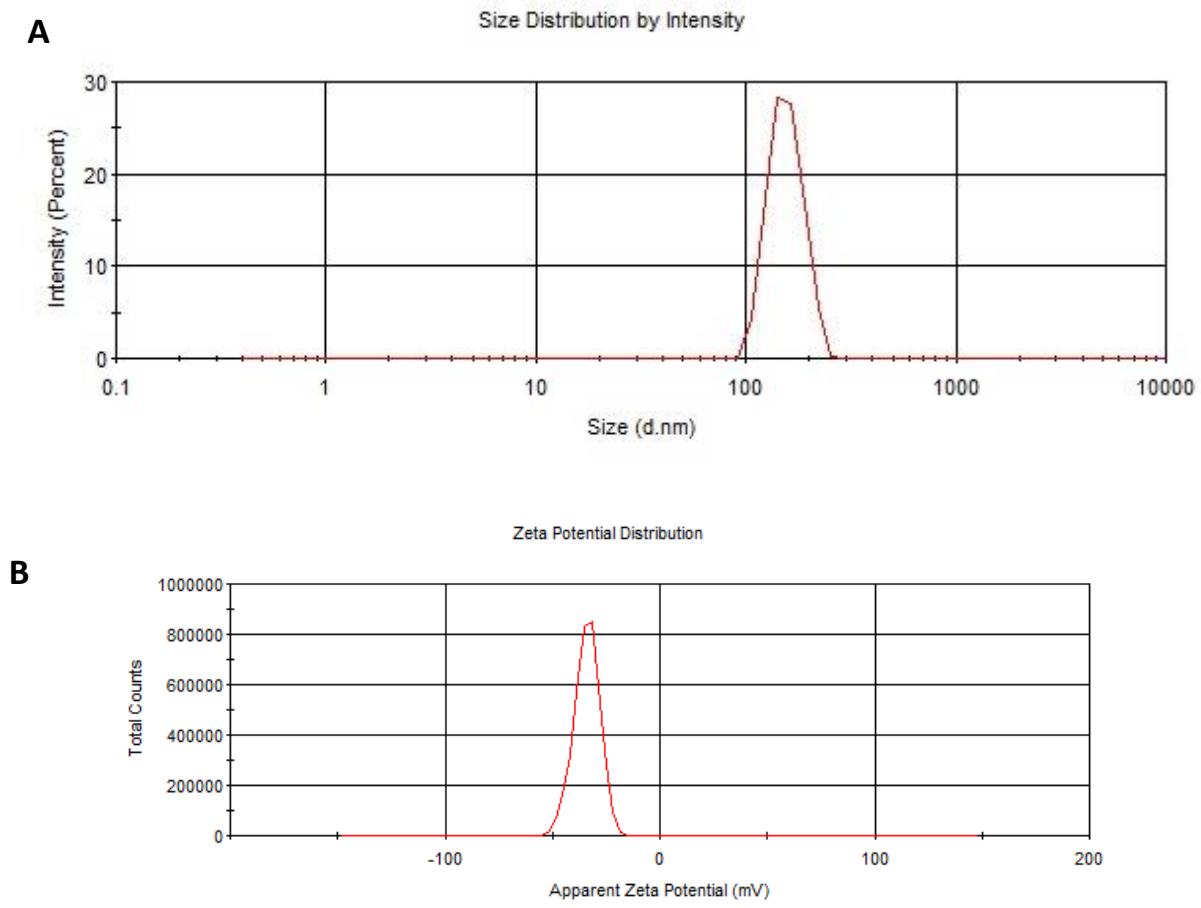
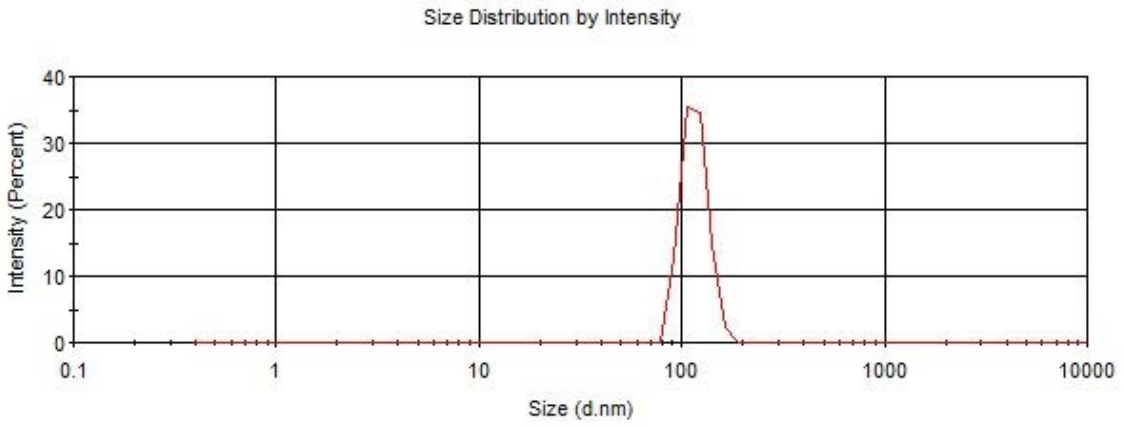


Figure 6

DLS analysis of **MSNs** (H_2O). A: Size distribution by intensity graph, 156 nm, PDI = 0.148. C: Zeta potential measurement ζ, -34 mV.

A



B

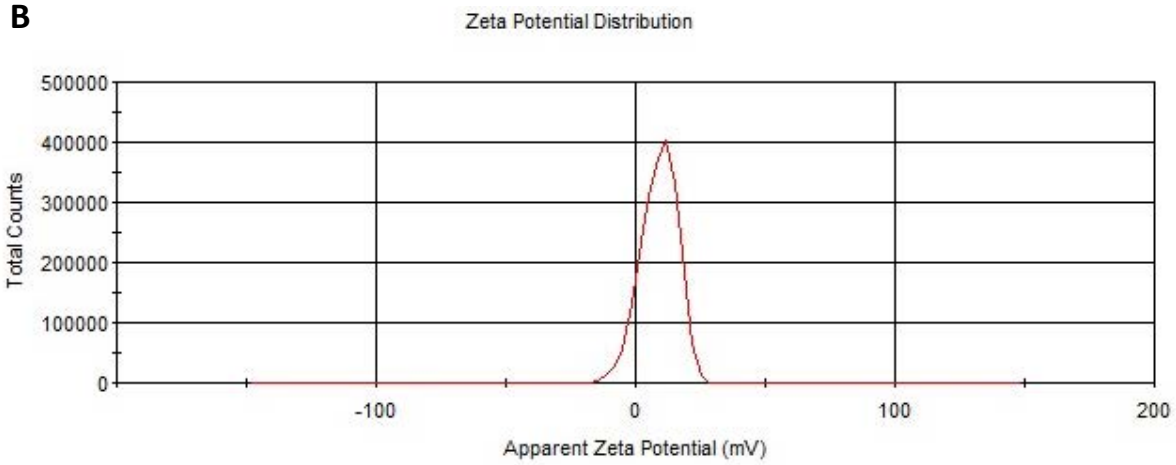


Figure 7

DLS analysis of **CPT loaded MSNs** (H_2O). A: Size distribution by intensity graph, 116 nm, PDI = 0.518. C: Zeta potential measurement ζ, +9 mV.

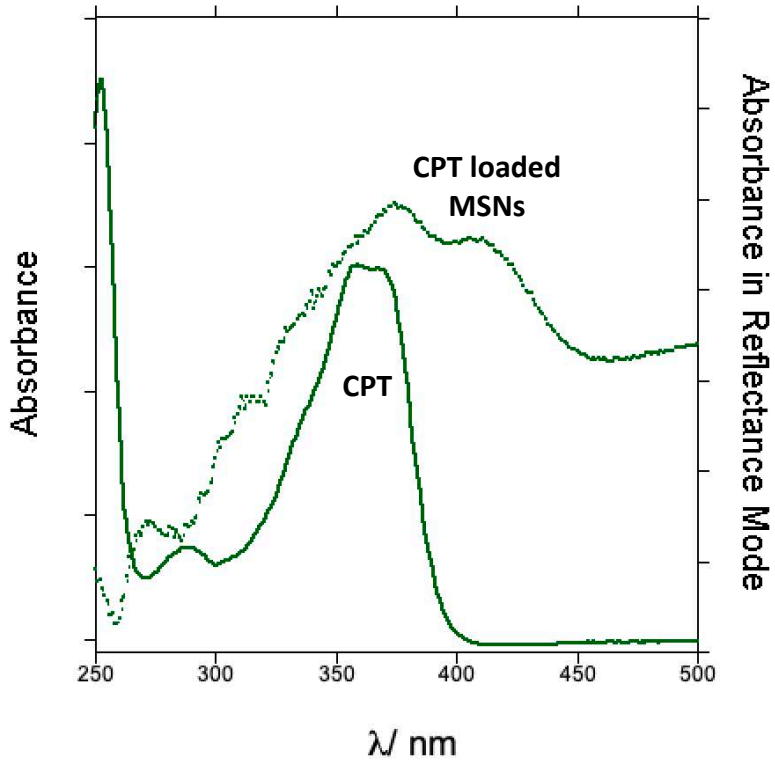


Figure 8

UV-Vis absorbance comparison of **CPT** (30 μM, MeOH) and **CPT loaded MSNs** (solid state).

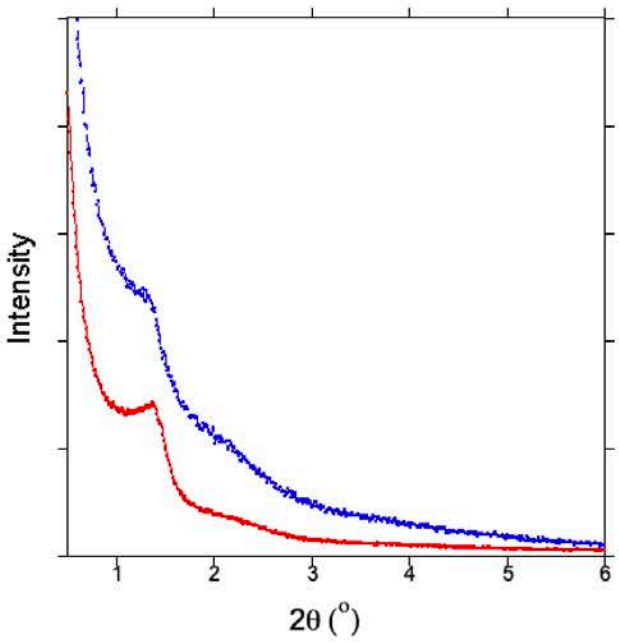


Figure 9

SAXD patterns of **L.MSN** (blue) and **CPT** loaded **MSNs** (red).

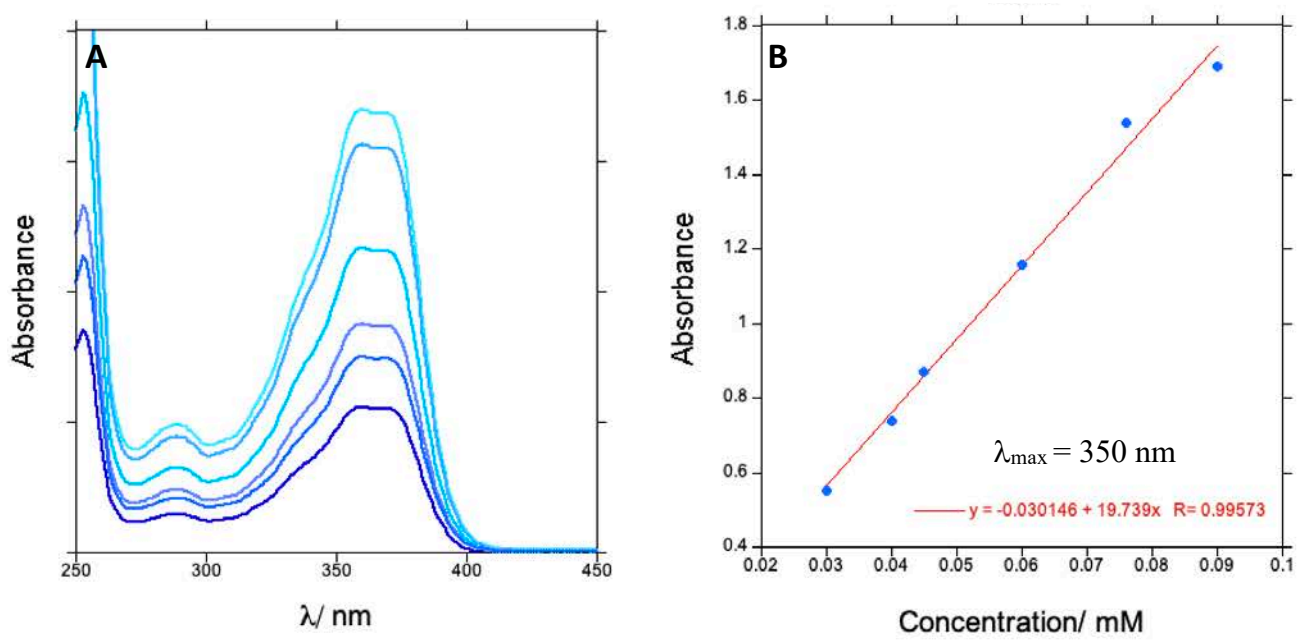


Figure 10

UV-Vis absorbance of **CPT** in MeOH to calculate the absorption coefficient ε using Beer Lambert's law. A: UV-Vis spectrum of **CPT** (0.03 mM, 0.04 mM, 0.045 mM, 0.06 mM, 0.076 mM and 0.09 mM, MeOH). B: Plot of absorption against concentration at λ_{max} = 350 nm, resulting in ε = 20000 mol^{-1} dm^3 cm^{-1}.

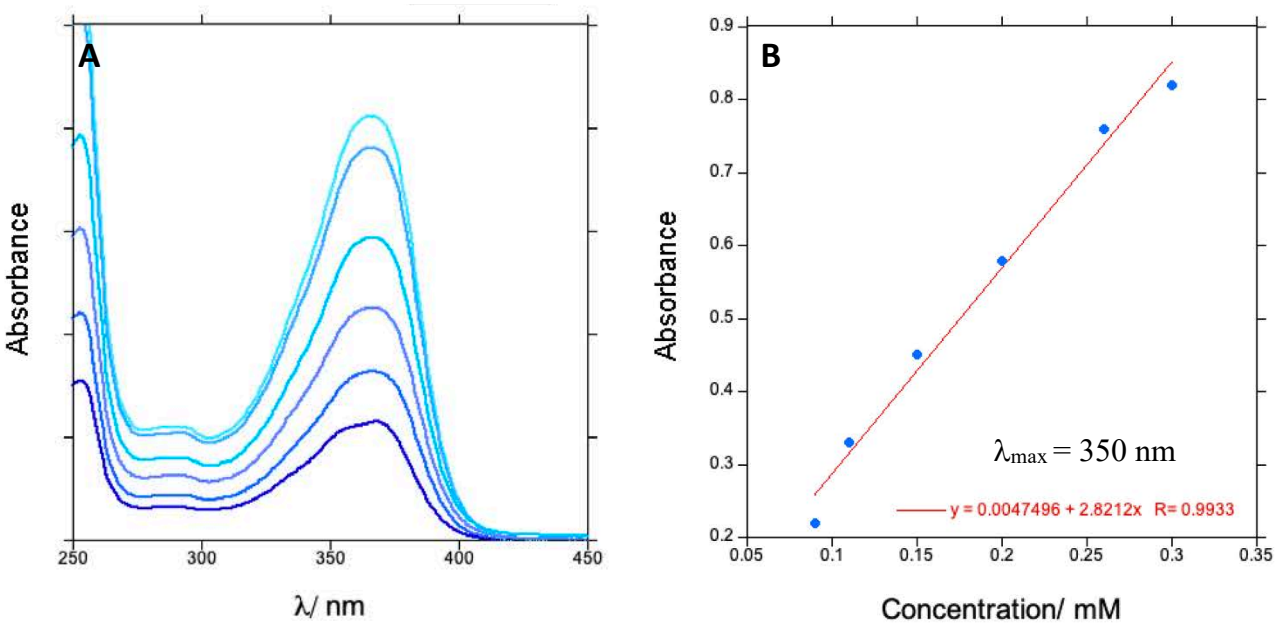


Figure 11

UV-Vis absorbance of **CPT** in H_2O to calculate the absorption coefficient ε using Beer Lambert's law. A: UV-Vis spectrum of **CPT** (0.09 mM, 0.1 mM, 0.15 mM, 0.2 mM, 0.26 mM and 0.3 mM, H_2O). B: Plot of absorption against concentration at λ_{max} = 350 nm, resulting in ε = 3000 mol^{-1} dm^3 cm^{-1}.

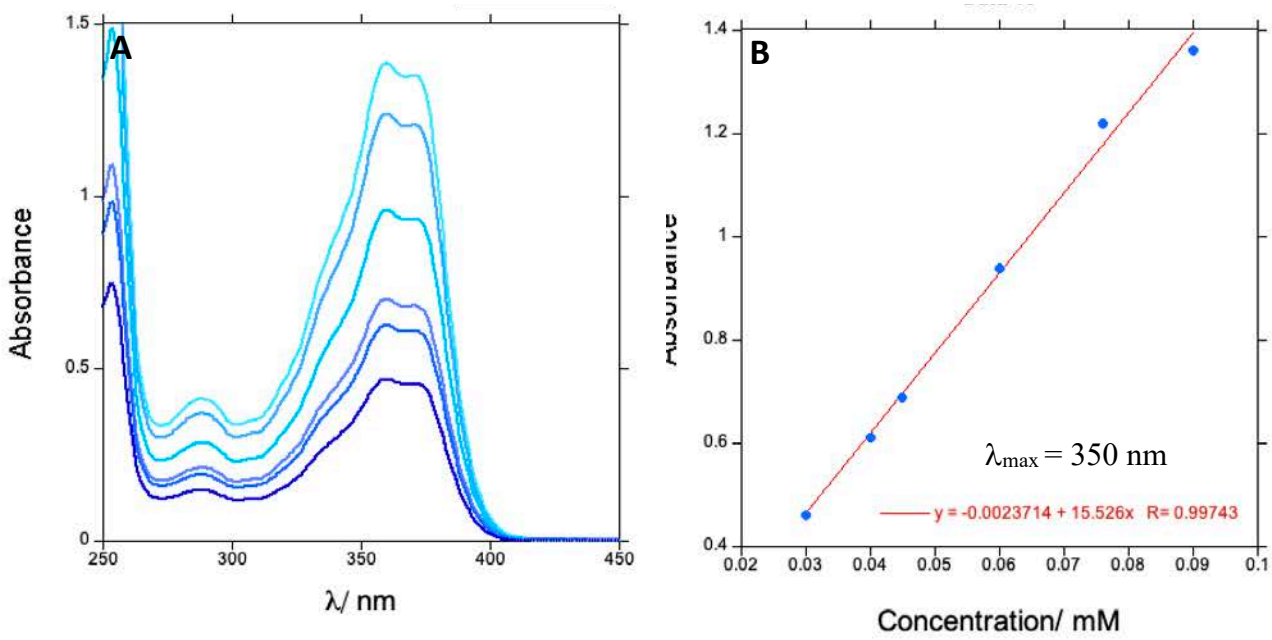


Figure 12

UV-Vis absorbance of **CPT** in EtOH to calculate the absorption coefficient ε using Beer Lambert's law. A: UV-Vis spectrum of **CPT** (0.03 mM, 0.04 mM, 0.045 mM, 0.06 mM, 0.076 mM and 0.09 mM, EtOH). B: Plot of absorption against concentration at λ_{max} = 350 nm, resulting in ε = 16000 mol^{-1} dm^3 cm^{-1}.

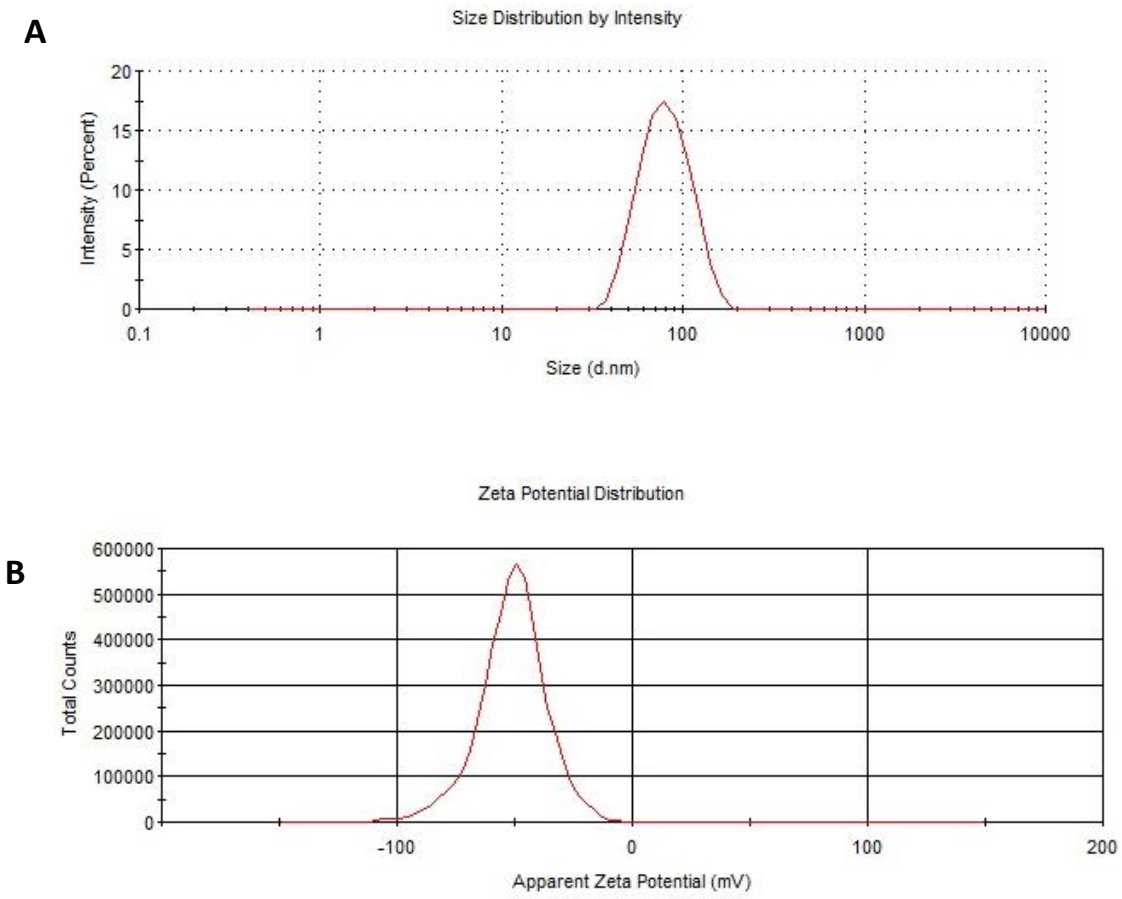


Figure 13

DLS analysis of **CPT0⊂SiO$_2$NP_1** (H_2O). A: Size distribution by intensity graph, 83 nm, PDI = 0.095. B: Zeta potential measurement z, -51 mV.

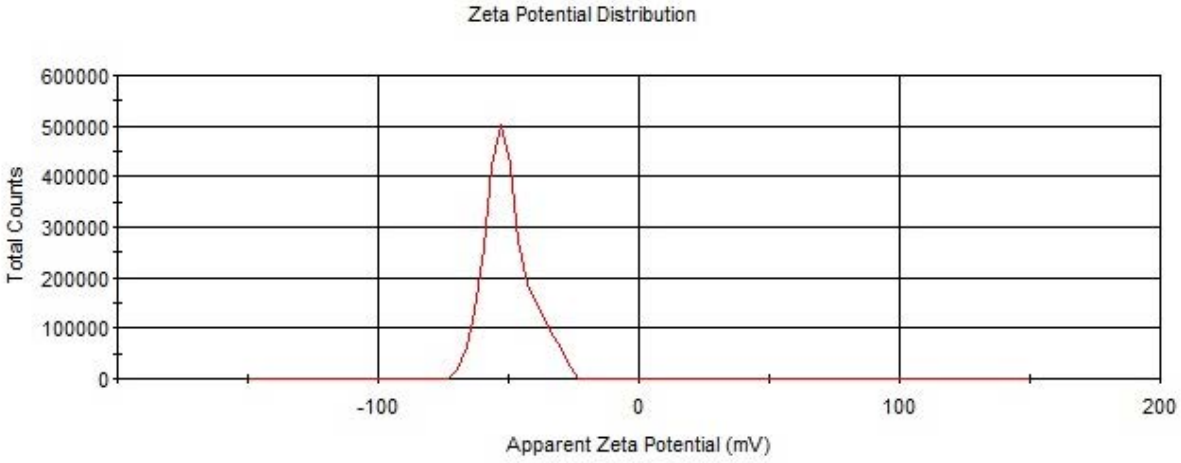


Figure 14

Zeta potential measurement ζ of **SiO_2NP** (H_2O), -50 mV.

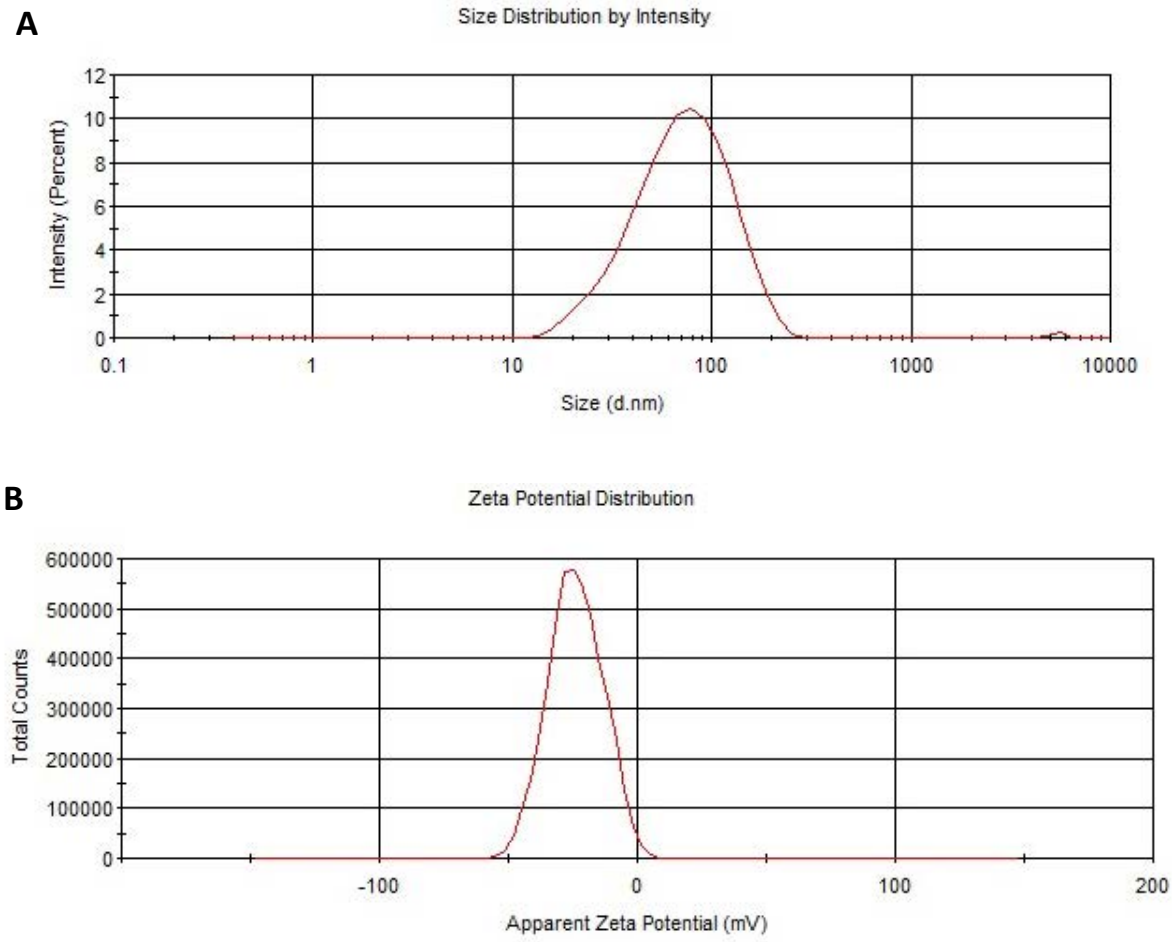


Figure 15

DLS analysis of **CPT0⊂Eu-L.SiO$_2$NP_1** (H_2O). A: Size distribution by intensity graph, 80 nm, PDI = 0.272. B: Zeta potential measurement ζ, -24 mV.

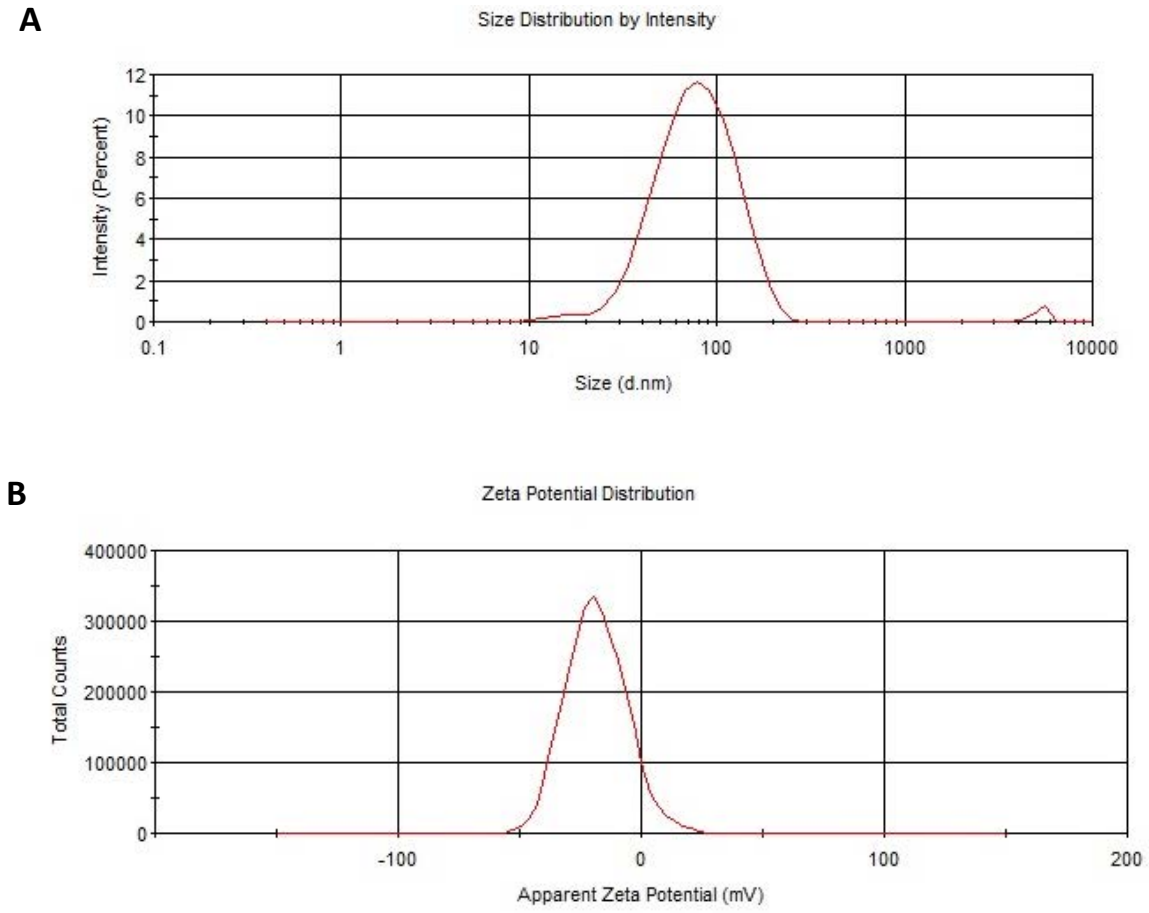


Figure 16

DLS analysis of **CPT0⊂Nd-L.SiO$_2$NP_1** (H_2O). A: Size distribution by intensity graph, 84 nm, PDI = 0.243. B: Zeta potential measurement ζ, -18 mV.

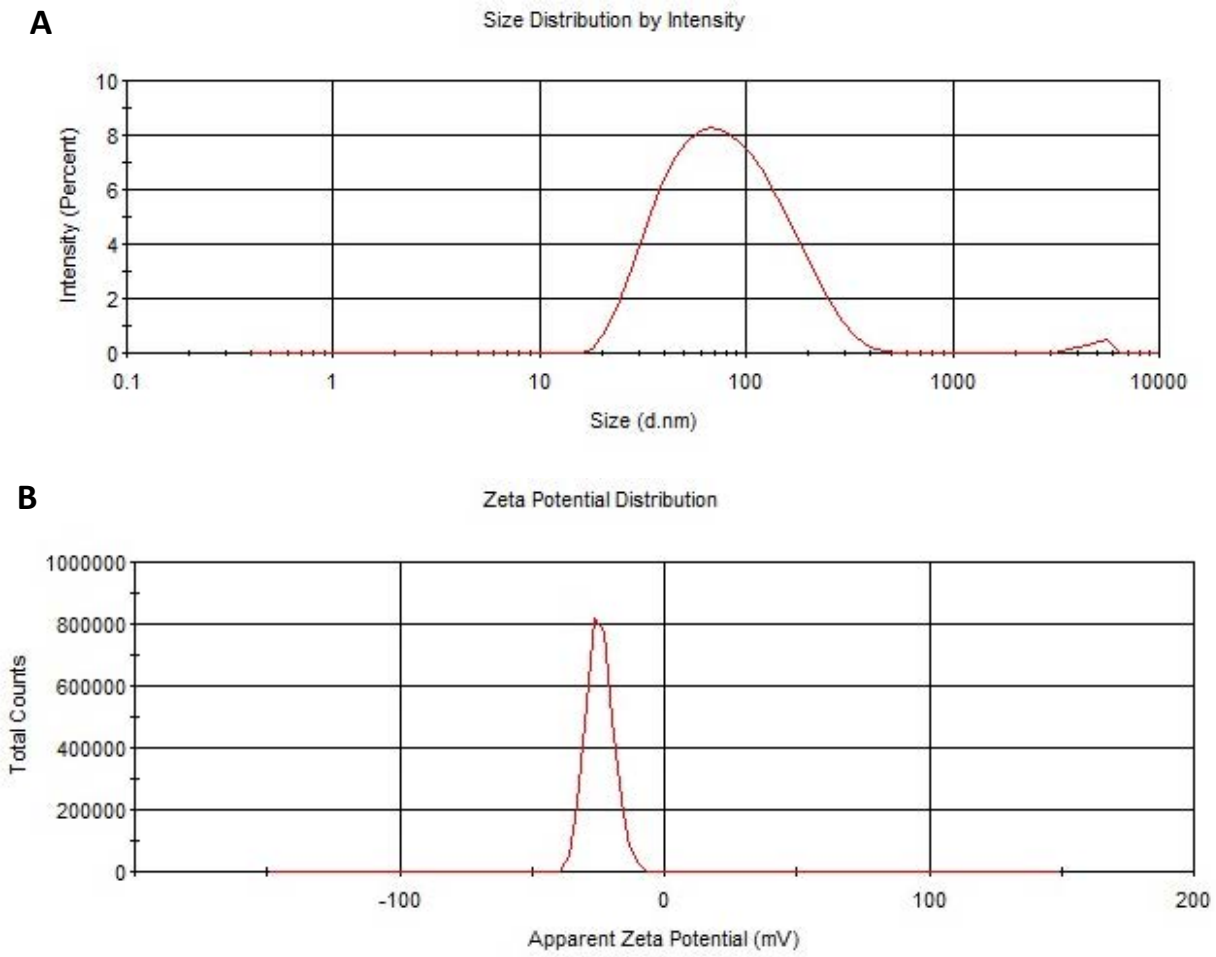


Figure 17

DLS analysis of **CPT0⊂Yb-L.SiO$_2$NP_1** (H_2O). A: Size distribution by intensity graph, 94 nm, PDI = 0.298. B: Zeta potential measurement ζ, -24 mV.

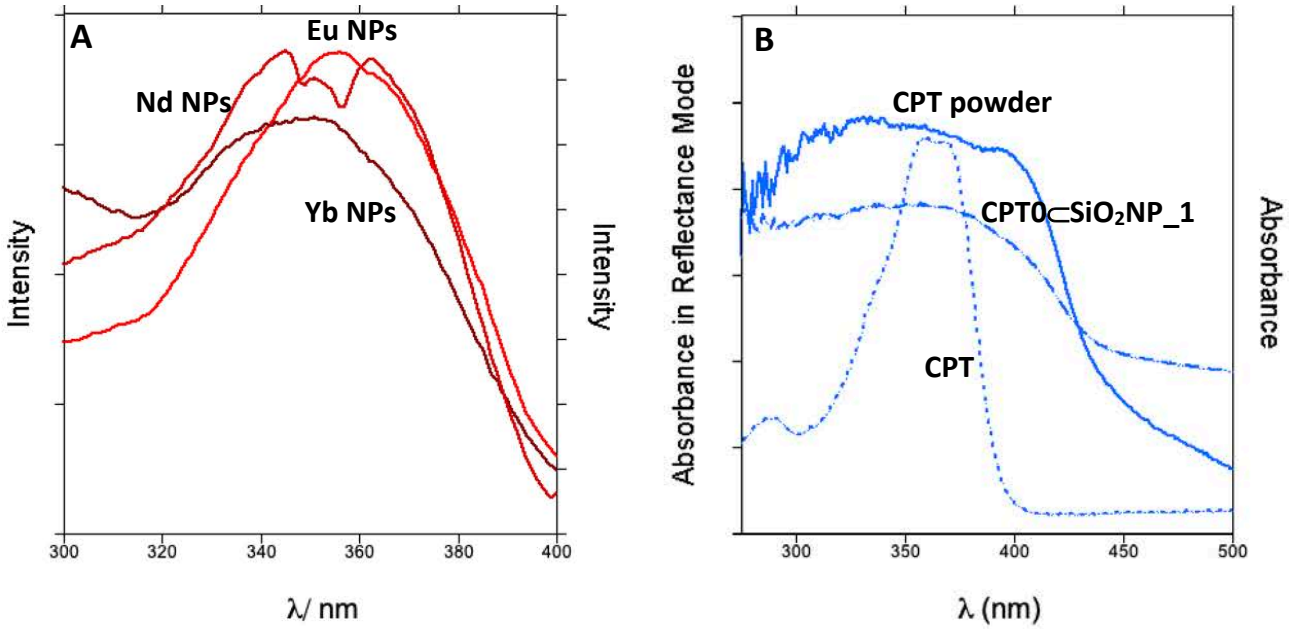
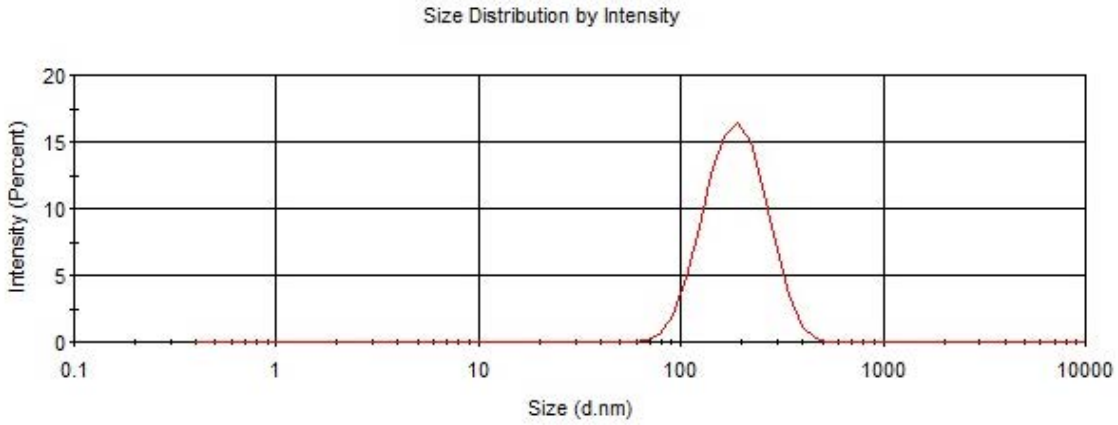


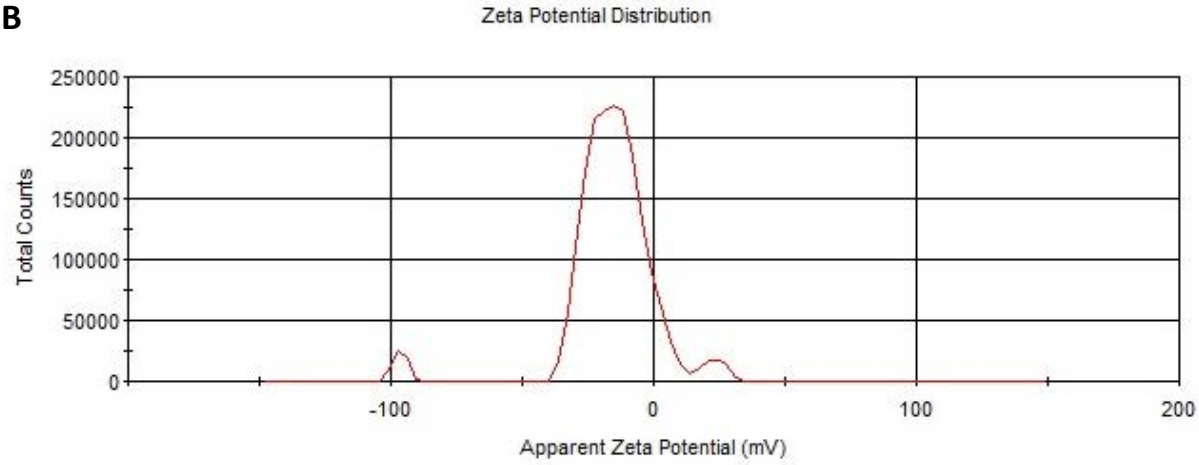
Figure 18

Comparison of **CPT⊂Ln-L.SiO$_2$NP** excitation spectra to **CPT** UV-Vis absorbance to show good agreement. A: Excitation spectra of **CPT0⊂Ln-L.SiO$_2$NP_1**, monitoring **CPT** excitation, Ln(III) = Eu (red), Yb (brown), Nd (maroon), at their respective emission bands; λ_{em} = 420 nm. B: UV-Vis absorbance comparison of **CPT** (30 μM, MeOH) (blue, dotted), **CPT powder** (solid state) (blue) and **CPT0⊂SiO$_2$NP_1** (solid state) (blue, dashed). Excitation spectra corrected for lamp response.

A



B



C

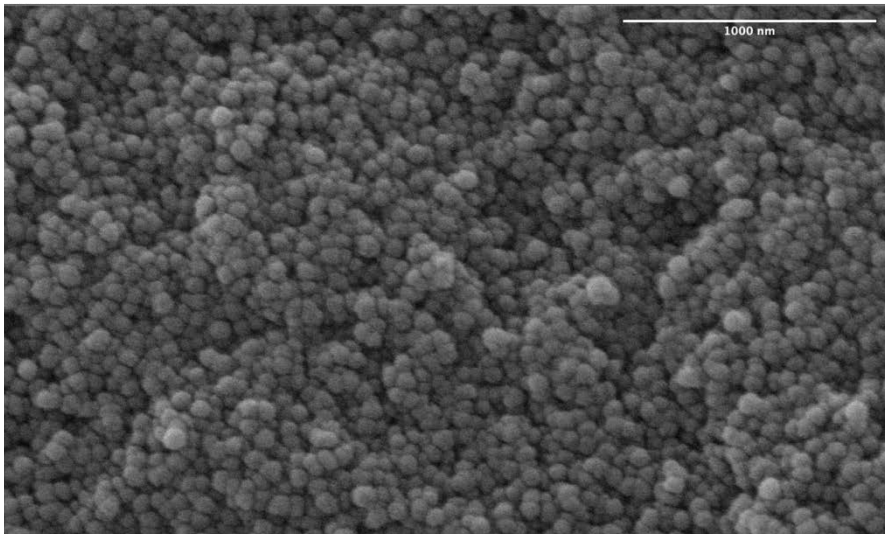


Figure 19

DLS analysis of **Eu-L.SiO$_2$NP_1** (H_2O). A: Size distribution by intensity graph, 196 nm, PDI = 0.383. B: Zeta potential measurement ζ, -15 mV. C: SEM image, average d = 78 nm (average taken from 15 NPs)

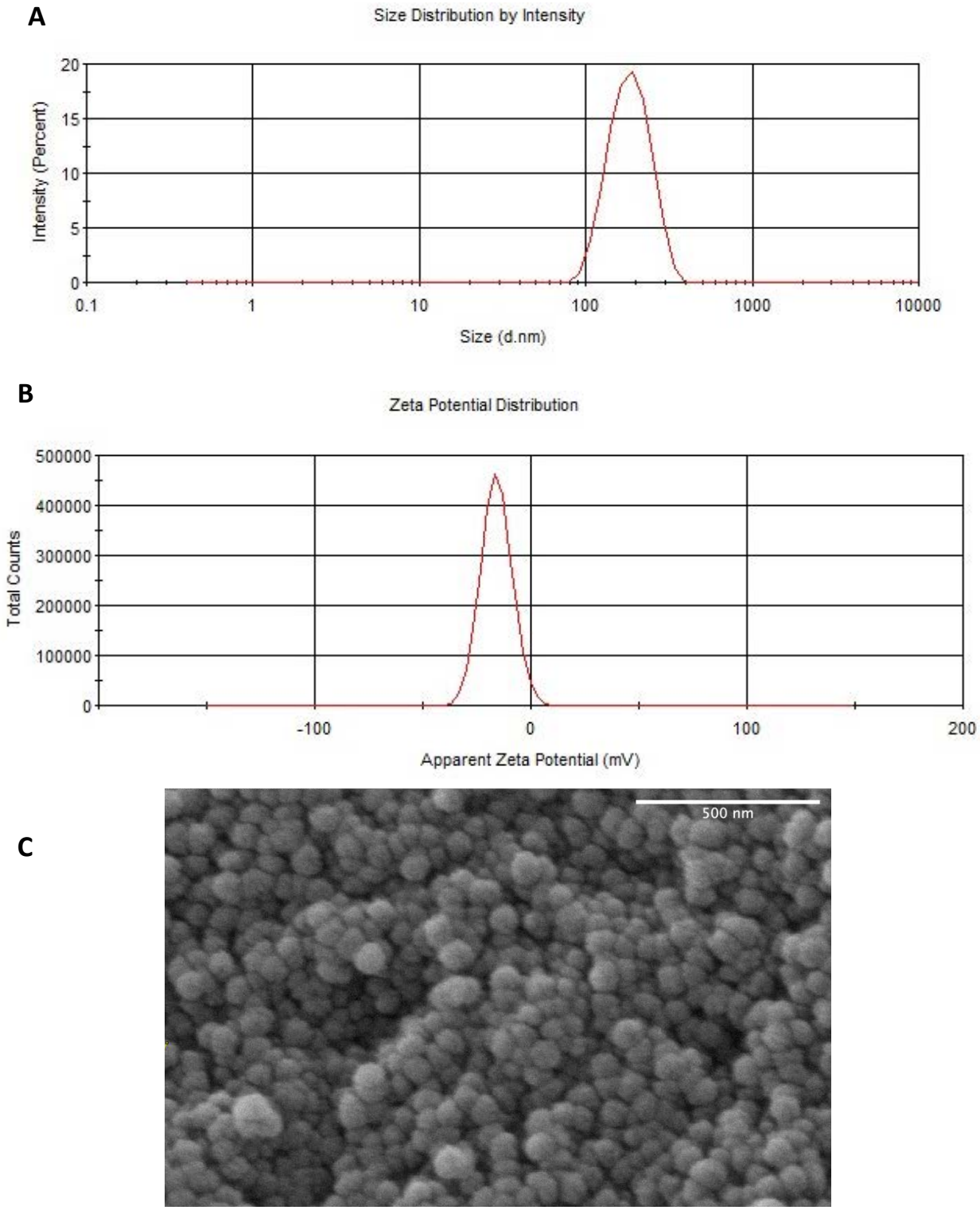


Figure 20

DLS analysis of **Nd-L.SiO$_2$NP_1** (H_2O). A: Size distribution by intensity graph, 189 nm, PDI = 0.356. B: Zeta potential measurement ζ, -16 mV. C: SEM image, average d = 80 nm (average taken from 15 NPs).

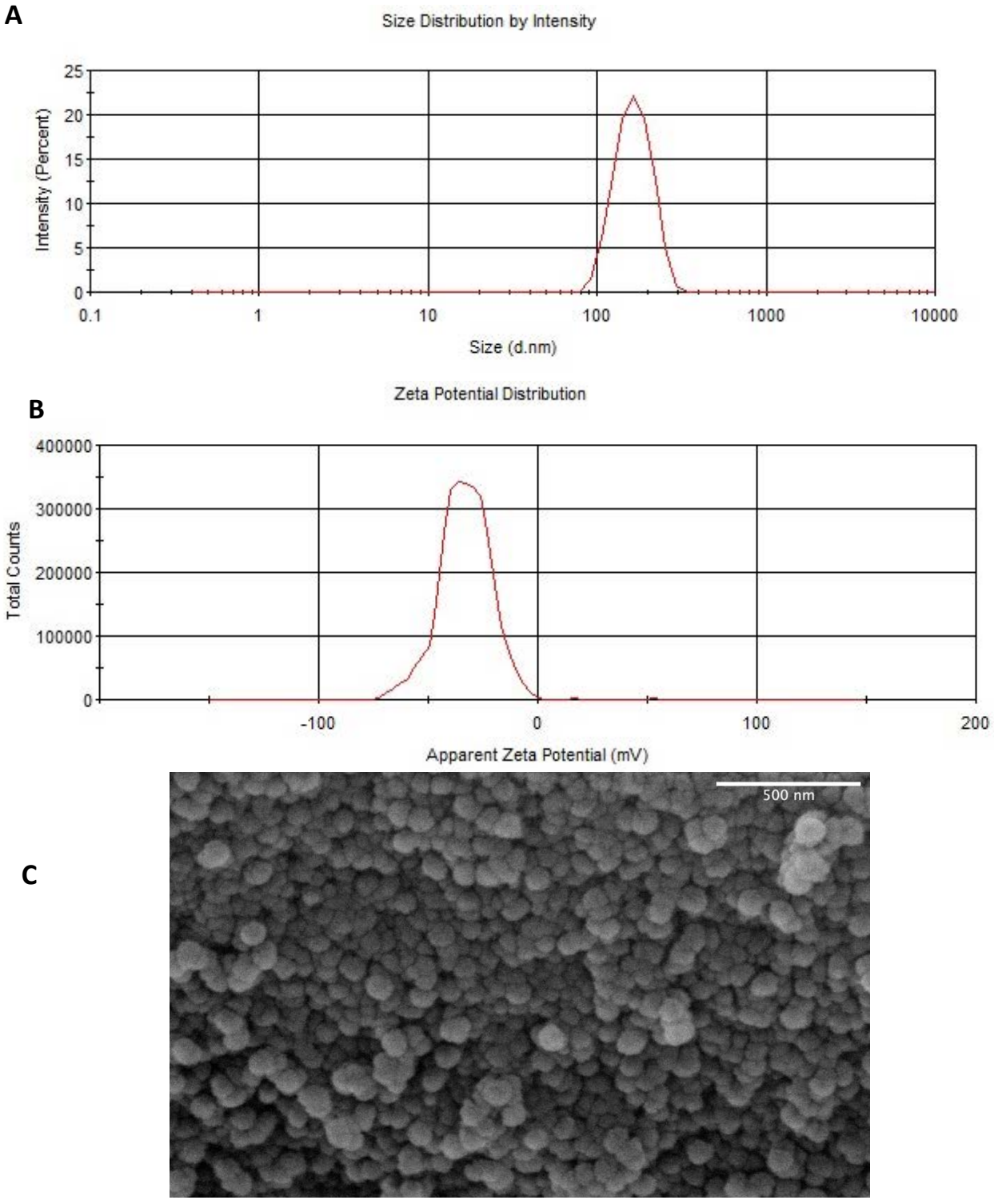


Figure 21

DLS analysis of **Yb-L.SiO$_2$NP_1** (H_2O). A: Size distribution by intensity graph, 167 nm, PDI = 0.403. B: Zeta potential measurement ζ, -33 mV. C: SEM image, average d = 72 nm (average taken from 15 NPs)

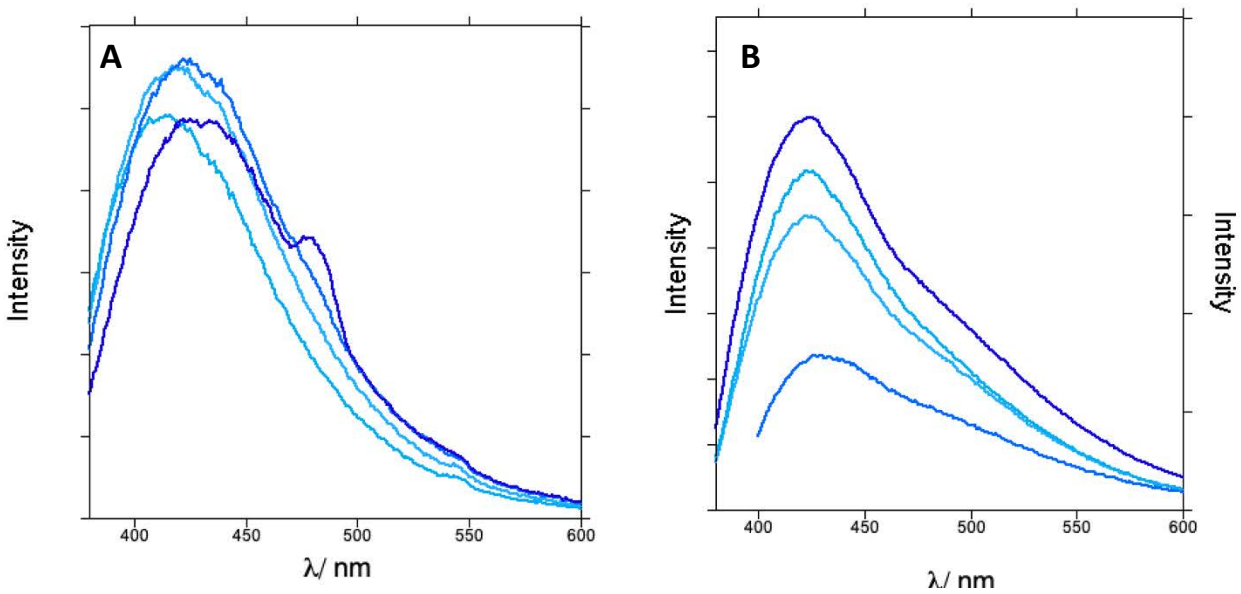


Figure 22

Solid state emission spectra of control experiments to show scattering from **SiO_2NP**. A: Emission spectra of **SiO_2NP** at different λ_{exc} (λ_{exc} = 345 nm turquoise, λ_{exc} = 350 nm light blue, λ_{exc} = 355 nm medium blue and λ_{exc} = 360 nm dark blue) demonstrating the change in emission wavelengths by the same increment as λ_{exc} changes, suggesting scatter. B: Emission spectra of **CPT0⊂SiO_2NP_1** at different λ_{exc} (λ_{exc} = 345 nm turquoise, λ_{exc} = 350 nm light blue, λ_{exc} = 355 nm medium blue and λ_{exc} = 360 nm dark blue) demonstrating no change in emission wavelength as λ_{exc} changes. Emission spectra corrected for PMT and instrument response.

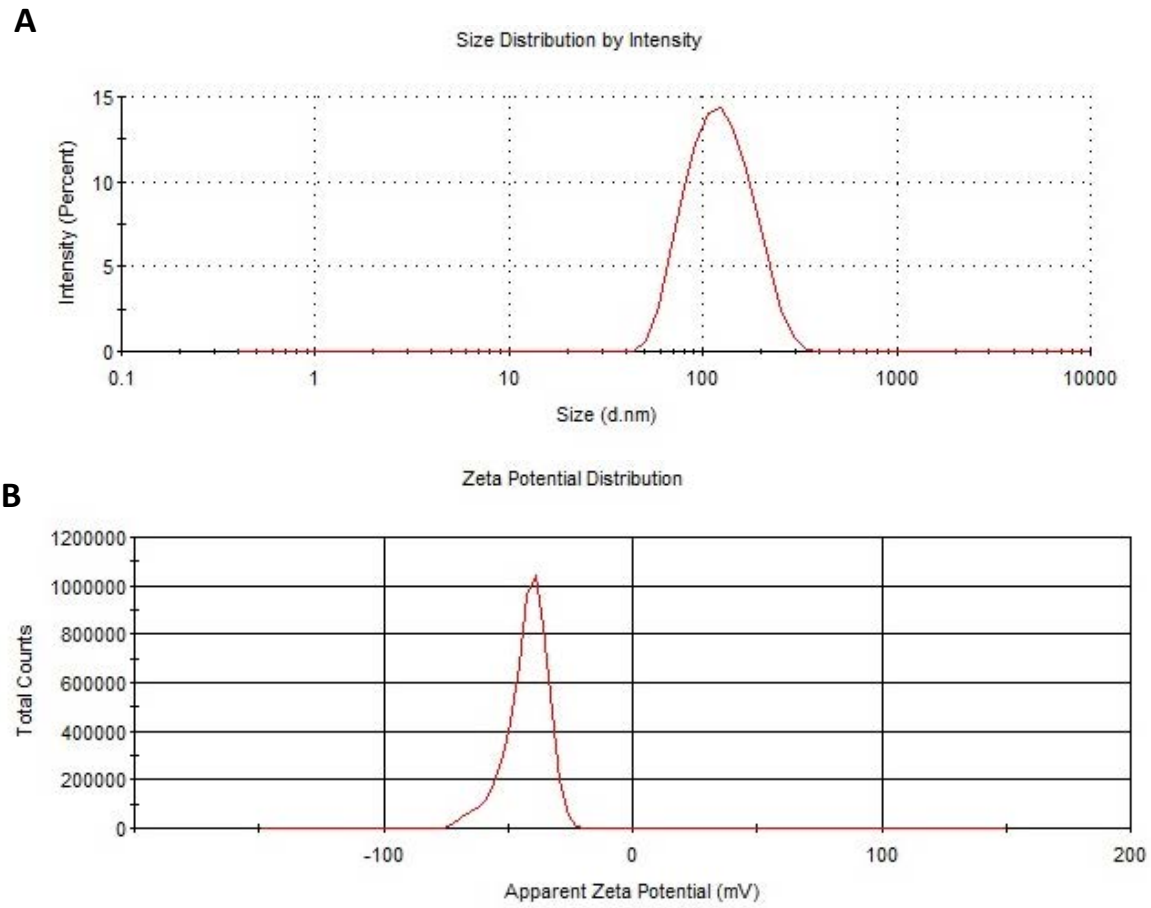


Figure 23

DLS analysis of **CPT3⊂SiO$_2$NP_1** (H_2O). A: Size distribution by intensity graph, 129 nm, PDI = 0.129. B: Zeta potential measurement ζ, -42 mV.

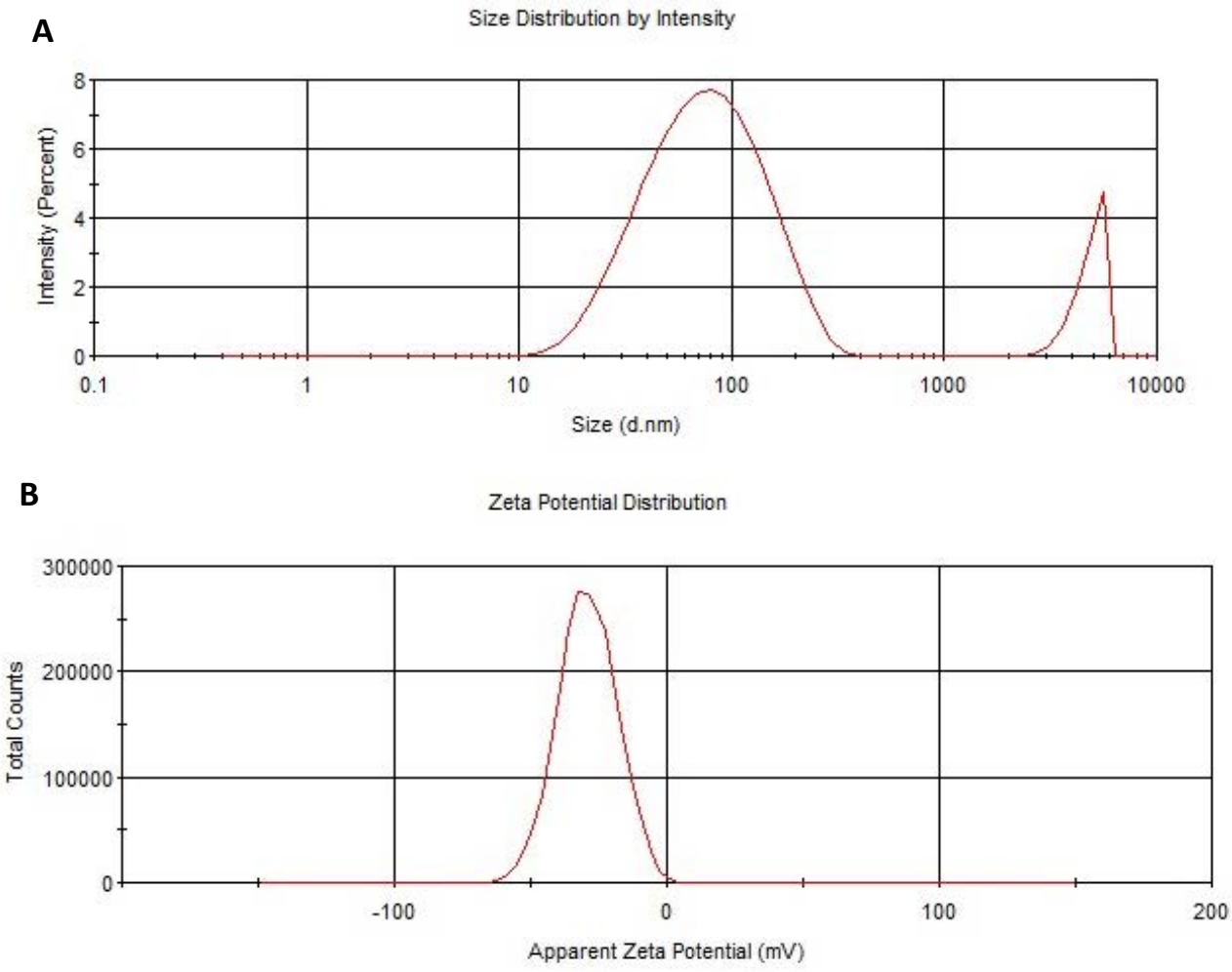
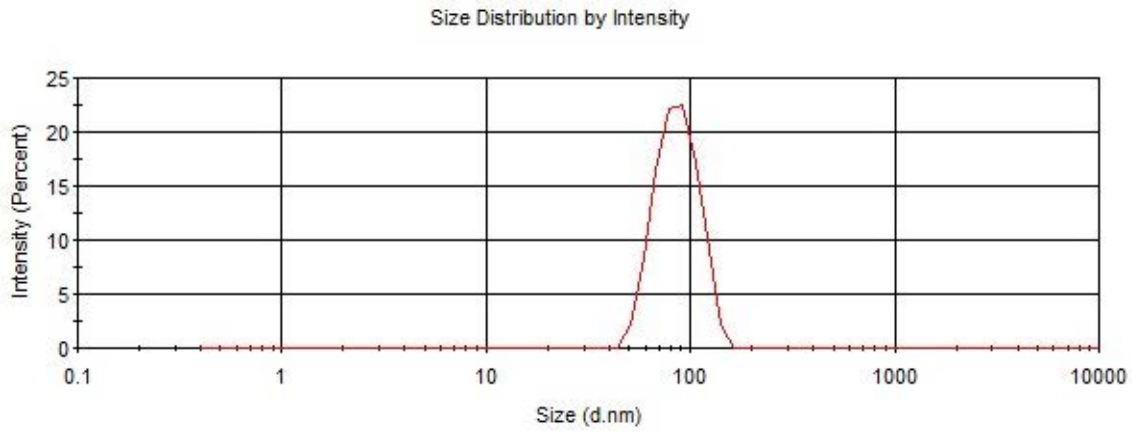


Figure 24

DLS analysis of **CPT3⊂Eu-L.SiO$_2$NP_1** (H_2O). A: Size distribution by intensity graph, 88 nm, PDI = 0.230. B: Zeta potential measurement ζ, -28 mV.

A



B

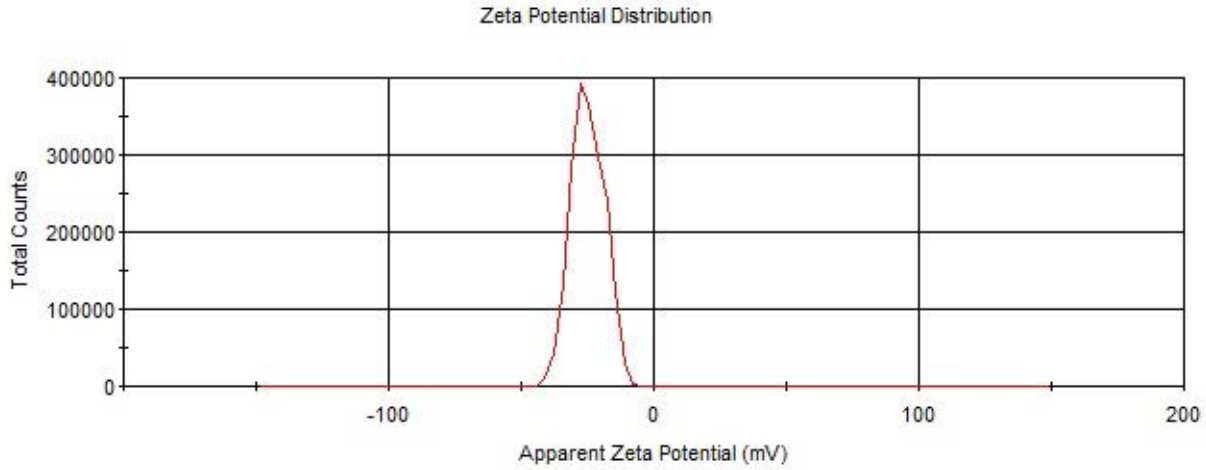


Figure 25

DLS analysis of **CPT3⊂Nd-L.SiO$_2$NP_1** (H_2O). A: Size distribution by intensity graph, 88 nm, PDI = 0.372. B: Zeta potential measurement ζ, -25 mV.

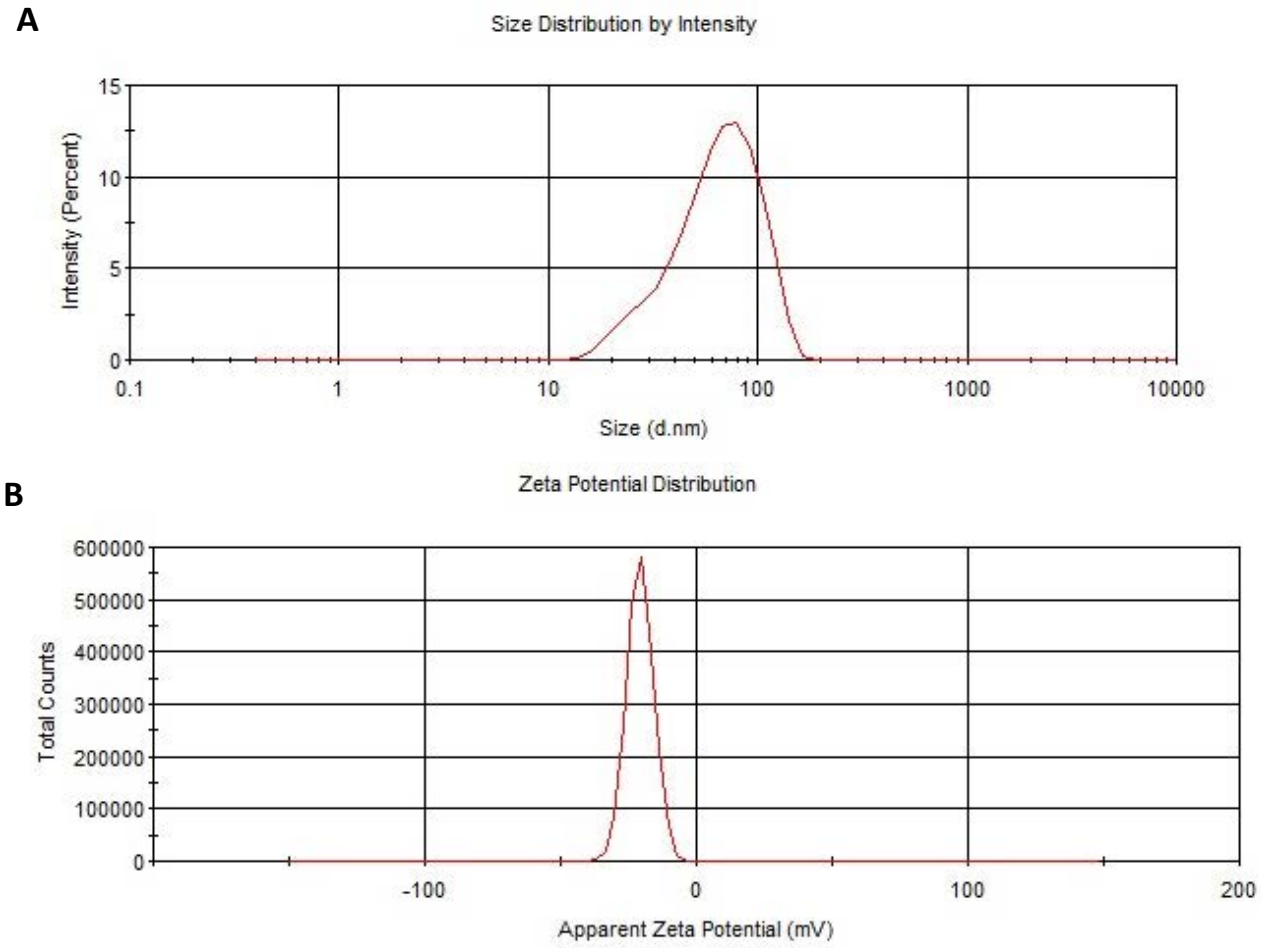


Figure 26

DLS analysis of **CPT3⊂Yb-L.SiO$_2$NP_1** (H_2O). A: Size distribution by intensity graph, 69 nm, PDI = 0.207. B: Zeta potential measurement ζ, -21 mV.

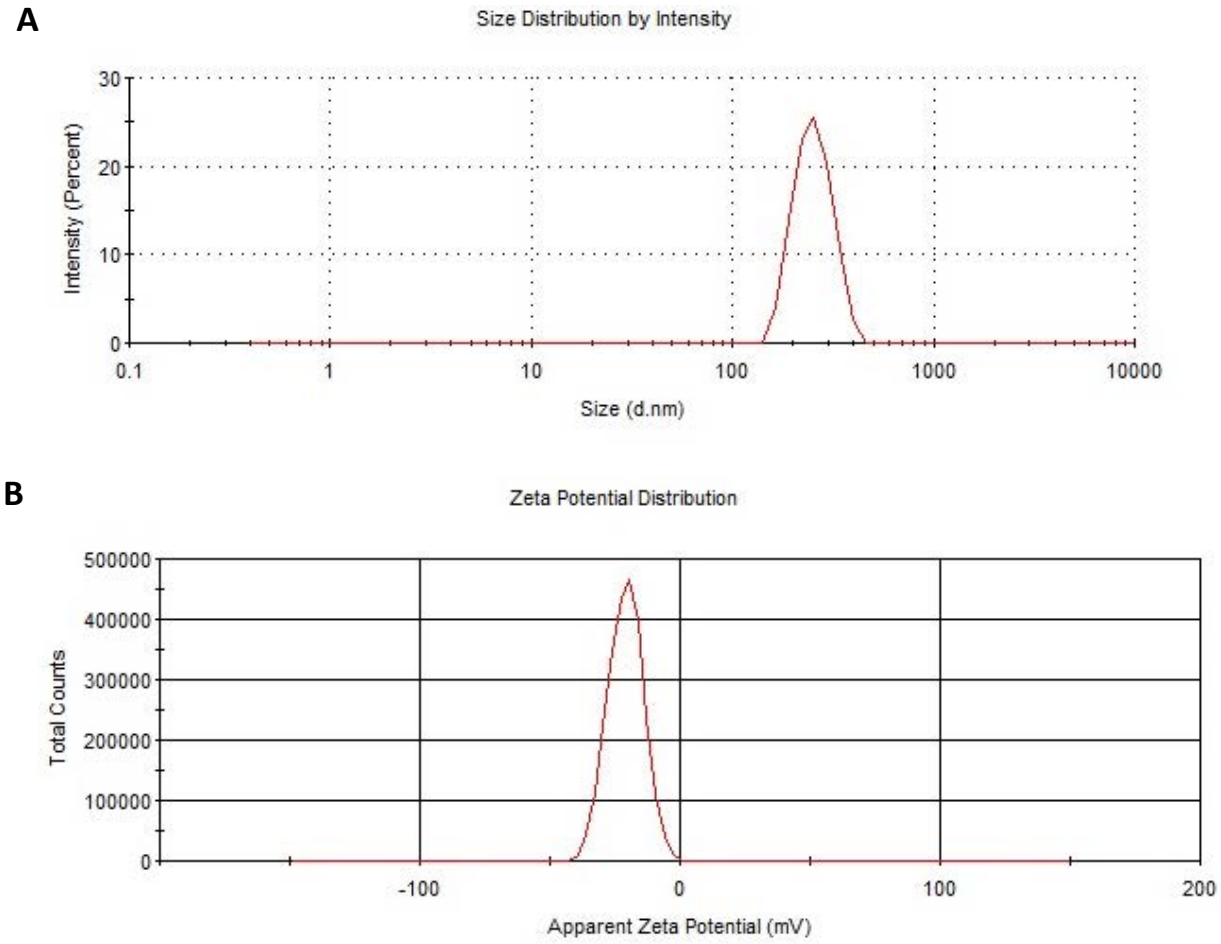


Figure 27

DLS analysis of **CPT0⊂SiO$_2$NP_2** (H_2O). A: Size distribution by intensity graph, 255 nm, PDI = 0.013. B: Zeta potential measurement ζ, -21 mV.

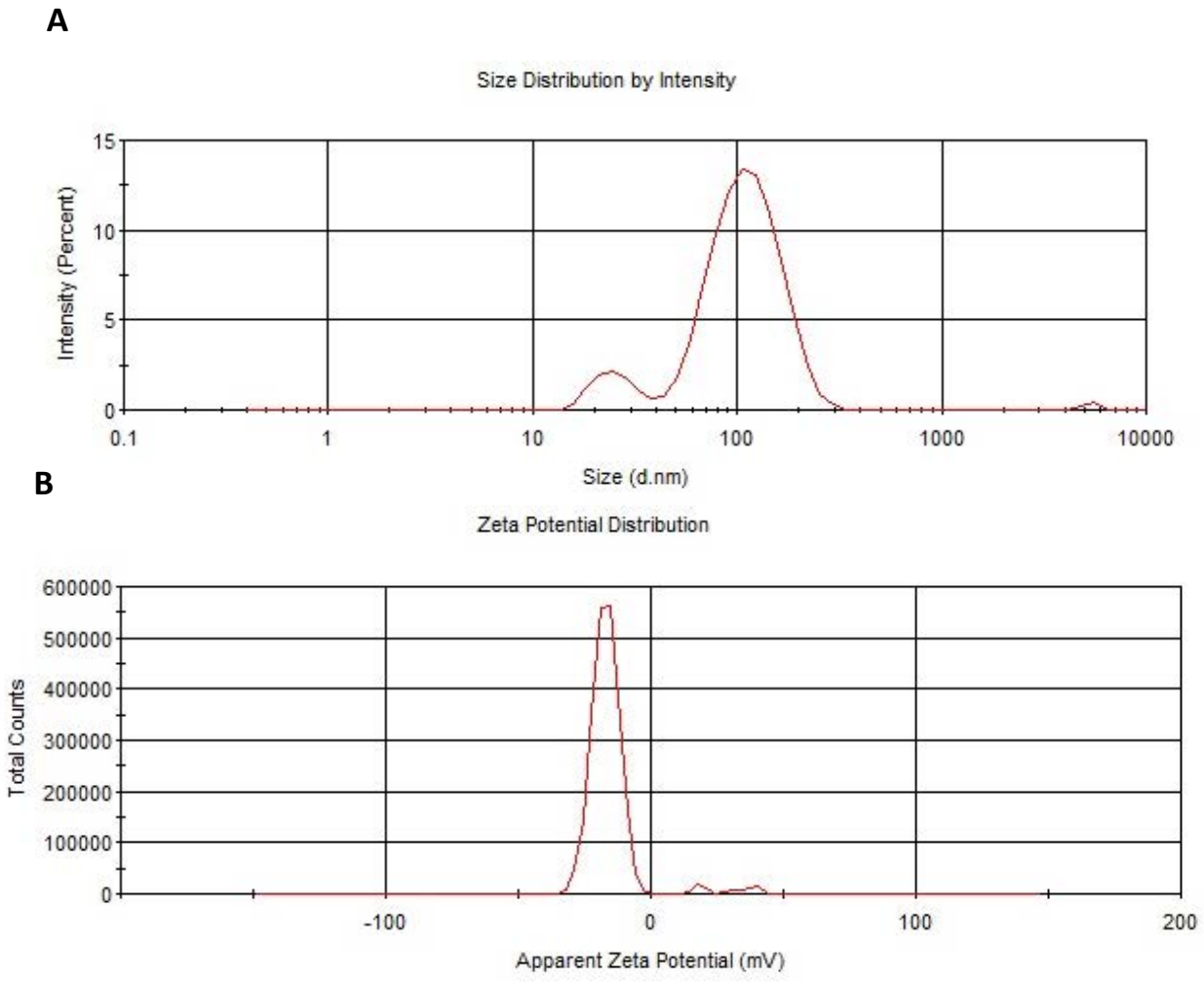


Figure 28

DLS analysis of **CPT0⊂Eu-L.SiO$_2$NP_2** (H_2O). A: Size distribution by intensity graph, 116 nm, PDI = 0.348. B: Zeta potential measurement ζ, -17 mV.

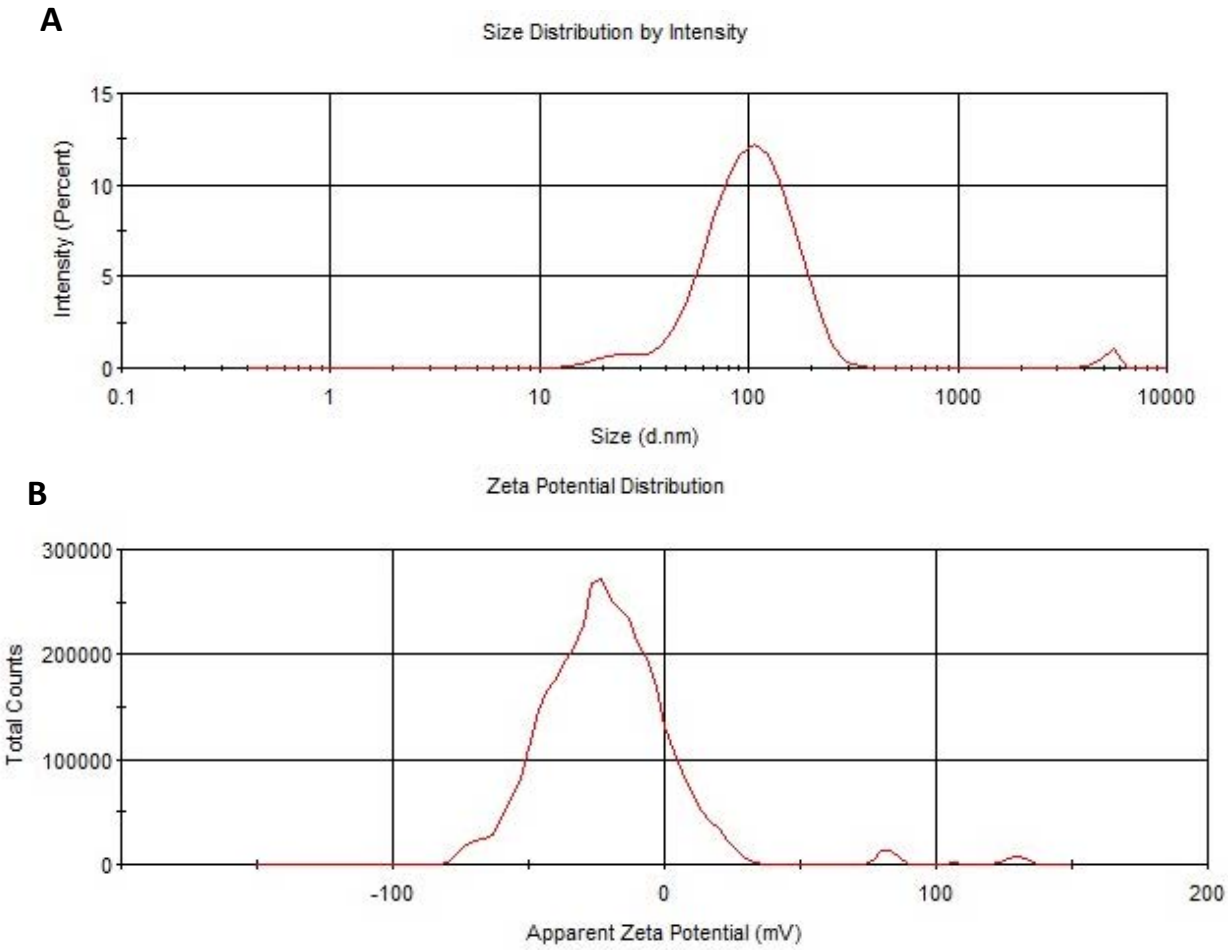


Figure 29

DLS analysis of **CPT0⊂Nd-L.SiO$_2$NP_2** (H_2O). A: Size distribution by intensity graph, 111 nm, PDI = 0.289. B: Zeta potential measurement ζ, -23 mV.

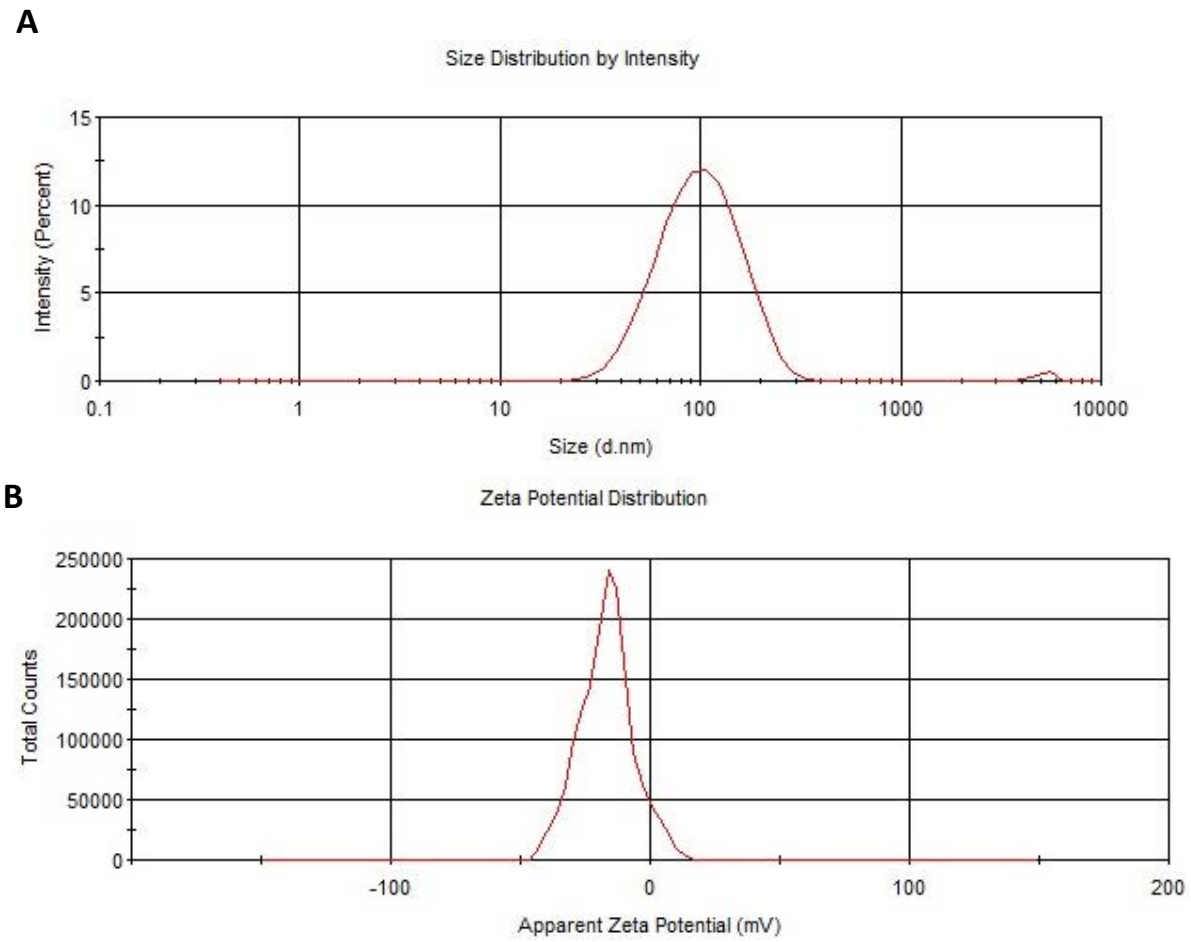
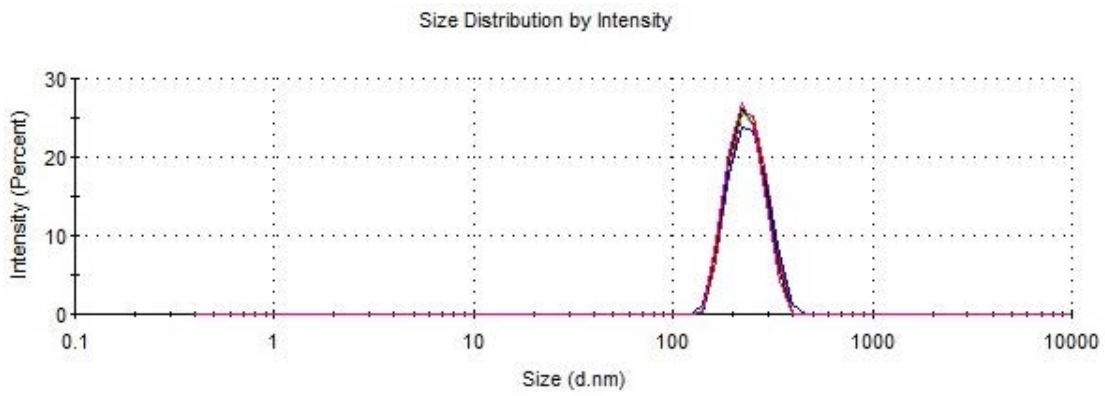


Figure 30

DLS analysis of **CPT0⊂Yb-L.SiO$_2$NP_2** (H_2O). A: Size distribution by intensity graph, 108 nm, PDI = 0.309. B: Zeta potential measurement ζ, -17 mV.

A



B

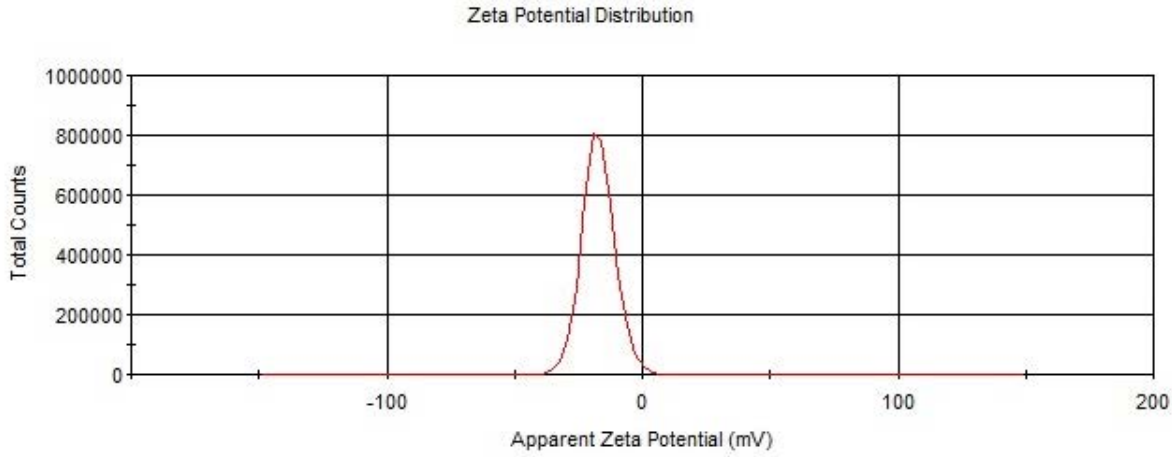
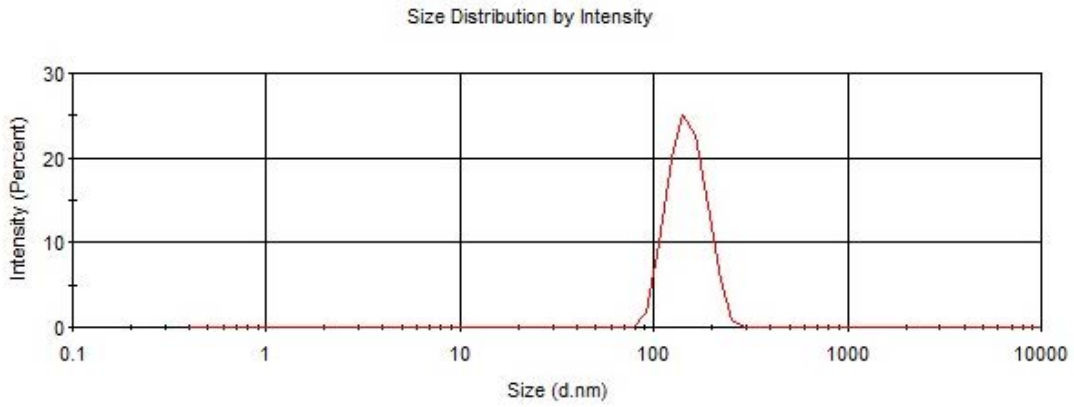


Figure 31

DLS analysis of **CPT3⊂SiO$_2$NP_2** (H_2O). A: Size distribution by intensity graph, 240 nm, PDI = 0.002. B: Zeta potential measurement ζ, -17 mV.

A



B

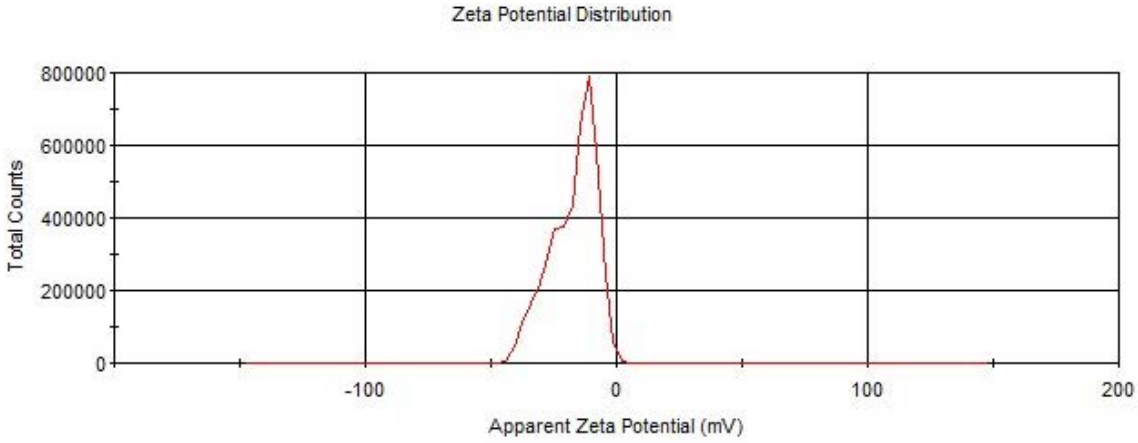


Figure 32

DLS analysis of **CPT3⊂Eu-L.SiO$_2$NP_2** (H_2O). A: Size distribution by intensity graph, 150 nm, PDI = 0.05. B: Zeta potential measurement ζ, -17 mV.

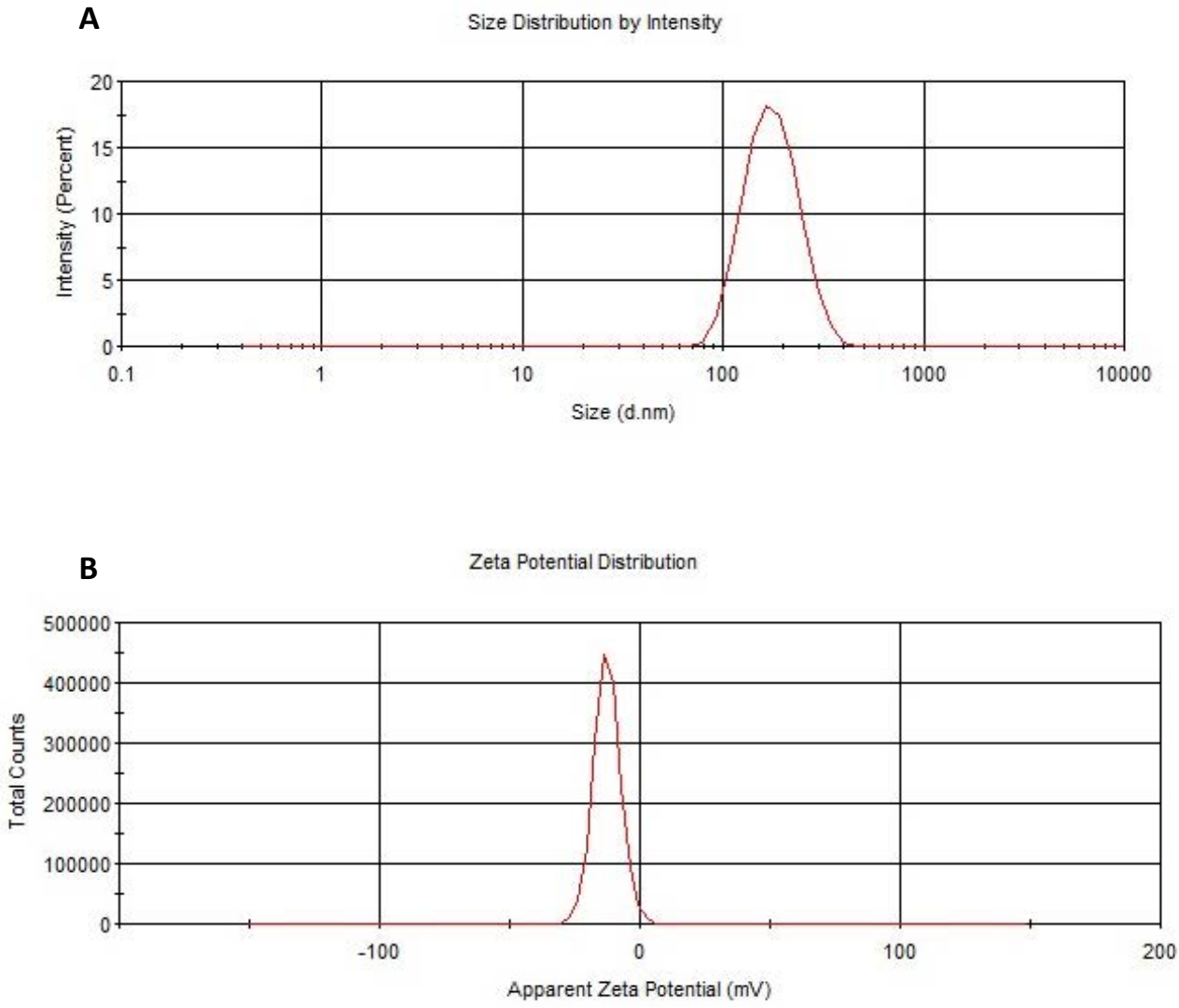
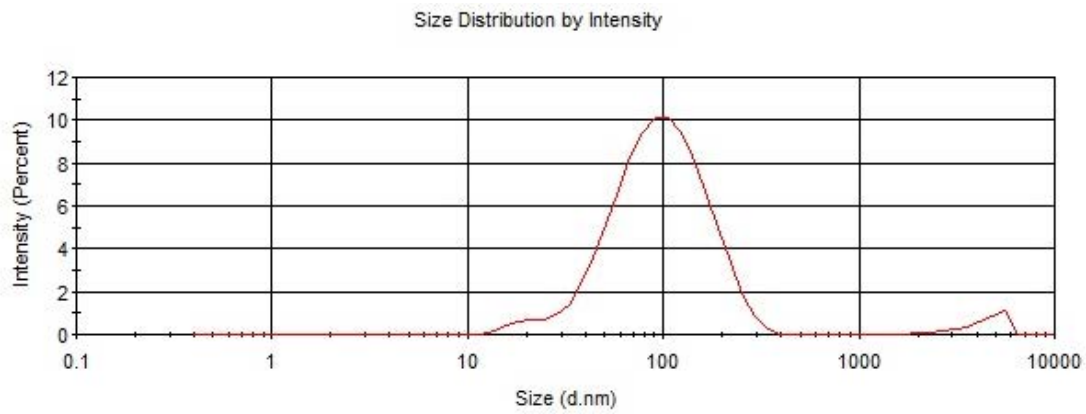


Figure 33

DLS analysis of **CPT3⊂Nd-L.SiO$_2$NP_2** (H_2O). A: Size distribution by intensity graph, 181 nm, PDI = 0.276. B: Zeta potential measurement ζ, -13 mV.

A



B

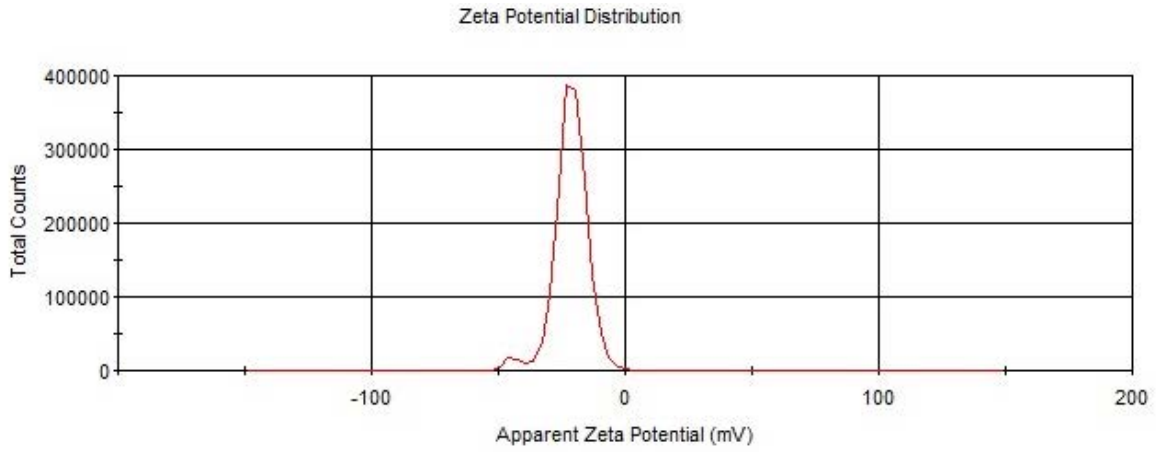


Figure 34

DLS analysis of **CPT3⊂Yb-L.SiO$_2$NP_2** (H_2O). A: Size distribution by intensity graph, 107 nm, PDI = 0.344. B: Zeta potential measurement ζ, -21 mV.

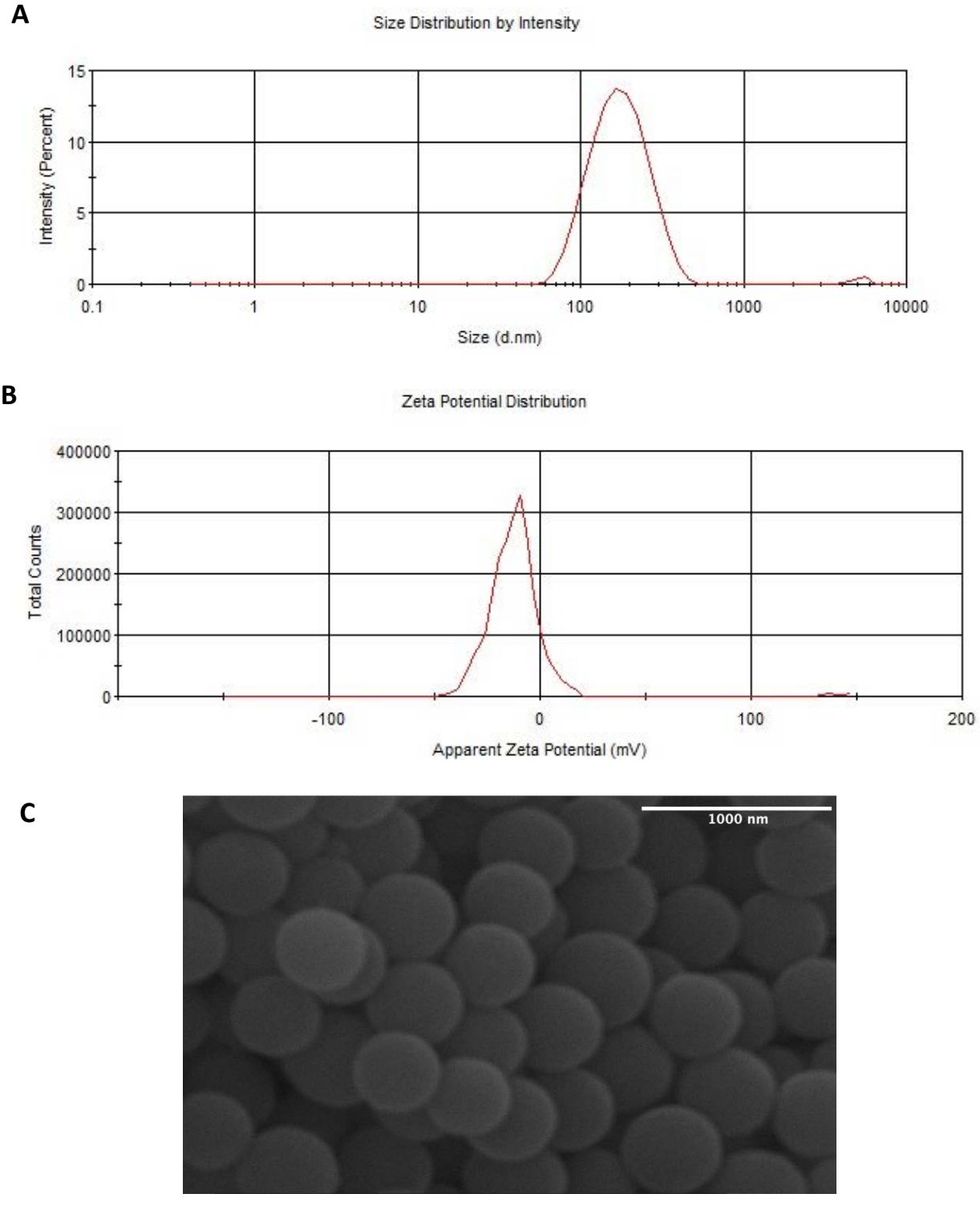


Figure 35

DLS analysis of **Eu-L.SiO$_2$NP_2** (H_2O). A: Size distribution by intensity graph, 183 nm, PDI = 0.241. B: Zeta potential measurement ζ, -13 mV. C: SEM image, average d = 442 nm (average taken from 10 NPs).

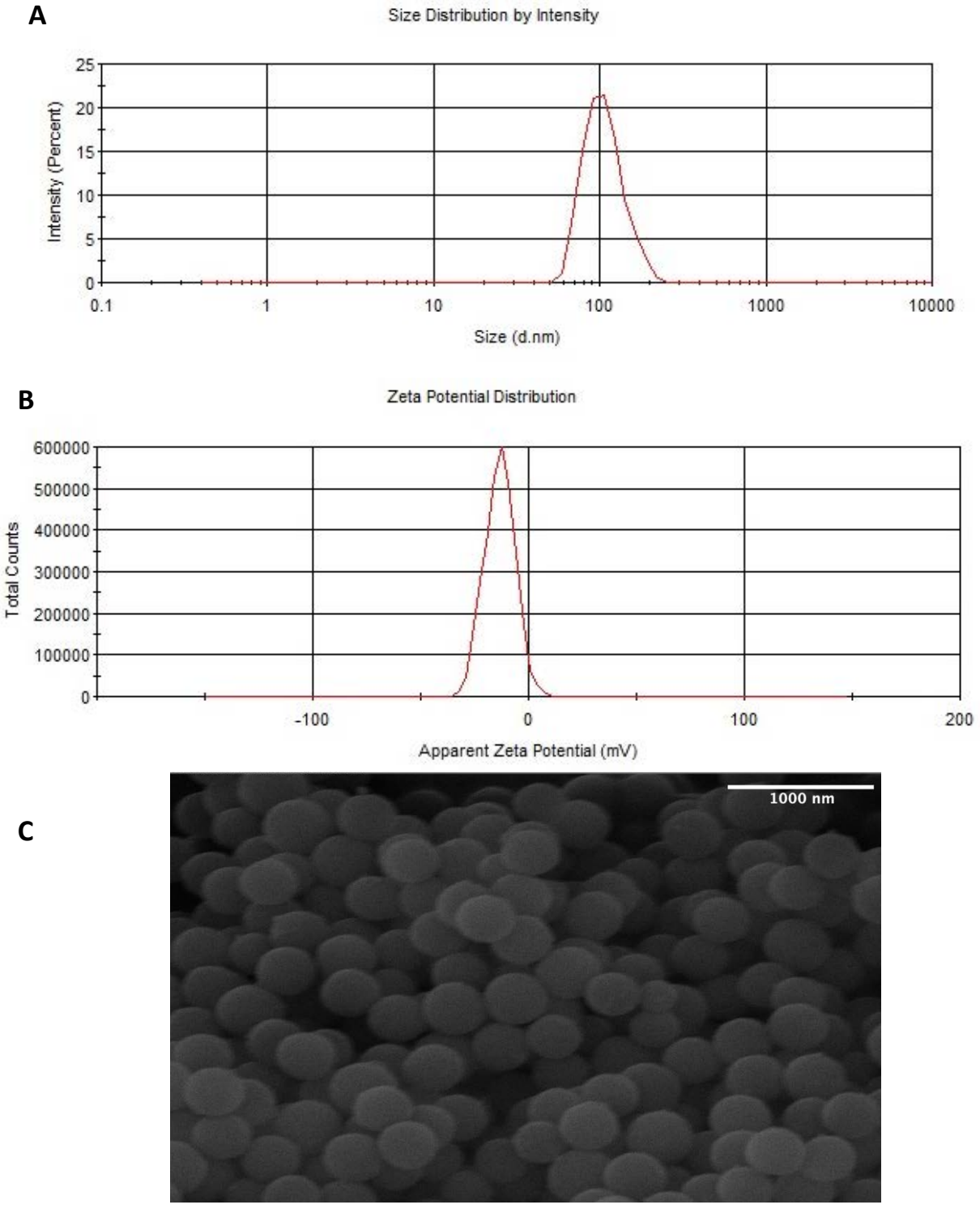
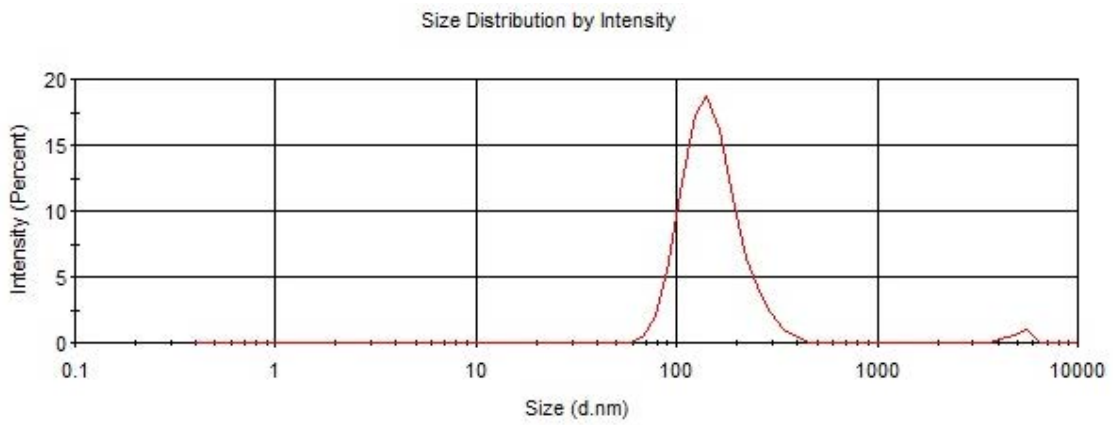


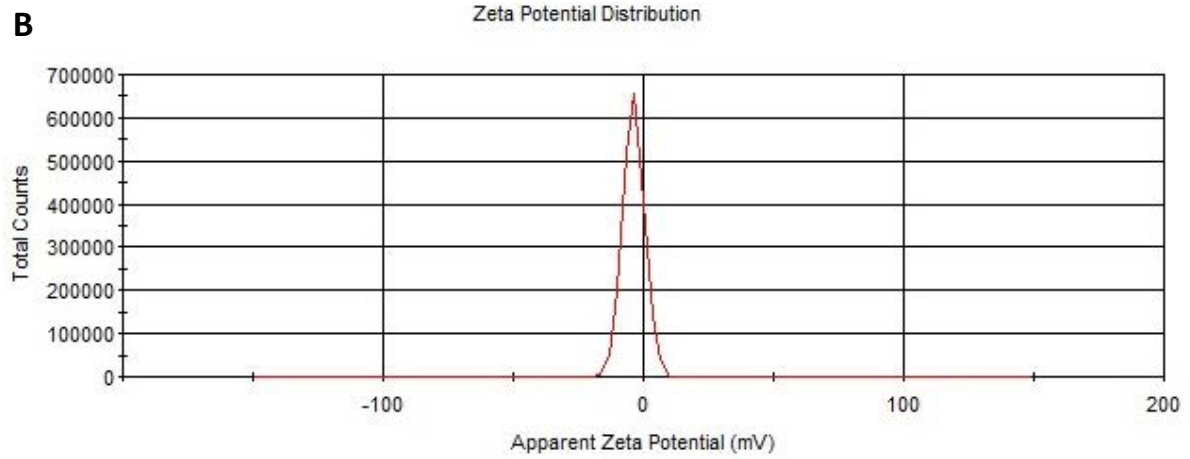
Figure 36

DLS analysis of **Nd-L.SiO$_2$NP_2** (H_2O). A: Size distribution by intensity graph, 108 nm, PDI = 0.346. B: Zeta potential measurement ζ, -13 mV. C: SEM image, average d = 355 nm (average taken from 10 NPs).

A



B



C

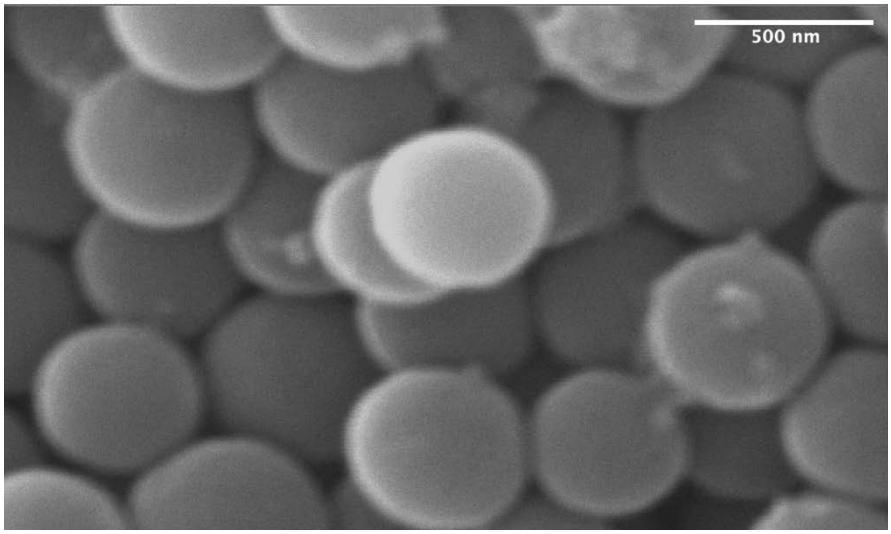


Figure 37

DLS analysis of **Yb-L.SiO$_2$NP_2** (H_2O). A: Size distribution by intensity graph, 155 nm, PDI = 0.283. B: Zeta potential measurement ζ, −4 mV. SEM image, average d = 430 nm (average taken from 10 NPs).

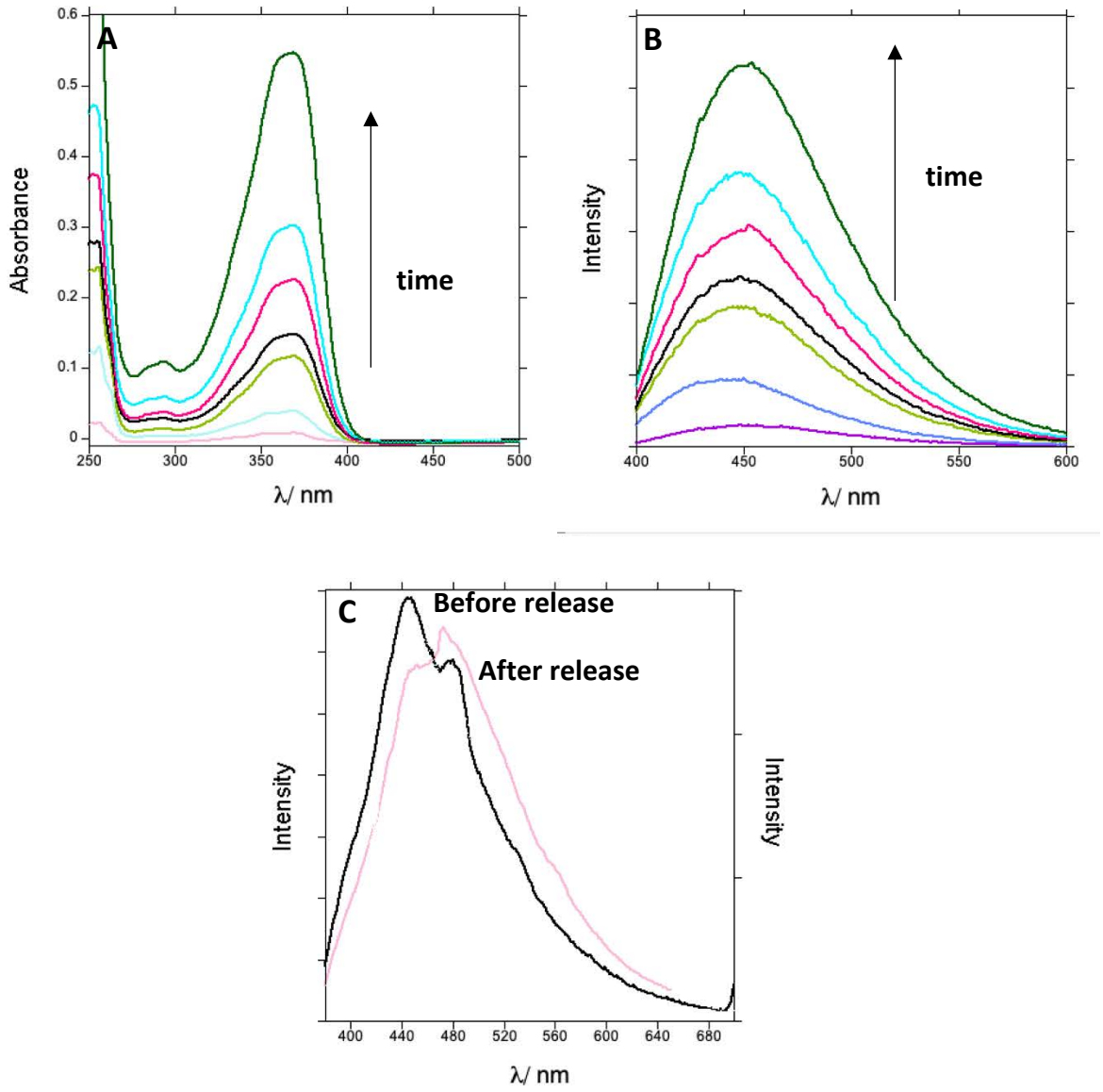


Figure 38

Release of **CPT** from **CPT3⊂SiO$_2$NP_1** (1 mg mL^{-1}, H_2O, 37 °C) up to 24 hrs studied by UV-Vis absorbance. A: UV-Vis absorbance of **CPT** released from **CPT3⊂SiO$_2$NP_1**. B: Emission of **CPT** released from **CPT3⊂SiO$_2$NP_1** showing a redshift in λ_{max}, λ_{exc} = 350 nm C: Solid state emission of dried **CPT3⊂SiO$_2$NP_1** NPs before (black) and after (pink) release showing a redshift in λ_{max}, λ_{exc} = 360 nm. Emission spectra corrected for PMT response.

Sample	Mass of CPT loaded per mass of SiO$_2$NP/ mg	Mass of CPT released/ mg	% Release
CPT3⊂SiO$_2$NP_1	0.07	2.28	3

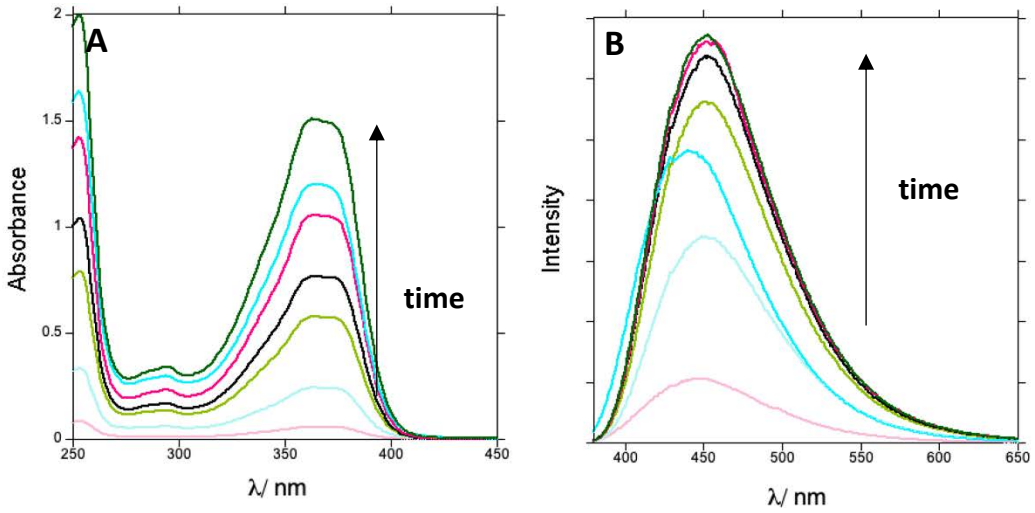


Figure 39

Release of **CPT** from **CPT5⊂SiO$_2$NP_1** (1 mg mL^{-1}, H_2O, 37 °C) up to 24 hrs studied by UV-Vis absorbance. A: UV-Vis absorbance of **CPT** released from **CPT5⊂SiO$_2$NP_1**. B: Emission of **CPT** released from **CPT5⊂SiO$_2$NP_1** showing a redshift in λ_{max}, λ_{exc} = 350 nm. Emission spectra corrected for PMT response.

Sample	**Mass of CPT loaded per mass of SiO$_2$NP/ mg**	**Mass of CPT released/ mg**	**% Release**
CPT5⊂SiO$_2$NP_1	0.2	0.96	21

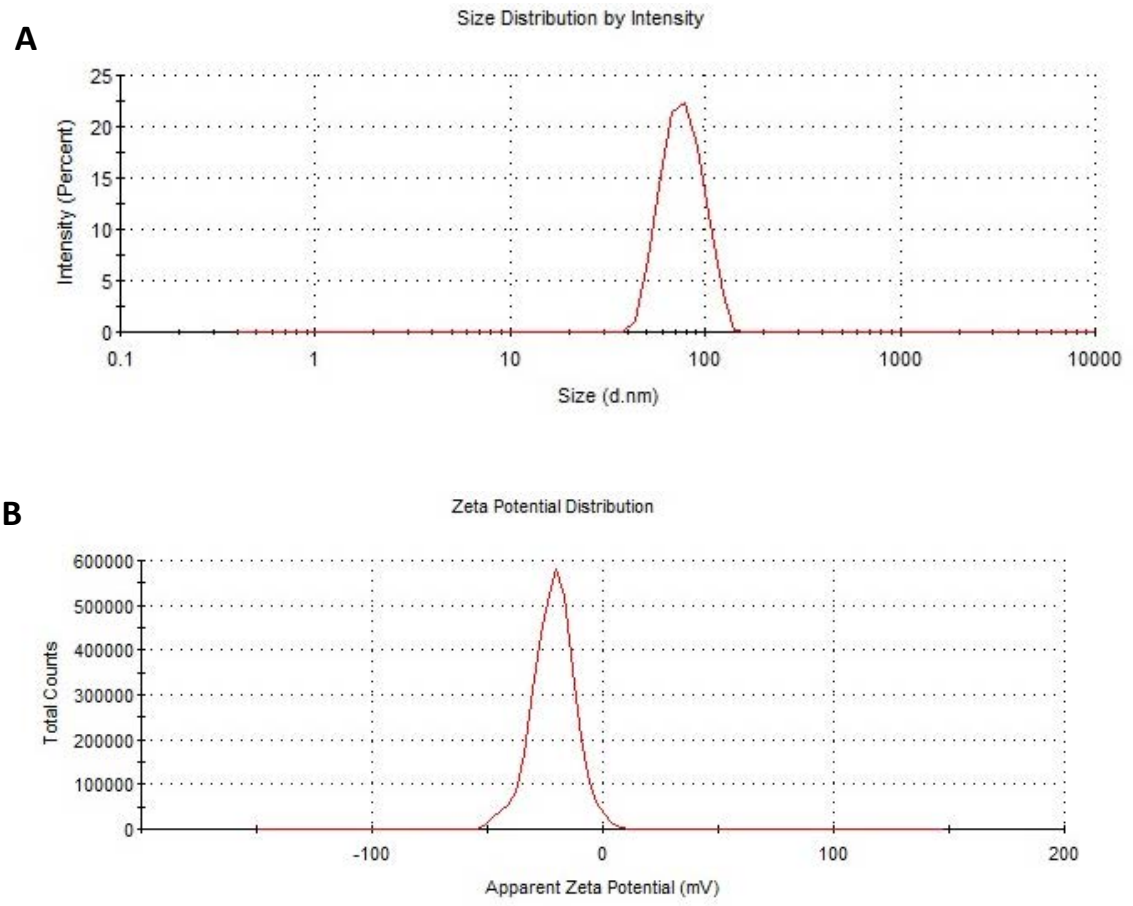


Figure 40

DLS analysis of **CPT5⊂SiO$_2$NP_1** (H_2O). A: Size distribution by intensity graph, 77 nm, PDI = 0.028. B: Zeta potential measurement ζ, -21 mV. C: SEM image, average d = 90 nm (average taken from 10 NPs).

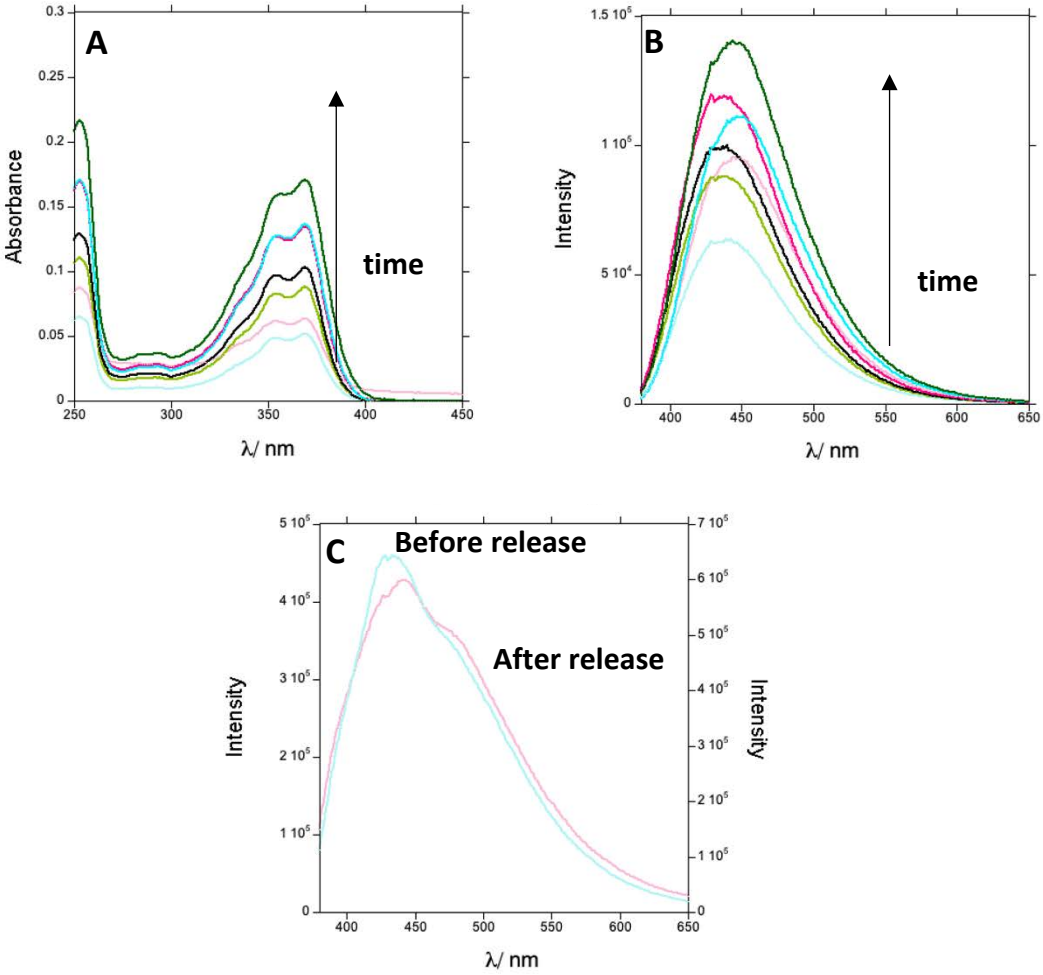


Figure 41

Release of **CPT** from **CPT loaded MSNs** (1 mg mL^{-1}, H_2O, 37 °C) up to 24 hrs studied by UV-Vis absorbance. A: UV-Vis absorbance of **CPT** released from **CPT loaded MSNs**. B: Emission of **CPT** released from **CPT loaded MSNs** showing a redshift in λ_{max}, λ_{exc} = 350 nm C: Solid state emission of dried **CPT loaded MSNs** NPs before (blue) and after (pink) release showing a redshift in λ_{max}, λ_{exc} = 360 nm. Emission spectra corrected for PMT response.

Sample	**Mass of CPT loaded per mass of SiO_2NP/ mg**	**Mass of CPT released/ mg**	**% Release**
CPT loaded MSN	0.02	0.55	4

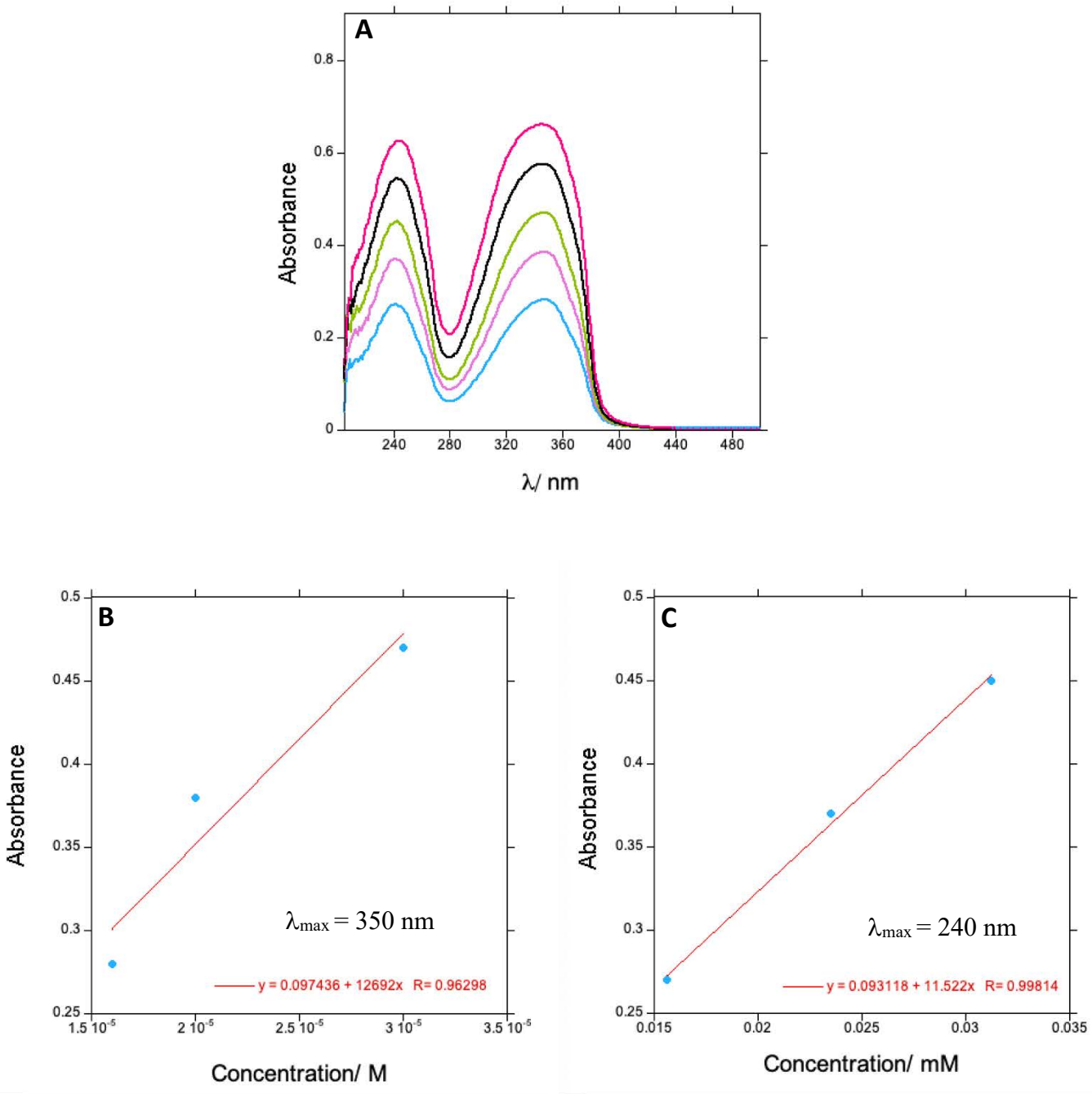


Figure 42

UV-Vis absorbance of **DBMSS** in MeOH to calculate the absorption coefficient ε using Beer Lambert's law. A: UV-Vis spectrum of **DBMSS** (0.0016 mM, 0.02 mM, 0.03 mM, 0.05 mM and 0.06 mM, MeOH). B: Plot of absorption against concentration at λ_{max} = 350 nm, resulting in ε = 13000 mol^{-1} dm^3 cm^{-1}. C: Plot of absorption against concentration at λ_{max} = 350 nm, resulting in ε = 12000 mol^{-1} dm^3 cm^{-1}.

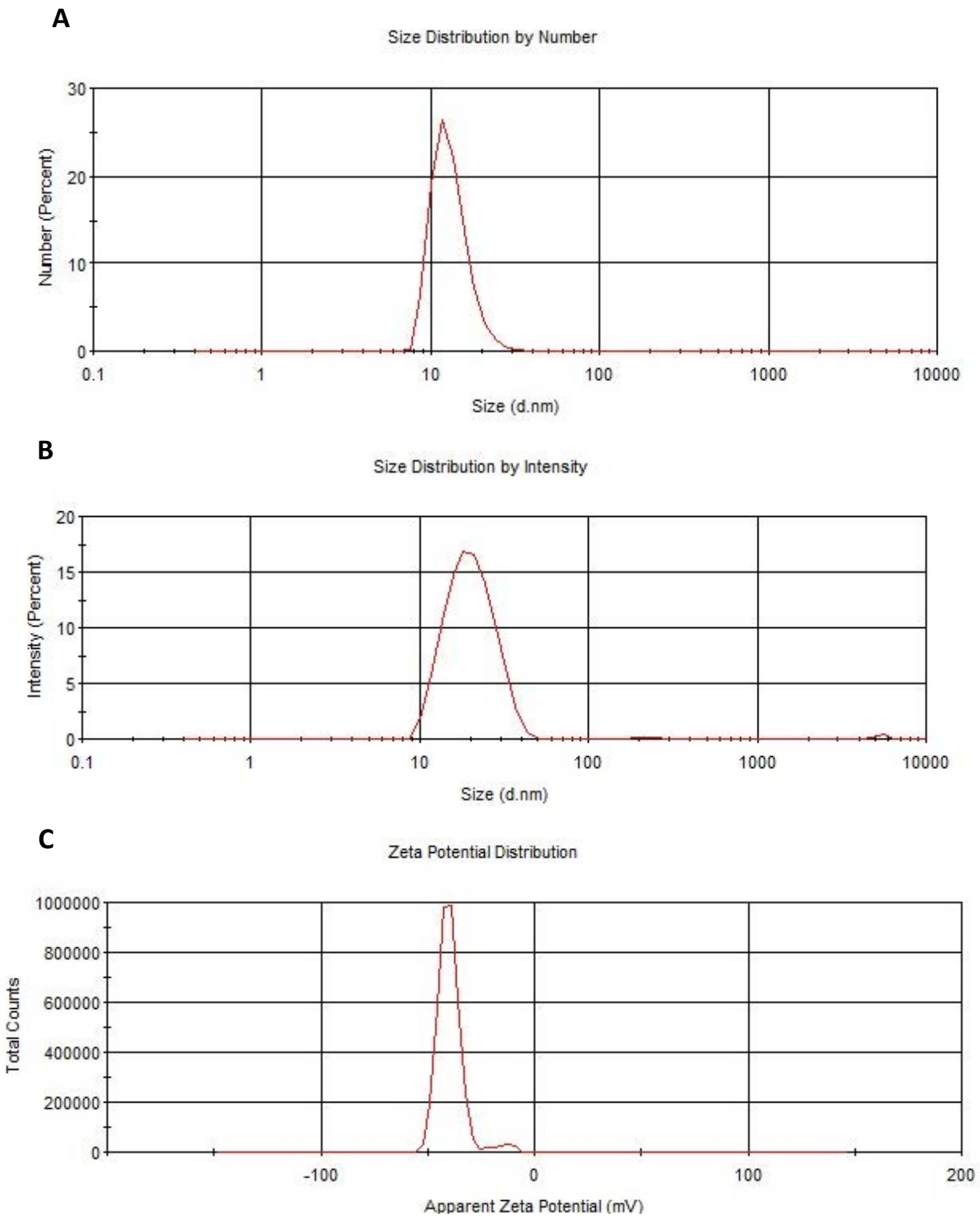


Figure 43

DLS analysis of **AuNP** (1.51 nM, H_2O). A: Size distribution by number graph, 13 nm, PDI = 0.154. B: Size distribution by intensity graph, 21 nm, PDI = 0.154. C: Zeta potential measurement ζ, -40 mV.

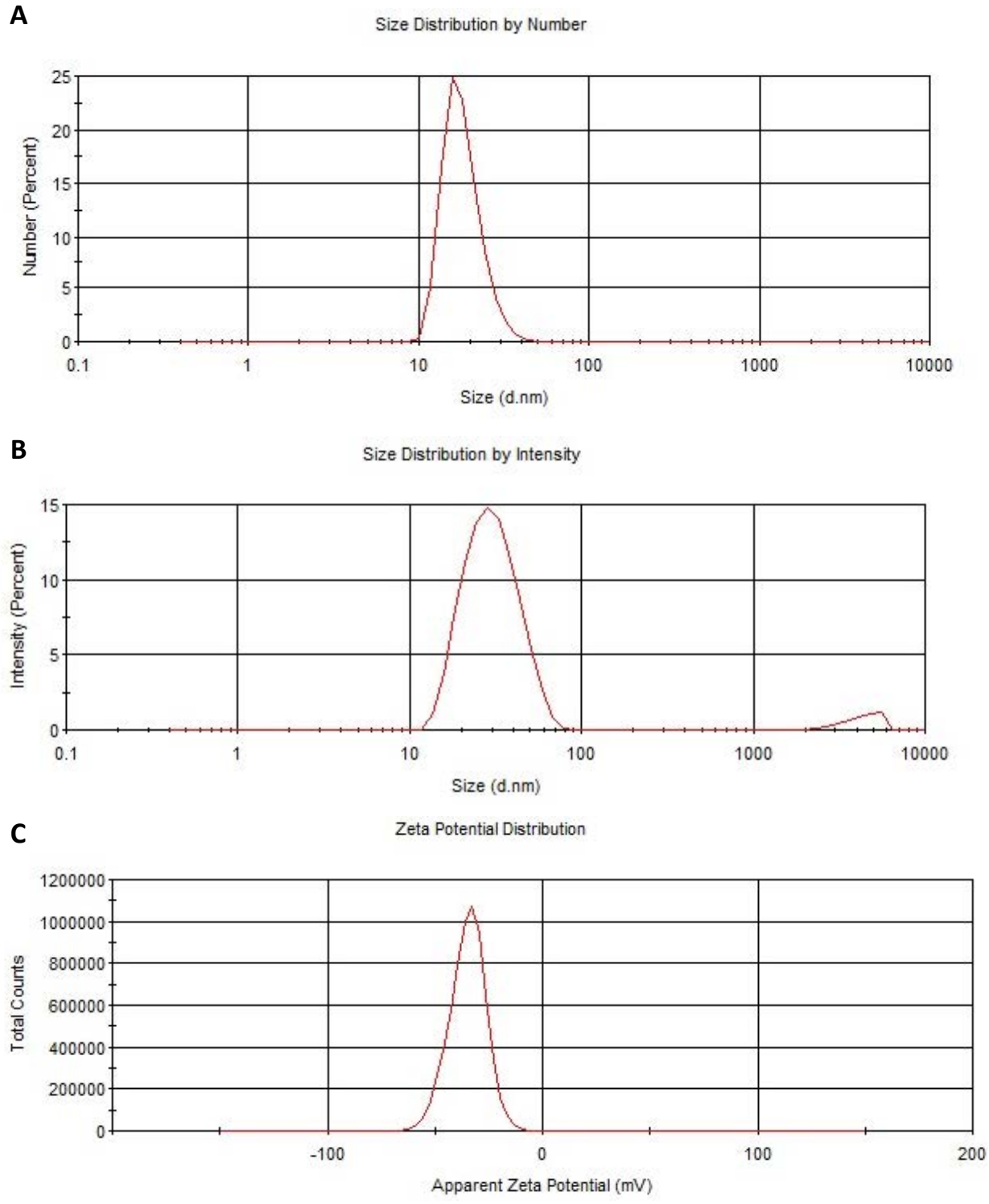


Figure 44

DLS analysis of **AuNP. Z** (0.7 nM, H_2O). A: Size distribution by number graph, 18 nm, PDI = 0.218. B: Size distribution by intensity graph, 31 nm, PDI = 0.218. C: Zeta potential measurement ζ, -35 mV.

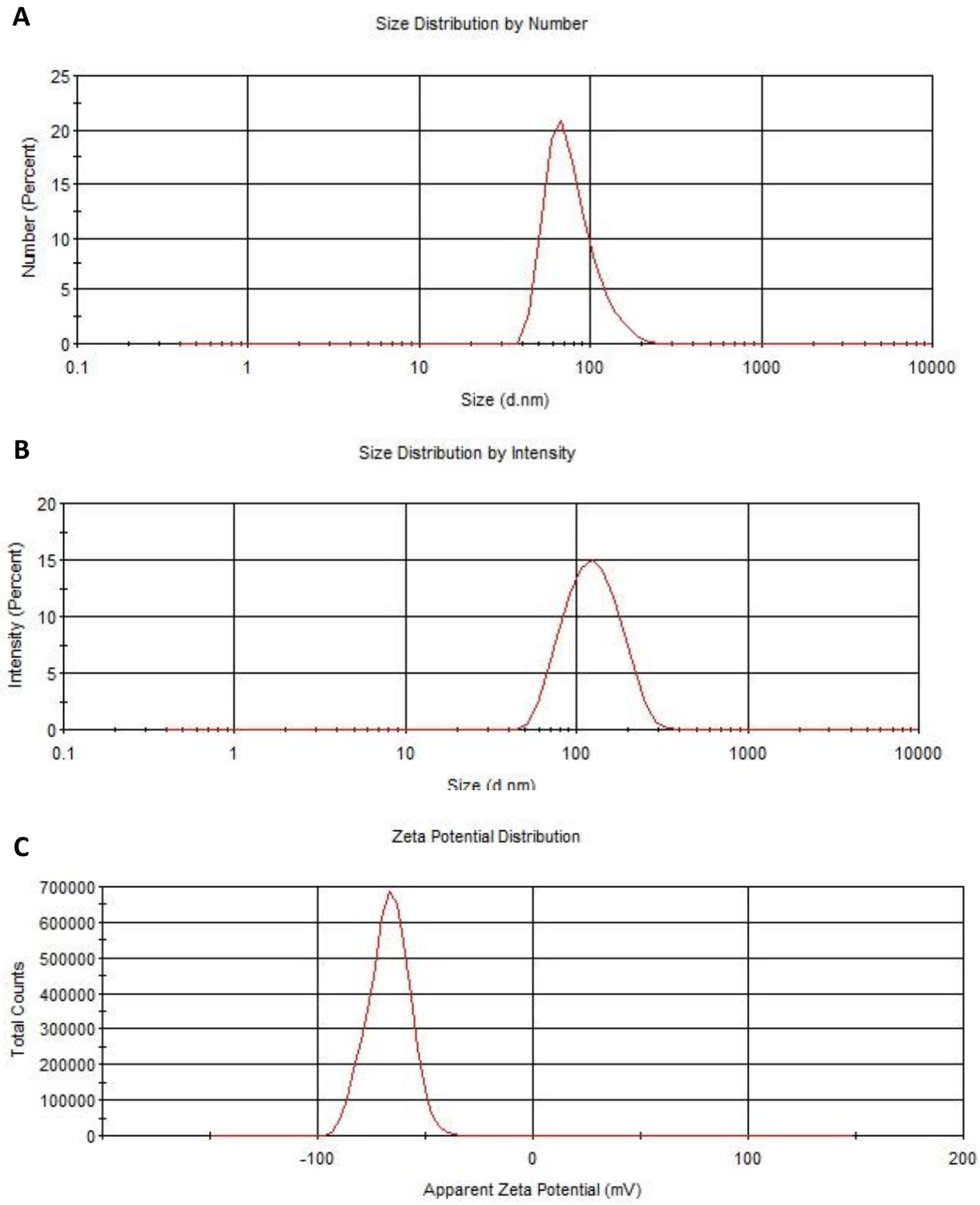


Figure 45

DLS analysis of **AuNP. Z + DBMSS** (final concentration 19.5 μM **DBMSS**) A: Size distribution by number graph, 78 nm, PDI = 0.171. B: Size distribution by intensity graph, 138 nm, PDI = 0.171. C: Zeta potential measurement ζ, -67 mV.

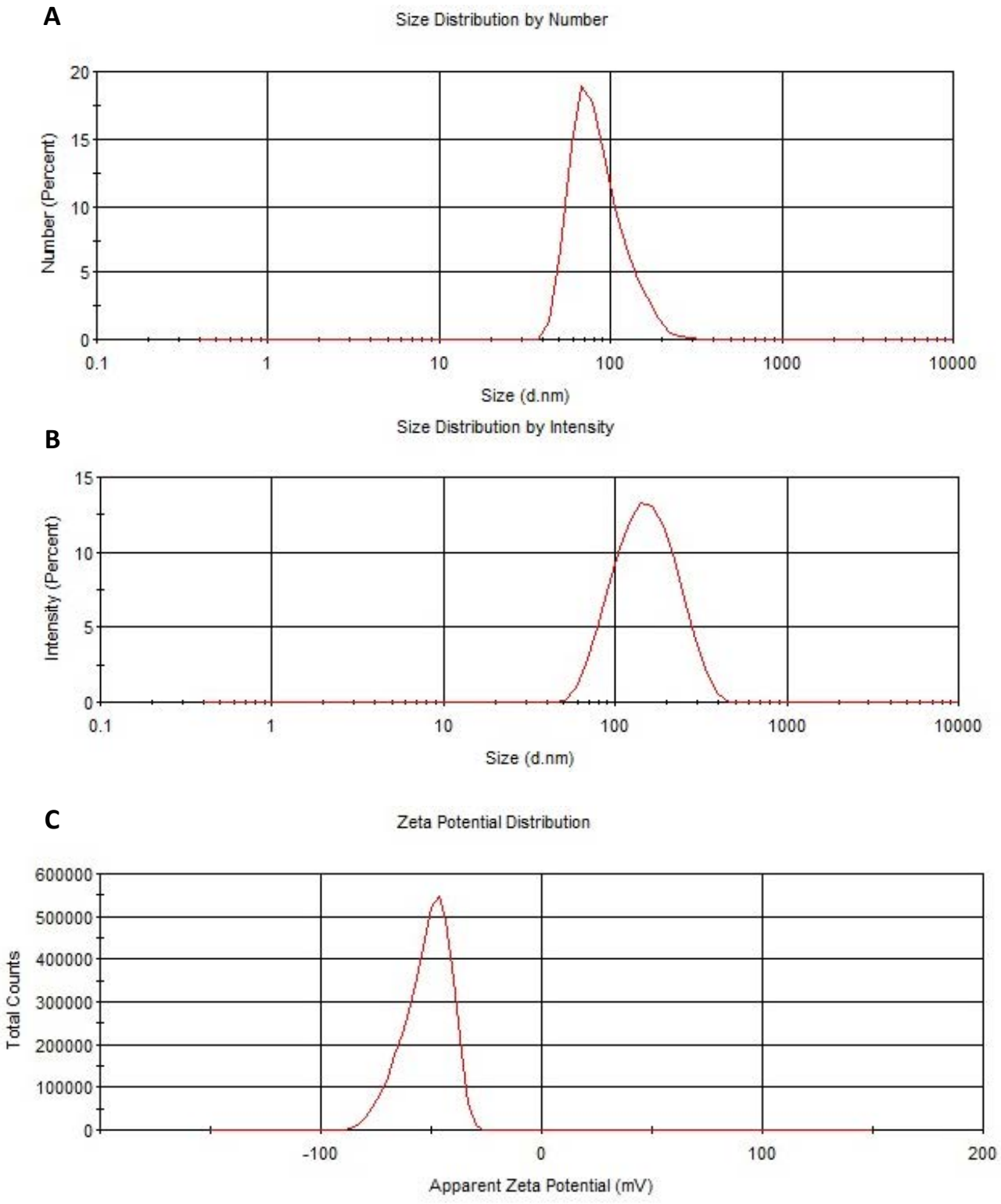


Figure 46

DLS analysis of **AuNP. Z + DBMSS + Eu(III)** (final concentration 19.5 μM DBMSS + 3.3 μM Eu(III)). A: Size distribution by number graph, 88 nm, PDI = 0.184. B: Size distribution by intensity graph, 161 nm, PDI = 0.184. C: Zeta potential measurement ζ, -52 mV.

Table 47

Table of values summarising data from ICP-MS and route to calculating number of Eu(III) complexes per NP.

Au Atoms/ ppb	**Eu Atoms/ ppb**	**Au : Eu Atoms**	**Au Atoms per NP**	**Eu(III) Complexes per NP**
505	26	20	$N = 30.9 \times d^3$ (67880)	3445
605	26	24	67880	2865
511	24	21	67880	3170

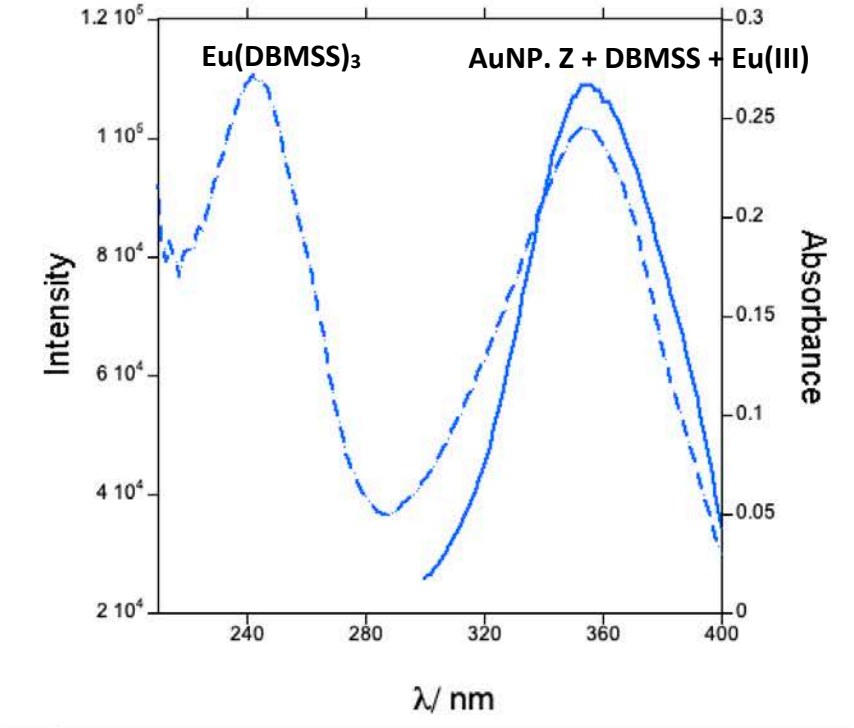


Figure 48

UV-Vis absorbance and excitation overlap of **DBMSS + Eu(III)** (blue, dashed) (**DBMSS** (0.05 mM, MeOH) coordinated to Eu(III) (0.017 mM, MeOH)) and **AuNP. Z + DBMSS + Eu(III)** (final concentration 19.5 μM **DBMSS**, pH 9). Excitation spectra corrected for lamp response.

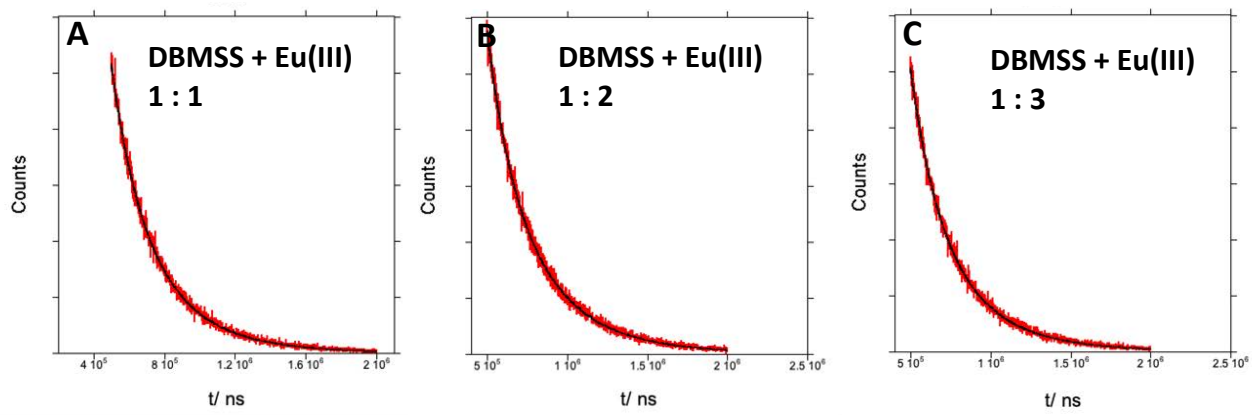


Figure 49

Lifetime of **DBMSS + Eu(III)** (1 : 1 (A), 2 : 1 (B), 3 : 1(C)) (a solution of **DBMSS** (0.05 mM, 10 % MeOH) titrated with Eu(III) (0.016 mM, 0.025 mM, 0.05 mM, 10 % MeOH) in H_2O) $\boldsymbol{\lambda}_{exc}$ = 350 nm and $\boldsymbol{\lambda}_{em}$ = 615 nm. % MeOH) in H_2O. Emission spectra corrected for PMT and instrument response.

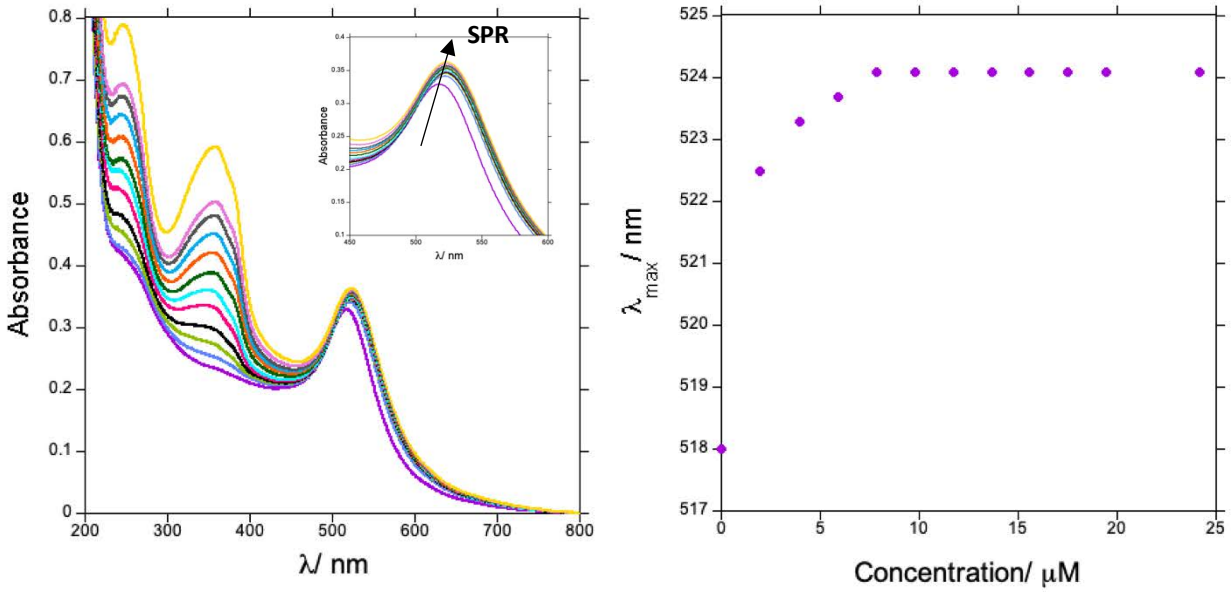


Figure 50

A: Change in SPR of **AuNP. PEG-SH + DBMSS** (0.88 nM **AuNP. Z** + 25 μM **DBMSS**) as μL additions of 1 mM **DBMSS** in MeOH is titrated in to a final concentration of 25 μM **DBMSS**. Figure 3.4.22, A insert shows the SPR shift from $\boldsymbol{\lambda}_{max}$ from 518 nm to 524 nm. B: A plot of $\boldsymbol{\lambda}_{max}$ against **DBMSS** concentration to show the binding on **AuNP**.

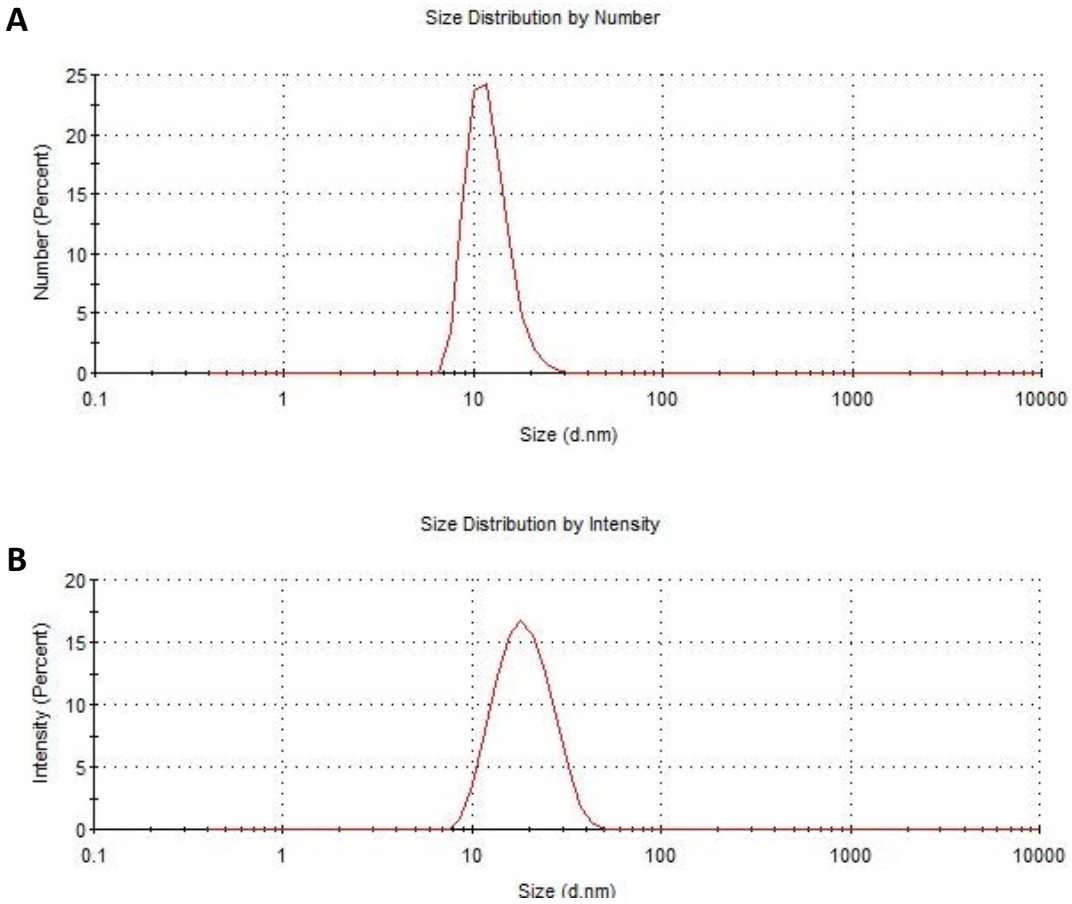
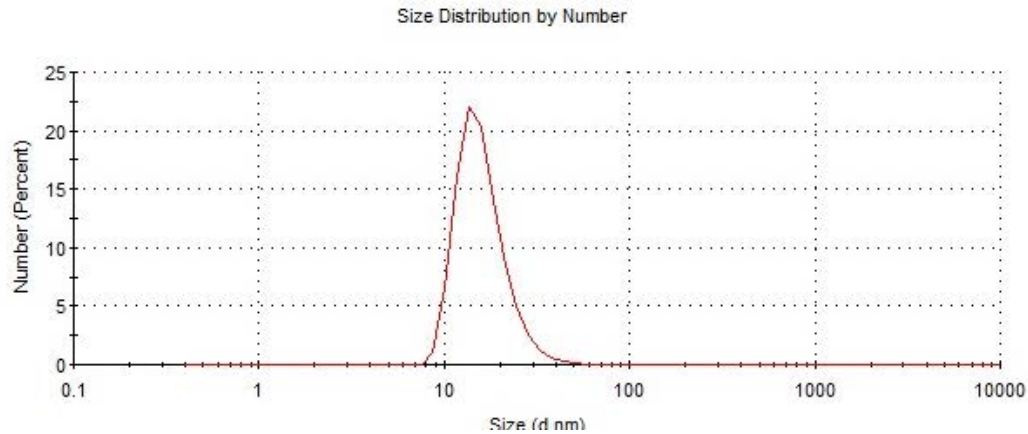


Figure 51

DLS analysis of **AuNP** (1.5 nM, H_2O, provided by I. Theofilou). A: Size distribution by number graph, 12 ± 3 nm, PDI = 0.123. B: Size distribution by intensity graph, 20 ± 6 nm, PDI = 0.123.

A



B

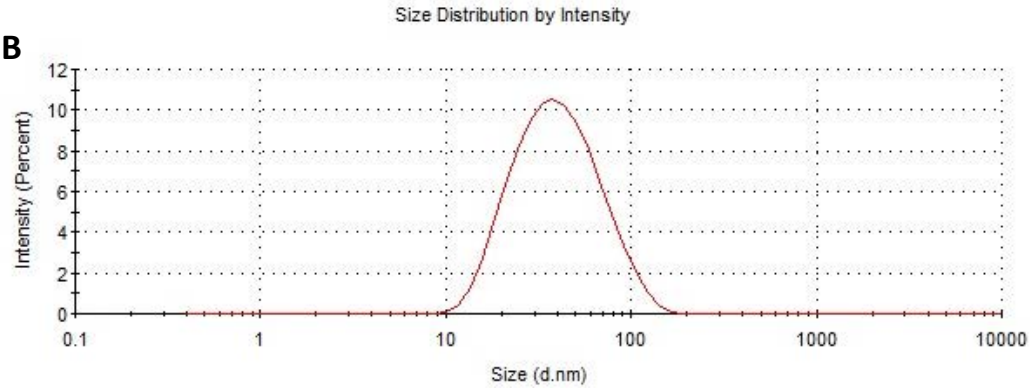


Figure 52

DLS analysis of **AuNP. PEG-SH** (1.8 nM, H_2O). A: Size distribution by number graph, 16 ± 5 nm, PDI = 0.235. B: Size distribution by intensity graph, 45 ± 24 nm, PDI = 0.235.

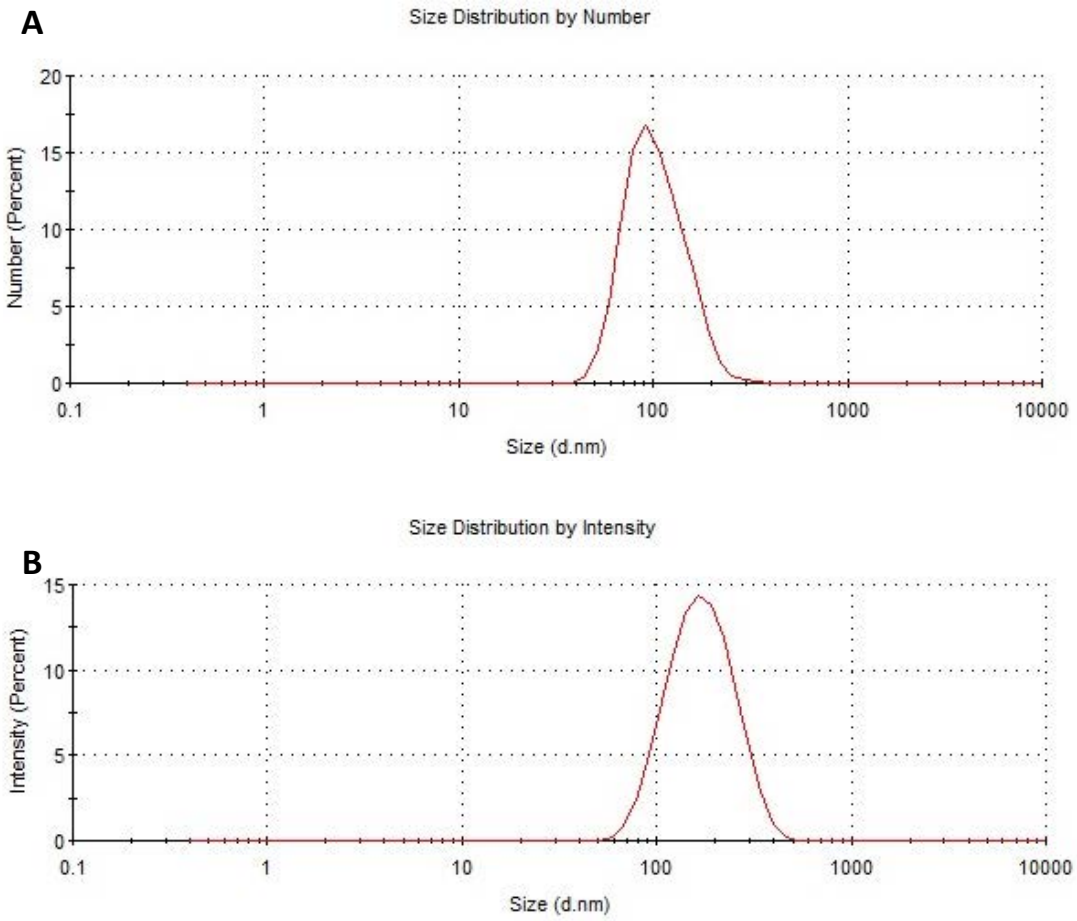


Figure 53

DLS analysis of **AuNP. PEG-SH** (2 nM, H_2O). A: Size distribution by number graph, 107 ± 40 nm, PDI = 0.216. B: Size distribution by intensity graph, 179 ± 68 nm, PDI = 0.216.